CYSENI

The 14th International Conference of Young Scientists on Energy Issues

Kaunas, Lithuania, May 25-26, 2017

Organized by

Lithuanian Energy Institute

Sponsors:

In cooperation with:

Chairman of the Conference dr. Sigitas Rimkevičius

Chairman of the Organizing Committee Vytautas Akstinas

INTERNATIONAL SCIENTIFIC COMMITTEE

Aleksandrs Ļvovs	Latvia	Mantas Marčiukaitis	Lithuania
Andres Siirde	Estonia	Namejs Zeltins	Latvia
Andris Kreslins	Latvia	Pierre-Etienne Labeau	Belgium
Anton Brin	Belarus	Panos M. Pardalos	USA
Alessandro Petruzzi	Italy	Ralf Ebinghaus	Germany
Bernhard Peters	Luxemburg	Sten Bergstrom	Sweden
Bjørn C. Hauback	Norway	Sigitas Rimkevičius	Lithuania
Darius Milčius	Lithuania	Sergej Zhdanok	Belarus
Enn Mellikov	Estonia	Svetlana Danilova-Tretiak	Belarus
Eugenijus Ušpuras	Lithuania	Victor A. Zhovyansky	Ukraine
Finn Ravndal	Norway	Vaclovas Miškinis	Lithuania
Florentin Paladi	Moldova	Virginijus Radziukynas	Lithuania
Luis E. Herranz	Spain	Vytautas Martinaitis	Lithuania
Myriam Lazard	France		

The Board of Reviewers was formed from the experts in the field of the Conference topics.

Board of Reviewers

Aleksandras Iljinas	Lithuania
Alessandro Petruzzi	Italy
Algirdas Gulbinas	Lithuania
Algirdas Jasinskas	Lithuania
Algirdas Maknickas	Lithuania
Andres Siirde	Estonia
Andrius Tamošiūnas	Lithuania
Andris Kreslins	Latvia
Anupras Šlančiauskas	Lithuania
Artur Rogoža	Lithuania
Antanas Kavolynas	Lithuania
Antanas Markevičius	Lithuania
Anton Brin	Belarus
Arturas Klementavičius	Lithuania
Artūras Šmaižys	Lithuania
Arvaidas Galdikas	Lithuania
Arvydas Adomavičius	Lithuania
Asta Malakauskaitė	Lithuania
Asta Narkūnienė	Lithuania
Audrius Dėdelė	Lithuania
Audrius Jonaitis	Lithuania
Aurimas Lisauskas	Lithuania
Aušra Pažėraitė	Lithuania
Benediktas Čėsna	Lithuania
Bernhard Peters	Luxemburg
Bjørn C. Hauback	Norway
Brigita Abakevičienė	Lithuania
Dainius Martuzevičius	Lithuania
Dainius Vaičiulis	Lithuania
Dalia Grigaliūnienė	Lithuania
Dalia Jankūnaitė	Lithuania
Dalia Štreimikienė	Lithuania
Dalius Tarvydas	Lithuania
Linas Miknius	Lithuania
Linas Paukštaitis	Lithuania
Liudvikas Pranevičius	Lithuania
Liutauras Marcinauskas	Lithuania
Luis E. Herranz	Spain
Mantas Marčiukaitis	Lithuania
Marija Eidukevičiūtė	Lithuania
Marijus Šeporaitis	Lithuania
Martynas Lelis	Lithuania
Mindaugas Jakubčionis	Lithuania
Mindaugas Krakauskas	Lithuania
Mindaugas Vaišnoras	Lithuania
Mindaugas Valinčius	Lithuania
Myriam Lazard	France
Namejs Zeltins	Latvia
Narimantas Listopadskis	Lithuania
Nerijus Pedišius	Lithuania
Nerijus Striūgas	Lithuania
Panos M. Pardalos	USA
Pierre-Etienne Labeau	Belgium
Povilas Krasauskas	Lithuania
Pranas Kuzas	Lithuania
Pranas Mierauskas	Lithuania
Raimondas Bliūdžius	Lithuania
Raimondas Pabarčius	Lithuania
Ralf Ebinghaus	Germany
Ramūnas Gatautis	Lithuania
Rasa Paleckienė	Lithuania
Reda Čerapaitė-Trušinskienė	Lithuania
Regina Kalpokaitė-Dičkuvienė	Lithuania
Renaldas Raišutis	Lithuania
Ričardas Krikštolaitis	Lithuania
Rimantas Pranas Deksnys	Lithuania

Danas Ridikas	Lithuania
Darius Albrektas	Lithuania
Darius Biekša	Lithuania
Darius Milčius	Lithuania
Darius Virbukas	Lithuania
Diana Meilutytė-Barauskienė	Lithuania
Diana Adlienė	Lithuania
Diana Šarauskienė	Lithuania
Egidijus Norvaiša	Lithuania
Egidijus Saulius Juodis	Lithuania
Egidijus Urbonavičius	Lithuania
Eglė Biekšienė	Lithuania
Eglė Jaraminienė	Lithuania
Enn Mellikov	Estonia
Ernestas Narkūnas	Lithuania
Eugenija Farida Dzenajavičienė	Lithuania
Eugenijus Perednis	Lithuania
Eugenijus Ušpuras	Lithuania
Farida Dzenajavičienė	Lithuania
Feliksas Zinevičius	Lithuania
Finn Ravndal	Norway
Florentin Paladi	Moldova
Gediminas Vasiliauskas	Lithuania
Gediminas Vilkevičius	Lithuania
Giedrė Streckienė	Lithuania
Giedrius Laukaitis	Lithuania
Giedrius Šiupšinskas	Lithuania
Gintautas Miliauskas	Lithuania
Grigorijus Duškesas	Lithuania
Inga Konstantinavičiūtė	Lithuania
Inga Radžiūnienė	Lithuania
Inga Stasiulaitienė	Lithuania
Inga Valuntienė	Lithuania
Irina Kliopova	Lithuania
Iveta Varnagirytė-Kabašinskienė	Lithuania
Rimantas Levinskas	Lithuania
Rita Plukienė	Lithuania
Robertas Alzbutas	Lithuania
Robertas Navakas	Lithuania
Robertas Poškas	Lithuania
Rolandas Jonynas	Lithuania
Rolandas Urbonas	Lithuania
Romualdas Kėželis	Lithuania
Romualdas Škėma	Lithuania
Saulė Milčiuvienė	Lithuania
Sergej Zhdanok	Belarus
Sigitas Kadiša	Lithuania
Sigitas Masaitis	Lithuania
Sigitas Rimkevičius	Lithuania
Simona Tučkutė	Lithuania
Stanislovas Vrubliauskas	Lithuania
Stasys Šinkūnas	Lithuania
Sten Bergstrom	Sweden
Svetlana Danilova Tretiak	Belarus
Tomas Deveikis	Lithuania
Tomas Sabonis	Lithuania
Vaclovas Kveselis	Lithuania
Vaclovas Miškinis	Lithuania
Vaidas Matuzas	Lithuania
Valdas Girdauskas	Lithuania
Valdas Ragaišis	Lithuania
Valentinas Klevas	Lithuania
Victor A. Zhovyansky	Ukraine
Vidas Lekavičius	Lithuania
Viktorija Bobinaitė	Lithuania
Viktorija Grigaitienė	Lithuania
Viktorija Mimaitė	Lithuania
Vilma Čipinytė	Lithuania
Violeta Makarevičienė	Lithuania
Violeta Pukelienė	Lithuania

Jolanta Dvarionienė	Lithuania	Violeta Vaitkevičienė	Lithuania
Jonas Baltrušaitis	USA	Virginijus Radziukynas	Lithuania
Juozas Gudzinskas	Lithuania	Virginijus Vileiniškis	Lithuania
Jūratė Karbauskaitė	Lithuania	Vitas Valinčius	Lithuania
Jūratė Kriaučiūnienė	Lithuania	Vykintas Šuksteris	Lithuania
Jurij Tonkonogij	Lithuania	Vytautas Liesionis	Lithuania
Justas Kažys	Lithuania	Vytautas Martinaitis	Lithuania
Karolina Čepurnienė	Lithuania	Vytautas Stankus	Lithuania
Karolis Gedvilas	Lithuania	Vytis Kopustinskas	Lithuania
Kęstutis Čiuprinskas	Lithuania	Vladislovas Algirdas Katinas	Lithuania
Kęstutis Valančius	Lithuania	Žaneta Simanavičienė	Lithuania
Kęstutis Venslauskas	Lithuania	Žaneta Stasiškienė	Lithuania
Kristina Brinkienė	Lithuania	Žilvinas Nakutis	Lithuania
Kristina Bočkutė	Lithuania	Živilė Rutkūnienė	Lithuania
Kristina Ukvalbergienė	Lithuania	Žydrė Kadžiulienė	Lithuania

Dear Reader of the Conference proceedings,

At Lithuanian Energy Institute the fourteenth **International Conference of Young Scientists on Energy Issues (CYSENI 2017)** was already organized**.** This conference brings together smart young researches and provides opportunities for exchange of ideas, knowledge improvement, development of their acquired abilities and contribute to increasing level of exercised research activities.

The initiative for such an event came from young and enthusiastic researchers of Lithuanian Energy Institute (LEI). They realised that there are a lot of young, smart and science-oriented young people who do research in the energy area and they do need a place and time to meet each other to share their views, generated ideas and present the latest results of research. The first Conference was organized in 2004. In 2007 this Conference became international and had participants from neighbouring countries (Belarus and Poland). In 2013 conference celebrated its 10 years anniversary. This time there were accepted 80 scientific papers. The authors were not just from Lithuanian institutions, but also from many foreign countries – Latvia, Estonia, Poland, Belarus, Ukraine, Moldova, Georgia, Romania, Nigeria, Indonesia and Taiwan.

This year we are pleased that young scientists further found the conference valuable to present their research results and share scientific experience. Conference event in Institute is usually full of pleasant atmosphere, interesting and valuable discussions and cheerful social programme. For the best papers of this year we have provided an opportunity to be published in journal **Energetika** (http://www.lmaleidykla.lt/ojs/index.php/energetika). The greetings and acknowledgments of the participants encourage us to keep these moments in mind and improve the future CYSENI conferences.

Hence, Lithuanian Energy Institute is glad to invite you to the next Conference of Young Scientists on Energy Issues (CYSENI 2018), which will be held on 23-25th May, 2018 in Kaunas, Lithuania. **We want to draw attention on it, because during the further conference we will celebrate the 15th anniversary of CYSENI and this conference will be marvellous event with many entertainments and new scientific ideas.**

Sincerely,
Conference Organizers

CONTENT

KEYNOTE SESSION (2)

I RENEWABLE ENERGY SOURCES (12)

II ENERGY EFFICIENCY AND RELIABILITY (4)

III SMART ENERGY NETWORKS (6)

IV ENERGY ECONOMICS AND POLICY (3)

V HYDROGEN ENERGY AND FUEL CELL TECHNOLOGIES (3)

VI FUSION ENERGY (2)

VII NUCLEAR FISSION AND RADIATION PROTECTION (3)

VIII COMBUSTION AND PLASMA PROCESSES (9)

IX THERMAL PHYSICS, FLUID MECHANICS AND METROLOGY (3)

X MATERIALS SCIENCES AND TECHNOLOGY (9)

XI GLOBAL CHANGE AND ECOSYSTEMS (3)

XII CROSS-CUTTING ENERGY ISSUES (2)

CYSENI 2017, May 25-26, Kaunas, Lithuania
ISSN 1822-7554, www.cyseni.com

MAJOR PHYSICS DISCOVERIES LEADING TO NUCLEAR POWER

Waclaw Gudowski
Royal Institute of Technology – KTH
Roslagstullsbacken 21, 114 21 Stockholm – Sweden
E-mail: wacek@neutron.kth.se

ABSTRACT

The turn of the XIX and XX century marked a profound revolution in the development of science and our understanding of the fundamental principles of the natural world. During the nineteenth century classical physics - the laws of motion formulated initially by I. Newton in 1687, electromagnetic field theory developed to maturity by J.C. Maxwell , and thermodynamics had reached an advanced state of development. The physical world seemed to be well understood based on the laws of motion, electromagnetism and thermodynamics. Much had been learned about the Earth and solar system as well. Estimates of the age of the Earth had risen from about 6000 years in the late eighteenth century to tens or hundreds of millions of years; and the view that life, the Earth, and the rest of the solar system had arisen in a single great upheaval in recent times had been replaced by the idea of gradual change over years.

Physicists of the end of 19th century believed that atoms consisted of hydrogen atoms (approximately) and they expected only minor refinements to get "an extra decimal place" of accuracy. But there were visible problems. Nothing was known about the fundamental structure of matter that gave rise to the Periodic Law - the very existence of atoms was largely conjectural. Geology and astronomy seemed in serious conflict since the apparent age of the geologic record could not be reconciled with the only power source for the Sun then conceivable, gravitational contraction. An important part of classical thermodynamics was stubbornly resisting resolution - the properties of blackbody radiation with its ultraviolet "catastrophy". By the end of 1900s it had become clear that within the existing framework of physics no solution of the blackbody problem was possible. Something important was missing. And soon the inadequacy of classical physics was proofed. The era of modern physics began with an unexpected discovery of x-rays. This lecture will take on a fascinating tour through the major discoveries of modern physics which resulted in mastering of the power of nuclear forces.

Keywords: nuclear power, x-rays

CYSENI 2017, May 25-26, Kaunas, Lithuania
ISSN 1822-7554, www.cyseni.com

THE ROAD TO NUCLEAR FUSION ENERGY: UPDATES ON ITER, AND DEMO PROJECTS

Francesco Maviglia
EUROfusion, Power Plant Physics & Technology (PPPT) Department
Building R3, Boltzmannstr. 2, 85748 Garching – Germany
E-mail: francesco.maviglia@euro-fusion.org

ABSTRACT

Nuclear fusion is one of the most promising research fields that can help to answer the increasing need of energy. A magnetic confinement device like a tokamak uses magnetic fields to contain a fully ionised gas, called plasma. Although controlled fusion is an extreme technological challenge, a fusion controlled power plant has several significant advantages over alternative energy sources: a) the isotopes of hydrogen, the fuel used for the reactions, are abundant in nature, b) the operations of a nuclear fusion plant are intrinsically safe, c) the research on fusion reactors based on magnetic confinement technologies (as tokamak) has no direct military applications, and d) fusion plants do not produce air pollution or greenhouse gases and do not represent radiological hazards because most of the radioactive materials produced can safely be disposed of and decay rapidly, with a half-life of around 10 years.

ITER is the next large experimental tokamak device, which is currently being built in southern France in the framework of a collaboration between China, Europe, India, Japan, Korea, Russia and the USA. ITER has the objective to demonstrate the scientific and technological feasibility of nuclear fusion allowing to achieve and study fusion plasmas under conditions very similar to those expected in a fusion power plant. It should produce 500 MW of fusion thermal power sustained for hundreds of seconds with a fusion gain Q = 10. In addition to the construction of ITER, a further technical program is being carried out in both physics and technology in order to prepare for the subsequent step, DEMO: a fusion power reactor that will demonstrate electricity production. DEMO should demonstrate tritium fuel self-sufficiency and first electrical power production.

Keywords: nuclear fusion, ITER, DEMO, fusion roadmap

CYSENI 2017, May 25-26, Kaunas, Lithuania
ISSN 1822-7554, www.cyseni.com

SELF-SUFFICIENT RENEWABLE ENERGY COMMUNITIES: THE IMPORTANCE OF SOCIAL CAPITAL

A. I. Patonia
University of St Andrews
MB20 Deans Court, North Street, FY16 9QT, St Andrews, Scotland
E-mail: aip4@st-andrews.ac.uk

ABSTRACT

Iceland represents one of the very few countries where transition from conventional to renewable energy fuels was launched and supervised by the state. What makes this country unique is its current total energy self-sufficiency based on locally-produced sustainable energy. On the other hand, Greenland – a similar autonomous nation from the same region – despite possessing significant renewable energy potential still has not reached its sustainable self-sufficiency. That is why in contrast to most of the researchers viewing the reason for the renewable energy failure there in the lack of governmental will and a firm transformation programme, this paper argues in favour of a very specific psychosocial factor being crucial for the success of such undertakings. In particular, social capital is seen as the key contributor towards the success of renewable undertakings. Demonstrating the case of the Isle of Eigg (Scottish Inner Hebrides), the research shows that the transition to a total renewable energy self-sufficiency can be launched as a grass-root movement without any particular state initiative. Later, the paper lists a number of factors that prevent social capital from solidification and thus hamper the transition towards renewable self-sufficiency. Viewed through the cases of Iceland and Greenland, these factors are seen to owe greatly to the geography and history of the sites undergoing transformations.

Keywords: Iceland, Greenland, renewable energy, hydropower, wind farm, geothermal energy

1. INTRODUCTION

With the thawing ice caps and extended time of ice-free navigation polar regions have recently gained additional attention as new potential sources of conventional fuels. At the same time, however, not all the Arctic countries rushed for the search of oil and gas. Despite being located close to the potential exploration and production sites, some of them made a rather unconventional turn towards a fully-fledged sustainable self-sufficiency. In particular, being a small nation potentially interested in exploiting the adjacent conventional natural resources, Iceland decided to focus primarily on its own renewable energy potential launching a governmental campaign on energy self-sufficiency based primarily on the geothermal sources and hydropower [1]. According to the National Energy Authority [2], 85 percent of the country’s energy mix in 2014 was covered with the mentioned renewables leaving the remaining 15 percent to the imported hydrocarbons used for local means of transportation. In the opinion of Driscoll, Theodorsdottir, and Richardson [3], with the current governmental desire to accomplish the overall transitionof the country to electric vehicles in the coming decade the total energy mix will fully be covered by renewable energy sources.

The case of Greenland – an autonomous counry within the Danish realm having similar geosocial characteristics to those of Iceland – the perspectives of future development of the energy sector do not seem to follow a similar sustainability path. In contrast to its fully-independent eastern neighbour, the autonomy has not developed its properly-functioning renewable supply scheme which could have replaced the imported carbohydrates. In the opinion of Carruth [4], this situation looks rather as a paradox in the face of the existing significanr hydropower potential of the island striving for a fully-fledged independence from Denmark. Some researchers, such as Kristjansdottir [5], explain it by the absence of the political will from the local government potentially gaining additional benefits from the current state of affairs when most of the energy is imported from the mainland. In the opinion of such scholars as Paldam [6], such a condition could be compared to the so-called ‘Dutch disease’ – a special case of the resource curse when non-resource industries of the mineral-rich countries do not gain impulse for development. In the opinion of the author[1], however, the lack of political interest and rent-seeking is what makes importing energy cheaper than the development of the local renewables.

In contrast to most of the previous pieces of research, this paper represents an alternative explanation of the causes of differences between Iceland and Greenland. Being a comparative case study in essence, the research hypothesises that specific geosocial conditions of both nations are directly connected to the degree of social capital, which ultimately affects the success of any renewable energy initiatives. In this connection, the paper first reviews the existing pieces of literature relevant to the hypothesis. Later, it focuses on the connection between the factor of geographic conditions and social capital. Finally, to further prove the stated idea it views the specific case of the Isle of Eigg (Scottish Inner Hebrides) where renewable energy initiatives started as grass-root movements.

2. LITERATURE REVIEW

Most of the researchers covering the aspects of sustainable energy development in the Arctic mention Iceland as a unique example of a country rationally utilising its peculiar geographical conditions. In particular, according to Kristjansdottir [5], the country’s gethermal fields evenly distributed throughout the country illustrate that uniqueness capable of powering the whole nation with unconventional and clean energy. In this respect, the case of Greenland is seen by the scholars as the one of lesser advantages due to its different phisical geography. In this context, the author attributes low-developed alternative energy sector of the Danish autonomy to almost complete absence of geothermal capacity in the island.

Another group of researchers comment on the climatic conditions of both territories influencing their distribution of population and thus energy strategies. Specifically, Rasmussen [7], describe Greenlandic settlements as the ones unevenly scattered along the coast of the island with very minimal concentration of them far away from the seashore. Hence, ice caps and rugged terrestrial conditions of the mainland can prevent the nation from elaborating a successfully-functioning energy grid notwithstanding the fact that the island possesses significant hydropower and wind power potential. In contrast to this view, Hilmarsson et al [8] state that milder climatic conditions leaving lesser territory covered with ice contributed to the more even dispersement of settlements in Iceland. In the opinion of the researchers, in contrast to Greenland, this could be seen as a precondition for the construction of an efficient energy network all over the country. Thus, apart from physical geography, the researchers believe human characteristics to shape the energy strategy of the Arctic nations

On the other hand, such researchers as Cilona [10] closely bind sustainable technology to the level of social capital in the country where it is applied. In his opinion, the probability of successful implementation of renewable energy sources directly correlates with the level of social kinship within this parcticular community. McShane et al [11] view kinship as an expression of societal affinity and trust which help to put through significant topics relevant to the wellbeing of every member of the community. In this context, lack of social capital within a society may directly influence its negative experience with the implementation of green solutions. Alternatively, high level of this indicator is assumed to contribute to nurturing sustainability applications within a particular community. At the same time, however, this aspect of national development is omitted in most research papers covering energy development in the Arctic.

To fill in this gap in the literature the current research explores the potential implications of social capital indicators for the development of energy sectors in Iceland and Greenland. As Rahn et

---

[1] Here and in the rest of the article the word ‘author’ means the author of the article

al [12] comment on the significant effect of geographical conditions and population distribution for the formation of the social capital, the paper analysis the potential effects of physical gepgraphy on psychosocial indicators of Iceland and Greenland and their subsequent energy development. In particular, elaborating on all the previously mentioned studies, the research suggests that milder climatic and geographical conditions of Iceland contributed to the more even distribution of the country's population all over its territory, which, in its turn, fostered social capital that shaped the green energy strategy of the nation. In contrast, Greenland is believed to owe its lesser success in terms of alternative energy to the lower level of social capital, which owes primarily to the scatteredness of the island's settlements because of the the climatic and geographical conditions.

3. SOCIAL CAPITAL AND SUSTAINABILITY

3.1. Basic geographical conditions of Iceland and Greenland

Geographically, Iceland and Greenland could be considered as both similar and different nations due to the islands' physical and human characteristics. The similarities of these nations are broadly described by Kristjansdottir [5], who comments primarily on the remote location of both places which should potentially instigate development of the self-sufficient energy systems due to the fact that shipping fuel to the islands ultimately leads to the rise in its prices and greater costs for the secondary products (including electricity).

On the other hand, the differences happen to be even more vivid if looked at from statistical perspective:

Table 1. Physical and human geography of Island and Greenland as of 2014

Country	Area	Population	Population growth	Population density
Iceland	103,000 km^2	323,202	0.7 %	3.2 inhabitants/ km^2
Greenland	2,166,000 km^2	56,483	-0.6 %	0.14 inhabitants/ km^2 (for the ice-free areas)

Source: [13], [14].

As represented in the table, despite possessing twenty times bigger territory, Greenland appears to be dramatically sparsely populated with the density of the ice-free areas not exceeding 0.14 inhabitants per square kilometer, which is 23 times less than the indicators of Iceland. Not only possessing six times fewer people, but also experiencing negative population growth, the country's human resources appear to differ from those of Iceland to a great extent.

When it comes to the geographic distribution of the population of both countries, the graphical representation of major settlements in both islands confirm the description of Hamilton and Rasmussen [9] who signified the biggest problem of Greenland in its population being scattered along the coast and absent in the middle of the island. In these circumstances, Iceland could be taken as a positive example of a nation where, despite being mostly concentrated along the coast, the settlements form a continuous circle along the whole coast ot the country [4]. This means that, in contrast to Greenland, no major communities are isolated from the rest of the country by geographical conditions. On the other hand, in Greenland, most of the settlements represent communities highly isolated from the remaining ones by geographical features and greater distances.

Judging by the data represented on the map in Fig. 1, it could be assumed that the idea of Diamond [16] attributing national development to geographical conditions could potentially be exemplified by the current comparative study: Iceland with more favourable geographical conditions is more developed than Greenland with less favourable ones.

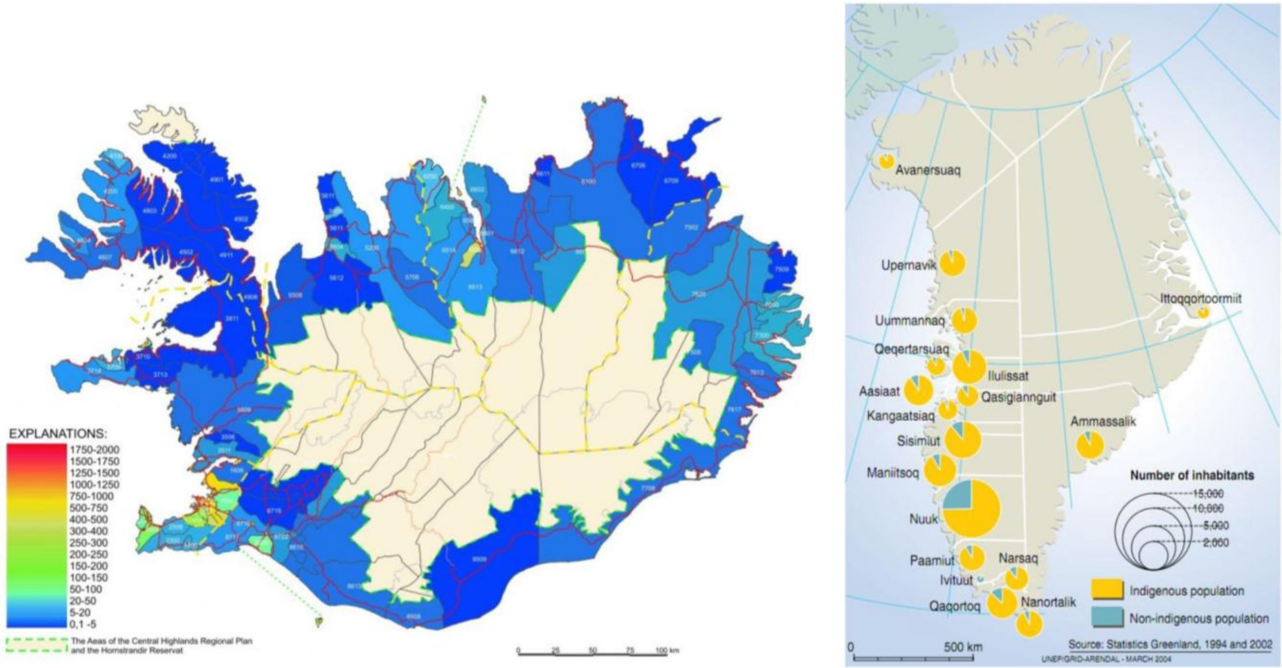

Fig. 1. Population density in Iceland and Greenland (source: [13], [14], [15])

3.2. Social capital in Iceland and Greenland

As displayed on Fig. 1, Iceland have greater possibilities to develop social capital through trust and kinship within its society due to the fact that its settlements are placed close to each other. On the other hand, Greenland in this sense could be seen as a disadvantaged place with lower chances to establish trust among people who have to rely on themselves due to greater geographical distances.

According to Robbins and Perrinicchio [17], social capital in isolated communities could be measured by the the number of criminal acts as the author assumes trust in particular society to be reflected by the crime rate – i.e. the lower the number of crimes, the greater the level of social capital. In such circumstances, the UN statistics on homicides speaks volumes on he significant differences between the nations.

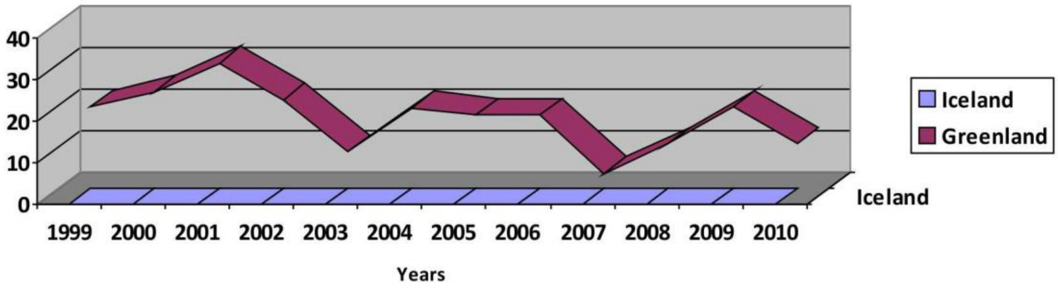

Fig. 2. Homicide cases per 100,000 citizens in Iceland and Greenland (1999–2010) (source: [18])

As it could be seen from the graph, the number of homicides in Greenland dramatically exceeds the almost non-existent one in Iceland. Even though the UN statistics has been officially revealed since 1999, in his paper analysing the criminal situation in Greenland in between 1985 and 2000 Chtistensen [19] provides evidence almost permanently high criminal record of the island for the whole period. In contrast to that, Baumer et al [20] comment on almost non-existent crime indicators in Iceland, where most of the severe acts are committed by foreigners. This could generally explain data represented by Fig. 2.

According to the Statistics Greenland [14], the island also greatly exceeds Iceland in terms of almost all other adverse criminal-related indicators. That is why, following the logic of McShane et al [11] binding high number of crimes to the general distrust in a society or community and thus low level of social capital, it should be assumed that the level of social capital in Greenland is very insignificant. On the other hand, viewing the UN statistics with respect to Iceland, the assumption relating to this country will be the opposite: due to the low level of criminal activity in the country the level of social capital is extremely high.

Thus, the link between geographical conditions and social capital could be represented through the following scheme:

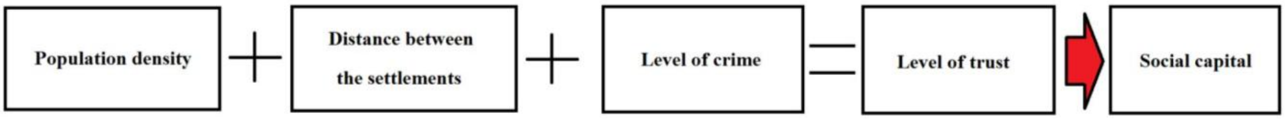

Fig. 3. The link between geographical conditions, social indicators and social capital (own work)

As seen from Fig. 3, social capital is assumed to be defined by a number of inter-dependent factors including population density, distance between the settlements and level of crime which all influence the level of trust in society or community defining this notion.

4. DISCUSSION

Since Cilona [10] assumes social capital to be important for the success of the green initiatives in a sociaty, the current comparative case study could illustrate this hypothesis through representing the situation in Greenland with its low level and underdevelopment in terms of green technologies and Iceland where total dependence on alternative energy sources is augmented by high social capital. Tracing the the improvised equation represented in Fig. 3 could indicate a number o problems in Greenland which influence the development of the nation’s alternative energy sector. In particular, low population density and distantly placed settlements instigating instilling the feeling of self-reliance into the population of the island prevent the country from developing trust and thus high level of social capital.

Even though the overall conditions in Greenland seem to be not suitable for the development of green energy technology, an alternative approach towards the nation’s renewable future could be found. Specifically, the example of the Isle of Eigg in the Scottish Inner Hebrides represents a case of the successful grass-root movement towards sustainable energy independence from the mainland. In this context, Chmiel and Bhattacharya [21] describe the renewable energy progress over there as the one that was inspired by a positive example of the coastal community of Findhorn, where the remoted local community decided to organize a fund to invest in local windfarm development in order to become independent from the state grid. According to the authors, the success of the terrestrial community was seen by the population of the Isle of Eigg as the possibility to replicate the approach. Even though the trust between the local population was not characterized as the one of extremely high level, the greater distrust to the secure energy supplies from the mainland instigated the process of gathering funds for the first windfarm and a couple of solar pannels [21]. Having conducted a cost-benefit analysis, the Scottish Government decided to support the local initiative of the Isle of Eigg with tax reliefs as the fuel delivery to the island would cost more money than locally-generated energy [22].

In such circumstances, the scattered settlements of Greenland could potentially implement the Scottish system of community initiatives. This, however, will most probably require the assistance not only from local Greenlandic authorities, but also from the Danish government as the autonomy appears to be an economically dependent region very much reliant on fuel and commodity supplied from the mainland. It is not clear, however, whether the Danish government will be willing to assist the islanders in their initiatives given the constantly raising issue of their independence.

5. CONCLUSION

This paper analysed the potential impact of social capital on energy development in the Arctic. Taking the example of two isolated communities – Iceland and Greenland – the research demonstrated how geographical factors could influence important social indicators that are crucial for the successful implementation of alternative energy policies. In particular, the case of Island explained the positive effect of high population density and lower distance between the settlements on greater kinship within the society, which ultimately influences trust and social capital. The example of greenland, on the other hand, demonstrated the opposite: extremely low population density augmented by great distances between most of the settlements negatively influence trust within society, which leads to low level of social capital.

In such conditions, the reseach builds on the theory binding social capital and the success of renewable energy initiatives providing arguments for the support of this idea. Specifically, the case of Greenland is taken to picture the detrimental effect of low social capital on the development of alternative power sources: the country is almost totally reliant on fuel supplies from the mainland. In contrast, Iceland demonstrate the opposite result: while posessing some fo the greatest trust levels in Europe, the country is almost totally running on renewables.

Finally, taking the example of the Isle of Eigg situated on the Scottish Inner hebrides, the research provides an example of potential solution to the problem of Greenland. In particular, community grass-root initiatives promoting renewable energy sources and local energy independence could become a way-out for the isolated Danish autonomy. Thus, even though the social capital of the island in general could be extremely low, locally-built trust in all the scattered communities could be utilised as an alternative solution for the problem.

REFERENCES

1. JOHANNESSON, Gudni A. Iceland – renewables as a national project. *Circle*, 2015, Vol. 3, No. 1, p. 16-18.
2. National Energy Authority of Iceland, 2017 [refered on the 5th of March in 2017 y.]. Link to the internet: <http://www.nea.is/the-national-energy-authority/energy-data/data-repository/>.
3. DRISCOLL, Patrick A., THEODORSDOTTIR, Asdis H., RICHARDSON, Tim, P. In the future of mobility electric? Learning from contested storylines of sustainable mobility in Iceland. *European Planning Studies*, 2012, Vol. 20, No. 4.
4. CARRUTH, Susan J. Developing renewable energy in discontiguous Greenland: An infrastructural urbanism of material practices. *Journal of Landscape Architecture*, 2016, Vol. 11, No. 1, p. 66-79.
5. KRISTJANSDOTTIR, Helga. *Sustainable Energy Sources and Economics in Iceland and Greenland*. New York: Springer, 2015. 79 p. ISSN 2191-5520.
6. PALDAM, Martin. Dutch disease and rent seeking: The Greenland model. *European Journal of Political Economy*, 1997, Vol. 13, No. 3, pp. 591-614.
7. RASMUSSEN, Rasmus O. Formal economy, renewable resources and structural change in West Greenland. *Groupe d'Etudes Inuit et Circumpolaires (GETIC) et l'Association Inuksiutiit katimajiit inc*, 2000, Vol. 24, No. 1, p. 41-78.
8. HILMARSSON, Agust et al. Incidence of first stroke: A population study in Iceland. *Arctic*, 2013, Vol. 71, No. 2, pp.13-27.
9. HAMILTON, Lawrence C., RASMUSSEN, Rasmus, O. Population, sex ratios and development in Greenland. *Arctic*, 2010, Vol. 63, No. 1, p. 43-52.
10. CILONA, Timothy. Sustainability, territorial resources and social capital. *International Journal of Sustainable Development and Planning*, 2017, Vol. 12, No. 4, p. 819-828.

11. MCSHANE, Connar J. et al. Connections: The contribution of social capital to regional development. *Rural Society*, 2016, Vol. 25, No. 2, p. 154-169.
12. RAHN, Wendy, M. et al. Geographies of trust. *American Behavioral Scientist*, 2009, Vol. 52, No. 12, p. 1646-1663.
13. Statistics Iceland, 2016- [referred on the 5th of March in 2017 y.]. Link to the internet: <http://www.statice.is/services/>.
14. Statistics Greenland, 2016- [referred on the 5th of March in 2017 y.]. Link to the internet: <http://www.stat.gl/?lang=en>.
15. National Land Survey of Iceland, 2009- [referred on the 3rd of March in 2017 y.]. Link to the internet: <http://www.lmi.is/en/>.
16. DIAMOND, Jared. Guns, gems and steel in 2003. *Antipode*, 2003, Vol. 35, No. 4, p. 829-831.
17. ROBBINS, Blaine and PETTINICCHIO, David. Social capital, economic development, and homicide: A cross-national investigation. *Social Indicators research*, 2012, Vol. 105, No. 3, p. 519-540.
18. United Nations Office on Drugs and Crime, 2013- [referred on the 3rd of March in 2017 y.]. Link to the internet: <https://www.unodc.org/documents/gsh/pdfs/2014_GLOBAL_HOMICIDE_BOOK_web.pdf>.
19. CHRISTENSEN, Martin et al. Homicide in Greenland 1985-2000. *Forensic Science, Medicine and Pathology*, 2016, Vol. 12, No. 1, p. 40-49.
20. BAUMER, Eric P. et al Crime, shame, and recidivism: The case if Iceland. *Criminology*, 2002, Vol. 42, No. 1, p. 40-59.
21. CHMIEL, Zbigniew, BHATTACHARYYA, Subhes C. Analysis of off-grid electricity system at Isle of Eigg (Scotland): Lessons for developing countries. *Renewable Energy*, 2015, Vol. 81, No. 2, p. 578-588.
22. CREANEY, Rachel, NIEWIADOMSKI, Piotr Tourism and sustainable development on the Isle of Eigg, Scotland. *Scottish Geographical Journal*, 2016, Vol. 132, No. 2, p. 210-233.

CYSENI 2017, May 25-26, Kaunas, Lithuania
ISSN 1822-7554, www.cyseni.com

THE POTENTIAL OF *FUCUS VESICULOSUS* SEAWEED AS A FEEDSTOCK FOR BIO-REFINERY INTEGRATED HYDROTHERMAL LIQUEFACTION

L. Jasiūnas
Aalborg University
Pontoppidanstræde 101, 9220 – Denmark
E-mail: lukas.jasiunas@ktu.edu

ABSTRACT

The paper focuses on assessing the potential of cold water brown macroalgae *Fucus vesiculosus* as a suitable biomass feedstock for biocrude production via supercritical hydrothermal liquefaction (HTL). The work undertook an integration-oriented approach: a bio-refinery concept with demineralisation and high added value product (alginate and fucoidan) extraction steps prior to residue valorisation in the form of HTL biocrude had been envisioned. The project scope included acid leaching (water, citric acid and the acidic aqueous by-product from a continuous HTL setup as agents), alginate extraction via H_2SO_4 and $NaCO_3$ bathing and fucoidan extraction using $CaCl_2$. Demineralisation was done to identify whether the inorganics (up to 33 wt.% on dry basis) present in the raw feedstock are in any way beneficial for effective conversion. Experiments showed that citric acid leaching with neutralisation resulted in the highest ash removal efficiency of 47%. The produced 6 sets of biocrudes were characterised by elemental and thermogravimetric analyses. Similarly, in order to obtain complete mass balances, all by-products (solid, aqueous and gaseous) were quantified and analysed. A biofuel precursor of acceptable yields and quality was sought. Such a product is also defined by low heteroatom concentrations and high energy recovery (ER). Short HTL (i.e. reaction time of 10 min instead of the baseline 15 min) and the extent of leaching residue neutralisation were also evaluated as a method to improve processing economics and ease potential integration. Non-neutralised citric acid leaching, alginate extraction and fucoidan extraction pre-treated seaweed led to higher biocrude yields compared to the results of short retention time, full neutralisation extent and baseline run experiments. The highest biocrude yield of 28 wt.% on dry ash free feedstock basis was recorded in the conversion of alginate extraction residues. This experimental run also led to the highest ER (53%) and HHV (44.3 MJ/kg) biocrude.

Keywords: biocrude, macroalgae, hydrothermal liquefaction, integration, added value products

1. INTRODUCTION

Increasing concern over climate change is driving the transportation sector towards change. There are many contending technologies that aim to collectively replace the use of fossil fuels. Hydrogen, electricity, electrofuels – all developing quickly. However, it is the assumption of many that an intermediary fuel is necessary in order not to collapse the widespread and well developed infrastructure of liquid fuels. Biofuels are an option for fulfilling this exact demand. A combination of sustainable cultivation and well planned integration might make biomass, the precursor of several types of fuels, a major player in future energetics. Its global abundance, short life cycles promise a more sustainable and anthropogenic CO_2 low world.

Macroalgae, also known as seaweed, are large multicellular algae species. These benthic (i.e. seabed dwelling) organisms grow near coastal areas, typically not lower than 50 meters below sea level. Here, their environment is virtually invariant in terms of water temperature and salinity [1]. However, seasonal solar irradiance variations have significant effects on the growth rates and chemical composition of macroalgae. Studies show that wild brown algae (e.g. of *Saccharina*, *Undaria*, *Sargassum*, and *Ecklonia* genera) exhibit growth rates of 3.3–11.3 kg dry weight / m^2 per year [1]. Such high biomass productivity sums up to a harvest potential of 2–10 dry tons / ha per year in Denmark alone [2]. Brown macroalgae are shown to have a maximum energy yield of over 45% throughout a growing period. A value significantly greater than the yields of most terrestrial biomass (e.g. energy crops: 30–35%, lignocelluloses: 20–25%). All thanks to their high productivity rates [3].

Chemical analyses carried out globally show that macroalgae samples differ significantly in composition. Variations are apparent across habitats, seasons and species. Seasonal differences in brown algae are expressed via storage carbohydrate (i.e. laminaran and mannitol) accumulation and subsequent release throughout the lighter and darker seasons, respectively [1]. High variation is also noticed in terms of ash content [1, 4]. In early spring, brown macroalgae are usually high in alginate, ash and protein but analyses show low carbohydrate concentrations [5]. As soon as the algae start to receive more light, their photosynthetic activity surges, leading to an increased sugar production. Correspondingly, the relative amounts of ash, alginate and proteins plummet [5].

Researchers worldwide have carried out numerous studies on various energy production technologies, using macroalgae as the input feedstock. They can be grouped into two major types: biochemical and thermochemical conversion. Direct combustion is excluded as an option due to the raw macroalgae containing high amounts of low melting temperature alkali metals. Otherwise, the pathway depends on the demanded output fuel. With the exception of solid fuel, the feedstock has shown potential for multiphase fuel production.

When compared to anaerobic digestion, hydrothermal liquefaction (HTL), commonly performed at reaction times in the order of several to tens of minutes, is capable of fast biofuel production [6]. Despite high levels of inorganics, alkali metals present in macroalgae are hypothesized to have a catalytic effect on the conversion. HTL of biomass is commonly carried out in alkaline media to reduce formation of solids and promote repolymerisation into liquid compounds. Partially confirmed by Anastasakis et al., when the researchers reached highest biocrude yields without using an external catalyst [6]. Previous studies show that HTL biocrude often exhibits a high energy density equivalent to at least 70% of that of fossil crude [7]. In case of macroalgae as feedstock, the lower energy content is a result of heteroatoms present in the biocrude. Nitrogen and sulphur originate from the proteins and sulphated carbohydrates, respectively, whereas oxygen is in all major polysaccharides. The higher nitrogen and sulphur content in algal biomass is shown to directly result in more contaminated biocrudes compared to lignocellulose derived alternatives [8].

Even though macroalgae have been used as a feedstock for HTL in many studies throughout the recent years [8, 9, 10], according to the author, liquefaction of post alginate and fucoidan extraction residues has yet to be performed. However, such feedstock was studied for energetic utilisation, using other conversion technologies such as anaerobic digestion [11], pyrolysis [12] and hydrothermal carbonisation [13]. The fact that HTL is capable of processing non-algae derived low value wet material, for example sewage sludge and manure, brings merit to a positive outcome of this study [14]. Here, the focus is set on utilising a residual material stream that is generated by macroalgae factories, which could potentially become modern bio-refineries producing both high value products and HTL biocrude at high capacities. The aim of the study was to show that alginate and fucoidan residues can indeed be converted to high quality biocrude for further upgrading and integration in the present liquid fuel infrastructure. Furthermore, the effects of raw macroalgae demineralisation were investigated as despite the extraction of high value organics, the post-processed algae are hypothesized to still contain inorganics. Experiments were also carried out to test whether extensive neutralisation of leaching residues is necessary and if shorter reaction times could benefit HTL of low quality algal feedstock.

2. MATERIALS AND METHODS

Multi seasonal samples of brown macroalgae *Fucus vesiculosus* were acquired for the experimental part of the study. Specifically, this algae was chosen due to its wide growth in the Baltic sea. In some Western parts of the sea, *F. vesiculosus* are in fact the only large, canopy-forming brown macroalgae. They grow along rocky coasts, in low depths [15].

Thermogravimetric analysis (TGA) was performed in an inert atmosphere (purged with nitrogen) using a PerkinElmer STA6000 TG/DSC analyser. Samples of 4–7 mg were heated to 950 °C at a temperature ramp rate of 10 °C/min. The nitrogen flow rate was set to 20 ml/min throughout the entire procedure. CHNS analysis was carried out on a Vario Macro Cube simultaneous CHNS analyser from Elementar. Here, samples of 70–80 mg were analysed in triplicates. Proximate and ultimate analyses bore the following compositional results: 54.16% volatiles, 20.23% fixed carbon, 22.42% ash, 36.90% elemental C, 6.06% H, 3.14% N, 1.12% S and 30.36% O by difference. In house moisture analysis (KERN MLS) showed that the freshly harvested *F. vesiculosus* algae contain 77.42 ±0.46 wt.% moisture. Higher heating values (HHVs) of the dried and milled macroalgae samples were measured in triplicates using an IKA C2000 basic bomb calorimeter.

1.1. Demineralisation

Initial screening tests were carried out on *Laminaria digitata* brown macroalgae as a part of a previous study. A combination of significant ash removal and relatively water-lean neutralisation procedure led to the decision that citric acid performed the best.

Following up on the results from the above study, a weak citric acid solution was chosen as the first leaching agent. Naturally, demineralisation with deionised water was also carried out in order to establish baseline results. Finally, with a view to investigate an alternative means to utilise one of the by-product streams of continuous HTL, the aqueous phase was used as the third leaching agent. Its acidic nature gives merit to investigate the de-ashing potential and thus valorise the otherwise challenging by-product. The raw aqueous product was a sample previously collected at the local semi-continuous HTL plant with a view to represent a real-life synergistic opportunity. The sample was slightly acidic with a pH level below 5.5 [16].

The raw macroalgae were pre-rinsed with cold water in order to remove any unbound inorganics as the first step. After the initial rinsing, the biomass is dried and milled (FOSS Cyclotec^{TM} 1093, particle size: ≤ 200 mm). In the case of citric acid leaching, the now dry and powdered macroalgae are mixed with a 1 wt.% citric acid solution (12.5 g solution / g macroalgae). The leaching process takes place overnight (18 hours of continuous stirring at 1000 rpm and at room temperature). As mentioned before, the procedure was adapted and modified from the performed screening tests on *L. digitata*. However, instead of a leaching time of 4 hours, in this study the samples were leached overnight in order to confirm that despite the weak acidity of the leaching agent, a longer retention time might compensate and increase demineralisation efficiency. This hypothesis was confirmed by achieving an ash removal of 47.15 wt.% compared to the initial 27.21%. After leaching, the mixture is centrifuged (SIGMA 6-16S centrifuge, for 5 minutes at 4000 rpm) in order to remove the leachate. Then, the neutralization/rinsing procedure takes place. Neutralization is a part of the study in order to process a non-acidic feedstock. It is done as alkaline processing media were found to suppress char formation from carbohydrates during HTL [16]. Deionised water is added to the residues (12.5 g water / g initial macroalgae) and stirred manually. Subsequent centrifugation is utilised for separation. Different numbers of the coupled rinsing-separating steps were enforced in order to set up for analysis of HTL of post-demineralisation macroalgae. The focus here is to determine whether a great neutralization extent is truly necessary for efficient HTL of acid leached macroalgae. The experimental design included drying (at least for 18 hours at 105 °C) the residues after 1, 4 and 8 rinsing repetitions (i.e. simulated water consumption ranging from 12.5 to 100 g / g of dry initial macroalgae). Ultimately aiming to dismiss the need for water-intensive post-treatment. The pH levels were measured initially, after the leaching period and after each rinsing step (WTW pH 3210 meter, accuracy of ±0.2 pH points). All results are reported as average values of triplicate experiments/measurements unless stated otherwise.

Only ≈ 50 ml of HTL water was available for the needs of this project. In order to accommodate for the required leaching medium, the available 50 ml were diluted with de-ionised water to reach a total volume of 300 ml. This being said, it is worthwhile to note that the pH of the solution did not change significantly, stabilising at pH 5.6 prior to mixing. The same acid solution-to-biomass ratio of 12.5 and the leaching conditions were kept.

1.2. Added value product extraction

The experimental flow of the performed alginate removal procedures was adapted from [17]. Three samples (sample size: 5 g) of the winter harvest *F. vesiculosus* were processed. Firstly, the rinsed macroalgae were dried and milled. Then, the powder was mixed with a 0.5M H_2SO_4 solution (13.58 g solution / g algae) and stored overnight (minimum 21 h) in a dark cabinet. Then, the mixture was centrifuged (5 min at 4000 rpm) and the liquid solution was removed. An intermediary washing step (13.58 g H_2O / g initial algae) with subsequent centrifugation (4000 rpm, 5 min) was performed to remove any residual acid. A 4% Na_2CO_3 solution (19.95 g Na_2CO_3 solution / g initial algae) was added to the residues. The mixture was stirred magnetically (800 rpm) for 2 hours. After soaking, the mixture was once again centrifuged to separate the solubles. A washing step (19.95 g water / g initial algae, mix, centrifuge, drain) took place next. All of the above process steps were carried out at room temperature. Finally, the residues were carefully removed from the centrifuge bottles and placed in an induction oven to dry for at least 18 hours at 105 ^{o}C.

The employed simulative fucoidan extraction procedure was adapted from [12]. Three samples (sample size: 5 g) of winter harvest macroalgae were analysed. The water rinsed macroalgae were processed mechanically via drying and milling. Subsequently fucoidan was extracted in a $CaCl_2$ solution. The extraction was finished throughout two steps: samples were exposed to two 20 min long magnetic stirring (1000 rpm) sessions in 1 wt.% $CaCl_2$ solutions (16.67 g solution / g algae). After each stirring, the mixtures were centrifuged at 4000 rpm for 5 min in and the separated liquid was removed. A similar procedure followed the two extraction-separation steps: the residues were mixed with water (16.67 g water / g initial algae) and centrifuged once more in order to remove any remaining calcium chloride. All steps were carried out at room temperature. Finally, the residues were oven dried at 105 ^{o}C for a minimum of 18 hours, cooled in a desiccator, weighed and stored in air tight containers until further processing.

1.3. Hydrothermal liquefaction

6 separate HTL runs were carried out throughout this study. The experiment list can be seen in Table 1. Here, the main focus was set on HTL of treated macroalgae, namely de-ashed, post fucoidan and alginate extraction. Additionally, effects of post de-ashing neutralisation and a shorter retention time were looked into.

Table 1. HTL experiment overview

Reference	Pre-treatment	HTL conditions	Hypothesis/Argument
Run 1	–	Normal	Baseline
Run 2	De-ashed		Demineralisation improves yield
Run 3	Fucoidan extraction		Effective HTL with fucoidan residues
Run 4	Alginate extraction		Effective HTL with alginate residues
Run 5	De-ashed and neutralised		Post de-ashing neutralisation is not necessary
Run 6	–	Short	High quality biocrude at a shorter reaction time

All experiments were carried out in stainless steel (grade 316) 12 ml micro reactors. Feedstock mass loadings of 20% (±2%) were used, and all reactions were carried out at 400 ^{o}C (±5 ^{o}C). Upon feedstock slurry preparation, the specific macroalgae powder was combined with distilled water to form the predefined mixture. A total of 5 g (±0.1 g) of the slurry was then loaded into the reactors. Nitrogen gas was used to simultaneously leak test (80 bar) and purge the reactors to evacuate atmospheric oxygen. Hereafter, two reactors and thermocouples were mechanically coupled to an agitator providing mechanical mixing of the reagents inside the reactors while being processed. The two reactors were then submerged into a preheated, fluidised sand bath and held normally for 15 minutes of retention time and 10 minutes in "short HTL" condition. The retention time was defined as the time that passes between the moment when the reactors have reached the pre-set temperature of 400 ^{o}C (±5 ^{o}C) and the instance of manually submerging the reactors into the cool (< 20 ^{o}C) water bath. After quenching in water for a minimum of half an hour, the separation procedure begins.

The first step of product separation was the weighing of the gaseous products, gas sampling and venting the remaining gases via top mounted valves. The remaining products consisted of solid residues, biocrude and an aqueous phase. The reactors were washed with acetone in order to remove all biocrude traces from the reactor. The liquid phase was then separated from the char by vacuum assisted mechanical filtration (VWR, particle retention: 5–13 mm). The solids present on the filter were then dried overnight at 105 ^{o}C and re-filtered with 250 ml of distilled water. The remaining solid residues were dried once again, weighed and defined as the water and acetone insoluble solids. Acetone was then evaporated from the homogeneous liquid fraction and the biocrude fraction was manually extracted after centrifuge-aided phase separation. The higher density extracts were defined as biocrude, whereas the aqueous by product was collected, dried, weighed and denoted as water solubles (WS). The yield of WS increased after adding the weight of the solids that indeed were soluble in water. Post reaction gases were weighed, adjusted for initial nitrogen addition and analysed via GC analysis. The aqueous products were weighed prior to and after in order to show the extent of experimental error due to water losses during acetone evaporation. The produced biocrudes were weighed, their proximate analyses were done via TGA and the water contents were measured via Karl Fischer titration, respectively. Finally, the produced solids were weighed, washed with water, dried, reweighed and ashed. This procedure was done in order to determine the acetone and water insoluble solids correctly and looking into how much inorganics are present in the by-product.

1.4. Calculation methods

The section describes all calculative methods that were used for determining both product/by-product yields and quality parameters such as biocrude higher heating value (HHV), hydrogen-to-carbon ratio (H/C) and oxygen-to-carbon ratio (O/C). Both biocrude and gas yields were calculated on a dry and ash-free (DAF) basis identically as shown in equation 1. Similarly, the yields of solids were calculated on a dry basis.

$$Yield_{biocrude} = \frac{Mass\ of\ biocrude}{Mass\ of\ dry,ash\ free\ feedstock} * 100\% \qquad [\%] \qquad (1)$$

Finally, the yield of WS was also determined on dry feedstock basis, by adding the weighed WSs and the amount of solids washed out with water (equation 2). This procedure was adapted in order to better represent the generated amount of WSs. Previously utilised methods of presenting the data as process water + WSs were shown to be inconsistent (i.e. variations in mass up to 25% among single run triplicate data). Such differences are believed to be caused by the non-automated evaporation step – depending on the duration of this step, more or less process water is lost. However, this does not impair the results of the study as preserving process water was never among the objectives. Furthermore, presenting dry WS data instead is more reliable.

$$Yield_{WS} = \frac{Mass\ of\ WS + mass\ lost\ during\ water\ washing\ of\ solids}{Mass\ of\ dry\ feedstock} * 100\% \qquad [\%] \qquad (2)$$

Due to the inability of measuring HHVs of the produced HTL biocrudes directly (i.e. micro reactors do not yield sufficient amounts), the study resorted to elemental HHV estimation. In order to represent the biocrude in a comparable manner, several HHV estimation formulas were tested against laboratory measurements or raw macroalgae, demineralisation and added value product extraction residues. The correlation derived by Friedl et al (equation 3) was shown to give most accurate results – all tested values were within 5% of the experimental measurements [18].

$$HHV = 0.00355 * C^2 - 0.232 * C - 2.230 * H + 0.0512 * C * H + 0.131 * N + 20.6 \qquad [\text{MJ/kg}] \qquad (3)$$

Hydrogen-to-carbon (equation 4) and oxygen-to-carbon ratios on an elemental basis were calculated for each of the produced biocrudes. Here, analysed sample masses are taken into account. Such quality parameters allow for direct comparison with biocrudes produced from other biomass sources, different HTL conditions and even fossil fuels. In literature, yet another ratio, the effective hydrogen-to-carbon ratio, is often presented in order to compensate for any water present in the produced biocrude. Contrary to such an approach, the study included measuring the total water content by Karl Fischer titration and subtracting the results both from biocrude yields and elemental composition.

$$\frac{H}{C} = \frac{\frac{H * m_{sample}}{100\% * m_{aH}}}{\frac{C * m_{sample}}{100\% * m_{aC}}} \qquad (4)$$

Energy recovered in the form of produced biocrudes was calculated as well in order compare the energetics of each HTL run, additionally to biocrude yield and quality. The recovered ratio is calculated on dry feedstock basis by equation 5.

$$ER = \frac{Mass\ of\ biocrude * estimated\ HHV}{Mass\ of\ dry\ feedstock * measured\ HHV} * 100\% \qquad [\%] \qquad (5)$$

2. RESULTS AND DISCUSSION

2.1. Demineralisation

All demineralisation runs (i.e. water, citric acid and HTL water washing) would require post processing neutralisation, should that prove to be necessary for effective macroalgae conversion. Naturally, after the water leaching step, macroalgae residues reached a pH level of 6 – same as measured on the fresh *F. vesiculosus*. Presumably caused by the inorganics present in the marine macroalgae. However, it did take 4 washing steps (i.e. 50 g water / g initial macroalgae) to reach a steady pH 7 reading. In the case of HTL water leaching, 5 washing steps brought the pH up to 6.9, compared to the initial pH of 5.6. This indicates that if the leaching agent is shown to perform well in terms of ash reduction, there would be no need for strong, dedicated acid solutions. However, further studies are necessary in order to show the full neutralisation extent required post non-diluted HTL water demineralisation. Finally, the addition of 1% citric acid lead to pH 3.8, the lowest initial pH level throughout the study. Furthermore, a mere pH 6.1 was reached after 8 washing steps (i.e. 100 g water / g initial macroalgae). This indicates an alarmingly high water consumption related to washing out the last acid residues or, alternatively, a need for an external alkaline agent. The latter could only be justified by high ash reduction and subsequent HTL performance, or if the addition of an alkaline catalyst would be synergistically beneficial. However, yet another aspect to take into account is the fact that each washing step comes at a cost. Organic matter is also lost throughout the neutralisation process. Although advanced techniques, such as reactive solvent citric acid extraction, might be able to reduce the water demand [19]. In this study, water washing was investigated as the cheap and widely available method. In the end, it is crucial to investigate whether neutralisation is at all necessary and if so, to what extent.

The first and most significant finding is that dry feedstock grinding combined with water leaching does indeed lead to a reduced ash content. A reduction of over 30% was reached, followed by further decreases in inorganics throughout subsequent "neutralisation" steps. The final ash content, measured after first reaching pH 7 (i.e. after washing step 4), of 13.71 wt.% resulted in an overall ash reduction of 38.85%. Besides that, the final baseline measurement (i.e. ash content after 8 H_2O washes) shows that there is no statistically significant change in inorganics post neutralisation.

In terms of ash reduction, HTL water performed worse than deionised water, resulting in 16.17 and 14.89 wt.% ash prior to and post neutralisation, respectively. The 2.51 wt.% of ash present in the leachate are thought to be the reason for why the agent's acidic effect was impaired. The ash is hypothesized to consist mainly, if not entirely, of the used catalyst, potassium carbonate which in turn will only add to the suspected high concentration of potassium salts in the marine feedstock. Interestingly, neutralisation did not decrease the ash content notably, as was the case in water leaching as well. Here a further reduction of just 1.28 wt.% was recorded, compared to the 1.9 wt.% drop in the case of pure water treatment. Judging solely based on ash reduction capacity, diluted HTL water leaching is slightly inferior with a maximal demineralisation capacity of 33.59%.

Finally, citric acid treatment showed highest ash removal performance with *F. vesiculosus*. The initially reached 14.53 wt.% were further reduced down to 11.85 wt.% after 8 washing steps, resulting in ash reductions of 35.19% and 47.15%, respectively. It is understandable that such results are brought on by the combined effects of both acid and water leaching. In terms of ash removal, 1% acid leaching is comparable to but slightly superior to extensive water leaching. The results are summarised in Table 2.

Table 2. Comparison of how the three leaching agents and subsequent neutralization steps influence final ash content of *F. vesiculosus*. Untreated macroalgae were determined to contain 22.42% ash

Leaching	**No. of H_2O washes**	**Ash [wt.%]**
Water	1	15.28 ± 0.20
Water	4	13.71 ± 0.33
Water	8	13.38 ± 0.36
HTL water	1	16.17 ± 0.91
HTL water	4	15.06 ± 0.96
HTL water	5	14.89 ± 0.59
Citric acid	1	14.53 ± 0.42
Citric acid	4	13.36 ± 1.36
Citric acid	8	11.85 ± 0.37

In order to properly compare the three investigated methods and discuss their performance, another dimension of comparing the leaching residues was included – HHV determination. All leaching agents lead to a higher quality energetic feedstock. And although the differences are minor, the claim that citric acid treatment performs best, is confirmed with a highest HHV of 16.16 MJ/kg compared to the initial 14.95 MJ/kg of the raw macroalgae. Based on this data, it would seem that extensive water washing is not beneficial as post neutralisation washes indicate lower HHV. The study explains this behaviour by claiming that in all cases, full demineralisation extents are reached prior to neutralising. Whereas subsequent water washes are more effective at removing organics. The above can also be argued by elemental analysis of the residues. In the case of citric acid leaching, when comparing residues post 1 and 8 H_2O washes, despite a drop-in inorganic of 2.68 wt.%, the fractions of elemental carbon and hydrogen increased just by 1.69% and 0.19%, respectively. Therefore, it is clear that macroalgae lose organics through subsequent water washing.

The author would like to point out that changes in nitrogen fraction were negligible (below 0.1 wt.%), whereas no conclusions could be drawn from sulphur content measurements.

Finally, comparing the generated amounts of post leaching residues of each treatment may shed even more light on the matter. As it turns out, the three treatments lead to slightly different quantities of residues initially – 61.75 wt.%, 65.15 wt.% and 68.66 wt.% with citric acid, HTL water and water leaching, respectively. This correlate well with the determined demineralisation effectiveness of the agents. Simply put, the more inorganics are removed, the less residue remains. Interestingly, no matter what leaching method was performed initially, the washing steps rendered the residues nearly identical by weight. This shows that neutralisation and subsequent washing is leaching agent independent in terms of residue generation.

2.2. Added value product extraction

The important finding here is that despite the high extent of extraction, post extraction residues added up to 41.88 wt.% and 68.17 wt.% of the initial feedstock mass in the cases of alginate and fucoidan extractions, respectively. This could be explained by the fact that the *F. vesiculosus*, harvested in late winter, were consuming their energy stocks throughout the cold season, when solar irradiance is at its lowest and the amount of inorganics surges. This is further confirmed by reported measurements of winter *F. vesiculosus* and autumn *S. latissima* – the latter is shown to contain more than double the amount of alginate [20, 21]. However, the possibility that structural differences among the two macroalgae genera add to such results cannot be ruled out.

Elemental analysis of the residues was carried out in order to evaluate the effect alginate and fucoidan extraction has on the elemental quantities of heteroatoms, specifically nitrogen and sulphur, present in the biomass. Elemental nitrogen was decreased by fucoidan extraction (1.84 wt.% compared to the initial 3.14 wt.%) but remained unchanged after alginate extraction. Sulphur removal via fucoidan extraction resulted in a logically decreased fraction of 0.37 wt.% (compared to the initial 1.12%).

Ash development is yet another characteristic of the residues that was studied. Fucoidan extraction did not influence the final ash content significantly. On the other hand, residues generated by alginate extraction exhibit a significantly higher amount of inorganics. Both fucoidan and alginate extractives were ashed in order to compare the de-ashing performance of the two procedures. Both sets of extractives showed similarly low amounts of dissolved inorganics. This confirms that the extraction methods, especially alginate removal, selectively dissolve organics and virtually no inorganics are lost. The produced ash samples differed in colour, namely light post fucoidan and dark – post alginate extraction. This served as a solid basis for further ash analysis in order to identify how this visual difference corresponds compositionally. Unsurprisingly, the inorganics present in fucoidan and alginate residues are dominated by calcium and sodium, respectively. The increased concentrations of these elements are caused by the fact that a single post extraction washing step does not remove all traces of $CaCl_2$ and Na_2CO_3. The high amounts of calcium are the reason for the unusually light colouration of fucoidan residues. However, ash composition of the raw macroalgae, shows a clear alkali and alkali earth metal dominance to begin with. Potassium, sodium, calcium and magnesium are the most abundant inorganics. Similarly, for both procedures, potassium, magnesium, manganese are extracted to a great extent. Meanwhile, concentrations of heavier metals: aluminium, copper, nickel and zinc remain nearly invariant. Notable differences occur with the migration of iron, strontium and phosphorous – in all cases alginate extraction seem to remove more of these elements. The addition of H_2SO_4 is the suspected culprit as the strong acid is commonly used as an effective demineralisation agent [22]. HHVs of the produced residues were measured and compared to the initial feedstocks. Both extraction procedures led to higher HHV values.

2.3. Hydrothermal liquefaction

2.3.1. HTL yields

Biocrude yields varied between 15.22 wt.% and 28.21 wt.% on DAF basis. As shown in Table 3, short HTL (run 6) and HTL of neutralised citric acid leaching residues (run 5) performed the worst in terms of biocrude yields. Meanwhile, the baseline run with raw macroalgae resulted in a yield of 19.36 wt.%. Finally, all three remaining biomass treatments (i.e. citric acid leaching, fucoidan and alginate extraction) led to increased biocrude yields. Alginate extraction residue conversion produced the most biocrude on DAF basis, 28.21 wt.%.

Next, it is interesting to look at the four phase HTL products in terms of measured mass yields. Runs 2, 3 and 5 led to highest production of solids. Fucoidan extraction residues performed the worst (0.35 g of solids), whereas alginate residues generated the least amount of solids (0.18 g). The difference is significant and definitely worth to consider. Runs 2 and 3 led to significantly lower amounts of WS, 0.08 g and 0.09 g, respectively. In comparison, the overall average of produced WS was 0.19 g, with run 1 generating the most, 0.28 g of WS. Gas yields were rather consistent throughout the experimental procedure with the exception of run 2, the citric acid leaching residues led to the highest amount of produced gases, 0.42 g, compared to the average of 0.35 g. The produced by-products were scaled with respect to each other in order to represent proportional yields and plotted on Fig. 1. Here the aim was to see whether it is possible to determine some kind of biocrude tendencies based on by-product yield distribution. In general, it seems that the worse performing runs (i.e. 1, 5 and 6) exhibit a slight tendency to form more WS and less gases. Whereas there is no correlation in terms of solids, as all three high biocrude yielding runs are spread out within the range of 16.40% to 41.85%, while the worse performing runs average out at 28.21%.

Table 3. Yield and quality summary of the produced biocrudes. Data presented in weight% are calculated on DAF basis

	Biocrude yield [wt.%]	**H/C**	**O/C**	**N [wt.%]**	**ER [%]**	**HHV [MJ/kg]**
Run 1	19.36	1.38	0.35	3.08	26.04	25.82
Run 2	21.59	1.22	0.1	2.75	49.14	42.34
Run 3	26.56	1.29	0.13	2.97	43.81	36.88
Run 4	28.21	1.36	0.14	3.02	53.02	44.3
Run 5	17.26	1.55	0.08	3.17	30.54	36.97
Run 6	15.22	1.54	0.05	4.33	29.28	38.44

HHVs of the biocrudes were estimated in order to calculate the energy recovery associated with the produced biocrudes. The results varied from as low as 25.82 MJ/kg in the case of run 1, up to 42.34 MJ/kg and 44.30 MJ/kg for run 5 and 6 biocrudes, respectively. The latter values are well within the range of conventional fossil crudes. In terms of HTL processing and energy efficiency, energy recovery in the main fuel product, the biocrude, is essential to evaluate the potential feasibility of the specific conditions or feedstock. Table 3 shows that runs 2, 3 and 4 perform the best with alginate residue HTL biocrude resulting in a ER of 53.02%. On the other end of the spectrum, run 1 (i.e. raw feedstock) exhibited an ER of just 26.04% while biocrudes from runs 5 and 6 contained < 30% of the initial feedstock energy.

2.3.2. Biocrude quality

Besides identifying the high biocrude yielding parameters, it is crucial to establish how the different HTL runs perform in terms of produced biocrude quality. This is first and foremost assessed by elemental H/C and O/C ratios. Here, the aim is to achieve a product of maximal hydrogen and minimal oxygen content. Runs 5 and 6 seem to perform the best with high H/Cs of < 1.54 and low O/C ratios between 0.05 and 0.08. However, when compared to the characterisation of fossil crude, upgrading via deoxygenation is necessary even for the best performing biocrudes. Runs 2, 3 and 4 also produced biocrudes of good quality. As indicated by the oxygen rich product of baseline run 1, it is clear that all pre-treatments/conditions (i.e. demineralisation, added value product extraction and even short retention) lead to superior biocrudes. Overall elemental analysis of the produced biocrudes is presented in Table 4. Proximate analysis of the produced biocrudes did not show significant differences in volatile matter and fixed carbon which averaged at 83.32 wt.% and 16.68 wt.% respectively. The high amount of volatiles is promising for further refining as only the volatile compounds can be distilled into lighter hydrocarbons such as diesel, jet fuel and gasoline.

Table 4. Elemental analysis of the produced HTL biocrudes

	C [wt.%]	**H [wt.%]**	**N [wt.%]**	**S [wt.%]**	**O [wt.%]**
Run 1	60.23	6.93	3.08	1.47	28.29
Run 2	77.96	7.94	2.75	0.54	10.81
Run 3	75.52	8.1	2.97	0.49	12.92
Run 4	74.63	8.44	3.02	0.51	13.41
Run 5	78.09	10.06	3.17	n.m.	8.68
Run 6	79.85	10.23	4.33	n.m.	5.58
n.m. – not measured					

A direct comparison between runs 2, 5 and 1, 6 is necessary in order to discuss whether either an extensive water neutralisation or a shorter retention time of 10 min benefits the biocrude yields and quality. In terms of biocrude yield (Fig. 1, Table 3), both neutralised residues and short retention led to very low results, with run 5 performing slightly better. It is difficult to define a tendency based on by-product distribution. Leached biomass runs exchanged gas and WS production, with the neutralised residues generating a higher amount of gases. On the contrary, short HTL produced proportionally less gas (Fig. 1). Coming back to Table 4, run 1 biocrude retained an alarmingly high amount of oxygen. Based on a significantly lower O/C ratio and a slight increase in H/C, a shorter retention is definitely the superior condition from this point of view. Meanwhile things are slightly less obvious with neutralised leaching residues – the O/C ratio remained nearly identical. Nonetheless, the H/C improved by more than 20%.

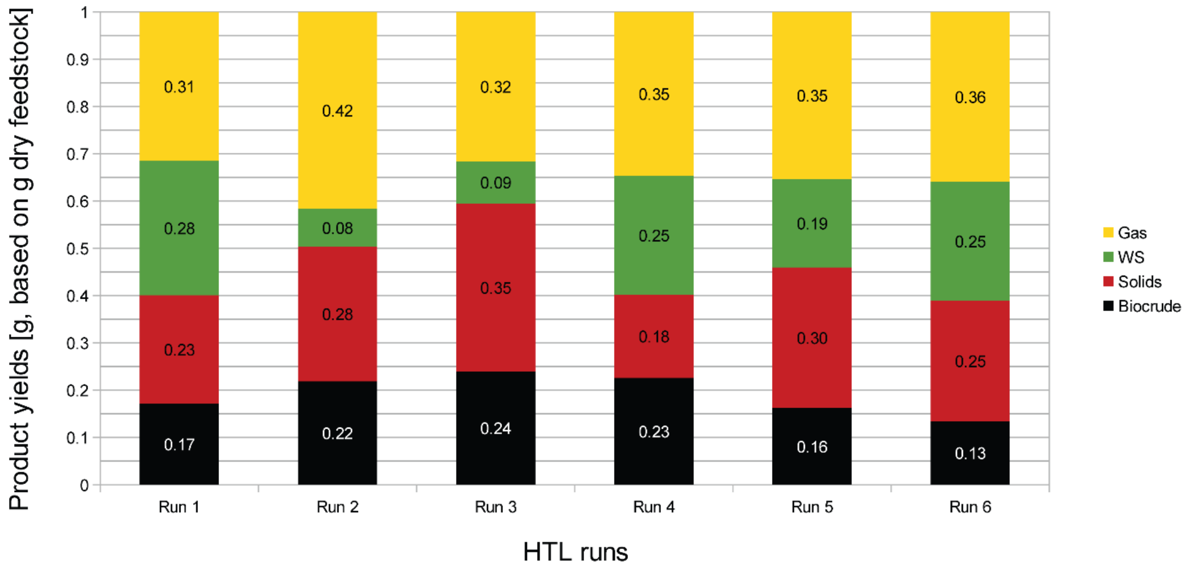

Fig. 1. Measured HTL product yields including biocrude, solids, water solubles and gases

2.3.3. Solids

The chemical composition analysis of the produced solids was limited to defining how much residual organics are present. With one exception, residual organics did not vary much throughout the six HTL runs, averaging at 70.87 wt.%. However, run 3 (fucoidan residues) varied significantly, comprising of just 52.54 wt.% organics. Going back to Fig. 1, since the gas yield of run 3 was average and the amount of produced WS significantly lower than in other runs, the fact that such a high fraction of solids was produced leads to think that more inorganics ended up in the solid phase by-product stream and thus reduced the apparent concentration of solid organics. Ash content both in the feedstock and HTL solids was measured, whereas the missing amount is assigned to WS, where the percentage is simply calculated based on the total yield of WS. This raises doubt in the potential of utilising the aqueous HTL product for direct water phase recirculation as effectively done with lignocellulosic feedstocks [16], or leaching. Ash analysis of run 1 solids (Table 5) revealed that with the exception of potassium and sodium, all measured metal concentrations increased compared to raw *F. vesiculosus*. This is expected as potassium and sodium salts are highly soluble in water and hence are believed to be washed out throughout the product separation procedure. Meanwhile, fears of reactor degradation are confirmed by the fact that concentration levels of stainless steel originating metals (i.e. chromium, iron, manganese, nickel and titanium) increased or, in the case of chromium and titanium, appeared.

Table 5. ICP ash analysis of raw macroalgae, citric acid leaching, fucoidan and alginate extraction residues and the solids produced in run 1

	Metal concentration [mg/g]														
Ash sample	**Al**	**Ba**	**Ca**	**Cr**	**Cu**	**Fe**	**K**	**Mg**	**Mn**	**Na**	**Ni**	**P**	**Sr**	**Ti**	**Zn**
Raw F. vesiculosus	0.85	0.03	42.83	-	0.13	1.93	104.9	30.65	0.48	49.03	0.73	10.35	4.05	-	0.19
Post Citric 8 washes	4.18	0.23	122.9	-	0.42	2.31	90.84	53.38	0.88	29.43	1.88	4.75	14.45	-	0.4
Post Fuc	3.70	0.13	253.53	-	0.21	4.04	13.34	2.96	0.13	6.48	0.97	4.51	3.58	-	0.26
Post Alg	5.01	-	8.33	-	0.11	0.36	3.2	1.1	-	95.76	0.58	1.03	0.32	-	0.05
Run 1 HTL solids	3.27	0.31	144.93	0.31	0.54	9.05	8.23	83.38	1.7	9.02	3.75	37.97	12.78	0.18	1.1

An additional water washing step was introduced post filtration in order to check whether there were any water solubles that were precipitated by the used acetone. The mere fact that a solvent was used in order to clean the reactors and separate the products might impair the reliability of the results. The gravimetrically separable biocrude is easily isolated without the use of external solvents in continuous HTL facilities [16]. The performed washing step revealed mass losses ranging from 7.96% to 54.15% in the case of run 4 and 3 solids, respectively. Here, the use of sulphuric acid during alginate extraction is hypothesized to have rendered the biomass residues recalcitrant to subsequent water treatments (i.e. low mass loss) due to the acid's structural destructiveness and demineralisation effectiveness. During the screening tests with *L. digitata*, sulphuric acid leaching was shown to break down crystalline macroalgae structures. Interestingly, mass losses across runs 1,6 and 2,5 remained virtually invariant at 37 wt.% and 22 wt.%, showing that neither extensive water neutralisation, nor halving the retention time influence the amount of WS that get precipitated during acetone filtration. All in all, it is obvious that without extra washing, reported amounts of produced solids risk to be neither acetone and water insoluble, nor representative for real-life in-line filtered HTL facilities.

2.3.4. Gases

Similarly to product yields, gas analysis shows that all HTL runs produce gases of similar composition (Fig. 2). The only major deviations were gaseous by-products of runs 3 and 4. Run 3 gases contained a significantly higher amount of CO, whereas run 4 in turn produced more H_2. Besides that, all produced gases were dominated by CO_2 (minimum of 84.61 vol.% and up to 91.61 vol.%) and contained traces of CO, H_2 and CH_4, indicating that the majority of oxygen is removed via decarboxylation and decarbonylation reactions.

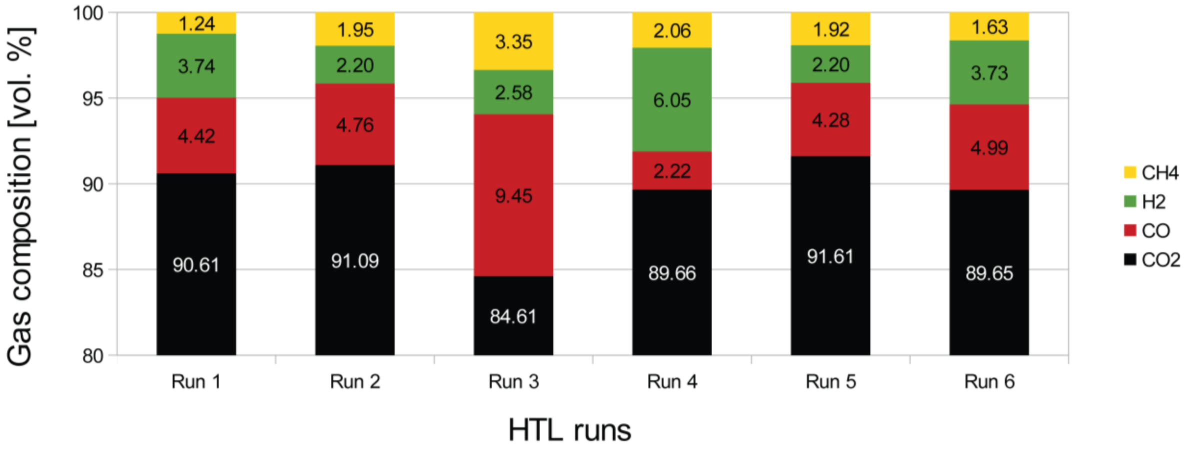

Fig. 2. HTL produced gas compositions across the experimental range

3. CONCLUSIONS

All three demineralisation methods led to reduced amounts of ash and consequently higher HHVs. Whereas the residual amounts levelled out already at mild neutralisation (washing step 4). Citric acid leaching with neutralisation resulted in the least ash, corresponding to an ash removal efficiency of 47.15%. Both alginate and fucoidan extractions led to highly different residual masses. However, alginate extraction led to residues with high ash concentrations. In all cases the residues had higher HHVs than the initial biomass samples.

Fucoidan and alginate extraction residues led to the highest biocrude yields, at 26.56 wt.% and 28.21 wt.%, respectively. Meanwhile, short retention and neutralised leaching residues resulted in the lowest yields. In terms of H/C and O/C ratios, on the other hand, the latter two performed the best, whereas raw *F. vesiculosus* biocrude exhibited a significantly higher O/C ratio. In terms of H/C, citric acid leaching and fucoidan extraction residues performed the worst. Despite slightly different tendencies in terms of biocrude yield, citric acid leaching and alginate extraction residue biocrudes exhibited the highest HHVs and ER. All initial hypotheses were confirmed:

- Run 2 – Demineralisation led to a slightly higher HTL biocrude yield;
- Run 3 – HTL of fucoidan extraction residues resulted in a relatively high biocrude ER;
- Run 4 – HTL of alginate extraction residues led to a high biocrude ER;
- Run 5 – Despite great quality in terms of H/C and O/C, neutralisation is not advised as it led to significantly lower yields and ER.

REFERENCES

1. S. J. Horn. Seaweed Biofuels: Production of Biogas and Bioethanol from Brown Macroalgae. VDM Publishing, 2009, isbn: 9783639153071.
2. Presentation by Anne-Belinda Bjerre. Macroalgae biorefinery – Production of bioethanol and protein for fish feed from brown seaweed, 2014.
3. M. Song, H. D. Pham, J. Seon and H. C. Woo, Marine brown algae: A conundrum answer for sustainable biofuels production, *Renewable and Sustainable Energy Reviews*, 2015, Vol. 50, p. 782–792, doi: 10.1016/j.rser.2015.05.021.
4. Presentation by A. B. Ross. Thermal conversion of macroalgae, 2011, Grenaa – Denmark.
5. A. B. Ross, J. M. Jones, M. L. Kubacki and T. Bridgeman, Classification of macroalgae as fuel and its thermochemical behaviour. *Bioresource technology*, 2008, volume 99(14), p. 6494-6504, doi: 10.1016/j.biortech.2007.11.036.
6. H. Chen, D. Zhou, G. Luo, S. Zhang and J. Chen, Macroalgae for biofuels production: Progress and perspectives, *Renewable and Sustainable Energy Reviews*, 2015, volume *47*, p. 427-437, doi: 10.1016/j.rser.2015.03.086.
7. K. Anastasakis and A. B. Ross, Hydrothermal liquefaction of the brown macro-alga Laminaria saccharina: effect of reaction conditions on product distribution and composition, *Bioresource technology*, 2011, volume 102.7, p. 4876-4883, doi: 10.1016/j.biortech.2011.01.031.
8. N. Neveux, A. K. L. Yuen, C. Jazrawi, Y. He, M. Magnusson, B. S. Haynes, A. F. Masters et al., Pre-and post-harvest treatment of macroalgae to improve the quality of feedstock for hydrothermal liquefaction, *Algal Research*, 2014, volume 6, p. 22-31, doi: 10.1016/j.algal.2014.08.008.
9. B. Jin, P. Duan, Y. Xu, F. Wang and Y. Fan, Co-liquefaction of micro-and macroalgae in subcritical water, *Bioresource technology*, 2013, volume *149*, p. 103-110, doi: 10.1016/j.biortech.2013.09.045.
10. K. Anastasakis and A. B. Ross, Hydrothermal liquefaction of four brown macro-algae commonly found on the UK coasts: an energetic analysis of the process and comparison with bio-chemical conversion methods, *Fuel*, 2015, volume *139*, p. 546-553, doi: 10.1016/j.fuel.2014.09.006.
11. K. N. Kerner, J. F. Hanssen and T. A. Pedersen, Anaerobic digestion of waste sludges from the alginate extraction process, *Bioresource technology*, 1991, volume *37*(1), p. 17-24, doi: 10.1016/0960-8524(91)90107-U.
12. J. Choi, J. W. Choi, D. J. Suh, J. M. Ha, J. W. Hwang, H. W. Jung et al., Production of brown algae pyrolysis oils for liquid biofuels depending on the chemical pretreatment methods.

Energy Conversion and Management, 2014, volume *86*, p. 371-378, doi: 10.1016/j.enconman.2014.04.094.

13. A. M. Smith and A. B. Ross, Production of bio-coal, bio-methane and fertilizer from seaweed via hydrothermal carbonisation, *Algal Research*, 2016, volume *16*, p. 1-11, doi: 10.1016/j.algal.2016.02.026.
14. D. C. Elliott, P. Biller, A. B. Ross, A. J. Schmidt and S. B. Jones, Hydrothermal liquefaction of biomass: developments from batch to continuous process. *Bioresource technology*, 2015, volume *178*, p. 147-156, doi: 10.1016/j.biortech.2014.09.132.
15. A. Graiff, D. Liesner, U. Karsten and I. Bartsch, Temperature tolerance of western Baltic Sea Fucus vesiculosus–growth, photosynthesis and survival, *Journal of Experimental Marine Biology and Ecology*, 2015, volume *471*, p. 8-16, doi: 10.1016/j.jembe.2015.05.009.
16. T. H. Pedersen, I. F. Grigoras, J. Hoffmann, S. S. Toor, I. M. Daraban, C. U. Jensen et al., Continuous hydrothermal co-liquefaction of aspen wood and glycerol with water phase recirculation. *Applied Energy*, 2016, volume *162*, p. 1034-1041, doi: 10.1016/j.apenergy.2015.10.165.
17. P. Vauchel, K. Leroux, R. Kaas, A. Arhaliass, R. Baron and J. Legrand, Kinetics modeling of alginate alkaline extraction from Laminaria digitata, *Bioresource Technology*, 2009, volume *100*(3), p. 1291-1296, doi: 10.1016/j.biortech.2008.03.005.
18. A. Friedl, E. Padouvas, H. Rotter and K. Varmuza, Prediction of heating values of biomass fuel from elemental composition, *Analytica Chimica Acta*, 2005, volume *544*(1), p. 191-198, doi:10.1016/j.aca.2005.01.041.
19. A. Keshav, P. Norge and K. L. Wasewar, Reactive extraction of citric acid using tri-n-octylamine in nontoxic natural diluents: part 1—equilibrium studies from aqueous solutions. *Applied biochemistry and biotechnology*, 2012, volume *167*(2), p. 197-213, doi: 10.1007/s12010-012-9682-z.
20. E. D. Obluchinskaya, G. M. Voskoboinikov and V. A. Galynkin, Contents of alginic acid and fuccidan in Fucus algae of the Barents Sea. *Applied Biochemistry and Microbiology*, 2002, volume *38*(2), p. 186-188, doi: 10.1023/A:1014374903448.
21. P. Schiener, K. D. Black, M. S. Stanley and D. H. Green, The seasonal variation in the chemical composition of the kelp species Laminaria digitata, Laminaria hyperborea, Saccharina latissima and Alaria esculenta. *Journal of applied phycology*, 2015, volume *27*(1), p. 363-373, doi: 10.1007/s10811-014-0327-1.
22. X. Liu and X. T. Bi, Removal of inorganic constituents from pine barks and switchgrass. *Fuel Processing Technology*, 2011, volume *92*(7), p. 1273-1279, doi: 10.1016/j.fuproc.2011.01.016.

CYSENI 2017, May 25-26, Kaunas, Lithuania
ISSN 1822-7554, www.cyseni.com

EXPERIMENTAL STUDY ON ASH FUSION CHARACTERISTICS OF AGROMASS AND WOODY BIOMASS

D. Čepauskienė
Lithuanian Energy Institute
Breslaujos st. 3, LT-44403 Kaunas – Lithuania
E-mail: Deimante.Cepauskiene@lei.lt

M. Valantinavičius
Lithuanian Energy Institute
Breslaujos st. 3, LT-44403 Kaunas – Lithuania
E-mail: Mantas.Valantinavicius@lei.lt

ABSTRACT

The use of the biofuel for energy purposes is one of the alternatives to fossil fuels. The increasing demand for biofuels leads to the introduction of non-woody biomass fuels into the market such as herbaceous plants, agricultural waste. The main problem using herbaceous plants and agricultural waste as agrofuels is that it is rich in alkali metals such as potassium and sodium, which react with other ash forming elements (chlorine, silicone, phosphorus, sulphur) and lead to different ash related operational problems.

In this study, chemical composition and melting behavior of ashes produced at 550 ºC were investigated. Two types of wood (spruce, betula pendula), three herbaceous plants (orchard grass, hemp, reed canary grass) and five types of agricultural crops (rye, wheat, buckwheat, canola straws and sunflower seeds) were investigated. Ash melting temperature of samples were determined using a high temperature furnace with a video camera. Ash elemental composition survey was conducted by inductively coupled plasma optical emission spectrometer (ICP-OES). Ash bulk structure were determined using X-ray diffraction (XRD).

Ash fusion characteristics (AFC) of selected agromass types shows that the highest shrinkage starting temperature (SST) was found to be hemps agromass which reaches 1079 °C. This is due to the composition of hemp ashes, because they are rich in calcium and low in potassium and sodium. It was also noticed that initial deformation temperature increases with decreased potassium and went up with increased calcium. The XRD results show that potassium in agromass mainly exists as potassium salts (chlorides, sulphates). Potassium salts have low melting temperatures and cause different ash related operational problems during energy conversion processes.

Keywords: Biomass, Biofuel, Ash, Ash Melting, Agromass, Woody Biomass

1. INTRODUCTION

A growing demand for energy, decreasing reserves of fossil fuel and increasing environmental pollution induce search for alternatives of fossil fuel. One of them is biofuel that could be used for energy needs. Agromass, i.e. agricultural plants, their parts and waste and herbaceous plants of short rotation could be used as alternative for wood to increase consumption of biomass in the energy sector. However, agrofuel made of agromass has the following negative properties: higher ash content, lower ash softening and melting temperatures, bigger content of sulphur, chlorine, alkali and alkaline earth metals. Even insignificant differences of chemical composition of ash can significantly change its melting characteristics [1]. Fly ash resulting from combustion begin to soften, melt and slag on surface under appropriate temperature. Slagging is associated with fly ash deposition and accumulation on heat exchange surfaces of furnace and heat exchanger. This leads to boiler contamination and as result boiler operation efficiency decreases [2].

Potassium (K) is one of the main elements that has the greatest impact on ash melting. Together with silicon (Si) potassium forms silicates that melt under low temperature of approximately 750 °C [3]. Due to high content of potassium not only K silicates but also other compounds of K (chlorides, sulphates, carbonates) can form during combustion. Melting point of these K compounds is low too, i.e. merely 770 °C [4]. Sodium (Na), same as K, reduces ash melting point. K and Na transformation mechanisms in ash are similar. Since effects of K are much higher and content of Na is very low, for this reason Na is not distinguished separately and is attributed to K [5].

This research mostly focuses on determination of chemical properties of ash of selected types of agromass and biomass. Ash fusion characteristics (SST, DT, HT, FT), the main elements (Ca, K, Si, P, Mg, Al, Na) and ash structure have been determined and ash content of each selected type of agromass and biomass has been assessed.

2. MATERIALS AND METHODS

2.1. Samples

Ten different samples of biomass divided into three main groups, i.e. agricultural waste, herbaceous plants and wood have been selected for analysis. Rye, wheat and buckwheat straws and canola straw pellets have been selected as agricultural waste. These products have been chosen because annual amount of this harvest waste is about 3 million tons and only a small part of it is used according to its original purpose (animal litter, feed). Sunflower seeds have been chosen too. In some cases, sunflower seeds are not suitable for food or feed production and such seeds need to be disposed. Pellets of orchard grass and reed canary grass and agromass of hemp have been selected from the group of herbaceous plants. Hemp is characterised by good energy properties that are very similar to wood properties. Two wood species, i.e. spruce and birch (with bark) have been selected for comparison.

2.2. Determination of ash content

Ash content is determined by mass balance after heat air under strict environmental conditions in muffle furnace Nabertherm. Test of each sample is repeated three times. Approximately 1 g of sample that is heated up in the furnace (its temperature shall be gradually raised up to 250 °C) for 30 to 50 minutes is used for determination of ash content. In order volatile substances would evaporate a sample must be kept for 60 minutes under such temperature. Then, a furnace temperature shall be raised up to 550 °C over a period of 30 minutes. Such temperature in the furnace shall be maintained for 120 minutes.

2.3. Ash fusion temperature test

In order to determine ash fusibility all samples are dried in the furnace under low temperature of 105 °C, pulverized and eventually ash is made of dry biomass under temperature of 550 °C. Ash obtained is pulverized with a pestle to obtain particles with a size of less than 0,075 mm. A moistened ash powder is used to form cylindrical ash samples with a size of 5×5 mm. Samples obtained are heated in ash fusion furnace Carbolite. A furnace temperature is raised up to 550 °C. Then temperature is gradually raised 5 °C/min and photos are made every interval of 2 °C. Records are made of temperatures under which a sample phase changes. The main four ash melting phases are: SST – shrinkage starting temperature or softening temperature, DT – deformation temperatute, HT – hemisphere temperature, FT – fusibility temperature.

2.4. Major elements determination in ash and biomass

Approximately 1 mg of biofuel (0,1 mg of ash) sample mineralized with H_2O_2 (30%), HNO_3 (65%) and HF (40%) is used for determination of the main elements. Temperature in mineralization device over 15 minutes is obliquely raised up to 190 °C. Such temperature is kept for 20 minutes.

When samples cool down to room temperature H_3BO_3 (4%) is added to vessels to neutralize HF. Samples are re-heated by raising temperature up to 150 °C. Such temperature is maintained for a period of 15 minutes. Concentration of elements is determined using ICP-OES.

2.5. X-ray diffraction XRD analysis

Volumetric structure of ash is determined using XRD BRUKER AXS DIFFRAKTOMETER D8 diffractometer. Each sample is scanned for 45 minutes using Θ–2Θ modification in the interval 20°–70°. A source of X-ray – CuKα1. Compounds are identified with help of EVA Search-Match program from PDF-2 database.

3. RESULTS AND DISCUSSION

Accomplished analysis of ash content of wood and agromass samples revealed that buckwheat and canola straws have the highest ash content, respectively 6.4% and 6.5% (Fig. 1).

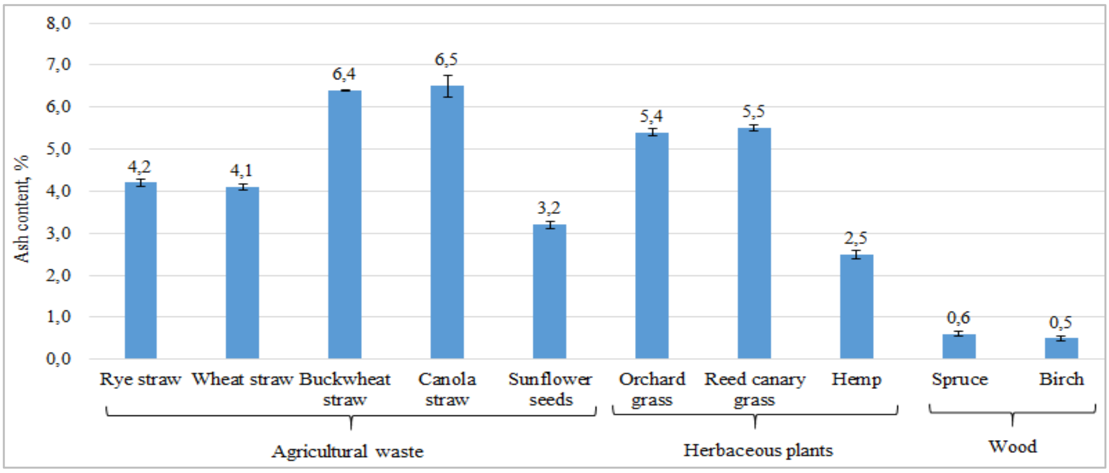

Fig. 1. Ash content (% db.) in wood and agromass

A determined ash content of wheat and rye was more than 2% lower (rye straws 4.2%, wheat straws 4.1%). A determined ash content of sunflower seeds was the lowest of all agricultural waste, i.e. 3.2%. Ash content of herbaceous plants is also similar to ash content of straw agromass (orchard grass 5.4%, reed canary grass 5.5%). However, ash content of hemp is the most divergent in this group because it is more than twice lower (2.5%) than ash content of other herbaceous plants. The lowest ash content has been determined in wood biomass. Ash content of spruce is 0.6%, ash content of birch is 0.5%. Ash content mostly depends on a content of non-combustible components that are present in the fuel. Their content is influenced by many factors: genetic plant properties, environmental factors, physiological and morphological characteristics. It has been determined that ash content also depends on plant parts used for production of biofuel. A test with four species of perennial plants (*sinensis* X *Giganteus Greef* & *Deuter*, *Arundo donax* L., *Cynara cardunculus* L. and *Panicum virgatum* L.) and two species of annual crops (sweet and fibre sorghum, *Sorghum bicolor Moench*) revealed that leaves in all cases are characterized by the biggest ash content. Almost twice bigger ash content compared to straws and almost 50% bigger ash content compared to reproductive organs has been determined [6]. The following factors influence ash content: a soil type, harvesting season, climate, type of fertilizer, its concentration and frequency of fertilization, impurities that fall in during preparation and transportation of fuel.

The four conventional ash fusion temperatures of all samples were compared in Fig. 2. Analysis of biomass and agromass ash fusibility revealed the highest ash fusibility temperature (FT) of the following products: buckwheat straws – 1549 °C, wood, i.e. spruce and birch respectively 1531 °C and 1526 °C. Canola straw ash fusibility temperature (FT) also exceeds 1500 °C. However, it should be emphasized that buckwheat and canola straw ash softening temperatures (SST) are very low, respectively 698 °C and 722 °C.

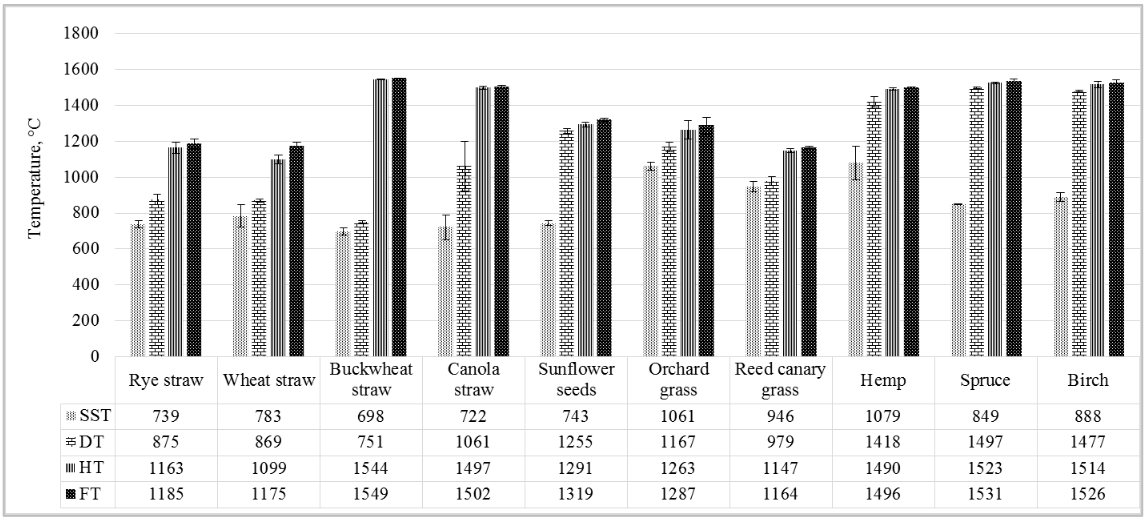

	Rye straw	Wheat straw	Buckwheat straw	Canola straw	Sunflower seeds	Orchard grass	Reed canary grass	Hemp	Spruce	Birch
SST	739	783	698	722	743	1061	946	1079	849	888
DT	875	869	751	1061	1255	1167	979	1418	1497	1477
HT	1163	1099	1544	1497	1291	1263	1147	1490	1523	1514
FT	1185	1175	1549	1502	1319	1287	1164	1496	1531	1526

Fig. 2. The ash fusion temperature of wood and agromass

When temperature is above ash softening temperature, then ash becomes very sticky and this results in slagging [7]. Hemp is considered to be one of the most potent herbal plants used in production of agrofuel because its combustion properties are very similar to combustion properties of wood. Ash softening temperature (SST) of hemp is higher than the same of wood, i.e. 1079 °C. Ash completely melts when temperature rises up to 1496 °C. Ash softening temperature (SST) of reed canary grass is 946 °C. However, ash begins to melt in the temperature of 1164 °C. Ash softening temperature (SST) of orchard grass is very high too, i.e. 1061 °C. It means that slagging does not manifest under lower temperature and boiler operation efficiency does not decrease. Ash softening temperature (SST) of sunflower seeds is very similar to ash softening temperature (SST) of other agricultural waste, i.e. 743°C. Use of fuel of such agromass is questionable because a process of slagging will start under very low temperature.

Ash fusion temperatures and slag formation depend on a component of the lowest fusibility temperature, distribution of elements in fuel and combustion conditions, and duration of combustion process because as longer fuel/ash is kept in high temperature, as more favourable are conditions for slagging [1]. Ash fusibility temperature also depends on temperature of biomass combustion. Ash fusibility characteristics of four types of biomass (ash, corn straw, Bermuda grass, bamboo) have been determined. Fusibility characteristics have been determined after biomass has been burned in temperature of 600 ºC and 815 ºC and influence on ash fusibility temperature has been observed. It has been found out that ash fusibility temperature is higher when biomass is burned in temperature of 815 ºC instead of 600 ºC. When biomass is burned in a higher temperature, then a higher ash fusibility temperature is obtained because substances of low fusibility temperature such as K and Cl evapotates and compounds of high fusibility temperature form [8].

Elemental composition of biomass and agromass has been determined using inductively coupled plasma optical emission spectrometer. Elemental composition of biomass/agromass and ash of nine samples has been determined. The results of analysis are shown in Table 1 and Table 2. The main elements that dominate in ash have been identified: Ca, K, Si, P, Mg, Al, Na.

Table 1. Major elements content (%) in biomass and agromass

	Ca	**K**	**Si**	**P**	**Mg**	**Al**	**Na**
Birch	0.14	0.05	0.03	0.25	0.02	–	0.22
Spruce	0.14	0.04	0.03	0.24	0.01	–	0.21
Reed canary grass	0.24	1.89	0.25	0.43	0.10	0.01	0.25
Hemp	0.70	0.17	0.31	0.31	0.08	0.05	0.24
Buckwheat straw	0.99	1.93	n/d	0.41	0.08	0.01	0.24
Wheat straw	0.26	1.27	0.85	0.35	0.09	0.02	0.24
Canola straw	1.15	2.08	0.27	0.36	0.14	0.03	0.30
Rye straw	0.34	0.98	0.90	0.36	0.10	0.04	0.27
Sunflower seeds	0.15	1.33	0.17	0.60	0.24	–	0.29

Results obtained show that the biggest content of Ca has been determined in canola and buckwheat straws, respectively 1.15% and 0.99%. However, it should be noted that the biggest concentrations of K have been also determined in these samples of agromass. The lowest content of all elements analysed have been determined in wood. Elemental composition of agromass of hemp is most similar to elemental composition of wood. However, content of Ca, Si, Mg and Al is bigger. Agricultural waste contains a lot of K, P and Na. Herbaceous plants (reed canary grass) have higher concentrations of K and P.

Table 2. Major elements content (%) in biomass and agromass ash

	Ca	**K**	**Si**	**P**	**Mg**	**Al**	**Na**
Birch	31.21	12.72	0.86	1.62	3.43	0.18	0.53
Spruce	29.43	12.78	1.56	1.35	2.39	0.33	0.55
Reed canary grass	4.77	45.71	7.89	2.80	1.85	0.17	0.47
Hemp	22.16	18.31	0.16	0.25	2.56	0.01	0.23
Buckwheat straw	19.22	41.86	n/d	2.66	1.38	0.16	0.60
Wheat straw	6.04	35.94	18.14	2.16	1.90	0.41	0.49
Canola straw	19.80	37.41	4.55	1.56	2.12	0.52	0.80
Rye straw	6.54	24.22	20.75	1.73	2.00	0.83	0.52
Sunflower seeds	5.02	47.62	0.31	10.26	3.03	0.05	1.11

As shown in the Table 2, ash of all samples have much higher concentrations of elements compared to biomass/agromass. A comparison of all results obtained shows that wood ash dominated by Ca and Mg is the most distinctive. Herbaceous plants (reed canary grass) contain mostly K, Si and P. Ash of sunflower seeds are the most distinctive among agricultural products. They had especially high concentrations of K, P, Mg and Na. Straw ash contains mostly K, Si and Al. Hemp ash is the most distinctive among all analysed agromass ash samples. Elemental composition of hemp ash is mostly similar to wood ash composition.

Several chemical changes of mineral substances that are present in the ash take place during combustion in high temperature. Silicon melts partially or completely and reacts with other elements that are present in the ash and first of all forms silicates of alkali metals (K and Na). Dissociation of carbonates, chlorides and other salts takes place. Alkali metals and heavy metals become volatile and evaporate [9]. To find out the reasons of ash melting at a certain temperature it is necessary to determine ash structure and to identify components that form ash.

Ash forming compounds have been identified using a method of X-ray diffraction. Analysis results indicating the qualitative presence of crystalline minerals in each ash and melted ash samples were listed in Table 3 and Table 4. It has been found out that ash does not have a clear crystal structure and oxides, silicates, carbonates, sulphates, and phosphates are the main components that form during combustion. Ash forming compounds are largely very different between selected groups of biomass and agromass. However, three main components that are most often found in biomass that is burned in temperature of 550 °C have been identified: calcium carbonate ($CaCO_3$), potassium sulfate (K_2SO_4) and potassium chloride (KCl).

Table 3. X-ray diffraction analysis (XRD) results for ash of wood and agromass

Ash	
Herbaceous plants	
Orchard grass	KCl, $Ca_4O(PO_4)_2$, SiO_2, $KCaPO_4$, $Na_2Ca_3Si_2O_8$, $KMg_2Al_{15}O_{25}$
Hemp	$CaCO_3$, $Ca_4O(PO_4)_2$, SiO_2
Reed canary grass	KCl, K_2SO_4, $Ca_4O(PO_4)_2$, SiO_2, $KCaPO_4$
Agricultural waste	
Rye straw	$CaCO_3$, $K_2S_4O_6$, SiO_2, $MgSiO_3$
Canola straw	KCl, $CaCO_3$, K_2SO_4, $K_2Ca(CO_3)_2$, Ca_2SiO_4
Buckwheat straw	KCl, $CaCO_3$, K_2SO_4, $K_2S_2O_6$, $K_2Ca(CO_3)_2$
Wheat straw	KCl, K_2SO_4, $KCaPO_4$, SiO_2
Sunflower seeds	KCl, K_2SO_4, MgO, K_2CS_3, NaS_2, CaP_4O_{11}
Wood	
Birch	$CaCO_3$, K_2SO_4, $K_2Mg(PO_3)_4$, KMnP, $MnSO_4$
Spruce	$CaCO_3$, K_2SO_4, $K_2Mg(PO_3)_4$, KMnP, $MnSO_4$

There is a little difference between ash structure of the same group‘s examples. Identical compounds that form wood (spruce and birch) ash have been determined. $CaCO_3$, K_2SO_4, potassium magnesium phosphate ($K_2Mg(PO_3)_4$), potassium manganese phosphide (KMnP) and manganese sulphate ($MnSO_4$) are the main components found in spruce and birch ash. Sunflower seed ash is the most distinctive by its ash structure among all types of agricultural waste. Compounds of potassium thiocarbonates (K_2CS_3), sodium sulphide (NaS_2) that have been found out exclusively in this ash sample have been identified. Very similar straw ash structure has been determined. The dominant components are KCl, $CaCO_3$ and K_2SO_4, whereas a vast majority of other compounds is dominated by K. The biggest problem is that agromass is dominated by K. During combustion of agromass K is converted into a gaseous form and forms gaseous compounds (KCl, K_2SO_4 and potash (K_2CO_3)). These gaseous compounds can condense on heat transfer surfaces and form sticky formations. As a result, heat transfer efficiency can decrease. On the other hand, a significant proportion of potassium remains in the bottom ash and can react with Si and form compounds of low melting point, and this can result in ash sintering and slagging [10]. Hemp ash is the most distinctive among herbaceous plants. The following three main compounds have been identified: $CaCO_3$, calcium oxophosphate ($Ca_4O(PO_4)_2$), silica (SiO_2) have been identified. Ash of other herbaceous plants also contained KCl, but no $CaCO_3$ has been identified in them. All other identified compounds largely coincide and are dominated by K, Ca and P.

Analysis of melted ash structure (Table 4) revealed that silicates, aluminates and oxides are the main components found in melted ash. Results show that aluminium oxide (Al_2O_3) and spinel ($MgAl_2O_4$) are compounds that were most often identified in melted ash of selected biomass and agromass. In this case it is also necessary to consider that ash was melted on porcelain plates. Therefore, peaks of aluminium oxide (Al_2O_3) and silica (SiO_2) seen in difractograms obtained may result from a tray.

Ash structure of melted herbaceous plants is different: melt of orchard grass ash is dominated by compounds with K, melt of reed canary grass ash is dominated by Mg, whereas hemp ash contains mostly Ca compounds. A structure of melted ash of agricultural waste is even more diverse. However, two main compounds, i.e. Al_2O_3 and $MgAl_2O_4$ that are typical for this entire group of agromass can be distinguished. Al_2O_3 and many other compounds with Ca have been identified in wood ash melt. It should be noted that a structure of melted ash of hemp is very similar to ash structure of wood biomass.

Table 4. X-ray diffraction analysis (XRD) results for melted ash of wood and agromass

Melted ash	
Herbaceous plants	
Orchard grass	Al_2O_3, $KCaPO_4$, SiO_2, $K_2Si_4O_9$, $K_{0,85}Al_{0,85}Si_{0,15}O_2$, KP_6O_{18}
Hemp	$MgAl_2O_4$, $Ca_2Al_2SiO_7$, $CaMg_2Al_6O_{12}$, $CaNa_3Al(P_2O_7)_2$, $CaAl_4O_7$
Reed canary grass	Al_2O_3, $MgAl_2O_4$, Si
Agricultural waste	
Rye straw	Al_2O_3, Si
Canola straw	$MgAl_2O_4$, $Ca_2Al_2SiO_7$, $Ca_3(PO_4)_2$
Buckwheat straw	Al_2O_3, $Ca_2Al_2SiO_7$, $CaAl_{12}O_{19}$, , $KAl_3Si_3O_{11}$, $MgAl_2O_4$, $KAlP_2O_7$
Wheat straw	Al_2O_3, $MgAl_2O_4$, $KAlSi_2O_6$, Si
Sunflower seeds	Al_2O_3, $MgAl_2O_4$, , MgO, Al_4C_3, $MgAl_2C_2$
Wood	
Birch	Al_2O_3, Al, $Ca_3Si_2O_7$, , $Al(PO_3)_3$
Spruce	Al_2O_3, $MgAl_2O_4$, $Ca_5(PO_4)_2SiO_4$, SiO_2, $Ca_3Al_2P_2Si_2O_{15}$, $Ca_3Al_2(SiO_4)_3$

New compounds often form and are identified during combustion process when chemical reactions of compounds that are present in ash take place. State of aggregation of some ash elements changes, they become gaseous and are removed. Compounds of higher melting point are found in melted ash. Some newly formed compounds are more resistant to high temperature. Other part of them continues to participate in the melting process. It should be noted that the main components identified in slag are Si, Al, Ca, K and O and the main components are $Ca_2MgSi_2O_7$, $KAlSiO_4$, SiO_2 [5].

4. CONCLUSIONS

1. Significantly lower ash content forms during wood combustion compared to agromass combustion. Ash content of canola and buckwheat straw is the biggest, respectively 6.4% and 6.5%. Ash content of both spruce and birch is more than ten times lower, respectively 0.6% and 0.5%.
2. Orchard grass and hemp ash softening temperatures are the highest, respectively 1061 °C and 1079 °C, whereas ash fusibility temperatures are respectively 1287 °C and 1496 °C. Buckwheat straw ash begins to soften first and at the lowest temperature of 698 °C, although its fusibility temperature is even 1549 °C. In this case a slagging process begins at relatively low temperature.
3. Wood ash is dominated by Ca and Mg, ash of herbaceous plants (reed canary grass) is dominated by K, Si and P, straw ash is dominated by K, Si and Al. Sunflower seed ash is the most distinctive as it contained very high concentrations of K, P, Mg and Na.
4. A fuel made of agromass of hemp is the most suitable for burning. Ash properties of this fuel are the most similar to properties of wood fuel ash.

REFERENCES

1. PATEL, B., GAMI, B. Biomass Characterization and its Use as Solid Fuel for Combustion. *Iranica Journal of Energy & Environment*, 2012, Vol. 3, No. 2, p. 123-128.
2. TEIXEIRA, P., LOPES, H., GULYURTLU, I., LAPA, N., ABELHA, P. Evaluation of slagging and fouling tendency during biomass co-firing with coal in a fluidized bed. *Biomass and Bioenergy*, 2012, Vol. 39, p. 192-203.
3. THY, P., JENKINS, B. M., GRUNDVIG, S.,SHIRAKI, R., LESHER, C. E. High temperature elemental losses and mineralogical changes in common biomass ashes. *Fuel*, 2006, Vol. 85, p. 783-795.

4. WANG, L., HUSTAD, J. E., SKREIBERG, Ø., SKJEVRAK, G., GRØNLI, M. A critical review on additives to reduce ash related operation problems in biomass combustion applications. *Energy Procedia*, 2012, Vol. 20, p. 20-29.
5. NIU, Y., TAN, H., HUI, S. Ash-related issues during biomass combustion: Alkali-inducted slagging, silicate melt-induced slagging (ash fusion), agglomeration, corrosion, ash utilization, and related countermeasures. *Progress in Energy and Combustion Science*, 2016, Vol. 52, p. 1-61.
6. MONTI, A., DI VIRGILIO, N., VENTURI, G. Mineral composition and ash content of six major energy crops. *Biomass and Bioenergy*, 2008, Vol. 32, p. 216-223.
7. VRUBLIAUSKAS, S., PEREDNIS, E. Biomasės ir iškastinio kuro mišinių deginimo ypatumai. *Energetika*, 2010, *Vol.* 56, p. 247-253.
8. FANG, X., JIA, L. Experimental study on ash fusion characteristics of biomass. *Bioresource Technology*, 2012, Vol. 104, p. 769-774.
9. NUNES, L. J. R., MATIAS, J. C. O., CATALAO, J. P. S. Biomass combustion systems: A rewiew on the physical and chemical properties of the ashes. *Renewable and Sustainable Energy Reviews*, 2016, Vol. 53, p. 235-242.
10. ELLED, A. L., DAVIDSSON, K. O., AMAND, L. E. Sewage sludge as a deposit inhibitor when co-fired with high potassium fuels. *Biomass and Bioenergy*, 2010, Vol. 34, p. 1546-1554.

CYSENI 2017, May 25-26, Kaunas, Lithuania
ISSN 1822-7554, www.cyseni.com

EXPERIMENTAL STUDY OF THE FORMATION OF CARBON SORBENTS FROM GRAIN HUSKS

A. N. Karnitski
The Institute of Power Engineering
National Academy of Sciences of Belarus
15/2 Akademicheskaya Street, 220072 – Minsk, Republic of Belarus
E-mail: Alex_Karnitski@mail.ru

ABSTRACT

The report gives preliminary results of the experimental study of the formation of carbon sorbents containing some amounts of common salt. They were established in experimental studies performed by using a muffle furnace of the Institute of Power Engineering of the National Academy of Sciences of Belarus. Not pre-treated samples of grain husks as well as samples pre-soaked in a salt solution were studied in the temperature range from 200 to 500 ^{o}C. The not pre-treated samples of grain husks had following parameters: a bulk density of 200 kg/m^3, humidity of 10.8%, ash content of 2.5%.The established results indicate that grain husks soaking in saline demonstrate higher yield of the sorbent mass over the entire range of temperatures studied. The maximal yield of sorbents in case of not pre-treated dry samples (humidity 10.8%) as well as in case of pre-soaked samples was achieved at a temperature of about 300 ^{o}C. Calorific value of sorbent samples obtained during pyrolysis of dry grain husks, pre-soaked in salt solution were also studied in performed experiments.

Keywords: carbon sorbents, pyrolysis, grain husks

1. INTRODUCTION

Carbon sorbents have been used in various industrial processes, such as neutralization of liquid wastes and gas emissions as well as in medicine, chromatography, etc. [1].

Coal, lignite, peat, various types of biomass, such as wastes of vegetable production, coconut shells, etc. have been used for their production [2, 3].

Some researchers are considering biomass as source of a bio-fuel. Different types of biomass including rice husks [4], melon seed husks [5] etc. were considered for reaching this aim.

Calorific values, elemental composition, proximate analyses and thermal kinetics of are examined as a rule in experimental studies of biomass. The aims of this and other studies were to investigate the pyrolysis process as well as composition of products, their thermochemical characteristics, elemental composition etc.

The present work pursued another goal, which was to study the formation of carbon sorbents containing a certain amount of sodium chloride. This can be achieved by pyrolysis of biomass pre-treated with aqueous solution of common salt. Such carbon sorbents can be used then as additives to feed of animals. Grain husks are one of the most suitable types of biomass, as it is very easy to impregnate them with a solution of common salt and in addition it is abundant in Belarus.

2. RESEARCH METHODOLOGY

This work was performed using a muffle furnace (SNOL 7,2 / 1300, 3.5 kW, Lithuania) of the Institute of Power Engineering of the National Academy of Sciences of Belarus. Experiments were carried out under isothermal conditions at temperatures of 200, 300, 400 and 500 °C.

Husk samples without any treatment (first series), as well as samples, presoaked in a solution of 2.2% NaCl salt (second series) were studied experimentally.

Grain husk has the following characteristics: bulk density 200 kg/m^3, humidity of 10.8%, ash content of 2.5%.

Grain husks were loaded into ceramic containers **a**, **b** and **c** (Fig. 1). The container **a** was covered with a layer of fiberglass. The container **b** was covered with a layer of fiberglass and had a ceramic tile over the fiberglass. The container **c** was covered with a layer of other insulation material and had a ceramic tile as an auxiliary cover on a top.

a **b** **c**

Fig. 1. Samples in container and their covers

Containers with samples were placed into the muffle furnace and were kept there at an appropriate temperature during 5 hours. This led to an increase in the pressure in the furnace chamber and possibly to an influence on the sorbent formation process. A more thorough study of this influence is planned for the future after the acquisition of the necessary equipment.

In a second series of experiment samples were soaked previously for 3 days in an aqueous solution of NaCl 2.2%. After this treatment, the excess of solution was decanted and samples were placed into containers.

The purpose of this treatment was to study the effect of soaking on the structure of the product produced in the process of husk pyrolysis.

In both the first and second series of experiment a dry weight of samples did not change and was 20, 17 and 9 grams for the containers a, b and c respectively.

The ash and moisture contents of samples of grain husks were determined in the work. The humidity of samples was determined by maintaining them in the muffle furnace at 120 ^{o}C for 3 hours. The ash content was determined while maintaining the sample in a muffle furnace at 650 ^{o}C for 2 hours. Table 1 shows humidity and ash content not pre-treated samples.

Table 1. Humidity and ash content of husk samples

	Humidity W, %	**Ash content A, %**
Husk samples	10.8	2.5

The humidity and ash content were evaluated by using formules:

$$W^a = \frac{m_s - m_s'}{m_s} \cdot 100\% \quad (1)$$

$$A^a = \frac{m_s - m_s'}{m_s} \cdot 100\% \quad (2)$$

where W^a – humidity of samples, %;

A^a – ash content of samples, %;

m_s' – mass of sample after pyrolysis, g;

m_s – mass of dry matter at the beginning of experiment, g.

3. RESULTS AND DISCUSSION

Pyrolyzed samples of grain husks are shown in Fig. 2 and 3. As can be seen, the structure and color of the formed product depends on the conditions of pyrolysis.

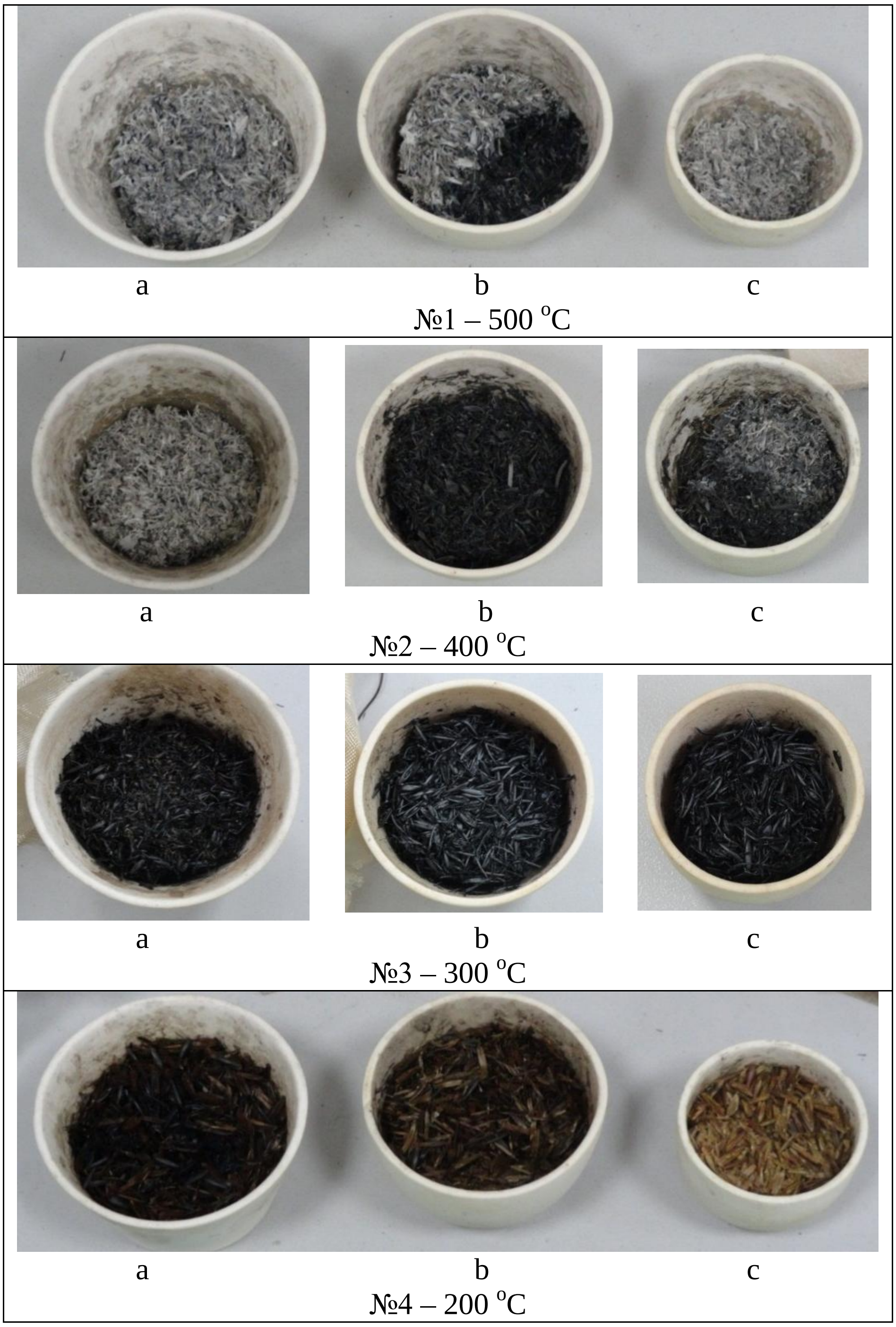

Fig. 2. Products of pyrolysis of not soaked samples

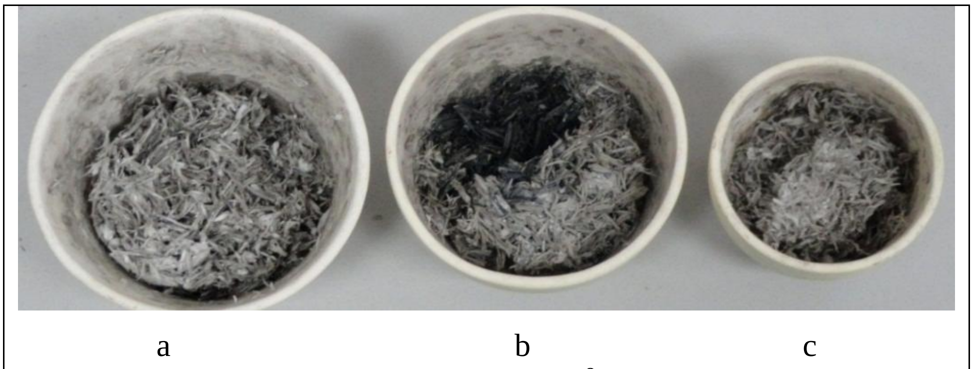

№5 – 500 ^oC

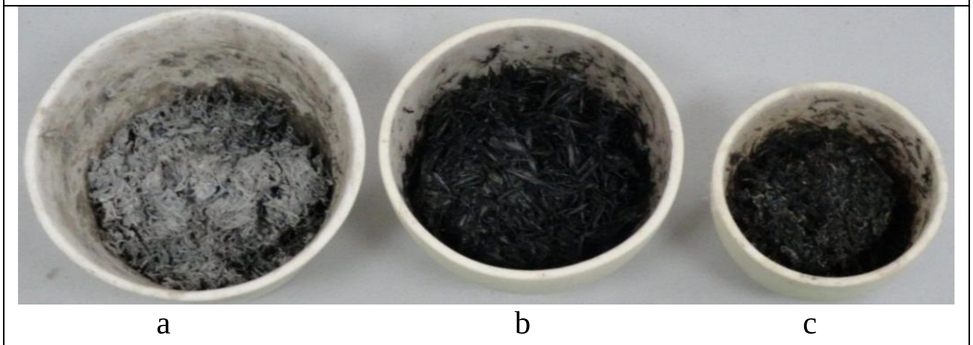

№6 – 400 ^oC

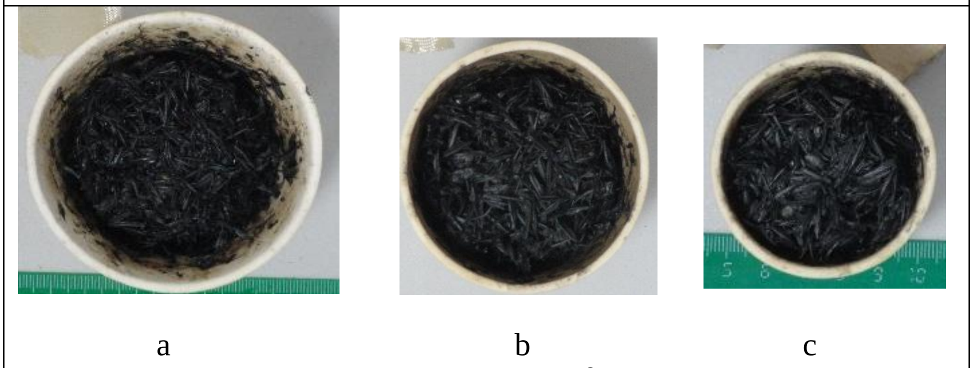

№7 – 300 ^oC

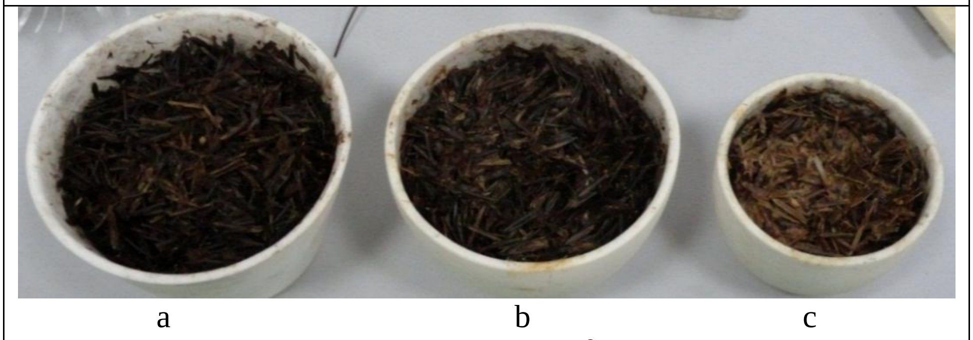

№8 – 200 ^oC

Fig. 3. Products of pyrolysis of presoaked samples

Experimental results of the first set (m'_s, m_s, η') are given in Table 2 and in Fig. 4.

Table 2. Experimental results established with not presoaked samples

Temperature	**№4 – 200 °C**			**№3 – 300 °C**			**№2 – 400 °C**			**№1 – 500 °C**		
Containers & covers	**a**	**b**	**c**	**a**	**b**	**c**	**a**	**b**	**c**	**a**	**b**	**c**
m_s, g	20	17	9	20	17	9	20	17	9	20	17	9
m'_s, g	12.58	13.52	7.7	3.12	6.03	3.1	0.82	4.3	1.12	0.48	3.2	0.28
η', %	62.9	79.5	85.6	15.6	35.5	34.4	4.1	25.3	12.4	2.4	18.8	3.1

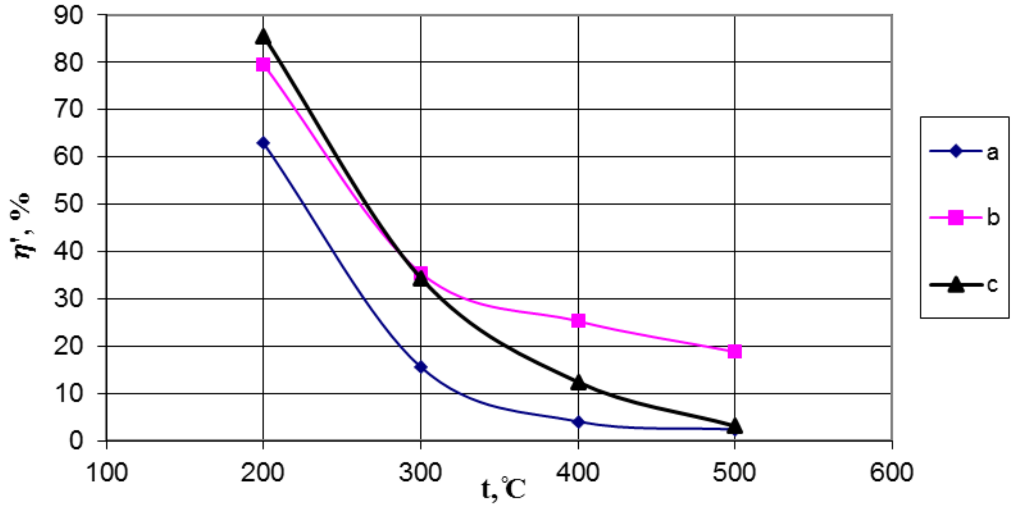

Fig. 4. Yield of sorbent formed by pyrolysis of not presoaked samples

Values of η' in Table 2 and Fig. 4 are calculated by using the formula:

$$\eta' = \frac{m_s'}{m_s} \cdot 100\% \tag{3}$$

Results of the second series of experiments (samples of grain husks soaked in saline solution) are presented in Table 3 and in Fig. 5.

Values of η'' in Table 3 and Fig. 5 are calculated from the formula:

$$\eta'' = \frac{m_s''}{m_s} \cdot 100\% \tag{4}$$

where m_s'' – is a final mass of presoaked sample.

Table 3. Experimental results with the presoaked sample

Temperature	**№8 – 200 °C**			**№7 - 300 °C**			**№6 – 400 °C**			**№5 – 500 °C**		
Containers & covers	**a**	**b**	**c**	**a**	**b**	**c**	**a**	**b**	**c**	**a**	**b**	**c**
m_s, g	20	17	9	20	17	9	20	17	9	20	17	9
m''_s, g	15.56	13.92	7.64	5.38	6.92	3.7	1.72	5.16	1.46	0.66	3.54	0.62
η'', %	77.8	81.9	84.9	26.9	40.7	41.1	8.6	30.4	16.2	3.3	20.8	6.9

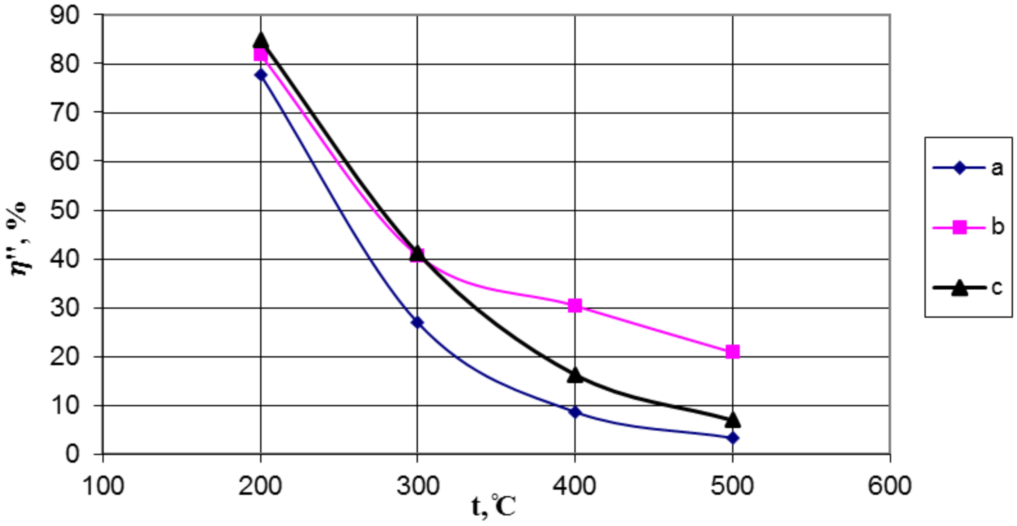

Fig. 5. The yield of sorbent formed by pyrolysis of presoaked samples

As follows from data presented in Table 2 and 3 as well as in Fig. 4 and 5, the weight of the final product depends on the temperature of pyrolysis as well as the conditions of heat insulation of containers.

In accordance with these data the yield of sorbent mass decreases with increasing temperature. This pattern is shown for both normal and presoaked samples. The maximum output of the sorbent is observed at a temperature of 200 ^{o}C. However, the visual characteristics of sorbents formed at this temperature indicate their poor quality that makes them unsatisfactory as additives to animal feed. For example, as can be seen from Fig. 2 and 3 samples formed at low temperature contain not pyrolysed fractions of grain husks. This is evidenced by the visual characteristics of the product produced at this temperature (brown-brown color of the product, its loose structure and the presence of material that was not pyrolysed). The optimum temperature at which the structure is provided as required for sorbents and a satisfactory amount of product in accordance with the data of this work is achieved at the temperature about 300 ^{o}C.

Comparison of the data presented in Tables 2, 3 and Fig. 4, 5 shows that the output of the sorbent mass in case of previously soaked husk is higher than in case of normal samples of husks.

It was found also that conditions of isolation influence the yield of product. According to established results, the weight of the product formed in containers covered additionally with ceramic tiles is higher than in experiments in which the insulation container carried only by fiberglass. This effect was observed for normal samples and for samples presoaked in salt solution.

Caloric values were determined by using a bomb calorimetry for some of sorbent samples obtained in the present studies. Results of such measurements are given in Table 4.

Table 4. Calorific value of the sorbent

Sample	**№1, 500 ^{o}C**	**№3, 300 ^{o}C**	**№4, 200 ^{o}C**	**№7, 300 ^{o}C**
Q, kJ/kg	26640	24603	19103	22587

The data in this table show that increasing the pyrolysis temperature leads to an increase in calorific value of the pyrolysis product. In was found that the calorific value of the product obtained from not soaked sample of husk was higher the calorific value of the product from previously soaked samples of husk. This difference appears to be due to the fact that the final product of pyrolysis of samples of previously soaked husk consists additionally some quantitates of sodium chloride. This leads to a decrease in carbon content and therefore to reducing the calorific value of the product of pyrolysis. However, it is possible that this difference is due to some other reason.

To clarify this issue, additional studies were conducted in which the formation of the sorbent has been studied from samples of husk presoaked in 2.2% – NaCl solution as well as from samples of husk pre-soaked in pure water.

In these experiments samples of husk weighing 7 grams were presoaked in 2.2% solution of NaCl and in pure water.

In the first case, the mass of solution was equal 40 g. It containing 39.12 grams of water and 0.88 grams of salt. After this operation the excess of solution was not decanted.

In the second case, samples weighing 7 grams husks soaked in pure water. Water weight was 39.12 grams as in the case of using 2.2% NaCl solution.

In order to improve the accuracy of the final results in both cases pre-soaked samples were placed in three identical containers and were dried in a muffle furnace for 4 hours at 150 °C. After this they were kept during 5 hours at the temperature 300 °C for performing of the pyrolysis process. Table 5 shows results established in these experiments.

Table 5. Comparison of pre-soaking in pure water and in 2.2% NaCl solution

	Samples presoaked in 2.2% NaCl solution			**Samples presoaked in pure water**		
m^*_s, g	1.68	1.70	1.76	1.52	1.56	1.64
η*, %	24.00	24.29	25.14	21.71	22.29	23.43
<η*>, %	24.48			22.48		

Here, m^*_s – final mass of sample without NaCl, g;

η* – mass yield without mass of NaCl, %;

<η*> – mass yield without NaCl, %.

The data in Table 5 show that the sorbent mass yield of product obtained from husk previously soaked in saline solution is higher than in the case of samples soaked in pure water.

Standard deviations of sorbent mass yields were also assessed for these series of experiments. This was done by using the following formula:

$$S = \sqrt{\frac{\sum_{i=1}^{n}\left(X_i - \overline{X}\right)^2}{(n-1)}} \qquad (5)$$

where S – standard deviation,

n – number of measurements,

X_i – results of the its measurements,

$\overline{X}$ – arithmetic average value of X_i.

It was found for samples pre-soaked in pure water the value of S equal to 0.873 and for samples pre-soaked in the 2.2% NaCl solution equal to 0.595.

4. CONCLUSIONS

- Experimental study of presoaked and not presoaked samples of husk have been conducted at isothermal condition at temperatures 200, 300, 400 and 500 °C.
- It was found that the pyrolysis temperature about 300 °C is optimal for producing of sorbents having necessary quality.
- The calorific value of sorbents obtained from husk increases with the temperature of pyrolysis and is about 26.000 kJ/kg at 500 °C.
- Presoaking of husk in the 2.2% NaCl solution increases the yield of sorbent.

REFERENCES

1. BELYAEV, E. Preparation and use of wood-based activated carbons for environmental purposes. *Khimiya rastitel'nogo syr'ya*, 2000, No. 2, p. 5–15.
2. KUMAR, M., GUPTA, R.C. *Energy Sources*, 1998, Vol. 20, No. 7, p. 575–589.
3. OLONTSEV, V., BORISOVA, I., SAZONOVA, E. Pyrolysis of coconut shells for the manufacture of carbon sorbents. *Khimiya Tverdogo Topliva*, 2011, No. 1, p. 47–52.
4. CHEN-PEI HSU, AN-NI HUANG, HSIU-PO KUO. Analysis of the Rice Husk Pyrolysis Products from a Fluidized Bed Reactor. *Procedia Engineering*, 2015, 102 (2015), p. 1183–1186.
5. NYAKUMA, B., Pyrolysis kinetics of Melon (Citrullus colocynthis L.) seed husk, arXiv preprint arXiv:1506.05419, 2015.

CYSENI 2017, May 25-26, Kaunas, Lithuania
ISSN 1822-7554, www.cyseni.com

INVESTIGATION OF PARTICULATE MATTER EMMITED FROM SMALL AND MEDIUM SCALE BOILERS SIZE DISTRIBUTION

V. Zaleskas, N. Pedišius
Lithuanian Energy Institute
Breslaujos st. 3, LT-44403 – Lithuania
E-mail: vladas.zaleskas@lei.lt

ABSTRACT

Strict limits are established for emissions from medium and large sized boilers and some EU countries are limiting PM_{10} emissions from small scale boilers and heating appliances as well. Emissions can be reduced by improving on the boiler design, but this way of reduction has it's limitations and of course, for existing boilers, which often exceed admissible limits, another solution – precipitation devices like electrostatic precipitators (ESP) or cyclones has to be used. Collection efficiency of the precipitators depend on their characteristics, such as geometry or voltage for ESP, but equally strongy depend on particulate matter. Precipitation efficiency usually is lower the smaller the particles are, also it depends on concentration of PM and even electric resistance in case of ESP. Thus it is important to obtain particle size distributions from emissions as well as precipitators and cleaned gases, which is the objective of this paper. Samples of PM were taken from multicyclones installed after 8 and 12 MW power boilers and distributions were very similar with two peaks at (0.2 to 0.3) μm and (4 to 7) μm. Another set of samples were taken before, from and after ESP of water heating boiler firing shale. Peak at (0.2 to 0.3) μm was observed in the three cases. All samples were analysed using PM spectrometer Promo 3000 H to obtain these PM size distributions.

Keywords: Particulate matter; particle size distribution; ESP

1. INTRODUCTION

Biofuel use as a renewable energy source is considered cleaner alternative to other types of fuel as gas or coal [1]. Especially when CO_2 emissions isn't considered as pollution if the amount of biofuel burnt isn't more than grown. Main disadvantage though, is pollution with particulate matter (PM). Higer PM emissions still in case of small scale boilers. PM pollution can cause health problems depending of the size of the particles. The smaller the particles the easier they get into respiratory system and deposit in lungs [2].

A number of factors determines the efficiency of precipitators. Namely, ESP performanse depends on dust density, because the higher dust density the more influence particle space charge has on electrohydrodynamic secondary flow and turbulence [3]. Electrical resistance is also very important. If it is too low then precipitated particles may give their charge to the wall and rejoin the flow. If it is too high, then high resistance layer of precipitated particles will affect performance of the ESP.

Not the least of the mentioned factors is particle size. Multicyclones most effective precipitate particles larger than 2 μm [4] and ESP are known to collect smaller particles much better, but even their efficiency steadily drops the smaller the particles become [5].

Extensive investigation was done by Saxony Anhalt State Environmental Protection Agency and University of Stuttgart, Institute of Process Engineering and Power Plant Technology [6]. Over a 100 different measurement campaigns performed, PM distributions determined for various plants and combustion units firing wood, coal, oil. The number includes measurements of PM in industrial production factories like cement production, metallurgy, etc. Considering only industrial plants and domestic stoves it was found that in more than 70% of the emission measurements the PM10 portion amounted to more than 90% and the $PM_{2.5}$ portion between 50% and 90% of the total PM emission. To measure PM distribution two eight- or six-stage Anderson Impactors were used and they gave comparable results. PM distribution results were represented by both frequency distribution (Y) over the PM diameter and cumulative frequency particle size distribution (D). Following their example we present our results using frequency distribution as well.

Also, important point to note is that PM distributions heavily vary even when the fuel is of the same type: can be one or two peaks at different PM diameter, also of different shapes and prominence.

This is continuation of work with purpose to collect PM distribution of different type of combustion systems that are using different types of fuel. Samples were collected from different precipitators or filters under operating conditions. This data can be used for research of ESP when choosing the particles to test ESP efficiency with and to optimize ESP for use in specific cases.

2. METHODOLOGY

PM size distributions were obtained using aerosol spectrometer system Promo 3000 H with sensors welas 2100 HP and welas 2500 HP. Spectrometer illuminates measuring volume with white light and measures intensity of 90 degrees scattered light and calculates equivalent diameter of the sphere. Promo 3000 H use white light to avoid specific light wavelength dependant phenomena like diffraction or interferention. This way calibration curve – the reflected light intensity dependance on particle diameter – is even and clear. Particle concentration is calculated by evaluating number of analyzed particles and volume of illuminated flow. Maximum concentration that 2100 sensor can measure is $2 \cdot 10^5$ particles/cm^3 and 800 particles/cm^3 for 2500 sensor.

Measuring ranges of the sensor can be changed. Possible ranges for 2100 sensor are (0.2 to 10) µm, (0.3 to 17) µm and (0.6 to 40) µm. For 2500 sensor they are: (0.3 to 17) µm, (0.6 to 40) µm and (2 to 105) µm. In our experiments we usually used 2100 (0.2 to 10) µm and 2500 (2 to 105) µm measuring ranges to get maximum range coverage.

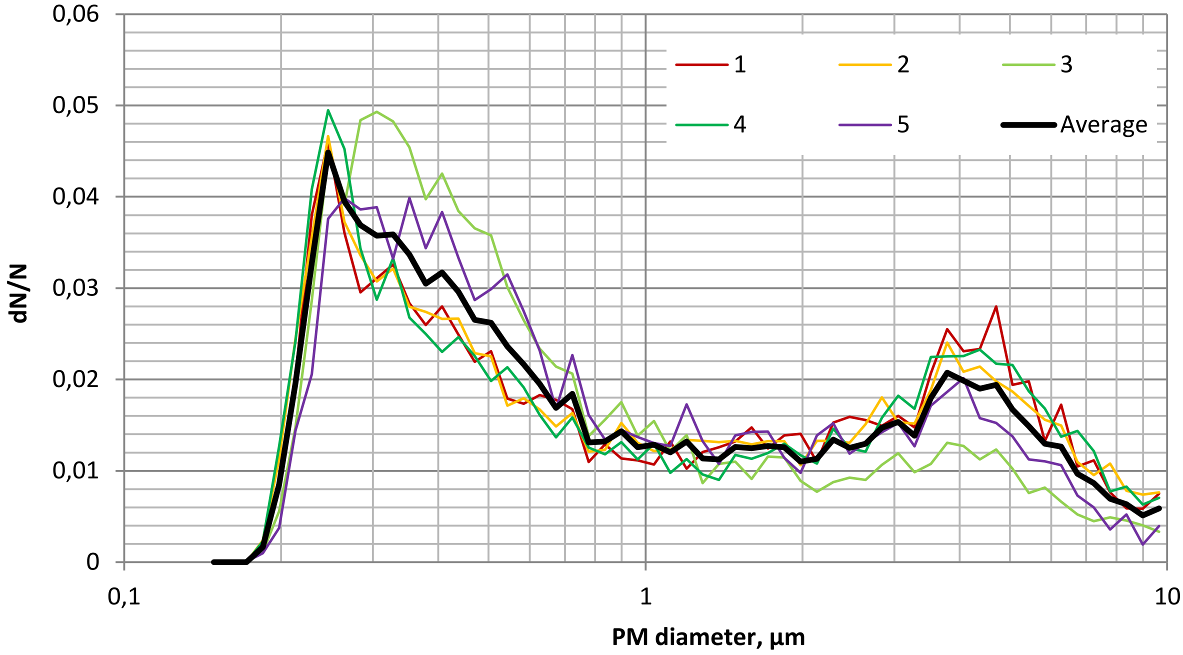

Fig. 1. PM distributions of the same sample of 5 consecutive time intervals and their average

Table 1. Number of analysed particles for the evaluation of measurement uncertainty

Interval No.	1	2	3	4	5	Average
Particles analyzed	7538	16284	5156	18640	3709	51327

In the first two cases we present here PM samples were taken from bunkers of multicyclones and in the 3rd case it filters were used to collect PM from the gas as well as a sample from ESP bunker. Samples were collected from boilers working at standard condition during nominal power mode. The samples then were put into a container and shook to create aerosol. Likewise, the filters were rumpled to unbind the particles and create the needed aerosol. Then aerosol was streamed through one or the other welas sensor at constant flow of 5 l/min.

Repeatability of such measurements can be evaluated comparing the distributions of the same sample from different time intervals. PM size distributions of the same sample and average distribution can be seen in Fig. 1. Number of particles analysed presented in Table 1. As we can see, even with vastly varying number of analysed particles per interval, meaning varying aerosol concentrations during the measurements, the distribution are very similar. Standart deviation was counted in PM size intervals that had more than 2% of all particles. Deviation fluctuated from 4% to 12.8 % at average of 9.6%. This is good estimation of measurement accuracy as it is main component of uncertainty. It is in par with measurement errors evaluated to be up to 10% for particles larger than 1.5 μm [5]. As explained in the paper, highest numbers of particles per interval was for (0.25 to 1.5) μm diameter particles, thus the errors were only (0.5 to 2) %, and because of lower number of particles the bigger they were the error increased up to 10%.

3. RESULTS AND DISCUSSION

3.1. Water heating boilers firing wood chips

3.1.1. Water heating boiler firing wood chips No. 1

Test samples were taken from bunkers of two multicyclones installed after identical 8 MW water boilers which are using wood chips as fuel. As we can see from PM distribution in Fig. 2 there are two peaks. One sharp spike measured only with welas 2100 (0.2 to 10) μm sensor, because it is at (0.2 to 0.3) μm particle diameters reaching up to 8% particle per interval.

Second, shallow peak is evident from results of both sensors. Distributions from 2500 (2 to 105) μm sensor overlap comparing both samples with around 5% particles per interval from 4 to 7 μm. Number of analysed particles were 55467 and 1204398 for sample No. 1 coresponding sensors welas 2100 and 2500 alike 71289 and 713994 for sample No. 2.

Comparing PM emmissions from 15 different firing units usint log wood, wood chips or pellers analysed in [6], we can see that they differ greatly. 175 kW firing plant using chips and working full power had a sharp peak at 0.2 μm and rather even distribution (0.8 to 9) μm with very shallow peak at 5 μm. 175 kW firing plant using chip board working at 139 kW power had lower and wider peak at (0.2 to 0.5) μm 50% higher and sharper peak at (5 to 6) μm than previous case. In case of 150 kW firing plant using chips PM size distribution of emissions from the plant when working third of the power had wider and lower peak at (0.2 to 0.5) μm same as with 175 kW plant, but lower peak at (6 to 7) μm. In any case, general trend of high peak at (0.2 to 0.3) μm and lower, wider peak at (4 to 7) μm is seen in [6] and well coincide with our results. Though the height of second peak varies 3 times in the mentioned cases. And even greater differences can be seen when comparing to cases when log wood or wood pellets were used as a fuel. When log wood was used the first peak usually was moved towards bigger diameters: from 0.4 μm even to 0.7 μm. Secondary peaks were low or not existent exept in single case of 450 kW firing plant working at 273 kW. The second peak in this case was very different: higher than most, including chips, with peak value at 2 μm. The case of wood pellets had PM distribution with high eak at (0.2 to 0.3) μm, but no noticable secondary peak.

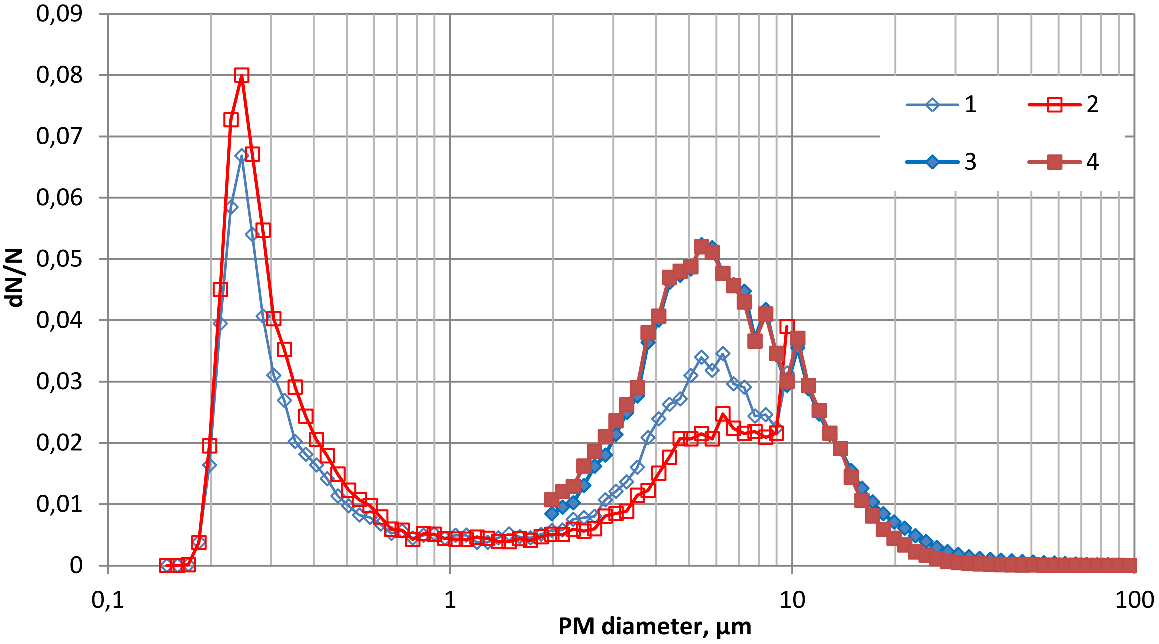

Fig. 2. PM distribution of two samples from multicyclones after 8 MW water heating boilers firing wood chips. PM distributions obtained with sensor 2100 using (0.2 to 10) µm measurement range: 1 – sample No. 1, 2 – sample No. 2; PM distributions obtained with sensor 2500 using (2 to 105) µm measurement range: 3 – sample No. 1, 4 – sample No. 2

3.1.2. Water heating boiler firing wood chips No. 2

Similar setup was selected for second test object. Samples were taken from bunkers of two multicyclones installed after 12 MW water boilers which are using same wood chips as fuel. As we can see from PM distribution in Fig. 3 there are the same two peaks: sharp spike around (0.2 to 0.3) µm up to 6% particles per interval for 2100 sensor and shallow peak with around 4% particles per interval for 2500 sensor from 2 to 6 µm. As we can see from comparing Fig. 2 and 3 the results are very similar with second test showing only bit lower peaks, but the same shape. Here, however, we can see that measuring 2nd sample with 2500 sensor the peak moved to smaller diameter range: from (4 to 6) µm to (2 to 5) µm. Number of analyzed particles were 93626 and 713244 for sample No. 1 corresponding sensors welas 2100 and 2500 alike 31744 and 373945 for sample No. 2.

Again, our previous results and other sources [4, 6] show that wood chip using boilers of different power emits PM with similar two peaks at (0.2 to 0.4) µm and (3 to 7) µm which well corresponds to these results.

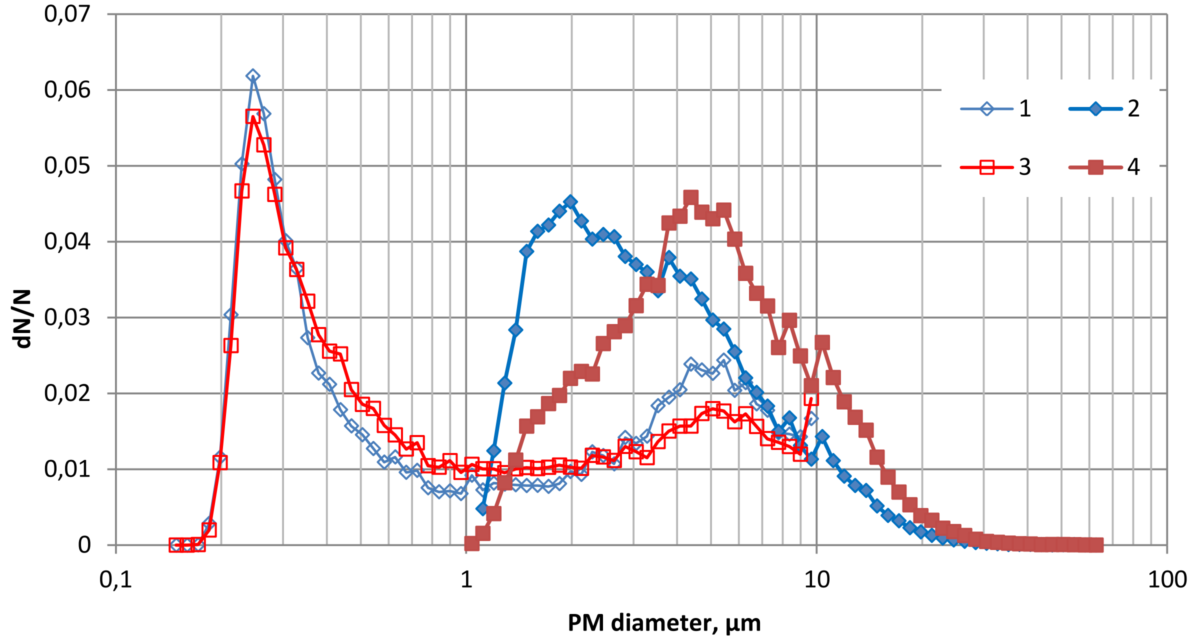

Fig. 3. PM distribution from multicyclones after 12 MW water heating boilers firing wood chips. PM distributions obtained with sensor 2100 using (0.2 to 10) µm measurement range: 1 – sample No. 1, 2 – sample No. 2, PM distributions obtained with sensor 2500 using (2 to 105) µm measurement range: 3 – sample No. 1, 4 – sample No. 2

3.2. Water heating boiler firing shale

Last case was chosen to be 115 MW water boiler that is using shale because we had unique opportunity to analyze what particles comes directly from the boiler, what particles are precipitated in ESP and what particles are emmited to the atmosphere during the measurement of ESP efficiency coefficient. 3 samples were tanken. Samples before and after ESP were taken using filters and sample from ESP bunker was taken as well. Results show only one peak at (0.2 to 0.3) µm particle diameters. The higher diameter particles the lower percentage of particles per diameter. ESP efficiency was determined to be very high, reaching 99.95% so it is natural, that distributions of PM from ESP and before ESP are very similar. The high majority of particles after ESP were around 0.2 µm, so graph for PM from ESP is lower at that range and higher if particle diameters are more than that comparing to PM distribution of particles before ESP. Distributions obtained with 2500 sensor show relatively constant level of particles at (2 to 6) µm diameters, but from 2100 sensor distributions we can see that in general such sized particles constitute small amount portion of PM. Understandably, no meaningful results were obtained from sample after the ESP using 2500 sensor. Number of analyzed particles were 232933 and 1572402 for sample before ESP corresponding sensors welas 2100 and 2500 alike 822889 and 58729 for sample from ESP and 711551 after ESP.

As mentioned before, according to [5] and other sources, ESP efficiency is lower the smaller the particles. Our results of showing almost only the smallest particles escaping the ESP is consistent with data from literature review.

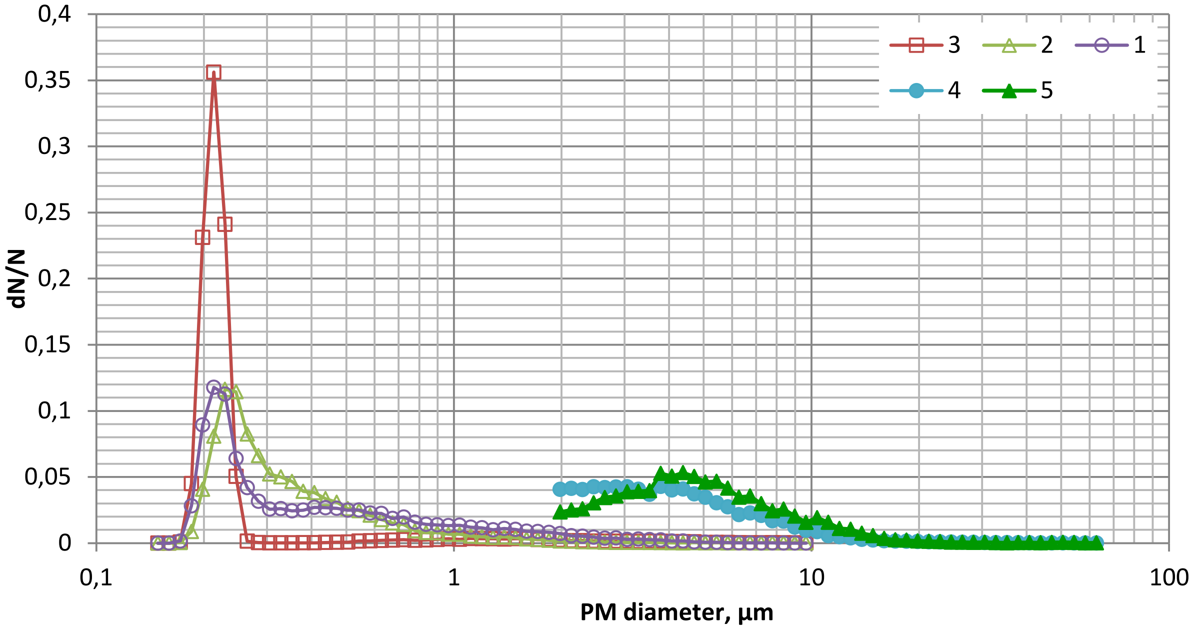

Fig. 4. PM distribution from ESP after water heating boiler firing shale. PM distributions obtained with sensor 2100 using (0.2 to 10) μm measurement range: 1 – before ESP; 2 – from ESP; 3 – after ESP; PM distributions obtained with sensor 2500 using (2 to 105) μm measurement range: 4 – before ESP; 5 – from ESP

4. CONCLUSIONS

PM samples from two objects each using 2 boilers with multicyclones were taken. Both of them were using wood chips as fuel. Particles of sizes (0.2 to 30) μm were observed of noticable levels. PM size distributions from 8 MW boilers' multicyclones match each other perfectly having two peaks at (0.2 to 0.3) μm and (4 to 7) μm. Distributions from 12 MW boilers follow the same trend with same first peak at (0.2 to 0.3) μm, but second peak from one of the samples was moved to lower diameter range (2 to 6) μm. Our results well coincide with general trend seen in literature of high peak at (0.2 to 0.3) μm and lower, wider peak at (4 to 7) μm. However the height of second peak varies 3 times in the analysed cases so it is important to collect more statistical data of how the peak position and prominence depend on factors like fuel, power both nominal and actual, etc.

Another set of samples were taken from 115 MW water boiler firing shale. Size distributions of particles before the ESP, from ESP and after ESP are presented. Since ESP efficiency coefficient was over 99,9% distribution of precipitated particles were very similar to distribution of PM sample before ESP. Mainly (0.2 to 0.3) μm diameter partciles were observed to leave ESP with very low number of larger particles, which can be explained by lower ESP efficience the smaller the PM diameter is.

5. LITERATURE

1. http://www.biokuras.lt/content_images/failai%20naujienoms/Biokuro%20poveikis%20aplinkai%20%20D%20%20Martuzevi%C4%8Dius%20%20KTU.pdf, 2017-03-06.
2. AMARAL S.S., JOÃO ANDRADE DE CARVALHO JR. J.A., COSTA M.A.M, PINHEIRO C. An Overview of Particulate Matter Measurement Instruments. Atmosphere 2015, 6, 1327–1345.
3. PODLINSKIA J., NIEWULISA A., MIZERACZYKA J., ATTENC P. ESP performance for various dust densitiesJournal of Electrostatics 66 (2008) 246–253.
4. TONKONOGIJ, J., PEDIŠIUS, N., STANKEVIČIUS, A., TONKONOGOVAS, A. Mažos ir vidutinės galios kietuoju kuru kūrenamų įrenginių kietųjų dalelių emisijų tyrimas. Energetika. 2015. T. 61. Nr. 3–4. P. 119–130.
5. NIEWULIS A., BERENDT A., PODLINSKI J., MIZERACZYK J. Electrohydrodynamic flow patterns and collection efficiency in narrow wire-cylinder type electrostatic precipitator. Journal of Electrostatics 71 (2013) 808 to 814.
6. EHRLICHA, C., NOLLA, G., KALKOFFA, W.-D., BAUMBACHB, G., DREISEIDLERB, A. PM_{10}, $PM_{2.5}$ and $PM_{1.0}$ – Emissions from industrial plants – Results from measurement programmes in Germany. Atmospheric Environment 41 (2007) 6236–6254.

CYSENI 2017, May 25-26, Kaunas, Lithuania
ISSN 1822-7554, www.cyseni.com

THE POTENTIAL OF THE LIVESTOCK FARMS AS A SOURCE OF ENERGY (EVIDENCE FROM THE BELGOROD REGION)

A. Karnaushenko, E. Shestova
Lomonosov Moscow State University
F. Poletaeva str., 109378 Moscow – Russia
E-mail: lisa07sh@mail.ru

ABSTRACT

The paper discusses the potential of livestock wastes as a source of energy, its energy efficiency and possibilities of the wide application. One of the regions of Russia – Belgorod region was an example of all the calculations, which were carried out. The main specialization of this territory is a cattle and poultry breeding. Due to the growing interest in alternative methods of producing energy and other positive effects coming out of this process, we have the method, which allows in addition to the energy problems to solve environmental issues. The paper describes the agricultural biomass and the biogas produced from that mass, as a resource for bioenergy. The available amount of the animal waste matter and the energy potential of it were calculated. The positive effects of biogas plants are several ecological functions, which can dispose of the waste and make fertilizer at the same time. This is a non-waste production and an efficient use of resources. The paper presents the classification of the selection factors of renewable energy sources. It can help to make the most rational choice of a type of RES. The result of the research was the substantiation of livestock farms' utilization efficiency as an energy resource, environmental components and the possibility of a widespread use of this method.

Keywords: renewable energy, bioenergy, livestock wastes, agricultural biomass, biogas, biogas power plant, energy efficiency, selection factors of RES, Belgorod region

1. INTRODUCTION

Due to the growing interest in alternative methods of producing energy and other positive effects coming out of this process, it becomes necessary to seek new opportunities for using energy-efficient technologies. A wide application of these technologies will not only have a positive effect on the operation of power stations, but will also solve environmental problems. One of such methods is the production and use of biogas. Agricultural biomass is a source of bioenergy, but also can be used as fertilizer (when applied to certain technologies). This is a non-waste production and efficient use of resources.

In this regard, the aim of the work was to identify the potential of agricultural wastes for use as a resource for energy in case of Belgorod region.

2. FACTORS OF RENEWABLE ENERGY SOURCES (RES) SELECTION

Renewable energy sources (RES), as well as technologies providing the energy generation process, have a sufficiently wide range. It suggests that by using combinations of certain sources and technologies, energy can be provided by any place on Earth.

Currently, priority is given to solar and wind plants in Russia, based on greater efficiency than other alternative methods of electricity production and the widespread distribution of solar radiation and wind resources. However, some circumstances can give priority to installations, which operates on other fuels.

In general, the choice of a renewable source is proposed to form the basis of the following factors combinations:

1. Natural factor is features of the geosystem, which form a sufficient number of a renewable energy source.

2. Socio-economic factor is the characteristics of an economic activity and the requirements of the population.

3. Political and economic factor is a political interest, an economic efficiency and profitability of projects.

4. The environmental factor is the requirement / danger of using / refusal of use a renewable energy source.

Usually in justification acceptance or rejection of the project, leading role is played by one or two factors. More often, the natural factor is taken as a basis, but this is not always the only correct solution. Taking into account all the factors, a rational choice of RES is able not only to provide the region with energy, but also to give impulse to the development in social, ecological and economic spheres.

3. MAIN TYPES OF RES IN THE BELGOROD REGION

The Belgorod region is located in temperate latitudes. The average annual duration of sunshine is about 2300 hours per year. According to the NASA information portal "Atmospheric science data centre" [4], the average annual amount of incoming solar radiation on a horizontal surface of the region territory is about 3.1 kWh/m² per day. If we consider similar indicators in Germany (the leader in the installed capacity of solar installations), there the average amount of incoming solar radiation is 2.9 kWh/m² per day. Therefore, it can be concluded that the Belgorod region is not inferior to the world leader in provided resources. This fact confirms that the use of solar energy in the region can be considered as rational in consequence of the natural conditions. However, solar cells can not occupy large areas intended for agriculture.

It should be noted that the region is water-deficit and do not have geothermal sources. Intensive development of lands led to deforestation of the territory. The forest cover is about 8–9%. The West and North East directions characterize the wind pattern of the Belgorod region in the warm season and South winds are in the cold period. The average annual wind speed in the region is 2.1–4.1 m / sec. The wind speeds within the region range from 3.84 to 5.88 m / sec. at a height of 50 m, which is in 1.5 times lower than in Germany. Nevertheless, due to wind energy with these characteristics it is possible to use wind energy in the private households.

However, the remaining factors also have to be carried over for consideration. The main role in the Belgorod region economy is played by two major industries: a mining and an agricultural. The mining always requires large energy expenditures, while the agricultural does not give obvious associations related to energy consumption. At the same time, if we consider the environmental factor of the region, the existence of mining processing plant (MPP) raises the issue of waste of this production, and agriculture raises organic waste and mineral fertilizers. At the same time, at the current stage of technology development, the MPP waste in the way of RES usually is not considered. In contrast to the MPP waste, the organic waste from agriculture is a valuable raw material for bioenergy. Therefore, agriculture needs to be examined detailed in case of choosing renewable energy sources.

There are two types of waste in agriculture: a crop and a livestock. Generally, the crop finds their use in the livestock sector as a litter, a fodder and a supplement. That is why almost all crop mass is used and we should pay attention to livestock biomass.

It is worth noting that the Belgorod region in 2016 reached the leading positions in the country for pork and poultry, and there are cattle breeding enterprises. More than 14 million tons of waste are generated in the region every year. The most common method of treatment these days is the separation of the total mass into liquid and solid fractions with each storing for composting or use as fertilizers. Only 4% of the total waste mass needs for use on cultivated areas. It makes possible to talk about the wide possibilities of using them as an energy resource.

4. AGRICULTURE WASTE AS A SOURCE OF ENERGY

It is possible to calculate the amount of waste from livestock and poultry by analysing production volumes. To receive the total weight, the value as the average weight of manure from one head has to be known and they can be calculated as follows:

Total mass = *number of heads* × *mass of manure from one head*

The mass of waste from one head of cattle or poultry varies depending on the age and sex structure and the intended purpose.

According to statistical data about the livestock structure [3] and "Methodological recommendations for the technological design of disposal systems for the use of manure" [2], the figures of manure and litter from one head are collected. Then, it is possible to estimate the approximate amount of manure (Table 1). A small cattle is not counted because almost all of them belongs to households. There is not big number of animals, not a significant amount of waste and a significant damage to the environment.

Based on the calculations, 16.6 thousand tons of manure from pigs, 15.3 thousand tons of bird droppings and 7.9 thousand tons of manure from cattle are formed in the territory of the region during the day. It is about 14.5 million tons of biomass for the year.

Table 1. Middle mass per day and per year of livestock waste in Belgorod region

		Excrements		
	Number of heads	**Weight of excrement, kg / head / day**	**including**	
		Total excrement, t / day	**Hard fraction**	**Liquid fraction**
Sows	277 400	11.37	3.12	8.25
		3 154	865	2 289
Fattening pigs	2 069 800	5.75	2.36	3.36
		11 901	4 885	6 955
Swines	2 774	11.1	3.86	7.24
		31	11	20
Young pigs	1 627 126	0.97	0.37	0.6
		1 578	602	976
Total	3 977 100	16 664	6 363	10 301
Poultry (chickens, turkeys, ducks)	51 320 200	0.30		
		15 396		
Total	51 320 200	15 396		
Cows	93 100	55	35	20
		5 121	3 259	1 862
Remaining	133 600	21	14.13	6.88
		2 806	1 888	919
Total	226 700	7 927	5 147	2 781
Total for the day, t		39 987		
Total for the year, t		14 595 255		

To assume the energy potential of raw materials, it is necessary to know the ratio of biomass and the energy and substance derived from it. The cycle of obtaining the final product: biomass - biogas - energy and matter, needs to be known.

Biogas is a product of biomass fermentation. Its characteristics have similarities with natural gas (Table 2) [1]. Thereby, biogas provides the possibility of using it for energy production.

Table 2. Comparison of natural gas and biogas

Components	**Natural gas**	**Biogas**
Methane	85–95%	55–80%
Carbon dioxide	Less than 1%	20–45%
Nitrogen	4–12%	–
Oxygen	Less than 0.5 %	–
Hydrogen	–	Less than 1 %
Hydrogen sulphide	50–100 mg/m^3	500–5000 mg/m^3
Calorific value	32–35 MJ/m^3	20–29 MJ/m^3

The biogas emission from one ton of biomass depends on the characteristics of the raw material. It varies from 30 to 1500 m^3/ton.

Taking into account that the average calorific value of biogas is 24.5 MJ/m^3 and one MJ = 0.278 kWh, it is possible to get 6.8 kWh of electricity from one m^3 of biogas. An average value was found by comparing these theoretical indicators with the characteristics of already operating biogas stations. As a result, a potentially electricity output of the total mass of livestock wastes in the Belgorod Region over the year was calculated (Table 3). The output was about 2 billion kWh/year of electricity, which is about 14% of the required electricity in the region and can cover the energy necessity of agriculture.

Simultaneously with the release of biogas, a rest is formed as an effluent, which is used as an organic fertilizer.

Table 3. Emission of energy and fertilizer (effluent) from livestock waste produced in biogas plant in the year

		Manure of pigs	**Manure of poultry**	**Manure of cattles**
	Biogas volume, m^3 per ton of raw material	70	70,5	45
	Mass of raw materials, t/year	6 082 360	5 619 540	2 893 355
Output from raw materials produced during the year	**Biogas volume, m^3**	425 765 200	396 177 570	130 200 975
	Electric power production, kW*h	979 259 960	911 208 411	299 462 243
	The effluent (slurry) emission, t	5 585 000	5 160 000	2 656 000

The assessment of electricity generation as a result of processing livestock waste allows us to make conclusions about the energy efficiency of production. When the biogas plant is in operation, energy is also used for the utilization of livestock waste and the effluent and energy are produced simultaneously. At the same time, part of the generated energy is returned to production for the operation of the station. Therefore, the station carries out work on waste utilization and fertilizer production by using its own energy. Thus, the station does not only consume energy from the electric grid, but even delivers it to the grid. In other words, the station works without the supplied power of the central power grid. Before the introduction of of biogas stations, the energy cconsumed from the grid went to the production fertilizers and waste management (Fig. 1).

As we found, the potential generation of electricity at biogas plants in the Belgorod region averages 2 billion kWh per year Considering that 25 to 50% of this energy goes to the needs of the stations, the free electricity output will be about 1 billion kWh per year.

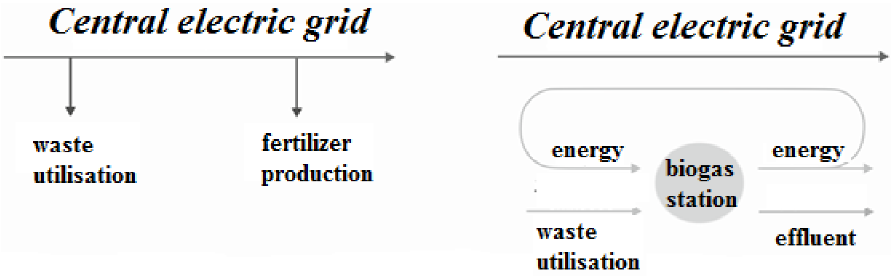

Fig. 1. The cycle of production and consumption of energy in absence and presence of biogas station

The biogas plants do not supply the region with energy only, but also contribute to the implementation of the ecological function, such as waste utilisation and the production of organic fertilizers. This creates a number of additional positive effects in addition to a direct function – the production of energy. This approach to the use of resources fits into the concept of rational nature management, involving the formation of cycles with minimum natural costs and maximum output of materials and energy.

5. DISCUSSION

Biogas stations in the Belgorod region are suitable for all four factors as a renewable energy source:

1. The natural factor. A sufficient amount of agricultural waste is generated in the region.

2. Socio-economic factor. In the Belgorod region, most of the areas and population are engaged in agriculture.

3. Political and economic factor. The widespread using of biogas plants does not only reduce the consumption of energy from the grid, but also delivers its own and produces an effluent, which an be used for the production of fertilizers.

4. Ecological factor. The introduction of agricultural waste utilization reduces their quantity, and also reduces the using of traditional (fuel) materials.

The conducted research showed the rationality of agricultural waste using, which can be used in other agricultural regions.

6. CONCLUSION

There are other directions for the development of alternative energy in the Belgorod region, despite the obvious natural factors. They are biogas stations based on livestock complexes, which allow developing the bioenergy in Russia. The proposed changes in the functioning of agriculture use a new energy source – livestock wastes, based on which it is possible to produce biogas with further conversion to electricity and obtaine a useful remainder – effluent. On the example of the Belgorod region, their positive effect was shown, which can be extended to territories with similar conditions.

REFERENCES

1. E.G. Savel'ev, Biotoplivo – *Jeffektivnyj istochnik jenergii, Teplofizicheskie osnovy jenergeticheskich tehnologij: sb. Nauch. Tr*. - Tomsk, 2010. - 281-284 p.
2. 1.10.15.02-08. *Metodicheskie rekomendacii po tehnologicheskomu proektirovaniju sistem udalenija i podgotovki k ispol'zovaniju navoza i pometa*. - Vzamen NTP 17-99; Vved. 01.10.2008. - 51 p.
3. Departament agropromyshlennogo kompleksa Belgorodskoj oblasti. Belgorod, 2010-2016. [referred on the 20th of February in 2016 y.]. Link to the internet: < http://belapk.ru/zhivotnovodstvo >.
4. Atmospheric science data center, 2016. [referred on the November in 2015 y.]. Link to the internet: < https://eosweb.larc.nasa.gov >.

CYSENI 2017, May 25-26, Kaunas, Lithuania
ISSN 1822-7554, www.cyseni.com

HEAVY METAL DISTRIBUTION IN RESIDUAL PYROLYSIS PRODUCTS OF ANAEROBICALLY DIGESTED SEWAGE SLUDGE

Marius Praspaliauskas
Lithuanian Energy Institute
Breslaujos st. 3, LT-44403 Kaunas – Lithuania
E-mail: Marius.Praspaliauskas@lei.lt

Nerijus Striūgas
Lithuanian Energy Institute
Breslaujos st. 3, LT-44403 Kaunas – Lithuania
E-mail: Nerijus.Striugas@lei.lt

ABSTRACT

The purpose of this work was to determine and compare the distribution of heavy metal in residual products namely char, tar and producer gas obtained during pyrolysis of digested and dried sewage sludge. Experimental investigations with anaerobically digested and dried sewage sludge were performed in laboratory fixed bed reactor. To avoid metal influence, the reactor tube was made from quartz tube. Pyrolysis of sludge was performed at following conditions: the temperature of reaction was set at 850 °C, the flow of nitrogen was 6 L min^{-1}. After the process completed all products were collected and mineralized for determination of metal concentration. For the evaluation of heavy metals in raw sludge and process products, prepared solutions were analysed with ICP-OES.

In this work, the characterization of all materials including raw sludge and products from sewage sludge pyrolysis was performed and the chemical, physical and energetic properties were determined. During the experimental run the composition of main producer gas compounds such as CH_4, CO, CO_2 and H_2 were analysed and yield of gas was measured. All products were collected and the mass balance was calculated. The product yield in all processes varied: tar and condensable about 30.7 ± 0.66 wt.%, char 41.8 ± 0,07 wt.%, gas 27.5 ± 0,65 wt.%. Finally, the experimental investigation reveals the fate of all found elements (Al, As, C, Ca, Cd, Cl, Co, Cr, Cu, Fe, H, K, Mg, Mn, N, Na, Ni, P, Pb, Sb, S, Si, Ti, V, Zn, Ba, Be, Se) and with special attention on heavy metals in the products of pyrolysis processes of dried sewage sludge. It was determined that after the thermal conversion the main part up to 94 wt.% of heavy metals was accumulated in the char. The metals such in the tar were found in such order Fe > Mn > Ti > Zn > Cu > Cr > Ni > Cd.

Keywords: sewage sludge, pyrolysis, heavy metals, char, condensate, tar

INTRODUCTION

Today, sewage sludge disposal in landfills, its burning and composting are the most common methods of sewage sludge utilization that are often used to reduce growing quantities of sewage wastes [1]. Sludge storage sites are considered the simplest decision in terms of removal of sewage sludge because it is a relatively cheap way of utilization. Storage sites are of a limited capacity and in order to avoid entry of hazardous substances into soil storage sites must be installed in accordance with the stringent environmental requirements [2].

Currently pyrolysis, i.e. a thermal process that takes place in the atmosphere of inert gas, becomes increasingly popular in management of solid waste. A volume of waste is reduced during this process by generating valuable by-products and obtaining chemically stable products [3]. It is considered that pyrolysis is the main alternative for utilization of sewage sludge. Pyrolysis is a fast thermal decomposition of solid organic material. The following three main fractions remain after a process of pyrolysis: resins with condensate, synthetic gas of high calorific value and a fixed carbon (char) [4]. A process of pyrolysis inhibits mobility of heavy metals in the product of pyrolysis (char). For this reason, a further use of char after a process of pyrolysis is more acceptable than after other thermal processes (burning or gasification). Pyrolysis is an alternative for aforementioned processes of sewage sludge processing. It is a relatively clean technology that quickly pays for itself [5]. The advantage of this technology lies in the fact that valuable products are obtained during the process and an amount of waste is reduced. Moreover, heavy metals are concentrated and pathogens are destroyed during pyrolysis [6].

Physico-chemical characteristics of sewage sludge char depend on the parameters of sewage sludge used as a raw material and a process of pyrolysis. The temperature parameters have the greatest effect on a process of pyrolysis because not only distribution of products (resins, gas, char) depends on temperature but also their properties [6]. As higher is temperature of pyrolysis as lower amount of char is generated. However, the resulting microstructure of char has a greater effect when compared to char generated in low temperatures. High temperature is maintained during the process, and then char loses a large part of carbon and other functional groups. Efficiency of such char decreases. Chemical composition, pH, a surface shape, thermal stability and a content of heavy metals are strongly influenced by temperatures of pyrolysis.

Notwithstanding the fact that researches of pyrolysis of sewage sludge are performed more and more often, there is not enough data on this topic. It is necessary to perform more studies and to accumulate as more information about distribution of heavy metals not only in chare but also in other products of pyrolysis as possible. Anaerobically digested and dried (10%) sewage sludge serves as an object of this paper. The objective of the paper was to determine elemental distribution in the products of pyrolysis (char, tar, condensate and gas) and compare the obtained results with results of other studies.

During the research a mix of condensate and resins has been separated into two separate factions, i.e. condensate and resins. To achieve the objective sewage sludge has been pyrolysed in the temperature of 850°C. Such temperature was selected to minimize a volumetric quantity of sludge and to avoid slagging into the reactor during the process. A large number of elements (Al, As, Ca, Cd, Co, Cr, Cu, Fe, K, Mg, Mn, Na, Ni, P, Pb, S, Sb, Si, Ti, V, Zn, Ba, Be, Se) has been selected to investigate how the aforementioned elements distribute individually in the products of pyrolysis. The pyrolysis products can be further used when there is sufficient knowledge of distribution of the mentioned elements. This could result in development of environmentally friendly process and even greater reduction of release of harmful substances into the environment.

1. ANALYSIS METHODOLOGY

1.1. Pyrolyzer and pyrolysis process

The schematic configuration of pyrolysis experiment is illustrated in Fig. 2. A special, vertical, lab-scale pyrolyzer was designed and successfully applied to conduct pyrolysis. The pyrolysis chamber is made up of quartz tube (internal diameter was 5 cm, length – 85 cm). Temperature profiles were obtained using a thermocouple positioned at the centre of reactor and middle of quartz tube which show that the sample reached the desired temperature according to the programed value. Approximately 270-320 grams of dry sewage sludge were loaded to a laboratory scale reactor. Before the experiment, nitrogen (with a constant flow rate of 4 L min^{-1}) was injected into the reactor for 3 min to maintain an inert atmosphere and heated at a constant heating rate of 15 °C min^{-1} to achieve the set-point temperature (850 °C) and maintained at this temperature for about 90 min. The pyrolysis experiments were performed according to a laboratory-scale fixed bed pyrolysis system under atmospheric pressure. The off-gases generated by the pyrolysis reaction were first allowed to pass through a cold trap to condense tar. Non-condensable gas (i.e. H_2, CO, CO_2, CH_4) were analysed with VISIT 03H analyser.

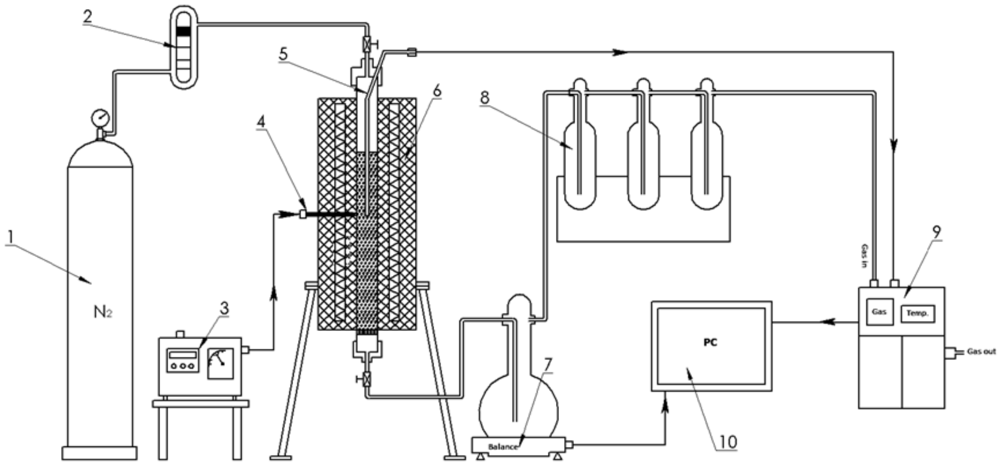

Fig. 1. The schematic configuration of pyrolysis experiment. 1. Nitrogen gas; 2. Reducer; 3. Temperature controller; 4. Thermocouple of reactor; 5.Thermocouple of sludge layer; 6. Furnance; 7.Balance; 8. Ice bath; 9. Gas analyser; 10. PC

Technical nitrogen was used as the carrier gas at a rate of 6 L min^{-1} to maintain an inert atmosphere. This flow rate was considered sufficient to prevent the accumulation of pyrolysis gas generated and at the same time to have no effect on the temperature of the surface of the sediment sample. After each run, the furnace was turned off and the reactor was allowed to cool down naturally to room temperature. The cooled samples were collected, weighed and subjected to elemental and heavy metal analysis.

The pyrolysis residue obtained from dry SS (sewage sludge) is subsequently referred to as SSCh (sewage sludge char), SST (sewage sludge tar) and SSC (sewage sludge condensate).

The experiment was repeated five times in order to ensure the mass balance and data reliability. The data reported in this paper are given as the mean value of five replicates.

1.2. Main thermochemical paremeters

From the collected sludge and char samples, moisture content was identified according to the specification CEN/TS 15414-1:2010, ash content of sludge, char, tar and condensate were determined according to the standard LST EN 15403:2011. Proximate analysis to determine the weight percentage of volatile matter was conducted using a TGA 4000 simultaneous TGA/DTA analysis method. Fixed carbon content was calculated as: *Fixed carbon (%) =100 (%) – Moisture content (%) – Volatile content (%) – Ash content (%).* Analysis of the elements C, H, N and S present to the solutions was performed using a Flash 2000 analyser. Carbon, hydrogen and nitrogen content were determined according to standard LST EN 15407:2011. Oxygen content was calculated as follows: *Oxygen content (%) =100 (%) – Carbon content (%) – Hydrogen content (%) – Nitrogen content (%) – Sulphur content (%) – Ash content.* Chlorine and sulphur content were estimated using an ISC-5000 DC ion chromatographic system according to the standard LST EN 15408:2011. The high heat value (HHV) of the solutions was determined using an IKA C5000 calorimeter according to the standard LST EN 15400:2011 for automated bomb calorimeters.

1.3. Heavy metal determination

At the first mineralisation step the samples (approximately 0.2–0.4 g) were flooded with 3 ml of concentrated nitric acid, 3 ml of fluoric acid and 1 ml of hydrochloric acid. The samples (in triplicate) were placed in a mineraliser and mineralised for 1 hour 10 minutes (at 800 W power, pLim: 60 bar, pRate: 0.5 bar/s), with 10 minutes allocated for heating, 45 minutes for mineralisation (in accordance with established parameters) and 15 minutes for cooling. After the second mineralisation, the samples were flooded with 18 ml boric acid (H_3BO_3 to avoid and eliminate fluoride toxicity) and again placed into a mineraliser for 1 hour 10 minutes (at 800 W power, pLim: 60 bar, pRate: 0,3 bar/s). After the mineralisation, the solution was poured into 50 ml flasks and diluted to 50 ml using deionised water. The analysis of the solutions (Al, As, Ca, Cd, Co, Cr, Cu, Fe, K, Mg, Mn, Na, Ni, P, Pb, S, Sb, Si, Ti, V, Zn, Ba, Be, Se) prepared from the different pyrolysis product samples were performed using an inductively coupled plasma optical emission spectrometer (ICP-OES) according to standards LST EN 15410:2011 and LST EN 15411:2011.

2. RESULTS AND DISCUSSION

2.1. Pyrolysis product yield

Fig. 1 shows the percentage distribution of pyrolysis products after final reaction. The yield of the pyrolysis product is a mass ratio of pyrolysis product to sludge samples. The sludge, char, tar and condensate mixture samples were weighed, and the syngas mass was calculated by finding the difference between added sewage sludge amount and char, tar and condensate mixture mass yield (Gas yield (g) = $SS_{(\text{add to reactor, g})} - SSCh_{(\text{mass after pyrolysis, g})} - SST_{(\text{mass after pyrolysis, g})} - SSC_{(\text{mass after pyrolysis, g})}$).

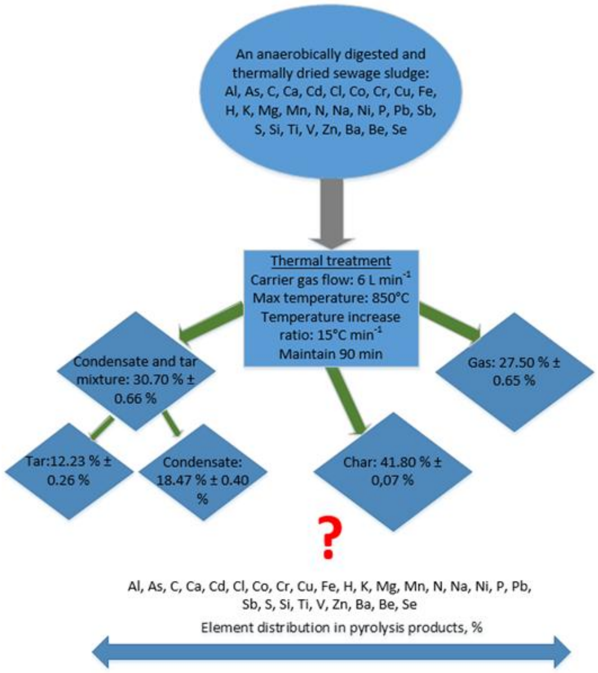

Fig. 2. Pyrolysis product residual yield

The calculations showed that char formed the biggest part of all pyrolysis products, about 41.8% ± 0.07%, condensate and tar mixture of the total balance of pyrolysis products comprised 30.70% ± 0.66%. After the separation, it was calculated that the part of condensate in total balance of products was 18.47% ± 0.40% and tar yield was 12.23% ± 0.26%. The water content obtained in this work was relatively low compared to the range between 20 and 70 wt.% reported in the literature (Fonts et al. 2012). Gas yield was calculated by difference and found that the gas consisted of 27.50% ± 0.65% in total balance of pyrolysis products. The appropriate composition of gas and the formation of condensate and tar mixture during pyrolysis process is presented in Fig. 3.

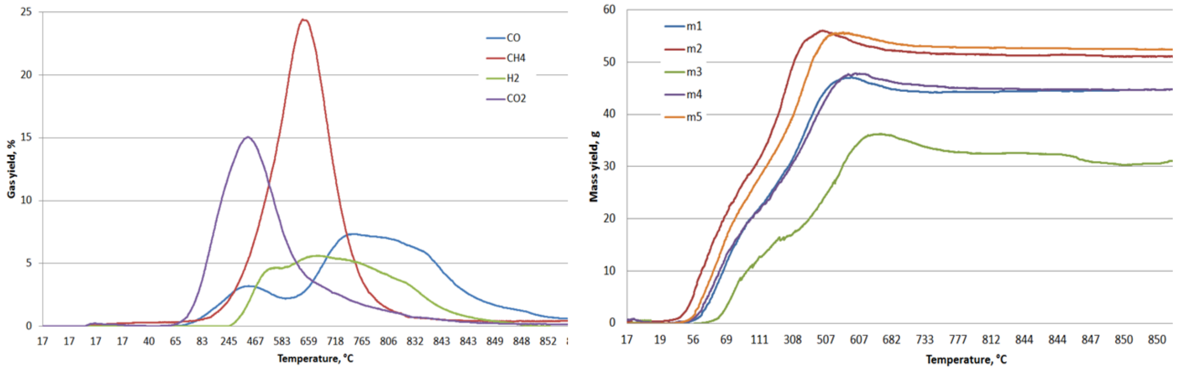

Fig. 3. Gas and mass (condensate and tar mixture) yield during pyrolysis process in laboratory fixed bed reactor

2.2. Chemical composition of sewage sludge and pyrolysis products

Selected proximate and ultimate analysis of anaerobically digested sewage sludge and its product before and after pyrolysis processing are given in Table 1. For proximate and ultimate analysis, the raw sewage sludge sample was dried in a furnace at 105°C. This approach preserves most of the volatiles in the sample even after drying.

Table.1. Main chemical parameters (average ± standard deviation)

Properties	Sewage sludge	Sewage sludge char	Tar	Condensate
Ultimate analysis (wt. %)				
Carbon, %	32.3 ± 0.26	25.97 ± 0.05	42.67±1.44	7.88±2.74
Hydrogen, %	5.04 ± 0.13	0.4 ± 0.04	5.36±0.19	1.05±0.02
Nitrogen, %	4.23 ± 0.42	1.3 ± 0.04	4.43±0.05	2.36±0.08
Sulphur, %	1.43 ± 0.04	1.03 ± 0.03	0.65±0.03	0.47±0.003
Oxygen (by difference), %	22.43	-	48.83	88.19
Chlorine, %	0.16 ± 0.05	0.27 ± 0.14	0.08 ± 0.01	0.004 ± 0.03
Proximate analysis (wt. %)				
Volatile matter, %	39.55±2.13	-	85.75 ± 1.40	5.90 ±0.43
Fixed carbon, %	22.98	24.25	-	-
Ash, %	34.57±0.04	71.41 ± 0.56	0.064 ± 0.004	0.046 ± 0.008
Moisture, %	9.84±0.02	4.34 ± 0.02	-	-
H/C	0.16	0.02	0.13	0.39
O/C	0.83	-	1.19	9.32
N/C	0.13	0.05	0.11	0.34
HHV, MJ/kg	13.50±0.05	9.58 ± 2.82	33.05 ± 0.07	-

The sludge and char displayed a very distinctive chemical composition. Its carbon content was much lower whereas its contents of ash. The ash content almost completely remains, which indicates that: (1) very little heavy metal runs off into the gas-phase syngas and the liquid-phase tar, and heavy metals almost entirely maintain in the solid-phase biochar; (2) the carbonaceous materials transform into hydrocarbon compounds as gas and aromatic hydrocarbons as tar[5].

The ratio of percentage H/C, as a carbonization degree parameter, is always lower than 0.5, thus suggesting the biochars with strong carbonization and high aromaticity can resist decomposition. The percentage O/C ratio of biochars is higher than that of activated carbon, which indicates the biochars with more polar-groups have higher hydrophilicity than some categories of commercial activated carbon [5]. These changes in H/C and O/C also illustrate that dehydrogenative polymerization and dehydrative polycondensation occur during pyrolysis, with significant loss of oxygen and aliphatic hydrogen [7]. The percentage N/C ratio has the same tendency like H/C and O/C.

The concentrations obtained in the sewage sludge, biochar, tar and condensate are shown in Table 2. The concentrations of As, Sb, V and Se was below the detection limit in the sludge and all products, and, therefore, were not analysed more detailed. The concentrations of all other elements were higher than that in the sewage sludge sample, reflecting the heavy enrichment of metals in the biochar, the exception was found only for Cd, which was not detected.

The results showed that total elemental contents in sewage sludge varied greatly, which were in the order of: Si > Ca > P > Fe > Al > K > Mg > Na > S > Zn > Mn > Ti > Ba > Cu > Pb > Cr > Co > Ni > Be > Cd. In order to understand the heavy metal distribution before and after pyrolysis, the heavy metal contents of sewage sludge were estimated from those of sewage sludge char Table 2 and Fig. 4.

Table 2. Element concentrations in sludge and sludge pyrolysis products

Element	**Sewage sludge**		**Sewage sludge char**		**Tar**		**Condensate**	
	AVG, mg/kg	**STD, %**	**AVG, mg/kg**	**STD, %**	**AVG, mg/kg**	**STD, %**	**AVG, mg/kg**	**STD, %**
Be	8.59	18.22	13.11	17.94	8.18	17.04	2.66	10.39
Ca	40566.67	9.99	81866.67	5.08	<0.01	-	7.10	14.80
Cd	6.17	11.99	<0.01	-	9.15	12.71	2.84	9.86
Co	20.09	16.73	18.85	18.25	12.35	14.12	4.20	10.94
Cr	52.07	2.31	85.06	14.60	<0.01	-	<0.01	-
Cu	124.37	11.54	263.50	2.48	23.86	11.65	5.96	5.34
Fe	20266.67	10.26	42240	6.53	132.03	10.16	6.78	10.99
Mg	7300	8.46	16472.50	4.69	23.45	22.88	8.02	16.22
Mn	1918.67	9.17	4127.50	8.22	5.77	17.56	1.37	13.03
Ni	17.39	17.13	38.17	4.18	<0.01	-	<0.01	-
Pb	73.77	13.73	165.70	9.46	16.43	16.53	8.85	7.28
Ti	919.07	9.21	2137.33	4.47	<0.01	-	<0.01	-
Zn	2610.67	11.72	5049.67	0.24	484.23	9.50	41.28	4.49
Al	10715	3.23	24490	0.78	18.54	2.93	8.40	2.76
Ba	461.70	3.80	1037.33	0.78	<0.01	-	<0.01	-
K	10299.50	5.22	21060	4.14	516.90	1.18	69.51	1.42
Na	3388.50	1.73	7715	0.99	76.83	6.91	54.53	2.44
P	27150	0.94	59470	1.43	64.64	2.79	24.03	10.36
S	2900.70	3.41	365.10	3.56	880.57	4.78	290.63	9.73
Si	75295	2.28	168733.33	2.59	<0.01	-	<0.01	-

The largest part of sewage sludge is comprised of Si (37%), Ca (20%), P (13%) and Fe (10%). The composition of char is almost adequate to sewage sludge and corresponds to Si (39%), Ca (19%), P (14%) and Fe (10%). Different chemical composition of tar and condensate was determined: in tar – S (39%), K (23%) and Zn (21%), in condensate – S (54%), K (13%) and Na (10%). The evaluation of elements, especially heavy metal distribution, shows that main part of the metals after pyrolysis remains in the sewage sludge char.

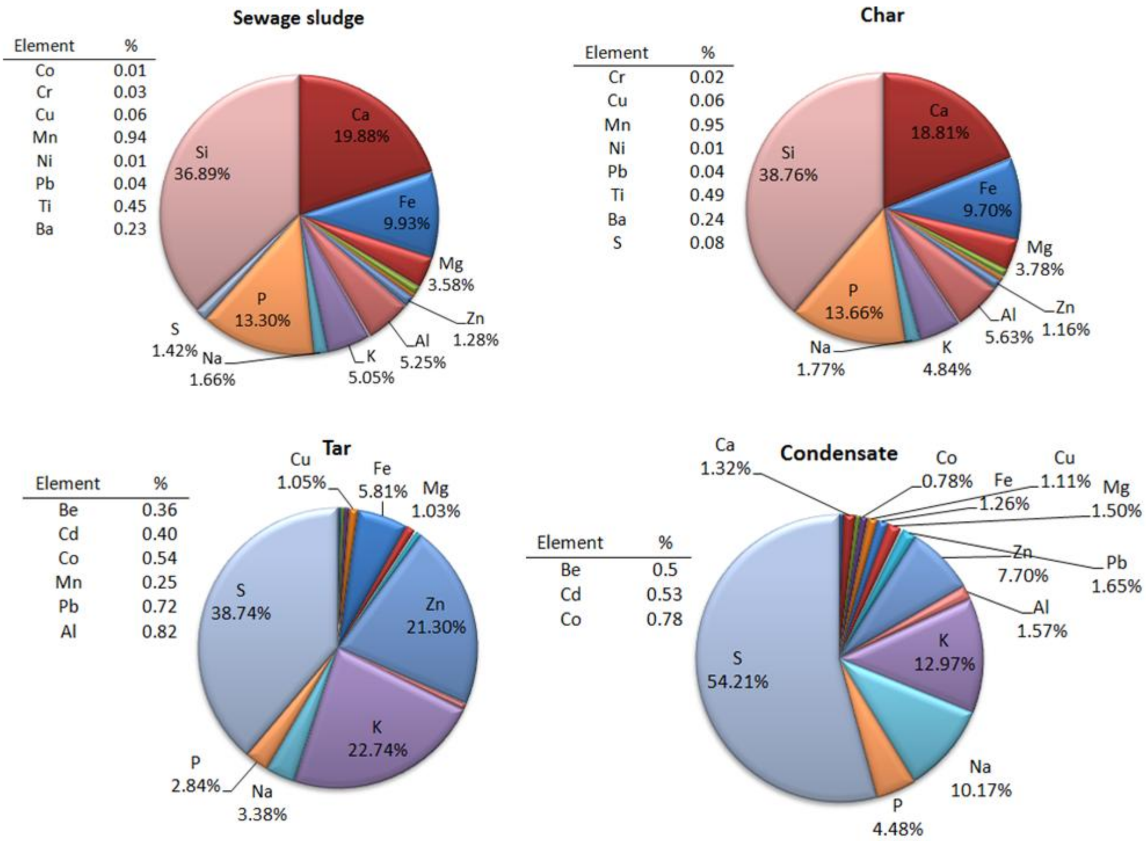

Sewage sludge:

Element	%
Co	0.01
Cr	0.03
Cu	0.06
Mn	0.94
Ni	0.01
Pb	0.04
Ti	0.45
Ba	0.23

Char:

Element	%
Cr	0.02
Cu	0.06
Mn	0.95
Ni	0.01
Pb	0.04
Ti	0.49
Ba	0.24
S	0.08

Tar:

Element	%
Be	0.36
Cd	0.40
Co	0.54
Mn	0.25
Pb	0.72
Al	0.82

Condensate:

Element	%
Be	0.5
Cd	0.53
Co	0.78

Fig. 4. Elemental distribution in sewage sludge and pyrolysis products of sewage sludge.
The results in tables near the diagrams present the values lower than 1%

Measured results showed that the total elemental contents in SS varied greatly, which were in the order of: Si > Ca > P > Fe > Al > K > Mg > Na > S > Zn > Mn > Ti > Ba > Cu > Pb > Cr > Co > Ni > Be > Cd. Almost the same variation of measured elements were determined in SSCh. The variation could be influenced by degradation and transformation of organic substances in SS. The concentrations in SSCh increased but variation left almost the same like in SS. The element concentrations in tar varied: S > K > Zn > Fe > Na > P > Cu > Mg > Al > Pb > Co > Cd > Be > Mn in condensate: S > K > Na > Zn > P > Pb > Al > Mg > Ca > Fe > Cu > Co > Cd > Be > Mn.

3. CONCLUSIONS

The elemental composition of sewage sludge depends on numerous factors such as: industry, city size, population, and the social aspects. A number of methods and technologies to reuse sewage sludge (utilisation) is known, but most of them have not been fully exploited, because of the specific characteristics of sewage sludge. Recently, the pyrolysis process is the most applicable method to reuse sewage sludge, due to the close energy and environmental relationship.

The char fraction retains most of the heavy metals present in the sewage sludge and is a by-product that has to be valorised in order to increase the feasibility of the process. The high ash content, together with a low carbon content and calorific value, makes char unattractive for energetic purposes. But it provides opportunity for its application as soil amendment in agriculture or as adsorbent in water treatment processes. Although a biochar may not be suitable for land application, it can still be mixed with coal and burned to generate power in a modern coal-fired facility equipped to capture heavy-metal emissions. Also, sewage sludge char can be used as an adsorbent for heavy metals, as it has a high affinity of the most volatile heavy metal Hg and to lesser extents of Pb, Cu, Cd, and Cr. Another option is to reduce the heavy-metal concentration initially present in the sewage sludge by activated carbon, acids, or other techniques and utilize the heavy metals as a resource in the metal industry.

The estimation of element distribution by percentage showed that biggest part of SS and SSCh is presented from ash-forming elements such as Si, Ca, P, and Fe. The percentage distribution of main heavy metals Co, Cr, Cu, Ni and Pb in the overall mass balance is less than 1%, although Be and Cd distribution in the overall mass balance is less than 0.01%. The elemental variation in liquid pyrolysis products is totally different than in SS or SSCh. The biggest part of SST and SSC composition consists of three elements such as S, Zn and K.

REFERENCES

1. MENDEZ, J., INGUANZO, M., PIS, J. Microwave-induced pyrolysis of sewage sludge. *Water Res*. 2002;36(13):3261-3264. doi:10.1016/S0043-1354(02)00017-9.
2. CHEN. Z., HU, M., CUI, B., LIU, S., GUO, D., XIAO, B. The effect of bioleaching on sewage sludge pyrolysis. *Waste Manag*. 2015;48:383-388. doi:http://dx.doi.org/10.1016/j.wasman.2015.10.002.
3. HEINRICH, A. Changes in Chlorinated Organic Pollutants and Heavy Metal Content of Sediments during Pyrolysis (7 pp). *Environ Sci Pollut Res - Int*. 2007;14(1):12-18. doi:10.1065/espr2006.07.322.
4. CHEN, F., HU, Y., DOU, X., CHEN, D., DAI, X. Chemical forms of heavy metals in pyrolytic char of heavy metal-implanted sewage sludge and their impacts on leaching behaviors. *J Anal Appl Pyrolysis*. 2015;116:152-160. doi:10.1016/j.jaap.2015.09.015.
5. CHEN, T., ZHANG, Y., WANG, H.. Influence of pyrolysis temperature on characteristics and heavy metal adsorptive performance of biochar derived from municipal sewage sludge. *Bioresour Technol*. 2014;164:47-54. doi:10.1016/j.biortech.2014.04.048.
6. YUAN, Y., YUAN, T., WANG, D., TANG, J., ZHOU S. Sewage sludge biochar as an efficient catalyst for oxygen reduction reaction in an microbial fuel cell. *Bioresour Technol*. 2013;144:115-120. doi:10.1016/j.biortech.2013.06.075.
7. ZHOU, L., LIU, Y., LIU S. Investigation of the adsorption-reduction mechanisms of hexavalent chromium by ramie biochars of different pyrolytic temperatures. *Bioresour Technol*. 2016;218:351-359. doi:10.1016/j.biortech.2016.06.102.

CYSENI 2017, May 25-26, Kaunas, Lithuania
ISSN 1822-7554, www.cyseni.com

GENERATION OF A TEST REFERENCE YEAR FOR DAUGAVPILS, LATVIA

M. Ruduks, A. Lešinskis
Department of Architecture and Building
Latvia University of Agriculture
Akadēmijas str.19, LV-3001 Jelgava – Latvia
E-mail: martins.ruduks@inbox.lv

ABSTRACT

Building performance analysis requires actual and reliable meteorological data. Since meteorological conditions vary significantly from year to year, there is a need to create a test reference year (TRY), to represent the long term weather conditions over a year. In this paper TRY data model was generated by analysing every 3-hour weather data for a 30-year period (1984–2013) in Daugavpils, Latvia, provided by the Latvian Environment Geology and Meteorology Centre (LEGMC). TRY model was generated according to standard LVS EN ISO 15927-4. The generated TRY contains from typical months that are included in TRY from a number of different years. The data gathered from TRY was compared with the climate data from the Latvian Cabinet of Ministers regulation No. 379, Regulations Regarding Latvian Building Code LBN 003-15. Average monthly temperature values in LBN 003-15 were lower than the TRY values, that indicate on climate changes in this location. The results of this study may be used in building energy simulations and heating-cooling load calculations for selected region. TRY selection process should include the most recent meteorological observations and should be periodically renewed to reflect the long term climate change.

Keywords: test reference year; climate analysis, climate change

1. INTRODUCTION

In Latvian legislation long-term climate data is reflected in the Latvian Building Code (LBN) 003-15 „Būvklimatoloģija” (Construction climatology), [1], where various climatic indicators are shown that represent the climatic situation in the territory of Latvia, providing information about the average monthly and yearly meteorological parameters. But this information is not enough to fully describe the region’s climatic conditions, because there is a necessity to define every day and every hour meteorological data values.

The need of such meteorological data worldwide led to the development of methodologies for generating the typical reference year (TRY) in the USA known as a typical meteorological year (TMY) [2]. TRY is a data set that contains a sequence of 8760 hourly values of chosen meteorological quantities. The requirement of TRY is that it has to correspond to an average year [3]. TRY provides every hour climatic parameter values, enabling to use these parameters for heating, ventilation and air conditioning (HVAC) device management and capacity optimization. One of the most important tasks to optimize these devices is to choose correct and precise outdoor air temperature that can be determined with TRY model [4].

Creation of TRY was introduced in 1978 by Hall et al. [2]. For a network of stations in the United States, a representative database consisting of weather data was created. Hall’s method has been used to successfully generate TRYs for a number of locations across the globe [2–3; 5–18].

LBN 003-15 describes climate parameters for ten cities of Latvia. These parameters have been calculated using data from 1961–1990 [1]. The aim of this research was to generate a representative climate database for one of these cities – Daugavpils, by employing the method according to standard LVS EN ISO 15927-4 [19]. Generation of TRY of Daugavpils would provide with hourly climate data that LBN 003-15 does not provide.

Geographical data for Daugavpils: latitude 55º56'03.05" N; longitude 26º39'33.18" E; on relatively flat, open area surface, elevated 124 m above sea level. Located 190 km from capital city of Latvia - Rīga (Fig. 1). Average annual temperature 5.5 °C [1].

The TRY is generated using the available weather data obtained from the station of Daugavpils by the Latvian Environment Geology and Meteorology Centre (LEGMC), covering the period from 1984–2013. LEGMAC database provides with 3-hour weather data values for the temperature and relative humidity. As TRY consists of every hour values, the necessary values are interpolated.

In the region there are only few studies that uses LVS EN ISO 15927-4 standard with 30-year weather data, it is Estonian TRY [8], TRY for Alūksne [11], TRY for Liepāja [12] and TRY for Dobele [13]. The aim of this research is to generate TRY for Daugavpils with most recent 30-year (1984–2013) climate data and compare results with similar research.

Fig. 1. Location of Daugavpils

2. METHODOLOGY

In this study, the ISO 15927-4 [19] method was used to construct the TRY. The selection proces of TRY has been previously descriebed in research of Ruduks and Lešinskis [11-13]. The primary selection was made on the basis of dry-bulb air temperature, cloud coverage (ISO 15927-4 suggest to use direct normal solar irradiance, but this parameter is not available for this station, so it was replaced with cloud coverage), and relative humidity. The wind speed was used for secondary selection. To guarantee that the selected year represents the Daugavpils climate as completely as possible, 30-year weather data where applied.

Climate data for TRY creation were obtained from LEGMC database from 1984–2013. LEGMC provides climate data with 3 hour interval, but TRY needs hourly climate data. The necessary data for TRY were calculated by linear interpolation.

In February, there may be 28 or 29 days, and it is not possible to compare years with different count of days; thus, 29. February was excluded from TMY creation. The rest of the days where rearranged in ascending order starting with the first hour of January till the last hour of December (8760 values).

For each climatic parameter p (dry-bulb temperature, cloud coverage and relative humidity), daily means $\overline{p}$ are calculated. For each calendar month m, the cumulative distribution function $\Phi_{p,m,i}$ of daily means over all the years in the data set is calculated using equation (1):

$$\Phi_{p,m,i} = \frac{K_i}{N+1} \tag{1}$$

where K_i – rank order of the i-th value of the daily means within that calendar month in the whole data set;

N – number of days in any calendar month in the whole data set.

For each year y of the data set, the cumulative distribution function $F_{p,y,m,i}$ of the daily means within each calendar month is calculated using equation (2):

$$F_{p,y,m,i} = \frac{J_i}{n+1} \tag{2}$$

where J_i – rank order of the i-th value of the daily means within that calendar month and that year; n – number of days in an individual month.

For each calendar month m the Finkelstein–Schafer statistic for parameter p, $FS_{p,y,m}$ for each year y of the data set is calculated using equation (3):

$$FS_{p,y,m} = \sum_{i=1}^{n} \left| F_{p,y,m,i} - \Phi_{p,m,i} \right|. \tag{3}$$

To normalize $FS_{p,y,m}$ for months of varying lengths, the results of equation (3) are divided by the number of days of the month (28, 30 or 31). For each calendar month individual months are ranked from the multiyear record in order of increasing value of $FS_{p,y,m}$. Monthly average $FS_{p,y,m}$ values of climate parameters dry-bulb air temperature, cloud coverage and relative humidity are added together and the same months of all years are ranked in the order of the increasing value of $FS_{p,y,m}$. From each calendar month, three candidate months with the lowest total ranking are selected. The monthly deviation of the wind speed of the three months is compared with the corresponding multi-year mean of calendar months. The month with the lowest deviation in wind speed is selected as the best month for inclusion in the TRY.

After the selection of the twelve calendar months for TRY, the months should be joined together. The first and the last eight hours of each month are adjusted by interpolation to ensure a smooth transition when months are joined to form a TRY. The adjustment also includes the last eight hours of December and the first eight hours of January, so that the test reference year can be used repeatedly in simulations [19].

3. RESULTS AND DISCUSSIONS

TRY was created combining months from different years based on their ability to follow the criteria described in materials and methods. Selected month/year combinations from which the TRY was created are shown in Table 1. Two months (May and October) were selected from year 2009, two months (February and April) from 1993 and three months (July, September, December) from 1991, but other months were selected from different years. Results displays that months were selected from all range of the observed period.

Table 1. The Month/Year combinations for the composition of TRY

Month	**Jan**	**Feb**	**Mar**	**Apr**	**May**	**Jun**
Year it was selected for TRY	2000	1993	1986	1993	2009	2005
Month	**Jul**	**Aug**	**Sep**	**Oct**	**Nov**	**Dec**
Year it was selected for TRY	1991	2011	1991	2009	1996	1991

Fig. 2 shows cumulative percentage curves for temperature for January, from the weather data used in this research. Comulative percentage for January 1987 is least similar (largest value of FS statistics) to the long tearm cumulative percentage for January but the comulative percentage for January 2012 is most similar (smallest value of FS statistics). January 2000 is selected for TRY when temperature, relative humidity, cloud coverage and wind speed are taken into account.

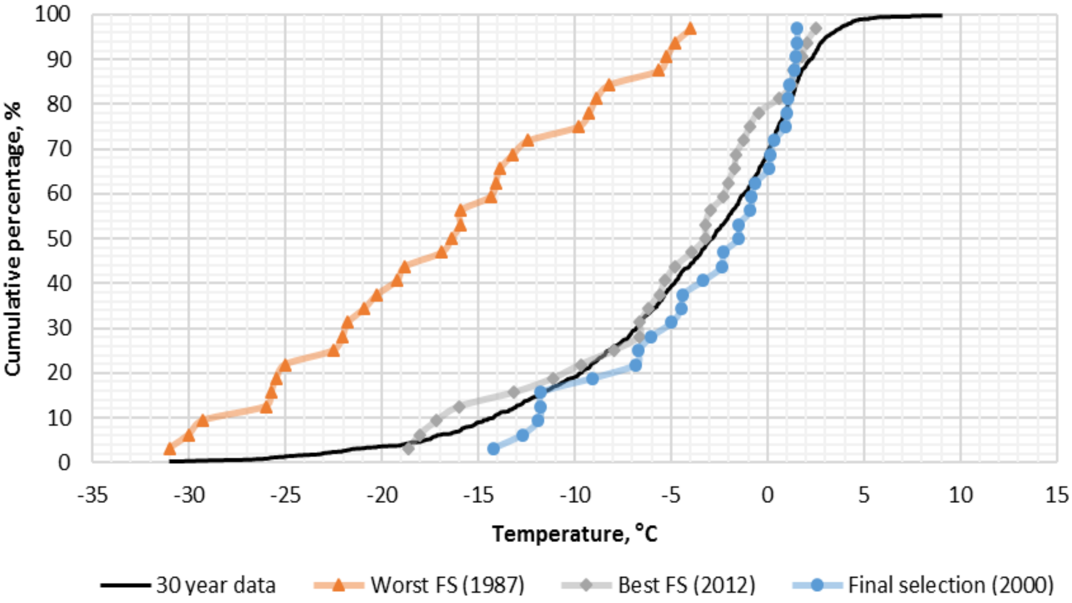

Fig. 2. Cumulative percentage for temperature for different Januaries

After selected months (Table 1) were connected and TRY was created, cumulative percentage for temperature (Fig. 3), temperature fluctuation (Fig. 4), temperature distribution (Fig. 5) and wind speed distribution (Fig. 6) was displayed. Results show similar tendencies with data from Estonian TRY [8], TRY for Alūksne [11], TRY for Liepāja [12] and TRY for Dobele [13].

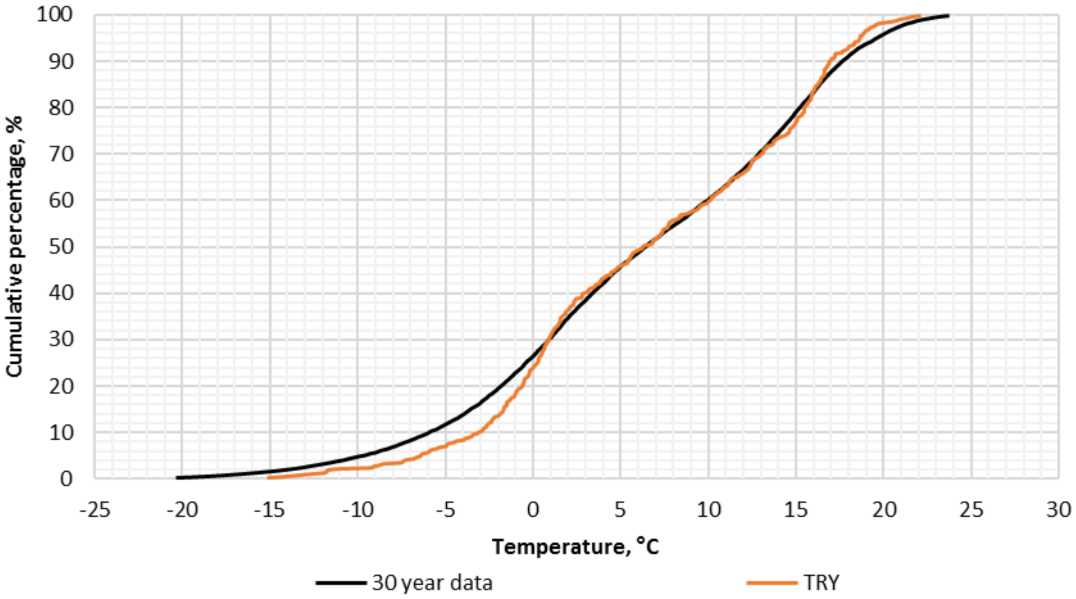

Fig. 3. Cumulative percentage for temperature

Fig. 4 shows how temperature values change in TRY model starting from the beginning of January until the end of December.

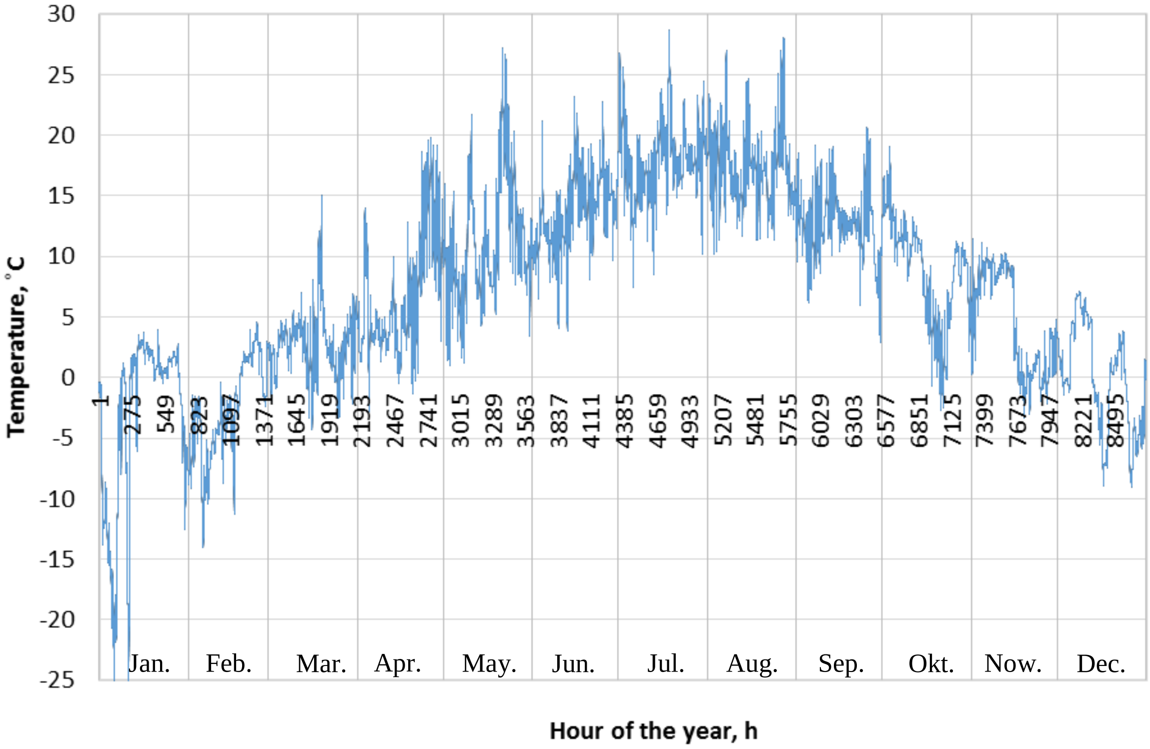

Fig. 4. Temperature fluctuation in TRY

When TRY model temperature distribution values are compared with 30-year average data (long term data) (Fig. 5), TRY model shows a good agreement with the long-term data. TRY model's maximum temperature value deviation from long-term data is 135 hours per year at 1 °C. The total TRY model's temperature deviation from 30-year average data is 1539 hours, compearing TRY for Alūksne deviation from 30-year average data is 1044 hours [11], TRY for Liepāja 1384 hours [12] and TRY for Dobele 1610 hours [13].

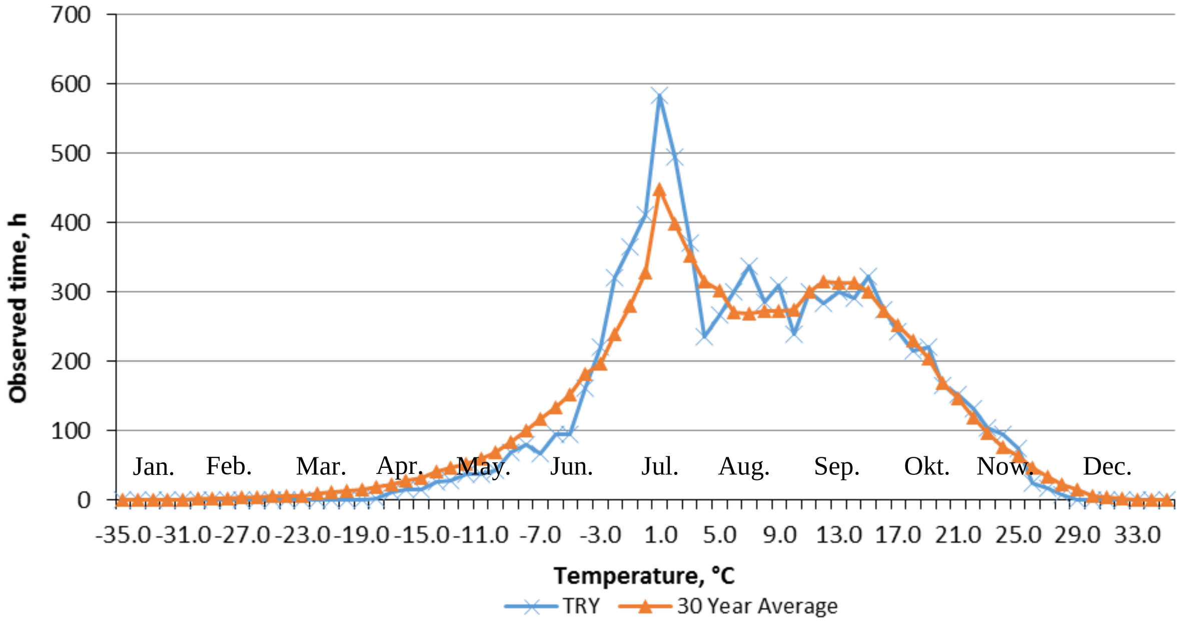

Fig. 5. Hourly temperature distribution for TRY and 30-year average data

Most typical wind speed value in TRY model is 2 m s^{-1}, it is observed for 1935 hours. TRY model's maximum wind speed value deviation from long-term data is 200 hours per year at 0 m s^{-1}. The total TRY model's wind speed deviation from 30-year average data is 518 hours. (Fig. 6).

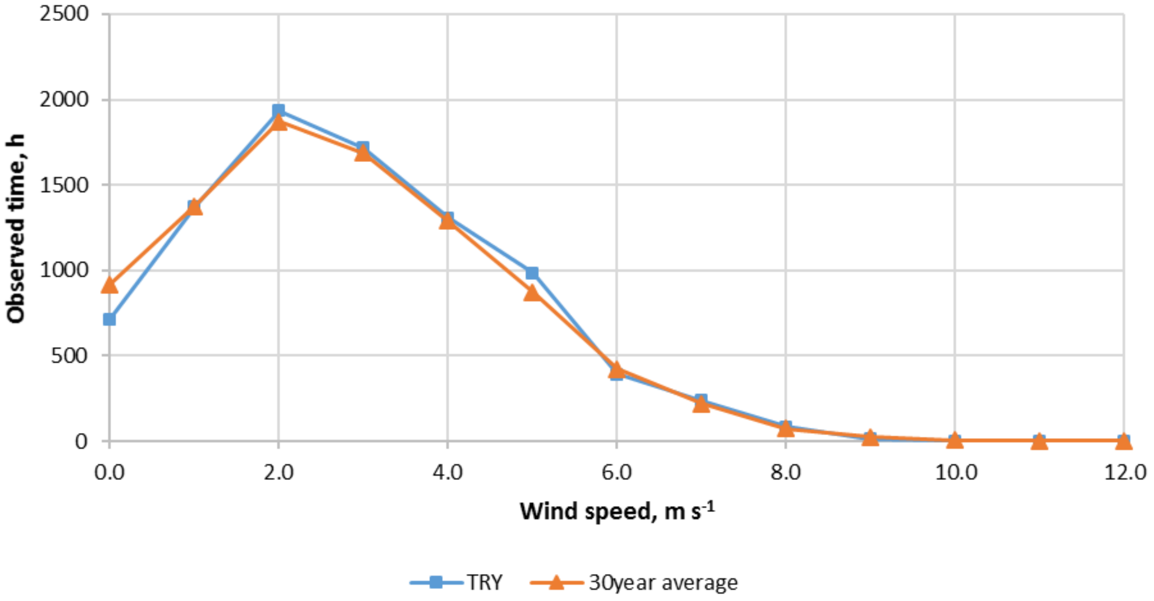

Fig. 6. Wind speed distribution for TRY and 30-year average data

One of the most important results that can be obtained from TRY models is shown in Fig. 7.

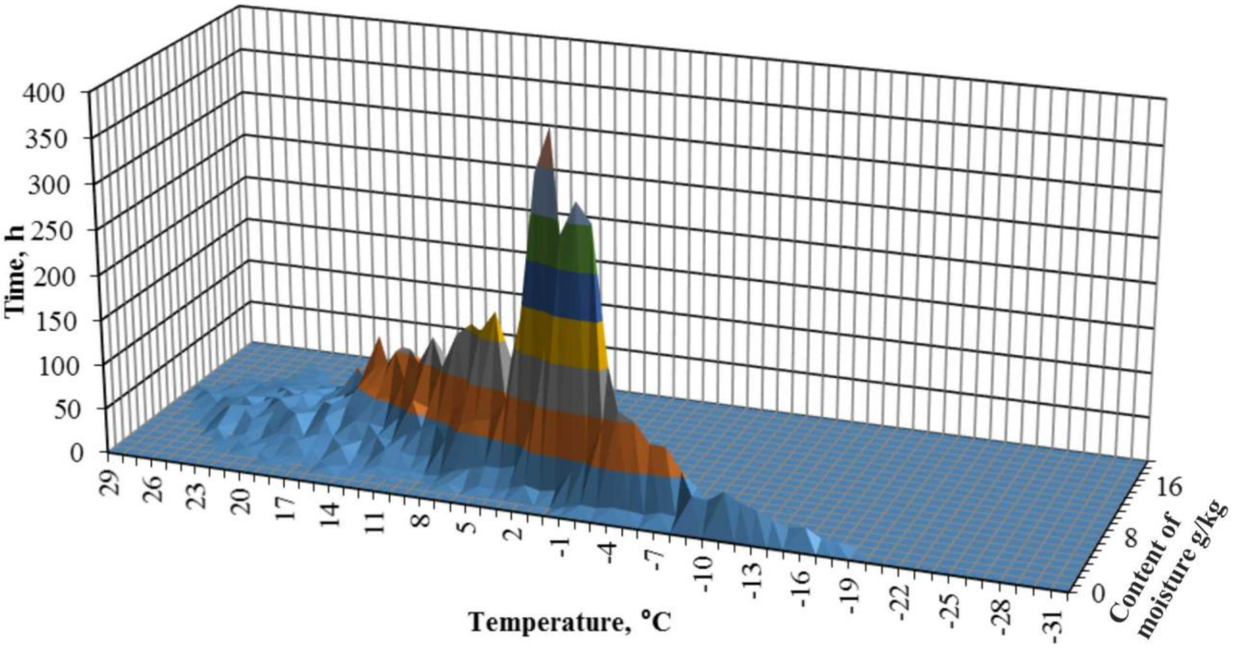

Fig. 7. Combination of temperature and content of moisture for TRY

This figure shows how many hours per year each temperature and content of moisture combination can be observed. Most typical content of moisture and temperature combination in TRY model is 4 g kg^{-1} at 1 °C. This combination can be observed for 364 hours (Fig. 7). Other models in Latvia show similar tendencies: TRY for Alūksne most typical combination is 4 g kg^{-1} at 0 °C and this combination can be observed for 339 hours [11], TRY for Liepāja most typical combination is 4 g kg^{-1} at 2 °C and this combination can be observed for 432 hours [12] and TRY for Dobele most typical combination is 4 g kg^{-1} at 1 °C and this combination can be observed for

353 hours [13]. These results can be used for HVAC system analysis and building energy simulations. Data from Fig. 7 gives an ability to calculate how long it will be necesary to use heating and cooling devices for buildings in this region, and chose optimal capasity for these devices.

Average year temperature value for TRY is 6.6 °C, but for 30-year average data it is 6.2 °C. Comparing results with LBN 003-15 values the difference is 1.1 and 0.7 °C respectively (Table 2). The difference with LBN 003-15 value can be explained by the fact that they have been obtained from 1961–1990, but TRY values were obtained from 1984–2013. The climate change can be the factor for the difference. There is no difference in average relative humidity value for TRY, LBN 003-15 and 30-year average data (Table 3).

Table 2. Average monthly temperature values (°C)

Month	**Jan**	**Feb**	**Mar**	**Apr**	**May**	**Jun**	**Jul**
30 year average	–4.6	–5.1	–0.7	6.5	12.3	15.9	17.8
TRY	–3.4	–2.6	–0.6	6.4	11.5	14.6	17.6
LBN 003-15	–6.7	–5.9	–1.8	5.2	12.1	15.7	16.9
Month	**Aug**	**Sep**	**Oct**	**Nov**	**Dec**	**Average**	
30 year average	16.4	11.3	6.3	0.9	–3.1	6.2	
TRY	16.8	12.1	4.4	4.1	–1.9	6.6	
LBN 003-15	15.9	11.2	6.1	1.0	–3.8	5.5	

Table 3. Average monthly relative humidity value (%) comparison from January till December

Month	**Jan**	**Feb**	**Mar**	**Apr**	**May**	**Jun**	**Jul**	**Aug**	**Sep**	**Oct**	**Nov**	**Dec**	**Average**
30 year average	87	84	78	69	69	74	75	78	83	85	89	88	80
TRY	85	81	81	69	67	75	71	78	84	92	90	88	80
LBN 003-15	85	83	79	73	70	72	75	78	83	85	88	88	80

Average year wind speed value for TRY and 30-year average data are the same 2.8 m/s, but difference with LBN 003-01 value is 0.4 m/s (Table 4). The difference can be explained by the fact that LBN 003-01 values have been obtained from 1961–1990, but TRY values were obtained from 1984–2013, and latest studies show that wind speed values decreases [20].

Table 4. Average monthly wind speed values (m/s)

Month	**Jan**	**Feb**	**Mar**	**Apr**	**May**	**Jun**	**Jul**
30 year average	3.3	3.1	3.1	2.9	2.6	2.3	2.1
TRY	3.2	3.3	3.3	2.8	2.6	2.2	2.1
LBN 003-15	3.5	3.4	3.4	3.3	3.0	2.9	2.7
Month	**Aug**	**Sep**	**Oct**	**Nov**	**Dec**	**Average**	
30 year average	2.1	2.4	2.9	3.1	3.2	2.8	
TRY	2.3	2.3	2.8	3.0	3.1	2.8	
LBN 003-15	2.6	2.9	3.3	3.7	3.5	3.2	

TRY models show similar tendencys when compearing TRY for Daugavpils and TRY models for different locations of Latvia, done by previosu research [11, 12 and 13] (Table 5). TRY model average year temperature values are higher than temperature values in LBN 003-15 in all cases. The highest difference detected in TRY of Dobele 1.3 °C, but lowest difference in TRY of Liepāja 0.8 °C. LBN values were obtained from 1961–1990, but TRY values are gaind from time period from 1984–2013. Tendency for all four researches to show increase in average year temperature value points out the result of global warming.

Table 5. Year average temperature comparison

Parameter/TRY	**Alūksne**	**Daugavpils**	**Dobele**	**Liepāja**
30 year average	5.4	6.2	7.1	7.8
TRY	5.4	6.6	7.2	7.5
LBN 003-15	4.5	5.5	5.9	6.7

4. CONCLUSIONS

The aim of this research was to generate TRY for Daugavpils and compare results with similar research. TRY was generated based on the recent 30-year (1984–2013) climate data and compared with similar research for other cities of Latvia. The average year value difference between TRY and LBN 003-15 for 4 cities is in range of 0.8–1.3 °C. The high average temperature difference between LBN and TRY values in only 20 year time period points out the impact of global warming. The difference points at the necessity of TRY creation, and the latest possible climate data should be used in TRY creation, to represent the latest meteorological conditions.

The results suggests that the research needs to be continued and TRY models need to be generated for other Latvian cities.

REFERENCES

1. LBN 003-15. *Noteikumi par Latvijas būvnormatīvu 003-15 "Būvklimataloģija" (Latvian Building Code 003-15 "Construction climatology")*, 2015- [reffered on 4th of March in 2017 y.]. Link to the internet <http://likumi.lv/ta/id/275013-noteikumi-par-latvijas-buvnormativu-lbn-003-15-buvklimatologija-> (in Latvian).
2. HALL, I.J., PRAIRIE, R.R., ANDERSON, H.E., BOES, E.C. Generation of a typical meteorological year. Denver 1978. Proceedings of the 1978 Annual Meeting of the American Section of the International Solar Energy Society. Denver: Sandia Laboratories. 1978.
3. SKEIKER, K. Generation of a typical meteorological year for Damascus zone using the Filkenstein–Schafer statistical method. *Energy Conversion and Management*, 2004, Vol. 45, p. 99-112.
4. GAUJĒNA, B., BORODIŅECS, A., ZEMĪTIS, J., PROZUMENTS, A. Influence of Building Envelope Thermal Mass on Heating Design Temperature. *IOP Conference Series: Materials Science and Engineering*, 2015, Vol. 96, No. 1, p. 1-8.
5. CHAN, A.L.S., Chow, T.T., Fong, S.K.F., Lin, J.Z. Generation of a typical meteorological year for Hong Kong. *Energy Conversion and Management*, 2006, Vol. 47, p. 87-96.
6. GUGGENBERGER, J.D., ELMORE, A.C., CROW, M.L. Predicting performance of a renewable energy-powered microgrid throughout the United States using typical meteorological year 3 data. *Renewable Energy*, 2013, Vol. 55, p. 189-195.
7. JIANG, Y. Generation of typical meteorological year for different climates of China. *Energy*, 2010, Vol. 35, p. 1946–1953.
8. KALAMEES, T., KURNITSKI, J. Estonian Test Reference Year for Energy Calculations. *In proceedings of the Estonian Academy of Science, Engineering*, 2006, p. 40-58.
9. KALOGIROU, S.A. Generation of typical meteorological year (TMY-2) for Nicosia, Cyprus. *Renewable Energy*, 2003, Vol. 28, p. 2317-2334.

10. LEE, K., YOO, H., LEVERMORE, G.J. Generation of typical weather data using the ISO Test Reference Year (TRY) method for major cities of South Korea. *Building and Environment*, 2010, Vol. 45, p. 956-963.
11. RUDUKS, M., LEŠINSKIS, A. Generation of a Test Reference Year for Alūksne, Latvia. *Proceedings of the Latvia University of Agriculture*, 2015, Vol. 33, No. 1, p. 46-54.
12. RUDUKS, M., LEŠINSKIS, A. Generation of a Test Reference Year for Liepāja, Latvia. *Proceedings of annual 22nd International Scientific Conference Research for Rural Development 2016"*, 2016, Vol. 1, No. 1, p. 175-181.
13. RUDUKS, M., LEŠINSKIS, A. Generation of a Test Reference Year for Dobele, Latvia. *Proceedings of the 13th International Conference of Young Scientist on Energy Issues*, 2016, p. II 46-54.
14. SKEIKER, K. Comparison of methodologies for TMY generation using 10 years data for Damascus, Syria. *Energy Conversion and Management*, 2007, Vol. 48, p. 2090-2102.
15. YANG, L., LAM, J.C, LIU, J. Analysis of typical meteorological years in different climates of China. *Energy Conversion and Management*, 2007, Vol. 48, p. 654-668.
16. ZANG, H., XU, Q., BIAN, H. Generation of typical solar radiation data for different climates of China. *Energy*, 2012, Vol. 38, p. 236-248.
17. ZARIŅŠ, M. *Klimata datu izvēle gaisa kondicionēšanas jaudas aprēķinam.* Jelgava: Latvia University of Agriculture, 2001. 59 p.
18. ZHANG, Q. Development of the typical meteorological database for Chinese locations. *Energy and Buildings*, 2006, Vol. 38, p. 1320-1327.
19. LVS EN ISO 15927-4. Latvijas Valsts Standarts. (Latvia State Standard). Ēku hidrotermiskie raksturlielumi. Klimatisko raksturlielumu aprēķināšana un izteikšana. 4. daļa: Ikstundas dati apkures un dzesēšanas ikgadējā enerģijas patēriņa novērtēšanai. (Hygrothermal performance of buildings - Calculation and presentation of climatic - Part 4: Hourly data for assessing the annual energy use for heating and cooling), 2005. (in Latvian).
20. GREEN, J.S., CHATELAIN, M., MORRISSEY, M., STADLER S. Estimated changes in wind speed and wind power density over the western High Plains, 1971-2000. *Theoretical and Applied Climatology*, 2012, Vol. 109, No. 3-4, p. 507-518.

CYSENI 2017, May 25-26, Kaunas, Lithuania
ISSN 1822-7554, www.cyseni.com

A LITERATURE REVIEW OF SMALL WIND TURBINES USAGE IN URBAN AREAS

V. Zimnickas, G. Gecevičius, A. Markevičius
Lithuanian Energy Institute
Breslaujos str. 3, LT-44403, Kaunas–Lithuania
E-mail: vaidotas.zimnickas@lei.lt

ABSTRACT

World is trying to reduce part of energy which is got/received from fossil fuels for a while now. One of the ways to do it is development of renewable energy, for example / e.g. wind energy. Only in Europe during year 2015 there was installed and connected to grid a total amount of 12800 MW of wind turbines. Because of such a rapid development of wind energy it is quite difficult to find a suitable place, where wind turbine would not disturb citizens, animals and would not influence landscape. One of possible solutions for this problem could be a development of small scale wind turbines in urban areas.

Small scale wind turbines have a lot of advantages: their influence to landscape is low, small wind turbines are more silent and do not cause instabilities in distribution networks. However wind flow in urban areas is very complicated. In urban areas there are many obstacles which cause separation of wind flow and increase wind flow turbulence. For this reason scientists face a lot of problems related to mathematical modelling, which is necessary for an adequate wind turbine place selection. To increase a number small scale wind turbines in urban areas it is important to understand the features of wind flow in cities and make cities' windiness map where the most suitable places for wind turbines would be determined.

The aim of this article is to overview the newest literature related to wind flow modelling in urban areas and compere the most usual models which are used for urban boundary layers.

Keywords: wind turbines, urban areas, CFD modelling

1. INTRODUCTION

Electric power is an inseparable part of our life. Electric power is necessary for daily needs of our society, we hardly imagine our lives without mobile phones, computers, microwaves and other electric devices. According to International Energy Agency by the year 2040th electric demand will grow about 69% compared with 2016 [1]. One of the main reasons why forecasting electric power growth is so high is the increasing number of inhabitants in urban areas. At the same time population growth in cities will cause increased electric power demand for heating and cooling. For this reason it is necessary to pay more attention to renewable energy resources, which are clean and environmentally friendly. A special attention should be paid to wind power because wind technology prices are shrinking, at the same time electric power made in wind turbines is becoming cheaper and more competitive to electricity produced by using other resources. An average electricity price for 1 kWh produced by wind turbine in Lithuania in 2015 was 0.075 eur/kWh; produced by solar panel – 0.142 eur/kWh [2]. At the same time an average electricity price for 1 kWh in market in 2015 was 0.042 eur/kWh [2].

Wind energy has a lot of potential in urban areas. It was shown that urban obstacles like high buildings could increase wind speed and also could help to increase performance of small scale wind turbines. However at the same time those obstacles increase turbulence intensity [3]. It is obvious that wind energy is one the best choices for trying to reduce dependence on fossil fuel .In order to maximize the usage of wind energy potential more wind speed parameter measurements should be taken and more attention should be paid to wind speed mapping in urban areas.

2. HORIZONTAL AXIS WIND TURBINES VS. VERTICAL AXIS WIND TURBINES

Wind energy has been used as an energy source for ships and mills for hundreds of years. In 1889 in the USA Charles Brush tried to use windmill to generate electricity. Till 20th century horizontal axis wind turbines (HAWTs) and vertical axis wind turbines (VAWTs) were developed in parallel. In 1922 S. J. Savonius invented the Savonius turbine. Few years later in 1931 Georges Darrieus patented his idea of VAWT with straight and bent blades. Different types of VAWT are presented in Fig. 1.

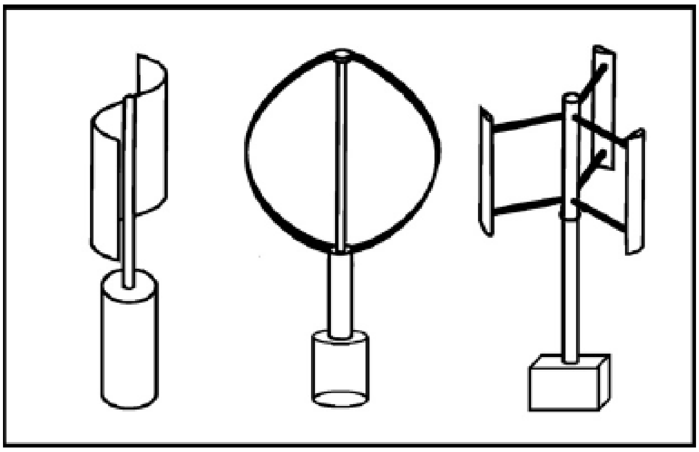

Fig. 1. On the left side – Savonius rotor; in the middle – Darrieus turbine; on the right side – an H-rotor [4]

However when it was proved that large scale HAWT is more efficient than VAWT, interest in VAWT technologies decreased and now we have the situation that absolute majority of wind turbines built around the world are HAWT. However there are scientists who believe that HAWTs are not so evidently better than VAWTs [5, 6].

2.1. VAWT advantages vs. HAWT advantages

HAWTs dominate when it is discussed about large scale wind turbines (installed power are 1MW – 3 MW). However for small scale wind turbines HAWTs are not so effective. The VAWT technology has some advantages that could make it more attractive to smaller size applications, especially in complex contexts like urban areas.

1. Main difference between VAWT and HAWT is that VAWT does not need any yaw mechanism, it is omni-directional, for this reason installation and maintenance costs of VAWT are smaller. Furthermore VAWTs have no power losses during the time that it takes to react to temporary changes in wind direction [7].
2. HAWTs have lower performance when turbulence intensity is high and they are mainly recommended for open city areas. The high variability of wind direction in urban areas is an extra disadvantage because with lower wind velocities start up time of HAWT increases. To avoid these problems horizontal axis wind turbine should be installed on large structures or in zones with low building density [8].
3. VAWTs create less noise and vibration compared with HAWT. There are two main sources of noise: aerodynamic noise and mechanical noise. The aerodynamic noise occurs due to rotation of turbine blades. Usually the speed of VAWT’s tips is about only half of HAWT’s tip speed, for this reason VAWTs generate less aerodynamic noise. Also VAWTs generate less mechanical noise because there are fewer moving parts than in HAWTs. Furthermore wind turbine generators create low frequency vibrations (above 16 Hz). Those vibrations could be transmitted to building constructions and could cause serious damage, if buildings are not industrial [9].

2.2. HAWT and VAWT performance under high turbulent air conditions

Fig. 2 illustrates the wind flow around tall buildings when incident wind velocity is 1 m/s. In this situation VAWT could work properly, but HAWT could not. Moreover in such case HAWT experiences additional strain, which might cause a damage to the turbine, with a consequent risk of an accident.

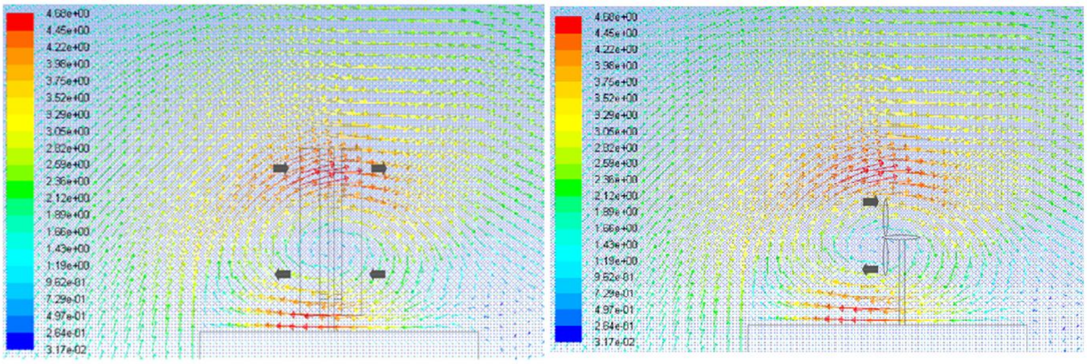

Fig. 2. Superposition of wind speed intensity of VAWT and HAWT when wind speed equals 1 m/s [9]

There are a lot of articles which try to estimate HAWT or VAWT alone, but there are only a few which compare both type wind turbine in same urban areas. Pagnini et al. (2015) [10] investigated the performance of HAWT and VAWT turbines in high turbulence urban areas. They built HAWT and VAWT in Savona city harbor where wind flows mainly in two directions: west-north (WN) (from the city to the sea) and from east-south (ES) (from the sea to city). The place which was chosen for wind turbine is unique for its unstable atmospheric conditions. They are unstable due to the thermal effect of the Mediterranean Sea. Measurements show that wind from ES direction dominates in interval from 0–6 m/s and higher than 16 m/s. Wind from WN direction dominates in 7–15 m/s range. The influence of turbulence intensity to wind turbine power is shown in Fig. 3 [10].

The effect of turbulence and wind gusts seems to affect HAWT power output more than VAWT. During high turbulence intensities HAWT is automatically stopped, while VAWT remains operational with the rated power almost to its maximum value. Fig. 3 represent power curves at three difference wind speed intensity: $I_u < 10\%$, $10\% < I_u < 20\%$ and $20\% < I_u < 40\%$, and compare them with manufacturer and measures power curves.

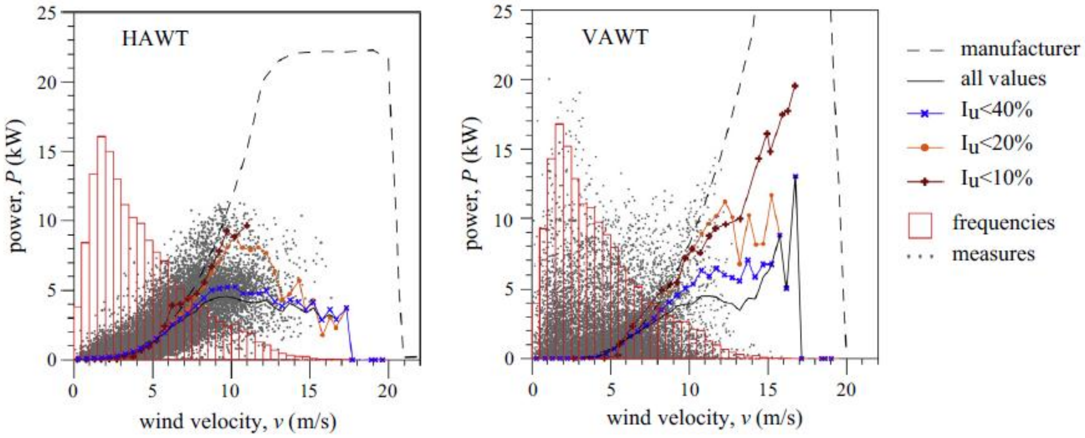

Fig. 3. Averaged power, experimental power curve and wind speed frequencies of HAWT and VAWT [10]

3. WIND FLOW IN URBAN AREAS

When we talk about wind energy development in urban areas we can use only small scale wind turbines. Installation of 1 kWh of small scale wind turbine costs about 5000 $ which is much more than for example large scale wind turbine which 1 kWh costs about 2000 $. For this reason electric energy produced by small wind turbines could be competitive only when location of wind turbine is chosen thoroughly [11].

Wind flow in urban areas is heavily influenced by such parameters as: orientation of the buildings to wind, their shape and space between two different buildings, the shape of the rooftops of the buildings.

3.1. Building's rooftop shape and height influence to wind flow

The shape of the rooftop could have a positive influence to wind flow if the location of the wind turbine on rooftop is chosen thoroughly. Abohela et al. (2013) [12] investigated influence of the shape of the rooftop and wind direction to wind flow around the buildings. They researched 6 most common rooftop shapes, illustrated in Fig. 4.

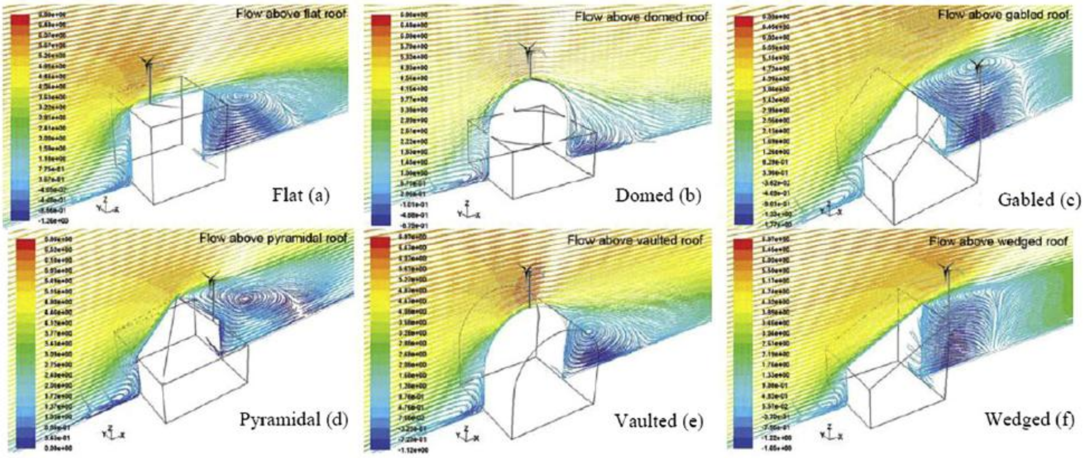

Fig. 4. The most common rooftop shapes, from the top to the right: flat, domed, gabled, pyramidal, barrel vaulted, wedged and wind flow around them [12]

Results show that all shapes of the rooftops have a positive influence to wind speed. Influence is the highest when wind flow is perpendicular to building. They discovered that the shape of the rooftop could accelerate wind in all cases in range between 9.3% for wedged rooftop and 56.1% for vaulted rooftop. These results validate other experiments which show that this wind acceleration could be reached only if wind turbine rotor lowest point would be at least 30% above the rooftop [13]. Also experiments made by Abohela et al. (2013) [12] show that the best location for wind turbine in all cases is different and depends on wind flow above the rooftop.

From the first look it could seem that the best place for wind turbine is on the highest building. However wind turbine which is placed on the highest building also might suffer from higher levels of turbulence. During researches Abohela with colleagues [12] discovered that turbulence intensity depends on the height of the building. They also found out that with increasing height of the building turbulence intensity may increase as well. However they got these results by modelling single-standing building and neglected other buildings. So this situation could be possible only in rural areas. In urban areas wind flow around buildings depends not only on particular building height but also on orientation to wind direction of other buildings and their height. There are numbers of studies which show positive influence of building height in urban areas [14, 15].

3.2. Vegetation influence to wind flow

One of the biggest challenges while modelling wind flow in urban areas is estimation of vegetation. It might be estimated in few ways:

a) All vegetation reflected as areas of increased surface roughness;
b) Vegetation modelled as a porous media;
c) Each plant modelled separately.

Vegetation reflected as increased surface roughness is not reliable because in that case in vegetated areas particular wind speed will be overestimated. Modelling each plant separately probably would give us the most accurate results, however this task could take a lot of time to create geometry and calculate possible problems. The most promising way to estimate vegetation is to model them as porous media. The wind speed reduction due to urban trees could be written as additional sink terms added to the turbulent momentum equation (Eq. 1) [16].

$$S_{ui} = -c_d L(z) \cdot U \cdot u_i \tag{1}$$

In this equation c_d is a drag coefficient, $L\ (z)$ is a equivalent leaf-area density of the plant at height z, U is the mean wind speed at height z, and u_i is wind velocity component. To parameterize the additional mechanical production of turbulence due to the trees could be written as additional source term added to turbulent kinetic energy equation (Eq. 2).

$$Q_{veg} = c_d L(z) \cdot U^3 - 4 c_d L(z) \cdot U \tag{2}$$

Illustrations of two different results of vegetation modelling are presented in Fig. 5. Fig. 5 shows the relative changes in the normalized wind speed. Blue colour represent decrese of wind speed and red increses. It is clearly seen that the model which shows trees as increased surface roughness areas overestimates wind speed. This model shows that the changes of wind speed caused by trees is between -2.5% and 2.5% (on the right side in Fig. 5). Nonetheless, more accurate method for tree modelling, such as porous media, shows speed reduction between -7.5% and -10% (on the left side Fig. 5).

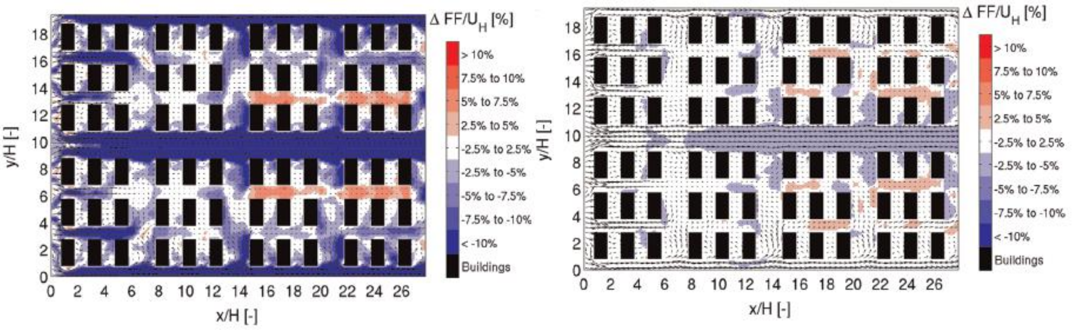

Fig. 5. Tree influence on wind flow in urban street canopy. On the left trees are modelled as porous media, on the right - as increased surface roughness areas [17]

4. WIND RESOURCE ESTAMATION IN URBAN ARAS

One of the first steps before using wind energy in urban areas is to establish an overview of the available wind resources. This overview would help to identify potentially suitable urban areas for high and low wind. The best way to identify these locations are long term measurements on-site, at multiple heights. However, as it was mentioned above, long term measurements for small scale installation are not financially rewarding. Indirect method must be used to assess the wind resources for small wind turbines [18].

One of those indirect methods has been proposed by Millward-Hopkins and colleagues [18]. They suggested a method for wind speed up-scaling in urban areas which is shown in Fig. 6.

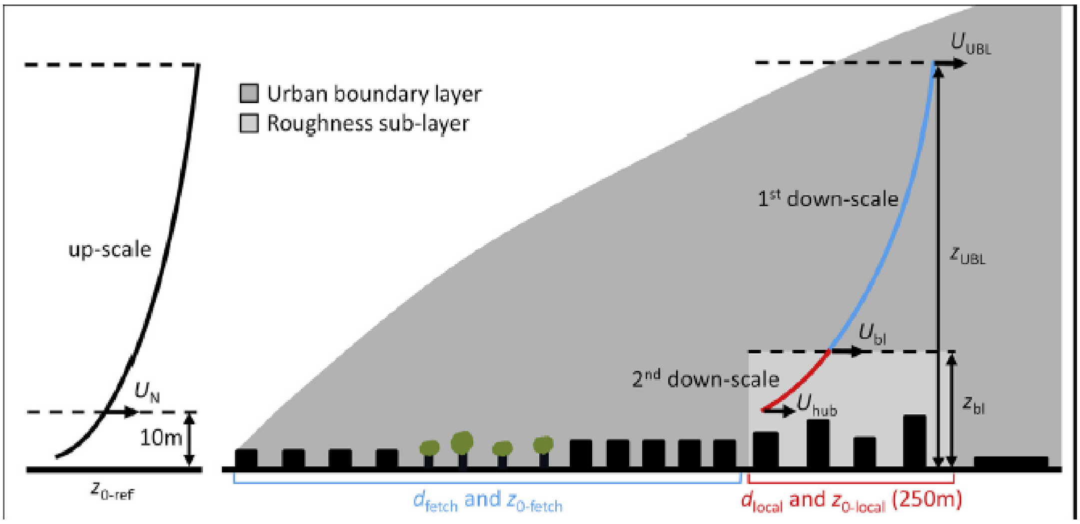

Fig. 6. Schematic diagram of wind speed change over urban areas [18]

In this method Millward-Hopkins with colleagues [18] suggest at first to up-scale wind speed from a regional wind climate to a height z_{ubl}, at which the frictional effect of the surface is negligible, by using standard logarithmic profile.

$$U_{ubl} = U_N \frac{ln(z_{ubl} - z_0)}{ln(10 - z_0)} \tag{3}$$

Second step in this method is down-scaling wind speed for turbine hub height using aerodynamic parameters which are appropriate for the urban area. The first down-scaling step is used to estimate the wind speed at Blanding height z_{bl}. Z_{bl} is the height below which the wind profile is considered to be determined by the local geometry.

$$U_{bl} = U_{ubl} \frac{ln[(z_{bl} - d_{fetch})/z_{0-fetch}]}{ln[(z_{ubl} - d_{fetch})/z_{0-fetch}]} \tag{4}$$

where $z_{0\text{-}fetch}$ – surface roughness, d_{fetch} – displacement height.

Second down-scaling step is used to estimate the wind speed at hub height.

$$U_{hub} = U_{bl} \frac{ln[(z_{hub} - d_{local})/z_{0-local}]}{ln[(z_{bl} - local)/z_{0-local}]} \tag{5}$$

$Z_{0\text{-}local}$ and d_{local} are surface roughness and displacement height for 250 m cell. Using method like this possibility to overestimate or underestimate wind speed still exists, however such methods are fast and relatively cheap which makes small wind turbines more attractive to investors [19].

5. CONCLUSIONS

1. The type and place for wind turbines should be chosen thoroughly. It is difficult to determine which turbine type is better because both types of wind turbines have their advantages and disadvantages which are revealed under certain environmental conditions. HAWT turbines are better than VAWT at larger scale and in places where wind speed is more stable. However VAWT has huge potential in places were wind speed is highly turbulent and omni directional.
2. CFD modelling should be used for choosing places for wind turbines, because wind flow in urban areas depends on many parameters like height of the buildings, shapes of the rooftops of the buildings, distance between different buildings. CFD modelling could be useful while estimating these dependencies and reducing costs related to this problem.

3. More attention should be paid to the influence of vegetation to wind flow in urban areas. Usually wind speed in urban areas is overestimated because of that reason. Tree influence in urban canopies reveals itself in different ways and depends on canopies width.
4. Usually wind resource estimation methods like long term measurements are not suitable for urban areas because such methods require huge financial resources. Indirect methods should be used more. More attention should be paid to development of such methods together with bigger attention to mapping urban areas.

REFERENCES

1. INTERNATIONAL ENERGY OUTLOOK, 2016 annual report.
2. ELEKTROS ENERGIJOS RINKOS STEBĖSENOS ATASKAITA UŽ 2015 METŲ IV KETVIRTĮ. Link to the internet: < http://www.regula.lt/SiteAssets/naujienu-medziaga/2016/2016-birzelis/elektra-ataskaita-2015_IV-ketv.pdf>.
3. DREW D.R., BARLOW J.F., COCKERILL T.T., Estimating the potential yield of small wind turbines in urban areas: A case study for Greater London, UK. *J. Wind Eng. Ind. Aerodyn.*, Vol. 115, 2013 p. 104-111.
4. ERIKSSON S., BERNHOFF H., LEIJON M., Evaluation of different turbine concepts for wind power. *Renewable & Sustainable Energy Reviews*, Vol. 12, 2008 p. 1419-34.
5. TJIU W., MARNOTO T., MAT S., RUSLAN M. H., Darrieus vertical axis wind turbine for power generation II: Challenges in HAWT and the opportunity of multi-megawatt Darrieus VAWT development. *Renewable Energy* Vol. 75, 2015, p. 560-571.
6. POPE K., DINCER I., NATERER G. F.M Energy and exergy efficiency comparison of horizontal and vertical axis wind turbines. *Renewable Energy* Vol. 35, 2010, 210-2113.
7. TUMMALA A., VELMANTI R. K., SINHA D. K., A review on small scale wind turbines. *Renewable and Sustainable Energy Reviews*, Vol. 56, 2016, 1351-1371.
8. ARAUJO A.M., VALENCIA D., ASIBOR A., ROSAS P., An approach to simulate wind fields around an urban environment for wind energy application. *Environmental Fluid Mechanics*, Vol. 13, 2013, p. 33-50.
9. SILVA F. T., SANTOS A. C., GIL M. C., Urban wind energy exploitation systems: Behaviour under multi directional flow conditions – opportunities and challenges. *Renewable and Sustainable Energy Reviews*, Vol. 24, 2013 p. 364-378.
10. PAGNINI L. C., BURLANDO M., REPETTO M., Experimental power curve of small-size wind turbines in turbulent urban environment. *Applied Energy* Vol. 154, 2015, p. 112-121.
11. GRIESER B., SUNAK Y., MADLENER R., Economics of small wind turbines in urban settings: An empirical investigation for Germany. *Renewable Energy*, Vol. 78, 2015, p. 334-350.
12. ABOHELA I., HAMZA N., DUDEK S., Effect of roof shape, wind direction, building height and urban configuration on the energy yield and positioning of roof mounted wind turbines. *Renewable Energy*, Vol. 50, 2013, p. 1106-1118.
13. WHITE L. V., WAKES S. J., Permitting best use of wind resource for small wind-turbines in rural New Zealand: A micro-scale CFD examination. *Energy for Sustainable Development*, Vol. 21, 2014, p. 1-6.
14. LIN LU., KE SUN., Wind power evaluation and utilization over a reference high-rise building in urban. *Energy and Buildings*, Vol. 68, 2014, p. 339-350.
15. YANG A.S., SU Y. M., JUAN Y. H., WANG W.S., CHENG C. H., Estimation of wind power generation in dense urban area. *Applied Energy*, Vol. 171, 2016, p. 213-230.

16. KARMAS A., PROSPATHOPOULOS J.M., CHAVIAROPOULOS P. K., YAKINTHOS K., Wind flow simulation over forested areas using a 3DRANS solver with a tree – scale approach. *Wind Eng.Ind.Aerodyn.*, Vol. 155, 2016, p. 149-158.
17. SALIM M. H., SCHULZEN K. H., GRAWE D., Including trees in the numerical simulations of the wind flow in urban areas: Should we care? *Wind Eng.Ind.Aerodyn.*, Vol. 144, 2015, p. 84-95.
18. MILLWAR-HOPKINS J. T., TOMALIN A. S., MA L., INGHAM D. B., POURKASHANIAN M., Mapping the wind resource over UK cities. *Renewable Energy,* Vol. 55, 2013, p. 202-211.
19. MILLWAR-HOPKINS J. T., TOMALIN A. S., MA L., INGHAM D. B., POURKASHANIAN M., Assessing the potential of urban wind energy in a major UK city using an analytical model. *Renewable Energy*, Vol. 60, 2013, p. 701-710.

CYSENI 2017, May 25-26, Kaunas, Lithuania
ISSN 1822-7554, www.cyseni.com

NEED FOR ADVANCING THE WAVE LOAD MODELLING ON MONOPILE OFFSHORE WIND TURBINES

A. Mockutė
University of Florence
Via Santa Marta, 3, 50139 – Italy
E-mail: amockute@dicea.unifi.it

ABSTRACT

This paper is introducing an ongoing doctoral research project on wave load modelling on monopile-supported offshore wind turbines, the state-of-the-art review and motivations behind it. Offshore wind provides a clean and inexhaustible source of energy with fewer noise and visual impact constraints. However, offshore wind technology is still very costly and the support structure accounts for a large part of the expense. Monopiles are the most common support type for offshore wind turbines, and they are prone to highly nonlinear excitations, such as 'ringing', when exposed to steep waves. These dangerous nonlinear effects are omitted if linear or weakly nonlinear wave theories are used, which is the case for the majority of current solvers. In addition, Morison's equation is normally used for hydrodynamic loading calculations in the industrial solvers due to its simplicity, but researchers have expressed doubts for its suitability where nonlinear effects count. The introduced doctoral research project therefore aims to improve current aero-hydro-servo-elastic solver without excessively compromising the computational efficiency. Work is conducted on two main areas: a potential flow Boundary Element Method code for fully nonlinear water waves, and a comparison study including Morison's equation, its corrections and FNV theory to determine most appropriate hydrodynamic loading model.

Keywords: Offshore wind energy, monopile-supported offshore wind turbines, wave load modelling, numerical solvers, nonlinear effects, ringing

1. INTRODUCTION

This paper is introducing an identified gap in advanced numerical modelling of offshore wind turbines, along with the chosen methodology for a doctoral research project which aims to fill it.

Climate change, exhaustible fossil fuels and the ever-increasing energy demand are creating a trilemma for which an environmentally friendly, economic and reliable energy source is needed, and wind energy is proving to fit this description [1–3].

Offshore locations provide higher wind speeds, steadier wind flow, and lesser issues with noise and visual impact, therefore allow for larger scale turbines, which can in turn generate greater amounts of electricity. For instance, the largest currently installed offshore wind turbine VESTAS V164-8MW with one rotation at rated speed produces enough to power an average UK household for 29 hours [4]. Consequently, offshore wind energy is playing an important role in the energy sector and is helping the governments meet their renewable energy targets.

Offshore wind turbines are large and expensive structures, therefore full-scale testing, especially at the initial phases and on innovative designs, is impractical. Scaled model tests are costly and time-consuming too, therefore cannot be carried out on every new concept. The most efficient method to check the viability of a location or to design offshore wind turbines is numerical simulation. Understandably, it needs to be thoroughly validated to ensure its reliability, and constantly advanced to keep the most appropriate balance between accuracy and required computational time [5].

More accurate modelling of the turbine loading and its response have multiple benefits. Firstly, it reduces the uncertainties, therefore helps to avoid overdesigning the structure, leading to reduced production cost. Secondly, correctly predicting failure modes contributes to increasing life expectancy of the system, and thus more appealing payback period [6].

The currently used codes for modelling the support structures of the offshore wind turbines were recently tested and compared in the Offshore Code Comparison Collaboration (OC3) [7], and its Continuation (OC4) [8]. In OC3 multinational participants used various codes to model NREL offshore 5 MW baseline wind turbine (a representative model developed for the use in conceptual evaluation studies, for details refer to [1]) in four phases: on (I-II) monopile with rigid and flexible foundations respectively, (III) tripod, and (IV) floating spar-buoy [7]. OC4 included two more supporting structures for the same baseline turbine – jacket support structure and DeepCwind semisubmersible [8]. All the support structures are illustrated in Fig. 1 along with the projects and depths they were modelled in.

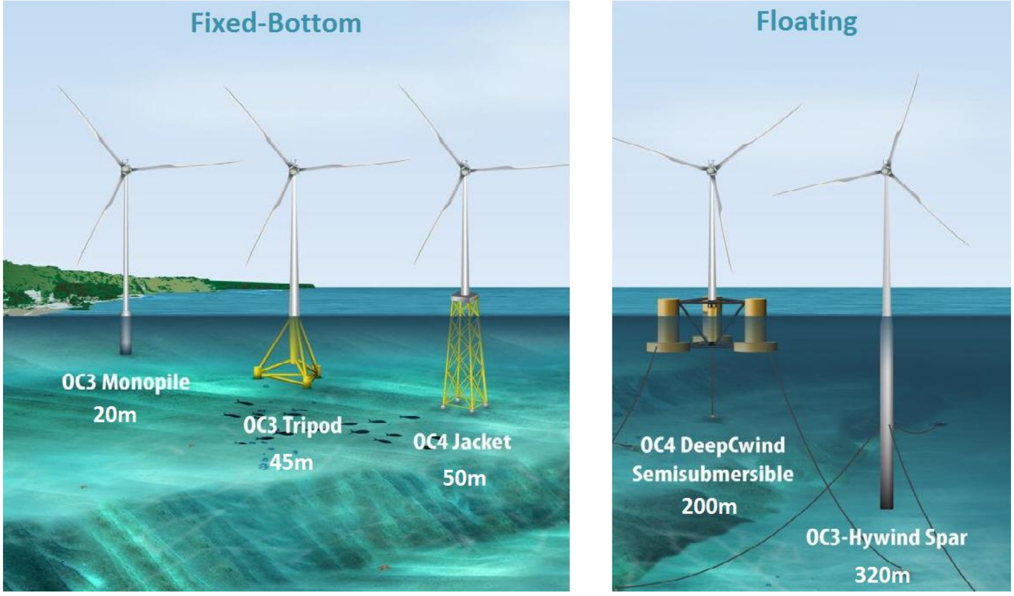

Fig. 1. The five studied support structures, the projects and depths they were modelled in. Courtesy of [10].

One of the concluding remarks of the OC3 and OC4 projects was that comparing code-to-code detects mismatches among the codes, but does not distinguish which code represents real case most accurately [11]. For this reason Offshore Code Comparison Collaboration Continuation, with Correlation (OC5) project is being carried out [10], making it fundamental for this research project. Phase Ia (Validation of Hydrodynamic Loading on a Fixed Cylinder) is focused only on hydrodynamic loads and reliability of their modelling approaches [12]. A simplified cylinder without a dynamic turbine is examined, because discrepancies in hydrodynamic loading modelling were noted in OC4 phase II but due to the complexity of semisubmersible structure it was impossible to investigate the subject at the time [11].

In the OC5 Phase Ib [12] a flexible cylinder (scaled version of OC3 monopile) was fixed to the floor of a wave tank with a sloped floor to include nonlinear wave transformation from deep to shallow water and the effects on the structure. Varied wave theories and hydrodynamic models were employed by participants to calculate the shear force at the seabed and the acceleration at the top. The key observations were the discrepancies in behaviour of the models in steeper waves where nonlinearities become significant. Second- and third-force peak components of the force signal were found to be much larger in shallower water than in deep. Although the values of these nonlinear contributions may not be very large, they have the possibility of exciting natural frequencies in the structure, resulting in fatigue issues such as ringing and springing. However, linear and weakly nonlinear wave models, which are commonly used in standard solvers, barely captured these peaks, implying that in the offshore wind turbine design process such dangerous phenomenon as ringing is likely omitted.

The structure of this paper is therefore as follows: Section 2 will explain the subject of interest – ringing, as well as the advances in the understanding and modelling of it, and its interaction with offshore wind turbines. The two main components needed to successfully capture nonlinear resonant phenomena are described in Section 3 and Section 4 along with the methodology chosen to advance them for the doctoral project. Section 5 will provide some concluding remarks and an outlook to future work.

2. RINGING

2.1. Introduction to ringing

Ringing has been first observed on offshore oil and gas platforms and reported in 1992, stating the danger it poses to offshore structures, in particular monopiles and tension leg platforms [13]. As described by Chaplin et al. [14] and illustrated in Fig. 2, "Unlike springing, ringing has a severely non-Gaussian nature, generates very high stress levels within a burst of only a few oscillations <…>."

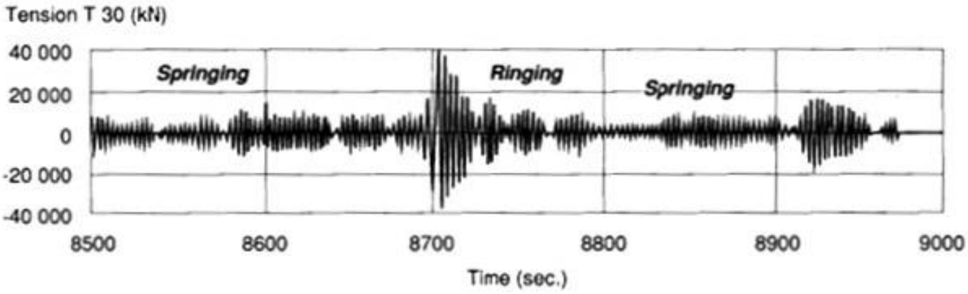

Fig. 2. Time series plot of an example springing and ringing response. Courtesy of [13]

However, its danger and nonlinearity are the only definite properties. As Schløer et al. (2016) [15] recently summarised, even though ringing has been investigated for over two decades now, there is still a great debate about the actual causes and effects of it.

Stansberg et al. (1995) [16] have conducted experiments on fixed vertical cylinders in irregular waves, creating conditions which would roughly correspond to large platforms placed in North Sea. The study found that high frequency forces corresponding to ringing phenomenon take place after a particularly steep wave has passed, and are caused by the third order wave forces, partly generated by second-order free-surface effects. This was also noted in the conclusions of OC5 Phase I [12] and highlights the need for a fully nonlinear wave kinematics model. Gurley and Kareem (1998) [17] have studied viscous effects on ringing and have shown that ringing is prompted by a wave of significantly larger amplitude than the rest of the wave train, and that asymmetric wave profile favours the formation of ringing, which reinstates that linear and weekly nonlinear wave theories may omit the ringing phenomenon in numerical modelling. Grue and Huseby (2002) [18] have studied vertical cylinders in Stokes waves, and by analysing the first seven harmonic components of the horizontal forces it was shown that ringing can be equally triggered in moderately steep transient waves, not only extremely steep ones. In the experiment conducted by Chaplin et al. (1997) [14] ringing was investigated by conducting two sets of experiments in steep non-breaking waves: on a single vertical cylinder held stationary, and then pivoted just above the floor. Three cylinders of diameters 70 mm, 100 mm and 127 mm were tested in seven waves of different characteristics, and the results were plotted on the (kA, kR)-plane along other experiments and relevant theoretical considerations, as shown in Fig. 3.

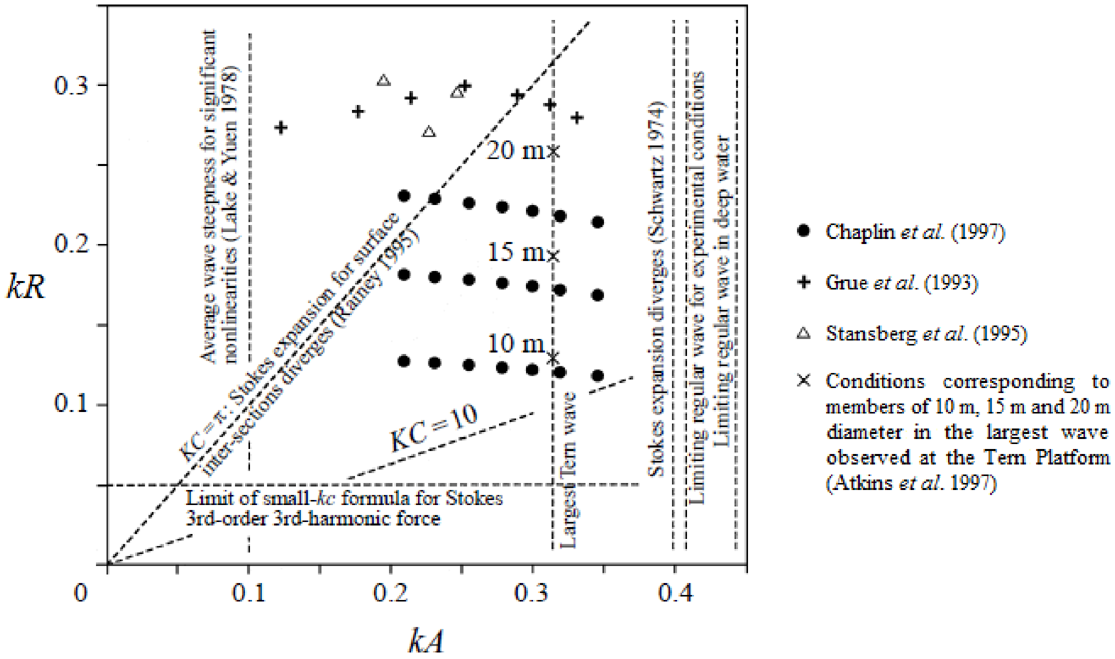

Fig. 3. Experimental and other conditions on the (kA, kR)-plane,
where k – wave number, A – wave amplitude, R – cylinder radius. Courtesy of [14]

To briefly explain the figure, the majority of the experimental conditions being in the Keulegan-Carpenter (*KC*) number range 3–10 implies that the tested cylinders are in the inertia-dominated regime instead of drag or diffraction, which is also confirmed by the Stokes first-order diffraction effects starting at $kR \approx 0.5$, outside of the scope of experiment. The data points falling to the right of $kA = 0.1$ denote that substantial phase speed nonlinearities are probable. The significance and relevance of ringing to the full-scale offshore structures is shown by the authors by augmenting the figure with the conditions corresponding to 10 m, 15 m and 20 m diameter cylinders being placed in the North Sea (at the location of the Tern Platform) during the highest extreme wave recorded during the 1990–92 (crosses on the vertical dashed line at $kA = 0.314$). This graph is of key importance as it shows that typical monopile supporting structures for offshore wind turbines would fit in the ringing-prone area of the (*kA*, *kR*)-plane.

Regrettably, the first phase findings of OC5 have revealed that particularly for higher *kR* values the majority of participants tend to underestimate 3rd harmonic forces which are vital to predict ringing [12].

2.2. State-of-the-art

Ringing and other nonlinear phenomena are an ongoing topic of interest, therefore work is continuously being conducted to understand them better. For example, there have been multiple research collaborations dedicated to it, such as the Wave Loads [19] and DeRisk [20] projects, besides other useful contributions, such as the findings from OC5 Phase Ib [12].

The numerical models that capture ringing are also being rapidly developed. Fully nonlinear wave solvers include CFD models, e.g. Waves2foam [21], finite difference potential flow solvers, such as OceanWave3D [22], or potential flow-based boundary element method model, e.g. [23], which is advanced as part of this doctoral research project, and will be described in Section 3.2.

In the first phase of OC5 project the participants with fully nonlinear wave kinematics have shown results closest to the ones observed experimentally [12]. The fully nonlinear potential flow solvers captured the forces in shallow water better than even the participants who used measured wave elevations as input. It is explained by the capability of fully nonlinear solver to directly model the influence of the nonlinear wave transformation over the sloped seabed, therefore stressing the importance of such technology and its development.

2.3. Effect of aerodynamic damping

Due to the fact that wind turbines are dynamic structures, ringing and other nonlinear phenomenon act on them differently than on static structures like offshore oil and gas platforms.

It was shown that the turbine is especially prone to such excitations when it is in parked configuration [24–27], which has most similarities with the behaviour of static structures. It is worrying because, except for the case of simply no or very low wind, it coincides with the most severe sea conditions – when the winds are above the cut-off speed, around 25 m/s [9], or when the turbine is not operating due to a fault, making it vulnerable.

In the analysis of turbine in power production state such nonlinear excitations in the response were negligible, and the assumed reason was aerodynamic damping in the direction of the waves which would diminish the vibrations [25]. However, most of the previous studies have been conducted on the co-directional wind and waves as they normally exert the largest loads on the structure. On the other hand, van der Meulen et al. [28] have investigated the effects of wind-wave misalignment on the monopile-supported offshore wind turbines in terms of fatigue loads and have found the largest accumulation of fatigue loads when wind and waves were misaligned. Similarly, the importance of aeroelastic damping was noted. Consequently, interest was sparked in the role of wind-wave misalignment to the sensitivity to wave nonlinearities.

This was investigated as part of this doctoral reseach project in a preliminary study on a turbine in both parked and operating conditions, in severe sea state with wind-wave misalignment angles varied between 0° and 90° [29]. The key results are presented in Fig. 4. They illustrate that with 90° misalignment between wind and waves the same shift in the response to match the natural frequency of the turbine is seen. The parked co-directional case (right) is critical with no aerodynamic damping and both wind and wave loading, therefore the magnitude of the response is much higher, but the misaligned operational case (left) has also shown shift and amplification of the response and higher accumulation of fatigue damage than co-directional operating case.

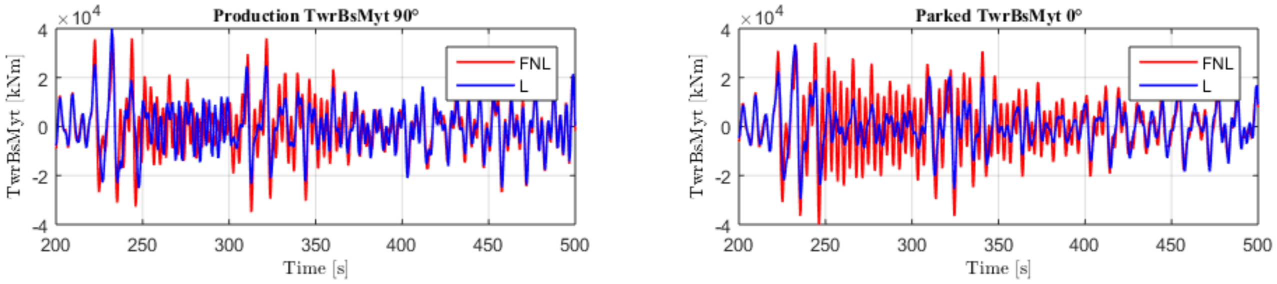

Fig. 4. Comparison between the tower base bending moment responses in power production 90° misalignment (left) and co-directional parked (right) cases using fully nonlinear (red) and linear (blue) wave kinematics in an event of wave nonlinearity significance. Courtesy of [29]

The preliminary study confirmed that in theory the resonant amplification can affect even dynamic structures like an operating wind turbine. It is therefore currently being extended to a systematic analysis with more misalignment angle distributions and wind and wave seeds for a better representation of the real environmental conditions where monopile-supported offshore wind turbines are placed.

To sum up, ringing is a dangerous phenomenon highly applicable to monopile-supported offshore wind turbines. In order to predict it in numerical simulations the solver has to have the ability to accurately model nonlinear wave-cylinder interaction, for which fully nonlinear wave kinematics and appropriate hydrodynamic loading models are needed. Both of these components and their implementation in this doctoral research project are discussed in greater detail in the following sections.

3. FULLY NONLINEAR WAVE KINEMATICS

3.1. Importance of fully nonlinear waves

As already shown in the previous section, the nonlinear resonant phenomena cannot be captured if linear or weakly nonlinear wave theories are used, which makes it a crucial consideration for this study. Moreover, the wave nonlinearities have been shown to affect the extreme and fatigue loads on the turbine. For example, Schløer et al. (2016) [15] have identified that wave nonlinearity has strong influence in the ultimate load analysis. Marino et al. (2017) [27] have shown simulations with fully nonlinear waves in comparison to linear wave kinematics yield up to 15% higher response in extreme loads and 10–17% higher accumulated fatigue loads depending on wind speed. This advises that the simplified wave model highly underestimates both the ultimate failure and the accumulated fatigue which affects turbine's lifetime and increases needed maintenance, therefore improving it would lead to safer and more efficient offshore wind turbine designs.

3.2. Potential flow-based BEM model

Work is carried out on a 2D potential flow-based higher-order Boundary Element Method (BEM) code for fully nonlinear wave propagation [23]. Boundary Element Method is commonly used for gravity wave modelling, and its suitability as well as advances in the methods for fully nonlinear wave tanks are summarised by Harris et al. (2014) [30].

Potential flow theory is deemed suitable for the analysis of gravity waves, because its main limitations are the assumption of incompressible and irrotational flow, which hold true up to the re-entry of the plunging breaking wave [31]. Modelling the wave up to re-entry is considered sufficient because the highest impact on the structure from the breaking wave is exerted before [19, 23].

The model is initialised with appropriate analytic theories, such as Rienecker-Fenton [32] for fully nonlinear waves. The only approximation of this theory is the truncation of the Fourier series, therefore the model is valid for deep and shallow waters and any wave steepness, with exceptions for the solitary wave limit and previously discussed re-entering of breaking wave.

The model also has the capacity to be coupled with hydro-aero-servo-elastic solvers for full dynamic response of the system.

3.3. Nonlinearities induced by sloping bottom

Monopile-supported wind turbines are commonly placed in coastal zone, where the sea bed slopes. The decreasing depth causes wave shoaling – gathering of nonlinearities which lead to an increasing steepness of the waves until the eventual breaking. To account for these accumulated nonlinearities a sloping bottom capability is added to the BEM code.

4. HYDRODYNAMIC LOADING MODELS

Wave kinematics alone are not enough to properly capture the amplifications and their effect, because the velocities and accellerations need to be converted into forces and moments by appropriate hydrodynamic loading models. For example, in the OC5 project, even though the participants with higher order wave models can capture the nonlinear nature of a breaking waves, the impulsive loading caused by them was not captured, leading to large differences between experiment and simulations [12].

For monopile supports, due to their slenderness, normally employed hydrodynamic loading model is Morison's equation. However, its appropriateness in certain situations, such as high nonlinearities and shallower depths, is doubted. Therefore alternatives and corrections have been proposed, e.g. slender-body corrections or perturbation models, which are discussed in the following subsections.

4.1. Morison‘s equation

Morison‘s equation has been proposed by Morison in 1950 [33]. It is applicable for slender structures where diffraction effects can be ignored and makes use of the mass and inertia coefficients. The coefficients need to be determined ideally from experiments, or alternatively from available practice guidelines, to be matched to the specific analysed case, making it semi-empirical.

When rightly calibrated, it is typically working well in linear and weakly nonlinear waves, and is therefore used by the majority of standard hydro-aero-servo-elastic solvers [12, 34]. However, it has limitations in more complex environments. For example, Paulsen et al. (2014) [35] found it to be mispredicting the higher-order harmonic forces, especially in shallower depths. Moreover, Chaplin et al. (1997) [14] determined that using Morison’s equation for peak force and moment predictions on stiffly supported cylinders led to underprediction which was increasing with the increase in the steepness of the waves. In the same study it was noted that addition of correction terms improved its performace, as described in the following subsection.

4.2. Corrections to Morison‘s equation

Improvements to Morison’s equation were first proposed by Rainey (1995) [36] and then investigated in detail and compared against experiments on cylinders by Chaplin et al. (1997) [14], as illustrated in Fig. 5. Slender-body corrections to Morison's equation are aimed to improve the accuracy of its inertia term in modelling potential flow loads, and consist of:

- (M) Morison inertia force – only the inertia component with coefficient of 2, integrated up to the instantaneous undisturbed water surface. Drag component (d) was added later, after the other corrections.
- (A) Axial divergence force – integrated along the length, like Morison inertia term.
- (I) Surface intersection force – applied as a point load at the instantaneous free surface intersection point.
- (D) Surface distortion force – removes the third-order error, also applied as a point load at the instantaneous free surface intersection point.
- (d) Drag force – based on drag coefficient of 1.

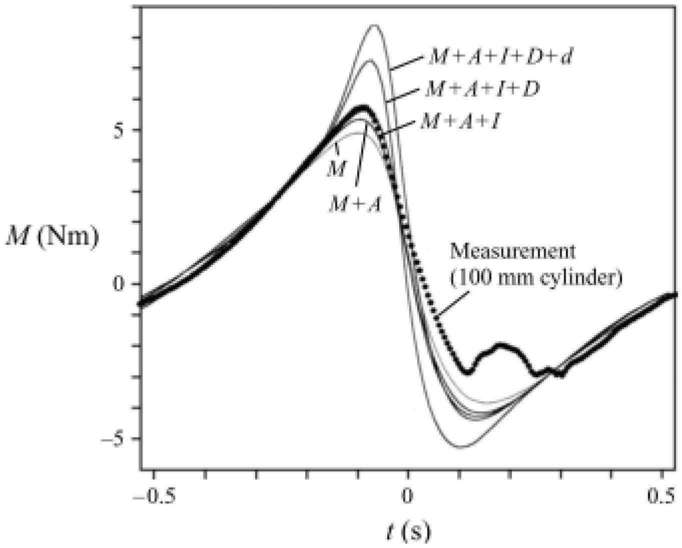

Fig. 5. Comparison of moment records on a cylinder between measurement and different corrections to Morison’s equation. Courtesy of [14]

Best agreement with experimental results in unsteady steep waves was found when Morison inertia term was improved by adding potential flow loads, namely axial divergence and surface intersection forces. These slender-body terms bring the Morison inertia term up to the accuracy of the second order in Stokes expansion.

4.3. Perturbation theories

Hydrodynamic loading has also been proposed to be modelled by the use of perturbation theories. The two most well-known are by Malenica and Molin (1995) [37] and Faltinsen, Newman and Vinje (1995), better known as FNV theory [38]. These theories directly take into account the third order loads, needed for capturing ringing phenomenon. The main difference between the two is that Malenica and Molin follow a classical Stokes perturbation technique to the third order, while FNV theory reconsiders the wave amplitude to be of the same order as the diameter of the structure. The original FNV theory was created for regular waves, but was quickly extended to irregular waves by Newman (1996) [39].

4.4. Comparison study

This doctoral research project involves conducting a systematic hydrodynamic loading model comparison study with the aim to assess which method is most suited to model the high nonlinearities. The models involved are Morison’s equation, Rainey’s slender-body corrections to it, and FNV theory. Study involves both flat and sloping bottom of the numerical wave tank, regular and irregular waves. It is expected to provide considerations for improved hydrodynamic loading models in strongly nonlinear waves, leading to more accurate modelling of monopile-supported offshore wind turbines.

5. CONCLUDING REMARKS

As the computational methods are improving and the computer capacities increase, much more advanced research can be conducted in the same amount of time. Consequently, there is a clear shift to understand and account for more nonlinear, non-Gaussian and in general more complex processes. Wave nonlinearities have been proven to have a strong influence on the loading and response of offshore structures, and the simplified most commonly employed hydrodynamic loading model is often untrusted in the cases of high nonlinearities; nonetheless, the current standard solvers do not account for a nonlinear wave-structure interaction, leading to omission of the phenomena that arise there, such as ringing.

Therefore work has been started within a doctoral research project to advance the models by modelling fully nonlinear waves on flat and sloping sea beds, and assessing which hydrodynamic loading model is most suited, in order to study these nonlinear effects in monopile-supported offshore turbine response. Accuracy of the enhanced wave loading model is to be assessed through comparisons with experimental data available in the literature. Results of the present study are expected to provide considerations for improved models in strongly nonlinear waves and to contribute to safer and more efficient future offshore wind turbine designs.

ACKNOWLEDGEMENTS

This work was funded by the European Commission’s Framework Program “Horizon 2020”, through the Marie Skłodowska-Curie Innovative Training Network (ITN) “AEOLUS4FUTURE - Efficient harvesting of the wind energy” (H2020-MSCA-ITN-2014: Grant agreement no. 643167).

REFERENCES

1. IPCC. *Climate Change 2014: Synthesis Report. Contribution of Working Groups I, II and III to the Fifth Assessment Report of the Intergovernmental Panel on Climate Change*. Geneva: IPCC, 2014. 151 p.
2. GLOBAL WIND ENERGY COUNCIL. *Global wind report: Annual market update 2015*. Brussels: GWEC, 2015. 76 p.
3. GLOBAL WIND ENERGY COUNCIL. *Global wind energy outlook | 2016*. Brussels: GWEC, 2016. 44 p.
4. RENEWABLEUK. *Offshore wind energy*. London: RenewableUK, 2016 - [referred on the 6th March 2016]. http://mhivestasoffshore.com/manuals/offshore_haynes_manual_2016.pdf .
5. BANIOTOPOULOS, C.; BORRI, C.; STATHOPOULOS, T. *Environmental Wind Engineering and Wind Energy Structures*, Wien New York: Springer Verl., 2010.
6. KARIMIRAD, M. *Offshore Energy Structures: For Wind Power, Wave Energy and Hybrid Marine Platforms*, Switzerland: Springer, 2014.
7. JONKMAN, J., MUSIAL, W. *Offshore Code Comparison Collaboration (OC3) for IEA Task 23 Offshore Wind Technology and Deployment*. Golden: NREL, 2010.
8. JONKMAN, J., ROBERTSON, A., POPKO, W., et al. Offshore Code Comparison Collaboration Continuation (OC4), Phase I – Results of Coupled Simulations of an Offshore Wind Turbine with Jacket Support Structure. ISOPE 2012. Proceedings of the 22nd Int. Society of Offshore and Polar Engineers Conf. Rhodes: Greece. 2012 June 17-22.
9. JONKMAN, J., BUTTERFIELD, S., MUSIAL, W., SCOTT, G. *Definition of a 5-MW reference wind turbine for offshore system development*, Golden: NREL, 2009.
10. ROBERTSON, A. *Introduction to the OC5 Project*, 2015 - [referred on the 6th March 2016]. http://www.sintef.no/Projectweb/Deepwind_2015/Presentations/ .
11. ROBERTSON, A., JONKMAN, J., VORPAHL, F. et al. Offshore Code Comparison Collaboration Continuation Within IEA Wind Task 30 : Phase II Results Regarding a Floating Semisubmersible Wind System. OMAE 2014. Proceedings of the 33rd Int. Conf. on Ocean, Offshore and Arctic Engineering. San Francisco: California, 2014 June 8-13.
12. ROBERTSON, A.; WENDT, F.; JONKMAN, J. et al. OC5 Project Phase Ib: Validation of Hydrodynamic Loading on a Fixed, Flexible Cylinder for Offshore Wind Applications. *Energy Procedia*, 2016, Vol. 94, No. C, p. 82-101.
13. Norewegian Petroleum Directorate, *Annual Report*, *1992*. Stavanger: NPD, 1992, pp. 118-119.
14. CHAPLIN, J. R. R.; RAINEY, R. C. T.; YEMM, R. W. Ringing of a vertical cylinder in waves, *J. Fluid Mech.*, 1997, Vol. 350, pp. 119-147.
15. SCHLØER, S., BREDMOSE, H., BINGHAM, H.B. The influence of fully nonlinear wave forces on aero-hydro-elastic calculations of monopile wind turbines. *Marine Structures*, 2016, Vol. 50, pp. 162-188.
16. STANSBERG, C. T.; HUSE, H.; KROKSTAD, J. R.; LEHEN, E. Experimental Study of Non-Linear Loads on Vertical Cylinders in Steep Random Waves. ISOPE 1995. Proceedings of the 5th Int. Offshore and Polar Engineering Conf. The Hague: Netherlands. 1995 June 11-16.
17. GURLEY, K. R., KAREEM, A. Simlulation of ringing in offshore systems under viscous loads. *J. Eng. Mech.*, 1998, p. 582-586.
18. GRUE J., HUSEBY, M. Higher harmonic wave forces and ringing of vertical cylinders. *Appl. Ocean Res.*, 2002, Vol. 24, No. 4, p. 203-214, 2002.
19. BREDMOSE, H., MARIEGAARD, J., PAULSEN, B.T. et al. *Final report for the Danish ForskEL Wave Loads project*. Report E-45, The wave loads project. DTU Wind Energy, 2013.

20. BREDMOSE, H.; DIXEN, M.; GHADIRIAN, A. et al. DeRisk— Accurate prediction of ULS wave loads. Outlook and first results. *Energy Procedia*, 2016, Vol. 94, p. 379-387.
21. TU-Delft. *Waves2FOAM – Detailed modelling of free surface flows*, 2015 - [referred on the 6th March 2016]. http://www.dsd-int.nl/2015/training/waves2foam-detailed-modelling-of-free-surface-flows/ .
22. ENGSIG-KARUP, A., BINGHAM, H.B., LINDBERG, O. An efficient flexible-order model for 3D nonlinear water waves. *J. Comp. Phys.*, 2009. Vol. 228, p. 2100-2118.
23. MARINO, E. *An Integrated Nonlinear Wind-Waves Model for Offshore Wind Turbines*, Florence: FUP, Firenze University Press, 2011.
24. MARINO, E.; BORRI, C.; LUGNI, C. Influence of wind–waves energy transfer on the impulsive hydrodynamic loads acting on offshore wind turbines, *J. Wind Eng. Ind. Aerodyn.*, 2011, Vol. 99, p. 767-775.
25. MARINO, E.; LUGNI, C.; BORRI, C. The role of the nonlinear wave kinematics on the global responses of an OWT in parked and operating conditions. *J. Wind Eng. Ind. Aerodyn.*, 2013, Vol. 123, p. 363-376.
26. MARINO, E.; NGUYEN, H.; LUGNI, C.; BORRI, C. Irregular Nonlinear Wave Simulation and Associated Loads on Offshore Wind Turbines. *J. Offshore Mech. Arct. Eng.*, 2015, Vol. 137, No. 2, p. 021901.
27. MARINO, E.; GIUSTI, A.; MANUEL, L. Offshore wind turbine fatigue loads: The influence of alternative wave modeling for different turbulent and mean winds. *Renew. Energy*, 2017, Vol. 102, p. 157-169.
28. VAN DER MEULEN, M.B., ASHURI, T., VAN BUSSEL, G.J.W., MOLENAAR, D.P. Influence of nonlinear irregular waves on the fatigue loads of an offshore wind turbine. TORQUE 2012. Oldenburg: Germany. 2012 October 9-11.
29. MOCKUTE, A., GIUSTI, A., MARINO, E., BORRI, C. Effects of wind-wave misalignment in the case of nonlinear hydrodynamic loading of offshore wind turbines. IN-VENTO 2016. Proceedings of 14th Conference of the Italian Association for Wind Engineering. Terni, Italy. 2016 September 25-28.
30. HARRIS, J.C.; DOMBRE, E.; BENOIT, M.; GRILLI, S.T. A comparison of methods in fully nonlinear boundary element numerical wave tank development. Proceedings of the 14émes Journées de l'Hydrodynamique. Val-de-Reuil: France. 2014 November 18-20.
31. NEWMAN, J. N. *Marine Hydrodynamics*. Cambridge: The MIT Press, 1977.
32. RIENECKER, M.M., FENTON, J.D. A Fourier approximation method for steady water waves. *Journal of Fluid Mechanics*, 1981, Vol. 104, p. 119-137.
33. MORISON, J.R., O'BRIEN, M.P., JOHNSON, J.W., SCHAAF, S.A. The force exerted by surface wave on piles. *Petroleum Transactions*, 1950, Vol. 154, p. 149-189.
34. JONKMAN, J. M., BUHL JR., M. *FAST User's Guide*. Golden: NREL, 2005.
35. PAULSEN, B.T., BREDMOSE, H., BINGHAM, H.B., JACOBSEN, N.G. Forcing of a bottom-mounted circular cylinder by steep regular water waves at finite depth. *J. Fluid. Mech.*, 2014, vol. 755, p. 1-34.
36. RAINEY, R.C.T. A new equation for calculating wave loads on offshore structures. *J. Fluid Mech.*, 1989, Vol. 204, p. 295-324.
37. MALENICA, S., MOLIN, B. Third-harmonic wave diffraction by a vertical cylinder. *J. Fluid Mech.*, 1995, Vol. 302, p. 203-229.
38. FALTINSEN, O.M.; NEWMAN, J.N., and VINJE, T. Nonlinear Wave loads on a slender vertical cylinder. *J. Fluid Mech.*, 1995, Vol. 289, p.179-198.
39. NEWMAN, J.N. Nonlinear scattering of long waves. Chapter in *Waves and Nonlinear Processes in Hydrodynamics*. Norwel: Kluwer Academic Publishers, 1996, p. 91-102.

CYSENI 2017, May 25-26, Kaunas, Lithuania
ISSN 1822-7554, www.cyseni.com

NOVEL APPLICATION OF STATISTICAL AND PHYSICAL METHODS FOR WIND POWER PREDICTION IN LITHUANIA

G. Gecevičius, M. Marčiukaitis, V. Zimnickas
Lithuanian Energy Institute
Breslaujos str. 3, LT-44403 Kaunas – Lithuania
E-mail: Giedrius.Gecevicius@lei.lt

G. Gecevičius
Kauno Kolegija, University of Applied Sciences
Pramones av. 20, LT-50468 Kaunas – Lithuania

ABSTRACT

Every year wind power installations gain more and more added power capacity around the world. However, effective integration of wind turbines energy generation is closely related to power system reliability. In order to ensure power system stability, it is necessary to improve accuracy and flexible adaptation of wind power prediction models. One of the ways to do that is a combination of forecasting models covering physical (wind speed conversion to power based on roughness and wind conditions) and statistical (autoregresion) power forecasting methods with different prediction horizons. Paper presents designed hybrid wind power prediction approach easily adaptable for local conditions. Tool was verified in four wind farms in Lithuania of different installed power capacity and technical characteristics. Analysed results revealed the importance of precisely chosen height of wind speed prediction from a numerical weather prediction model, evaluation of surface roughness and height coefficients to the accuracy of wind power predictions. Designed hybrid forecating model makes opportunity to improve wind power prediction accuracy by 1–2 percent.

Keywords: power generation, wind power prediction, hybrid forecasting approach

1. INTRODUCTION

Global power consumption grew very rapidly during last 15 years, and it is forecasted, that it will grow in future also, because new power generation plants are necessary to meet increasing energy demands. To compare, 24.5 GW of new power plants capacity was built across the European Union in 2016, and renewables made 86% of that. Besides, wind turbines alone added more than 50% of all installed power capacity of total installations [1]. Despite positive impact of RES regarding environmental requirements and relative low energy price, development of renewable energy sources brings negative impact too [2–4]. Wind speed is very volatile and to assure optimal wind turbines control in power system is not very easy. One of the ways to solve these issues is to improve accuracy of wind power forecasting. Although many wind power forecasting methods and models have been designed, there is still no optimal model suitable for different terrains and different time horizons [5, 6].

Wind power prediction methods can be separated to two different approaches. One of them is statistical methods and the second one – physical power prediction methods. First group covers methods related to historical relations between variables, and they are best suitable for short term power prediction. Second group – physical approach methods – are based on wind prediction from numerical weather forecasting system, when wind speed is corrected according local conditions and converted to wind power. Besides, hybrid models, which integrate statistical and physical methods exist also. But there is still lack of very careful evaluation of meteorological and topographic conditions like orography, roughness, wind shear and turbulence impact on the accuracy of wind power prediction [7–9]. Paper presents analysis of local topographic conditions and statistical methods, also indicates best tools for short, mid- and long term wind power forecasting.

2. OBJECT AND METHODS

In order to analyse the influence of local conditions for power forecasting, four wind farms were chosen. These farms are situated in Western part of Lithuania (Fig. 1).

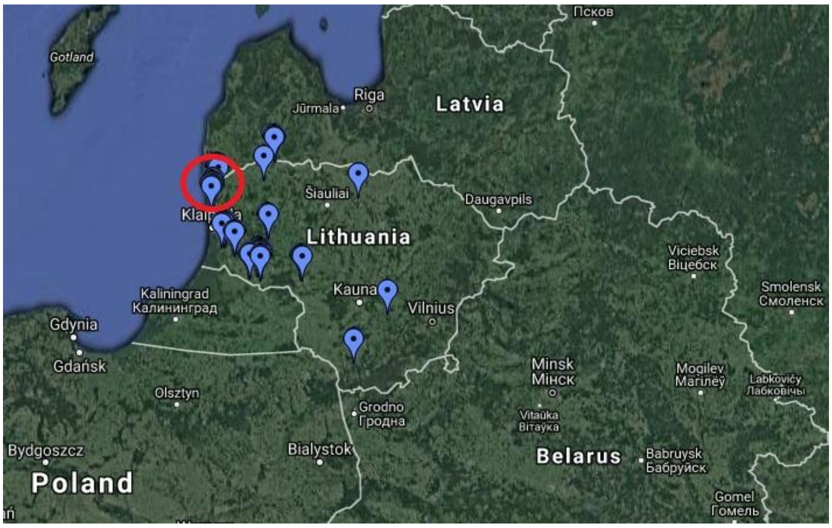

Fig. 1. Locations of analysed wind farms

Presented wind farms consist of turbines with different parameters, when hub height varies in 78–108 m limits, generators power in 2–2.75 MW and rotor diameters in 82–108 m (Table 1).

Table 1. Technical parameters of wind farms and turbines

Name of Wind Farm (WF)	Power Capacity of WF (MW)	Number of Wind Turbines	Power Capacity of Wind Turbine (MW)	Hub Height of Wind Turbines (m)
Benaiciai WF	34	17	2	98
Ciuteliai WF	39.1	17	2.3	108
Laukzeme WF	16	6	2.75	100
Sudenai WF	14	7	2	78

The evaluation of wind speed distribution by Weibull equation were approximated (Eq. 1).

$$f(v) = \frac{k}{c}\left(\frac{v}{c}\right)^{k-1} exp\left[-\left(\frac{v}{c}\right)^{k}\right] \tag{1}$$

where *c* is the scale parameter; *k* is the shape parameter; and *v* is wind speed. To count *k* and *c* parameters equations 2 and 3 respectively are used.

$$k = \left(\frac{\sum_{i=1}^{n} v_i^k ln(v_i)}{\sum_{i=1}^{n} v_i^k} - \frac{\sum_{i=1}^{n} ln\,(v_i)}{n}\right)^{-1} \tag{2}$$

$$c = \left(\frac{1}{n}\sum_{i=1}^{n} v_i^k\right)^{\frac{1}{k}} \tag{3}$$

where v_i is wind speed, which does not equal to zero; *n* is number of measurements.

Power output of wind turbine can be estimated using parametric models that are characterised by various functions. Polynomial regression function in the analysed case is presented in following equation:

$$p(v) = a_0 + a_1 v + a_2 v^2 + \ldots + a_n v^n \tag{4}$$

where p – estimated power (kW), v – wind speed (m/s), n – the order of polynomial. a_i – parameters of the polynomial function to be estimated ($a_i \in \mathbf{R}$. $i = 0$. 1. …. n). Sixth order polynomial function was analysed in the paper.

To evaluate goodness-of-fit of the analysed models measure of normalized mean absolute percentage error (MAPE) is calculated by the following formula:

$$n\text{MAPE} = \frac{1}{n}\sum_{i=1}^{n}\frac{\left|p_i(P) - \hat{p}_i(P)\right|}{p(NP)}\cdot 100\% \tag{5}$$

where p_i – factual wind power, kW, $\hat{p}_i$ – predicted power, kW, $p(NP)$ – nominal wind power, kW.

ARIMA model defined as ARIMA (p. d. q) is presented in Eq. 6.

$$y_t = \acute{a} + \sum_{i=1}^{p} \ddot{o}_j + \sum_{j=1}^{q} \grave{e}_j e_{t-j} + \dot{a}_t \tag{6}$$

This equation can be expressed equation number 7:

$$y_t = \alpha + \phi_i Y_{t-1} + \ldots + \phi_p Y_{t-p} + + \theta_i \varepsilon_t - 1 + \ldots + \theta_q \varepsilon_t - q + \varepsilon_t \tag{7}$$

where α is the constant term, ϕ_i is the i-th autoregressive parameter; ϕ_j is the j-th moving average parameter; e_t is the error term at time t, and y_t is the value of the wind speed observed at the time t.

For the physical wind power prediction – wind speed and wind direction from numerical weather prediction (NWP) system were used. Wind speed and wind direction forecasted to 50, 80, 100 and 150 m height. At this case, a source of NWP system High resolution local area model (HIRLAM) was used. For the evaluation of local topography conditions Wind atlas analysis and application software 9 (WAsP 9) was used. Both programmes cover resolution of 5×5 km squares, and describe topographical conditions in four squares.

3. RESULTS

As mentioned before, wind turbines are located in Western part of Lithuania, where wind speed at 10 m height is 4.53 m/s at and 6.42 m/s at 50 m height with 342 W/m^2 power density (Fig. 2). In Western part of Lithuania prevailing wind direction is from west direction, where is the coast line of the Baltic sea, and this region has largest wind resources in Lithuania.

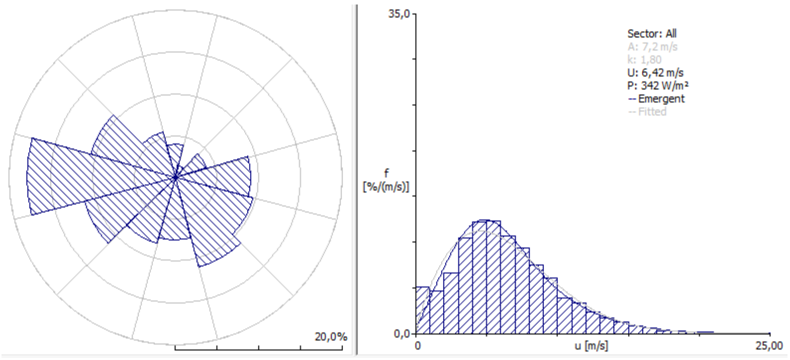

a b

Fig. 2. Wind rose and Weibull distribution of wind speed in Western part of Lithuania

3.1. Statistical wind power prediction approach

Wind power forecasting time horizons can be separated to 3 main ranges – short, mid- and long term prediction periods. Short term period covers 6 hours ahead and is concentrated to real time grid operation and control action. To compare, midterm and long (24–48 hours) term power prediction methods are used for economic load dispatch planning, operational security in electricity market and also maintenance planning. Statistical methods are used usually for short term wind power prediction. Most of them are auto regression functions, where relations between numbers are used. One of auto regression methods including integrated moving average examples calls ARIMA. Besides this method can be used for last steps seasonality evaluation and it is called (S)ARIMA (Fig. 3).

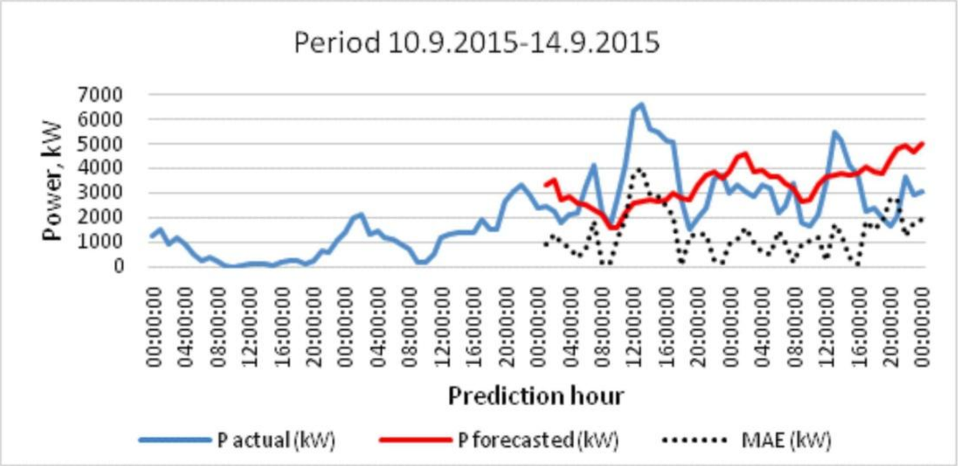

Fig. 3. Wind power forecasting during low wind speed period in Sudenai wind farm

Wind speed prediction based on statistical methods is best suitable for stable wind speed and not effective, when wind speed is changing from low to high wind speed or vice versa. Definition of lower wind speed in this paper, describes wind speed, when at the moment generated wind power is two times lower than nominal power, e.g., when nominal power of wind turbine is 2000 kW, lower wind speed can be classified when power is 1000 kW and less, respectively wind speed 8.5 m/s and less. In contrary, higher wind speed definition describes wind speed when it is higher than 8.5 m/s.

Analysed power prediction output in Sudenai wind farm is presented in Fig. 3 and covers low wind speed period. Results indicate, that maximum power prediction MAE was 4001 kW, and as a result of that, nMAPE varied in 0.5–29% limits. For the midterm period (6 hours ahead) the acuaracy of wind power prediction was suffiecient.

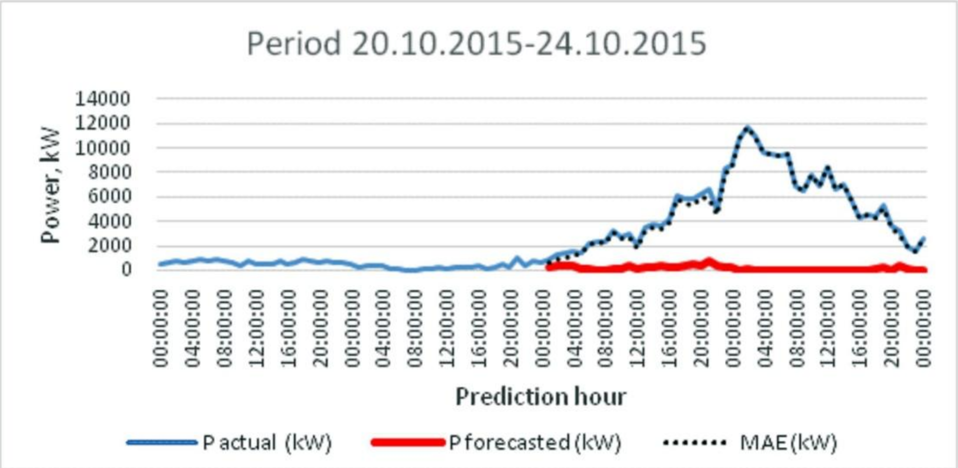

Fig. 4. Wind power forecasting during low and high wind speed period in Sudenai wind farm

To compare wind power prediction during lower and higher wind speed conditions, maximum MAE dramatically increased during time horizon, and varied in range 600–10835 kW, when maximum nMAPE was 83 percent (Fig. 4). These results indicate the unsuitability of such method for midterm and long term wind power forecasting, when speed varies from low to high or vice versa.

Table 2. Wind power prediction errors during different wind periods and time horizons in Sudenai wind farm

Forecasting period h	**Wind speed m/s (High and Low)**				**Average**
	L-L	L-H	H-L	H-H	
3	4.20	10.44	9.78	8.78	**8.30**
6	3.68	11.33	12.53	14.70	**10.56**
12	4.04	16.32	17.57	24.32	**15.56**
24	5.45	26.02	16.57	30.06	**19.52**
48	5.26	36.46	18.29	35.89	**23.98**
Average	**4.53**	**20.12**	**14.95**	**22.75**	–

Comparison of nMAPE’s of four different wind intensity periods is presented in Table 2. It was noticed, that during all kind of wind periods, wind power prediction errors increase is directly related to time horizon, when during the 3-48 h ahead period nMAPE increased from 8.3% to 23.98%. To evaluate short term time horizon, lowest errors were recognised during low wind speed period with 3.68% and highest during high wind period with 14.70%.

Evaluation of low, high and mixed wind speed conditions during 48 h time horizon presents large prediction errors, except during low wind speed conditions, when maximum nMAPE reaches 5.26%.

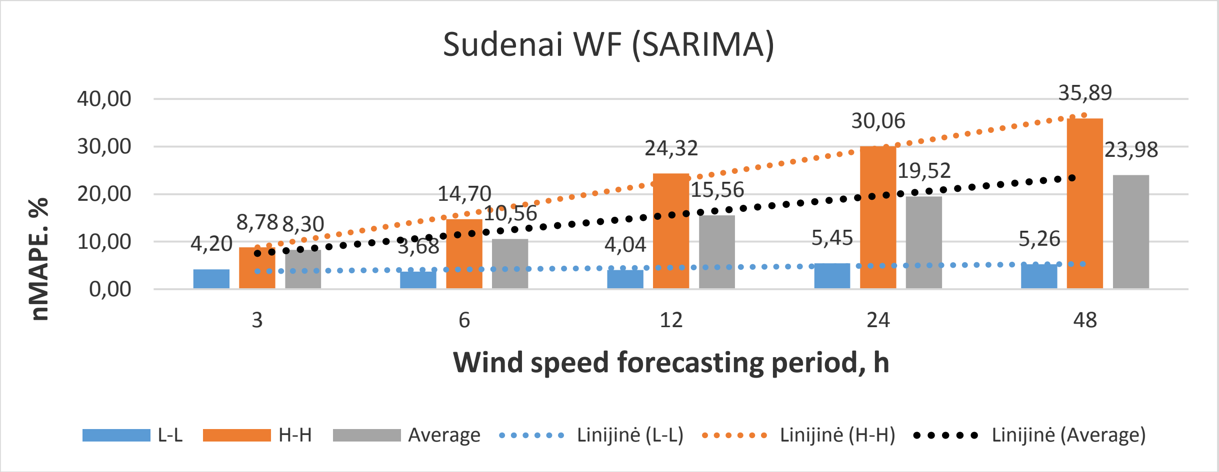

Fig. 5. Comparison of wind speed prediction errors during different wind and time periods

Variations of wind power forecasting errors during lower wind speed period are not significant, and this method is suitable for long range power prediction. On the opposite, wind power forecasting errors variations between higher wind speed period are very rapidly increasing and gain 36% percentage error at 48 h horizon. To conclude the part of statistical approach methods, it is necessary to mention, that for short term wind power forecasting statistical methods can be used, and for midterm and long term periods they are not the best choice.

3.2. Physical wind power prediction approach

Wind power can be forecasted by physical methods also. Such kind of model includes many steps, like evaluation of topographic, meteorological condition, wind conversion to power and statistical part in order to find relation between model predicted and actual wind speed. Besides, it is very important to separate the best methods, which can best approximate wind turbines power curves in order to reduce power forecasting errors. Analysis of nMAPE based on physical approach is presented in Table 3. Results indicate, that the most suitable wind speed forecasting point is at 100 m height, despite the fact, that wind speed at different points is recalculated to turbines' hub height. Moreover, it is important to mention, that hub height of wind turbines varies in 78–108 m limits.

Table 3. Comparison of wind farms power forecasting errors using wind source (HIRLAM) from different heights (Resoliution 10x10 km)

Title of WF	**nMAPE %**				
	50 m	**80 m**	**100 m**	**150 m**	**Average**
Benaiciai WF	13.0	11.3	10.7	11.5	11.6
Ciuteliai WF	13.8	10.8	11.3	10.6	11.6
Laukzeme WF	11.8	10.6	10.2	12.0	11.1
Sudenai WF	10.6	9.2	8.8	9.6	9.6
Average	12.3	10.5	10.3	10.9	–

However, to improve wind power prediction accuracy, more detailed analysis of topographic conditions is necessary. Topographic conditions consist of roughness, orography and obstacles. Example of local roughness and height variations assessment is presented in Fig. 5.

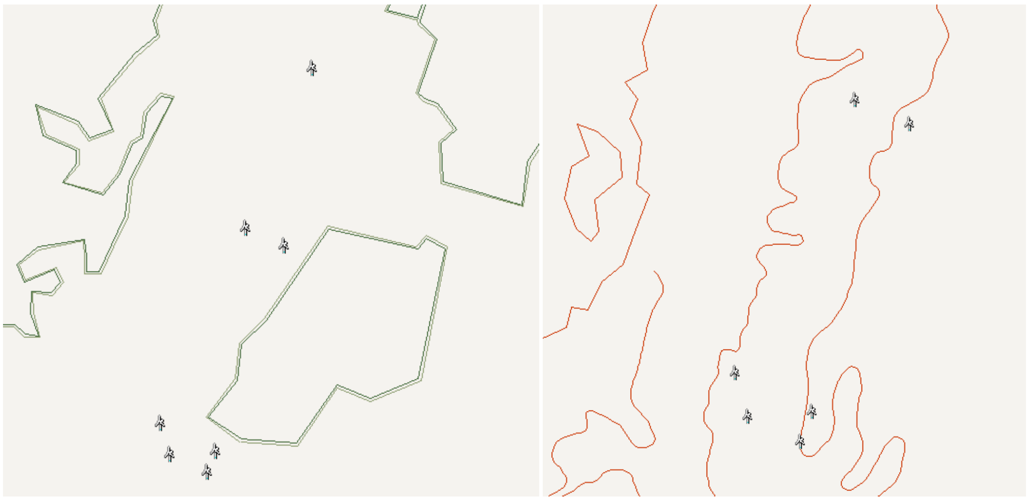

(a) (b)

Fig. 5. Example of roughness (a) and topography (b) modelling using WAsP 9 software in Sudenai wind farm (Resolution 10×10 km)

Wind farms usually are located in open areas by the coast line or higher locations, where very flat site surface prevails. However, in many cases, it is important to analyse local area surface roughness in different wind directions. In Table 4 comparison of fixed and flexible in different wind directions roughness coefficient, is presented. It was noticed that in case of usage of flexible surface coefficient, nMAPE were significant lower.

Table 4. Comparison of wind speed power prediction errors using fixed and flexible by wind directions roughness coefficient

Sudenai WF	North	East	South	West	Average
Fixed roughness coef.	***0.145***	***0.145***	***0.145***	***0.145***	–
50	7.57	11.63	15.18	11.86	11.56
80	**6.55**	8.39	10.23	9.71	**8.72**
100	**7.20**	7.45	8.96	10.62	**8.56**
150	11.15	12.52	12.10	**15.64**	12.85
Average	8.12	10.00	11.62	11.96	–
Flexible roughness coef. in different directions	***0.068***	***0.092***	***0.079***	***0.029***	–
50	7.24	10.36	**12.76**	10.44	10.20
80	**6.55**	8.39	10.23	9.71	**8.72**
100	**6.73**	7.58	9.41	9.51	**8.31**
150	7.96	8.62	9.45	11.63	9.41
Average	7.12	8.74	10.46	10.32	–

Comparison of wind power prediction errors (nMAPE) including and excluding surface height variations coefficient presented in Table 5. Results revealed, that including wind speed coefficient, wind power forecasting errors are not significant, but, however, lower.

Table 5. Comparison of wind power prediction errors including and not including speed up coefficient resulted by topography

Sudenai WF	North	East	Sought	West	Average
Wind speed up (topography). %	0.43	0.05	0.43	0.03	–
50 m	7.23	10.35	12.61	10.44	**10.16**
80 m	6.55	8.39	10.23	9.71	**8.72**
100 m	**6.78**	7.57	9.33	9.51	**8.30**
150 m	8.07	8.64	9.50	11.64	**9.46**
Average	**7.16**	**8.74**	**10.41**	**10.33**	–
Wind speed up not included	–	–	–	–	–
50	7.24	10.36	12.76	10.44	**10.20**
80	6.55	8.39	10.23	9.71	**8.72**
100	**6.73**	7.58	9.41	9.51	**8.31**
150	7.96	8.62	9.45	11.63	**9.41**
Average	**7.12**	**8.74**	**10.46**	**10.32**	–

Analysed statistical and physical approach for wind power generation prediction confirmed, that statistical methods are best suitable for short term wind power forecasting, and physical methods and models – for mid- and long term power prediction. However, in many cases, for optimal real time grid power regulation, electricity market, load and maintenance planning actions, it is necessary to design new hybrid model, where combination of statistical and physical methods is possible. Paper suggests to combine methods, which can reduce power prediction errors by 1–3% and make wind energy development worldwide even more attractive.

4. CONCLUSIONS

- Statistical method SARIMA is best suitable for short term wind power prediction during lower speed period with nMAPE 3.68% and 10.56% during lower and higher wind conditions. For long term power forecasting horizon SARIMA method is not suitable.
- Physical approach methods are best suitable for long range power forecasting. To improve such kind of wind power prediction accuracy, it is necessary to include evaluation of wind turbines sites surface roughness and height variations.
- Suggested hybrid approach is best suitable for different range (short, mid-, long term) of wind power forecasting in order to assure optimal grid control, electricity market and wind turbines maintenance planning actions.

REFERENCES

1. WETSTONE, G., THORNTON, K., HINRICHS-RAHLWES, R., SAWYER, S. SANDER, M., TAYLOR, R., RODGERS, D., ALERS, M., LEHMANN, H., ECKHART, M., HALES, D. *REN21*, 2016, Global status report 2016. ISBN 978-3-9818107-0-7.
2. ALBADI, M., H., EL-SAADANY, E., F. Overview of wind power intermittency impacts on power systems. *Electric Power Systems Research*, 2010, Vol. 80, No. 6, p. 627–632.
3. GRASSI, S., CHOKANI, N., ABHARI, R., S. Large scale technical and economical assessment of wind energy potential with a GIS tool: Case study Iowa. *Energy Policy*, 2012, Vol. 45, p. 73–85.
4. PATHAK, K., SHARMA, M., BUNDELE, M. A critical review of voltage and reactive power management of wind farms. *Renewable and Sustainable Energy Reviews*, 2015, Vol. 51, p. 460–471.
5. ONER, Y., OZCIRA, S., BEKIROGLU, N., SENOL, I. A comparative analysis of wind power density prediction methods for Canakkale, Intepe region, Turkey. *Renewable and Sustainable Energy Reviews*, 2013, Vol. 23, p. 491–502.
6. FOLEY, A., M., LEAHY, P., G., MARVUGLIA, A., MCKEOGH, E., J. Current methods and advances in forecasting of wind power generation. *Renewable Energy*, 2012, Vol. 37, No. 1, p. 1–8.
7. DE TOMMASI, L., GIBESCU, M., BRAND, A., J. A dynamic wind farm aggregate model for the simulation of power fluctuations due to wind turbulence. *Journal of Computational Science*, 2010, Vol. 1, No. 2, p. 75–81.
8. ZOLFAGHARI, S., RIAHY, G., H., ABEDI, M. A new method to adequate assessment of wind farms' power output. *Energy Conversion and Management journal*, 2015, Vol. 103, p. 585–604.
9. PENG, H., LIU, F., YANG, X. A hybrid strategy of short term wind power prediction. *Renewable Energy*, 2013, Vol. 50. p. 590–595.

CYSENI 2017, May 25-26, Kaunas, Lithuania
ISSN 1822-7554, www.cyseni.com

LONG-TERM UPPER WIND DYNAMICS: VARIABILITY AND TRENDS

M. Savenets, **I. Dvoretska**
Ukrainian Hydrometeorological Institute
Nauky Av. 37, 03028 Kyiv – Ukraine
E-mail: mihails@e-mail.ua

G. Kruchenitsky
Central Aerological Observatory
Pervomayskaya Str. 3, 141700 Dolgoprudny – Russia

ABSTRACT

Long-term wind variability plays important role in energy budget formation of Earth’s climate system. Air motion has two energy components: kinetic and dissipative – that part of energy motion, which transfers to the heat because of friction in viscous energy interval of turbulence. Wind speed trends show the direction of energy redistribution between these two components. The most significant wind speed trends observed in lower troposphere on 1000–700 hPa levels, where they are negative, and in on 300–250 hPa levels, where they are positive. The most significant trends reach values about 0.9–1.2 per decade with determination coefficients up to 16%.
Significant long-term wind fluctuations have 18.6 years’ period with first two overtones and undertones. It shows the determinative role of tidal harmonic constituents in climate variability.

Keywords: long-term, upper wind, trend, fluctuations, tidal harmonic constituents

1. INTRODUCTION

For understanding the relevance of information about long-term wind dynamics throughout all troposphere and how it could be used for solving different applied problems on the near-ground levels, we should clarify two principles. Firstly, almost all long-term changes in wind dynamics that could be observed near the surface, are the result of numerous feedbacks and processes existing in all troposphere and upper atmospheric levels [1]. It means, that we could not properly understand possible climate changes on the surface without upper air data [2, 3]. Secondly, all industrial and scientific fields that use seasonal wind data and based on climate information, must predict future meteorological conditions and be ready for significant changes. It means, that long-term variability and trends of wind speed and direction allow to find answers about expected climate situation in the future. Consequently, researches of long-term wind dynamics are very relevant for energy industry, transport and construction industry. Moreover, as air motion consists of kinetic and dissipative components, long-term analysis helps to descry energy redistribution between them. It plays important role in energy budget and climate change.

Long-term wind data is necessary and widely used on the different stages of designing and building of energy objects [4–6]. Wind power industry process statistic data of wind on 850 hPa (~1.5 km), 700 hPa (~3 km) and 500 hPa (~5 km) levels for maximal wind energy estimation [7–9]. Wind information on upper tropospheric levels is used for power plants planning in mountain regions. It is clear, that long-term wind variations cause significant changes in maximal wind energy. Extreme wind has negative effects on the turbines [10]. Usually the strongest wind in 50-year period is used. Strong winds, together with hoarfrost, are the most dangerous phenomenon for power lines [4], thus probability of strong winds in different intervals should be calculated. Wind speed blowing at a right angle to a high-voltage line can cool the line [11]. In this case, the long-term wind dynamics could give important information about possible future changes. Sidewind influence drift of aircrafts [4, 12]. Knowledge about long-term dynamics answers on very important question – is there any possibility of wind direction changes and what will be the angle between runways on airport and possible wind directions. Another example could be found on the designing stage of railway network [13]. The sum action of strong winds during long period influence on electrical lines and cause deformation and sidelong displacement. So, railway designing depends on long-term wind characteristics. Meteorological conditions are determinative for stationary object in the sea and near shorelines [4, 14]. Information about long-term wind dynamics permit to define maximal probability of dangerous situations.

This study aims to define trends and significant long-term variations of upper wind that formed main features of wind distribution on the surface. Research contains evidence about determinative role of external geophysical factors in climate formation and role of the wind in energy budget.

2. METHODOLOGY

This work is continuation of previous researches of aerological climate above Ukraine and adjacent territories [1, 2]. The data, involved in this research, represents upper air soundings from meteorological stations that are present in Wyoming University databases [15]. Daily data were selected on 13 standard isobaric levels from 1000 hPa (~0.1 km) to 30 hPa (~24 km). Analysis of long-term dynamics should be based on monthly residuals of seasonal variations data. Seasonal (short-term) dynamics were presented earlier [1, 2], where daily data were averaged to monthly values. Database of residuals was obtained by authors after research presented in [1]. Total period for analysis of long-term dynamics is approximately 30 years from 1979 to 2010. Initially, for short-term dynamics, 13 stations were used: 6 on the territory of Ukraine and 7 on the adjacent territories [1]. Starting from 1994 majority of Ukrainian aerological stations do not have regular observations. That’s why, among of all Ukrainian stations, only Kyiv has enough data for providing long-term analysis. Except Kyiv (Ukraine), long-term variations and trends were calculated for Kursk, Voronezh, Rostov-na-Donu, Tuapse (all Russia), Bucharest (Romania) and Legionovo (Poland). On the levels, less than 100 hPa (higher than 14 km), there are also not enough data for accurate long-term analysis. For Legionovo station it is possible to provide calculations up to 250 hPa level (~10 km).

All calculations for long-term analysis consist of three parts: trends estimation, computation of long-term variations and residuals verification (similarity to white noise). Trends estimation was made on monthly residuals of seasonal variations. Significance was calculated using Fisher test. Computation of long-term variations was made after trends exclusion using harmonic analysis. Main attention should be paid on tidal harmonic constituents – low frequency variations caused by gravitational interaction between the Earth and the Moon. It is well known period in 18.613 years [16–18] that called nodal tidal cycle. If variation with main period is significant, it is possible to see significant variations of two – three overtones and undertones. In case of tidal harmonic constituents, period of second overtone is about 9.3 years, third overtone – 6.2 years. Period of second undertone is 37.2 years and third undertone – 55.8 years. All variations with specified periods could be significant for long-term wind dynamics.

After exclusion of trends and significant long-term variations residuals should be tested on similarity to white noise. There were used integrated periodogram of residuals. It shows how close residuals are to white noise. As energy in white noise distribute by frequency evenly, residuals without variations and trends should have the same energy distribution [19]. Firstly, for periodogram computation there were calculated amplitudes of 1000 variations with periods from 3 to 32 years distributed by frequency evenly using harmonic analysis. Secondly, for integrated periodogram there were used equation:

$$A = \sum_{i=1}^{n} A_{i-1} + \sqrt{A_{f_i} + A_{f_{i-1}}} \tag{1}$$

where A – integrated amplitude for n variations of residuals; A_{i-1} – integrated amplitude on previous step; A_{fi} – amplitude of i-variation with frequency f_i; A_{fi-1} – amplitudes of previous variation with f_{i-1} (lower) frequency.

If residuals are close to white noise then A_i increase linearly with increasing of frequency f_i.

3. RESULTS AND DISCUSSIONS

3.1. Trends estimation

Trends, which were calculated on monthly residuals of seasonal variations, are not significant throughout all troposphere (Table 1). Blue color show significant negative trends, red color – significant positive trends. Not significant trends are absent in the table. Significant wind speed trends mainly distributed in the lower troposphere on 1000–700 hPa levels (~0.1–3 km). All trends are negative except Voronezh station on the 1000 hPa level where positive trend is observed (Fig. 1). The highest determination coefficients are on Kyiv station – 15.5%, Tuapse – 14.8%, and Legionovo – 14.7%. Significant trends disappear on the south (Bucharest, Rostov-na-Donu, Tuapse) with the height increasing.

Table 1. Values and determination coefficients (%) of significant wind speed trends per decade

	Bucharest		**Kyiv**		**Kursk**		**Voronezh**		**Rostov**		**Tuapse**		**Legionovo**	
Level, hPa	**A**	**R^2**	**a**	**R^2**	**a**	**R^2**	**a**	**R^2**	**a**	**R^2**	**a**	**R^2**	**a**	**R^2**
1000	-0.3	5.1	-0.6	15.5	nd*	nd*	0.3	3.0	-0.3	2.5	-0.9	14.8	-0.6	14.7
850			-0.3	2.4	-0.6	4.9	-0.6	2.6					-0.3	1.8
700			-0.6	2.2	-0.9	4.8	-0.6	1.8					-0.6	2.2
500					-0.9	1.8	-0.6	1.5					-0.9	2.0
400							-0.9	1.2			-0.9	1.9	-0.6	1.0
300	1.2	2.8							-1.2	1.4				
250	1.2	3.1			0.3	2.9							0.3	1.5
200					0.3	4.4							nd*	nd*
150													nd*	nd*
100			0.3	3.6					0.3	2.1			nd*	nd*

*nd – no data on the level

There is no spatial regularity of trends distribution in the middle troposphere. 300 hPa (~9 km) is the primary level where values become positive. In the upper troposphere, significant trends observed in Bucharest, Kursk and Legionovo, where they disappear in tropopause and lower stratosphere. Trend values vary from 0.3 to 1.2 per decade. Only for Kyiv and Rostov-na-Donu trends are significant in lower stratosphere.

Wind plays important role in Earth' energy budget. Wind has two components: kinetic and dissipative. Dissipative component is a part of energy motion, which transfers to the heat because of friction in viscous energy interval of turbulence. It means that decreasing of wind speed cause increasing of turbulence and, as result, heating. Negative trends show energy redistribution from kinetic to dissipative component. Wind speed negative trends in lower troposphere (Table 1) show that natural processes of energy dissipation play significant role in modern global warming.

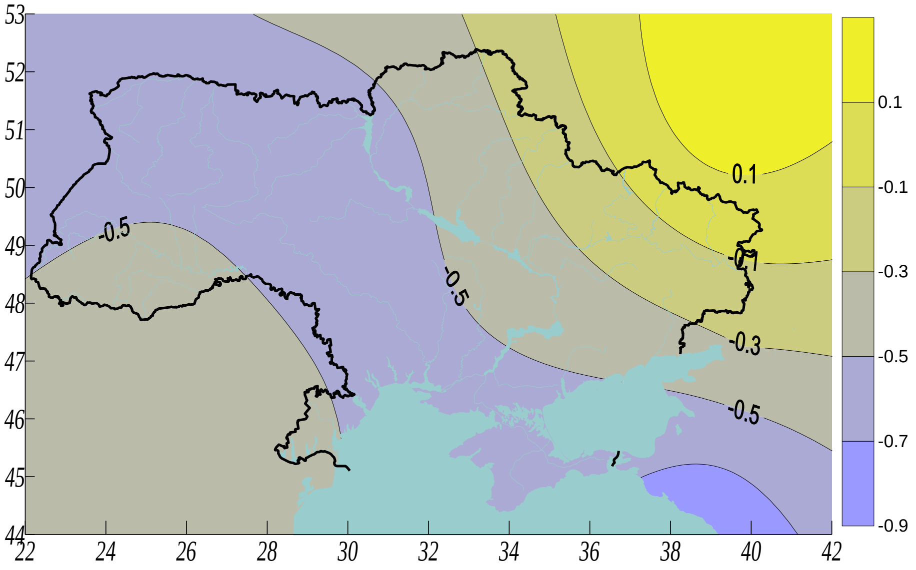

Fig. 1. Spatial distribution of wind speed trends on 1000 hPa level

Wind direction trends are not significant throughout all troposphere in Kyiv, Kursk and Legionovo. They observed on 1000–850 hPa level (~9 km) in Voronezh, Rostov-na-Donu and Tuapse. All trends in boundary level are negative and vary from -0.6 (Voronezh) to -0.9 (Tuapse) with determination coefficient less than 1.7%. On the lower stratosphere layer trends are positive and observed only in Bucharest and Rostov-na-Donu with the highest value 0.3 on the 100 hPa level (~16 km). It means that wind direction above Ukraine and adjacent territories is stable.

According to other researches based on aerological soundings data [20–21], wind speed decrease in lower troposphere and increase in middle and upper troposphere in Europe and North America. But the level, where trends change sign to positive vary from 850 hPa to 500 hPa.

3.2. Long-term variations

Wind speed long-term variations on 1000 hPa level (~0.1 km) differ from each other. Main variation in 18.6 years, dedicated to tidal harmonic constituents, is significant for Bucharest, Kyiv and Legionovo. Wind speed dynamics form also under second (37.2 years) and third (55.8 years) undertones and second overtone (9.3 years). For Rostov 6.2-years' period is also significant (Fig. 2). There are no definite long-term variations in Voronezh. For Tuapse only 9.3-years' variation exist.

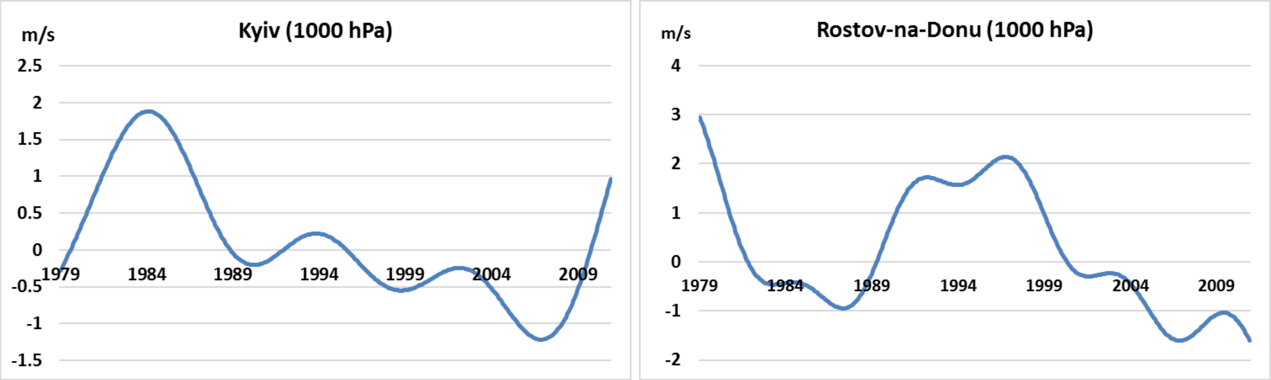

Fig. 2. Long-term wind speed dynamics on 1000 hPa level in Kyiv and Rostov-na-Donu

Amount of wind speed long-term variations decrease with height increasing. The most changeable dynamics in troposphere is typical for Kyiv. Above boundary layer on 700–500 hPa (~3–5.5 km) there are two significant variations: 9.3 and 55.8 years. Middle and higher troposphere is sensitive to 6.2-years fluctuations. For Legionovo 9.3-years’ variation observed up to 250 hPa (~10 km) level (Fig. 3).

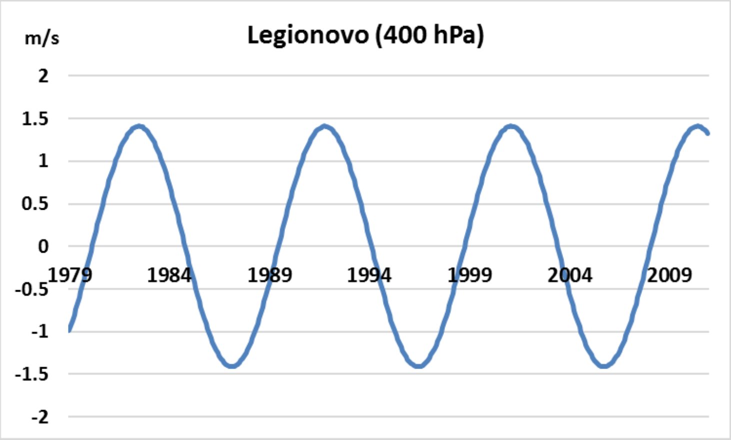

Fig. 3. Typical long-term wind speed variation in middle troposphere in Legionovo

On other stations significant variations distribute differently. They also coincide with tidal harmonic constituents. Wind speed dynamics in Tuapse and Kursk is the most stable: most heights do not have any long-term fluctuations. In Bucharest amplitudes of variations reach 38 m/s in upper troposphere. On that layer all variations connected to gravitational interaction between Moon and Earth are significant. For Rostov and Voronezh stations there are no significant wind speed variations on the heights more than 5 km.

Wind direction dynamics is more unstable than it is observed for wind speed. But only on two layers large fluctuations are observed. First layer is boundary, where maximals variations during last 30 years reach 115 degrees amplitudes (Bucharest). In Legionovo and Kyiv (Fig. 4) it is observed 58–65 degrees amplitudes. All variations also coincide with tidal harmonic constituents. Long-term fluctuations on 1000 hPa levels are very important for industry, thus they should be included in wind dynamics forecast models for solving problems in transport, energy and building industry.

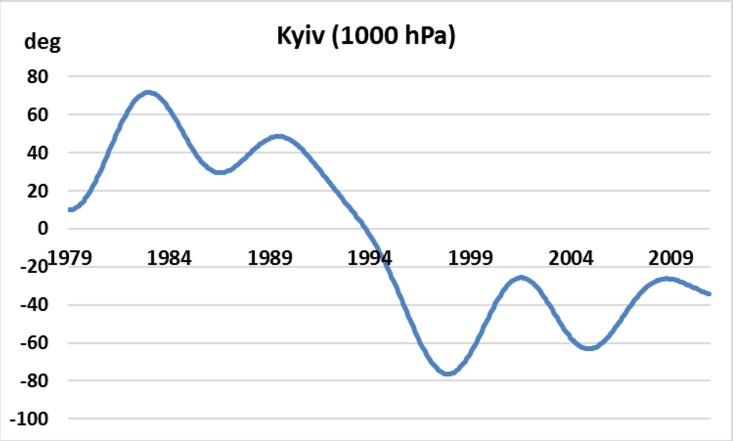

Fig. 4. Long-term wind direction dynamics on 1000 hPa level in Kyiv

Second layer is lower stratosphere. These heights are very important for understanding global circulation and its changes. All stations, except Bucharest and Tuapse, is characterized by changes in wind direction within 80–100 degrees. On Tuapse station variations are not significant. For Bucharest station fluctuations reach higher values up to 150 degrees. In upper troposphere – lower stratosphere the most important role plays low frequancy variations with period more than 18.6 years. The highest impact on direction changes has third undertone of tidal constituents with period 55.8 years.

Computation of long-term upper wind variations for Ukraine were first made in this research. Impact of nodal tidal cycle on wind speed and wind direction also was firstly estimated.

3.3. Residuals verification

Quality and accuracy of calculations could be defined after trends and variations exclusion. In ideal situation only white noise should remain. Analysis on similarity to white noise using integrated periodogram of residuals show good results with the worst time series about 94% (Table 2). Such values are for wind direction in Bucharest on 250 hPa level (~10 km), Rostov-na-Donu on 100 hPa level (~14 km) and wind speed in Bucharest on 200 hPa level (~11 km). Such similarity to white noise after variations exclusion based on tidal harmonics constituents once again prove that gravitational interaction plays determinative role in climate variability.

Table 2. Residuals similarity to white noise (%)

	Bucharest		**Kyiv**		**Kursk**		**Voronezh**		**Rostov**		**Tuapse**		**Legionovo**	
Level, hPa	**wd.**	**ws.**	**wd.**	**ws.**	**wd.**	**ws.**	**wd.**	**ws.**	**wd.**	**ws.**	**wd.**	**ws.**	**wd.**	**ws.**
1000	95	99	99	99	nd*	nd*	99	99	99	96	99	99	99	99
850	97	99	99	99	99	99	99	99	99	97	99	99	99	99
700	99	98	98	99	98	99	96	97	99	98	99	99	99	99
500	99	99	99	99	98	99	97	96	99	99	97	99	98	99
400	99	99	96	99	98	99	98	98	99	99	99	99	99	99
300	99	99	97	99	98	98	98	97	99	99	99	99	99	99
250	94	99	97	99	98	99	98	97	98	99	96	99	99	99
200	99	94	98	98	99	99	98	97	99	99	99	99	nd*	nd*
150	96	99	98	99	98	99	99	97	99	99	99	99	nd*	nd*
100	96	99	99	97	99	99	99	95	94	97	99	99	nd*	nd*

wd. – wind direction, ws. – wind speed
*nd – no data on the level

4. CONCLUSIONS

Long-term dynamics of wind speed and wind direction in troposphere differ and depends on height. Wind speed trends are negative in lower troposphere and positive in upper troposphere. Negative trend in lower troposphere shows that energy dissipation plays improtant role in modern climate change. The most negative trends reach 16% of determination coefficients. Positive trends is characterized by lower values. Wind direction trends are not significant on most heights.

Long-term wind variability forms under gravitational interaction between Moon and Earth with the main period in 18.6 years and its overtones and undertones. There were firstly calculated impact which nodal tidal cycle has on temporal wind distribution. The highest wind speed amplitudes reach 38 m/s. Wind direction could vary up to 115 degrees.

Residuals similarity to white noise shows that analysis of long-term dynamics were made properly and accurately. Similarity to white noise is more than 94%.

REFERENCES

1. SAVENETS M.V., DVORETSKA I.V., KRUCHENITSKY G.M. Vertical distribution and seasonal variability of wind over Ukraine and adjacent territories. CYSENI 2016. Proceedings of annual conference of young scientists on energy issues. Kaunas: Lithuanian Energy Institute. 2016 May 26-27.
2. КРУЧЕНИЦКИЙ Г.М., ДВОРЕЦКАЯ И.В., САВЕНЕЦ М.В. Климат термобарических полей над территорией Украины. Оптика атмосферы и океана. Физика атмосферы: тезисы докладов XX международного симпозиума. Новосибирск: ИХКГ СО РАН. 2014, 23-27 июня.
3. BRONNIMANN S. et al. *Climate Variability and Extremes during the Past 100 Years*. Springer Science + Business Media B.V. 2008. 358 p. ISBN: 978-1-4020-6765-5.
4. ХАНДОЖКО Л.А. *Экономическая метеорология*. СПб.: Гидрометеоиздат. 2005. 491 с. ISBN: 5-286-01505-0.
5. LEFEBVRE G. et al. Environmental, Energy and Climate Change II. Energies from New Resources and the Climate Change. Springer International Publishing. 2016. 268 p.
6. EMEIS S. Wind energy meteorology: atmospheric physics for wind power generation. Springer-Verlag Berlin Heidelberg, 2013. 201 p.
7. D.J. DE RENZO. *Wind power: recent developments*. Front Cover D.J. De Renzo. William Andrew, Inc., 1979. 347 p.
8. LORENZ E. Available potential energy and the maintenance of the general circulation. Tellus 7, 1955. 271-278 pp.
9. MILLER, L.M., F. GANS, A. KLEIDON: Estimating maximum global land surface wind power extractability and associated climatic consequences. *Earth Syst. Dynam*. 2, 1-12 (2011).
10. LANDBERG L. *Meteorology for wind energy*. John Wiley & Sons Ltd. 2016. 227 p. ISBN: 9781118913444.
11. *Energy and Environment*. Increasing the capacity of Existing power lines. A cool way to increase existing overhead power line capacity. Link to the internet <https://energy.gov/sites/prod/files/2013/12/f5/inl_powerline_cooling_factsheet.pdf>.
12. БОГАТКИН О.Г. Авиационная метеорология. СПб.: Изд. РГГМУ. 2005. 328 с. ISBN:5-86813-137-1.
13. MATSHCHKE G., SHULTE-WENING B., Measures and Strategies to Minimise the Effect of Strong Cross Winds on High Speed Trains. Proceedings of the World Congress of Railway Research WCRR ’97, Florenz, Italy, 1997. Nov. 16-17.

14. BITNER-GREGERSEN E.M., EIDE L.I., HORTE T., SKJONG R. *Ship and Offshore Structure Design in Climate Change Perspective*. Springer. 2014. 76 p. ISBN: 978-3-642-34137-3.
15. *Atmospheric soundings*. University of Wyoming, College of Engineering. Link to the internet: < http://weather.uwyo.edu/upperair/sounding.html >.
16. Z. KOWALIK, J. LUICK. *The oceanography of tides*. Link to the internet: < https://www.uaf.edu/files/sfos/Kowalik/tide_book.pdf >.
17. YASUDA I. The 18.6-year period moon-tidal cycle in Pacific Decadal Oscillation reconstructed from three-rings in western North America. Geophysical Research Letters, Vol.36, L05605, doi:10.1029/2008GL036880. 2009.
18. Manual of Harmonic Analysis and Prediction of Tides. Government Printing Office. Washington. 1958. 332 p.
19. H. von STORCH, F.W. ZWIERS. *Statistical Analysis in Climate Research*. Cambridge University Press. 2002. 495 p. ISBN: 0-521-01230-9.
20. Z.ZHAO, Y.LUO, Y.JIANG. Is global strong wind declining? Advances in Climate Change Research. Vol 2. 2011. pp.225-228.
21. R. VAUTARD et al. *Nothern Hemisphere Atmospheric stilling partly attributed to an increase in surface roughness*. Nature Geoscience 3 (17). 2010.

CYSENI 2017, May 25-26, Kaunas, Lithuania
ISSN 1822-7554, www.cyseni.com

RHEOLOGICAL STUDY ON CO_2 HYDRATE SLURRIES FOR SECONDARY REFRIGERATION

Y. Salehy, P. Clain
Léonard de Vinci Pôle Universitaire, Research Center
92916 Paris La Défense, France
E-mail: yasmine.salehy-shablizi@devinci.fr

A. Boufares, V. Osswald, A. Delahaye, L. Fournaison
Irstea GPAN
1 rue Pierre Gilles de Gennes, CS 10030, Antony 92761 Cedex France

ABSTRACT

To help the fight against climate change, the Kigali deal has planned to eliminate hydrofluorocarbon's use (HFC) in industrial sytems. HFCs are powerful greenhouse gases with a high global warming potential. Moreover, HFCs are commonly used as refrigerant within secondary refrigeration processes for cold production. A solution to limit their negative environmental impact would be to reduce the amount of HFC by using a phase change slurries (PCS) in the secondary loop. A PCS is composed of solid phase change particles (solid-liquid) in a liquid transportation phase. The most used one are ice slurries. The issue incontered with these PCS are the high amount of energy needed to produce and stabilze the system. Clathrate hydrates are crystalline particles where gas molecules are trapped in water cages. Due to their high energy densities (higher than water), hydrate slurries, in particular CO_2 hydrates, are relevant two-phase secondary fluids because they enhance the energy efficiency of secondary refrigeration systems. The suitable temperature above 0 °C allows hydrate slurries to be used in chiller systems. However, the pressure needed is more than 1 MPa. To reduce the euilibrium pressure, many studies have demonstrated that quaternary salts such as tetra-n-butylphosphonium bromide (TBPB) are effective promoters. Indeed, they have the ability to be stable at the atmopheric pressure. In this study, the rheological behaviour of mixed CO_2 – TPBP hydrate slurries in various experimental conditions on a dynamic loop for cold distribution was investigated. An exhaustive state-of-the-art on the rheological studies of hydrate slurries in aqueous solution has pointed out that hydrate slurries are non-newtonian fluids. However, the rheological behaviour could be different for a same kind of hydrate slurry according to the litterature. Moreover, the litterature review also highlighted that the most used measurement method for the apparent viscosity is the capillary viscometer. We used the generalized form of Rabinowitsh and Mooney equation for determining the needed caracterisation coefficient and then the apparent viscosity of the mixed CO_2 – TBPB hydrate slurry as a function of the hydrate slurry fraction. Three different solid volume fraction have been studied 11.50%, 14.2% and 16.4%. In the semi-empirical Herschel-Bulkley's model experimental datas of pressure drop and volume flows are measured and used. The experiments have confirmed that hydrate slurries are non-newtonian fluids. The results also shown the shear thinning behaviour of the slurry. Indeed the behaviour index decreases as the solid fraction increases. This work is primordial for designing and sizing a new efficient refrigeration system based on this innovative material.

Keywords: CO_2, tetra-n-butylphosphonium bromide (TBPB), Hydrate slurries, rheology, dynamic loop, secondary refrigeration

CYSENI 2017, May 25-26, Kaunas, Lithuania
ISSN 1822-7554, www.cyseni.com

THE CHALLENGE OF GREEN CONSUMPTION BEHAVIORS

V. Varanavicius
Lithuanian Energy Institute
Breslaujos str. 3, 44403 Kaunas, Lithuania
E-mail: v.varanavicius@gmail.com

ABSTRACT

Modern consumers have embraced sustainable lifestyles and sustainable consumption that do not damage the environment and also do not compromise the future. According to the recent reports, enhanced society awareness on various environmental problems has changed consumers' behavior and also induced them on social responsibility. Moreover, positive mind-set towards the environment has been increasing over the years. Investigations of published academic papers about green consumption have revealed that this field is highly unexplored. With this in mind, the overall purpose of the study is to examine the consumer behavior concepts that lead to changes. The aim of the study is reached via three-fold objectives. Firstly, it examines the consumer behavior concepts. Secondly, it presents the models of consumer behavior. Finally, examines the challenges that appear in implementing green consumption behaviors. The novelty of this study paper could be constituted by the fact that it is extensive in terms of displayed models and concepts. Moreover, the conclusions of this study present significant theoretical and also practical implications for green consumption behaviors. Hence, the significance of the article lies on that the gap of green consumption behavior understanding is narrowed. Accordingly, it puts forward an important foundation for the future investigations.

Keywords: consumer behavior, green consumption, energy saving

1. INTRODUCTION

Modern consumers have embraced sustainable lifestyles and sustainable consumption that do not damage the environment and also do not compromise the future. Positive mind-set towards the environment has been increasing over the years. Investigations of prior published academic papers considering the green consumption behaviors which center the attention on the pioneering ways for its attainment have revealed that this field is highly unexplored. With this in mind, the overall purpose of the study is to examine the consumer behavior concepts that lead to changes.

The novelty of the study: It is constituted by the fact that it is extensive in terms of displayed models and concepts. Moreover, the conclusions of this study present significant theoretical and also practical implications for green consumption behaviors.

The object of this study is: green consumer behavior in respect to energy consumption.

The problem of the study is: how energy consumption influences the green behavior?

The aim of the study is: To analyze the challenges of green consumption behavior.

The objectives of the study are two-fold:

1) To analyze the element of consumer behavior from theoretical point of view.
2) To investigate energy consumption and green consumption concept.

The methods of the study are:

Logical and comparative analysis of literature;
Graphics;
Synthesis and deduction.

2. CONSUMER BEHAVIOUR

The traditional economic theory of customer preference is based on four main elements: customer income, market price of goods, customer preferences and behavior assumption about the maximum of achievable benefit. When exist the limited income, the customer is choosing the preferred goods by using the method to ensure getting the maximum benefit, also which is allowed by limited income. (Begg et al., 2005)

It is important to detail realized customer rationality. The classical users or consumers usually are those who maximize their benefit from various purchase options. Seeking to get the highest benefit consumer has to have overall information: the group of possible purchase options and the prices of each good. It is admitted that the role of information is very important for the customer behavior when real life situation is analyzed. The rational choice is possible only when the context of perfect information availability exist. (Nunes, 2002)

It is worth to mention, that the consumer choices, tastes that have the high impact on the choice is valued. The consumer preference theory has not much information about nature of customer behavior, structure and environment. The individual and collective consumer preferences are known as much as it was analyzed through the rational consumption during the process of consumer decision making. It is said that economy is promoted, that there is no constrains on desire of individual goods or services. The wishes of the consumer is unlimited, this is the constraint for theory which says that customer is willing to get the highest values. However, the main factors that make influence are the individual taste, preferred costs and benefit. Thus the role of information is said to have the highest influence that allows making the rational decisions to the consumer. To sum up, the one constraint is the assurance of needed information to ensure the rational decision making, including the costs and the benefit that correlates with each other. (Brennan, 2007)

Otherwise Fogli (2006) admitted that increased clientele depend not only on customer satisfaction but rather on customer behavior: repeating purchases, larger or more frequent purchases, also a positive word of mouth from friends and colleagues. Customer satisfaction serves as a help to forecast the future behavior and Oliver (2006) indicates that customer satisfaction is an important antecedent of behavioral intentions and actual behavior. Regarding Čavoški, Marković (2015): "Consumer behaviour can be described as a set of activities prospective customers undertake in searching, selecting, valuing, assessing, supplying and using of products and services in order to satisfy their needs and desires."

Moreover, Choy, Lam & Lee (2011) presented the conceptual model (see picture below) of essential relationships among three objects.

Fig. 1. Interrelationships among customer satisfaction, service quality and behavioral intentions (ref.)

The provision of the conceptual model contributes for practitioners. It offers a positive relationship between customer satisfaction and service quality and it's both dimensions (technical and functional qualities), also provides the positive impact of customer satisfaction towards behavioral intentions.

3. ENERGY CONSUMPTION

It can be stated that equalizing energy consumption in respect to consumers behavior is not possible. On the other hand, it can be described as consequences of behavior, such as turning on the lights or thermostat level reduction (Becker, 1981). The impact of household behaviors is enormous. Households are one of the largest final energy users in the EU, accounting for 26.2% of total energy consumption in 2001. In 2002, households contributed 10% of CO2 emissions in the EU-15. (European Environment Agency, 2004)

It is important to mention that authors divide the two types of energy consumption in households, the table below show the types of energy saving behavior.

Table 1. Energy saving behavior types. Source. Abrahamse et al. (2005)

Behavior Types	**Examples**
Productive behavior	Investments with clear nature Ceiling Insulation Walls insulation Double windows installation
The behavior which decrease energy consumption	Recurring operational actions Turning off the light Keeping windows closed Turning off equipment

It is worth mentioning that these behavior types may be considered from the economic perspective, as an example can be taken that the consumption behavior can be related with the monetary aspect. On the other hand the energy consumption can be seen as value approach, as an example energy consumption behavior may be influenced by saving the environment that persons are cared about.

According to Geller (2002), there is still not clear which behavior type – the productive behavior or the behavior which decrease energy consumption is more effecting on energy saving. It is also said that behavior that decease energy consumption creates the conditions for developments of behavior changes in the long term perspective. However, the author Abrahamse et al. (2005) states that productive behavior is more effective when seeking for energy saving and environmental sustainability.

Nevertheless, there is an environmental awareness and concern, mostly this does not translate into a real action – behaviour. Kollmuss, A. & Agyeman, J., (2002). Green behaviour is the shared responsibility of individual citizens, public authorities and industry (Sonigo, 2012).

4. GREEN CONSUMPTION

There is so called „green consumption or green behavior, which identifies the behavior that minimizes harm to the environment as much as possible, or even benefits it (Abrahamse et. al., 2005). Practical examples could be identified as energy use minimisation and waste reduction. Addressing Cushman-Roisin(2012) idea it means 'doing good and avoiding bad'.

The Four 'A's approach is rooted in social marketing and identifies the Four A's which focus on the necessary conditions to improve green consumption and behavior:

- Accessibility – green products and services must be easy accessible, which may also include cancelling products that are damaging to the environment.
- Affordability – sustainable consumption must be affordable for everyone, especially low-income households.
- Attractiveness – sustainable consumption needs to be translated into clear personal benefits, such as better health and improved quality of life.
- Awareness – sustainable consumption requires a level of environmental knowledge, for example, gained through information brochures and educational handouts.

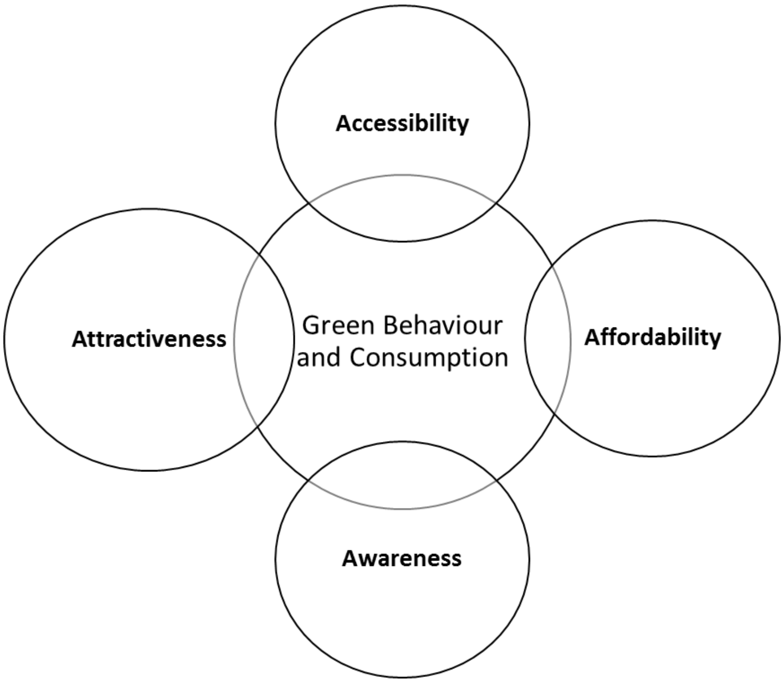

Fig. 2. Four A’s which focus on the necessary conditions to improve green consumption and behavior. Source. Science of Environment policy. Future Brief: Green behaviour, 2012

An approach similar to the Four ‘A’s has been adopted by the international company Unilever in its five levers of behavior change, which propose that the desired behavior must be made understood, easy, rewarding, desirable and habitual.

5. CONCLUSIONS

1. The traditional economic theory of customer preference is based on four main elements: customer income, market price of goods, customer preferences and behavior assumption about the maximum of achievable benefit.
2. The classical users or consumers usually are those who maximize their benefit from various purchase options.
3. Green behavior is the shared responsibility of individual citizens, public authorities and industry.
4. Affordability, accessibility, attractiveness and awareness are necessary conditions to improve green consumption and behavior.

REFERENCES

1. Abrahamse, W., Steg, L., Vlek, C., Rothengatter, T., (2005). A review of intervention studies aimed at household energy conservation. Journal of Environmental Psychology, Netherlands, No. 25, p. 273-291.
2. Becker, L., Selingman, C., Fazio, R., Darley, M., (1981). Relating Attitudes to Residential Energy Use. Environment and Behavior, No. 13, p. 590-609.
3. Begg, D. K. H., Fischer, S., Dornbusch, R., Damian Ward, D., (2005). Economics, 8th Edition, McGraw-Hill Education, Berkshire.
4. Brennan, T., (2007). Consumer preference not to choose: Methodological and policy implications. Energy Policy, No. 3, p. 1616-1627.
5. Čavoški, S., Marković, S., Analysis of Customer Behaviour and Online Retailers Strategies Using the Agent-Based Simulation. Management (1820-0222). 2015, Issue 77, p. 13-24. 12 p.
6. Choy, J.,Y., Lam S.Y., Lee, T.,C., (2011), Service Quality, Customer Satisfaction and behavioral intentions: review of literature and conceptual model development. International Journal of Academic Research, 4(3).
7. Cushman-Roisin, B. (2012) Green behaviour (homo ecologicus). [Presentation] [Electronic source] Retrieved from http://engineering.dartmouth.edu/~cushman/courses/engs44/GreenBehavior.pdf (Date of access: 01.12.2016).
8. European Environment Agency (2004) Analysis of greenhouse gas emission trends and projections in Europe 2004. Luxembourg: Office for Official Publications of the European Communities. [Electronic source] Retrieved from http:// www.eea.europa.eu/publications/technical_report_2004_7 (Date of access: 01.12.2016).
9. Fogli, L. (2006). Customer Service Delivery: Research and Best Practices. USA: John Wiley & Sons, Inc.
10. Geller, S., (2002). The Challenge of Increasing Proenvironment Behavior. Handbook of Environmental Psychology. Wiley, New York.
11. Kollmuss, A. & Agyeman, J. (2002) Mind the Gap: Why do people act environmentally and what are the barriers to pro- environmental behavior? Environmental Education Research 8:3, 239-260.
12. Nunes, P., (2002) .Using factor analysis to identify customer preferences for the protection of a natural area in Portugal. European Journal of Operational Research.
13. Oliver, R.,L. (1999). Whence consumer loyalty?. Journal of Marketing, 63, 33-44.
14. Science of Environment policy. Future Brief: Green behaviour, (2012). [Electronic source] Retrieved from http://ec.europa.eu/environment/integration/research/newsalert/pdf/FB4_en.pdf (Date of access: 01.12.2016).
15. Sonigo et al (2012) Policies to encourage sustainable consumption, Final report prepared by BIO Intelligence Service for European Commission (DG ENV). [Electronic source] Retrieved from http:// ec.europa.eu/environment/eussd/pdf/report_22082012.pdf (Date of access: 01.12.2016).

CYSENI 2017, May 25-26, Kaunas, Lithuania
ISSN 1822-7554, www.cyseni.com

ADVANCED EXERGETIC ANALYSIS OF A HEAT PUMP PROVIDING SPACE HEATING IN BUILT ENVIRONMENT

V. A. Voloshchuk
National Technical University of Ukraine "Igor Sikorsky Kyiv Polytechnic Institute"
Politehnichna st. 56, 03056 Kyiv – Ukraine
E-mail: Volodya-28@yandex.ru

ABSTRACT

In addition to conventional exergy-based methods, advanced exergetic analysis considers the interactions among components of the energy-conversion system and the real potential for improving each system component. This type of analysis has been applied so far mostly to refrigeration machines and industrial heat pump systems where only single modes (nominal ones) were investigated. When applying exergy-based methods for the heat pumps providing space heating variation of operational regimes should be taken into account.

The scope of the paper is to demonstrate application of the detailed advanced exergetic analysis on a wastewater source heat pump for space heating in varying operational modes.

In order to determine thermodynamic parameters of the refrigeration vapor compresion cycle in different operating modes (off-design modes) during a heating season the simulation model has been used. The model is based on quasi-steady state approach.

The analysis is performed for a typical Ukrainian house. Daily weather data within a heating season for the city of Rivne located in the western part of Ukraine were used for the evaluation.

It has been shown that within a heating season both the absolute values and the shares of exergy destruction can be different for different operational modes. For correct exergetic assesment of such type of heat pump it is not sufficient to analyze only single modes (for example, design modes). It is proposed to calculate annual (for the whole heating season) values of exergy destruction.

According to results obtained from the conventional (without splitting the exergy destruction) exergetic analysis the priority for improvement should be made in the following order: condenser (32% of exergy destruction ratio), throttling valve (28%), evaporator (22%) and compressor (18%). These results are misleading to some extent. The throttling process is completely irreversible and there are no ways of improving this process with the help of increasing thermodynamic efficiency in it. Some part of exergy destruction in the compressor depends on irreversibilities in the condenser and the evaporator but not on the compressor itself.

The advanced exergy-based assesment includes splitting the exergy destruction within each component of the heat pump into unavoidable, avoidable, endogenous and exogenous parts as well as a detailed splitting of the avoidable exogenous exergy destruction.

In addition to conventional exergy analysis the advanced one has provided more precise information concerning location, magnitude and causes of thermodynamic inefficiencies in the investigated heat pump. The results obtained from the advanced exergetic analysis demonstrate that in all four components of the heat pump exergy distruction takes place. But only 1181 kW·hr or 50% of the total annual exergy destruction in the heat pump can be avoided which is distributed among the components in the following manner: 303 kW·hr in the compressor, 316 kW·hr in the condenser, 246 kW·hr in the throttling valve and 316 kW·hr in the evaporator. About 40% of avoidable thermodynamic inefficiency is exogenous. 50% of the avoided seasonal exergy destruction in the heat pump is caused by irreversible heat transfer in the evaporator. Exergy destruction which can be avoided in the heat pump with the help of decreasing heat transfer irreversibility in the condenser accounts 43%. Only 7 % of the avoided exergy destruction in the investigated unit belongs to the compressor.

Due to variation of operational modes from year to year the values of exergy destruction in the same components of the investigated heat pump can be different. For example, in the analyzed case avoidable parts of seasonal exergy destructions in the components of the heat pump for warm and cold years can be 14–26% lower and bigger respectively as compared with a middle year.

Keywords: advanced exergetic analysis, heat pump, heating, variability

CYSENI 2017, May 25-26, Kaunas, Lithuania
ISSN 1822-7554, www.cyseni.com

CAUSAL RELATIONS BETWEEN ENERGY CONSUMPTION, ECONOMIC STRUCTURE AND ECONOMIC GROWTH IN EU COUNTRIES

A. Zuoza
Lithuanian Energy Institute
Breslaujos g. 3, LT-44403 Kaunas – Lithuania
E-mail: andrius.zuoza@lei.lt

V. Pilinkienė
Kaunas University of Technology,
Donelaičio str. 20-334, LT-44309 Kaunas – Lithuania

ABSTRACT

The questions about country's energy consumption and their influence on economic growth are one of the main points on the agenda of the environmental and economic policy. Especially the politicians, from less developed countries, often argue that high environmental requirements allows to have less energy consumption, which could cause reduction of countries economic growth. Simultaneously European Commission has decided to increase energy efficiency, with hope, that this will have a positive impact on the environment and also stimulate the economy. However, there are discussions that such ambitious target can have a negative influence on the economic growth. With this paper we investigating relations between energy consumption, country's economic structure and economic performance. The research was done across 27 EU countries. In this paper country's economic structure is considered as a mix of 10 socio-economic indicators, taken from The World Banks World development indicators database. All countries were grouped into the three groups, and Granger causality check was performed for each country. The results of the research are not suggesting any clear conclusions about relations between energy consumption and economic performance in the EU countries.

Keywords: economic structure, energy consumption, economic growth

1. INTRODUCTION

One of the main goals declared in the Europe 2020 strategy [1] of the European Commission is to achieve a 20% increase in energy efficiency by 2020 (compared to 1990). Furthermore in 2014 EU countries had agreed to set a new, more challenging, energy efficiency target – to achieve not less than 27% increase in energy efficiency by 2030. Eurostat specified that energy intensity is used as overall energy efficiency indicator [2]. Energy intensity of the economy is measured as a ratio between the gross inland consumption of energy and the gross domestic product (kg of oil equivalent per 1 000 EUR). The gross inland consumption of energy is calculated as the sum of the gross inland consumption of five energy types: coal, electricity, oil, natural gas, and renewable energy sources.

Evidence of a causal relationship between energy intensity and economic growth has a significant impact on political agenda. And such question is even more important for developing countrieswhich often need large increases in energy production and consumption to keep up with the expansion of their economies [3]. However in the discussions is more commonly to use gross inland energy consumption instead of energy intensity. In this paper, energy consumption will be also used instead of energy intensity.

The causal relationship between energy consumption and economic growth has been examined by numerous researchers. Gross inland energy consumption and economic growth causality relationship were tested for different countries or their groups, with different methods, different time periods. As mention by Payne [4] and Ozturk [5] there is four main hypothesis for economic grow and energy consumption testing:

- Growth hypothesis. The main idea here is that energy consumption has unidirectional causality to economic growth. For example, if there exists unidirectional causality running economic growth to energy consumption, it may be implied, that energy conservation policies may be implemented with little adverse or no effects on economic growth [6].
- Conservation hypothesis. This is the opposite of growth hypothesis, which in general state, that economic grow cause energy consumption.
- Neutrality hypothesis. This hypothesis state, that there is no causality between energy consumption and economic growth. This hypothesis would imply, that energy conservation policy does not affect economic growth [6].
- Feedback hypothesis. This hypothesis confirms bidirectional causality between energy consumption and economic growth.

As well as Payne [7] and Ozturk [5] and Lekavičius [8] noted, that there are a couple of statistical methods for causal relationship examination, but the most popular is Granger causality, Toda-Yamamoto causality, Pedroni panel cointegration, autoregressive distributed lag, maximum entropy bootstrap, Panel-Corrected Standard Errors estimators, etc.

From the literature surveys done by Al-mulali [9], Ozturk [5] or Chiou-wei et al. [10] can be seen, that main focus of most studies is concentrated on developing countries and US.

Al-mulali [9] investigated the relationship between GDP growth and renewable and non-renewable energy consumption in 82 developing countries categorized by geographical region (East Asia, Pacific, Europe, Central Asia, Latin America, the Caribbean, Middle East, North Africa, South Asia, the Sub-Saharan African). However, countries in the same geographical region can have a very different economic situation and this was not been taken into account.

Chiou-wei et al. [10] suggested using nonlinear Granger causality test to examine the causal relationship between energy consumption and economic growth. Their study confirms neutrality hypothesis for the US, Thailand and South Korea. However, empirical evidence on Philippines and Singapore reveals a unidirectional causality running from economic growth to energy consumption while energy consumption may have affected economic growth for Taiwan, Hong Kong, Malaysia and Indonesia.

Gaspar et al. [11] noted that gross domestic product could be very inefficient for evaluating country development. As an alternative, he suggests to use an Index of Sustainable Economic Welfare (ISEW) and investigate ISEW and energy consumption relationships.

Such a big amount of studies and their controversial results shows a significant meaning of this subject and should be further investigated. However, the lack of studies where the relation between energy consumption and economic growth in EU countries were investigated shows that important of this question can be misinterpreted. Also it was not found any papers, where countries economic structure was taken into account.

This paper aims to group similar EU countries and then investigate relations between energy consumptions and country’s economic growth in groups.

In the next section methodology for country grouping and causality relationship is discussed. Section three presents’ empirical results and discussions and conclusions are set out at the end of the paper.

2. METHODOLOGY

2.1. Grouping of the countries

In order to check for causality evidence between countries economic structure and energy consumption, all 27 European Union (EU) countries were grouped into the three groups.

In this paper countries economic structure is understood as a collection of sustainable development criteria’s [12]. From all sustainable development criteria’s, mentioned by Bivainis and Tamošiūnas [12] only ten socio-economic criteria were selected. The complete criteria list is mentioned below:

- Agricultural land (% of land area);
- Energy imports, net (% of energy use);
- Electric power consumption (kWh per capita);
- CO2 emissions (metric tons per capita);
- GDP per capita (current US$); Number of infant deaths;
- Employment in industry (% of total employment);
- Employment in services (% of total employment);
- Life expectancy at birth, total (years);
- Merchandise exports/imports ratio by the reporting economy (current US$).

Multi-criteria decision-making method [13] was used to combine countries into the groups. Multi-criteria decision-making method is typically used for solving problems, which was decribed by multiple criteria.

First, each country data was ranked by each criterion. Second, weighted rank for last five years for each criterion was calculated. Third, final rank was constructed by adding all weighted ranks for one country. Fourthly, all countries were divided into three groups:

- The first group included countries with ranks from 1 to 10;
- The second group included countries with ranks from 11 to 20;
- The third group included countries with ranks from 21 to 27.

2.2. Granger causality test

Due to the simplicity of computations Granger causality test [14] is a popular method for causality analysis in economics [15]. This test was designed to detect a correlation between the current value of one variable and the past values of another variable. The original definition of Granger causality does not account for latent confounding effects and does not capture instantaneous and non-linear causal relationships, though several extensions have been proposed to address these issues [15].

Grangers causality test consider a bivariate VAR model with two time series X_t and Y_t [16]:

$$\begin{aligned} \Delta Y_t &= \alpha_{12} + \sum_{i=1}^{T11} \beta_{11i} \Delta Y_{t-1} + \sum_{j=1}^{T12} \beta_{12j} \Delta X_{t-j} + v_{12t} \\ \Delta X_t &= \alpha_{22} + \sum_{i=1}^{T21} \beta_{21i} \Delta X_{t-1} + \sum_{j=1}^{T22} \beta 2_{12j} \Delta Y_{t-j} + v_{22t} \end{aligned} \tag{1}$$

where Δ is the difference operator, T is the lag order, α and β are parameters for estimation, ν_t is an error term. All data was tested with lags (T) from 1 to 5.

By testing for Granger causality from *X* to *Y*, the null (H_0) hypothesis is described as:

H_0: $\beta_{12j} = 0$, j = [1,q].

If H_0 is rejected it suggests that the past value of *X* has a significant linear predictive power on the current value of *Y*. It normally denotes that *X* Granger causes *Y*, and vice versa [10].

In this paper two null hypotheses were tested:
H_{01}: Countries total energy consumption does not Ganger cause gross domestic product.
H_{02}: Gross domestic product does not Ganger cause the total energy consumption.

For unit root testing Dickey-Fuller [17] test was performed. The null hypothesis is that the gross domestic product and energy consumption in each country have a unit root, against the alternative that they do not.

Significance level (p) for all statistical calculation was set by 0.05.

All statistical computation and model buildings were done using R programming language (version 3.2.3).

3. RESULTS AND DISCUSSIONS

After ranking all countries in tree groups were categorized and shown in Fig. 1 in alphabetical order.

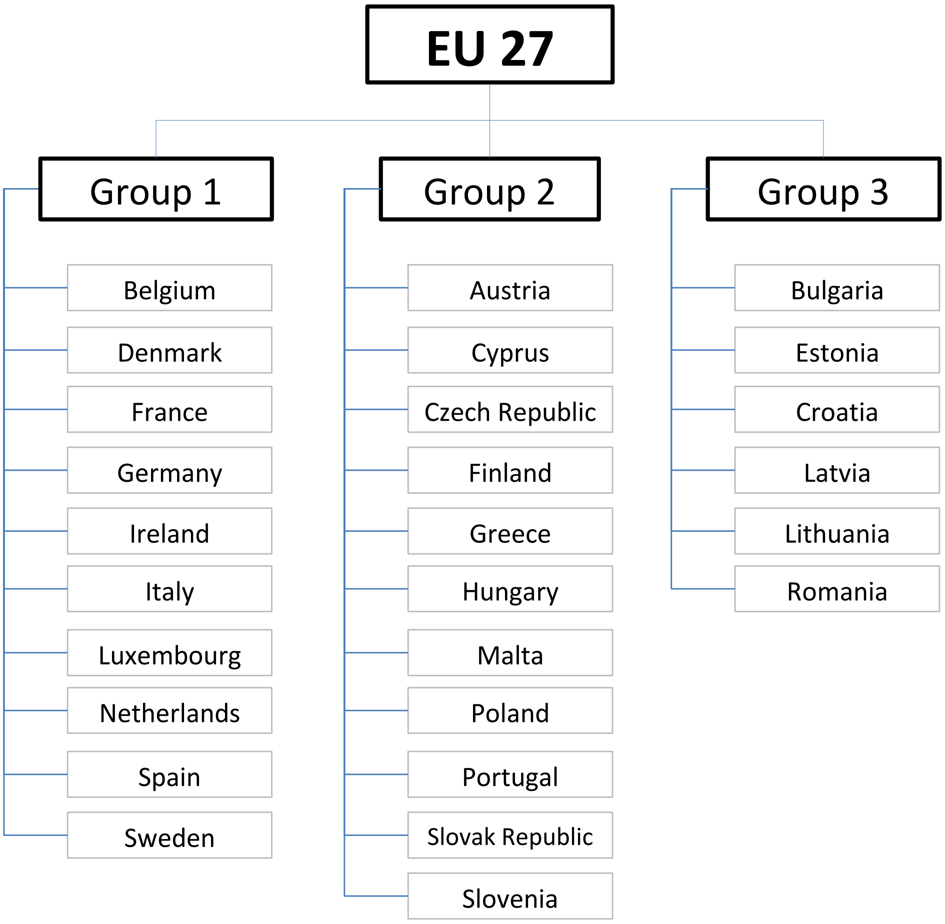

Fig. 1. Categorized EU countries in alphabetical order

Before performing Granger causality test and to avoid the problem of spurious regression, Dickey-Fuller test was conducted for all countries. Table 1 reports the results of unit root tests for all countries total energy consumption and real GDP. For all series, the null hypothesis of a unit root in levels cannot be rejected significantly, which suggest that all series are nonstationary. However for most series in first difference is stationary at a 0.05 significance level.

Table 1. Dickey-Fuller test results

Countries	**Energy consumption**		**GDP**	
	Level	**First difference**	**Level**	**First difference**
		Group 1		
Belgium	0.212; 0.834	-6.382; < 0.000	1.668; 0.114	-2.758; 0.014
Denmark	-0.523; 0.608	-7.001; < 0.000	1.645; 0.118	-2.801; 0.013
France	0.510; 0.616	-7.314; < 0.000	1.457; 0.163	-2.940; 0.010
Germany	-0.484; 0.635	-8.079; < 0.000	1.063; 0.303	-3.191; 0.006
Ireland	0.882; 0.390	-2.937; 0.010	1.459; 0.163	-2.328; 0.033
Italy	-0.233; 0.819	-2.974; 0.009	1.240; 0.232	-3.174; 0.006
Luxembourg	0.939; 0.361	-2.815; 0.012	2.609; 0.018	-2.597; 0.019
Netherlands	0.551; 0.589	-7.223; < 0.000	1.549; 0.140	-2.886; 0.011
Spain	0.554; 0.587	-1.786; 0.093	1.282; 0.217	-2.455; 0.026
Sweden	-0.202; 0.843	-6.648; < 0.000	1.734; 0.101	-3.529; 0.003
		Group 2		
Austria	1.385; 0.184	-5.552; < 0.000	1.622; 0.123	-2.849; 0.012
Cyprus	0.219; 0.829	-2.868; 0.011	1.431; 0.170	-2.478; 0.025
Czech Republic	-0.008; 0.994	-4.480; < 0.000	1.466; 0.161	-3.143; 0.006
Finland	0.401; 0.694	-4.826; < 0.000	1.548; 0.140	-3.160; 0.006
Greece	0.041; 0.968	-1.052; 0.308	0.521; 0.609	-2.058; 0.056
Hungary	-0.985; 0.338	-3.742; 0.002	1.218; 0.240	-3.203; 0.006
Malta	-0.104; 0.919	-8.927; < 0.000	3.546; 0.002	-2.428; 0.027
Poland	-0.209; 0.837	-4.117; 0.001	1.728; 0.102	-3.664; 0.002
Portugal	0.283; 0.780	-2.849; 0.012	1.270; 0.221	-2.795; 0.013
Slovak Republic	-0.275; 0.787	-6.743; < 0.000	2.081; 0.053	-2.648; 0.018
Slovenia	0.589; 0.564	-5.233; < 0.000	1.258; 0.226	-2.867; 0.011
		Group 3		
Bulgaria	-1.521; 0.147	-3.346; 0.004	2.047; 0.056	-2.634; 0.018
Estonia	0.387; 0.704	-2.440; 0.027	1.220; 0.239	-2.628; 0.018
Croatia	0.416; 0.683	-4.962; < 0.000	1.912; 0.073	-2.583; 0.020
Latvia	-0.419; 0.681	-3.770; 0.002	0.957; 0.352	-2.915; 0.010
Lithuania	-0.676; 0.508	-3.776; 0.002	1.617; 0.124	-3.133; 0.006
Romania	-1.800; 0.090	-2.519; 0.023	1.368; 0.189	-2.916; 0.010

Notes: 1. First reported number is Dickey-Fuller test statistic. 2. Second reported number – p. value

Because the first difference of Spain energy consumption and Greece GDP and energy consumption data also are nonstationary, they are excluded form future analysis.

For each country, the five VAR models, using the series in first difference, between energy consumption and GDP were constructed.

Table 2. Granger causality test results

Countries	**Lag 1**		**Lag 2**		**Lag 3**		**Lag 4**		**Lag 5**	
	H_{01}	**H_{02}**	**H_{01}**	**H_{02}**	**H_{01}**	**H_{02}**	**H_{01}**	**H_{02}**	**H_{01}**	**H_{02}**
					Group 1					
Belgium	1.61 (0.23)	0.02 (0.89)	1.13 (0.36)	2.25 (0.15)	0.47 (0.71)	2.91 (0.10)	0.86 (0.54)	3.48 (0.10)	1.9 (0.38)	2.49 (0.31)
Denmark	1.29 (0.27)	0.85 (0.37)	2.6 (0.12)	**5.3** **(0.02)**	1.93 (0.20)	**4.2** **(0.046)**	0.84 (0.56)	1.87 (0.25)	5.39 (0.16)	0.92 (0.59)
France	1.11 (0.31)	0.02 (0.88)	1.01 (0.39)	0.19 (0.83)	1.6 (0.27)	1.3 (0.34)	2.33 (0.19)	4.8 (0.06)	3.15 (0.26)	2.04 (0.36)
Germany	**5.57**	0.19	2.54	0.4	1.56	1.57	5.06	2.35	2.35	1.55

Countries	**Lag 1**		**Lag 2**		**Lag 3**		**Lag 4**		**Lag 5**	
	H_{01}	**H_{02}**	**H_{01}**	**H_{02}**	**H_{01}**	**H_{02}**	**H_{01}**	**H_{02}**	**H_{01}**	**H_{02}**
	(0.03)	(0.67)	(0.12)	(0.68)	(0.27)	(0.27)	(0.052)	(0.19)	(0.32)	(0.44)
Ireland	0.38 (0.55)	1.35 (0.27)	0.68 (0.52)	1.89 (0.20)	0.7 (0.58)	1.65 (0.25)	0.72 (0.61)	0.7 (0.62)	0.22 (0.92)	3.76 (0.22)
Italy	0.95 (0.35)	1.09 (0.31)	0.83 (0.46)	0.8 (0.47)	0.26 (0.85)	3.51 (0.07)	0.25 (0.90)	1.34 (0.37)	0.78 (0.64)	0.93 (0.59)
Luxembourg	0.47 (0.51)	0.08 (0.78)	0.61 (0.56)	0.06 (0.94)	0.59 (0.64)	**6.18** **(0.02)**	3.71 (0.09)	3.1 (0.12)	0.98 (0.57)	**35.52** **(0.03)**
Netherlands	0.17 (0.69)	2.21 (0.16)	0.54 (0.60)	1.98 (0.18)	0.31 (0.82)	2 (0.19)	0.09 (0.98)	1.63 (0.30)	0.81 (0.63)	**31.86** **(0.03)**
Sweden	1.74 (0.21)	0.62 (0.44)	1.06 (0.38)	0 (1)	0.9 (0.48)	1.05 (0.42)	0.5 (0.74)	1.76 (0.27)	3.28 (0.25)	4.29 (0.20)
Group 2										
Austria	1.12 (0.31)	1.11 (0.31)	1.41 (0.28)	1.17 (0.35)	1.54 (0.28)	1.42 (0.31)	3.35 (0.11)	1.95 (0.24)	3.67 (0.23)	0.85 (0.62)
Cyprus	0.95 (0.35)	0.21 (0.65)	0.4 (0.68)	0.22 (0.81)	0.34 (0.79)	0.16 (0.92)	0.16 (0.95)	0.27 (0.89)	0.74 (0.66)	0.31 (0.87)
Czech Republic	2.13 (0.17)	3.95 (0.07)	1.19 (0.34)	2.35 (0.14)	1.37 (0.32)	1.39 (0.32)	1.89 (0.25)	0.96 (0.50)	2.64 (0.30)	0.3 (0.88)
Finland	**5.52** **(0.03)**	**5.81** **(0.03)**	1.64 (0.24)	2.8 (0.10)	0.91 (0.48)	1.72 (0.24)	0.4 (0.80)	0.93 (0.52)	0.42 (0.81)	1.38 (0.47)
Hungary	0.09 (0.77)	0.33 (0.57)	0.28 (0.76)	0.93 (0.42)	0.72 (0.57)	**4.52** **(0.04)**	1.68 (0.29)	**10.2** **(0.01)**	4.9 (0.18)	3.87 (0.22)
Malta	0.12 (0.73)	0.85 (0.37)	1.84 (0.20)	0.21 (0.81)	0.86 (0.50)	1.04 (0.42)	0.69 (0.63)	0.53 (0.72)	1.07 (0.55)	2.63 (0.30)
Poland	1.68 (0.22)	1.02 (0.33)	1.04 (0.39)	1.32 (0.31)	3.78 (0.06)	1.27 (0.35)	1.97 (0.24)	1.38 (0.36)	0.65 (0.70)	6.53 (0.14)
Portugal	0.04 (0.85)	0.02 (0.89)	0.19 (0.83)	0.06 (0.94)	0.11 (0.95)	0.23 (0.87)	1.09 (0.45)	0.09 (0.98)	**34.81** **(0.03)**	0.08 (0.99)
Slovak Republic	**4.92** **(0.04)**	0.03 (0.86)	1.89 (0.2)	0.21 (0.82)	1.53 (0.28)	**6.25** **(0.02)**	1.28 (0.39)	5.35 (0.047)	1.02 (0.56)	3 (0.27)
Slovenia	0.02 (0.89)	0.03 (0.87)	0.63 (0.55)	0.08 (0.92)	0.66 (0.60)	1.87 (0.21)	2.81 (0.14)	2.45 (0.18)	2.64 (0.30)	8.77 (0.11)
Group 3										
Bulgaria	0.51 (0.49)	0.32 (0.58)	1.04 (0.39)	0.58 (0.57)	4.09 (0.05)	**4.85** **(0.03)**	2.09 (0.22)	5.04 (0.053)	7.17 (0.13)	4.78 (0.18)
Estonia	1.28 (0.28)	3.31 (0.09)	0.36 (0.70)	2.69 (0.11)	0.24 (0.86)	1.91 (0.21)	**6.94** **(0.03)**	1.73 (0.28)	2.22 (0.34)	2.09 (0.35)
Croatia	1.56 (0.23)	1.32 (0.27)	0.24 (0.79)	1.03 (0.39)	0.21 (0.88)	1.12 (0.40)	0.34 (0.84)	1.45 (0.34)	1.02 (0.56)	1.32 (0.48)
Latvia	0.1 (0.76)	**7.42** **(0.02)**	0.32 (0.73)	3.3 (0.08)	0.67 (0.59)	1.78 (0.23)	0.31 (0.86)	0.7 (0.63)	1.86 (0.39)	0.31 (0.88)
Lithuania	2.51 (0.14)	0 (1)	2.75 (0.11)	0.25 (0.78)	1.31 (0.34)	0.29 (0.83)	2.96 (0.13)	0.41 (0.79)	4.64 (0.19)	1.58 (0.43)
Romania	0.71 (0.41)	0.58 (0.46)	0.61 (0.56)	0.69 (0.52)	1.43 (0.30)	0.81 (0.52)	0.89 (0.53)	2.59 (0.16)	0.83 (0.63)	4.28 (0.20)

Notes: 1. First reported number is F statistic. 2. Second reported number is p. value. 3. All marked values are – statistical significant. 4. H_{01}: Countries total energy consumption does not Ganger cause gross domestic product (Growth hypothesis); H_{02}: Gross domestic product does not Ganger cause total energy consumption (Conservation hypothesis).

For each country in all three groups five VAR models, using the series in first difference, between energy consumption and GDP was constructed (all results are shown in Table 2). Each model used a different number of lag (from 1 to 5). The testing period was 1995–2013.

In only 44% of explored countries (i.e. in 11 from 25) Granger causality was confirmed.

The results in Table 2 show that in 1st group causality between total energy consumption and gross domestic product was found only for Germany (Lag 1, F = 5.57, p = 0.03). This result confirms Narayan and Smyth [18] conclusions, but it is opposite to Balcilar et al. [19] conclusions. These differences can be explained by different testing period and different method used by Balcilar et al.

In the 1st group Ganger causality between gross domestic product and total energy consumption was found for Denmark (Lag 2, F = 5.3, p = 0.02 and Lag 3, F = 4.5, p = 0.046), Luxembourg (Lag 3, F = 6.18, p = 0.02 and Lag 5, F = 35.52, p = 0.03) and Netherlands (Lag 5, F = 31.86, p = 0.03).

The results shows that in 2nd group causality between total energy consumption and gross domestic product (i.e. Growth hypothesis) was found for Finland (Lag 1, F = 5.52, p = 0.03), Portugal (Lag 5, F = 34.83, p = 0.03) and Slovak Republic (Lag 1, F = 4.92, p = 0.04). Findings about Portugal confirm Narayan and Prasad [20] conclusions and partly Shahbaz [21] conclusions. In 2nd group Ganger causality between gross domestic product and total energy consumption was found for Finland (Lag 1, F = 5.81, p = 0.03), Hungary (Lag 3, F = 4.51, p = 0.04 and Lag 5, F = 10.2, p = 0.01) and Slovak Republic (Lag 3, F = 6.25, p = 0.02). Findings about the Slovak Republic contradict Narayan and Prasad [20] conclusions. Finland was the only one country there both two causalities were founded.

In the 3rd group, Granger causality between total energy consumption and gross domestic product was found only for Estonia (Lag 4, F = 6.94, p = 0.03). Also in this group causality between gross domestic product and total energy consumption was found for Bulgaria (Lag 3, F = 4.85, p = 0.03) and Latvia (Lag 1, F = 7.42, p = 0.02).

As mentioned by Balcilar et al. [19] it could be, that splitting testing period to smaller sub-periods by significant structural changes, will have a significant impact on results.

4. CONCLUSIONS

The purpose of this paper was, after grouping EU 27 countries in groups, to investigate for causality between countries energy consumption and gross domestic product. Granger causality test was used for causality testing.

EU 27 countries was grouped into three groups – to the 1st group was assigned – Belgium, Denmark, France, Germany, Ireland, Italy, Luxembourg, Netherlands, Sweden; to the 2nd group was assigned – Austria, Cyprus, Czech Republic, Finland, Hungary, Malta, Poland, Portugal, Slovak Republic, Slovenia; to the 3rd group was assigned – Bulgaria, Estonia, Croatia, Latvia, Lithuania, Romania. Spain and Greece were excluded from the analysis.

Causality between total energy consumption and gross domestic product was found (i.e. Growth hypothesis was confirmed) for Germany (Lag 1, F = 5.57, p = 0.03), Finland (Lag 1, F = 5.52, p = 0.03), Portugal (Lag 5, F = 34.83, p = 0.03), Slovak Republic (Lag 1, F = 4.92, p = 0.04) and Estonia (Lag 4, F = 6.94, p = 0.03).

Causality between gross domestic product and total energy consumption was found (i.e. Conservation hypothesis was confirmed) for Denmark (Lag 2, F = 5.3, p = 0.02 and Lag 3, F = 4.5, p = 0.046), Luxembourg (Lag 3, F = 6.18, p = 0.02 and Lag 5, F = 35.52, p = 0.03), Netherlands (Lag 5, F = 31.86, p = 0.03), Finland (Lag 1, F = 5.81, p = 0.03), Hungary (Lag 3, F = 4.51, p = 0.04 and Lag 5, F = 10.2, p = 0.01), Slovak Republic (Lag 3, F = 6.25, p = 0.02), Bulgaria (Lag 3, F = 4.85, p = 0.03) and Latvia (Lag 1, F = 7.42, p = 0.02).

Finland was the only one country where both two causalities were founded.

These results don’t allow any conclusions about similarities in groups to be done.

The outcome of this paper can be upgraded by testing for nonlinear causality. The current paper was concentrated only to the macro level. By splitting energy consumption into the sectors and gross domestic product into components, may have a significant impact on results. It is also possible that if the testing period will be divided to smaller sub-periods, later on causality could be observed. Sub-periods should be associated with significant political or economical changes. Future research should pay attention to these points.

REFERENCES

[1] E. Marlier and D. Natali, *Europe 2020: towards a more social EU?*, no. 69. Peter Lang, 2010.

[2] Eurostat, “Energy intensity of the economy,” 2017. [Online]. Available: http://ec.europa.eu/eurostat/en/web/products-datasets/-/TSDEC360. [Accessed: 01-Mar-2017].

[3] N. Cantore, M. Calì, and D. W. te Velde, “Does energy efficiency improve technological change and economic growth in developing countries?,” *Energy Policy*, vol. 92, no. November, pp. 279–285, May 2016.

[4] J. E. Payne, “A survey of the electricity consumption-growth literature,” *Applied Energy*, vol. 87, no. 3. pp. 723–731, 2010.

[5] I. Ozturk, “A literature survey on energy-growth nexus,” *Energy Policy*, vol. 38, no. 1, pp. 340–349, 2010.

[6] J. Asafu-Adjaye, “The relationship between energy consumption, energy prices and economic growth: time series evidence from Asian developing countries,” *Energy Econ.*, pp. 615–625, 2000.

[7] J. E. Payne, *Survey of the international evidence on the causal relationship between energy consumption and growth*, vol. 37, no. 1. 2010.

[8] V. Lekavičius, “Modelling the Impact of Changes in Energy Supply on the National Economy,” 2013.

[9] U. Al-mulali, “GDP growth – energy consumption relationship: revisited,” *Int. J. Energy Sect. Manag.*, vol. 8, no. 3, pp. 356–379, Aug. 2014.

[10] S. Z. Chiou-wei, C. Chen, and Z. Zhu, “Economic growth and energy consumption revisited: Evidence from linear and nonlinear Granger causality,” *Energy Econ.*, vol. 30, no. 8, pp. 3063–3076, 2012.

[11] J. dos S. Gaspar, A. C. Marques, and J. A. Fuinhas, “The traditional energy-growth nexus: A comparison between sustainable development and economic growth approaches,” *Ecol. Indic.*, vol. 75, pp. 286–296, Apr. 2017.

[12] E. Bivainis and T. Teodoras, “Darnus regionų vystymasis: Teorinis diskursas,” *Ekon. ir Vadyb. Aktual. ir Perspekt.*, vol. I, no. 8, pp. 30–36, 2007.

[13] E. Triantaphyllou, “Multi-criteria decision making methods: a comparative study,” *Interfaces (Providence).*, vol. 44, pp. 81–84, 2000.

[14] C. W. J. Granger, “Investigating Causal Relations by Econometric Models and Cross-spectral Methods,” *Econometrica*, vol. 37, no. 3, pp. 424–438, 1969.

[15] M. Eichler, “Causal inference in time series analysis,” *Causality Stat. Perspect. Appl.*, pp. 327–354, 2012.

[16] C. A. Sims, “Macroeconomic and Reality,” *Econometrica*, vol. 48, no. 1, pp. 1–48, 1980.

[17] D. Dickey and W. A. Fuller, “Distribution of the estimates for autoregressive time series with a unit root,” *J. th Am. Stat. Assoc.*, vol. 74, no. 366, pp. 427–431, 1979.

[18] P. K. Narayan and R. Smyth, “Energy consumption and real GDP in G7 countries: New evidence from panel cointegration with structural breaks,” *Energy Econ.*, vol. 30, no. 5, pp. 2331–2341, 2008.

[19] M. Balcilar, Z. A. Ozdemir, and Y. Arslanturk, “Economic growth and energy consumption

causal nexus viewed through a bootstrap rolling window," *Energy Econ.*, vol. 32, no. 6, pp. 1398–1410, 2010.

[20] P. K. Narayan and A. Prasad, "Electricity consumption-real GDP causality nexus: Evidence from a bootstrapped causality test for 30 OECD countries," *Energy Policy*, vol. 36, no. 2, pp. 910–918, 2008.

[21] M. Shahbaz, C. F. Tang, and M. Shahbaz Shabbir, "Electricity consumption and economic growth nexus in Portugal using cointegration and causality approaches," *Energy Policy*, vol. 39, no. 6, pp. 3529–3536, 2011.

CYSENI 2017, May 25-26, Kaunas, Lithuania
ISSN 1822-7554, www.cyseni.com

REVIEW OF THERMAL ENERGY STORAGE TECHNOLOGIES INTEGRATION IN SMART GRID

B. Pichon, P. Clain
Léonard de Vinci Pôle Universitaire, Research Center
92916 Paris La Défense, France
E-mail: bastien.pichon@devinci.fr

H.M. Hoang, T. Dufour, A. Delahaye, L. Fournaison
Irstea GPAN
1 rue Pierre Gilles de Gennes, CS 10030, Antony 92761 Cedex France

ABSTRACT

Because of global warming, governments want to use more and more renewable energy, which are unstable sources of energy. With the strong industrial development, energy consumption, electrical in particular, is growing rapidly. As a consequence, energy policies tend to reduce consumption. In order to achieve an optimum result, the electrical network as well as every distribution network systems will have to undergo major transformations in order to adapt to new requirements. In spite of the lack of investment and deployment , Thermal Energy Storage (TES) is a good way to integrate renewable energies into the distribution network. It can act directly on the heat networks and will have impact on the production systems and therefore on the energy consumption. Indeed, TES systems are relevant tools to participate in demand management. They widely guarantee an improvement of the energy efficiency and the control of the energy since TESs are used to manage the relationship between the demand of each consumer and energy availability. The Demand Side Management (DSM) is a principle of Smart Grid which aims to improve the capacity of the distribution system to adapt to consumer needs by optimizing demand and consumption.
A study was carried out to show the different TES systems, in order to compare their advantages and disadvantages and the parameters of each of them, in order to finally determine the production technologies, storage system and consumption strategies to be considered and integrated in the Smart Grid for the most optimal result.

Keywords: Thermal energy storage, DSM, Smart Grid

1. INTRODUCTION

The concept of controlling energy demand is designed for the first time in the wake of the oil shocks of 1973 and 1979. Indeed, the affected countries launched energy management programs in such a way to consume the available resources in the most effective way. The term Demand Side Management (DSM) was first used by the Electric Power Research Institute in 1980 to encompass the actions of managing the load (load management) of the power grid, energy efficiency and energy saving.

Today the energy system is not optimized to ensure a necessary distribution of the network. Indeed, the use of the production capacity does not exceed 55% and the transmission network is below 50%. In addition, energy production mainly depends on two types of power stations: the power stations generating the base load and the latter trigger at peak loads.The power plants for base load provide the minimum energy at a load factor of about 85% while those for peak loads work only few hours a year.

These commissioning operations are expensive and emit a lot of CO_2. The network also faces the emergence of non-dispatchable renewable energies which can not be put into service according to the needs of the network: productions must be consumed as soon as they are produced.

The common factor in all problematic issues is the balance that must be struck between supply and demand. This balance is difficult to obtain because the demand is volatile and can not currently be managed in real time by the network managers. Insofar as basic power stations are very inefficient, the peak power stations are triggered by large variations in consumption.

As described in [1] by conducting DSM actions, it is possible to move or clear consumptions, which has the consequences of linearizing the consumption and thus the energy production. The DSM has several advantages for both the electricity grid operators and the end-user.

In the same line, it is also an opportunity to alleviate the increase in consumption of full hours due to air conditioning in urban areas. In addition to this, space problems related to the installation of more powerful transformers will be solved by the use of cold storage systems.

The fault management will also be more successful, therefore the power grid will be more robust for consumers with critical load. At the customer level, profits are mainly financial. DSM can allow the end user to reduce the cost of energy bills while maintaining the same level of comfort.

Storage is an essential element in controlling energy demand. Some hours of consumptions that take place at full hours are simply shifted without harming the comfort of the end user. This is the case, for example, with heating and air conditioning usingstorage solutions. These storage solutions are part of distributed energy resources which are elements that fit into the Smart Grid and enable the demand for energy to be reached.

Future intelligent networks will integrate a notion of storage to smooth the load curve. In this case, storage is also used for the energy produced by non-dispatchable technologies. The portion of electricity consumption for heating and air conditioning is 35% in the tertiary sector in Ile de France region. Domestic hot water and heating have a share of more than 70% in private homes. It is therefore essential to plan consumption items, especially since they are the ones that have the biggest impact on consumer demand profile. In order to answer this problem this work is interested in the use of thermal energy storage (TES) methods: heat and cold and the study of the corresponding systems and their most optimal strategies as well as their integration in Smart Grid (SG) modeling models.The goal of the Smart Grid is to improve the distribution system's ability to adapt to consumer needs and optimize demand and consumption.The distribution systems are not adapted to the stated specifications. It is necessary to use and study the production and distribution methods, and improve the consumption algorithms for the royalty flow, which produces the amount of energy in a given time [2].

The aim of this study is to propose several strategies for controlling production and energy consumption in an intelligent network in order to optimize the configuration and operation of the production and thermal storage devices for the lowest power installed possible. The idea is to move the operation of refrigeration and heat units in order to improve the performance of production systems and take into account the internal and external parameters that come into play.

2. INTEGRATION TES WITHIN A SG

In order to meet objectives of the model Smart Grid, scientific community has worked to integrate thermal energy storage on it. The term Smart Grid is to be taken in the broadest sense as "Smart energy system" [3]. Indeed, most of the models emphasize on the combination of several sources of energy in order to smooth energy loads and optimize consumption.

A projection between 2004 and 2025 has been studied [4] in order to analyze the impact of the combination of several distribution networks in order to optimize the consumption of each energy resource (Fig. 1). This estimation is based on the integration of renewable energies and previous works [5] [6] [7] on the relocation of heat pumps and the impact of DSM strategies.

The study assesses the positive effect of DSM strategies related to the introduction of heat pumps systems powered by the excess derived from renewables energies. The use of heat pumps provides an interesting reduction in the electricity excess, helping to avoid grid stability problems when a large share of renewable sources is introduced.

Futhermore, the study of the DSM strategy confirms its feasibility in keeping the users comfort while a proper TES is included in the heating system (red lines).

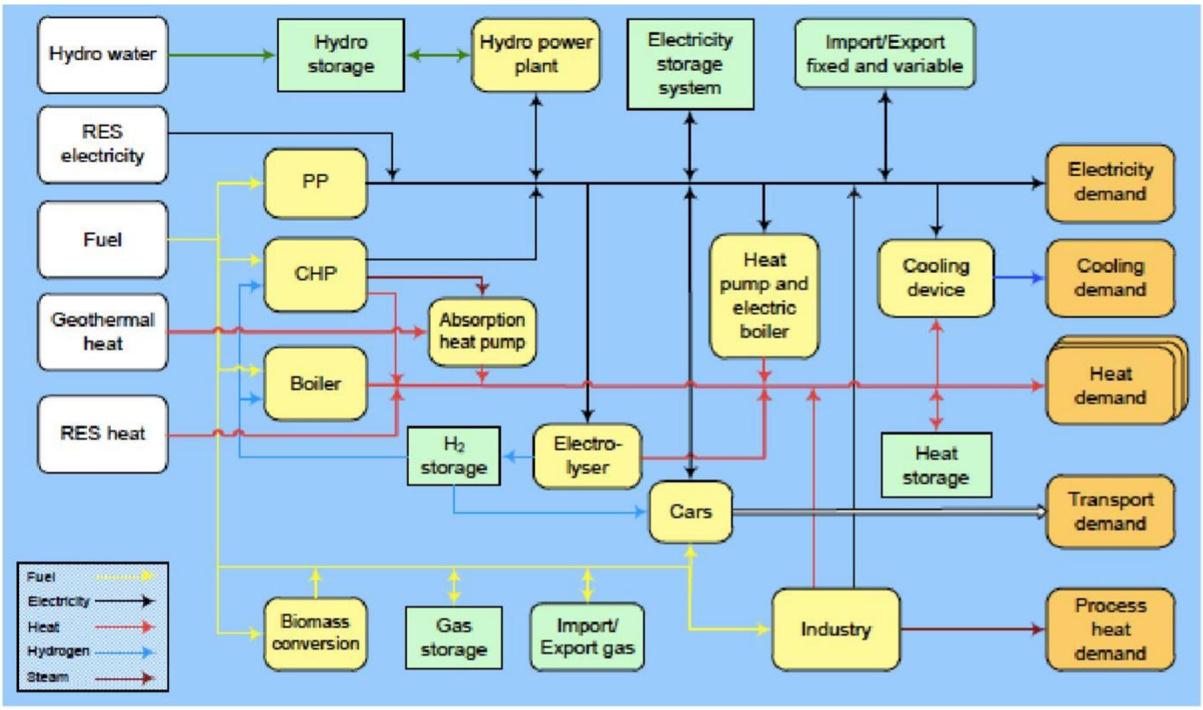

Fig. 1. Energy Plan model

This type of system offers flexibility and interaction between different energy sources and between different production systems.

Moreover, to improve the flexibility and energy efficiency, the insertion of thermal storage is studied for cogeneration, since heat demand can be decoupled from production because one has this flexibility to produce electricity by simultaneously storing thermal energy.

Combined Heat and Power (CHP) is a particularly attractive production system for a distribution network adapted to the Smart Grid because there is a possibility of interaction between gas distribution systems and electricity distribution systems. It simultaneously produces thermal and electrical energy, which is why it features a gas boiler and a heat pump. With such a system there is an optimization of the consumption of different sources of energy.

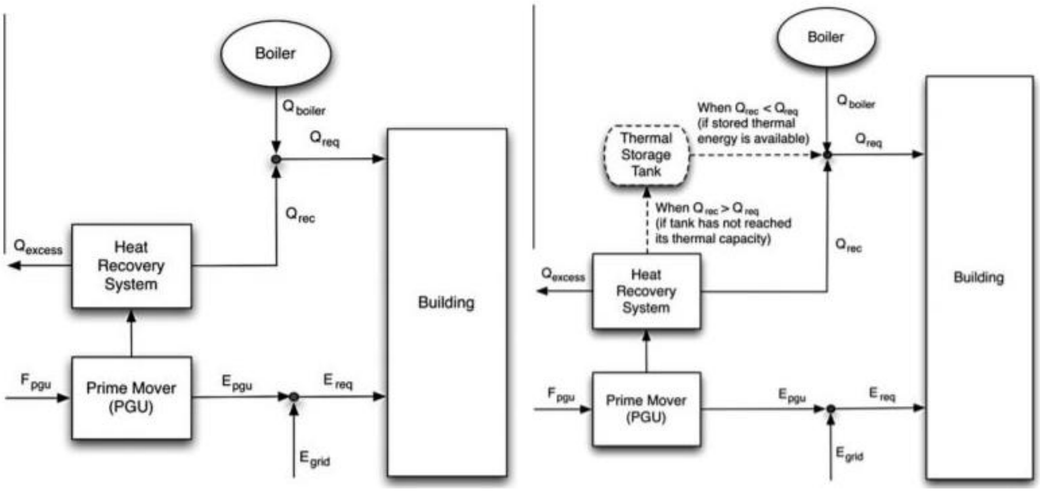

Fig. 2. CHP without and with TES [8]

Since the TES thermal energy storage is an additional cost to a cogeneration device, its addition to cogeneration must provide an economical advantage as well as a energey efficiency. This is why such a device must considerably reduce or eliminate completely the need for additional heating with another thermal production.

Smith *et al.* [8] carried out a study on insertion of CHP and TES on different buildings (Fig. 2). Their calculation is based on an ideal device, their results are therefore not general and varies according to several parameters (type of boilers, type of storage, external climate). Their results showed that the storage of heat energy does not provide an advantage in addition to cogeneration. Since the buildings concerning this study are hospitals, hotels that requires much more electrical energy than thermal energy.

To evaluate the energy efficiency of such technologies there are other parameters considered. A building located in a colder climate will have better result regarding this efficiency since the demand will be greater. However, the demand also varies over time during the year and the seasons, the climate is not the same from day to day. Besides, the change in temperature is even more important between day and night.

J.Vandewalle *et.al.* [3] was directly concerned with the impact of storage by first comparing a gas demand reference with a simulated gas demand. Then other points such as the size of the tank and way to store, when and how to store thermal energy were also discussed. Their results showed that TES increases the electrical revenues of cogeneration: 25% decrease in cost compared to the case without thermal energy storage and 50% decrease compared to the case without storage and cogeneration.

3. APPLICATION OF TES IN SG

3.1. Indirect electrical storage

The TES applications will be studied in this section, their operation is influenced by the demand of the user. Buildings in Europe account for 40% of the consumption of heating and hot water. It is necessary that these needs are adapted and controlled to meet demand and optimize power consumption.

By carrying out actions of DSM, it is possible to move or delete consumptions, which has the consequences of linearizing the consumption, and therefore the production of energy. The DSM has several advantages for both the electricity grid operators and the end-user. Controlling energy demand is an opportunity for system operators to reduce marginal costs of production. Indeed, as when a part of the consumption at peaks is offset, the most expensive and most polluting power plants have no longer to be put into service. However, it depends very much on the behavior of the end user.

Demand-side management is a method of matching energy production and demand. DSM programs can be directed to peak clipping, valley filling, load shifting and strategic conservation. Among the means of DSM, the TES can be used for this load distribution. By projecting in 2025, C.Brandoni *et.al.* [4] showed with a numerical model that the use of heat pump linked to thermal storage allows reducing the electricity consumption with more than satisfactory results (30% with new technologies and regulationns, and up to 50% with TES) taking into account well all the regulations that will evolve until 2025.

DSM strategies aim to flatten the consumption curve. However, attention must be given to the risk of shifting consumption peaks, i.e. to apply the same strategies for different production systems and TES. For example, moving all refrigeration productions at night because the temperature is lower, so the efficiency of these production systems is better but such a strategy could cause a peak of consumption at night.

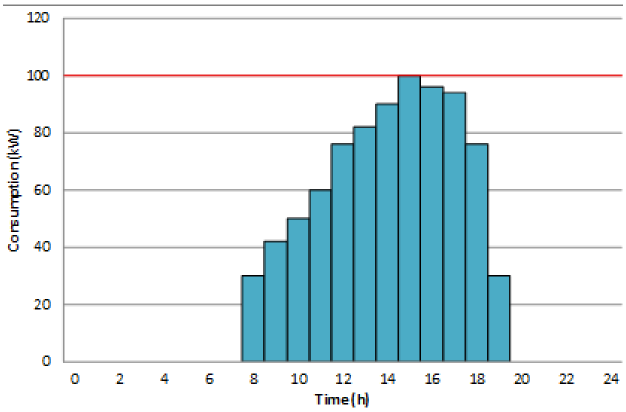

Fig. 3. Consumption histogram (Dumas, 2002)

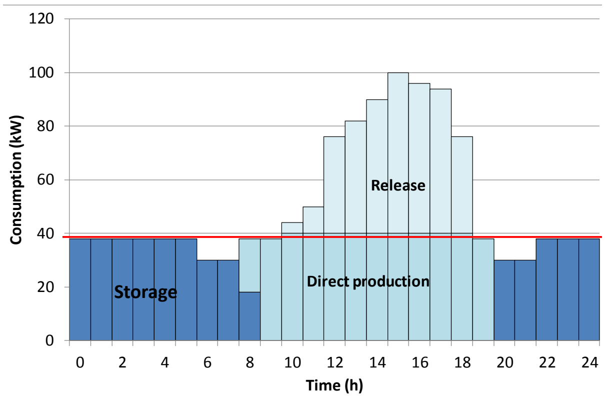

Fig. 4. Consumption histogram with storage (Dumas, 2002)

Four criteria are important for DSM [9]:

- Energy-efficient end-use device.
- Supporting equipment and systems to allow the shaping of the load distribution.
- Control system to start or stop (manage strategies) end-use devices as required.
- Communication system between end users and external parties.

The TES technologies, their characteristics, strategies and existing tests to meet DSM expectations must be determined.

3.2. Choice of a Thermal Energy Storage Technology

For thermal energy storage to be as optimal as possible there are several important parameters to consider in order to evaluate the efficiency of such a system.

The *storage capacity* must be taken into account: the amount of energy available in a storage system after being loaded is important to define the energy that can be used.

This is why the maximum amount of energy accumulated per unit mass or volume (*energy density*) plays a role on the storage system: important criterion due to space constraints in buildings.

Loading performance such as charging and discharging time is also not negligible, efficient and fast charging and discharging times will be more interesting for a consumer.

The *reliability* of a storage system affects the relationship between its installation and its performance over time, since its durability determines the energy savings or even the financial savings that can impact this system. The number of times in which the storage unit can release the energy level for which it was designed after each recharge determines its durability and thus the reliability of this storage.

The *available power*, i.e. the maximum power of charge or discharge, is an important criterion that will influence the storage efficiency which is the ratio between the released energy and the stored energy.

In the same line, the power available during the discharge is one aspect to be taken into account. While the amount of stored thermal energy is determined by the storage size, the heating or cooling power depends mainly on the storage device configuration. Among the thermal energy stores, laminated water tanks represent the most fully developed, commercially available technology with good efficiency at low cost in the temperature range for buildings.

For a laminated water tank, the power is strictly related to the flow of the tank, which can not be too high so as not to reduce stratification and reduce storage efficiency. For a latent TES, the power is related to the system configuration and to the thermal conductivity of the material, generally not too high.

However, Phase Change Materials (PCM) are a good option [10] [11]. A PCM is a material with a high heat density during melting or solidying in a range of temperature, thus it is able to store or release large amounts of energy. Future developments in TES are limited and one of the most interesting opportunities is related to the development of phase change materials and their integration into the system [12]. The presently studied PCMs have phase change temperatures between 22–25 °C. However, there is a lack of PCM in the temperature range below 15–20 °C [13]. Thermochemical storage systems are being developed and only prototype systems are available.

Hewitt.carried out a study on response times on PCM [14]. The loading and unloading times are influenced by the integration of the storage with the Demand-Response.

Finally, if the investment on the installation does not have an economical and efficient return such a device is unnecessary for the consumer. *Capital and operational costs* must therefore be taken into account for the entire life of the system. Some comparisons according to some of these criteria are performed [15].

3.3. Strategy for DSM

Such a distribution system is strongly influenced by its behavior, and therefore by the application of strategies. But we must not neglect the influence this may have on thermal comfort. The TES allow these consumption strategies to be applied and to maintain user comfort even when the electrical consumption is stopped by using thermal storage (Fig. 5). In order to allow such a management of the strategies and regulation of the loads it is necessary to understand its functioning [16] and to use intelligent controllers for the buildings of each micro-grid.

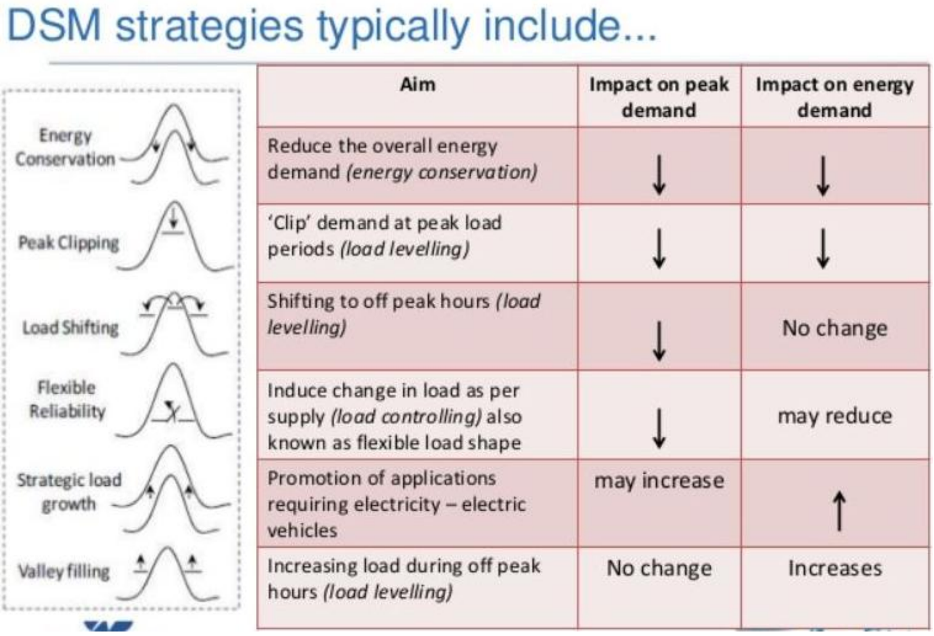

DSM strategies typically include...

Aim	Impact on peak demand	Impact on energy demand
Reduce the overall energy demand *(energy conservation)*	↓	↓
'Clip' demand at peak load periods *(load levelling)*	↓	↓
Shifting to off peak hours *(load levelling)*	↓	No change
Induce change in load as per supply *(load controlling)* also known as flexible load shape	↓	may reduce
Promotion of applications requiring electricity – electric vehicles	may increase	↑
Increasing load during off peak hours *(load levelling)*	No change	Increases

Fig. 5. DSM Strategies [1]

The consumption of the TES can be optimized if it is able to function in an intelligent way, such as automata. They must be able to evaluate their consumption in real time according to various predefined parameters such as temperature, the price of production of the energy market to avoid peaks of consumption. In order to be able to respond to such an operation, it is necessary to apply the most appropriate consumption strategies according to the situation, the parameters and the type of appliances. Guérard *et al.* present the different strategies possible according to any type of device concerning consumption, storage or both [1].

---

[1] https://www.slideshare.net/TataPowerDDL/demand-side-management-61048795

4. CONCLUSION

This paper shows the impact and importance of the integration of TES for a more optimal heat network. It presents some configurations based on this kind of system and its advantage to use it in an intelligent network. The thermal energy storage is necessary in order to optimize future distribution networks. But in order to develop this approach, we must define the objectives of this system and its advantages:

First point to highlight is the energy management. Indeed, the thermal energy storage makes it possible to have a better control of the system production operations. This optimization is the reflection of the consumption cut-off explained in the paper. In this case, there is an improvement in the flexibility of the distribution. This can involve a reduction in the installed capacity of 30 to 70%. Second point thermal storage improves the efficiency of the production system. This management involves moving the refrigeration units (at night) or hot groups (in the middle of the day) at their most favorable time to produce thermal energy. This process improves the performance of the condenser or compressor due to climate conditions. There is therefore an improvement in energy efficiency.

In future works, a wider study of the problem will be performed by applying the TES in a model that is constrained to the objectives of the Smart Grid.

5. REFERENCES

[1] Guerard.Guillaume, Pichon.Bastien ir Nehaï.Zeinab, Demaned-Response: let the devives take our decisions, SmartGreens, 2017.

[2] M.S.Srinivas, Distribution Load flows: A brief review, IEEE, 2000.

[3] J.Vandewalle, N.Keyearts ir W. D'haeseleer, The role of thermal storage and natural gas in a smart Energy system for different commercial bulding types., 2012.

[4] C.Brandoni, G.Ciriachi, F.Polonara ir A.Arteconi, Heat Pumps and Demand Side Management for Renewable Energy Integration in Sustainable Communities, International Conference and Utility Exhibition 2014 on Green Energy for Sustainable Development, 2014.

[5] A.Arteconi, C.Brandoni, CM.Bartolini ir F.Polonora, “Assessment of the impact of local energy policies in reducing greenhouse gas emissions, Aravossis K, Brebbia CA, editors. Environmental economics & investment assessmen, 2010.

[6] C. Brandoni ir F. Polonara, The role of municipal energy planning in the regional energy-planning process, Energy, vol. 48, pp. 323-338, 2012.

[7] G. Comodi, L. Cioccolanti, F. Polonara ir C. Brandoni, “Local authorities in the context of energy and climate policy, Energy policy, vol. 51, pp. 737-748, 2012.

[8] Smith, D.Amanda, J. Mago, Fumo ir Nelson, Benefits of thermal energy storage option combined with CHP system, 2013.

[9] A.Arteconi, F.Polonara ir H. N.J., Domestic demand-side-management (DSM): Role of heat pumps and thermal energy storage (TES) systems., Applied Thermal Engineering, 2013.

[10] C. Veerakumar ir A. Sreekumar, Phase change material based cold thermal energy storage: Materials, techniques and applications – A review, ELSEVIER, 2016.

[11] W. A. Qureshi, N.-K. C. Nair ir M. M. Farid, Demand Side Management through efficient thermal energy storage using phase change material, IEEE, 2008.

[12] J.Baker, New technology and possible advance in energy storage, Energy Policy, 2008.

[13] V. Tyagi ir D.Buddhi, PCM thermal Storage in buldings: a state of art, Renew Sustain Energy, 2007.

[14] NJ.Hewitt, Heat pump and energy storage- the challenge of implemantation,, APPLIED ENERGY, 2012.

[15] A.Arteconi, N.J.Hewitt ir F.Polonara, State of the art of thermal storage for demand-side management, Applied Energy, 2012.

[16] LEE.Hollad, Karayaka, H.Bora, Tanaka, L.Martin, Bal ir Aaron, An Empirical Method for Estimating thermal system parameters based on operating data in smat grids, IEEE, 2014.

CYSENI 2017, May 25-26, Kaunas, Lithuania
ISSN 1822-7554, www.cyseni.com

MONTE CARLO SIMULATION OF DISTRICT HEATING SYSTEM SHORT-TERM OPERATION

I. Dimoulkas, M. Amelin
KTH Royal Institute of Technology
Brinellvägen 8, 114 28 Stockholm – Sweden
E-mail: iliasd@kth.se

ABSTRACT

Modern district heating (DH) systems consist of various types of energy generation units like combined heat and power (CHP) plants, heat only boilers, electric heaters, heat pumps and heat storage facilities. Short-term operation of such systems refers to the unit commitment and energy dispatch during the following period. The operation scheduling is done in a way to minimize the operation costs and maximize the profits. However, the coupling of heat and power generation in the CHP units, the use of electric power to produce heat in the electric boilers and the heat pumps and the possibility to store heat for later use in the heat storage tanks, makes the short-term operation scheduling of such systems a quite challenging task. Furthermore, power which is produced by CHP units can be sold in electricity markets. This makes the operation scheduling problem even more complex as the uncertainty of the electricity prices in the markets should be considered when making decisions about how much power will be produced. To make optimal decisions under uncertainty, various mathematical optimization methods have been developed like Monte Carlo simulation, stochastic programming and robust optimization. In this paper, a deterministic short-term operation model of a DH system is proposed which provides the optimal unit commitment, power/heat dispatch and power trading in the electricity markets for each hour of the following day. Three types of electricity markets are considered: the day-ahead (spot) market, the intraday market and the balancing (real-time) market. The model is used to run a Monte Carlo simulation on a case study system. In every iteration of the simulation, a set of electricity prices and volumes in the electricity markets is initially created using autoregressive models (AR, SARIMA, ARMAX). Then the model is solved to get the optimal operation scheduling and the profits of the DH system. Two different system configurations are also considered. In the first, there is no heat storage while in the second there is a heat storage capacity of 500 MWh_{th}. Results show that the mean optimal value of the Monte Carlo simulation converges to a solution after approximately 300 runs. Each run needs approx. 1.5 seconds for solving the model. This means that the method is quite fast as it takes about 7.5 minutes for the solution. Furthermore, regarding the two different system configurations, results show an increase of approx. 11% in daily mean profit when heat storage is used.

Keywords: district heating, combined heat and power, short-term operation, Monte Carlo simulation, electricity markets, heat storage

CYSENI 2017, May 25-26, Kaunas, Lithuania
ISSN 1822-7554, www.cyseni.com

INTEGRATION OF THE BLOCKCHAIN IN A SMART GRID MODEL

Z. Nehaï, G. Guerard
Léonard de Vinci Pôle Universitaire, Research Center
92916 Paris La Défense, France
E-mail: Zeinab.nehai@devinci.fr

ABSTRACT

Nowadays, one of the principal concerns of the scientific community is the energy transition and energy efficiency. Indeed, the expansion of objects consuming and IoT leds to a significant increase in energy demand. To find a solution to this phenomenon is essential. Currently, one of the solutions that can be applied is the Smart Grid. It would optimize the energy consumption by setting consumption patterns, adapted to a specific situation, taking into account different parameters like the pricer, the user preferences, or the parameters of the appliances of the house. Promoting renewable energies such as solar or wind power, are also part of the issues of the Smart Grid. The goal is to promote local energy production, and then avoid the energy transport loses over long distances. However, the produced energy by renewable energies is erratic, thus a numerical management is needed. A blockchain is a distributed, decentralized transaction ledger, which is owned, maintained and updated by each user. It carries peer-to-peer energy exchanges among citizens of a same microgrid, without a central control body, based on smart contracts. The smart contracts will have the role to automatically satisfy some conditions or rules of consumption, among citizens. These contracts might contain the user preferences or the consumption patterns of appliances. A city contains several microgrids, each with their own blockchain, the inhabitants would have solar panels or other energy sources, and then would feed those which claim energies by making a transaction following the smart contracts. This paper focuses on these peer-to-peer transactions in a microgrid validated by a blockchain.

Keywords: Peer to Peer, Blockchain, Smart Contract, Game Theory

1. INTRODUCTION

In its balance sheet for the year 2015, RTE (Réseau de Transport d'Electricité /Electricity transmission network) reports an electricity consumption of 475.4 TWh in France[1]. This growth in consumption concerns not only France but the whole world. The world's electricity consumption in 2013 is 21 538 TWh[2]. This phenomenon tends to increase, due to many electrical appliances and the IoT. Today, connected objects are integral parts of our everyday life, from the simple watch to the whole house.

Worldwide, 48% of the electrical energy comes from fossil energy, which leads to a major problem due to the scarcity of these energies (e.g. oil, coal, natural gas)[3]. In addition to the scarcity, this kind of energy pollutes considerably the environment, both atmosphere and waters, due to greenhouse gas emissions. It is in the interest of all to come up with solutions. The energy consumption increases from year to year. Getting to better management of our energy consumption seems paramount. A possible solution could be the exploitation of renewable energies as primary energy. This would amount to integrate a numerical regulation of the energy production. The solution of renewable energies is a good initiative, but it does not remain without flaws. The disadvantages of renewable energies are their intermittent production, it depends on the weather (sun, wind, tide).

A numerical aspect able to manage these disadvantages could optimize the integration of clean energies within the current production system. It is in this perspective that the Smart Grid was born [1], by setting up a network connected to homes, consumer's appliances and renewable energy

---

[1] http://rte-france.com
[2] https://www.edf.fr
[3] https://worldenergy.org

power plant, in order to smooth consumption curve. Another digital aspect could achieve an optimization of the consumption, it is the Blockchain technology.

To arrive at a conclusion on the feasibility of integrating Blockchain into a Smart Grid model, it is necessary to know the issues and parameters to be considered. For this purpose, an in-depth study of this technology is expected, to have an overview of what is happening in terms of Blockchain, the different types existing, or the technological advances of the field through the scientific community.

The Blockchain is a kind of transaction history, like a huge ledger that appeared with the Bitcoin [2]. This technology allows for peer-to-peer monetary transactions without a central control body. The Blockchain is based on the decentralization of the data in order to remove the central part representing the confidence part of the current system. The Bitcoin has given birth to other types of Blockchain, like the Ethereum [3]. It has a peculiarity that is the implementation of smart contracts, contracts allowing to establish various rules, between the protagonists. More recently, an Energy Blockchain was created[4] to promote local energy production. Peer-to-peer energy transactions could reduce the high electrical demand for the existing grid, and Blockchain could secure and memorize transactions.

2. THE BLOCKCHAIN TECHNOLOGY

2.1. Environmental situation

The current state of the environment requires the implementation of local energy production, based on renewable energy, in order to manage the rise in electricity consumption leading to an increase in energy production (Fig. 1), it induced to CO2 emissions which is proportional to the population growth. It has a direct impact on the power lines because, due to the excessive demand, the lines no longer support the excessive electrical flow, i.e a peak consumption at full hours, and a drop in off-peak times. In order to lighten the lines, it is necessary to smooth consumption curve, and for this it would be interesting to use its own electrical production.

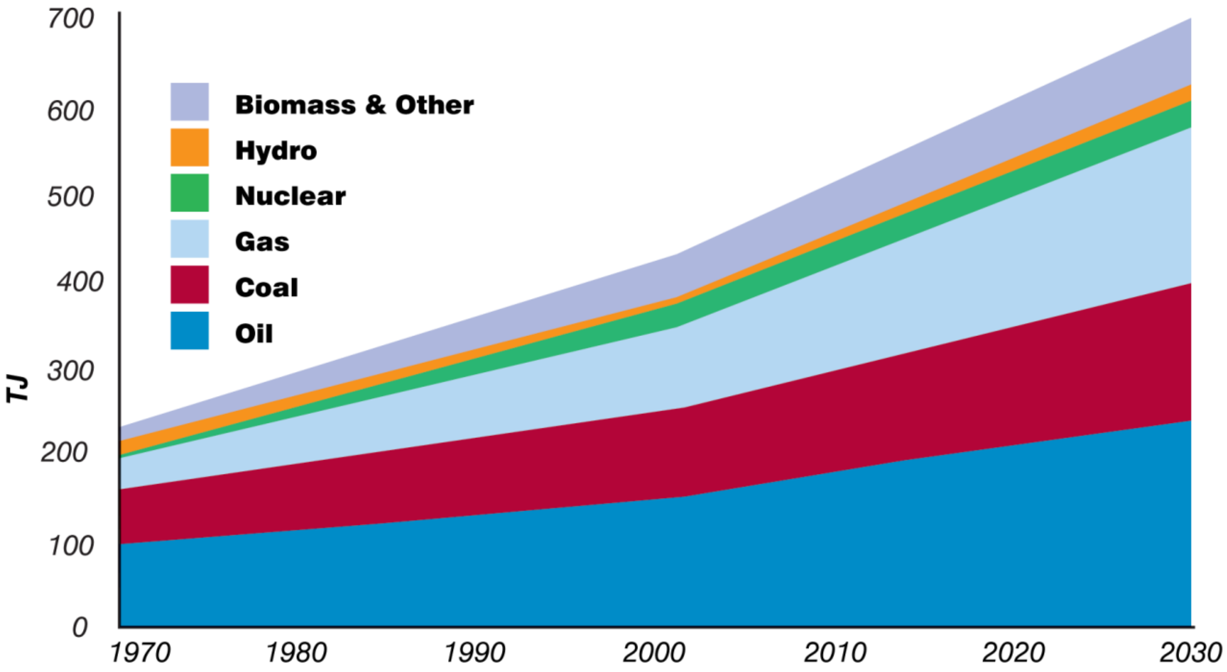

Fig. 1. Primary energy consumption, past and future
(*Source:* OECD/IEA *World Energy Outlook* 2004)

---

[4] https://solarcoin.org/fr/

Promoting local energy production means the integration of renewable energies within the existing network. However, this integration requires good management because these energies, such as wind or solar, generate electricity intermittently, which is why digital management seems essential in order to achieve a stable electrical system.

This digital management could be the Smart Grid but not only. A peer-to-peer energy transaction between neighborhood would be a good solution. That’s why we thought to integrate a Blockchain in the large scale Smart Grid project [1].

2.2. Definition and examples

2.2.1. Bitcoin

This famous technlogy was born with the Bitcoin [2], we count several types of Blockchain with each a specific application. Globaly, a Blockchain allows to decentralize data and to perform peer-to-peer transactions [4], [5]. For the Bitcoin the transactions are only monetary. The Fig. 2 illustrates a bitcoin transaction between two people.

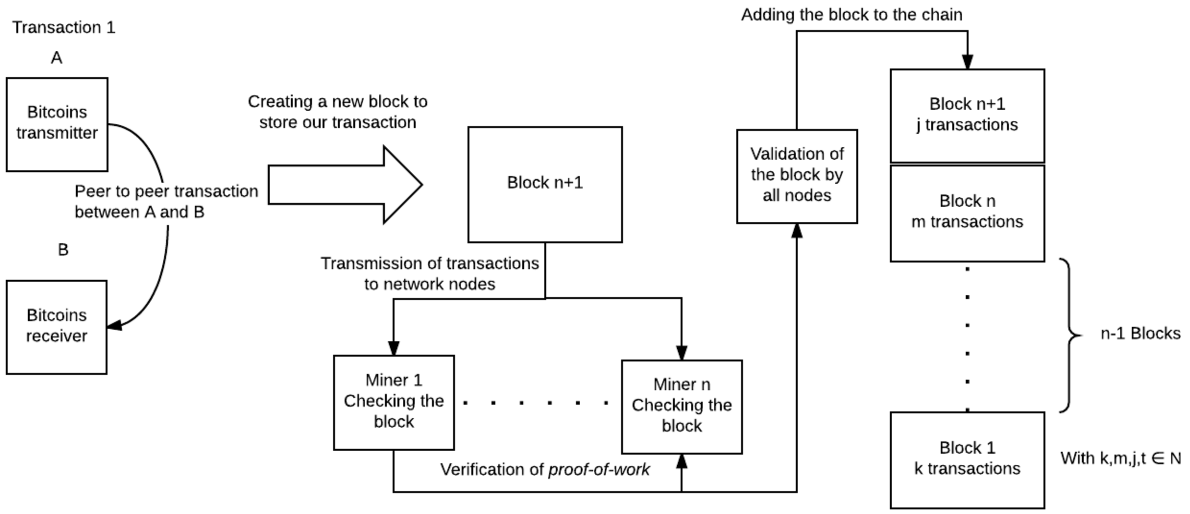

Fig. 2. A bitcoin transaction

The transaction can be divided into three parts:

1. The willingness to make a transaction (specifying the amount and the receiver), this creates a new block.
2. All miners of the network check the blocks, based on the *proof-of-work* protocol (PoW) (calculation algorithm for checking whether a work has been performed) [2], [5], [6].
3. The validation of the block, and the addition of the latter to the oldest chain.

2.2.2. Ethereum

The Ethereum Blockchain was created by Vitalik Buterin [3]. He judged that the Bitcoin is not performing enough and possessing too many flaws. He devised a Blockchain capable of overcoming these failures.

The principle remains the same as for the Bitcoin, it is a matter of a transaction in peer-to-peer, this time based on smart contracts. The transaction exchanges ethers [7].

The difference with the bitcoin, in addition to smart contracts, is that the validation is based on a *proof-of-stake* (PoS) [3], [8], [9]. It is no longer a proof of work but a proof of possession, it consumes less energy than the bitcoin.

A smart contracts is nothing more than a code [10], stored in the blockchain, it could be not modify, so if you want to change some parameters of the contract, you should remove it and create another one.

2.2.3. SolarCoin[5]

This new application of Blockchain seems promising because it allows to achieve an optimization of the electrical consumption. Nowadays, there is not much information about the solarcoin, nevertheless in Brooklyn in the USA an energy exchange system was established based on the Blockchain Ethereum[6]. This system is limited to a microgrid, it allows to exchange energy produced from solar panels of the inhabitants of this same microgrid. Each MWh produced makes the producer benefit from a SolarCoin.

2.3. Pros and Cons of blockchain's technology

Not all blockchains have the same specificities and areas of application. Despite its growing popularity, it is nevertheless a subject of controversy and debate. Any new technology has its advantages and disadvantages, we could maybe minimize the disadvantages and bring out the good aspects. The three Blockchains that interested us for our research are: Bitcoin, Ethereum, and SolarCoin. So we weighed the pros and cons of these different blockchain, to highlighted the points to improve or avoid (Table 1).

Table 1. Pros and cons of different Blockchain

Blockchain technology	Pros	Cons
Bitcoin	Decentralized data	PoW
	Peer-to-peer transaction	Only monetary transactions
		Public blockchain
Ethereum	Smart contracts	Smart contracts
	PoS	Lack of security
Solarcoin	Energy transaction	Same as Ethereum

In regards to Bitcoin, the heaviest disadvantage remains the consensus protocol (PoW). Its mode of operation remains rather long and very greedy in energy [3].

PoS is often referred to as a PoW solution, because of its green consumption electricty. But it should not believed that the PoS is the miracle solution. One of its cons is its lake of security [9], because by comparing with the PoW, PoS does not ask for work in return for its validations.

Ethereum is characterized by its Smart Contracts, and it seems very useful. But if contracts are badly programed, the system could be ill-suited.

Finally, concerning SolarCoin it is difficult to decide on its advantages and disadvantages because it is not very widespread, there is not enough information about this technology. However, it is based on the Ethereum platform therefore the disadvantages of Ethereum apply to Solarcoin. The innovative aspect remains its energy transaction.

3. THE BLOCKCHAIN APPLIED TO THE SMART GRID

After knowing the various variants of the Blockchain and retaining the interesting points concerning them, we tried to develop a Blockchain adapted to a smart grid model. This first blockchain approach is a combination of several blockchains, which gives us the ElectricChain[7], in reference to the electrical aspect of the chain. The aim is to set up a microgrid electric network, as

---

[5] https://solarcoin.org/fr

[6] http://brooklynmicrogrid.com/

[7] http://www.electricchain.org/

in the case of the Brooklyn district[8], to allow the inhabitants of the same microgrid to exchange their energy production, not only solar energy, but all other energy produced (wind, solar, battery, other), and so benefit Energycoin for every kWh of energy produced. And thus promote the production of local energy and alleviate the high energy production, in order to achieve an erasure of the curve of energy consumption. The decentralization aspect provides peer-to-peer exchange flexibility.

By merging the initial Smart grid model and the ElectricChain, Fig. 3 summarizes the process which relates the progress of a transaction between two inhabitants of the same microgrid.

Background:

- “A” produced 8 kWh, he consumes 5 kWh, he still has 3 kWh.
- “B” needs 4 kWh.
- A smart contract is established between those two persons (transaction rules).

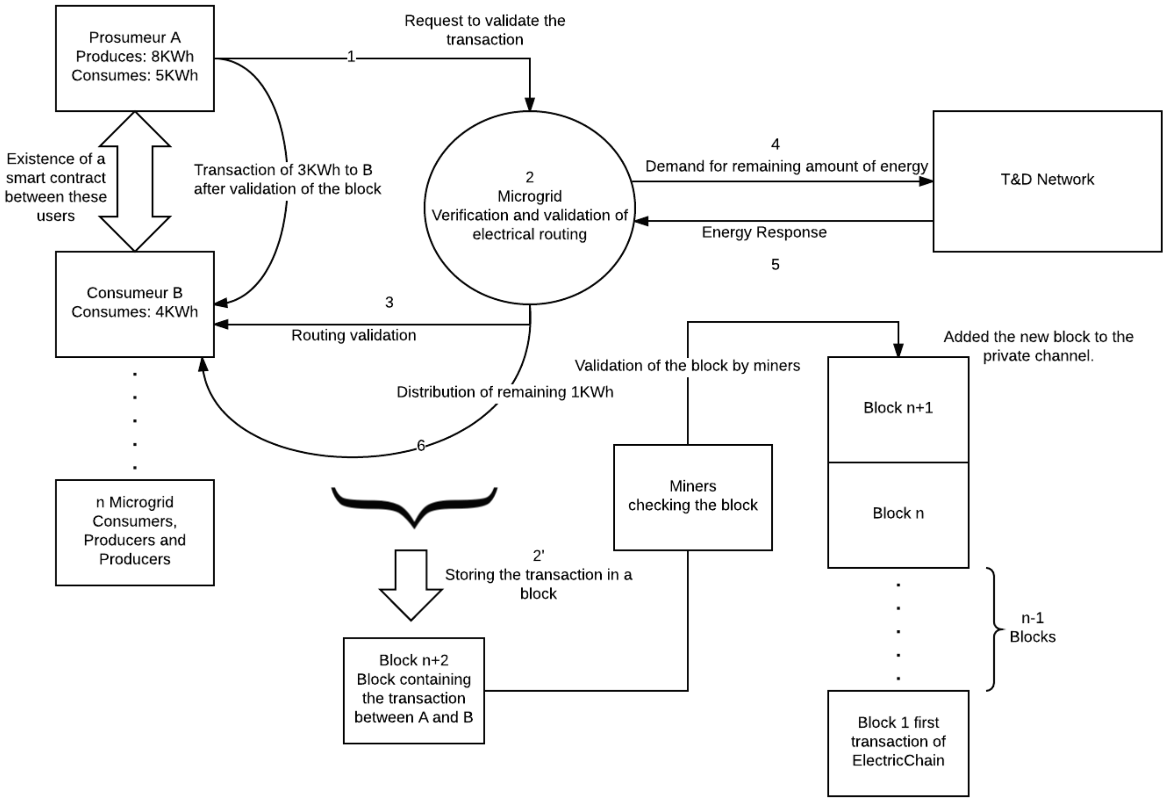

Fig. 3. Process of an energy transaction

Microgrid level:

1. A Transaction wanted to be carried out between two persons of the same microgrid according to the rules of the smart contract (A and B), “A” wants to send 3 kWh to “B”.
2. The microgrid checks whether it is possible to perform a transaction, based on the electrical routing and the power line support.
3. Once the routing is validated, the microgrid allows to “A” to transmit the amount of energy to “B”, concerning the capacity of the lines to support the transaction.
4. The microgrid demand the 1 kWh left for “B” to the T&D network for meeting conditions of the transaction.
5. The network provides the remaining 1 kWh to the microgrid.
6. Finally, the microgrid sends to “B” the 1 kWh.

---

[8] http://brooklynmicrogrid.com/

Miners level :

1. A transaction wanted to be carried out between two persons of the same microgrid according to the rules of the smart contract (A and B), “A” wants to send 3 kWh to “B”.
2. The transaction between “A” and “B” is stored in a block with other transactions, and ready to be verified by miners. If the PoS is verified, the block is validated and then stacked on the oldest chain.

In this new model, the smart contracts possess the strategies and consumption patterns [1] of the Blockchain participants. So, as smart contracts are stored in the chain, to add or remove consumption strategies, it will be necessary to remove the smart contract to replace it with the smart contract updated, because let’s remember, the blocks can not be altered.

4. ITEMS STILL TO BE DEALT WITH

This first approach of Blockchain applied to the Smart Grid is not without flaws. Several points still need to be improved and deepened. We have compiled these points in Table 2.

Table 2. Areas for improvement

	Questions to ask
1	Is it possible for a user to leave a blockchain when he has knowledge of certain private data?
2	If it is possible to join or leave a blockchain network, what will be the procedure to follow?
3	Is it possible for a neighbor to switch from one ElectricChain to another?
4	Should we include a monetization aspect?
5	If one wishes to exchange this currency with another currency of another Blockchain, is it possible to have an equivalence?
6	Could a non-energy consumer buy Energycoins in any way?
7	Could the Energycoin only be resold against the energy of a neighbor, or the conventional network?
8	Is it better to return this energy to consumers and thus benefit from a profitability in its production?
9	In the full period, is it better to feed on the classical network or the blockchain network?
10	What pattern should be applied for known situations?
11	How to remove the third part in the system, which is the microgrid?

The choice in the consumption pattern shown in Fig. 4, illustrates the different possibilities of algorithm consumption. It is difficult to know which path will be the best, because several parameters are involved (peak of consumption, price of the energy, energy produced by the prosumers, … etc).

It is also important to note that, from Fig. 3, it can be seen that the transaction can not be done without a third organ. Indeed, concerning the routing of the energy, the presence of EDF (Électricité de France/ French Electricity), or other organization as such seems to be indispensable to allow the validation of a transaction from an energy routing point of view.

This shocks the very concept of Blockchain, which is to establish a peer-to-peer transaction system without a central body. Today, it is impossible to remove the electrical routing part of the network. As we can see in the Fig. 4.

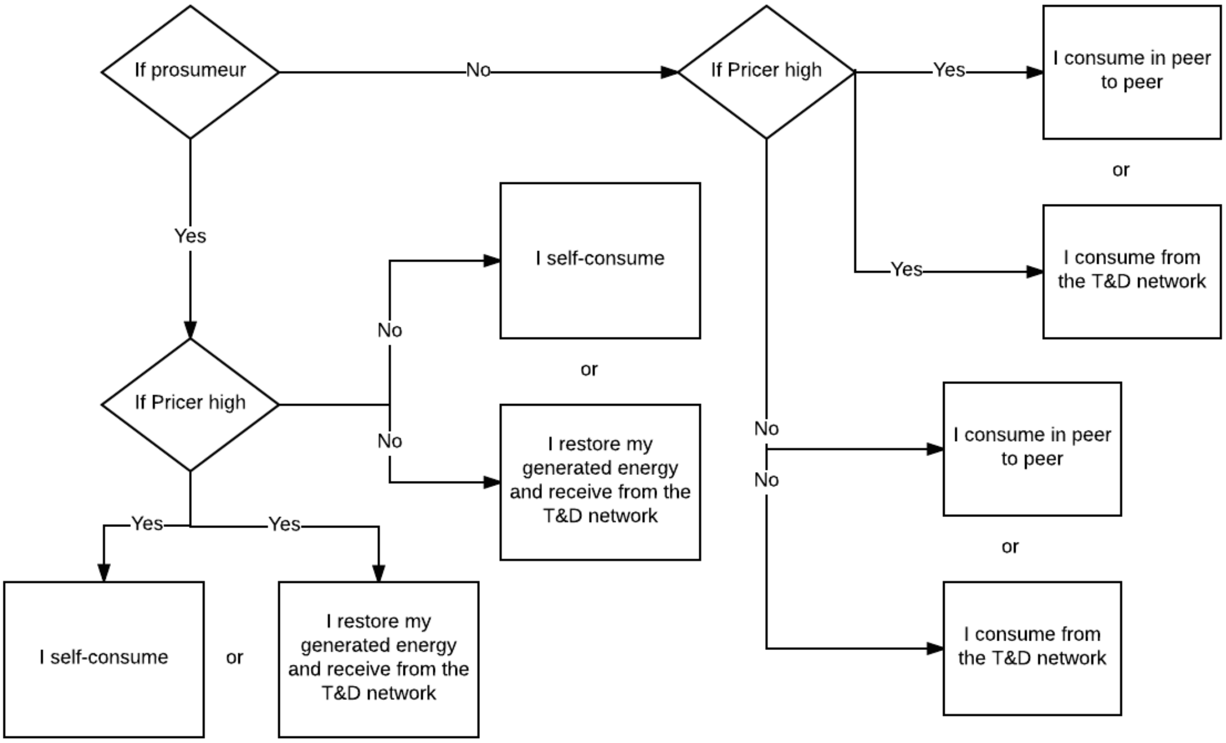

Fig. 4. Problems about the consumption algorithm

5. CONCLUSION

The importance of the Blockchain in a Smart Grid does not seem obvious but it is the case. This means of exchanging energy could promote the production of renewable energy locally, thus avoiding energy losses in the lines. On that day, we do not have concrete answers on questions in Table 3, but we have plans to resolve the problems encountered.

Our model is based on the installation of several ElectricChains in the same city, in order to distribute and homogenize the demands in electricity and thus avoid too much disruption of the network. Dividing a city's network into a microgrid [11] would allow for better management of energy flows and peer-to-peer transactions.

The aspect that we did not want to integrate into the model is a monetary aspect because it would imply a tendency to haggle the energy produced and possibly get to an energy traffic. If this is the case, it is necessary to establish tariff standards.

To be rewarded with an amount of energy produced, the producer will benefit a certain amount of energycoin.

REFERENCES

1. GUERARD, Guillaume; PICHON, Bastien; NEHAÏ, Zeinab. Demand-Response : let the devices take our decisions. SMARTGREENS 2017. Porto: Portugal 6th International Conference on Smart Cities and Green ICT Systems. 2017 April 22-24.
2. NAKAMOTO, Satoshi. Bitcoin : Peer-to-peer electronic cash system. http://bitcoin.org/, 2008.
3. BUTERIN, Vitalik. A next generation smart contracts and decentralized application platform. http://ethereum.org/. December 2013.
4. MIGNOT, Sylvain. Le bitcoin, nature et fonctionnement. Banque et droit. February 2015.
5. CHRISTIDIS, Konstantinos; DEVETSIKIOTIS, Michael. Blockchain and smart contracts for the internet of things. IEEEAccess, 2016.

6. SWAN, Mélanie. *Blockchain, Blueprint for a new economy*. O'Reilly Media, 2015. ISBN 978-1-4919-2049-7.
7. WOOD, Gavin. Ethereum a secure decentralized generalised transaction ledger final draft. http://gavwood.com/, 2014.
8. CASTRO, Miguel; LISKOV, Barbara. Practical byzantine fault tolerance. Proceeding of the Third Symposium on Operation System Design and Implementation, 1999.
9. KING, Sunny; NADAL, Scott. Ppcoin: Peer-to-peer crypto-currency with proof-of-stake, 2012.
10. DELMOLINO, Kevin; ARNETT, Mitchell; KOSBA, Ahmed; MILLER, Andrew; SHI, Elaine. Step by step towards creating a safe smart contract: Lessons and insights from a cryptocurrency lab. Financial Cryptography and Data Security, 2015.
11. KONASHEVYCH, I.O. Advantages and current issues of blockchain use in microgrids. Electronic modeling, 2016.

CYSENI 2017, May 25-26, Kaunas, Lithuania
ISSN 1822-7554, www.cyseni.com

STUDY OF APPROACHES TO INCIPIENT FAULT DETECTION IN POWER TRANSFORMER BY USING DISSOLVED GAS ANALYSIS

R. Liepniece, S. Vitolina, J. Marks
Riga Technical University
Azenes Street 12/1, LV-1048 – Latvia
E-mail: ruta.liepniece@edu.rtu.lv

ABSTRACT

To maintain the reliability of power transmission it is important to detect the incipient fault of power transformer as early as possible. If the fault of power transformer is not detected promptly, it can evolve resulting in high repair costs or even failure of power transformer. The most commonly used method for power transformer fault detection is the dissolved gas analysis (DGA) of transformer oil. Various methods have been developed to interpret the data of dissolved gas analysis, but not many are applicable for detection of incipient fault.

In the framework of this research two standards were used: IEEE C57.104-2008 "Guide for the Interpretation of Gases Generated in Oil-Immersed Transformers" and Standard of Latvian Electrotechnical Committee LEK 118 "Transformer Oil Inspection Standards". Detection of the incipient fault of power transformer is included in both, however, approaches recommended in these standards vary to a great degree – one approach mostly indicates that transformers are in good condition, but the second approach mostly results in warning about incipient fault, which must be confirmed by additional evaluation.

The objective of this paper is to determine the most suitable approach to detect the incipient fault of a power transformer. For this purpose DGA data of 48 oil-filled power transformers have been analysed. These transformers are with rated voltage 110/20 kV and rated power within the range from 6.3 MVA to 40 MVA; all of them have active on-load-tap-changer (OLTC). The DGA data has been provided by Latvian Transmission System Operator (Augstspriegumatīkls, JSC).

Current DGA data interpretation approach described innational standard LEK118 states that the limits of fault gas concentration are divided into 3 levels: normal operation of a transformer; detection of incipient fault; detection of existing fault, and that the interpretation of DGA data is carried out by evaluating the concentrations of dissolved gases in oil. However, the case study indicate that only for 10 of 48 transformers condition is indexed as a normal operation, while the other transformers have been identified either with incipient fault or an existing fault. The obtained results conflict with the real maintenance situation since additional tests or repair works were not appointed based on DGA measurement results.

Different multi-step approach based on ideas of standard IEEE C57.104 is proposed, where the first step is evaluation of value of total dissolved combustible gas (TDCG), followed by evaluation of individual fault gases in the second step, and additional analysis of acetylene concentration due to large proportion of faults in OLTC and trend of TDCG generation rate in the final step. The proposed approach allowed decreasing the number of transformers that were mistakenly diagnosed with existing fault, although their operation is normal. Study showed the necessity to adjust TDCG values given in national standard, therefore several variations of TDCG concentrations are proposed and tested in this paper as case studies.

Keywords: power transformers, dissolved gas analysis, incipient fault, reliability

CYSENI 2017, May 25-26, Kaunas, Lithuania
ISSN 1822-7554, www.cyseni.com

SMART GRID: FROM RAW DATA TO A DIGITAL MODEL

E. Cathelineau, G. Guerard, L. Levy
Leonard de Vinci Pôle Universitaire, Research Center
92916 Paris La Défense – France
E-mail: loup-noe.levy@devinci.fr

ABSTRACT

One of humanity's main objectives in the years to come is to drastically reduce our greenhouse gas emissions and to ensure energy efficiency. But at the same time the need for electrical power is rising and new products, requesting great amounts of electrical energy, such as electric cars and IoT (Internet of Things), are introduced in the market.

Reaching governmental and world goals about energy transition can only be made through the massive integration of renewable energy sources into the electrical grid. The sources of renewable energy being decentralized, it is necessary to design an adapted energy grid to handle them. To face this challenge, simulation tools and numerical methods must be used to optimize transport, distribution and consumption of electricity, hence there is a need of prediction and forecasting tools.

Different physical factors are involved in the electric power transmission, such as impedance, intensity, conductor's properties and weather. Using these different factors, we can build different algorithms calculating voltage in real time in every cable. These estimations will enable electricity to take the optimal path to decrease lost.

Renewable energy production being irregular, increasing their number implies to predict consumptions and energy storage or discharge in real time. This is why the consumption patterns of every device connected to the grid must be organized in order to optimize the global consumption of the grid with the use of a combination of several fields such as game theory, IoT and grid's communication and artificial intelligence.

Keywords: Multi-Agent Systems, Agent-Based Model, Complex System, Game Theory

1. INTRODUCTION

We are facing many challenges today regarding energy. It has become clear that it is essential to diminish our greenhouse gases to decrease the impact of the human's activity on the environment. Furthermore, our current energy consumption is made in such a way that a great deal of our energy is being lost during transportation, or is lost because we are unable of evening and balancing demand and consumption, making overproduction the only way to avoid power outage. Finally, the important daily consumption peaks require the use of fossil fuel power plants: polluting but reactive enough to adapt to such quick increase of consumption.

Since COP21, France has made the engagement to diminish its greenhouse emission by 75% by 2050 compared to 1990. But the consumer's comfort must suffer as little as possible from the changes made to the energy system. So we must give the same services for a lower energy consumption, we must therefore increase energy efficiency in the French electrical network.

Furthermore, such development could be made in an increasingly decentralized way and come from the initiative of citizen or collectivites. The European Economic and Social Committee (EESC) concluded, in a report of January 2015, after the study of European example, that the deployment of renewable energies was more present and faster in the states which gave the citizen the possibility to start their own energy initiatives. It advocates to the states to have as a priority to allow the citizen to make the subject of renewable energy production their own.

To face those challenges, it is necessary to rethink the electrical network. It will have to integrate the recent technological breakthrough from a variety of different domains to allow a smarter and a more environment friendly production. This new grid has a name: The Smart-Grid.

A Smart Grid is an intelligent energy grid [5]: it means that it is capable of adapting, predicting and communicating with the different agents it is interacting with (production, consumers, weather...) to optimize production, transport and consumption of energy. It can be seen as a complex system optimizing efficiency, reliability and robustness of the electrical grid. It is made of intelligent nodes interacting autonomously to deliver power to the consumers by integrating advanced control and communication techniques.

It can be divided in three parts:

- The devices: consuming, storing or producing energy.
- The micro-grid: those are the nodes of the grid. They have the size of Eco-district; they manage distribution of energy to (and between) the devices.
- Transmission [6]: the energy circulates in the high-voltage cable from the power plant to the transformers where it is distributed in low or middle voltage in the microgrid.

2. TRANSMISSION

The demand of electricity has already increased of 25% since 1990. The transmission of the electricity consists of routing energy produced by different centers of productions to consumers [8].

A high voltage(400 or 225 kV) [7] must be maintained to avoid significant losses during transport, mainly due to the Joule effect.

Presently, the network market doesn't work in real time but from predetermined situation. The network is composed of intensity and voltage sensors on the lines taking measures on the networks, mainly at the transformers and the electricals stations. The aim of our project is to adapt the lines in real time, dynamic line rating [3] and integrating others factors like weather to choose the best way for the electricity. The weather is a new factor important with the objectives of the important integration of renewable energy. The self-healing of the network is also a new objective.

Our aim is to use physical data of the network and to transform them in numerical data, in a graph. It's important to use numerical data [1], because the numerical calculations are more reliable and faster than human calculations. Moreover, the data must be collected directly at the root. We want to avoid the losses that are too important and optimize the routing of process.

2.1. From physical data to numerical data

In this part, we focus on a small part of the French network. We realize the routing between the city of Beaulieu and Niort. The lines between the two cities have a voltage of 225 or 90 kV. The aim is to have the maximum flow at the lowest cost.

In the first step, we realize a curve of power as function of cost. We have obtained the following formula with the ohm's law.

$$Losses = RP^2/U \qquad (1)$$

U refers to voltage in Volt;
P refers to power in Watt;
R refers to resistor in ohm;
Losses refers to losses in Joule.

With this formula, we have the voltage of the lines from maps of RTE (French Electricity transmission network). We have as unknown the power and the losses.

To find the values of the resistors we use the Pouillet's law because we know the section and the materials of the lines(see Table 1). We see that the losses are more important when the power is higher.

Table 1. Table of resistor values

Lines	Voltage (kV)	Value of resistance (ohm)
1-(54 km)	225	0,918
2-(30 km)	225	0,51
3-(35 km)	225	0,595
4-5-(13 km)	225	0,221
6-7-8-(3 km)	90	0,1275

In the second step, we realize three linear regressions on the curve that we obtained before, where the using rate is the most important on the lines, because we know that the lines are more used for a certain power. For example, the lines with a 225 kV voltage, the using rate is more important between 200 and 340 MW. When we realize our linear regression, we obtain the equation ax + b. The coefficient **a** represent the cost of the losses in Joules. The coefficient **a** changes in function of the power in the lines. With these coefficients, we can modelize our lines from the cost and the capacity(power of the lines).

2.2. Numerical data

We want to take the physical data, and transform it in graph to apply the Busacker & Gowen algorithm. The complex network theory is important for the complex system such as Smart Grid, and provides mathematical tools to model its structure.

The complex network of Smart Grid change at each time, so it's important to model this functions by taking into account the dynamics[2]. The separation of each criteria in a dedicated graph (like voltage or…) is important to simplify modelling. The overall adhesion function is defined as an aggregation of several spaces.

In this manner, a modification in a space is instantaneous. The Smart grid is governed by a number of qualitative and quantitative criteria, for example the voltage of the power lines or the weather, etc. Finally, graphs are a very useful modelling tool in the context of complex systems to manage acquaintances between agents and be able to follow the dynamics of relationships between them [10].

Now that we have modelized our lines numerically, we want to choose the best path between all the lines (meaning the path with maximum flow and the minimum cost) [4].

We represent our lines this way:

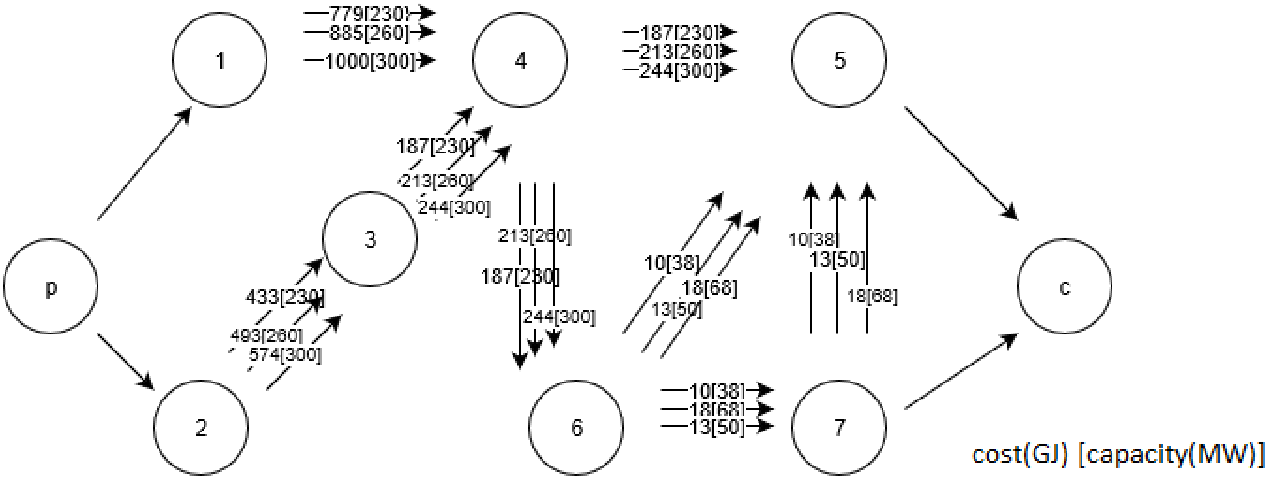

Fig. 1. Graph representing the electric lines in function of cost and capacity

To choose the best path, we search the minimal cost. At each iteration we want to determine the shortest path using only the cost. To find the shortest path we use the Bellman Ford Algorithm

(Fig. 1). Next, we saturate the founded path, we watch the capacity minimum on the path, and we send the new flow cost:

$$New\_flow\_cost = \left(\sum_{i=1}^{total\_line} \mathrm{cost}\_line_i * x_i\right) * (\min(non - zerovalues\ from\ capacity\_line_i * x_i)) \quad (2)$$

x_i: x_i =1 if the line i is used otherwise $x_i = 0$.

We compute the shortest path, and if it is the end of the algorithm, there is no path between producers and consumers. The total cost is equal to:

$$\sum_{i=1}^{total\_line} flow_i * \mathrm{cost}\_line_i \quad (3)$$

total_line: Total_line is the entire number of lines of the network (Fig. 1).

2.3 Analysis of data

We want to understand where the flow is saturated if the demand is growing. We don't consider the cost now. We have two schemes, the augmenting path and the flow max at the min cost. The min-cut give information where the grid has bottleneck. A min-cut at a source means the production isn't enough. A min cut at a sink means the consumption is well defined. A feed back to the consumers actives a process that determines a new path for electric transmission. Then, routing is updated, ect. Until demand is equal to consumption.

When a consensus is reached, we don't use the data at the consumption level [11]. We use a weighted average formula to estimate the consumption of each microgrid.

$$2\sum_{x=1}^{n} \frac{f_{i,x}x}{n(n-1)} \quad (4)$$

where $\mathbf{f}_{i,x}$ is the flow which arrive or depart of **i** at the **x** occurrence.

Now, we want to realize the feedback if the demand isn't satisfied. The feedback are composed of two steps, first we put the producers to infinity and we realize the min cost flow. If the demand isn't satisfied we have two solutions, decrease the demand or look the cut min to see if it's a lines problem. The second step consists of putting the consumers to infinity and realizing the min cost flow. If the consumption is too high, we need to increase the production, and if there is a problem on the lines we must decrease the demand.

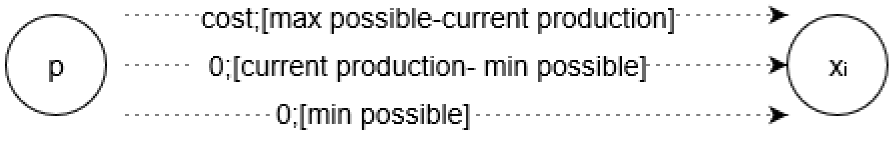

Fig. 2. Minimum and maximum variation production of power stations

Max possible: Max possible is the maximum evolution of the production in comparison with iteration i-1;

Min possible: Min possible is the minimum evolution of the production in comparison with iteration i-1;

x_i: x_i refers to the consumers;

P: p refers to the source of production.

We can see the current production in the middle edge(Fig. 2). In the upper edge we see the maximum production and the cost of this evolution. In the lower edge we can see the minimum production (Fig. 2).

The last step consists of scheduling the production. Each plant has a known variation across time. In order to find the best schedule of production for the next step (i.e in 5 minutes), we use both known variations and the estimated consumption from formula (3). Thus, each source of the graph has three acts of increasing cost where the first one refers to the lowest value, the second to the current production and the last to the highest value. Cost of each areas depends of the kind of the plant (coal, nuclear, etc.).

3. DISTRIBUTION: THE MICRO-GRID

The main challenge in distribution and consumption of energy is avoiding the formation of daily consumption pikes and levelling consumption of the grid in general. Today no satisfying solution have been found to answer those challenges, and creating a model of efficient management of consumption is a key step in the creation of a microgrid.

Demand-Side Management (DSM) is the management of demand in order to reduce and to level consumption. Automating this decision making to optimize consumption is called Demand-Response (DR). It is on the DR aspect of DSM (automatization of demand-side management) that we are going to focus on in this part of the article.

Such a heterogeneous and large system as the micro-grid needs physical data-processing, and mathematical tools to be apprehended. In this context, complex systems theory is important to approach the concepts of microgrid and Demand Response as explained further in the article.

3.1. Decentralized demand-side management

It would be tempting to centralize decision making, to organize consumption from a “higher point of view”. But centralized control of thousands of smart meters would be an extremely complex task. It would require an enormous calculation power and would be problematic regarding private life of the users. Indeed, it needs an exhaustive knowledge of the device, the habits and preferences of each users.

Hence the notion of Decentralized Demand-Side Management (DDSM), in which the system is self-organized and therefor does require a central intelligence, but creating an efficient DDSM is a complex task.

Indeed, on this graphic representing the different consumption curves in function of the different DR types we can see that the use of real time pricing (RTP) as the use of Time of use (TOU) – created to optimize consumption – are actually creating induced peaks. It is therefore very important to develop new tools allowing us to organize the consumption without those important drawbacks [9].

3.2. Definition and application of game theory and complex system

The consummers in a smart grid can be seen as several agents acting according their own rules and with the objective of maximizing their gains (in this case it would be compfort: consuming as much as you want when you want for as little as you want). Developing the rules that define the consummers and the smart grid so that by acting in their interest the “players” (consummers) also act for the common good (the whole grid) is apllying game theory to electricy consumption. A system composed of a large population of connected agents is said to be complex if there is an emergent dynamic resulting from the actions of every of the agents rather than imposed by a central intelligence. Their collective self-organized behaviour is hard to predict by locally observing the behaviour of the agents [13, 14]. The microgrid matches perfectly this definition and therefor represents a complex system. To study it and create an efficient model it is therefore necessary to use the tools allowing us to study complex systems. We created our model by using a multi-agent modelling environment (NetLogo).

3.3. The model

Our model represents a small microgrid composed of four buildings. Our goal is to obtain a minimal consumption for a maximal comfort and to avoid brutal changes in the global consumption of the microgrid. This will be achieved by having each device to adapt accordingly to the global situation of the microgrid. Our goal is to even consumption, to diminish the amplitude of the peaks.

In each of the houses there are a number of devices, each of a different breed: some have batteries others don't, some are cyclic other aren't etc. These devices are going to turn themselves on or off according to their own set of functions and rules. Their behaviour will depend on global variables of the microgrid (global consumption of the microgrid, time of day…) as well as on local variables (consumption of the house, current agent state, value of its batteries, and the steps of its consumption patterns…).

Each agent represents a device with its parameters and values. The device will choose a consumption scheme according to his situation. The devices with a battery can choose to charge or to discharge their batteries. The devices may choose to defer their consumption if they can. This way each device, in function of its different properties, has a variety of schemes it can choose to adopt.

With regulation activated in the microgrid, each device will be able to attempt to regulate the system according to this principle: if the global consumption goes beyond the average value plus a tolerance value that is specific to the device, then the devices will set itself on battery mode so that the global value gets closer to its average value to avoid important variations. If every device had the same threshold tolerance value, then they would all react at the same time, causing an important variation in the global consumption (see Fig. 3) and therefor a peack. Therefore, the variation of the threshold value has to be adapted to the system so that it stays stable. The same principle is applied for the deferable devices.

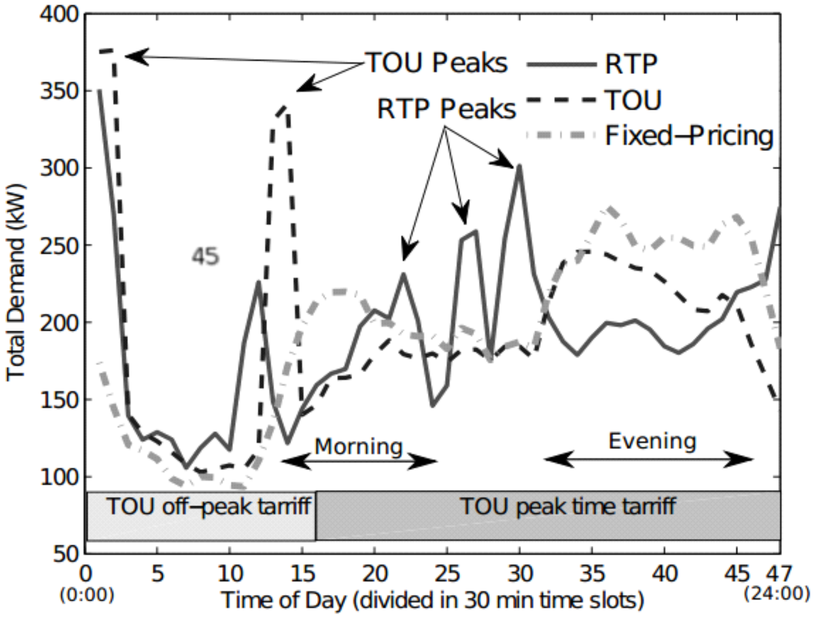

Fig. 3. Consumption curves of a modelled micro-grid with different price incentives [12]

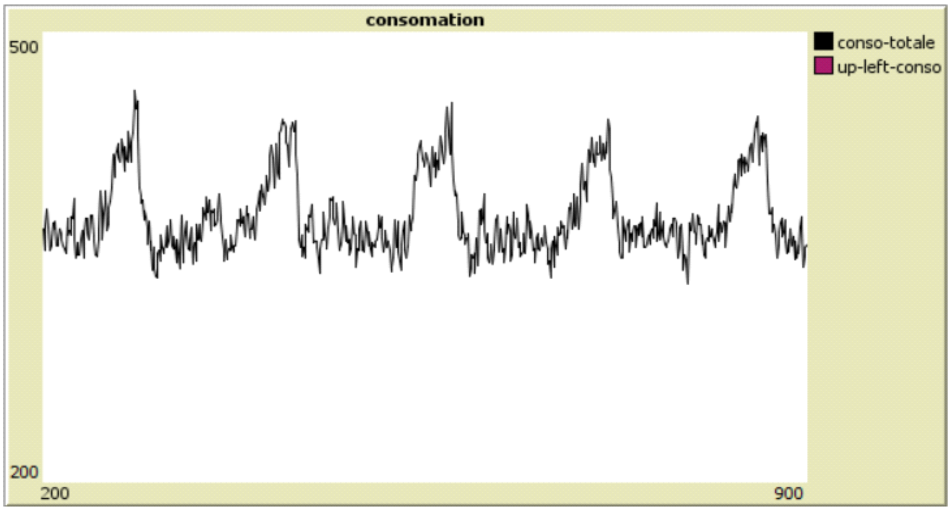

Fig. 4. Consumption curve of the model in function of time

The global consumption is a cyclic curve. In the "evening" the consumption grows higher and falls rapidly after midnight. The model has been studied running with three different kind of operation, the first without any regulation, the second with a well-adjusted regulation and the third with an improperly adjusted regulation. The unit of time is of 1/144 of a day.

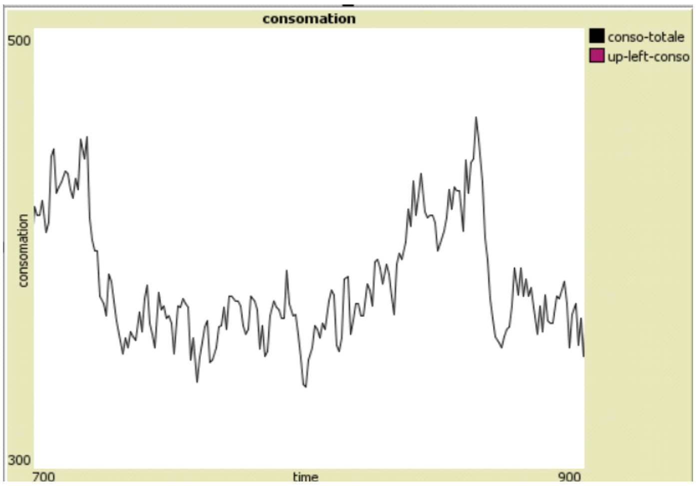

Fig. 5. Curve with no regulation

We can see in Fig. 5 the curve representing the consumption in function of the time during a "day" with no regulation.

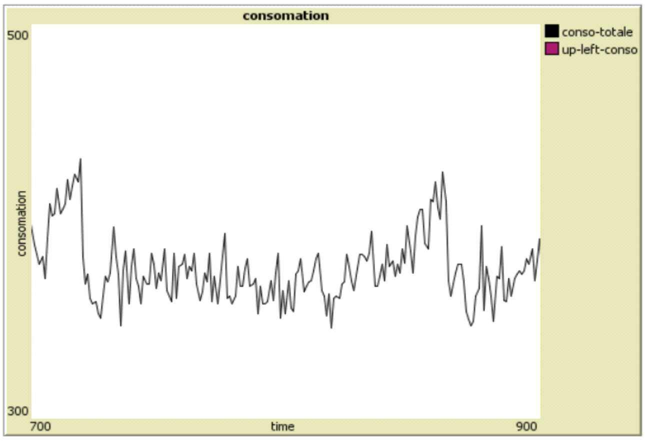

Fig. 6. Curve with a well-adapted regulation

With a well-adjusted regulation, it is visible on figure 6 that even though the consumption is far from being smooth (due to the small number of devices) we can see that the pikes are much smaller than with the non-adapted regulation, and that in general the values stay always closer to the average.

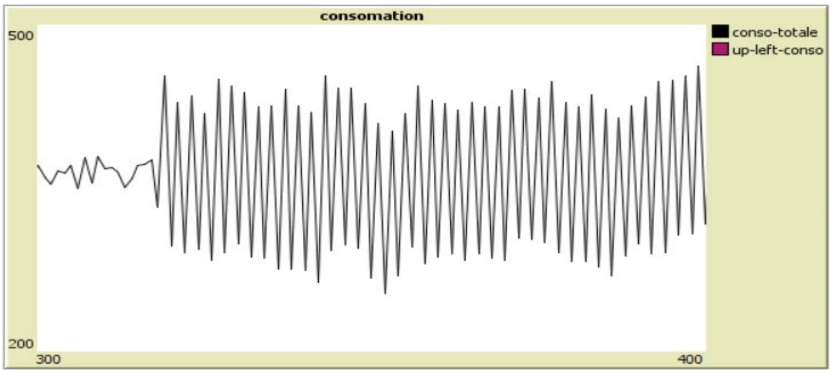

Fig. 7. Curve with an ill-adapted regulation

The devices can have a response that is not adapted to the grid. For example if they are too reactive (as a whole) they will put the system off balance. In the case of a regulation that is not well adapted to the size of the grid (Fig. 7) the answer of the devices facing an under-consumption or an over-consumption will be too important and the system will become unstable. It can be explained by a bad repartition of the "consumption-mode-changing-threshold-value" (the consumption value of the grid that makes the device change his mode of consumption). The solution to this issue was to create a process in which the consumption-mode-changing-threshold-value of the device is updated regularly so it can adapt to the changes in the grid (Fig. 8).

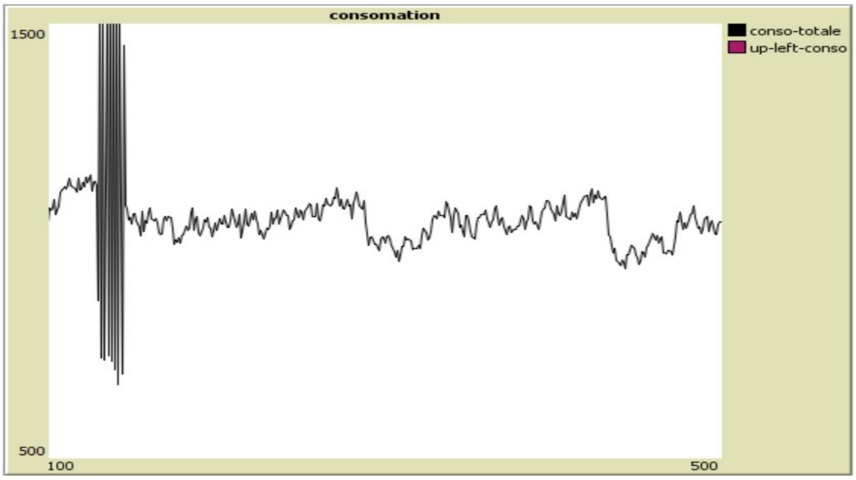

Fig. 8. Curve with auto-adapting regulation

Here, the regulation was started around 140 ticks (unit of time). The system went off balanced, but by adjusting its threshold value, it managed to find balance again.

4. CONCLUSION

A Smart Grid is a complex and constantly evolving system. This is why we must use adapted tools of simulation and prediction.

For the routing of electricity, we recover physical data, and we include this data in numerical graph. From this graph, we can establish the best path to deliver the best flow at minimal cost. The energy distribution agent-based model was based on Decentralized-demand-side-management.

Composed of intelligent devices adapting their consumption schemes to the state of the microgrid, it was able to significantly even consumption and diminish major pikes. It is a case study of decentralized-demand side management using intelligent devices with positive results.

Thus, whether it is transmission or distribution, modelling seems to be an essential element in the creation of a functional Smart Grid.

REFERENCES

1. J.Momoh Smart Grid: *Fundamentals of design and analysis.*
2. <http://lemag.rte-et-vous.com/dossiers/le-poste-electrique-100-transition-energetique-100numerique> .
3. Dynamic Line Rating for overhead lines – V6 CE TSOs current practice RGCE SPD WG .
4. Dynamic Line Rating Systems for Transmission Lines Steven Bossart, Senior Energy Analyst and Ronald Staubly, Technical Project Officer.
5. Smart Grid: Overview, Issues and Opportunities. Advances and Challenges in Sensing, Modeling, Simulation, Optimization and Control S. Massoud Amin.
6. Smart Transmission Grid: Vision and Framework Fangxing (Fran) Li, Senior Member, IEEE, Wei Qiao, Member, IEEE, Hongbin Sun, Member, IEEE, Hui Wan, Member, IEEE, Jianhui Wang, Member, IEEE, Yan Xia, Member, IEEE, Zhao Xu, Member, IEEE, and Pei Zhang, Senior Member, IEEE.
7. <https://ei.haas.berkeley.edu/education/c2m/docs/Math4SmartGrid.pd .>
8. Distribution load flows: A brief review M S Srini .
9. Impact of Smart Grid on Distribution System Design Richard E. Brown.
10. A Context-Free Smart-Grid Model Using Pretopologic Structure, Guillaume Guerard, Soufian Ben Amor, and Alain Bui.
11. Demand Response: Let the devices take our decisions, B.Pichon and Z.Nehaï
12. Sarvapali D. Ramchurn, Perukrishnen Vytelingum, Alex Rogers, and Nick Jennings “Agent-Base Control for Decentralised Demand Side Management in the Smart Grid”, the 10th International Conference on Autonomous Agents and Multiagent Systems - Vol. 1, Pages 5-12, 2011.
13. D. MacKay. Sustainable energy without the hot air. UIT, Cambridge, 2009.
14. Murat Ahat1, Soufian Ben Amor , Marc Bui , Alain Bui , Guillaume Guérard, Coralie Petermann, “Smart Grid and Optimization”, American Journal of Operations Research, 2013, 3, 196-206.

CYSENI 2017, May 25-26, Kaunas, Lithuania
ISSN 1822-7554, www.cyseni.com

FUEL PROPERTIES AND FERTILIZATION COST OF UKRAINIAN CORN STOVER

V. O. Antonenko
Institute of Engineering Thermophysics of the National Academy of Sciences of Ukraine.
2a Zhelyabova Street, 03680, Kyiv – Ukraine
E-mail: viacheslavon@gmail.com

ABSTRACT

In order to provide reliable and efficient thermal conversion, it is necessary to understand the physical and chemical properties of corn stover. The properties of corn stover depend on species, climatic and weather conditions, soil type, fertilizer input etc. Thus, it is necessary to study the fuel from various locations.

The present paper describes analysis results of corn stover from a single location in Kyiv region, Ukraine. The soil was fertilized with anhydrous ammonia 80 kg/ha. Elemental composition (W, A, C, H, S, N, O, Cl), calorific values, ash melting temperatures and ash chemical composition of the samples have been tested.

The comparative analysis of the samples with foreign analogues has been carried out. It is shown that the test samples of corn stover from Kyiv region are characterized by ash initial deformation temperatures of 1160–1200 °C. These temperatures are higher than the average agricultural biomass values and typical for woody biomass. The relatively high ash melting temperature reduces risks of sintering and deposit formation on the furnace inner surface.

In the case of removing straw from a field, the soil may suffer from nutrient depletion. The fertilization value of biomass as a soil fertilizer have been also studied and compared.

Keywords: bioenergy, biomass, corn stover, calorific value, elemental composition, ash melting, ash chemical composition, fertilization value

1. INTRODUCTION

Ukraine is the 5th largest corn harvester in the world. Considerable amounts of corn stover is formed while growing the plant. These by-products can be used for energy. Energy potential of corn stover is 3.08 Mtoe [1]. Fuel properties of the corn stover include elemental composition, calorific value, ash melting temperature and ash chemical composition. These properties influence combustion and equipment performance.

During combustion, chlorine evaporates completely and forms HCl, Cl_2 and alkaline compounds. While gas temperature decreases, the chloride alkalis condense on the metal surfaces causing corrosion. The studies [2], [3] show, that NOx formation occurs at temperatures in the range of 800–1100 ^{o}C and mainly depend on the fuel nitrogen content, combustion chamber design and method of air inlet. Ash content affects the equipment, ash removal system and the particulate matter emission rate. Ash can cause complications during combustion in boilers. Ash deposition can reduce the heat transfer intensity and cause corrosion [4]. Thus, along the heat exchange surfaces the flue gases should be cooled below the ash initial deformation temperature (ta). Therefore, the higher ash initial deformation temperature simplifies the problem of ash deposition. The ash melting is affected by overall ash composition pattern. It is believed that the interaction of various elements is of decisive importance. It is very likely that the content of Ca, K and Si are the most important elements for the ash melting characteristics [5].

The mineral and chemical composition of a biomass ash depends on the plant composition. However, in the real conditions an actual amount of inorganic elements can be supplemented with additional components of soil and atmospheric dust while harvesting, transporting and storage of the fuel [6]. Biomass ash mainly consists of inorganic elements oxides: SO_3, P_2O_5, SiO_2, Fe_2O_3, Al_2O_3, CaO, MgO, Na_2O, K_2O, Mn_3O_5, TiO_2.

Oxides of potassium K_2O and phosphorus P_2O_5 are macro nutrients and play an important role in the use of ashes as fertilizer. Significant amounts of nutrients are taken out of soil in case of corn stover and wheat straw alienation. In order to determine the real price of these products, the farmers should consider the fertilizer cost used for subsequent reimbursement of nutrients removed [7].

The corn stover properties usually depend on different factors: e.g. climate condition, weather, soil properties, fertilizer input etc. In Ukraine, 44% of area is covered with humus (blacksoil). Most of agriculture activity is concentrated within humus areas. Moreover, farmers are used to dig the corn stover into the soil in order to minimize fertilizer input. Therefore, careful comparative analysis of fuel properties from different locations is needed. The research aims to compare fuel properties of the Ukrainian corn stover with the analogues and other biomass types. The paper also aims to define fertilization value of corn stover comparatively to other biomass.

2. METHODOLOGY

Samples of the corn stover were taken directly after the harvest. Location: Kyiv Oblast, Severynivka. Date: 16 November 2015, 12-00 PM. Plant species: KVS-380.

Samples: Corn cob (1); Corn stalk (2).

Fig. 1. Corn stover samples

Indicators and methods of determination are presented in Table 1. All of the tests, except chemical composition of ash, were conducted according to ISO (the International Organization for Standardization). Noteworthy that the chemical composition of ash determination methodology is based on GOST 10538-87. The standards in Table 1 are initially dedicated to solid mineral fuel (coal, lignin etc.). However, we applied these methods for corn stover analysis that may result in some inaccuracy.

Table 1. List of indicators and standards

#	**Indicator**	**Standard**
1	Moisture content, analytical	ISO 589-81 Solid mineral fuel. Methods for determination of moisture
2	Total moisture, as received	ISO 589-81 Solid mineral fuel. Methods for determination of moisture
3	Ash, on dry basis	ISO 1171-97 Solid mineral fuel. Methods for determination of ash
4	Sulfur, on dry basis	ISO 334-92 Mineral solid fuel. Determination of total sulfur. Method Eshka
5	Chlorine, on dry basis	ISO 587-97 Mineral solid fuel. Methods for determination of chlorine
6	Volatile, on dry ash-free basis	ISO 562-81 Solid mineral fuel. Methods for determining the release of volatile matter
7	The temperatures of ash fusibility (deformation t_A, hemisphere t_B, fluid t_C)	ISO 540-81 Solid mineral fuel. Methods for determination of ash melting
8	Higher calorific value on dry ash-free basis	ISO 1928: 1995, IDT Mineral solid fuel. Determination of Higher calorific value by combustion in a bomb calorimeter and calculation of the lower calorific value

#	Indicator	Standard
9	lower calorific value on dry ash-free basis	ISO 1928: 1995, IDT Mineral solid fuel. Determination of Higher calorific value by combustion in a bomb calorimeter and calculation of the lower calorific value
10	Element composition, on dry ash-free basis:	
	- organic carbon	ISO 625-96 Solid fuel. Methods for determination of carbon and hydrogen
	- organic hydrogen	ISO 625-96 Solid fuel. Methods for determination of carbon and hydrogen
	- nitrogen	ISO 333-96 Solid mineral fuel. Methods for determination of nitrogen
	- oxygen	ISO 1994-76 Solid fuel. Methods for determination of oxygen
	- organic sulfur	ISO 157-96 Solid mineral fuel. Determination of forms of sulfur
11	The chemical composition of ash	GOST 10538-87 Solid fuel. Methods for determining the chemical composition of the ash

3. RESULTS AND DISCUSSIONS

Elemental composition, calorific value, ash melting temperature and ash chemical composition of Ukrainian KVS-380 corn stover samples: cob (1) and stalk (2); as well as the average values of same indicators for three different types of biomass: corn stalk (3), wheat straw (4), pine chips (5), according to database ECN Phyllis, are shown in Table 2.

Table 2. Characteristics of Ukrainian corn biomass samples and average fuels

Sample/average fuel indicator	Ukrainian KVS-380 corn stover		Database average value		
	Corn cob	Corn stalk	Corn stalk	Wheat straw	Pine chips
	1	2	3	4	5
Moisture, W_r, %	7.7	10.5	6.25	9.71	8.83
Ash. A_d, %	2.1	5.6	6.37	6.08	0.7
Volatiles, V_{daf}, %	85.3	81.9	81.31	81.37	84.26
Carbon, C_{daf}, %	49.08	50.04	42.76	48.72	52.01
Hydrogen, H_{daf},%	6	6.07	5.36	5.97	6.25
Nitrogen, N_{daf},%	1.0	1.0	1.17	0.72	0.14
Oxygen, O_{daf}%	43.69	42.78	39.83	44.39	41.43
Sulfur, S_{daf},%	0.23	0.11	0.23	0.14	0.1
Chlorine, Cl_d, mg / kg	100	1500	2098	4479	603
Calorific value					
High, Q^{s}_{daf}, MJ / kg	18.963	19.377	18.4	19.2	20.68
Low, Q_{ir}, MJ / kg	15.767	15.016	17.11	17.99	19.36
Ash melting temperatures					
Initial deformation, ta, °C	1200	1160	989	924	1200
Hemisphere, tb, °C	1250	1180	1 203	1161	1252
Fluid, tc, °C	1330	1260	1 243	1224	1259
Ash Chemical Composition, %					
	3.65	4.36	5.99	3.7	1.62
	1.66	3.37	4.88	3.55	3.39
	67.36	55.9	59.01	53.47	36.2
Fe_2O_3	4.99	3.99	4.34	1.01	2.74
SO_3	5.08	4.46	1.99	0.88	6.86
P_2O_5	2.8	9.45	2.93	7.02	27.56
SiO_2	3.53	4.28	4	2.28	3.26
Na_2O	0.85	1.3	0.44	1.11	0.67
K_2O	5.75	7	11.84	18.01	7.57
Mn_3O_5	0.09	0.12	NA	0.1	NA
TiO_2	0.45	0.24	NA	0.06	0.12

3.1. Elemental composition

The elemental composition of presented biomass types does not vary significantly in volatile matter V_{daf}, carbon C_{daf}, hydrogen H_{daf} and oxygen O_{daf}. The sulfur S_{daf} content in the samples of cob (1) and stalk (2) are 0.23% and 0.11% respectively. These values are typical for other solid biomass fuels of agricultural and woody origin. Sulfur affects the formation of sulfur oxides SO_x and alkaline sulfates that may condense on the metal surfaces and on particles of fly ash. Higher calorific value Q^s_{daf} of the samples (1) and (2) is about 19 MJ/kg. Nitrogen content N_{daf} in the samples (1) and (2) is 1.0%, which is typical for biomass of agricultural origin. Although, the nitrogen content of pine chips (5) is slightly lower – 0.14%.

Significant differences are spotted in ash and chlorine content, as illustrated in Fig. 2 below.

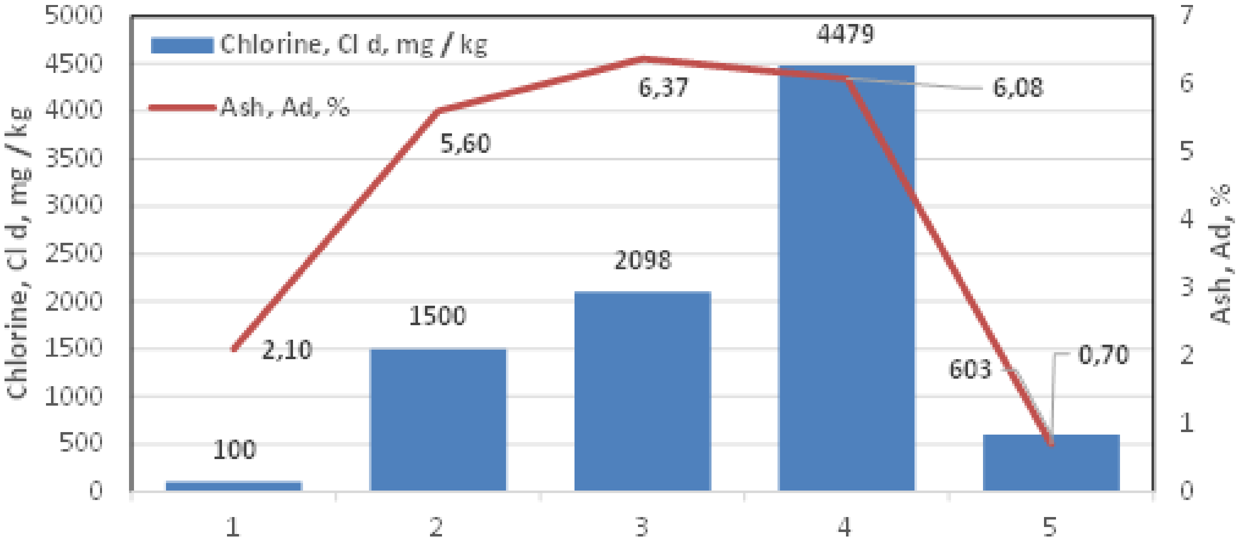

Fig. 2. Ash and chlorine content differences

Ash content A_d of the samples (1) and (2) is 2.1% and 5.6% respectively, which is typical for agro-based biomass. Chlorine concentration Cl_d in the corn stalk sample (2) is 1500 mg/kg, which is higher than the average value of pine chips (5), but lower than the average values of corn stalk (3) and wheat straw (4). However, the chlorine content of the corn cob sample (1) is 100 mg/kg, which is even lower than the average for pine. Relatively low chlorine content in the samples of Ukrainian corn stover potentially leads to lower formation of HCl, Cl_2 and alkaline compounds during burning. That potentially reduces the corrosion risks.

3.2. Ash melting behaviour

The Fig. 3 illustrates the ash melting temperatures of the Ukrainian corn stover samples and average biomass fuels. The samples of Ukrainian corn cob (1) and stalk (2) are characterized by higher ash initial deformation temperature, unlike average corn stalk (3) and wheat straw (4), and are similar to wood.

Relatively high ash melting temperature of Ukrainian corn stover samples may occur due to soil peculiarities, climate conditions and farming traditions (e.g. fertilizer input, crop rotation etc.). High ash melting temperature of Ukrainian corn stover defuse requirements for the boiler additional systems and steel quality. As a result, the Ukrainian corn stover potentially may be fired within relatively cheap wood-fired boilers.

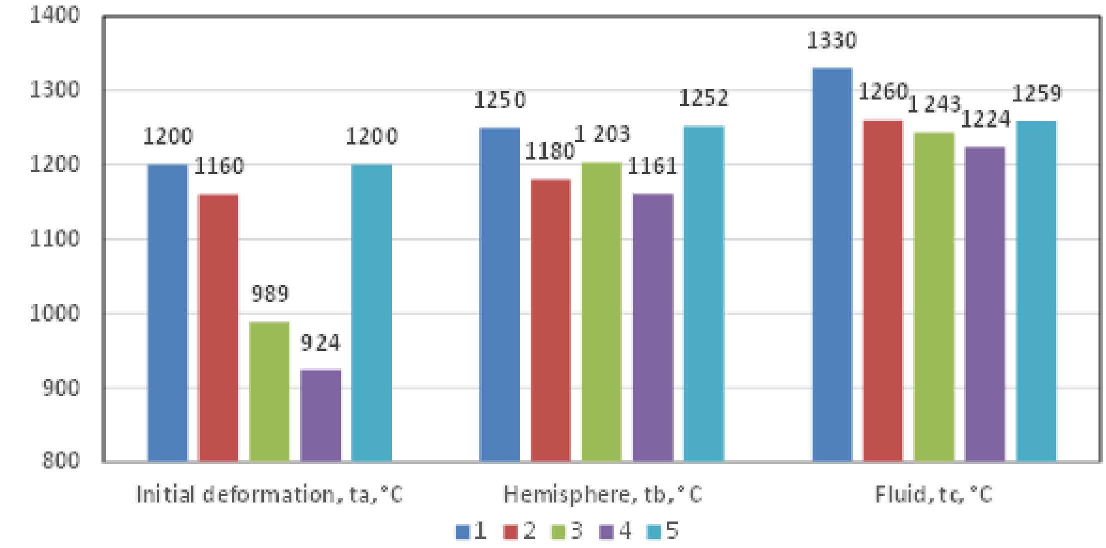

Fig. 3. Ash melting temperatures

3.3. Ash chemical composition

Fig. 4 demonstrates ash chemical composition of Ukrainian corn stover samples and average biomass fuels. It is found that K_2O content of the Ukrainian stover samples (1) and (2) is lower than average value of agricultural biomass (3) and (4). However, dependence of ash chemical composition to ash melting temperature of the Ukrainian corn stover samples is uncertain yet.

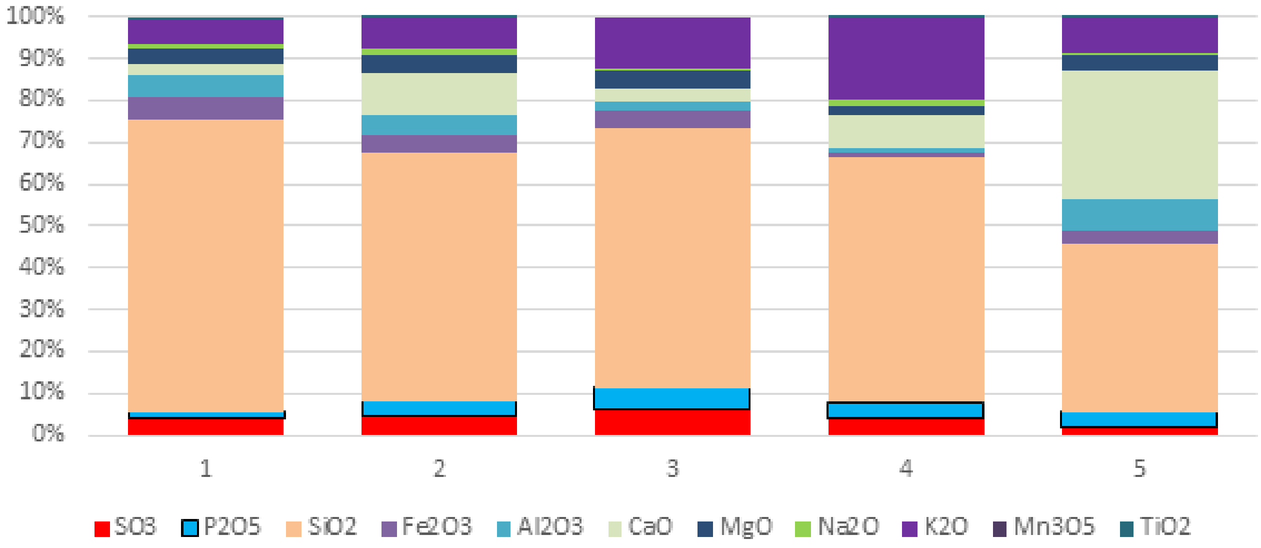

Fig 4. Ash chemical composition

3.4. Fertilization value

Fig. 5 shows the distribution of macronutrients of the Ukrainian corn stover samples and average biomass fuels on dry basis (See Table 2).

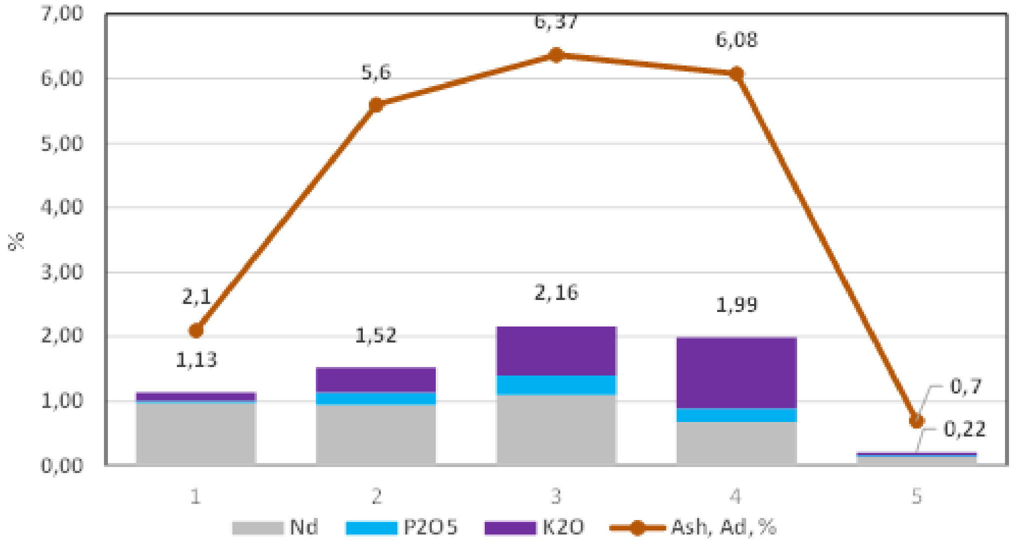

Fig. 5. Biomass macronutrients content

According to study [8], the cost of fertilizers in recalculation on elements are: N – 629 EUR/t, K_2O – 565 EUR/t and P_2O_5 – 1031 EUR/t. Figure 6 shows the fertilization cost of Ukrainian corn stover samples and the average biomass fuels when using the plant as a fertilizer.

Fig. 6. Fertilization cost of biomass, EUR/t on dry basis

In other words, the diagram shows the cost of nutrients that farmer should compensate with fertilizers in case of plant alienation instead of being plowed into the ground.

4. CONCLUSIONS

In general, the corn stover is more complex fuel in comparison to wood due to high ash content and, in some cases, chlorine. The study shows that the samples of corn stover of Ukrainian origin have elemental composition similar to agricultural biomass. However, the chlorine concentration is noticeably lower than the average value of agro fuel and is close to average value of pine chips. Relatively low chlorine content plays important role in preventing corrosion of steel elements.

The ash melting temperatures of the Ukrainian corn cob and stalk samples are 170–270 ^{o}C higher than average agricultural biomass and equal to woody biomass. The high ash melting temperatures tails a better combustion performance and opportunity to use traditional wood-fired boilers for corn stover combustion.

The agricultural biomass usually has a high content of macronutrients that are used in agriculture. A farmer should be reimbursed in case of plant alienation for fuel instead of being digged into the ground. The fertilization value of the Ukrainian corn stover samples is 7.2–10.1 EUR per dry ton.

REFERENCES

1. T. ZHELIEZNA, G. GELETUKHA Prospects for the use of agricultural residues for energy production in Ukraine, UABio Position Paper N7, February 2014.
2. LECKNER, B. and KARLSSON, M., Gaseous emissions from circulating fluidised bed combustion of wood. *Biomass and Bioenergy*, 1993, vol. 4, no. 5, pp 379-389.
3. KILPINEN, P. Kinetic modelling of gas-phase nitrogen reactions in advanced combustion processes, 1992, Report 92-7, *PhD thesis*, *Abo Akademy University*, Abo, Finland.
4. MICHAL HOLUBCIK, JOZEF JANDACKA, MILAN MALCHO ASH Melting Temperature Prediction From Chemical Composition Of Biomass Ash, ISSN 1848-0071, *Faculty of Mechanical Engineering*, *University of Žilina*, Žilina, Slovakia.
5. J. van Soest, J. Renirie, S. Moelchand, A. van der Meijden and J. Plijter New Insights in the Ash Melting Behavior and Improvement of Biomass Energy Pellets Using Flour Bond, 2011, *Journal of Energy and Power Engineering*, no 5, pp. 685-691.
6. WANDA WILCZYēSKA-MICHALIK1*, RENATA GASEK1, MAREK MICHALIK, Mineral and chemical composition of the biomass ash. Goldschmidt 2012 Conference Abstracts.
7. David D. Tarkalson, Brad Brown, Hans Kok, and Dave L. Bjorneberg, Impact of Removing Straw from Wheat and Barley Fields: A Literature Review <http://eeca-ru.ipni.net/article/EECARU-2184> .
8. S. DRAGNEV, T. ZHELIEZNA, G. GELETUKHA Opportunities For Harvesting By-Products Of Grain Corn For Energy Production In Ukraine, UABio Position Paper N 16 April 06, 2016.

CYSENI 2017, May 25-26, Kaunas, Lithuania
ISSN 1822-7554, www.cyseni.com

THE EVALUATION OF LITHUANIAN HOUSEHOLDS’ WILLINGNESS TO PAY FOR MICROGENERATION TECHNOLOGY

Ilona Ališauskaitė-Šeškienė,
Lithuanian Energy Institute
Breslaujos 3, Kaunas, LT-44403 – Lithuania
E-mail: seskiene@lei.lt

ABSTRACT

Trying to find the right balance between economic, social and environmental aspects of sustainable development is not easy. However, scientists agree, assessment of households’ willingness to pay (WTP) can be very useful tool for planning the development of renewables in communities. This method stands out because of its’ ability to reflect the preferences of energy consumers towards various renewable energy sources (RES) technology, i.e., it calculates the financial contribution people are willing to make in order to prevent or remedy environmental damage. Most of existing research generally supports that people are willing to pay extra for renewable energy nonetheless, zero WTP or negative WTP may exist as well. Negative WTP indicates respondents should be compensated in order to choose to use a product with the particular attribute, while zero WTP means respondent does not have to be paid for using such products nor is he willing to sacrifice to procure a good. In this paper the research, which adopted choice experiment approach, has been completed on WTP of individual houses owners’ for particular RES technology in Lithuania. The selected RES technology, namely microgeneration technology, comprised of solar photovoltaic, biomass boilers, solar thermal and micro-wind. Study has shown Lithuanian households have mostly negative WTP for selected microgeneration technology.

Keywords: renewable energy sources (RES) technology, microgeneration technology, choice experiment, willingness to pay (WTP)

INTRODUCTION

Many factors need to be taken into consideration when investing in a renewable energy technology and lessons can be learnt from sustainable development when selecting the optimal solution for supplying clean energy – not all renewable energy technologies may always provide the most sustainable option, bearing in mind certain specific area [1]. The important goal is trying to find the right balance between economic, social and environmental aspects of sustainable development, which together act as guiding principles to ensure that factors which are considered for a renewable energy technology is relevant for sustainable development [1].

A strong correlation between environmental attitude and ecological behavior intention has been established – it is important to know the attitudes of energy consumers since their attitudes are the foundations of their resulting behavior [2–3]. According to [3], in democratic societies, inputs to the planning and decision-making process include not only expert opinions, but public feelings and perceptions as well, the problem being that rational individual behavior may conflict with the common good and prevent the efficient use of public resources. “Nowadays most of the citizens expect, more than in the past, their government or administration not only to warn them of major environmental–energy–climate problems, but also to prepare them for enacting timely policy responses” [4].

Consequently, not only societies need sustainability assessment of renewable energy technologies – it needs to assess the trade-offs between alternative sources in order to choose the most beneficial one [5]. Although, over the years, there has been an increase in public awareness of the adverse environmental effects of the consumption of fossil fuels [3], nonetheless, in order to make socially optimal renewable energy investment, external costs and benefits of renewables, which may appear, need to be taken into account [6]. What is more, some benefits and costs of renewables and their technology do not have monetary values, therefore, different economic valuation techniques were derived in order to evaluate them [7]. Ultimately, societies must develop a good understanding of the environmental impacts and especially, the marginal rate of valuation between different kind of energy sources and between different types of renewables [5].

Assessment of willingness to pay (WTP) “calculates the financial contribution people are willing to make in order to prevent or remedy environmental damage” [3]. Although this integrated assessment method answers the question, what premium are energy customers willing to pay for environmentally friendly energy, it “should not be interpreted as actual willing to pay but rather as an index of consumer’s relative preferences for certain outcomes over other outcomes” [8]. Households satisfaction with renewable energy and WTP have significant impact on state policies aiming to promote renewable energy sources [9] [10] [11]. According to [10], “given that renewable energy use is in an early stage and that it can influence the consumer behavior in a way to increase the market performance, development of new strategies orientated to sustainable energy consumption can have a positive impact if properly explained in terms of consumer demand.” Furthermore, as consumers become more environmentally conscious and willing to pay a higher price for green energy – utilization of RES becomes ever more widespread [2]. And once the benefits of renewables will be recognized by a larger percentage of population – cost of renewable energy technologies will drop [7]. Moreover, because many renewable energy resources throughout Europe are concentrated by their nature in remote areas, WTP can be also used as a tool for planning the development of renewables in remote communities [12]. Such remote communities, with low population densities, limited conventional energy sources, lack of infrastructure, low levels of economic activity, physical access constraints and long distances to external markets, could benefit through the generation of local income and employment while using a strategy to meet their energy demand as much as possible from local renewable sources [12].

The aim of this paper is to evaluate Lithuanian households’ WTP for microgeneration technologies. This kind of research, which has never been conducted before in Lithuania, adopted choice experiment approach, and was completed on WTP of individual houses owners’ for particular RES technology comprised of solar photovoltaic, biomass boilers, solar thermal and micro-wind.

1. WTP METHOD USED IN SUSTAINABILITY ASSESSMENT

Assessment of WTP for climate change mitigation measures is one the main aspects currently world’s focus is concentrated on [13]. In general, consumers’ voluntary renewable energy purchases through green power marketing are highly important, when it comes to policy mechanisms that can support renewable generation sources [14]. In many countries energy production is based on a variety of energy sources (including solid mineral fuels, oil, gas, nuclear power and RES) and is an important contributor to economic development [3]. Examinations of voluntary contributions for the energy generated from RES have already received a lot of attention [15]. “As renewable energy activities grow and require more funding, the tendency in many countries is to move away from methods that let taxpayers carry the burden of promoting renewables, towards economic and regulatory methods that let energy consumers carry the burden” [16]. Concept that consumers share responsibility for pollution and its cost has been increasingly accepted [17]. In some jurisdictions, the prices of many energy resources have increased over the last decades, in part to account for environmental costs [17].

As any other method, WTP has its’ own advantages and disadvantages. Based on the previously examined studies, author has concluded a table:

Table 1. Advantages and disadvantages of WTP method

Types	**Cited authors**	**Advantages**	**Disadvantages**
Willingness to pay (WTP)	[3] [4] [5] [6] [9] [10] [11] [12] [30] [31] [32] [33]	• Takes into account attitudes of energy consumers • Takes into account external costs and benefits of renewables • Have significant impact on state policies aiming to promote RES • Helps energy consumers, households, to become more conscious • The larger percentage of population recognizes the benefits of renewables, the more quicker cost of renewable energy will drop • Can be used as a tool for planning renewables in remote communities.	• Significant differences can be found between values derived from two different WTP methods while applying them to the same target group of respondents

2. MICROGENERATION TECHNOLOGIES

Social acceptance of renewable energy innovation has often been discussed in the context of large renewable technology projects, acceptance having been seen as rather passive consent by the public [18]. However, according to [18], renewable energy technologies, applied in households, do not only impact in individuals' environments, e.g. noise or spoiling the landscape, but also necessitate their active acceptance in terms of the willingness to install these technologies in their homes. These particular technologies, microgeneration technologies, are defined as renewable energy generation technologies that are installed in households, such as [19–20]:

- solar photovoltaic (PV) – solar roof panels, comprising thin layers of semiconductor material, convert sunlight to electrical energy. Output is determined by the area of the panels, their efficiency, and the brightness of natural light available;
- micro wind – a roof or pole mounted turbine converts kinetic energy of wind to electrical energy. Output is determined by turbine size and wind speed;
- solar thermal – a roof, shade structure or other location absorb solar energy mounted collectors (panels), heat water or other fluids, and can also power solar cooling systems. Solar thermal systems differ from PV systems, which generate electricity rather than heat. Output is determined by the area of the panels, their efficiency, and the brightness of natural light available;
- heat pumps – thermal roof panels use sunlight to heat water. Output is a function of available sunlight, panel area and panel efficiency;
- biomass boilers and pellet stoves – usually wood chips or pellets, and used for space heating and hot water needs. Requires space for boiler and fuel storage.
- small scale CHP – this concept means combined heat and power generation systems with electrical power less than 200 kW [21]. Although technically CHP is not a "renewable", it is assigned to renewable technology because of its' potential to save significant amounts of energy and reduce carbon emissions [22]. This type of technology can be divided into mini-CHP and micro-CHP. Mini-CHP is taken to be in the range of a few kilowatts to 100 kW and may serve a group of dwellings or a commercial site, whereas micro-CHP is suitable to serve a single dwelling and has no agreed size limit, but 10 kW of electrical power might be appropriate [21].

Nowadays microgeneration technology is still the growing trend [23]. After all, balancing market depends on the behavior of market participants [23]. Microgeneration at the level of households is an interesting subject because of its large potential, the possibly limited control by market players and grid operators and the current lack of continuous metering of residential and small business consumers [23].

3. ESTIMATION LITHUANIAN HOUSEHOLDS' WTP

In this paper the research, which adopted choice experiment approach, has been completed on WTP of individual houses owners' for particular RES technology in Lithuania. The selected RES technology, namely microgeneration technology, comprised of solar photovoltaic, biomass boilers, solar thermal and micro-wind. Household owners were presented with the sets of alternative combinations of attributes of particular microgeneration technologies and asked to choose the one more preferred alternative form each set of two. Repeated choices of household owners from sets of alternatives revealed the trade-offs they are willing to make between attributes and thus between microgeneration technologies [19]. The attributes included were (i) installation costs, (ii) monthly energy bill, (iii) length of the warranty period, (iv) inconvenience of system, and (v) degree of possibility for sharing. Each of them had four levels. As regards the inconvenience of system, the four levels correspond to special circumstances associated with different technologies of energy generation, i.e. climatic conditions and the time of the day (daylight requirement), the need for additional fuel, generation of noise during the operation, and none of these. The attribute of sharing possibility captures the preferences of inhabitants in regards to cooperative use of renewable energy sources. Table 2 gives the options possible for each attribute.

Table 2. Attributes and their levels used in the discretionary choice experiment

Attribute	Level 1	Level 2	Level 3	Level 4
1. Installation costs, EUR	1500	3000	4500	6500
2. Monthly energy bill, EUR/month	16	30	35	38
3. Length of the warranty period, years	2	5	10	13
4. Inconvenience of system	Weather	Fuel	Noise	None
5. Degree of possibility for sharing	Very low	Low	Moderate	High

In many cases results of studies of WTP vary widely, which, according to [24], is the result of different methodologies and intermittent preferences of customers [24–25]. And although most of existing research generally supports that people are willing to pay extra for renewable energy [26] [27–28], zero WTP or negative WTP may exist as well. Negative WTP indicates respondents should be compensated in order to choose to use a product with the particular attribute [29], while zero WTP means respondent does not have to be paid for using such products nor is he willing to sacrifice to procure a good.

In this research in order to account for differences in tastes, a mixed logit model was employed. Installation costs were chosen as a fixed parameter thus ensuring higher stability of the model and more reasonable estimation of the WTP. The remaining parameters were included as random ones assuming normal distribution. Installations costs, monthly bill, and warranty period entered into the model as continuous variables, whereas operation requirements and degree of sharing – as dummy variables (no special requirements for operation and very low possibility for sharing were taken as base levels). And the estimation of mixed logit model with opt-out (when respondent has a opportunity not to choose any of given answers) allowed for the dependent variable was carried out.

Table 3 presents the results of survey – the increase in monthly bill by 1 EUR requires decrease in installation costs of 90 EUR on average in order to maintain the same level of utility in case of opt-out model. The increase in warranty period of one year is worth 241 EUR on average. The respondents were eager to pay about 3000 EUR in order to avoid noise related to operation of the energy generation facility. Note that the confidence intervals for the aforementioned attributes indicated significant WTP, whereas the estimates for possibility of share include zero values. This suggests the respondents attributed no clear value to possibility for sharing of the energy generation.

Table 3. Estimates of the WTP for different attributes

	Bill (EUR)	Warranty (years)	Requirements for operation			Possibility for sharing		
			Weather	Fuel	Noise	Low	Moderate	High
Opt-out								
$E(WTP_k)$	-90	241	-1219	-1716	-2973	170	-115	234
CI	-107	161	-1919	-2315	-4144	-507	-827	-368
	-73	322	-518	-1117	-1802	848	598	836

Notes: (i) *CI* stands for the 95% confidence interval based on the delta method; (ii) Requirements for operation are compared to case of no requirements; (iii) Degrees of possibility for sharing are compared to very low possibility.

4. CONCLUSIONS

Although microgeneration technology is still the growing trend and most of existing research generally supports that people are willing to pay extra for renewable energy, in Lithuania, however, this is not the case. Study has shown Lithuanian households would pay extra only for warranty of selected microgeneration technology, comprised of solar photovoltaic, biomass boilers, solar thermal and micro-wind, however in all other cases they prefer to be compensated in order to choose that particular technology with particular attribute. However this was only the pilot study and further investigation needs to be taken. Nevertheless study proved it is possible to conduct Lithuanian households attitudes towards renewable energy and measures should be taken to help improve users' perspective towards them.

REFERENCES

1. LUONG, S., LIU, K., & ROBEY, J. (2012). Sustainability Assessment Framework for Renewable Energy Technology. *Technologies for Sustainable Built Environment Centre. Reading: Informatics Research Centre*, 1-8.
2. EK, K. (2005). Public and private attitudes towards "green" electricity: the case of Swedish wind power. *Energy Policy, 33*(13), 1677-1689.
3. STIGKA, E. K., PARAVANTIS, J. A., & MIHALAKAKOU, G. K. (2014). Social acceptance of renewable energy sources: A review of contingent valuation applications. *Renewable and Sustainable Energy Reviews, 32*, 100-106.
4. ZOGRAFAKIS, N., SIFAKI, E., PAGALOU, M., NIKITAKI, G., PSARAKIS, V., & TSAGARAKIS, K. P. (2010). Assessment of public acceptance and willingness to pay for renewable energy sources in Crete. *Renewable and Sustainable Energy Reviews, 14*(3), 1088-1095.
5. KOSENIUS, A., & OLLIKAINEN, M. (2013). Valuation of environmental and societal trade-offs of renewable energy sources. *Energy Policy, 62*, 1148-1156.
6. BERGMANN, A., HANLEY, N., & WRIGHT, R. (2006). Valuing the attributes of renewable energy investments. *Energy Policy, 34*(9), 1004-1014.
7. MENEGAKI, A. (2008). Valuation for renewable energy: a comparative review. *Renewable and Sustainable Energy Reviews, 12*(9), 2422-2437.
8. WOOD, L. L., KENYON, A. E., DESVOUSGES, W. H., & MORANDER, L. K. (1995). How much are customers willing to pay for improvements in health and environmental quality? *The Electricity Journal, 8*(4), 70-77.
9. GEORGESCU, M., & HERMAN, E. (2014). Social corporate responsibility regarding household consumer satisfaction with the electric power supply services. *Amfiteatru Economic, 16*(35), 123-137.

10. LUNGU, C. I., DASCALU, C., CARAIANI, C., & BALEA, E. C. (2014). Econometric approach of the scenarios regarding the impact of the consumer's empowerment and companies' responsibility for environment sustainability on the electricity market performance. *Amfiteatru Economic, 16*(35), 187-200.
11. STREIMIKIENĖ, D., & MIKALAUSKIENE, A. (2014). Lithuanian consumer's willingness to pay and feed-in prices for renewable electricity.
12. HANLEY, N., & NEVIN, C. (1999). Appraising renewable energy developments in remote communities: the case of the North Assynt Estate, Scotland. *Energy Policy, 27*(9), 527-547.
13. ŠTREIMIKIENĖ, D., & ALIŠAUSKAITĖ-ŠEŠKIENĖ, I. (2014). Lietuvos gyventojų pasirengimo mokėti už atsinaujinančius energijos išteklius vertinimas. *Energetika, 60*(3).
14. WISER, R., PICKLE, S., & GOLDMAN, C. (1998). Renewable energy policy and electricity restructuring: a California case study. *Energy Policy, 26*(6), 465-475.
15. ZORIĆ, J., & HROVATIN, N. (2012). Household willingness to pay for green electricity in Slovenia. *Energy Policy, 47*, 180-187.
16. TURKENBURG, W. C., BEURSKENS, J., FAAIJ, A., FRAENKEL, P., FRIDLEIFSSON, I., LYSEN, E., . . . SINKE, W. C. (2000). Renewable energy technologies. In J. Goldemberg (Ed.), *World energy assessment: energy and the challenge of sustainability* (pp. 219-272) United Nations Development Programme.
17. DINCER, I. (2000). Renewable energy and sustainable development: a crucial review. *Renewable and Sustainable Energy Reviews, 4*(2), 157-175.
18. SAUTER, R., & WATSON, J. (2007). Strategies for the deployment of micro-generation: Implications for social acceptance. *Energy Policy, 35*(5), 2770-2779.
19. SCARPA, R., & WILLIS, K. (2010). Willingness-to-pay for renewable energy: Primary and discretionary choice of British households' for micro-generation technologies. *Energy Economics, 32*(1), 129-136.
20. WILLIS, K., SCARPA, R., GILROY, R., & HAMZA, N. (2011). Renewable energy adoption in an ageing population: heterogeneity in preferences for micro-generation technology adoption. *Energy Policy, 39*(10), 6021-6029.
21. STREIMIKIENE, D., & BALEŽENTIS, T. (2013). Multi-criteria assessment of small scale CHP technologies in buildings. *Renewable and Sustainable Energy Reviews, 26*, 183-189.
22. CLAUDY, M. C., MICHELSEN, C., O'DRISCOLL, A., & MULLEN, M. R. (2010). Consumer awareness in the adoption of microgeneration technologies: An empirical investigation in the Republic of Ireland. *Renewable and Sustainable Energy Reviews, 14*(7), 2154-2160.
23. VAN DER VEEN, REINIER AC, & DE VRIES, L. J. (2009). The impact of microgeneration upon the Dutch balancing market. *Energy Policy, 37*(7), 2788-2797.
24. KRAEUSEL, J., & MÖST, D. (2012). Carbon Capture and Storage on its way to large-scale deployment: Social acceptance and willingness to pay in Germany. *Energy Policy, 49*, 642-651.
25. POORTINGA, W., STEG, L., VLEK, C., & WIERSMA, G. (2003). Household preferences for energy-saving measures: A conjoint analysis. *Journal of Economic Psychology, 24*(1), 49-64.
26. AKCURA, E. (2015). Mandatory versus voluntary payment for green electricity. *Ecological Economics, 116*, 84-94.
27. BORCHERS, A. M., DUKE, J. M., & PARSONS, G. R. (2007). Does willingness to pay for green energy differ by source? *Energy Policy, 35*(6), 3327-3334.
28. NOMURA, N., & AKAI, M. (2004). Willingness to pay for green electricity in Japan as estimated through contingent valuation method. *Applied Energy, 78*(4), 453-463.

29. JAMES, J. S., RICKARD, B. J., & ROSSMAN, W. J. (2009). Product differentiation and market segmentation in applesauce: Using a choice experiment to assess the value of organic, local, and nutrition attributes. *Agricultural & Resource Economics Review, 38*(3), 357.
30. ADAMOWICZ, W., LOUVIERE, J., & WILLIAMS, M. (1994). Combining revealed and stated reference methods for valuing environmental amenities. *Journal of Environmental Economics and Management, 26*(3), 271-292.
31. BOXALL, P. C., ADAMOWICZ, W. L., SWAIT, J., WILLIAMS, M., & LOUVIERE, J. (1996). A comparison of stated preference methods for environmental valuation. *Ecological Economics*, *18*(3), 243-253.
32. ROE, B., TEISL, M. F., LEVY, A., & RUSSELL, M. (2001). US consumers’ willingness to pay for green electricity. *Energy Policy, 29*(11), 917-925.
33. ŠTREIMIKIENĖ, D., & BALEŽENTIS, A. (2014). Assessment of willingness to pay for renewables in Lithuanian households. *Clean Technologies and Environmental Policy*, *17*(2), 515-531.

CYSENI 2017, May 25-26, Kaunas, Lithuania
ISSN 1822-7554, www.cyseni.com

ANALYSIS OF THE APPLICATION OF RENEWABLE ENERGY SOURCES FOR ROAD PUBLIC TRANSPORT

P. Mačiulis
Lithuanian Energy Institute
Breslaujos str. 3, Kaunas, LT-44403 – Lithuania
E-mail: povilas.maciulis@gmail.com

ABSTRACT

The transport sector is one of the major polluter of greenhouse gases and other pollutants. The transition from the use of fossil fuels to renewable energy in transport requires co-ordinated changes and a kind of co-evolution of the transport sector and the energy sector. As alternative fuels compete with conventional fuels for a place in public awareness and acceptance, one of their most visible applications is in public transportation. Buses, shuttles and other type of road public transport, that carry people in large numbers, stand to gain much from using alternative fuels. The transition requires new technologies to be implemented in energy and transport sectors. The required changes depend on the different technology pathway. Coordinated efforts by stakeholders are more likely to occur if there is synergy between these developments and added value. Finding such synergies may help to overcome technical, economical, environmental and institutional barriers. Private investors, technology companies and policy makers need to know what alternatives are identified to accelerate the transformation of road transport towards significantly lower carbon emissions. In this paper is analized three renewable energy technology directions: battery-electric, hydrogen and biofuels.

Keywords: renewable energy in transport, renewable energy sources, public transport

1. INTRODUCTION

The scientific community has reached a agreement that human-induced global climate change will lead to widespread economic and social disruptions in future decades if we do not take immediate steps to diminish its causes. Emissions from the combustion of fossil fuels significantly contribute to climate change by increasing the buildup of greenhouse gases in the atmosphere (Bauen et al., 2009). There is a pressing need to accelerate the development of advanced energy technologies in order to address the global challenges of clean energy, climate change and sustainable development (Battaglia et al., 2008). The transport sector is one of the major polluter of greenhouse gases and other pollutants. Road transport activity and gross domestic product have historically shown a strong correlation, although a slight decoupling has been observed in recent years in industrialised countries (Contestabile et al., 2011). Concern over the negative impacts of global warming, coupled with increasing unease about our nation's dependence on foreign oil has prompted interest in the renewable energy sector and the development of alternatives to fossil fuels (Battaglia et al., 2008). Berger (2015) argue that diesel buses currently dominate the public transport market due to their high productivity, low deployment costs, technological maturity, operational reliability and flexibility. There is a range of alternative fuels and energy carriers that have the potential to be used in the transport system by 2050 and which have the potential to reduce transport‘s greenhouse gases emissions. These include mixing biofuels with conventional fuels, which can be used in conventional wehicles, and alternative energy carriers, such as electricity and hydrogen, which would require potentially significant modifications to powertrains (Skinner, Hodgson, 2010). Many cities and bus operators are struggling with the currently conflicting objectives of shifting to zero emission public transport while keeping operational flexibility and maintaining budgets under control (Berger, 2015).

The European Union has invested much effort and resources into developing and implementing policies and initiatives to enable a clean, secure and de-carbonised energy future for our communities, especially for our transport systems. The European Union has set itself ambitious targets for reducing emissions in the years ahead. For 2050, EU leaders have defined the goal of reducing Europe's greenhouse gas emissions by 80% compared to 1990 levels (Bauen et al., 2009). Promoted by trends such as urbanisation, a shift in societal values towards more sustainability and the need to increase energy security as well as a more holistic perspective on costs, transition in public transport is placed firmly on the agenda of national and local governments in Europe (Berger, 2015). Transition has to be planned to avoid disruption. It also underlines the importance of investing in new technologies and the need for policy incentives, such as green procurement, to stimulate market introduction of clean technologies (Contestabile et al., 2011).

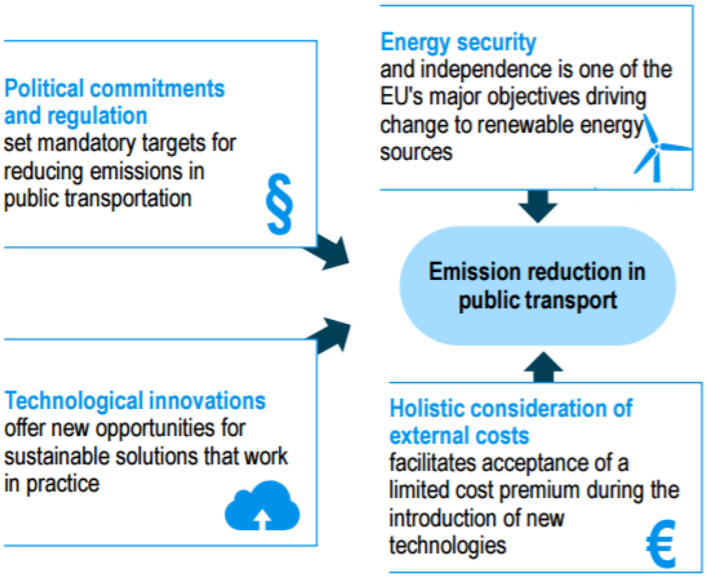

Fig. 1. Trends supporting emissions reduction in public transport (Berger, 2015)

Private investors, technology companies and policy makers need to know what alternatives are identified to accelerate the transformation of road transport towards significantly lower carbon emissions (Skinner, Hodgson, 2010). National and espacially local governments and decision-makers need to make sustainable and cost-efficient decisions that on one hand contribute to global, European Union and national goals and on the other hand fulfil the specific requirements of each individual city (Nesterova, Verbeek, 2013). There is no doubt that Europe and the world are facing a paradigm change in the future as we move from our present fossil fuel based energy systems to a new energy and fuel mix which will include several alternatives: battery-electric, hydrogen and biofuels. The aim of this article is to compare three different renewable energy technology application for road public transport.

2. BATTERY-ELECTRIC

There is still research needed to explore the best combination of fuel type and vehicle concept for a given condition, location and user profile. An over-all assessment has to consider factors ranging from greenhouse gases emission, air pollution and energy security to fundamental production items, as well as the availability and reuse of raw materials in well-towheel studies and life cycle assessments. In most cases, battery electric vehicles powered by regenerative energy are obviously the best option (Jacobson, 2009). Electric buses support the transition process towards a more sustainable public transport. The different electric bus systems in the market use basically the same traction system to convert electricity into propulsion. The supply of electricity is the defining difference between them. A simple and proven concept is for example the trolley bus. It is continuously connected to overhead wires, which cover the energy demand at any time. However, the overhead wire system causes high invest costs and maintenance efforts (Brunton, 2000).

The electrification of road transport establishes yet another link between the energy and mobility sectors as well as a new domain of services in regards to the management of Electric Mobility as for the first time it brings together utilities and grid operators with the makers and users of the automobile (ERTRAC, 2009).

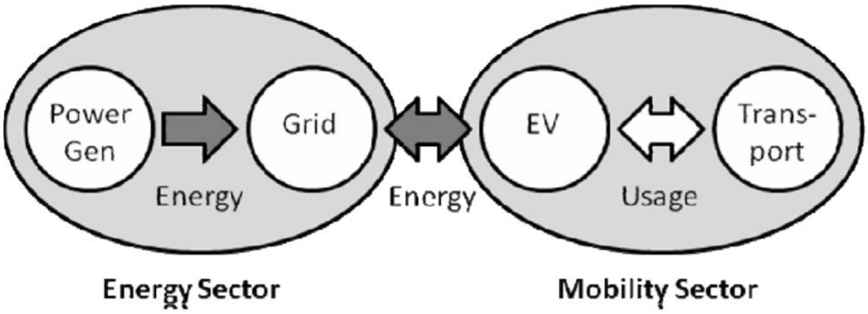

Fig. 2. Electrification of road transport links the energy and mobility sectors (ERTRAC, 2009)

A shift to an electric bus fleet necessitates an understanding of the technology. The design of an electric bus and the necessary infrastructure depend on the application scenarios. The battery size depends on the drive cycle, terrain features and other operating conditions. The battery system preference depends on the operating conditions of the vehicle (Contestabile et al., 2011). The cost is determined by the bus and the battery size, battery type and carrying capacity. Having a fundamental understanding of the technology landscape and application scenarios is important. Understanding future developments and industry expectations will give a sense of the direction in which the electric bus sector is heading (Lund, Kempton, 2008).

For charging of electric vehicles a public and private infrastructure is needed. Public parking structures or lots close to residential areas, the work place or a shopping mall as well as private garages will necessarily be equipped with charging stations, also curb side solutions must be found for charging "on the go". The deployment of electric vehicles will thus require major investments in the charging infrastructure for the electric vehicles in the city, in public and public spaces, e.g. bus depots. (ERTRAC, 2009)**.** There are two types of charging technologies:

- Conductive charging Conductive charging requires a physical connection between the electric vehicles and electric vehicle supply equipment at the charging station. This technology has been historically the most popular option for accessing grid electricity for various charging applications. The automotive standard voltage plugs and sockets interface between the distribution lines and the on-board sockets. All battery systems currently use the conductive charging technology (Antti, 2015).
- Inductive charging uses an electromagnetic field to enable the exchange of energy between the electric vehicles and the charging station. In this method, no physical contact is needed between the energy source and the vehicle. Inductive charging works by using an induction coil placed within a charging station to create an electromagnetic field. A second induction coil, placed on the electric vehicles, takes power from the electromagnetic field and converts it into an electrical current that is used to charge the on-board battery (Nizam, 2013).

''Vehicle-to-grid'' (V2G) power technology is one of the many energy storage technologies, which may be part of making a flexible energy system that can better utilise fluctuating renewable energy sources. V2G is built on top of plug-in electric drive vehicles (EVs), which already displace petroleum by using electricity as the carrier for transportation energy. V2G refers to adding the capability to deliver power from the vehicle to the grid, but ''V2G'' is also used to imply that power flow, whether to or from the vehicle, is controlled in part by needs of the electric system, via a real-time signal (Lund, Kempton, 2008). The most important role for V2G may ultimately be in emerging power markets to support renewable energy. The two largest renewable sources likely to be widely used in the near future, photovoltaic (PV) and wind turbines, are both intermittent. At low levels of penetration, the intermittency of renewable energy can be handled by existing mechanisms for managing load and supply fluctuations (Kempton, Tomic, 2005) The vehicle to grid concept, however, goes well beyond charging and paying. The EVs' batteries can be integrated as a buffer for the fluctuating influx of electricity from renewable energy sources which would optimize the efficiency of the whole system. This requires the routing of energy and power to be bi-directional, from the grid to the vehicle and vice versa, and it calls for smart control devices that adapt the batteries' state of charge to both the anticipated driving range needs of the user and to the stability requirements of the grid. (ERTRAC, 2009).

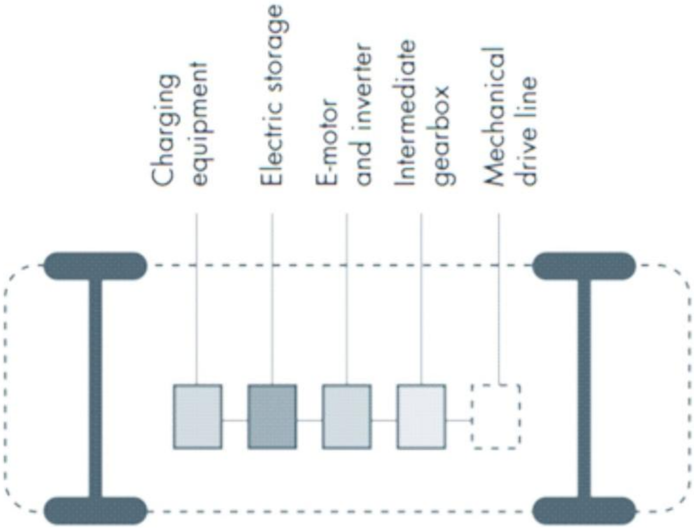

Fig. 3. Example of electric powertrain (Nesterova, Verbeek, 2013)

The deployment of electric vehicles in the network will require the provision of the supporting infrastructure and systems, and their integration in the full mobility system in a wide scale. Rail public transport that uses electric energy provides sustainable mobility solutions as well and will growingly be an alternative to private vehicles in the future (Kempton, Tomic, 2005). Given the limitations of the electric vehicle, its intelligent integration into the existing urban transport infrastructure is essential. Intelligent ICT solutions enabling proper traffic management, managing the change between different modes of electric transport or giving travel advice will optimize the efficiency of the transport system, make it conveniently useable, and thus acceptable for the public. This contribution therefore will cover all relevant modes of possibly electric transport: individual motorized transport and public transport vehicles for urban delivery and logistics other vehicles, in particular public fleets of vehicles. (ERTRAC, 2009).

3. BIOFUELS

Biofuels – liquid and gaseous fuels derived from organic matter – can play an important role in reducing CO2 emissions in the transport sector, and ehancing energy security (IEA, 2011). Biofuels can be produced from a wide range of biomass feedstock. Liquid biofuels technically can be used for propulsion in all transport modes and can be used with existing power train technologies, for certain biofuels with minor technical modifications, and existing re-fuelling infrastructures in various blending ratios depending on biofuel types (Malca, Freire, 2010). Biofuels are also the primary route for the decarbonisation of synthetic fuels, methane and LPG (Pringle, 2011). By 2050, biofuels could provide 27 percent of total transport fuel and contribute in particular to the replacement of diesel (IEA, 2011).

Given the right conditions, biofuels have been shown to have a great potential to reduce greenhouse gases emissions. Safeguard long-term ecological sustainability is one of the reasons why biofuels have been introduced in the first place. (Bauen et al, 2009). The projected use of biofuels could avoid around 2.1 gigatonnes of CO2 emissions per year when produced sustainably (IEA, 2011). The criteria to measure the sustainability of any given biofuel must cover a wide range of environmental and social factors and include metrics on resource use efficiencies as well as direct and indirect environmental impacts. Criteria example – total energy inputs versus outputs, crop yields versus inputs and etc. (Pringle, 2011). Production and use of biofuels can also provide benefits such as increased energy security, by reducing dependency on oil imports, and reducing oil price volatility. In addition, biofuels can support economic development by creating new sources of incomein rural areas. IEA (2011). The potential of biofuel production from both traditional crops and energy crops is determined by the area of land, which can be made available, the yield of that land, and the use of biomass and co-products in other sectors (Malca, Freire, 2010). There are two types of biofuel production: first and second generation.

First generation biofuels are made from biomass based on agricultural feedstock. Examples of feedstock for production of ethanol are corn, sugar beets, wheat and sugar cane. Different types of biodiesel are made from rapeseed, sunflower, soy beans etc. Biogas is methane produced in water treatment plants or from waste. Fossil fuel natural gas also consists of methane and therefore biogas could be used in natural gas vehicles or it could be injected into existing natural gas grids (Larson, 2006).

Second generation biofuels are produced from the whole of the plant, not just the sugar or oil-rich parts. They can be produced from biomass. These biofuel technologies are not yet commercially viable (Pringle, 2011). In general terms these are biofuels that have a high greenhouse gas emission reduction potential and have no adverse effects on food prices, biodiversity and labour circumstances. For example, these biofuels are made from non-food cellulose feedstock such as waste wood, straw and cellulose based waste (Larson, 2006). The second generation of ethanol can also be made from chemical treatment of cellulose to extract sugar to make ethanol. Hydrated biooils, for instance, is a new product that can replace diesel. It is based on different types of vegetable oil and waste animal fat (Malca, Freire, 2010).

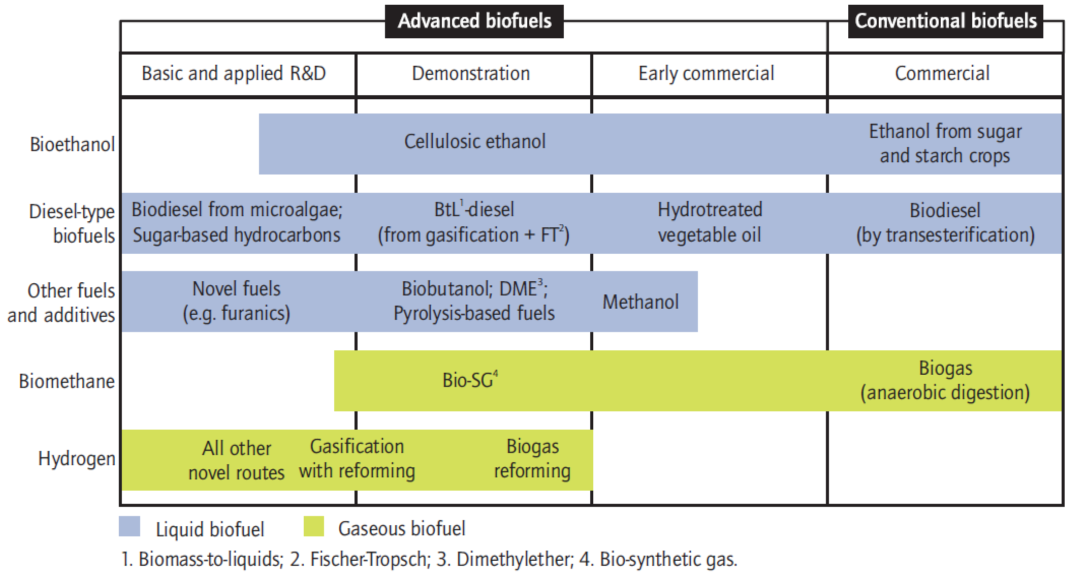

Fig. 4. Commercialisation status of main bioful technologies (Bauen et al., 2009)

There are few important advantiges of biofuel. only slight motor modifications of the diesel bus are necessary in order to use biofuels and to achieve significant reduction in emissions. (Pringle, 2011). Such fuels have the advantage that they can be used in existing vehicles, although in some instances modifications are required, particularly with higher blends or pure biofuels. (Skinner, Hodgson, 2010) The use of biogas would clearly depend on their being vehicles available that could use natural gas, either in its compressed (CNG) or liquefied (LNG) form. In road transport, a limited but increasing number of natural gas vehicles are in use, but these are generally seen as a short-term option that has the potential to pave the way for increased use of biomethane. Pringle, D. (2011), Biogas can be produced through anaerobic digestion of feedstocks such as organic waste, animal manure and sewage sludge, or from dedicated green energy crops such as maize, grass and crop wheat (IEA, 2011).

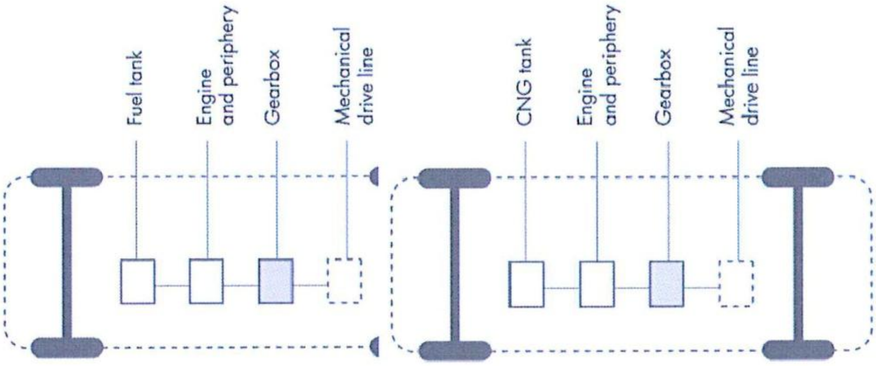

Fig. 5. Example of diesel powertrain (on the left) and CNG powertrain (Nesterova, Verbeek, 2013)

Biogas is used as transportation fuel in a number of countries, but in Europe it has only reached a major breakthrough in Sweden. All of the biogas plants in Sweden that are in the planning or construction phase will be equipped with possibilities to deliver a biogas that is upgraded to natural gas quality, either for direct use as vehicle fuel or for injection into the natural gas grid (Jönsson, Persson, 2003). In Sweden, renewable fuels now make up two thirds of total fuel consumption of buses in public transport, new statistics show. Biodiesel is the most popular choice of renewable fuel, followed by biogas and ED95 ethanol (Malca, Freire, 2010). When diesel buses are adjusted to use biofuels, each type and blend of biofuel requires specific minor motor modifications. Therefore buyers must have a clear initial understanding of what kind of biofuel or biofuel blend will be used in the specific bus. Same filling infrastructure as for diesel can be used: widespread presence of filling stations across Europe. In some cases a special tank for biofuels may be needed. Same filling infrastructure as for diesel can be used but specific pump for bioethanol has to be installed as well as larger storage tank (Nesterova, Verbeek, 2013). For many biofuels there are concerns about availability and wider sustainability impacts. With respect to liquid biofuels, there are concerns about the potential competition with food crops for both land and water resulting from an increased demand for certain feedstocks (Skinner, Hodgson, 2010).

4 HYDROGEN

Hydrogen is the most abundant element on the earth although it is not found in nature in its energy rich molecular state – H2. Hydrogen is the simplest element. Each atom of hydrogen has only one proton. The sun is basically a giant ball of hydrogen and helium gases. In the sun’s core, hydrogen atoms combine to form helium atoms (called fusion process) and gives off radiant energy. This radiant energy sustains life on earth as it drives the photosynthesis in plants and other living systems, and is stored as chemical energy in fossil fuels (Berry, 1996). Hydrogen has been used as an industrial gas for more than 100 years. The direct use of hydrogen for energy purposes is mainly for power and heat generation. Today this sector only plays a minor role. This is likely to change over the coming decades when hydrogen may become an energy carrier as important as electricity and may even be used to buffer store intermittent, renewable energy (Herzog et al., 2000).

Hydrogen is a not a resource for example like petroleum. Hydrogen is an energy carrier that must be manufactured from a primary energy resource. It can be produced from natural gas or coal at a cost on par with the price of petroleum (Barbier, 2001). Hydrogen is an energy carrier, meaning it can store and deliver energy in a useable form. It can be produced using abundant and domestic energy resources including fossil, nuclear, and renewables (Berger, 2015). Hydrogen can be produced with electricity from 100% renewable energy sources. Hydrogen is relatively inexpensive to manufacture at large scales (Sandman, 1998). Steam reforming of methane is currently the cheapest and most common way to manufacture hydrogen. Electricity can be used to create hydrogen via electrolysis. Emissions from steam methane reforming are essentially limited to carbon dioxide, but even these could be mitigated by sequestering the carbon dioxide underground in geological formations (Skinner, Hodgson, 2010). Due to its low volumetric energy density, hydrogen is stored and transported as a compressed gas (CGH2 or GH2) or in liquefied state (LH2) at about - 253 °C. Hydrogen’s low boiling point makes liquefaction very energy intensive but decreases transportation costs. It is an energy carrier that can be derived from a wide range of energy sources, both fossil and renewable (Herzog et al., 2000).

Hydrogen can play a central role as a potential alternative and clean transport energy carrier producing zero CO2 emissions at the exhaust. The contribution of fuel cell vehicles will depend on developments in hydrogen and fuel cell technologies, as well as in electrical energy storage for competing pure electric wehicle. When fuel cells are used to power a vehicle, the only output from the tailpipe is water. There are no greenhouse gas or criteria emissions. Fuel cell vehicles also promise more than two times the efficiency of traditional combustion technologies – for vehicles, this can mean a more than 50 percent reduction in fuel consumption compared to a conventional vehicle with a gasoline engine (Berger, 2015). Skinner, Hodgson (2010) emphasize that hydrogen fuel cells offer significant potential to reduce greenhouse gases emissions from road transport in the longer term, although, as with other potential alternative fuels and energy carriers, this depends on the way in which the hydrogen is produced. Berger (2015) stated, that hydrogen as a road fuel yields significant potential for carbon neutrality on a well-to-wheel basis along the entire hydrogen value chain, including production and means of delivery. Operating fuel cell buses can be achieved with zero CO2 emissions along the entire hydrogen value chain. By using hydrogen produced from renewable energy sources only, one standard fuel cell bus would save approximately 800 tonnes of CO2 in its lifetime of 12 years compared to a conventional diesel bus (Herzog et al., 2000).

Hydrogen buses are electric buses that feature a longer lifetime and lower maintenance costs than diesel buses in the long run as abrasion is expected to be lower. The fuel cell converts chemical energy of hydrogen into electrical energy. Several complementary zero emission powertrains are currently available in the market (Berger, 2015) Three types of bus technologies running on hydrogen are already available on the market: fuel cell engine without battery, hydrogen internal combustion engine and combined hydrogen with electric battery (Farrella et al., 2003). Hydrogen can be stored in four main ways: compressed, as a liquid, in hydride form bound to metals, or on the surface of solid porous materials or carbon nano-tubes. One of the positive characteristics of hydrogen is that it disperses very quickly, meaning that hydrogen concentrations under normal pressure dissolve to incombustible levels very quickly (Sandman, 1998). This also means that under ambient air pressure hydrogen has very little energy density per unit of volume compared to other vehicle fuels. Hydrogen also rises very quickly and therefore is less of a threat outdoors (Herzog et al., 2000). Skinner, I., Hodgson, I. (2010) argue, that the possibility to use the existing natural gas infrastructure as a bridging technology for hydrogen distribution is being considered. One of the largest and most obvious issues for hydrogen fuel is to minimize the costs of the delivery system. In general, larger refueling sites would be preferable, especially those close to the point of hydrogen production, which today are refineries.The more intensively these sites are used, the greater their cost is spread over different users and the lower the marginal cost for any individual user.In addition, the fewer the number of refueling sites that an application needs the better (Farrella et al., 2003).

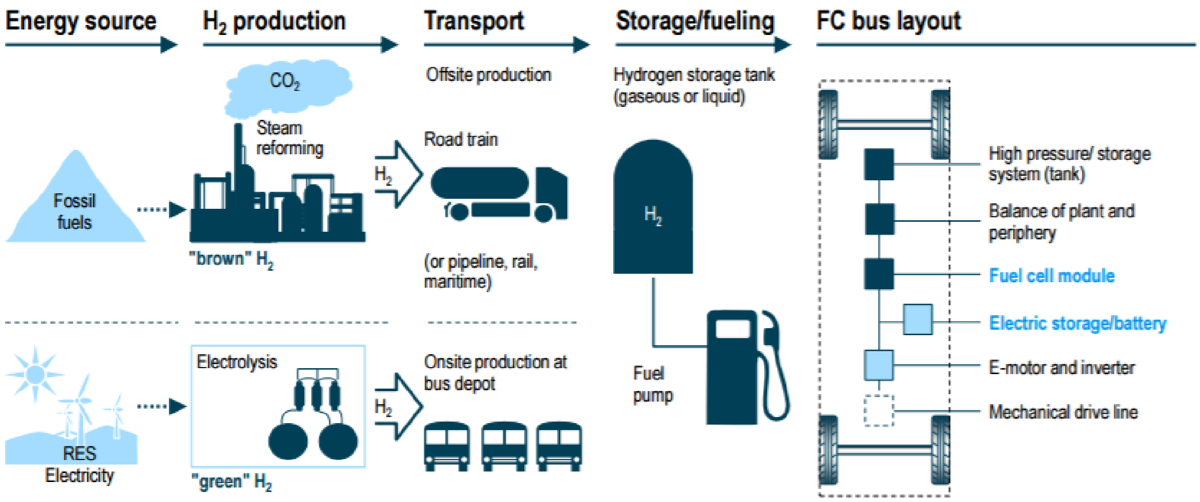

Fig. 6. Hydrogen value chain and fuel cell bus layout – simplefield presentation (Berger, 2015)

The forms of hydrogen storage that are currently being tested are compressed hydrogen and liquid hydrogen. While hydrogen has a high burn/explosive velocity, it has less explosive power than other fuelair mixes. Except in extremely high concentrations, hydrogen is not toxic to humans (Sandman, 1998). Hydrogen is odorless and tasteless. While the flame of burning hydrogen is visible under daylight conditions, it is a lot less so than flames from other fuels due to the lack of soot. A hydrogen flame can be most easily identified by the mirage-like effect on the air over and around the flame, as it otherwise does not produce significant heat radiation (Farrella et al., 2003). The challenges of hydrogen storage dictate that hydrogen powered vehicles will generally perform more poorly than their petroleum-powered counterparts. For example, the low volumetric density of hydrogen storage may reduce payload volume or decrease range.The importance of these decreases in performance varies strongly across modes (Herzog et al., 2000). Skinner, Hodgson (2010) state, that fuel cell vehicles currently have an advantage in range over electric vehicles due to greater energy storage densities for hydrogen relative to electrical energy storage. The cost of developing new hydrogen refuelling infrastructure is significan: it is much higher in comparison to developing a recharging infrastructure for electric vehicles (Skinner, Hodgson, 2010). Hydrogen needs completely new infrastructure throughout the whole chain from production over distribution and storage in filling stations and on-board the vehicles (Berger, 2015). The cost of using hydrogen as a transportation fuel would be less for larger than smaller vehicles, since larger vehicles (such as bus) tend to have less tightly constrained volumetric limitations (Farrella et al., 2003).

5. COMPARISON OF ALTERNATIVES

Road transport today is dominated by oil-derived fuels and internal combustion engines, which makes it unsustainable both economically and environmentally (IEA-RETD, 2015). Diesel buses currently dominate the public transport market. Alternative fuels are currently more costly than conventional fossil fuels (Berger, 2015). One of the main advantages of the diesel bus is its long term history of implementation, well known operational performance and disruptions represent a serious threat to road transport affordability and reliability, the lack of which significant availability of necessary fuelling infrastructure (Contestabile et al., 2011).

Needful transition from oil-derived fuels and conventional internal combustion engine powertrains, replacing these with low-carbon, renewable fuels and alternative low-emission, high-efficiency powertrains. (Contestabile et al., 2011). The rate at which these alternative fuels and powertrains are introduced as substitutes for conventional road transport fuels and powertrains should ideally be compatible with achieving international energy and environmental policy goals. A comparative assessment of different renewable energy source and bus technology needs to take calculations of energy efficiency, greenhouse gas emissions, energy consumption, and macro-economic cost elements for parts of the system (Herzog et al., 2000):

1. **vehicles**, including purchase and maintenance, comprising in the analysis life cycle aspects for production and disposal;
2. **fuels**, integrating the impacts along the whole pathway from the primary energy source to the final use for propulsion of a transport carrier;
3. **infrastructure**, including creation and maintenance as well as macro-economic cost elements for single fuel and multiple fuel fuelling and distribution infrastructure.

Countries and municipalities are operating under different financial, social and environmental conditions so there cannot be one clear fuel or technology option for all public buses (Lave et al., 2000). The list below presents an summarized overview of some of the main factors which influence the choice of alternative bus technology and fuel type (Evans et al., 2014):

- **Subsidies, tax incentives, funds etc.** The availability of financial support for the introduction of alternative fuels and technologies, including tax incentives (reduced vehicle tax for cleaner vehicles, lower tax on cleaner fuels etc.) and subsidies/grants, varies substantially from country to country.
- **Total cost of ownership/life cycle cost.** Cost remains the primary decision factor for the majority of public authorities. However the extent to which authorities are able to take into account the life cycle cost/total cost of ownership of a vehicle can have a major bearing on the selection of vehicle type. Many alternative fuel/technology options have higher upfront investment costs, both in terms of the vehicles, and the infrastructure required, but can demonstrate cost savings over the life of the vehicle due to lower fuel consumption/prices, and potentially longer lifespans and lower maintenance costs.
- **Prioritisation of air pollution or CO2 emissions.** A major determining factor in fuel/technology selection is your priority in terms of environmental performance.
- **Availability of fuel and refuelling infrastructure.** The highly differentiated availability of a refuelling infrastructure for alternative fuel types has a major impact on the practicality of selecting certain vehicle types. The type of area being served by a bus route (whether urban, short distance, high occupancy, or rural, long distance, low occupancy for example).
- **Topography, route and climate.** The physical conditions under which the buses will operate can also have a major impact on the right choice of fuel/technology – for example how hilly a route is, the distance between stops, the density of passenger occupation, conditions of extreme heat and extreme cold.
- **Scope of replacement activities.** The extent to which a new technology may be introduced will also be in part determined by the approach to bus replacement within the fleet. The introduction of a new refuelling infrastructure will likely only be cost effective where a major fleet overhaul is occurring. Where individual vehicles are being replaced, different fuel/technology choices may be most appropriate.
- **Whole Fleet.** A greater benefit may be achieved by replacing a high number of vehicles which provide modest CO2 and/or air quality related improvements rather than one or two buses which provide significant improvements.

6. CONCLUSION

The table below presents generalized results of application of different bus technology. Comparison substantiated by scientific articles and studies, including JRC (2007), McKinsey & Co (2010), IEA-RETD (2015), Sørensen (2009), Contestabile et al. (2011), Evans et al. (2014), Lave et al. (2000), Berger (2015). Biofuels that are oxygenates could also help reduce emissions from combustion, but it is important to emphasize, that only electricity and hydrogen have zero emissions of air pollutants at point of use. In this comparison were limited evaluated technical, economic and environmental impacts of alternatively fuelled vehicles. For example reducing external costs such as air pollution in cities has clear societal benefits, which are not included in this analysis. So, the next stage of these analysis should focus on particular case which has particular economics, sustainability and performance factors across the entire value chain.

Table 1. Comparison of operational performance of different bus technology

		Energy source - bus technology		
Comparison criteria		**Biofuel**	**Hydrogen**	**Battery-electric**
1	Reducing GHG emmision	medium-hight	hight	hight
2	Level of energy security	medium-hight	medium-hight	hight
3	Route flexibility	hight	hight	medium
4	Reducing noise	low	hight	hight
5	Current market penetration	medium-hight	low	medium
6	Purchase price	medium-low	hight	medium-hight
7	Additional infrastructure investment	medium-hight	hight	hight
8	Safety (filling and charging)	hight	medium	hight
9	Refuelling / recharging time	low	low	hight
10	Technology suppliers	medium	low	medium
11	Exploitation costs	hight	medium	low
12	EU coverage with fuelling infrastructure	medium	low	medium
13	Energy consumption	medium-hight	medium-hight	medium-low
14	Possibility of bus technology to adapt to another fuel	hight	low	low
15	Exploitung market opportunities: trading balance, employement and GDP benefits	medium-hight	hight	hight
16	Current fuel/ energy source availability	medium	low	hight
17	Investment risk (from the supply/industry)	hight	hight	hight
18	Financial barriers from energy carrier dimension	hight	low	low

REFERENCES

1. Antti, L. (2015) Evaluation of Electric Buses, Alto University. Link to the internet http://www.ecv.fi/@Bin/211333/ECV-seminaariesitys_10-3-2015_Evaluation-ofEBuses_Antti-Lajunen.pdf.
2. Barbier, F. (2001) Hydrogen and fuel cell: the European and French projects, Actualite Chimique 12, pp. 81–84.
3. Battaglia, J., Battey , H., Brooks, S. (2008) The Potential Role of Biofuels in New Jersey to Reduce Carbon Emissions from Electricity Generation, Columbia University for the New Jersey Department of Environmental Protection.
4. Bauen, A., Berndes, G., Junginger, M., Londo, M., Vuille, F. (2009), Bioenergy – a sustainable and reliable energy source, A review of status and prospects, IEA Bioenergy.
5. Berger, R. (2015) Fuel Cell Electric Buses – Potential for Sustainable Public Transport in Europe, A Study for the Fuel Cells and Hydrogen Joint Undertaking.
6. Berry, G. D., Pasternak, A. D., Rambach, G. D., Smith, J. R., Schock, R.N. (1996), Hydrogen as a future transportation fuel. Energy 21, pp. 289–303.

7. Brunton, L. J. (2000) Why not the trolleybus? In Proceedings of the IEEE Seminar on Electric, Hybrid and Fuel Cell Vehicles, Durham, UK.
8. Contestabile, M., Offer, G., Jaegar, F., Slade, R. (2011) Battery electric vehicles, hydrogen fuel cells and biofuels. Which will be the winner? ICEPT Working Paper, Imperial College Centre for Energy Policy and Technology.
9. ERTRAC (2009) The Electrification Approach to Urban Mobility and Transport, Strategy Paper Version 5.0.
10. Evans, N., Clement, S., Wimmer, F., Chesterton, V. (2014) Clean Buses – Experiences with Fuel and Technology Options, ICLEI – Local Governments for Sustainability.
11. Farrella, A., Keithb, D., Corbettc, J. (2003) A strategy for introducing hydrogen into transportation, Energy Policy 31, pp. 1357–1367.
12. Herzog, H., Eliasson, B., Kaarstad, O. (2000). Capturing greenhouse gases.Scientific American 282, pp. 54–61.
13. IEA (2011) Technology Roadmap Biofuels for Transport OECD/IEA, Renewable Energy Division. Paris.
14. IEA-RETD (2015) Driving renewable energy for transport – Next generation policy instruments for renewable transport (RES-T-NEXT), IEA Implementing Agreement for Renewable Energy Technology Deployment (IEA-RETD), Utrecht.
15. Jacobson, M. (2009) Review of solutions to global warming, air pollution, and energy security, Stanford University.
16. Jönsson, O., Persson, M. (2003) Biogas as transportation fuel, Swedish Gas Centre, Fachtagung 2003, pp. 98-111.
17. JRC (2007) Well-to-wheels analysis of future automotive fuels and powertrains. In the European context, European Commission Joint Research Centre.
18. Kempton, W., Tomic, J. (2005) Vehicle-to-grid power implementation: From stabilizing the grid to supporting large-scale renewable energy, Journal of Power Sources, pp.1–15.
19. Larson, E. (2006) A review of life-cycle analysis studies on liquid biofuel systems for the transport sector, Energy for Sustainable Development, Volume 10, pp. 109–126.
20. Lave, L., Maclean, H., Hendrickson, C., Lankey, R., (2000) Life-cycle analysis of alternative automobile fuel/propulsion technologies. Environmental Science and Technology 34, pp. 3598–3605.
21. Lund, H., Kempton, W. (2008) Integration of renewable energy into the transport and electricity sectors through V2G, Energy Policy, volume 36, pp. 3578–3587.
22. Malca, J., Freire, F. (2010) Uncertainty Analysis in Biofuel Systems An Application to the Life Cycle of Rapeseed Oil, Journal of Industrial Ecology, Volume 14, Number 2, pp. 332–334.
23. McKinsey & Co. (2010) EU powertrain coalition, A portfolio of power-trains for Europe: A fact-based analysis. The role of Battery Electric Vehicles, Plug-in Hybrids and Fuel Cell Electric Vehicles.
24. Nesterova, N., Verbeek, R. (2013) Smart choices for cities Clean buses for your city, CIVITAS WIKI.
25. Nizam, B. (2013) Inductive Charging Technique, International Journal of Engineering Trends and Technology 4 (4). Link to the internet http://www.ijettjournal.org/volume-4/issue-4/IJETT-V4I4P311.pdf.
26. Pringle, D. (2011) BIOFUELS: THE NEXT GENERATION, Supported by How innovation can brighten Europe’s energy future, The Energy Technology Roadmap, Science Business Publishing Ltd.
27. Sandman, F. J. (1998) Sea transportation of hydrogen. In: Saetre, T.O. (Ed.), Hydrogen Power: Theoretical and Engineering Solutions. Kluwer Academic Publishers, Boston, pp. 529–542.
28. *Sørensen, B. (2009)* Comparison between hydrogen fuel cell vehicles and bio-diesel vehicles, Roskilde University, Institute of Mathematics and Physics, Energy & Environment Group, Denmark.

CYSENI 2017, May 25-26, Kaunas, Lithuania
ISSN 1822-7554, www.cyseni.com

ESTIMATION OF INTEGRAL IMPACTS OF THE CLIMATE CHANGE ON THE RUSSIAN ENERGY SYSTEM

E. V. Kasilova, V. V. Klimenko, A. G. Tereshin
Moscow Power Engineering Institute
Krasnokazarmennaya str, 111250 Moscow – Russia
E-mail: e.v.kasilova@gmail.com

ABSTRACT

The impacts of the climate change on the energy systems around the world are highly site-specific. Effects for Russia are not completely understood yet, especially for power industry. However, they are already detected and will be more pronounced during the entire current century, as the Russian territory is one of the areas around the world where the climate change is developing most rapidly.

The climate warming deteriorates efficiency of the thermal engines. This effect is one of the significant climate related vulnerabilities of the power industry and counteracts to the well established effect of decreasing the domestic energy demand observed for temperate and boreal areas. The aim of the presented study is to estimate the impact of the climate change on the efficiency and the fuel consumption of thermal power plants and gas transportation compression drive for Russian conditions.

An original climate model was applied to simulate the change of the air temperature across Russia for the twenty-first century. The model takes into account both anthropogenic and natural climate driving factors and allows simulation of regional features of the climate change. Impact analysis for the power generation and gas-compression application was done using generalised characteristics of the units being in operation nowadays. Different scenarios were considered for a fleet of power units under a variety of renovation strategies.

The effects for the power industry and gas transportation system were simulated taking into account seasonal and spatial heterogeneity of the climate change across the Russian territory. The established estimations have been used to study the integral impact of the climate change on the energy systems. The main challenges and opportunities of the energy systems under the climate change were identified for boreal and temperate regions.

Keywords: Climate change, efficiency, power industry, gas transportation, simulation

1. INTRODUCTION

Issues of the climate change and its impact on society are among the most discussed topics both in everyday news and in academic research works for years. It’s clear at the moment that further climate warming is unavoidable during the entire 21st century and will impact all areas of the world and all fields of human activities.

The energy industry is stated to be vulnerable to the climate change. The dominating processes which determine this vulnerability are highly regional-specific [1]. Energy systems of USA and Europe were analysed quite in detail in a number of recent works [2–7]. Others regions of the world still require further investigation.

2. CLIMATE CHANGE IN RUSSIA

The territory of Russia belongs to the areas across the world where the climate changes were manifested most significantly during the entire twentieth century. The strongest part of climate warming in Russia was observed since begin of 1980th. There was a known pause in this warming process about the year 2000 caused by specific of atmospheric circulation processes which intensively counteracted anthropogenic influences. After that the climate warming continued with resulting a Russia-mean warming rate averaged for 30 years as high as 0.4 ^{o}C per 10 years [1, 8].

Climate changes are highly regional and seasonal specific. Warming in European part of Russia is concentrated manly on winter and spring with moderate summer warming. At the same time, summer warming is strongly pronounced in the northern part of Western Siberia [1, 8]. Such a complicated climate change patterns makes analysis of the climate impacts quite a challenge.

Energy studies in Russia for the climate change were mainly concentrated on the energy demand changes [8]. Some fundamental works in the early 2000s forecasted pronounced decrease of space heating demand with some increase of cooling needs varying from negligible to moderate across the country [9, 10]. Correctness of these findings was confirmed during the next years of observations and research [11, 12] and is perfectly consistent with the latest results for energy demand for Canada and northern regions of China that are similar to Russia by climatic conditions [13–15].

Energy supply for Russia is known to be deteriorated by the climate warming [8, 16]. However, few works dedicated to that problem are concentrated on climatic processes itself [16, 17] and don’t provide any quantitative estimations for their impacts on the energy system.

A scope of this study is to present the first estimation for the integral climate change effects on the energy supply in Russia The study was concentrated on the steam and gas turbines as the most common equipment of the modern energy industry.

3. METHODS

3.1. Simulation of the regional climate change

An original climate model was used to obtain projections for the annual and seasonal air temperatures in different Russian regions during the twenty-first century [18]. The model applies linearization of the climate response to variations of the principal climatic driving factors, based on approach of [19]. The whole set of natural and anthropogenic climate driving factors considered is as follows:

1) solar activity;
2) change of the Earth orbital parameters;
3) volcanic activity;
4) atmospheric circulation processes;
5) concentration of greenhouse gases (both CO2 and other multiatomic gases);
6) anthropogenic sulfur aerosols.

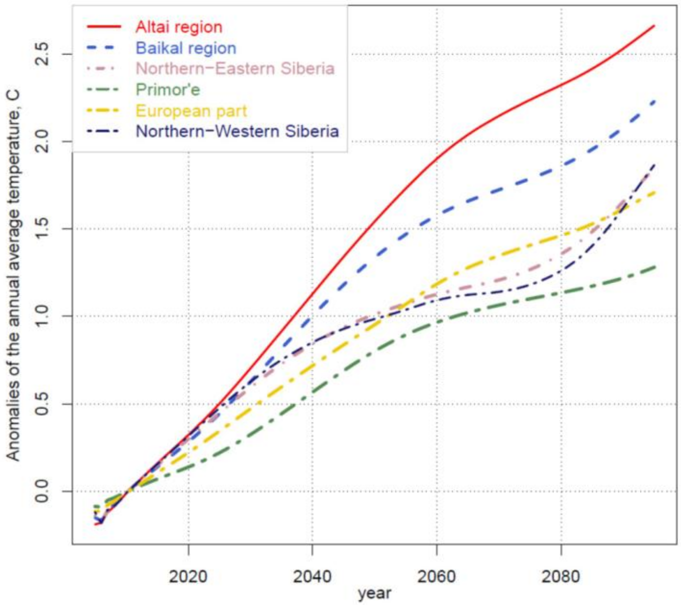

Fig. 1. The projected trends of the mean annual temperatures in the Russian regions in the twenty-first century

The carbon dioxide concentration was calculated by a separate model of the global carbon cycle with implementation of an original forecast for the world energy development [12]. The quantitative estimation of the climate response on the change of each climatic factor was obtained by combination of a non-stationary energy balance model based on [20] supplemented with empirical impacts study. Simulations of all considered climatic factors were integrated into the climate model using statistical approaches and implemented as a C++ project used for further calculations [21].

The model was developed in the Global Energy Problems Laboratory more than 25 years ago and has been verified by meteorological observation data in a number of preceding works and was repeatedly confirmed to be quite reliable for practical applications [9, 10, 22].

The projections of the annual air temperatures obtained for a number of geographical regions of Russia are presented in Fig. 1. The simulation results are generally consistent with multimodel ensemble estimations obtained by global circulation models of the international project CMIP5 with the scenario RCP 4.5 [23] up to the year 2050 which was chosen as the time horizon for the present impact study. The reference years used in impact studies for comparison with future climate conditions were 1966–2010 according to the recommendations of the World Meteorological Organisation.

3.2. Sensitivity study for steam turbine units

Efficiency drop of a steam turbine due to the increase of the ambient temperature may be evaluated by the change of the condenser pressure. The ratio of the turbine power drop ΔN assosiated with the condenser pressure change Δp is 1% to 1 kPa for the power equipment currently being in operation on Russian thermal power plants [24]. Nuclear plants are more vulnerable to deterioration of condenser vacuum with elevated $\Delta N/\Delta p$ values of about 1.5%.[24]

Condenser pressure determines the condenser temperature t_c which is one of the main parameters influencing the heat processes in the condenser and condenser sensitivity to variations of the ambient air temperature t_a.

Experimental data for the water saturation curve [25] were used for calculation of the condenser pressure corresponding to the temperature t_c. The resulted steam turbine power sensitivity to the condenser temperature change Δt_c was estimated using typical ranges of the steady-state operation pressure as 0.23% for the thermal power plants and 0.44% for nuclear ones per 1 degree Celsius of ambient air temperature change.

A relationship between the condenser temperature t_c and the ambient air temperature t_a is governed by two group of the effects:

1) heat and mass transport processes in the condenser

2) heat transfer between the condenser cooling water and the atmosphere.

The first group of the effects was represented in the condenser simulation model established for the purpose of this study. Impact of the ambient air temperature t_a to the cooling water temperature t_c was estimated using empirical coefficients accounting for the type of cooling systems used and climatic conditions in the different Russian regions.

The condenser model was based on a classical VTI (abbreviation of the original name of the All-Russian Thermal Engineering Institute) approach [26, 27]. The VTI method was developed as a generalisation of a huge amount of experimental data obtained for condensation processes with the parameters corresponding to the industry-scale power units. The method is applicable for the whole range of design and operational parameters of the modern power units and demonstrates more stable accuracy as compared with concurrent approaches [28].

The VTI method was implemented into the condenser model in the R simulation environment. A parametrical study was conducted to estimate the sensitivity S_c of the condenser temperature t_c to the changes of the cooling water temperature t_w for the whole parameters range inherent for the steam turbine units being currently installed on the Russian power plants. The sensitivity value was defined as follows

$$S_c = dt_c / dt_w \tag{1}$$

The obtained sensitivity values were applied to estimate the impact of the water temperature change on the turbine electric power ΔN_{el}

$$\Delta N_{el} \approx \Delta t_w \cdot S_c \left(t_w \right) \tag{2}$$

The linear approach is an appropriate one as the change of water temperature change due to the climate warming is of order of a few degrees.

A dependence of the sensitivity value on the water temperature and velocity of the cooling water is shown in Fig. 2. The values of the condenser design and operation parameters (the outer diameter of the condenser tubes, the number of tube-side passes, the specific steam rate etc.) were set up equal to the most typical values for the Russian power equipment [24, 28].

The thick curve on the picture is a border separating the nominal velocity values in the upper picture part from the decreased velocities corresponding to turbine operation by the air temperature much lower as compared to the design point.

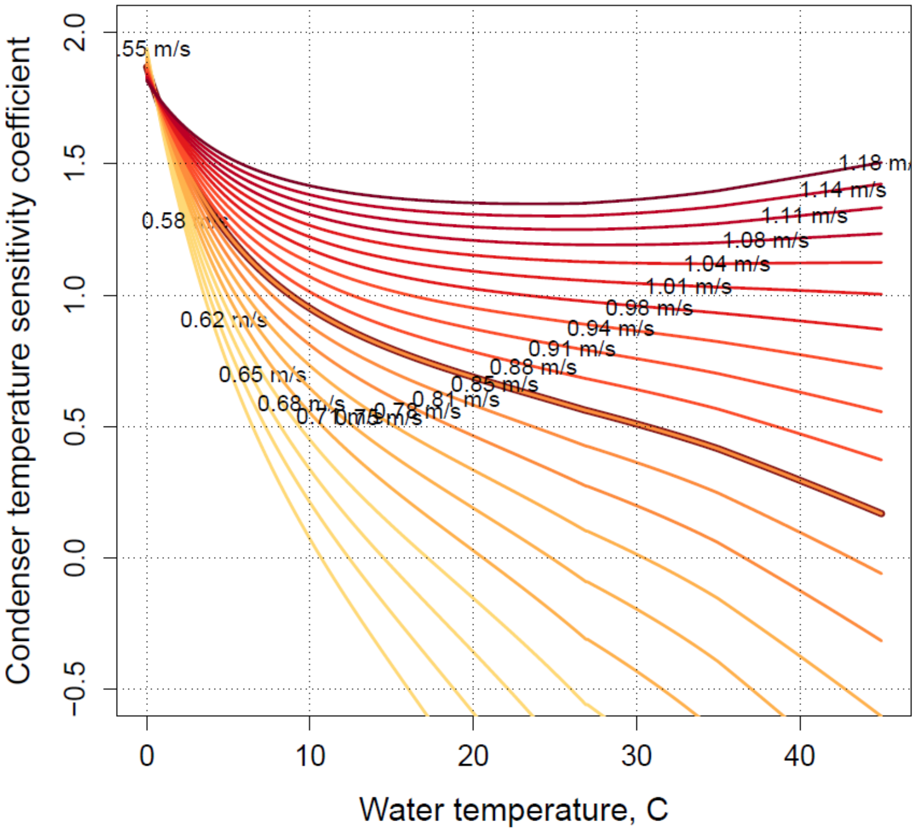

Fig. 2. Map of the condenser temperature sensitivity coefficients S_c by the range of cooling water velocities

The mean sensitivity values S_c for each water temperature value was estimated as an average by all possible nominal velocity values.

The water temperature value t_w is determined by a water cooling technology used and climatic conditions on the operation site. The most widely used in Russia cooling technologies take cooling water directly from the natural or artificial water reservoirs. The relation of the water temperature in rivers and ponds to the air temperature may be represented by a S-type curve [29]. Strictly speaking, the value of the $t_w(t_a)$ curve slope dt_w/dt_a, is site-specific. However, due to the lack of such data for

Russian hydrological systems, the dt_w/dt_a were estimated by the long-term annual average air temperature for each geographical region combined with the results of hydrological studies for the rivers located in moderate climatic conditions across the world.

3.3. Sensitivity study for gas turbine units

The dependence of the efficiency of a gas-turbine unit (GTU) η on the ambient air temperature t_a is nonlinear [31]. The increase in the ambient air temperature deteriorates the performance of the unit due to both heating of the low-temperature outlet and reducing efficiency of the compression process. In addition, different values of the ambient temperature require different patterns of GTU regulation resulting to the knees in the unit temperature characteristics.

The unit efficiency is nearly constant at low t_a. Starting from a certain value t_a^* ranging from -5 to –12 °C the rise in the air temperature causes the drop of η. The sensitivity of the GTU efficiency to the air temperatures increases when t_a rises and typically is in the range 0.5..1.0 percent points per 10 ^{o}C by $t_a > t_a^*$.

The parametric calculations in this study were based on the characteristics of the General Electric gas turbine MS9001E with nominal power of 126 MW and nominal efficiency of 34%. With regard to its power and performance, this unit occupies an intermediate position between large power plants and gas-turbine drive of gas pumping large units.

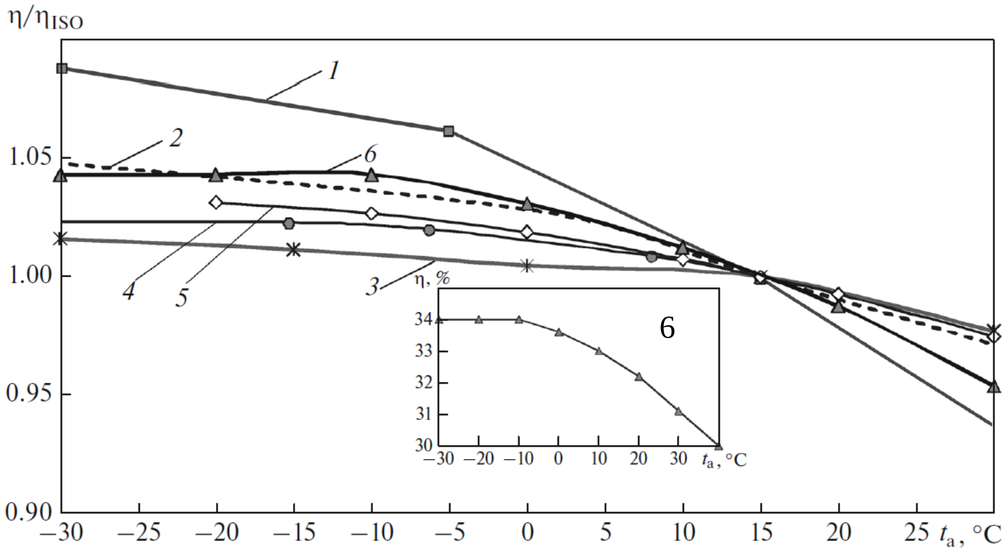

Fig. 3. Dependence of the efficiency on the ambient air temperature for different gas turbines; η is the efficiency at the given temperature, η_{ISO} is the efficiency by the standard conditions: 1 – GTE-6; 2 – GTK-25R; 3 – GE LMS100; 4 – Siemens V64 3A; 5 – Alstom GT13E2; 6 – GE MS9001

4. RESULTS AND DISCUSSION

4.1. Steam turbine units

The steam turbine units currently dominate power generation in Russia being the most widely used technology both by installed capacity and the power generated [30]. Work of steam turbines was simulated for the seven largest regional subsystems of the Russian energy system located respectively in the north-west, central and south areas of the European part of Russia, in the middle reaches of the Volga river, in the Urals industrial region, in the south regions of Siberia and in the south part of Russian Far East (Fig. 4). Isolated energy systems and stand-alone units weren’t considered in the study as their overall installed capacity is less than 10% of the total capacity installed.

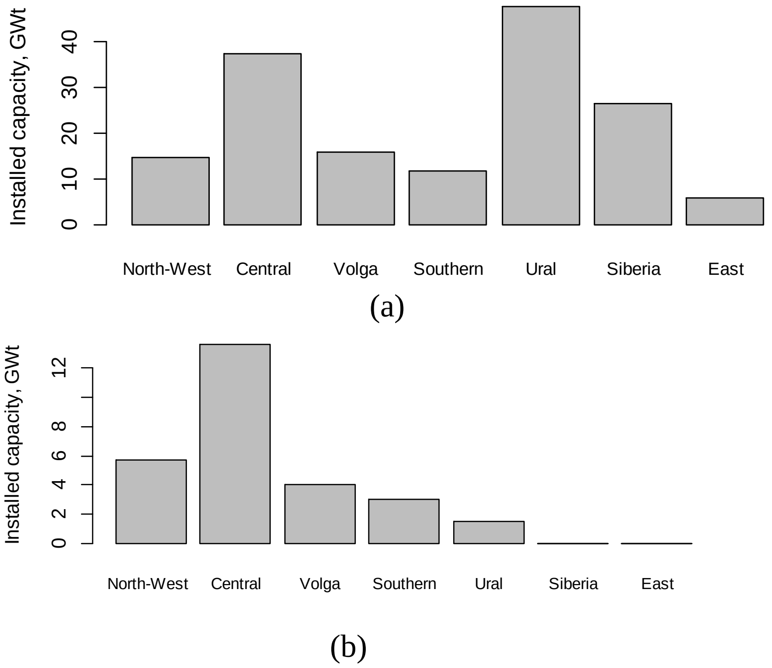

(a)

(b)

Fig. 4. Installed capacity of power plants: a – thermal power plants; b – nuclear power plants [30]

The total power drop of the steam turbines in each region was evaluated using sensitivity values estimated as described above. The typical water temperatures were taken using data [28] for different water cooling technologies being currently applied on the Russian power plants. Those are direct cooling by the river stream, or using water from the cooling ponds, or cooling towers.

The power drop due to 1°C air temperature rise is significantly higher for the nuclear plants than for the thermal ones (Table 1) with 0.4–0.6% and 0.2–0.3% respectively.

Table 1. Estimation of the climate change impact on the steam turbines efficiency by regional energy systems with different water cooling technologies

Energy system region	**Annual air temperature t_a, °C**	**dt_w/dt_a**	**Power drop per 1°C air temperature change**					
			Thermal power plants			**Nuclear power plants**		
			direct	ponds	towers	direct	ponds	towers
North-West	4.6	0.85	0.27	0.24	0.23	0.52	0.46	0.44
Central	6.7	1	0.31	0.27	0.27	0.60	0.52	0.51
Volga	6.1	1	0.31	0.28	0.27	0.60	0.53	0.52
Southern	9.0	1	0.30	0.27	0.26	0.58	0.52	0.49
Urals	3.5	0.7	0.22	0.20	0.18	0.43	0.38	0.35
Siberia	0.0	0.7	0.26	0.21	0.19	0.50	0.41	0.37
Far East	1.0	0.7	0.25	0.21	0.19	0.48	0.40	0.36

The integral power drop compared to the modern conditions (i.e.1966–2010) was estimated as

- 600 MW for the thermal power plants to 2030; 900 MW to 2050;
- 200 MW for the nuclear power plants to 2030, 300 MW to 2050.

That means that the total decrease of the power in the whole power system due to the climate warming will be as big as an output of a single large nuclear power plant. However, a thermal power station working with a moderate efficiency of 30% to compensate this decrement will spend additionally only about 3 million tonnes of coal equivalent (tce). That is at least one order of magnitude higher as compared with saving of about hundred millions tce due to space heating demand reduction associated with the climate warming [32].

4.2. Gas turbine units

Two main applications of gas turbines in Russia are drive of gas-compressor units for the natural gas transport system and electricity generation including combined cycle power plants. The Russian gas transport system is a huge gas pipeline network, whose operating pressure is maintained by compressor stations. Typically, such stations are located on gas pipelines at every 100–150 km. More than 80% of compressor stations use gas turbines for compressor drive consuming a small share of the transported gas.

The calculations were performed for 18 territorial units corresponding to subsidiary gas pipeline companies. The values of the installed gas-turbine drive capacity were estimated for each territory using the publicly available statistical data. Installed capacity was assumed to be constant for each territory as the first inertial approach.

Calculations for the change of fuel consumption by the gas turbines were done considering further climate conditions for each territory separately. The increase in the fuel consumption due to changes in the climatic conditions is 0.2% by 2030 and 0.3% by 2050 for all considered territories except the Far East. In the Far Eastern region, the combination of relatively low air temperatures and a comparatively slow warming rate leads to a weaker impact of warming on GTU fuel consumption than in other regions of Russia. The total increase of the fuel consumption by the gas pipeline network will reach about 90 thousand tce by 2030 and approximately 120 thousand tce by 2050.

Electricity-generating gas turbines are still quite rare in Russia with a share in the total electricity-generation as low as 3%. However, in recent years, the number of combined-cycle plant is increasing with the share of gas-turbine power usually amounting to 70%. According to Russia's Energy Strategy, in the near future combine-cycle units should become the main type of the power generating facilities being constructed in Russia. Besides, gas turbines are widely used nowadays to cover peaks of the energy load. Their application should expand in the coming decades both for electricity generation and cogeneration purposes.

Thirteen regions of Russia accounting for more than 75% of Russia's gas-turbine installed comprise the impact study. Three development scenarios for the electric power industry were considered, i.e., inertial, which corresponded to the current state of the installed capacity of electricity-generating GTU, optimistic, and moderate.

The installed capacity utilization factor was assumed to be 0.5 for independent gas turbines and 0.8 for the combined-cycle plants. The calculation results for the existing GTU fleet (inertial scenario) are presented in Table 2.

Table 2. The change of the power gas-turbine installed capacity N_{GTU} and the increase in the fuel consumption ΔB due to the climate change

Indicator	**Inertial scenario**		**Moderate scenario**		**Optimistic scenario**	
	2030	**2050**	**2030**	**2050.**	**2030**	**2050**
N_{GTU}, MW	18 800	18 800	22 600	41 400	60 200	88 400
ΔB, thousand tce	37	46	81	135	118	215

The total fuel consumption increase in the power industry due to the reduction of the gas turbine efficiency because of the climate warming may constitute about 40 thousand tce by 2030 and approximately 50 thousand tce by 2050 for the inertial scenario.

The optimistic scenario assumes that the commissioning rates of the gas turbines and combined-cycle plants will remain the same over the next 35 years as in 2009–2015, i.e., about 2 GW/year. Generally, such a value corresponds to the development plans of the Russian energy system for the nearest four years. These rates are approximately half of those taken for scenarios of [35]. In the moderate scenario, the growth in the GTU installed capacity is twice slower.

5. SUMMARY

1. The climate change deteriorates efficiency of the power equipment on the entire territory of Russia. The corresponding efficiency drop depends on both increase of the air temperature and its initial values. Besides, the climate change will reduce the operating efficiency of compressor drives in the gas transmission system where the compressors are mainly driven by the gas turbine units.
2. The power drop of the steam turbines constitutes about 0.2–0.3 and 0.4–0.6 percent points per 1^{o}C for thermal and nuclear power plants respectively; the average efficiency decrease of the gas turbines is of order 0.1 percent points per 1 ^{o}C.
3. The total output decrease of steam power units will be as high as 0.8 GW (600 MW and 200 MW divided between thermal and nuclear plants respectively) by 2030 and 1.2 GW (900 and 300 MW) by 2050. The total increase of the gas turbines fuel consumption will reach 130 thousand tce by 2030 (90 thou tce for the gas compression units and 40 thou tce in the power industry) and approximately 170 thou tce (120 and 50 thou tce, respectively) by 2050. The implementation of more optimistic development scenarios for the power industry will increase this effect 1.5–2.0 times by 2050.
4. Despite such high absolute values of climate change impacts on the power and efficiency of the turbines, the decrease of space heating demand due to the climate warming dominates the climate induced change of the Russian energy balance. Fuel saving due to the last effect is at least one order of magnitude higher as compared with considered effects. To the end of 21st century, the climate warming will induce decrease of fuel spend for space heating about 100 mln tce yearly with only 3 mln tce rise of fuel consumption due to turbines’ efficiency deterioration under more warm climate conditions.
5. The response of the gas and steam turbines on the change of the air temperature was found to be qualitatively and quantitatively different. That may mean a need to adjust control strategy of the combined-cycle power plants to the changing climate.

The authors acknowledge a grant for young scientists from the Ministry of Education and Science of the Russian Federation for supporting E.V.Kasilova (a grant number MK-1494.2017.8).

REFERENCES

1. IPCC, CLIMATE CHANGE 2014: Impacts, Adaptation, and Vulnerability. Part A: Global and Sectoral Aspects. *Contribution of Working Group II to the Fifth Assessment Report of the Intergovernmental Panel on Climate Change*, Ed. by Field C. B., Barros V. R., Dokken D. J. et al. (Cambridge Univ. Press, Cambridge, 2014). [referred on the 6th of March in 2017 y.]. Link to the internet < http://www.ipcc.ch/report/ar5/wg2/ >.
2. VLIET, M. T. H., YEARSLEY, J. R., LUDWIG, F. et al. (2012) Vulnerability of US and European electricity supply to climate change. *Nature Climate Change, 2012,* Vol. 2, No. 9, p. 676–681.
3. RÜBBELKE D., VÖGELE, S. Short-term distributional consequences of climate change impacts on the power sector – who gains and who loses? *Climatic Change*, 2013, Vol. 116, No. 2, p. 191–206.
4. DOWLING, P., The impact of climate change on the European energy system. *Energy Policy*, 2013, Vol. 60, p. 406–417.
5. CHANDRAMOWLI, S. N., FELDER, F.A. Impact of climate change on electricity systems and markets: A review of models and forecasts. *Sustainable Energy Technologies and Assessments*, 2014, No. 5, p. 62–74.

6. JAGLOM, W. S., MCFARLAND, J. R., COLLEY, M. F., et al., Assessment of projected temperature impacts from climate change on the U.S. electric power sector using the Integrated Planning Model. *Energy Policy*, 2014, Vol. **73**, p. 524–539.
7. STANTON, M. C. B. , DESSAI, S., PAAVOLA, J. A systematic review of the impacts of climate variability and change on electricity systems in Europe. *Energy*, 2016, Vol. 109, p. 1148–1159.
8. *Roshydromet's Second Assessment Report on Climatic Changes and Their Consequences on the Territory of Russian Federation*, Ed. by V. M. Kattsov and S. M. Semenov Moscow: Rosgidromet, 2014. [in Russian].
9. KLIMENKO V.V., KLIMENKO A.V., TERESHIN A.G. et al. Changes of the heating period parameters on the European part of Russia due to the global warming. *Izvestiya Akademii nauk. Energetika*. 2002, No. 2, p. 10–27 [in Russian].
10. KLIMENKO V.V., TERESHIN A.G., BEZNOSOVA D.S. et al. Changes of the heating period parameters on the Asian part of Russia due to the global warming. *Izvestiya Akademii nauk. Energetika*. 2004, No. 4, p. 135–145 [in Russian].
11. KLIMENKO V.V., KLIMENKO A.V., TERESHIN A.G. et al. Changing pattern and amount of the residential and commercial energy consumption in response to economic and climatic factors. *Thermal Engineering*, 2012, Vol. 59, No. 11, p. 807–815.
12. KLIMENKO V.V., KLIMENKO A.V., TERESHIN A.G. Experience in Constructing Distant Forecasts of World Energy Impact on the Earth’s Atmosphere. *Izvestia RAN. Physics of Atmosphere and Ocean*, 2015, Vol. 51, No. 2, p. 158–168.
13. VIEIRA, M.J.F., LARAMEE, L.L., MOORE, A. R. Projected Climate Change Impacts on Energy and Peak Demand in Manitoba. *Report submitted to Climate Change Impacts and Adaptation Division, Natural Resources Canada.* 2015. [referred on the 6th of March in 2017 y.]. Link to the internet https://www.hydro.mb.ca/corporate/research_and_development/projected_climate_change_impacts.pdf >
14. Embracing Energy Efficiency: Ensuring Yukon Benefits from Climate Moderated Heating Demand. *Report prepared for the Government of Yukon Energy Branch*. 2015. .[referred on the 6th of March in 2017 y.]. Link to the internet < http://www.energy.gov.yk.ca/pdf/Embracing-Energy-Efficiency-Climate-Moderated-Heating-Demand-Assessment.pdf >
15. SHI Y., GAO X., XU Y. et al. Effects of climate change on HDD & CDD and potential energy demand in the household sector of China. *Clim Res*. 2016, Vol. 67, No.2, p.135–149.
16. SHKOL’NIK, I.M., MELESHKO, V.P., STADNIK, V.V. et al. Influence of the climate change on energy supply and demand in Russia. RGO Proceedings. 2014, Vol. 573, p. 92–222 [in Russian].
17. AKENT’EVA, E.M., TYUSOV, G.A. Using of a program complex ClimPACT for estimation of the climatic factor influence on electricity generation. RGO Proceedings. 2015, Vol. 578, p. 86–100 [in Russian].
18. KLIMENKO Vladimir V., KLIMENKO Alexander V., ANDREICHENKO Tatiana N. et al. *Energy, Nature, and Climate*. Moscow: Moscow Power Engineering Institute, 1997. 200 p. [in Russian].
19. SCHONWIESE, C.-D., STAHLER, U. Multiforced statistical assessments of greenhouse-gas-induced surface air temperature change 1895–1985. *Climate Dynamics*, 1991, Vol. 6, No. 1, p. 23–33.
20. HARVEY, L. D. D., SCHNEIDER, S. H. Transient climate response to external forcing on 1-1000 year time scales. Part I: Experiments with globally averaged, coupled, atmosphere and energy balance models. *Journal of Geophysical Research*, 1985, Vol. 90, No. D1, p. 2191–2205.

21. MIKUSHIN, D. N. AND MIKUSHINA, O. V. *The Software Complex for Climatic Research “GEPL Research Environment,”*Certificate 2016611074 RF, Proposed Dec. 8, 2015; Registered Jan. 26, 2016.
22. KHRUSTALEV, L.N., KLIMENKO V.V., EMELYANOVA L.V. et al.“Dynamics of permafrost temperature in southern regions of cryolithozone under different scenarios of climate change,” *Kriosfera Zemli*, 2008, Vol. 12, No.1, p. 3–11 [in Russian].
23. KNUTTI, R. // IPCC Working Group I AR5 snapshot: The rcp45 experiment. World Data Center for Climate. 2014. doi:10.1594/WDCC/ETHr4 .
24. ARONSON, K.E., BLINKOV, S.N., BREZGIN, V.I. et al. Heat transfer equipment of the power units. Electronic handbook. <https://openedu.urfu.ru/files/book/ >
25. ALEXANDROV, A.A., GRIGORIEV, B.A. The tables of thermophysical properties of water and steam . Moscow: Moscow Power Engineering Institute, 1999. 165 p. [in Russian].
26. BERMAN, L.D., Heat transfer with steam condensation on a bundle of horizontal tubes. *Thermal Engineering*, 1981, No. 28, p. 218–224
27. BERMAN, L.D., ZERNOVA E.P. *Directions to calculation of the surface condencers of large steam turbines of thermal and nuclear power plants*. Moscow: Soyuzteckenergo, 1982. 106 p.
28. BRODOV, Yu.M., SAVEL’EV, R.Z., Condensing units of the steam turbines. Moscow: Energoatomizdat, 1994. 288 p.
29. MOHSENI, O, STEFAN, H.G. Stream temperature/air temperature relationship: a physical interpretation. *Journal of Hydrology*, 1999, Vol. 218, No. 3–4, p. 128–141.
30. *Report on the Operation of the United Power System of Russia in 2016.* System Operator of the United Power System, 2015. [referred on the 6th of March in 2017 y.] Link to the internet: <http://www.so-ups.ru>
31. KLIMENKO, V.V., KLIMENKO, A. V., KASILOVA, E. V. et al. (2016) Performance of Gas Turbines in Russia under the Changing Climatic Conditions. *Thermal Engineering*, 2016, Vol. 63, No. 10, pp. 690–698.
32. KLIMENKO, V.V., TERESHIN, A.G., MIKUSHINA, O.V. Changes of the climatic parameters and their role for the heating system of the country. *Informational and analytical system Rosteplo*. [referred on the 6th of March in 2017 y.]. Link to the internet: < http://www.rosteplo.ru/Tech_stat/stat_shablon.php?id=2572 >

CYSENI 2017, May 25-26, Kaunas, Lithuania
ISSN 1822-7554, www.cyseni.com

POSSIBLE REDUCTION OF ALUMINIUM HYDROXIDE IN HYDROGEN GAS PLASMA

M. Urbonavičius, Š. Varnagiris, D. Girdzevičius, D. Milčius
Lithuanian Energy Institute
Breslaujos st. 3, LT-44403 Kaunas – Lithuania
E-mail: Marius.Urbonavicius@lei.lt

ABSTRACT

Efficient hydrogen generation from reaction between plasma modified Al powder and water proceeded leading to non-hazardous byproduct ($Al(OH)_3$) formation. Such byproduct could be used in chromatography, pharmaceuticals, water treatment or catalyst converters production. Also it could be reduced back to aluminium and used in Al-water reaction again. Current industrial reduction of alumina is based on electrochemical process releasing huge amount of greenhouse gases into the atmosphere.

In this study, experiments were carried out in vacuum chamber to examine the reduction of $Al(OH)_3$ by non-thermal hydrogen and hydrogen/argon gas plasma. Hydrogen is a powerful reducing agent. Hydrogen plasma contains variety of active particles (ions, electrons, excited and neutral atoms) which could break down bonds between aluminium and oxygen atoms resulting efficient reduction process. In order to increase the reduction potential, temperature of samples (500 °C) was increased using tungsten heater. Magnetron with Al cathode ($P = 260W$) was used as a plasma source. Impulse DC power supply was used for power control. Initial and reduced alumina/aluminium hydroxide samples were characterized by scanning electron microscopy (SEM), energy dispersive X-ray spectroscopy (EDS) for elemental analysis, X-ray diffraction (XRD) for microstructure analysis.

Keywords: aluminium, glow discharge, vacuum, hydrogen plasma, reduction

1. INTRODUCTION

Efficient hydrogen production for on-board application can be realised using the reaction between modified aluminium metal and water. The reaction byproduct is stable and non-corrosive aluminium hydroxide ($Al(OH)_3$). It could be used as flame retardant, adsorbent in chromatography or in manufacturing processes of paper, glass, ceramics, lubricants, cosmetics and antacid drugs [1–3].

Furthermore, the Al-water byproduct could be reduced back to aluminium metal. Currently, industrial production of aluminium from alumina is based on the Bayer process followed by the electrochemical Hall-Heroult method. High green-house gas emission (0.7 kg CO_2/1 kg Al) and enormous energy consumption (0.055 GJ/1 kg Al) are the main drawbacks of this aluminium production route [4, 5].

It is known that reduction of metal oxides in plasma is feasible [6–8]. Hydrogen could be used as a powerful reducing agent. Aluminium metal could be obtained from aluminium oxide, according to the reaction $Al_2O_3 + 3H_2 \leftrightarrow 2Al + 3H_2O$ [9]. In this case hydrogen gas (or CH_4) plasma or its mixture with noble gas could be employed because of presence of the highly reactive atomic hydrogen, ions and electron-excited H_2 molecules ($2H$, $2H^+$, $2H^{2+}$, $2H^{3+}$, H_2^*) [10]. Additionally, heavy and energetic ions of noble gases lead to physical bombardment of metal oxide. Usually the process takes place in thermal plasma (1200–2000 °C) which is used as high-enthalpy source for the thermal decomposition [11]. High temperature enhances the reaction kinetics and chemical reactivity [12]. Kitamura et al. [13] showed the possible reduction of Fe_2O_3, Cr_2O_3, TiO_2 and Al_2O_3 in thermal Ar/H_2 plasma. Removal of oxide film was detected after stainless steel samples were exposed to hydrogen plasma at elevated temperature [14]. Another approach could be carbothermic reduction of aluminium oxide by thermal treatment of CO gas plasma [4, 15]. However, plasma reduction of aluminium oxide still remains a challenge.

Here we present a non-thermal plasma reduction process under vacuum conditions using pure H_2 and H_2/Ar mixture as working gas. The main advantage of the vacuum is lowered temperature (compared with atmospheric plasma) during the reduction process of Al-water byproduct [4]. Hydrogen molecules are partly ionised and dissociated under plasma conditions which result the formation of chemically reactive species. Whereas argon ions perform physical desorption. Value of Gibb‘s free energy change (T = 1000 °K) for the reduction of aluminium oxide with hydrogen plasma is negative (-53.73 kJ/mol) and with molecular hydrogen is positive (246 kJ/mol) [16]. Positive value represents that aluminium oxide would not be reduced using molecular H_2 at 1000 °K.

The aim of this work is the reduction of the Al-water reaction byproduct back to aluminium metal which could be reused in reaction with water again.

2. METHODOLOGY

A schematic view of the experimental setup is shown in Fig. 1. Specimens were prepared after hydrogen generation via reaction between plasma modified aluminium and water. Further the byproduct samples were dried in air at room temperature. The reduction of the byproduct received after Al-water reaction was investigated in vacuum chamber under the glow discharge plasma treatment. Magnetron with aluminium cathode was used for plasma generation. The byproduct samples were treated at 260 W for 1 hour. Plasma reduction was performed at 16 Pa pressure of pure hydrogen and mixture of hydrogen/argon gases. In order to increase and maintain temperature (500 °C) of the samples tungsten heater was employed. Chemical reaction rate could be increased by elevated temperature.

A scanning electron microscope (SEM, Hitachi S-3400N) was used to investigate surface morphology of the aluminium-water byproduct and samples reduced in hydrogen gas plasma. Elemental composition was determined and compared by energy dispersive X-ray spectroscopy (EDS, Bruker Quad 5040). The microstructure of as-received and reduced samples were characterised via X-ray diffraction analysis using Bruker diffractometer operated in the θ - θ configuration. The measurements were performed at 2θ angle in the range 20°–70° using Lynx eye linear position-sensitive detector in steps of 0.01°. EVA *Search – Match* software was used for peaks identification.

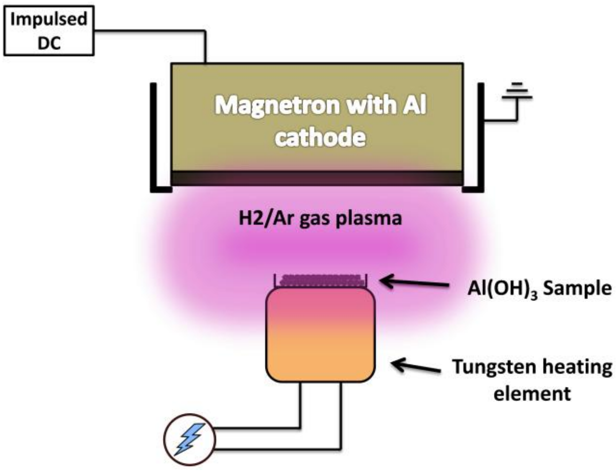

Fig. 1. Principal scheme of Al-water byproduct reduction in non-thermal H_2 and H_2/Ar plasmas

3. RESULTS AND DISCUSSIONS

3.1. SEM and EDS analysis

Surface morphology of Al-water byproduct and samples reduced in glow discharge plasma with pure H_2 and H_2/Ar mixture was investigated by SEM (Fig. 2; scale bar – 10 μm). Views of Al-water byproduct powder (Fig. 2a) did not show any significant changes after reduction in plasma with different ratio of H_2/Ar gases (Fig. 2 (b-e)). All samples consisted of similar irregularly-shaped agglomerates with rough surface. Size of agglomerates varied from 3 to 10 µm. However, it was noticeable that powder colour changed from white to light grey after plasma treatment. Presumably surface morphology remained unchanged because of insufficient reduction process.

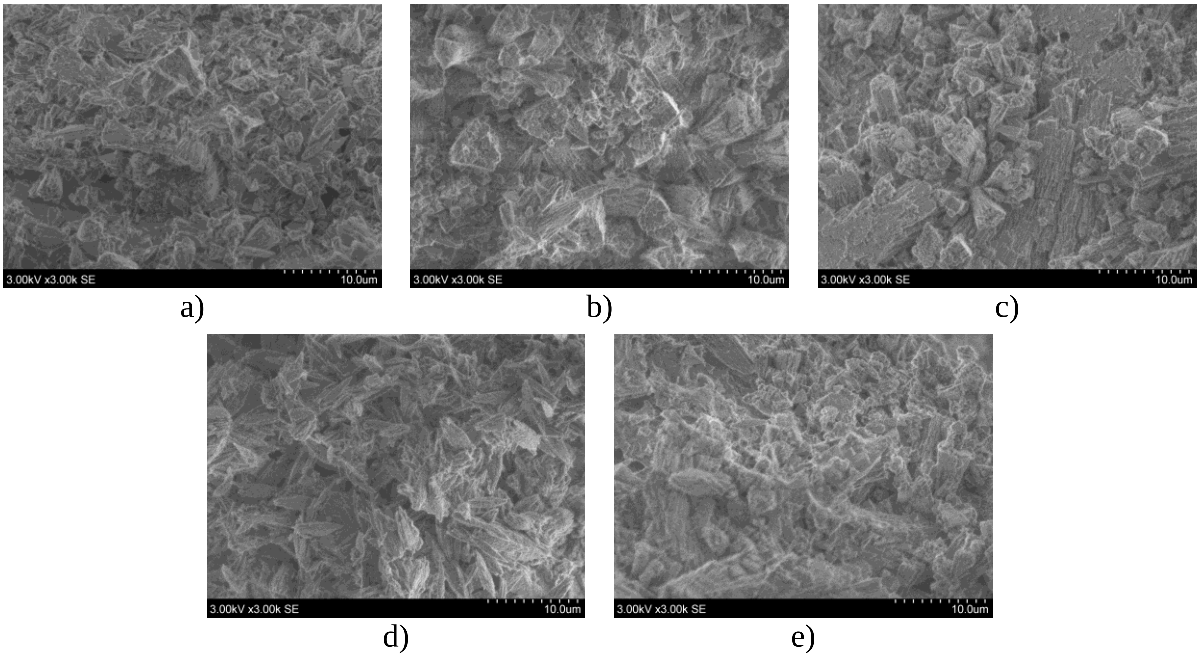

a) b) c)
d) e)

Fig. 2. SEM views of the Al-water reaction byproduct (a) and samples reduced in plasma at constant temperature (500 °C) and power (260 W) for 1 h varying ratio of mixed gases: (b) pure H_2; (c) H_2:Ar = 1:1; (d) H_2:Ar = 3:1; (e) H_2:Ar = 1:3

Chemical composition of as-received byproduct and plasma reduced samples is summarised in Table 1. Al-water byproduct consisted of 72.53 at.% of oxygen, 25.75 at.% of aluminium and 1.72 at.% of carbon. Whereas, samples reduced in non-thermal plasma presented the significant change in oxygen and aluminium concentrations. O/Al ratio was reduced after plasma treatment which showed that stoichiometry of Al-water byproduct was altered by oxygen loss. Hydrogen plasma is possible to induce chemical desorption of oxide while argon gas induce sputtering process. However the plasma treatment did not result the complete reduction. Changed stoichiometry showed that only polymorphic transformation (dehydroxylation) occurred. As well the comparison between chemical compositions of initial byproduct reduced in pure H_2 and H_2:Ar plasmas did not indicate a noticeable difference. Small carbon content is related with sample holder and adventitious carbon adsorbed on the powder surface.

Table 1. EDS elemental composition of Al-water byproduct and plasma reduced samples

Samples	**O, at.%**	**Al, at.%**	**C, at.%**	**O/Al ratio**
Initial byproduct	72.53	25.75	1.72	2.81
Pure H2	62.74	35.79	1.47	1.75
H_2:Ar = 1:1	62.94	35.53	1.53	1.77
H_2:Ar = 3:1	60.51	37.56	1.93	1.61
H_2:Ar = 1:3	61.66	36.18	2.16	1.70

3.2. XRD analysis

Structure of Al-water byproduct (Fig. 3a) and structural transformations after reduction experiments in plasma were characterised by XRD technique (Fig. 3 (b-e)). Fig. 3a demonstrates spectra of predominant monoclinic $Al(OH)_3$ (bayerite) with small peaks of Al and AlO(OH) (boehmite) which are left components after Al-water reaction. TOPAS software was used for structural refinement and crystallite size calculation of XRD spectra. In Fig. 3a crystal state concentrations were estimated: 95.54% of $Al(OH)_3$, 2.51% of AlO(OH) and 1.96% of Al. Calculated crystallite size of $Al(OH)_3$ was 60 nm. The hydroxide peaks vanished and structural transformation occurred after reduction process. Nano crystalline orthorhombic AlO(OH) structure was identified after reduction with pure H_2, $H_2:Ar = 1:1$ and $H_2:Ar = 3:1$ plasmas (Fig. 3 (b-d)). Mean crystallite size of AlO(OH) was 3–4 nm. Reduced sample demonstrated almost amorphous structure (one AlO(OH) peak registered) when plasma consisted of higher argon content than hydrogen (Fig. 3e). It seems that structural transformation of bayerite ($Al(OH)_3$) to boehmite (AlO(OH)) could be attributed to the elevated temperature which induced structural dehydration ($Al(OH)_3 = AlO(OH) + H_2O$). XRD results are in agreement with SEM and EDS results which indicated the presence of polymorphic transformation but not the reduction effect.

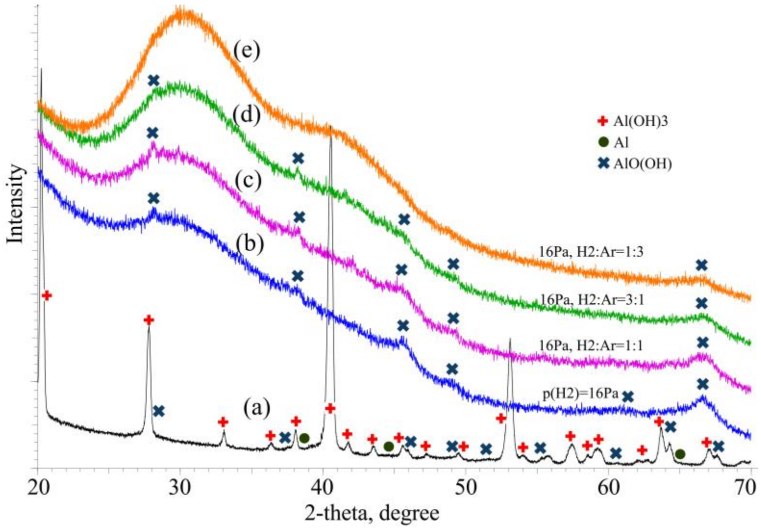

Fig. 3. XRD patterns of the Al-water reaction byproduct (a) and samples reduced in plasma at constant temperature (500 °C) and power (260 W) for 1 h varying ratio of mixed gases: (b) pure H_2; (c) $H_2:Ar = 1:1$; (d) $H_2:Ar = 3:1$; (e) $H_2:Ar = 1:3$

Physical and/or chemical plasma reduction processes could be applied for aluminium hydroxide. However, reduction of aluminium hydroxides in H_2 (H_2/Ar) plasma is not so simple. Some factors should be taken into account, such as location of material in the plasma reaction zone, processing time, temperature and reverse reaction, where atomic hydrogen recombines rather than reacting with the oxide [16, 17]. Another challenge is related to the water formed as the byproduct during the reduction process. Presence of water could increase the probability for the re-oxidation reaction [17]. According to the Ellingham diagram, small amount of impurities (eg.: water vapour) could hinder the reduction process [8].

4. CONCLUSIONS

Morphologic changes were not observed by scanning electron microscope after reduction of Al-water byproduct in plasma. All samples composed of irregularly-shaped agglomerated particles. Meanwhile, EDS elemental composition showed oxygen loss and aluminium growth after plasma reduction process. Altered H_2 and Ar ratio had no influence on elemental concentrations of reduced samples. XRD analysis showed drastic structural transformation after samples reduced in plasma. Instead of aluminium hydroxide reduction, thermal transformation of bayerite to boehmite occurred. Presumably thermal treatment had the leading effect, while plasma was as additional source for reduction process. Aluminium oxide reduction in plasma is a challenging process which could be affected by insufficient processing time and temperature, reverse reaction and the presence of impurities.

Future experiments require higher plasma concentration at the surface of treated sample and higher temperature.

REFERENCES

1. RAZAVI-TOUSI, S.S., NEMATOLLAHI, G.A., EBADZADEH, T., AND SZPUNAR, J.A. Modifying aluminum-water reaction to generate nano-sized aluminum hydroxide particles beside hydrogen. *Powder Technology*, 2013, Vol. 241, p. 166–173.
2. LIU, H., TSE, J.S., HU, J., LIU, Z., et al. Structural refinement of the high-pressure phase of aluminum trihydroxide: In-situ high-pressure angle dispersive synchrotron X-ray diffraction and theoretical studies. *Journal of Physical Chemistry B*, 2005, Vol. 109, No. 18, p. 8857–8860.
3. DAIMATSU, K., SUGIMOTO, H., KATO, Y., NAKANISHI, E., et al. Preparation and physical properties of flame retardant acrylic resin containing nano-sized aluminum hydroxide. *Polymer Degradation and Stability*, 2007, Vol. 92, No. 8, p. 1433–1438.
4. HALMANN, M., STEINFELD, A., EPSTEIN, M., AND VISHNEVETSKY, I. Vacuum carbothermic reduction of alumina. *Mineral Processing and Extractive Metallurgy Review*, 2014 Vol. 35, No. 2, p. 126–135.
5. BALOMENOS, E., PANIAS, D., AND PASPALIARIS, I. Energy and exergy analysis of the primary aluminum production processes: A review on current and future sustainability. *Mineral Processing and Extractive Metallurgy Review*, 2011, Vol. 32, No. 2. p. 69–89.
6. RAINS, R.K. AND KADLEC, R.H. The reduction of Al_2O_3 to aluminum in a plasma. *Metallurgical Transactions B*, 1970, Vol. 1, No. 6, p. 1501–1506.
7. HUCZKO, A. AND MEUBUS, P. Vapor phase reduction of chromic oxide in an Ar-H2 Rf Plasma. *Metallurgical Transactions B*, 1988, Vol. 19, No. 6, p. 927–933.
8. VESEL, A., MOZETIC, M., AND BALAT-PICHELIN, M. Reduction of a thin chromium oxide film on Inconel surface upon treatment with hydrogen plasma. *Applied Surface Science*, 2016, Vol. 387, p. 1140–1146.
9. BRAATEN, O., KJEKSHUS, A., AND KVANDE, H. The possible reduction of alumina to aluminum using hydrogen. *The Journal of The Minerals, Metals and Materials Society*, 2000, Vol. 52, No. 2, p. 47–53.
10. LYUBOCHKO, V.A., MALIKOV, V.V., PARFENOV, O.G., AND BELOUSOVA, N.V. Reduction of aluminum oxide in a nonequilibrium hydrogen plasma. *Journal of Engineering Physics and Thermophysics*, 2000, Vol. 73, No. 3, p. 580–584.
11. BULLARD, D.E. AND LYNCH, D.C. Reduction of titanium dioxide in a nonequilibrium hydrogen plasma. *Metallurgical and Materials Transactions B*, 1997, Vol. 28, p. 1069–1080.
12. WATANABE, T., SOYAMA, M., KANZAWA, A., TAKEUCHI, A. AND KOIKE, M. Reduction and separation of silica-alumina mixture with argon-hydrogen thermal plasmas. *Thin Solid Films*, 1999, Vol. 345, p. 161–166.
13. KITAMURA, T., SHIBATA, K., AND TAKEDA, K. In-flight reduction of Fe_2O_3, Cr_2O_3, TiO_2 and Al_2O_3 by Ar-H2 and Ar-CH_4 plasma. *ISIJ international*, 1993, Vol. 33, p. 50–58.

14. MOZETIČ, M., VESEL, A., KOVAČ, J., ZAPLOTNIK, R., MODIC, M., BALAT-PICHELIN, M. Formation and reduction of thin oxide films on a stainless steel surface upon subsequent treatments with oxygen and hydrogen plasma. *Thin Solid Films*, 2015, Vol. 591, p. 186–193.
15. BALOMENOS, E. AND PANIAS, D., FRIEDRICH, B., JARONI, B. Carbothermic reduction of alumina: A review of developed processes and novel concepts. *Proceedings of EMC*, 2011, p. 729–744.
16. SABAT, K.C., RAJPUT, P., PARAMGURU, R.K., BHOI, B., MISHRA, B.K. Reduction of oxide minerals by hydrogen plasma: An overview. *Plasma Chemistry and Plasma Processing*, 2014, Vol. 34, p. 1–23.
17. ZHANG, W., SADEDIN, D.R., REUTER, M.A. AND MCCALLUM, J.C. The de-oxidation of partially oxidized titanium by hydrogen plasma. *Materials Forum*, 2007, Vol. 31, p. 76–83.

CYSENI 2017, May 25-26, Kaunas, Lithuania
ISSN 1822-7554, www.cyseni.com

Ni-NaCl POWDERS PRODUCTION USING MAGNETRON SPUTTERING

JOSÉ RAMÓN DÍAZ ORDAZ
Vytautas Magnus University
Faculty of Natural Sciences
Physics Department
Vileikos g. 8, LT-44404 – Lithuania
E-mail: IronhideX1@gmail.com

Darius Milčius
Lithuanian Energy Institute
Center for Hydrogen Energy Technologies
Breslaujos g. 3, LT-44403 – Lithuania
E-mail: Darius.Milcius@lei.lt

ABSTRACT

Nickel extraction and manipulation involve plenty environmental and safety dangers. Being almost as harmful as cobalt, high airborne nickel nanoparticles concentrations (over 1.0 mg/m^3) produce severe injuries if inhaled as they present a high surface-to-volume ratio that greatly increases their reactivity. Ni-NaCl powders were produced using DC magnetron sputtering. The created structures allow transporting the Ni structures without harm to environment from production site to the final user.

The research focuses on the analysis of received structures surface morphology and elemental composition. Characterization of powders and nanoparticles is performed by combining scanning electron microscopy (SEM), energy-dispersive X-ray spectroscopy (EDS) and X-ray photoelectron spectroscopy (XPS). SRIM modeling shows possibility to change Ni structures geometry by initiating penetration of Ni particles into salt substrate during deposition.

Keywords: powders, magnetron sputtering, nickel, impurities on the material surfaces

INTRODUCTION

Nanoparticles (NPs), considering under this category particles with Ø ≤ 100 nm, have been extensively developed for facing industrial needs in so different areas as the electrical, optical, biochemical and biomedical.

Particularly nickel nanoparticles (Ni NPs) are widely used in batteries and fuel cells applications, especially as materials for electrodes and catalysts. There are other interesting uses as pigments in coatings focused on electromagnetic interference (EMI) shielding applications [1, 2].

During the last years, several studies have been conducted to develop a green and environmentally suitable NPs production method, capable of producing highly pure homogeneously sized particles [2] with different structures. Some of these methods include ball milling [3], inert-gas condensation [4], reverse micelles systems [2], hydrothermal, micro-emulsion synthesis [5] and plasma technologies [6].

Nickel extraction and manipulation involve plenty environmental and safety dangers. Being almost as harmful as cobalt, high airborne nickel nanoparticles concentrations (over 1.0 mg/m^3) produces severe injuries if inhaled as they present a high surface-to-volume ratio that greatly increases their reactivity. Traditionally is accepted that when the particles concentration increases, so does their toxicity [7]. However, as nanoparticles tend to agglomerate when the concentration per volume increases, they are more dangerous in small quantities, as they preserve their reactivity. Nickel can cause allergy through skin contact and penetrate through inhalation to the digestive, respiratory and nervous systems [7] eventually leading to cancer problems. Moreover, while refining it through the Mond process [8] (that is extensively used in industry) certain toxic exhaust gases may be involved in the production stage, such as carbon oxide [CO] and nickel carbonyl [$Ni(CO)_4$].

Attaching of Ni NPs to NaCl grains allows increasing the transportation safety, preventing eventual leakages and airborne dust formation; and decreasing the NPs agglomeration risks.

It is possible to achieve well-defined dimensioned particles with a narrow size distribution and limited particle aggregation through magnetron sputtering [9, 10]. This technology has some particular pros: allows working directly with pure nickel instead of needing a compounded source (due to the Ni tendency of spontaneously oxidize when exposed to air), which implies no contamination from solvent or precursor molecules on the surface, and no heating required for decomposing precursors; excess nickel is recoverable from the chamber after sputtering; there is no liquid waste; and it is a method relatively easy to adapt and scale up to industrial production [9, 10].

The DC planar magnetron main drawbacks are the low deposition rate on the substrate, the production time and the ions relatively low energy. Authors as Veith et al. reported a measured by ICP rate of 1.37 wt. %, which implies an efficiency loss around 99 %; even working with a rotating substrate holder for improving the chance of getting a homogeneous deposition [9]. However, it is intrinsically connected to the technology, as 80 % of the supplied electric energy is transformed to heat and therefore lost.

Several researchers have carried out experiments related to this area [9, 11, 6] since the first results were obtained by Takeuchi et. all [6]. Although magnetron sputtering had been widely used for thin film deposition of nickel, there were not many previous attempts of generating powders with commercial purpose [3].

The technological novelty of proposed work is related to development of industry suitable technique of Ni clusters synthesis on water soluble substrates. The main aim of this work was to produce Ni clusters on the salt substrates, dissolve substrates in water afterward and analyse Ni particles surface morphology, elemental composition and crystalline structure using SEM, EDS and XPS methods. In order to estimate Ni particle attachment and possible penetration into salt substrate SRIM modelling results also presented and discussed.

METHODOLOGY

At the first step several models with SRIM software were developed for estimating the Ni NPs attachment to the substrate.

SRIM is a modelling tool that is based on the Monte Carlo algorithms. This software allows defining the stopping/range tables and the TRIM calculation of the sputtered particles. It was used for setting the ideal energy range within the particles attachment to the substrate is guaranteed, depending on a Gaussian distribution.

DC magnetron sputtering were used for nickel particles synthesis on salt substrates (Fig. 1).

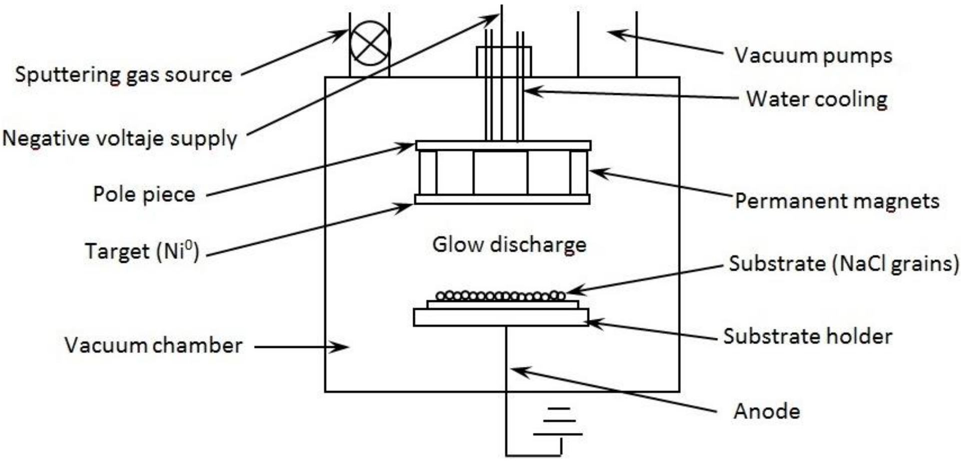

Fig. 1. Magnetron sputtering system configuration

The main parameters during sputtering process were: distance between magnetron and salt substrates (10 cm), magnetron power (420 W), carrier gas (argon), and deposition time (15 min).

Investigation of the particles size and shape was done through scanning electron microscopy (SEM) technique with a Hitachi S-3400N. An elemental distribution was researched by energy-dispersive X-ray spectroscopy (EDS) with a BRUKER QUANTAX 5040. Besides, the chemical state and the purity grade was checked by X-ray photoelectron spectroscopy (XPS) with a PHI-5000 Versaprobe.

RESULTS AND DISCUSSION

1.1. SRIM models

The preliminary hypothesis was that the Ni NPs could have enough energy from the magnetron so that they could penetrate inside the substrate surface by hard-landing phenomena. Therefore, attachment could be improved by increasing particles energy or decreasing substrate packing (i.e. increasing temperature).

SEM images obtained from the NaCl characterization showed that the surface length (considered as the diameter of the sputtered zone) of an average NaCl crystal was 2500 Å (the average clusters size is around 2 µm). Considering all Ni clusters as spheres; for avoiding cluster instability (critical breaking of internal structure) the maximum penetration range was set on 0.8 of the cluster diameter (2000 Å).

Considering a different approach, the model focuses on analysing the sputtering of the Ni NPs over the NaCl crystal, so the particles handling would be facilitated. With an average kinetic energy of 0.5 keV mainly there will be incorporation of NPs to the substrate by soft-landing. It is shown that the expected average penetration will be up to 100 Å.

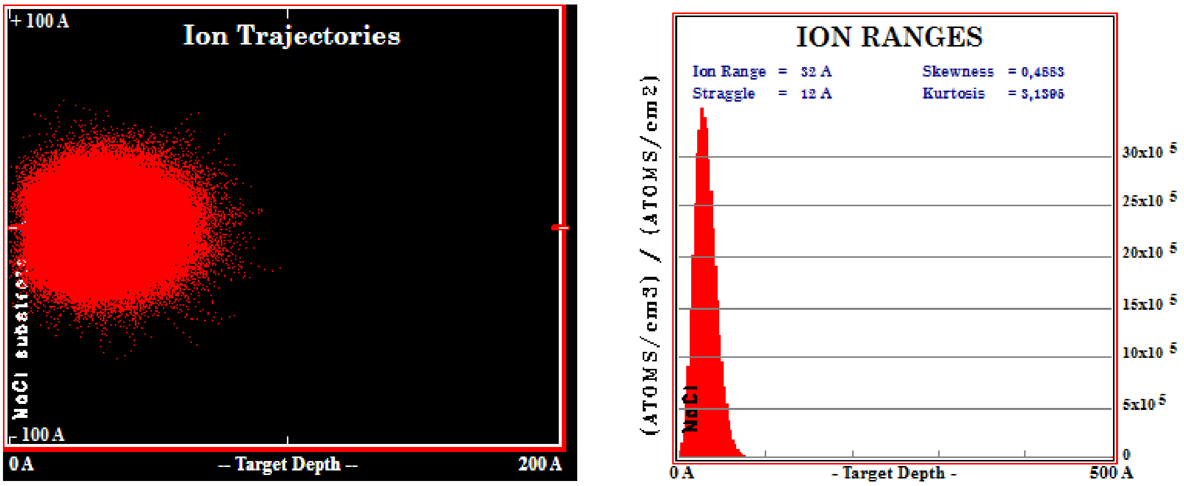

a) b)

Fig. 2. SRIM modelling results. (a) Ion trajectories from Z-axis and aerial views (model by SRIM); (b) particles distribution along the penetration range, 0–200 Å

1.2. NaCl characterization

Two table salt brands provided the NaCl substrate: a thick grained rock salt with a 97.5 % purity; and a fine-grained marine salt with a 99.7 % purity and including an iodine supplement of 20–40 mg/kg.

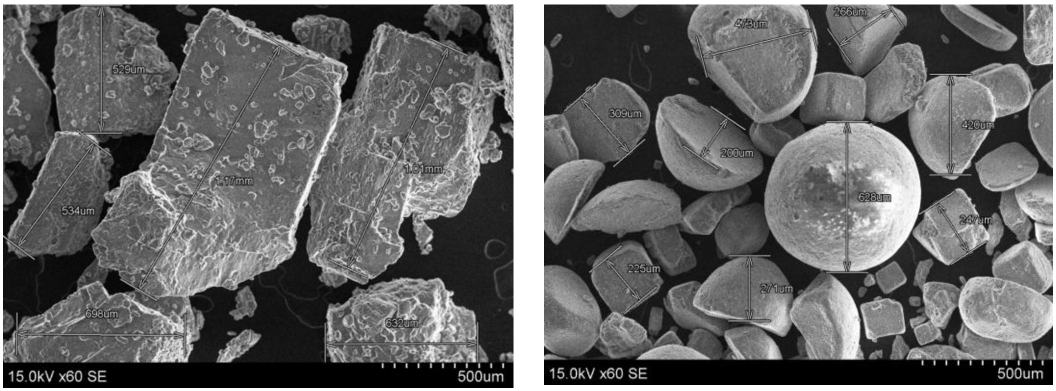

a) b)

Fig. 3. Initial salt: (a) thick grained rock salt; (b) fine-grained marine salt

The salt particles SEM analysis (Fig. 3) revealed that in case of thick grained rock salt the particles size in range from about 500 µm up to 1 mm. The particles geometry is close to non uniform rectangular shape. In case of the fine-grained marine salt we see rounded particles with the size from 100 µm up to 700 µm.

The elemental composition analysis done by EDS is showed in Table 1. In both salts several impurities were detected. In case of thick grained rock salt it is calcium and sulfur and in case of fine-grained marine salt – sulfur. These additional impurities can form componds with nickel after deposition and removal from salt.

Table 1. EDS analysis of thick grained rock salt and fine-grained marine salt

Element	Thick grained rock salt	Fine-grained marine salt
Oxygen, at. %	5.17	3.32
Sodium, at. %	48.84	49.36
Chlorine, at. %	45.08	47.10
Calcium, at. %	0.68	-
Sulfur, at. %	0.23	0.23

1.3. Ni-NaCl powders/Ni particles characterisation

Ni-NaCl powders were produced using magnetron sputtering technique. Elemental mapping analysis show that Ni (red color) distributes uniformly on both salts (Fig. 4).

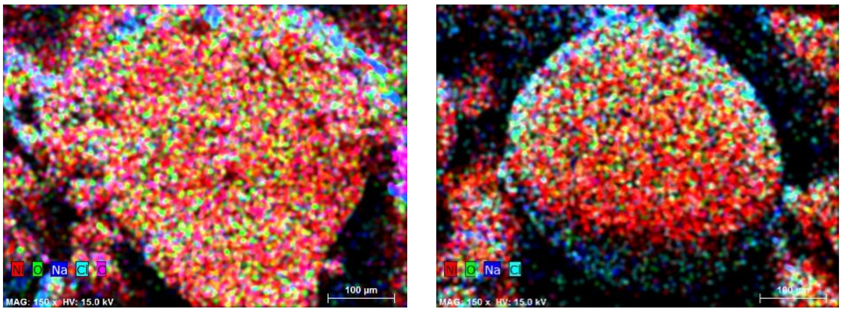

a) b)

Fig.4. Distribution of Ni on salt crystals for (a) thick grained rock salt; (b) fine-grained marine salt

The produced Ni-NaCl powders were immersed in distiled water and in ultrasonic bath for 15 min. Few cycles of immersion were repeated with the partial water change everytime. The received Ni particles were flake like structures (Fig. 5).

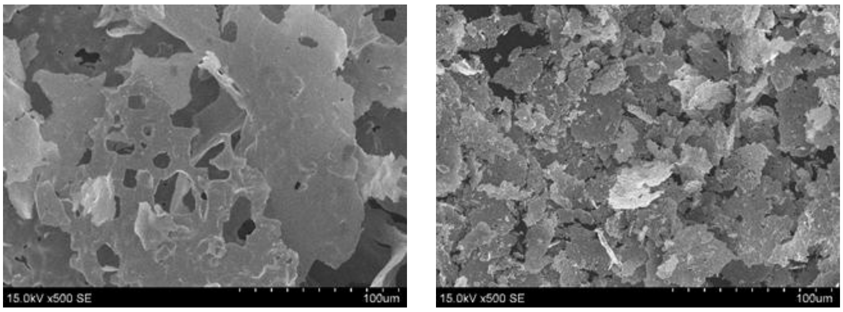

a) b)

Fig. 5. Ni structures after removal from (a) thick grained rock salt; (b) fine-grained marine salt

The SEM analysis revealed that geometry of Ni structures were very sensitive to the geometry of the salt substrate. The use of bigger substrates (thick grained rock salt) leads to the synthesis of more than twice bigger flakes in comparison to fine-grained marine salt. Ni particles form uniform structures on the salt surface repeating the substrate geometry and it leads to the formation of different Ni structures.

Detailed XPS analysis showed the presence of impurities forming structures in the received Ni flakes (Fig. 6).

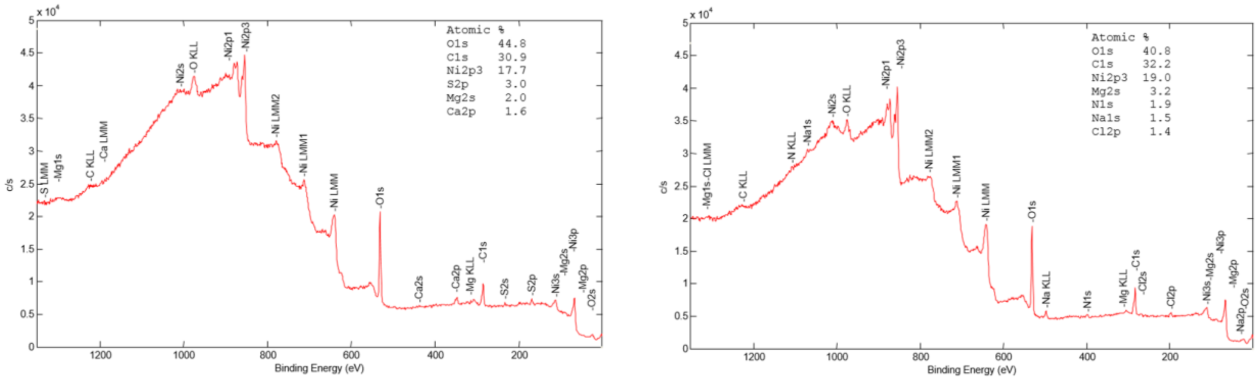

a) b)

Fig. 6. XPS graphs of Ni structures received from (a) thick grained rock salt; (b) fine-grained marine salt

It is important to point out that Ca impurities which we found in initial thick grained rock salt becomes attached to Ni particles after salt removal. The presence of Mg impurities was also very important in both cases. Up to now it remains unclear where this Mg amount came from; although it could be an undetected component of the original salt. Further XPS analysis of the substrate should be carried out.

CONCLUSIONS

Ni-NaCl powders, resulting in different-sized size structures, were produced by magnetron sputtering. Ni particles were distributed uniformly on salt surface and it led to formation of flake like Ni structures after salt removal. Simple and non-expensive dissolution of salt in distilled water could be used for Ni structures removal from salt substrates. The combined EDS and XPS elemental composition analysis showed that Ca impurities were present in both of the cases: initial thick grained rock salt and on the surface of received Ni structures after salt removal. It shows importance of the quality of the substrate. The substrates must be with minimum amount of impurities in order to receive pure Ni structures after salt removal. The SRIM modelling results show possible penetration of Ni particles in near surface region of salt substrate. These results lead to conclusion that by changing Ni ions energy during deposition there is possibility to change Ni penetration depths and to have different in size and shape Ni structures after salt removal.

The presented results confirms possibility to produce Ni-NaCl powders which can be transported in safe way from production site to the end user. Ni remains attached to NaCl and there is no possibility to have environment contamination with harmful Ni particles.

AKNOWLEDGEMENTS

This work was financially supported by The European Social Fund under project with SFMIS code: VP1-3.1-SMM-10-V-02-019.

REFERENCES

1. LUCCHINI, M. A., TESTINO, A., LUDWIG, C., KAMBOLIS, A., EL-KAZZI, M., CERVELLINO, A., RIANI, P., CANEPA, F. Continuous synthesis of nickel nanopowders: Characterization, process optimization, and catalytic properties. *Applied Catalysis B: Environmental*, 2014, Vol. 156-157, p. 404-415.
2. WIEDWALD, U., HAN, L., BISKUPEK, J., KAISER, U., ZIEMANN, P. Preparation and characterization of supported magnetic nanoparticles prepared by reverse micelles. *Beilstein Journal of Nanotechnology*. 2010, No. 1, p. 24-47.
3. TAKEUCHI, A., WISE, H. High dispersion platinum catalyst by RF sputtering. *Journal of Catalysis*, 1983, Vol. 83, Iss. 2, p. 477-479.
4. BOUCHAT, V., MOREAU, N., COLOMER, J-F., LUCAS, S. On Some Applications of Nanoparticles Synthesized in the Gas Phase by Magnetron Discharges. *Journal of Surface Engineered Materials and Advanced Technology*, 2013, No. 3, p. 184-189.
5. BEYGI, H., BABAKHANI, A. Microemulsion synthesis and magnetic properties of $Fe_xNi_{(1-x)}$ alloy nanoparticles. *Journal of Magnetism and Magnetic Materials*, 2017, No. 421, p. 177-183.
6. TAKEUCHI, A., WISE, H. High dispersion platinum catalyst by RF sputtering. *Journal of Catalysis*, 1983, Vol. 83, Is. 2, p. 477-479.
7. KALIKMANOV, V. I. Classical nucleation theory. *Lecture Notes in Physics*, 2012, No. 860, p. 17-41.
8. CRUNDWELL, F. K., MOATS, M. S., RAMACHANDRAN, V., ROBINSON, T. G., DAVENPORT, W. G. Carbonyl refining of impure nickel metal. *Extractive Metallurgy of Nickel, Cobalt and Platinum Group Metals*, 2011, p. 269-280.
9. VEITH, G. M., LUPINI, A. R., PENNYCOOK, S. J., OWNBY, G. W., DUDNEY, N. J. Nanoparticles of gold on γ-Al_2O_3 produced by dc magnetron sputtering. *Journal of Catalysis*, 2005, No. 231, p. 151-158.
10. KELLY, P. J., ARNELL, R. D. Magnetron sputtering: a review of recent developments and applications. *Vacuum*, 2000, No. 56, p. 159-172.
11. YOUNG-MIN, K., KYOU-HYUN, K., BYOUNGMOON, K., HANSHIN, C. Size and morphology manipulation of nickel nanoparticle in inductively coupled thermal plasma synthesis. *Journal of Alloys and Compounds*, 2016, No. 658, p. 824-831.

ATTEMPT TO REGENERATE MgO TO Mg UNDER HYDROGEN PLASMA CONDITIONS

Dalius Girdzevičius, Marius Urbonavičius, Šarūnas Varnagiris, Darius Milčius
Lithuanian Energy Institute
Breslaujos str. 3, LT-44403, Kaunas – Lithuania
E-mail: dalius.girdzevicius@lei.lt

ABSTRACT

Magnesium hydride is considered as a potential hydrogen storage solution capable to store up to 7.66 wt% of hydrogen. On the other hand, MgH_2 can be used as a source to power portable devices on demand realizing its reaction with water and consequent hydrogen supply to fuel cells. Hydride reaction with water in liquid phase or steam ensures hydrogen generation and formation of $Mg(OH)_2$ or MgO respectively. Regeneration of hydrolysis byproducts to Mg is needed in practical point of view – process becomes environmentally friendly when Mg powder can be hydrogenated repeatedly. High temperature treatment, resulting increased energy consumption, is required to remove undesired compounds. Current work aims to apply hydrogen plasma for efficient magnesium oxide reduction to Mg. Hydrogen is known as a reducing agent in metal industry, thus, hydrogen plasma is suggested as a technique for regeneration. Results presented in this paper clearly demonstrate importance of an accurate selection of working conditions, especially taking into account temperature and time of treatment. The largest decrease in MgO crystalline concentration (up to 8.98%) was fixed when hydrogen plasma treatment was in process at 750 °C for 3 hours. Magnesium powder was investigated before and after the treatment in hydrogen plasma. Surface morphology was identified by scanning electron microscopy (SEM), elemental composition of the surface – by energy dispersive X-ray spectrometry (EDS), crystalline structure was determined using X-ray diffraction technique (XRD).

Keywords: regeneration, magnesium oxide, reduction, plasma, hydrogen, hydride

1. INTRODUCTION

Magnesium hydride (MgH_2) as an appropriate solution for hydrogen storage has been intensely studied since 1912 [1]. Despite hydrogenation/dehydrogenation reaction and thermodynamic limitations, Mg has relatively high gravimetric (7.66 wt%) and volumetric (110 g H/l) densities. Consequently, various attempts to enhance unfavorable properties are investigated. It usually includes ball milling, alloying, catalysts and thin film hydrides [1], [2], [3].

Furthermore, attention to MgH_2 is paid not only because of its potential applicability for hydrogen storage, but for on-demand hydrogen generation during powder/water reaction as well. According to pre-described technique, hydrogen yield can reach 15.2 wt% following two possible reactions [4], [5]:

$$MgH_2 + 2H_2O \rightarrow Mg(OH)_2 + 2H_2,\ [4] \tag{1}$$

$$MgH_2 + 2H_2O \rightarrow MgO + 2H_2,\ [6] \tag{2}$$

These equations depict MgH_2 reaction with water and steam respectively. Such hydrolysis lead to formation of magnesium hydroxide or oxide as by-products. Despite possible applications of $Mg(OH)_2$ (e.g. flame retardant, smoke suppressant, neutralizer for acidic wastewater, natural antacid in medicine, etc.) [7], [8], [9] or MgO (e.g. pH modifier in industrial applications, component in fireproof materials, acid trace neutralizer in paper production, electric insulator, fuel additive, etc.) [10], [11], regeneration is considered as a solution to ensure re-use of powder in hydrogenation.

Pidgeon process is widely dominated method for Mg extraction during thermal reduction reaction between calcined dolomite and ferrosilicon. Vacuum pressure of approximately 10 Pa and temperature of 1100–1200 °C are needed to ensure this operation [12]. Economic aspect makes this technique the most popular in China which is known as the main supplier of Mg metal [13]. Carbon as a reducing agent is usually used for industrial reduction of metal oxides to obtain pure metals as well. Carbothermic reduction ensures low cost of reductant and high production efficiency [13]. However, generated carbon oxides are not desirable compounds according to environmental requirements determined by responsible international institutions [14]. Moreover, reversion reactions and consolidation of fine Mg are challenges that must be overcome [13]. Reaction between metallic aluminum and magnesium oxide was also proposed as possible solution to reduce MgO. In this case, process requires introduction of new material and increase temperature above 850 °C [15]. Laser-induced MgO regeneration is considered as an alternative way to produce Mg too. This process starts when CO_2 laser is focused on a mixture of oxide and reductant (e.g. C) leading to high operation temperature and subsequent evaporation. In order to create an effective system solar powered laser together with the reducing agent is proposed [16].

The objective of this paper is to apply hydrogen plasma for an efficient MgO reduction to Mg excluding addition of catalyst and reducing operating temperature. Hydrogen is known as a reducing agent in metal industry, thus, hydrogen plasma is suggested as a technique for regeneration. It plays an important role because of its composition of energetic atoms, ions and other particles creating favorable thermodynamic properties compared to molecular hydrogen [14].

2. EXPERIMENTAL TECHNIQUES

Regeneration of oxidized Mg powder (315–630 μm) was done in hydrogen plasma environment ensuring its generation around the sample. Tungsten heating source was placed below the sample. It was in contact with the stainless steel substrate ensuring adequate heat transfer. Hydrogen consumption was 600–650 ml/h during experiments. Optimal process conditions were determined by changing working temperature (500, 750, 1000 °C) and time (3, 6 hours). Constant pressure of 16 Pa was maintained during all experiments. DC power supply was set to 600 V.

Configuration of oxidized Mg regeneration system is shown in Fig. 1.

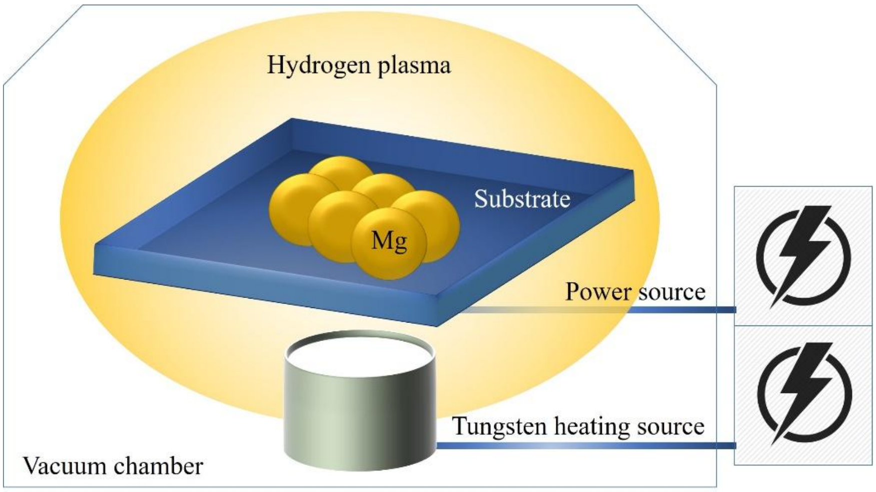

Fig. 1. Principle scheme of powder regeneration system

Mg powder characterization was done before and after regeneration in hydrogen plasma. Scanning electron microscopy (SEM, Hitachi S-3400N) was used to analyze surface morphology. Energy dispersive X-ray spectroscopy (EDX, Bruker Quad 0540) was employed to find out the elemental composition. Microstructural characterization of the samples was done using diffractometer (Bruker D8) with an appropriate software (EVA Search Match) for identification of the peaks. Consequently, quantitative analysis of crystalline concentrations were estimated using TOPAS software.

3. RESULTS AND DISCUSSION

SEM images summarize alterations of particle surface morphology caused by regeneration of oxidized Mg powder (Fig. 2). As-received oxidized Mg (Fig. 2a) depicts relatively smooth surface compared to samples treated in hydrogen plasma environment. Such processing of the powder effects surface restructuring (Fig. 2c) and induces formation of modest islands/clusters (Fig. 2b, d). The reason of these changes can be attributed to working conditions (temperature, pressure, time) and probable consequent variation of elemental composition. Mg powder regenerated at 500 °C and 1000 °C for 3 hours reveal clustering (Fig. 2b, d). Higher temperature causes more distinct growth of crystal structure.

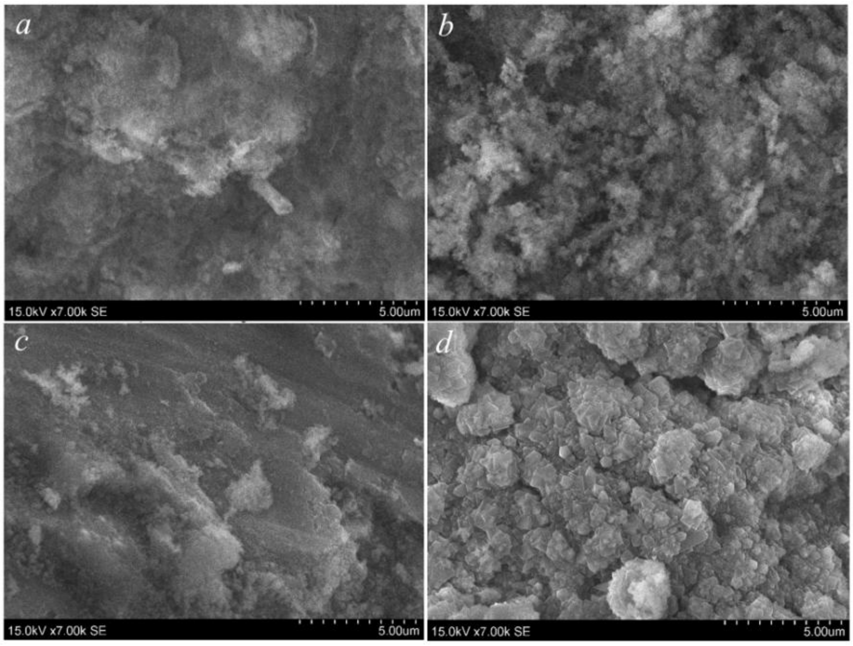

Fig. 2. SEM images. As-received oxidized Mg (a), Mg regenerated in hydrogen plasma (b – 500 °C, c – 750 °C, d – 1000 °C; 3 hours)

Elemental composition dependence of regeneration temperature is indicated in Fig. 3.

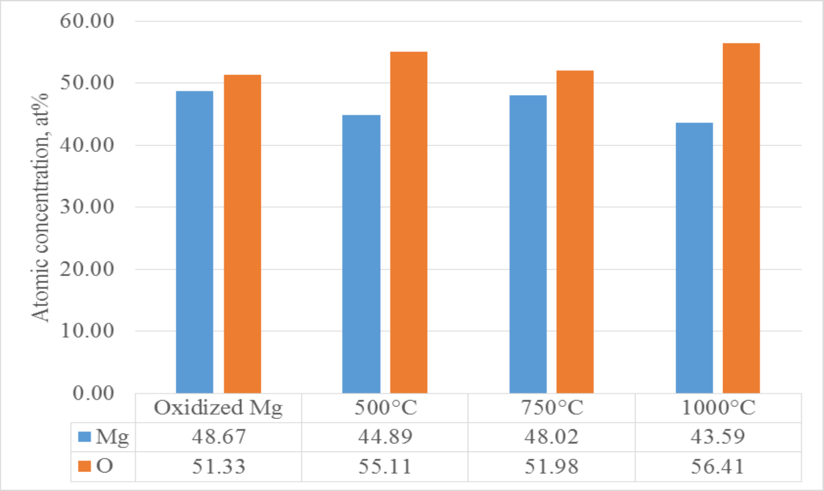

Fig. 3. Elemental composition of Mg powder at different working temperatures (time of regeneration in hydrogen plasma – 3 hours)

Variable ratio of Mg:O does not show any correlation with increased working temperature. Moreover, it is important to mention that none of regenerated samples demonstrates reduction in atomic concentration of oxygen. This ratio decreases for samples treated at 500 °C and 1000 °C under hydrogen plasma, while oxide reduction procedure at 750 °C gives very similar results with as-received oxidized Mg powder.

Fig. 4 reveals summarized element mapping results of characteristic as-received and plasma treated Mg powder. Small islands of relatively pure Mg are fixed in as-received and regenerated (at 750 °C) samples (Fig. 4a, c). On the contrary, even distribution of oxygen is measured in the rest of Mg powder (Fig. 4b, d). According to visual assessment of all samples, it can be stated that efficiency of oxide reduction in hydrogen plasma relates to selection of optimal working conditions and depends on shape of the sample, i.e. spherical powder may have shadows where the surface is not affected by plasma.

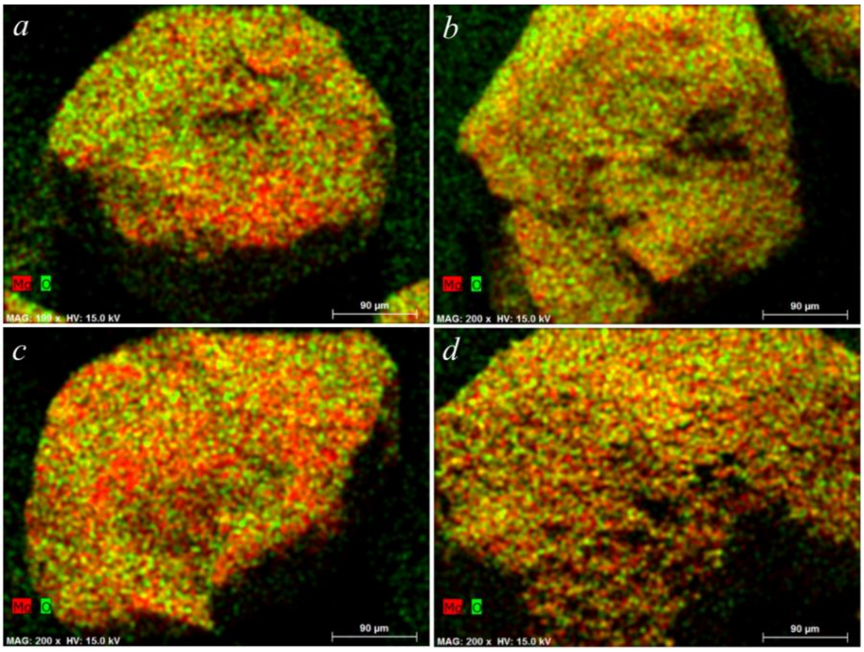

Fig. 4. Element mapping. As-received oxidized Mg (a), Mg regenerated in hydrogen plasma (b – 500 °C, c – 750 °C, d – 1000 °C; 3 hours)

The XRD spectra (Fig. 5) of analyzed Mg powder reveal growth of crystalline MgO at working temperatures of 500 °C and 1000 °C, while decrease of these peaks is noticed at 750 °C. This result is in good agreement with elemental analysis presented above, i.e. the highest MgO intensity is fixed when working temperature is at 1000 °C, and the lowest – at 750 °C. This leads to interim conclusion that an appropriate working temperature is one of the key factors in process of oxygen reduction.

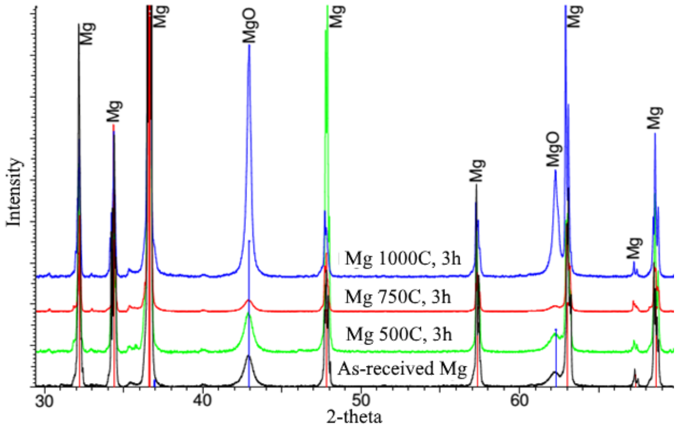

Fig. 5. XRD patterns of Mg powder treated in hydrogen plasma at different working temperatures for 3 hours

Crystalline concentrations were measured using Topas software (Fig. 6). As expected, a slight decrease in MgO content was fixed only at working temperature of 750 °C. This concentration was lower than as-received Mg powder. Consequently, other samples demonstrated significant increase in crystalline concentration of MgO.

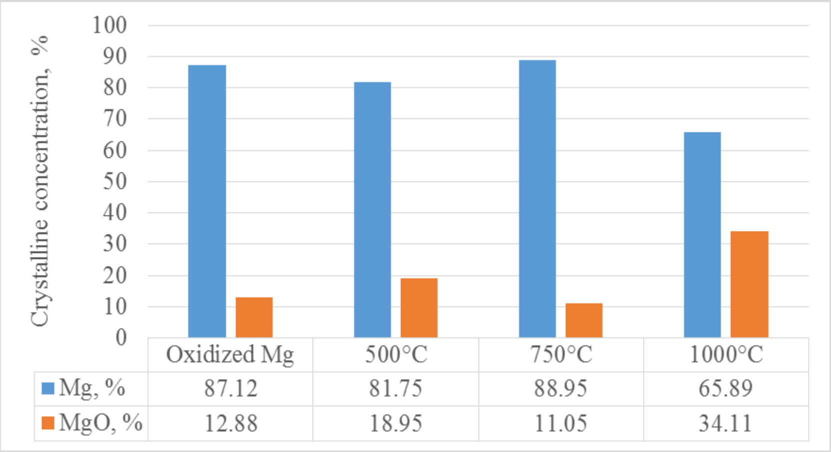

	Oxidized Mg	500°C	750°C	1000°C
🟦 Mg, %	87.12	81.75	88.95	65.89
🟧 MgO, %	12.88	18.95	11.05	34.11

Fig. 6. Crystalline concentrations of Mg and MgO of Mg powder treated in hydrogen plasma at different working temperatures for 3 hours

Therefore, 750 °C was confirmed as optimal working temperature for oxide regeneration in hydrogen plasma. In order to understand regeneration efficiency dependence on time, experiment was extended up to 6 hours.

XRD diffractograms reveal how time of regeneration affects alteration of crystal structures (Fig. 7). Only fractional decrease in intensity of MgO peaks is noticed in regenerated Mg powder compared with as-received oxidized Mg. Generally, spectra of plasma treated samples are very similar.

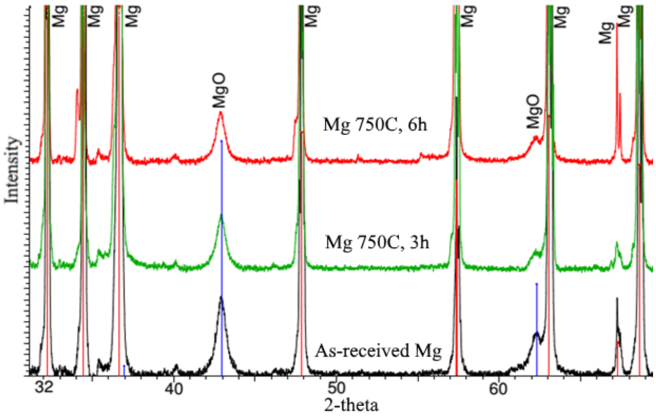

Fig. 7. XRD patterns of Mg powder treated in hydrogen plasma at different time of regeneration

Quantitative assessment of crystalline concentrations shows negative effect of extended regeneration (Fig. 8). Despite the fact that an amount of MgO decreased, still it was more than in the sample treated in hydrogen plasma for 3 hours.

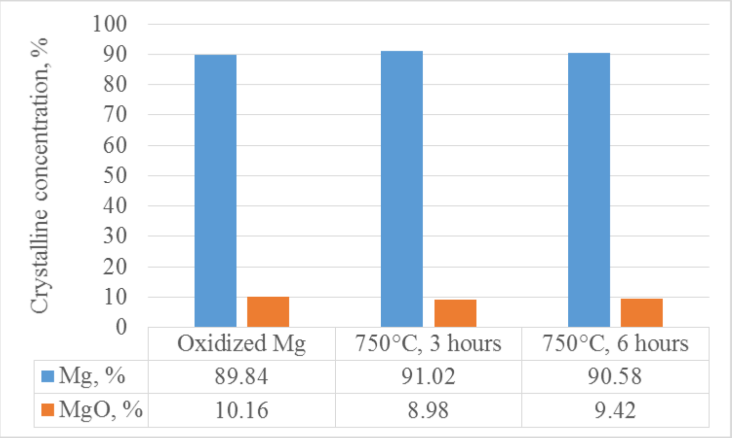

Fig. 8. Crystalline concentrations of Mg and MgO of Mg powder treated in hydrogen plasma at different time of regeneration

4. CONCLUSION

Experimental results lead to the conclusion that regeneration efficiency of oxidized Mg powder strongly depends on appropriate working conditions, including factors of time and temperature during treatment in hydrogen plasma. Moreover, it must be noted that there is no direct relation between temperature increase and decrease of MgO concentration. Although reduction of oxide is relatively insignificant, it is worth to be mentioned that the process of regeneration does not require extreme conditions, i.e. highest temperatures or time extension. In our case, the best regeneration efficiency was obtained when hydrogen plasma induced regeneration was done at 750 °C for 3 hours.

REFERENCES

1. JAIN, I. P.; LAL, C.; JAIN, A. Hydrogen storage in Mg: A most promising material. *International Journal of Hydrogen Energy*, 2010, Vol. 35, No. 10, p. 5133–5144.
2. LOTOTSKYY, M.; SIBANYONI, J. M.; DENYS, R. V.; WILLIAMS, M.; POLLET, B. G.; YARTYS, V. A. Magnesium-carbon hydrogen storage hybrid materials produced by reactive ball milling in hydrogen. *Carbon*, 2013, Vol. 57, p. 146–160.
3. CRIVELLO, J. C.; *et al.* Review of magnesium hydride-based materials: development and optimisation. *Applied Physics A: Materials Science and Processing*, 2016, Vol. 122, No. 2, p. 1–20.
4. GIRDZEVIČIUS, D.; MILČIUS, D. Electrical power generation with PEM FC using hydrogen supply through Mg-Ni reaction with water. *Energetika*, 2016, Vol. 62, No. 1–2, p. 19–27.
5. UESUGI, H.; SUGIYAMA, T.; NAKATSUGAWA, I. Production of Hydrogen Storage Material MgH_2 and its Applications. Link to the internet: < http://www.biocokelab.com/dcms_media/other/MgH2.pdf >
6. KINDLER, A.; HUANG, Y. Refinements in an $Mg/MgH_2/H_2O$-Based Hydrogen Generator. Link to the internet < https://ntrs.nasa.gov/archive/nasa/casi.ntrs.nasa.gov/20100042209.pdf>
7. Magnesium Hydroxide ($Mg(OH)_2$) Nanoparticles - Properties, Applications. Link to the internet: http://www.azonano.com/article.aspx?ArticleID=3367>
8. Magnesium Hydroxide: Formula, Uses & Side Effects. Link to the internet: <http://study.com/academy/lesson/magnesium-hydroxide-formula-uses-side-effects.html>
9. Magnesium hydroxide Formula – Magnesium hydroxide Uses, Properties, Structure and Formula. Link to the internet:

<http://www.softschools.com/formulas/chemistry/magnesium_hydroxide_uses_properties_structure_formula/249/>

10. Magnesium Oxide (MgO) Industrial Applications. Link to the internet: <http://www.baymag.com/applications/industrial.php>
11. Magnesium Oxide (MgO) Nanoparticles - Properties, Applications. Link to the internet: <http://www.azonano.com/article.aspx?ArticleID=3353>
12. LI, R. B.; ZHANG, S. J.; GUO, L. J.; WEI, J. J. Numerical study of magnesium (Mg) production by the Pidgeon process: Impact of heat transfer on Mg reduction process. *International Journal of Heat and Mass Transfer*, 2013, Vol. 59, No. 1, p. 328–337.
13. BO YANG, C.; TIAN, Y.; QU, T.; YANG, B.; QIANG XU, B.; NIAN DAI, Y. Production of magnesium during carbothermal reduction of magnesium oxide by differential condensation of magnesium and alkali vapours. *Journal of Magnesium and Alloys*, 2013, Vol. 1, No. 4, p. 323–329.
14. SABAT, K. C.; RAJPUT, P.; PARAMGURU, R. K.; BHOI, B.; MISHRA, B. K. Reduction of oxide minerals by hydrogen plasma: An overview. *Plasma Chemistry and Plasma Processing*, 2014, Vol. 34, No. 1, p. 1–23.
15. GRJOTHEIM, K.; HERSTAD, O.; TOGURI, J. M. The Aluminum Reduction of Magnesium Compounds. *Canadian Mining and Metallurgical Bulletin*, 1962, Vol. 602, p. 396–399.
16. MOHAMED, M. S.; *et al.* Laser-induced magnesium production from magnesium oxide using reducing agents. *Journal of Applied Physics*, 2008, Vol. 104, No. 11, p. 113110-1 – 113110-7.

CYSENI 2017, May 25-26, Kaunas, Lithuania
ISSN 1822-7554, www.cyseni.com

DIELECTRIC PROPERTIES OF ALUMINA CERAMICS FOR FUSION APPLICATIONS

D. Cruz, R. Vila
CIEMAT – National Fusion Laboratory
Avda. Complutense 40, 28040 Madrid – Spain
E-mail: darioandres.cruz@ciemat.es

B. Gómez-Ferrer
Université et INSA de Rouen,
Avenue de l'Université BP12, 76801 Rouen – France

ABSTRACT

The insulating materials for radio frequency (RF) windows and different antenna supports for heating systems and some diagnostics are still an unresolved issue in future fusion machines such as DEMO. Alumina ceramic (Al_2O_3) is one of the main candidate materials for these systems. The dielectric properties, such as electrical permittivity (ε) and loss tangent (tan δ), determine its power losses. Therefore, tan δ values need to be low, between 10^{-6} and 10^{-3} depending on the application. However, due to the crucial role of the manufacturing process in determining its final dielectric properties, there is the need to undertake a joint effort with the industry in order to validate a standard manufacturing route that ensures a supply of ceramic material with homogeneous and standardized dielectric properties for future fusion machines.

In DEMO, these ceramic materials will be operated under extreme conditions. They will be exposed to considerable levels of neutron irradiation. Radiation Induced Conductivity (RIC) and Radiation Induced Electrical Degradation (RIED) are phenomena that influence notoriously on the dielectric performance of these materials. Therefore, their optimum properties must be tested under relevant irradiation conditions. Hence, it is important to accurately characterize their dielectric properties before irradiation to be able to compare them with the future post neutron irradiation results. Furthermore, other types of radiation such as beta and gamma are also used in the irradiation scheme to provide more information on the variation of dielectric properties of ceramics due to radiation effects.

In this work, loss tangent and permittivity values of some pre-irradiated candidate materials will be presented as well as the measuring techniques used at CIEMAT. Different manufacturing routes were used for each batch of samples to systematically test the effect on the loss tangent. The dielectric properties were measured using two different methods, depending on the frequency range: from 1kHz to 100MHz, the half-power-gap variation method (JAPAN E&M – DPMS 1000) was used at several discrete frequency points, at room temperature and in a N_2 atmosphere. The upper frequencies were covered with a closed cylindrical resonant cavity. The dielectric properties are obtained from the comparison of the characteristics of the resonance with and without the sample inside the resonator. These techniques have the advantage of covering the very broad range of frequencies required for alumina applications in fusion (from kHz to GHz) and giving the best accuracy for very low losses.

Results revealed that depending on the type of material and the manufacturing route, ceramics have better performance at different frequency ranges. Thus, changes in the manufacturing route have enhanced or undermined the dielectric properties of the ceramic. However, the different routes present deviations in the measured dielectric loss between samples from the same batch. Therefore, assuring the reproducibility of the samples is the next objective.

Keywords: Fusion, DEMO, ceramics, dielectric properties, pre-irradiation

CYSENI 2017, May 25-26, Kaunas, Lithuania
ISSN 1822-7554, www.cyseni.com

INFLUENCE OF BREEDER BLANKET MODULE SIZE VARIATION ON NEUTRON ACTIVATION INVENTORIES

A. Tidikas, G. Stankūnas
Lithuanian Energy Institute, Laboratory of Nuclear Installation Safety
Breslaujos str. 3, LT 44403 Kaunas – Lithuania
E-mail: andrius.tidikas@lei.lt

ABSTRACT

Water Cooled Lithium Lead (WCLL) blanket module is one of the key concept designs for tritium and neutron breeding. WCLL type modules are considered to play substantial role in the next generation fusion power plants such as DEMO. As for 2015 DEMO model, 4 iterations of breeder blanket modules were proposed with key differences in radial lengths and thickness as well as dimensional differences in inner structures such as breeding zone, shielding zones and manifold. Such changes were made in respect to its nuclear, thermohydraulic and thermomechanical performances. In this work neutronic characteristics of WCLL modules were analysed in terms of fusion power increase and dimensional changes in the blanket geometry. Such characteristics include activity and decay heat. Numerical experiment was carried out with MCNP particle transport code and FISPACT activation calculation code.

Keywords: nuclear fusion, FISPACT, MCNP, neutron activation, DEMO, WCLL

1. INTRODUCTION

Nuclear fusion is a promising source of relatively clean and cheap enenergy for our future needs. However in order to harness such energy, there are still many engineering and physics issues that needs to be solved. Some of these issues are related to nuclear safety as currently the most endearing solution is magnetic plasma confinement reactors that runs with deuterium-tritium fuel. Although the amount of tritium during the operation of the reactor isn't very high, it can get trapped inside the reactor structural materials. Furthermore During the fusion reaction a high neutron flux is being produced. Aside from being main heat carriers in the reactor, neutrons do play essential part in activation processes, thus making materials radioactive and dangerous to environment and the reactor itself. Current fusion devices are not supposed to produce any tangible amount of activated materials, however in future large fusion reactors such as ITER or DEMO, material activation is unavoidable factor concerning device operation and decomissioning [1].

DEMO (stands for demonstration power plant) reactor might be the first prototype of commercial reactor. Its development and design constantly being changed with regards to newly attained knowledge from other fusion projects and emerging techinques. Crucial component for such reactor is a module called breeding blanket. Breeding blanket mainly serves as neutron multiplyer and tritium producer. There are few types of breeding blankets, that in principle differs in coolant type and breeder zone. For this study water cooled lithium lead (WCLL) breeding blanket is selected for examination [1].

In this work, activity inventories and decay heat output of DEMO WCLL equatorial breeding blanket modules are examined in terms of recent change in Reactor nominal power and slight geometry changes seen in Fig. 1. Compared to 2014 DEMO baseline Model in 2015 version fusion power was significantly increased from 1570 MW to 2037 MW. Major radius was changed from 9.0 to 9.072 m while minor radius from 2.25 to 2.927 m. Such changes were introduced in order to reduce parasitic neutron absorbtion by blanket structural steels. Such absorbtion not only make device less efficient, but also impair tritium breeding in blanket.

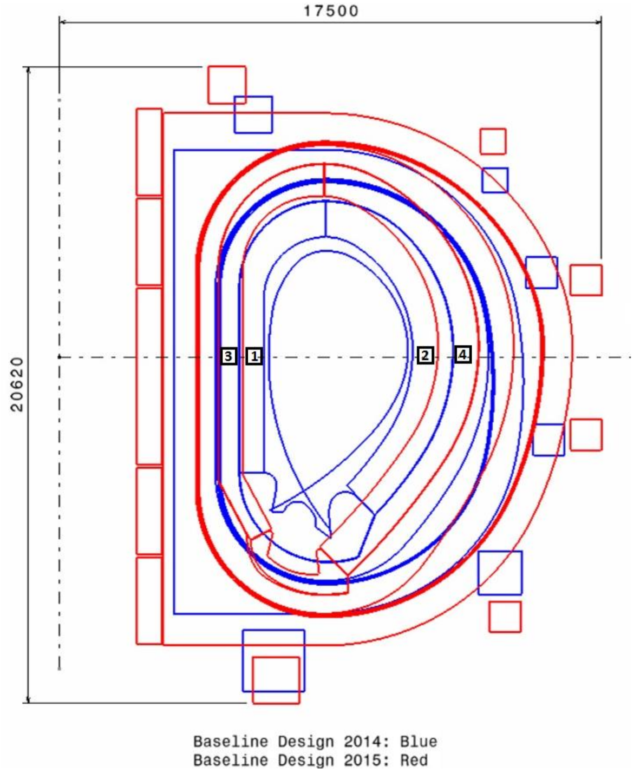

Fig. 1. Comparison of reactor vacuum vessel cross section geometric change. 1 and 2 blanket module localizations for 2014 IB and OB modules respectively, 3 and 4 for 2015 IB and OB modules [2]

2. METHODS AND MATERIALS

Water Cooled Lithium Lead blanket (WCLL) design is based on water cooling, other prominent designs includes helium as primary or secondary coolant. With DEMO reactor change, there were also changes made in blanket geometry.

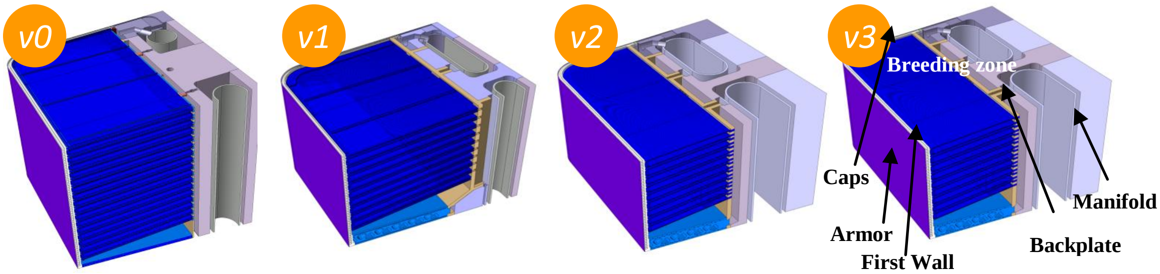

Fig. 2. DEMO HCPB Blanket module evolution [2]

Fig. 2 shows one evolutionary path from 2014 design towards 2015 for helium cooled pebble bed (HCPB) blanket. Same overall geometry change also applies to WCLL blankets. There are only slight variations in inner structure composition fractions that are presented in Table 1. Investigated WCLL modules were divided into six different segments that corresponds to different materials or compositions: armor (AR), first wall (FW), breeder zone (BZ), caps (CP), backplate (BP) and manifold (MF). Armor is made from tungsten alloy and serves as a plasma facing material. First wall and caps are made from EUROFER steel and acts as a cladding and heat exchanger for the module. The Core component of breeder zone is PbLi alloy. It has tritium breeder, neutron multiplier and heat transfer medium functions. Backplate is EUROFER based support construction and manifold includes auxiliary structures for cooling and tritium extraction [3].

MCNP [4] calculations for 2014 and 2015 baseline design were used in this work in order to obtain neutron spectra for breeding blanket segments. The neutron spectra, in form of VITAMIN-J 175 groups [5], were calculated for equatorial inboard (IB) and outboard blanket (OB) module localizations for each segment. IB module is located further from central axis of fusion device, while OB is closer. The differences in spectra between breeder zone of 2014 and 2015 models are shown in Fig. 3.

European Activation System: Easy-2007 is used as a primary tool for the determination of dominant radionuclides in structural materials after irradiation together with EAF-2010[6] nuclear library. Its code FISPACT [7] is being utilized for simulation of irradiation process [2]. Model of irradiation is simplified: infinite slab of material is being irradiated by neutron flux in pulses corresponding to operation of fusion device. Input data consists of composition, density and masses.

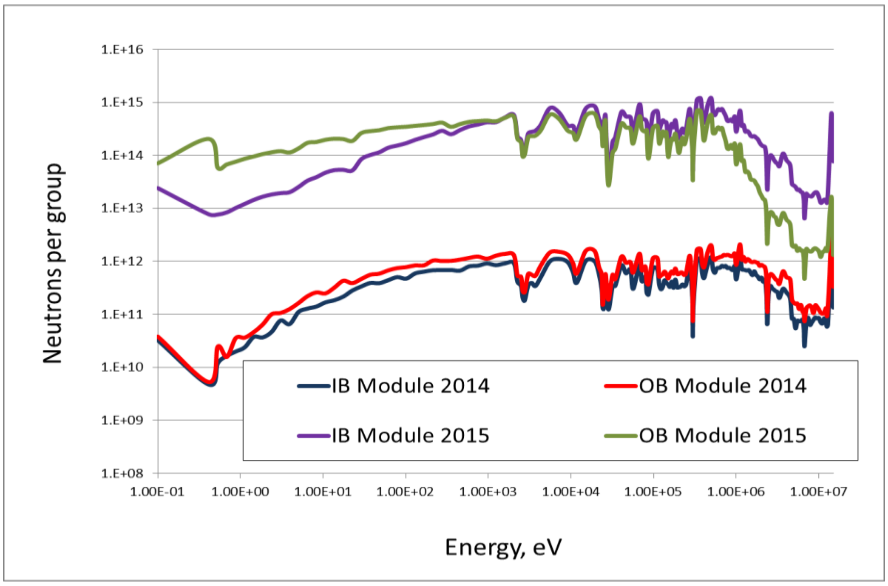

Fig. 3. Neutron spectra used for IB and OB modules

First irradiation sequence lasts for 1888 days with 0.3 MW m^{-2} neutron load on the slab surface. Another sequence consists of 48 pulses: material is exposed to 1 MW m^{-2} load for 4 hours. Pulse sequences were performed one after another with one hour delay. Neutron activation related properties were analyzed for 1000 years period after last irradiation sequence starting with zero second after irradiation ends. In the time frame the interval and its change was selected in accordance to different stage of reactor utilizition. Period from the very first second after shutdown and up to the month provides data that might be usefull during regular power plant operation and maintenance. Subsequent period up to 100 years would corresport to plant decomissioning and material storage. 100 years and up period is dedicated for evaluation of long term fissile material presence in the reactor.

Table 1. Investigated materials and their compositions [8]

WCLL DEMO						
Volume, %	**Armour**	**FW Vol.**	**Breeder module**	**Caps**	**Backplate**	**Manifold**
EUROFER		89.5	18	95.2	100	74.4
Water		10.5	1.9	4.8		4.8
PbLi (90% Li_6)			80.1			9.2
Tungsten	100					
Void (vacuum)						11.6
Total	**100**	**100**	**100**	**100**	**100**	**100**

3. RESULTS AND DISCUSSION

Activity and decay heat values for all segments of 2014 and 2015 models were obtained and are displayed in Figs. 3–6. Roughly all segments can be divided by radial distance. Neutron flux is highest at armor segment and gradually decline while moving towards manifold construction. Activity and decay heat dependence on distance is shown in Fig. 7.

In most cases, but not all, inboard modules exhibit higher activities and decay heats than outboard modules. In the early stages of shutdown such values range within the factor of ~2–5 for 2015 model and within the factor of ~3–10 for 2014 model. The maximal difference applies to armor and first wall segments, however 2014 model manifold IB/OB segments also has quite significant variance in activation characteristics. This difference might be caused either by geometry flaws present in the model. With cooling time increment such tendencies remains with only slight shrink in differences.

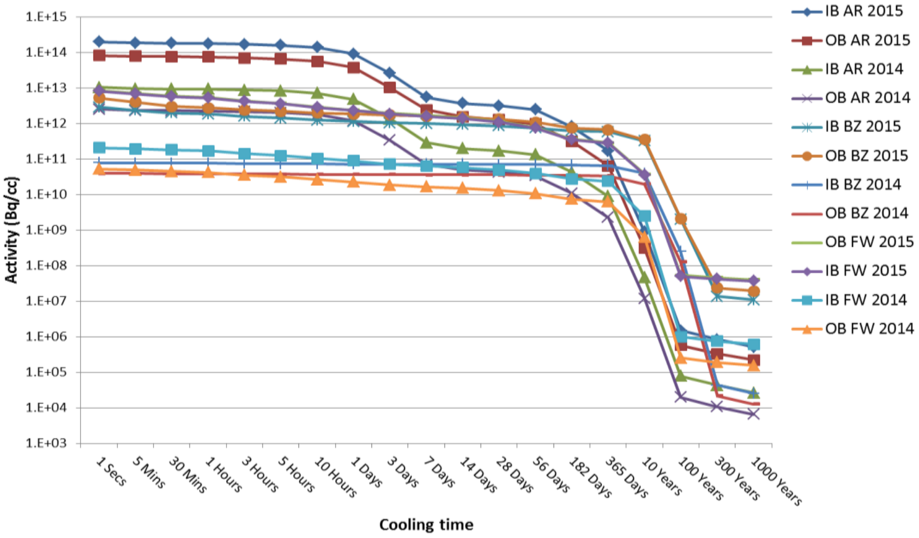

Fig. 3. Activity dependence on time after shut down for armor (AR), first wall (FW), breeder zone (BZ)

Comparing 2014 and 2015 Model side by side gives us following results: all 2015 model obtained values are higher as expected. At the start of shutdown, for armor localization it varies by a factor ~10–20, for first wall by a factor of ~40, for breeder zone by a factor of about 100 and more, for a backplate by a factor of ~100, for caps by a factor of ~50–100 and for manifold by about 100 and more. With increment of time such difference is more pronounce and in parts increase by the factor of ten, but not more.

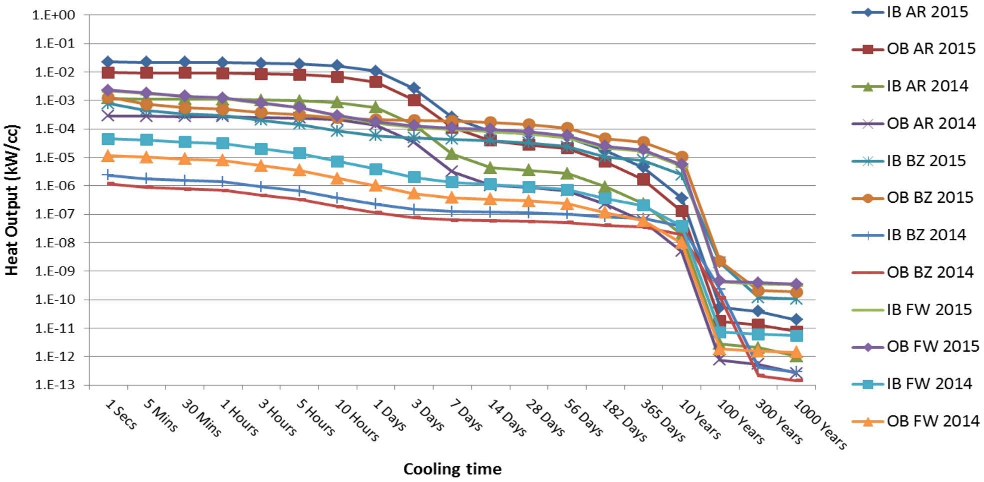

Fig. 4. Decay heat dependence on time after shut down for armor (AR), first wall (FW), breeder zone (BZ)

Armor is made of tungsten alloy. Its activity and decay heat characteristics are highly dependent on W-187 and Re-188 isotopes. In seven day span influence of these isotopes are comparable with other radionuclides. Later on, W-185 isotope makes up the largest part for activity inventories for armor segment. In 1 year period armors activity falls below the activity of breeding zone segment. For the first wall, caps, backplate and manifold principal radionuclides correspond to EUROFER composition as tritium from water activation is being removed from the module and tritium retention and absorption are not taken into consideration in this study. Key activity and decay heat contributors in EUROFER are Mn-56, Cr-51 and V52. There are slight variation between these and other radionuclides in hierarchy across the investigated module segments, however these variations are not very drastic. In 10 years after shutdown, the most prominent radionuclide is Fe-55, moreover in such timeframe overall activity starts to fall rapidly.

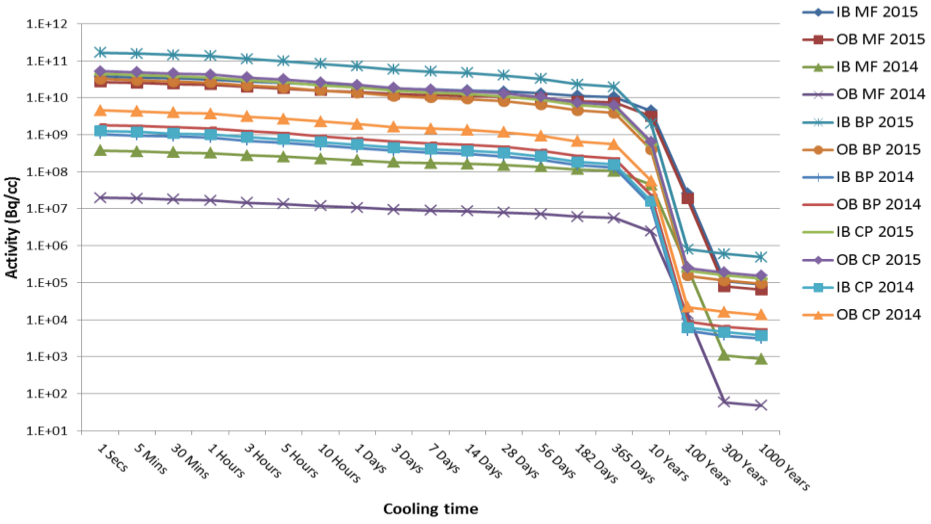

Fig. 5. Decay heat dependence on time after shut down for caps (CP), backplate (BP), manifold (MF))

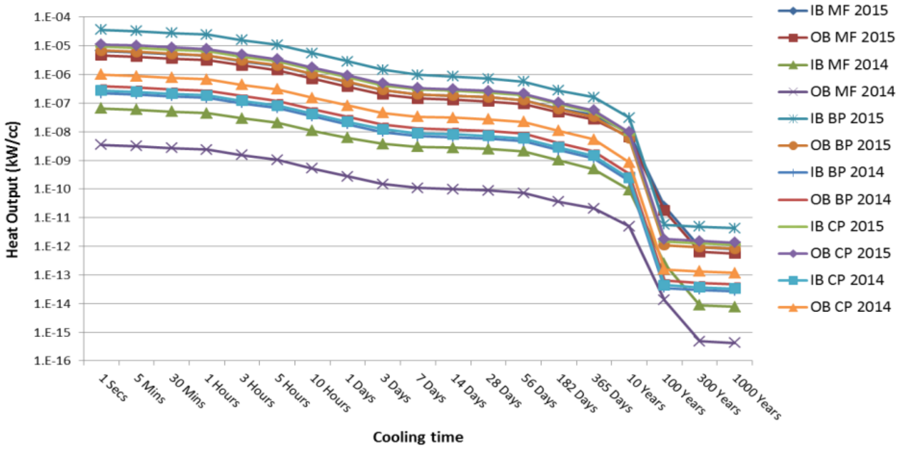

Fig. 6. Activity dependence on time after shut down for caps (CP), backplate (BP), manifold (MF))

Breeder zone is mostly made of PbLi alloy, however almost all lithium activation products consist of tritium that is removed from the system and of Li-8 radionuclide with very short half-life. Essentially activity and decay heat of breeder zone are dominated by EUROFER activation products, nonetheless significant part is also affected by lead activation products that become more prominent with cooling time increment. Such effect is seen in manifold segment in Fig. 7, that has fraction of PbLi alloy. Fig. 7 shows activity dependence on radial distance along the IB blanket module of 2015 DEMO model. In this graph Breeder zone is divided into 4 sections. In the graph on the right sudden drop at the begging and at the 82.3 cm mark happens because 2 cm length armor, first wall and caps layers doesn’t scale well with 20 cm length breeder zone section.

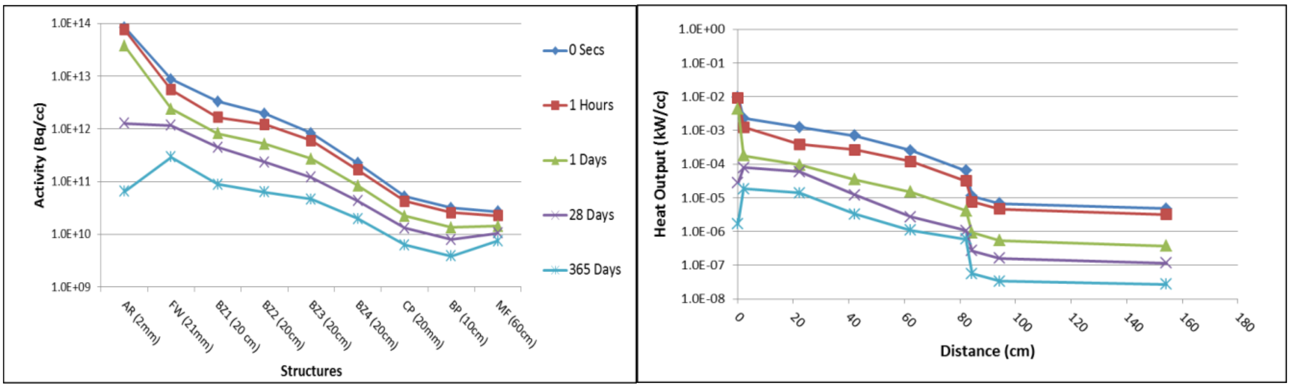

Fig. 7. Activity and decay heat dependences on radial distance

4. CONCLUSIONS

After geometry change and increase in power from 1570 MW to 2037 MW, activity and decay heat in equatorial inboard and outbord water coolled lithium lead blanket modules changed substantially. Overall obtained values using 2015 model in respective segments were higher by the factor of 20–100 and more with a tendency of incresment along radial distance compared to 2014 model.

Differences among inboard and outboard models ranges from 2 to 5 times for 2015 model and from 3 to 10 for 2014 model.

Radionuclide analysis showed, that with exception of tungsten armor in all other parts of the module the most significant activation products belongs to EUROFER alloy with minor variances. Tungsten armor activity inventories decreases significantly in a week period of time after shutdown, while EUROFER based segments retain relatively steady for a year and more.

Acknowledgements: This work has been carried out within the framework of the EUROfusion Consortium and has received funding from the Euratom research and training programme 2014–2018 under grant agreement No 633053. The views and opinions expressed herein do not necessarily reflect those of the European Commission.

REFERENCES

1. COOK I. *Et al*, *European Fusion Power Plant Studies, Euratom/UKAEA Fusion Association, Culham Science Centre, 2004.*
2. GONZÁLEZ F. A. G. *Design Engineering / HCPB Design Report 2015.*
3. STORK D. et al. *Materials R&D for a timely DEMO: Key findings and recommendations of the EU Roadmap Materials Assessment Group.*, Fusion Engineering and Design 89 1586–1594 2014.
4. PELOWITZ D. B. *MCNP6 User's Manual Version 1.0, LANL Report LACFP-13-00634*: Rev 0 2013.
5. VONTOBEL P., PELLONI S. JEF Report 10: JEF/EFF Based Nuclear Data Libraries, OECD NEA DATA BANK1987.
6. SUBLET J. CH. *The European Activation File:EAF-2010 neutron-induced cross section library.*, Euratom/CCFE fusion association, 2010.
7. FOREST R. A. *FISPACT-2007: User manual.*, EURATOM/UKAEA Fusion Association, Culham Science Centre, Abingdon, Oxfordshire UK 234 2007.
8. Technical Specifications EUROFER Material Database F4E-2008-GRT-010 (PNS-MD) Fusion for Energy (2008).

CYSENI 2017, May 25-26, Kaunas, Lithuania
ISSN 1822-7554, www.cyseni.com

DEVELOPMENT OF VVER-1000/V-320 MODEL FOR SEVERE ACCIDENT ANALYSIS WITH ATHLET-CD CODE

M.V. Frankova, M. P. Vyshemirskyi
State Enterprise "State Scientific and Technical Center on Nuclear and Radiation Safety"
V. Stusa Street, 35-37, 03142 – Ukraine
E-mail: mv_frankova@sstc.com.ua

ABSTRACT

In the framework of state nuclear and radiation safety reviews of assessments and analyses developed by the Utility for Ukrainian nuclear power plants (NPP) the State Scientific and Technical Center on Nuclear and Radiation Safety (SSTC NRS) experts conduct a large number of transients and accidents analyses to ensure validity of results and conclusions provided by the Utility. Nowadays, the vast majority of Utility calculations of severe accident (SA) scenarios are performed with application of MELCOR 1.8.5 code. Use of alternative up-to-date thermal-hydraulic code ATHLET-CD 3.0A for review calculations ensures greater independence of regulatory assessments and provides higher confidence in analysis results adequacy. This paper briefly describes SSTC NRS thermal-hydraulic model of VVER-1000/V-320 reactor facility for severe accident analyses with application of ATHLET-CD 3.0A code and demonstrates results of its approbation. For test calculation the total station blackout (SBO) with stuck open pressurizer pilot operated relief valves was chosen. The calculation results confirmed capabilities of the model and code to simulate such severe accident phenomena as core heating and melting, melt relocation, fission products release, their transport and deposition.

Keywords: NPP, VVER, initiating event, severe accident, SBO, ATHLET-CD, core damage

1. INTRODUCTION

To ensure validity of results and conclusions provided by the Utility for Ukrainian nuclear power plants (NPP) the experts of the State Scientific and Technical Center on Nuclear and Radiation Safety (SSTC NRS) perform a large number of accident analyses. The vast majority of severe accident (SA) analyses in Ukraine are performed with application of MELCOR 1.8.5 code. The up-to-date thermal-hydraulic code ATHLET-CD 3.0A can become an alternative tool for performing calculations of SA in the reactor core.

This paper provides a brief description of the development and approbation of VVER-1000/V-320 model for ATHLET-CD 3.0A code. Use of alternative code for review calculations ensures greater independence of regulatory assessments and provides higher confidence in analysis results adequacy.

2. GENERAL INFORMATION ON COMPUTER CODE ATHLET-CD 3.0A

The thermal-hydraulic system code ATHLET-CD 3.0A (Analysis of THermal-hydraulics of LEaks and Transients with Core Degradation) is being developed by Gesellschaft für Anlagen- und Reaktorsicherheit (GRS). The ATHLET-CD 3.0A structure is modular, both to provide a variety of models for the simulation and to provide an optimum basis for further development. For a comprehensive simulation of the thermal-fluid dynamics in the nuclear steam supply system, the ATHLET 3.0A system code has fully been integrated.

ATHLET 3.0A is an advanced best-estimate code which has been initially developed for the version simulation of design basis and beyond design basis accidents (without core degradation) in light water reactors, including VVER and RBMK reactors [2]. ATHLET code is composed of several basic modules for the simulation of the different phenomena involved in the operation of a light water reactor [2]:

- thermo-fluiddynamics (TFD);
- heat transfer and heat conduction (HECU);
- neutron kinetics (NEUKIN);
- control and balance-of-plant (GCSM).

The one-dimensional, two-phase fluiddynamic models are based on a five-equation model supplemented by a full-range drift-flux model, including a dynamic mixture-level tracking capability. Moreover, a two-fluid model based on six conservation equations is provided. The heat conduction and heat transfer module allows a flexible simulation of fuel rods and structures. The nuclear heat generation is calculated by a point kinetics or by a one-dimensional kinetics model [3].

A general control simulation module is provided for a flexible modelling of Balance-of-Plant and auxiliary plant systems. Systematic code validation is performed by GRS and other organizations.

The time integration of the thermo-fluiddynamic model is performed with the general purpose ODE- solver FEBE (Forward-Euler, Backward-Euler). It provides the solution of a linear system of ordinary differential equations (ODE) of first order, splitting it into two subsystems, the first being integrated explicitly, the second implicitly. Generally, the fully implicit option is used in ATHLET. Each thermo-fluiddynamic object provides a subset of the entire ODE system, which is integrated simultaneously by FEBE. Other independent modules (e.g. large models with own time advancement procedure) can be coupled without structural changes in ATHLET by means of dedicated interfaces [1].

The ATHLET-CD code has been developed for accidents resulting in major core damage. The 3.0A version of the code was generaly improved since previous version (2.2 A). This improvmets vere dedicated to thermo-fluiddynamics, heat conduction, neutron kinetics, FEBE etc. This modifications improved code performance and reduced the number of errors, which occured while performing of calculations.

3. BRIEF DESCRIPTION OF VVER-1000/V-320 MODEL FOR ATHLET-CD 3.0A COMPUTER CODE

3.1. General description of core modification

The VVER-1000/V-320 model for ATHLET-CD 3.0A code was developed according to the general requirements formulated in the ATHLET [1] and ATHLET-CD [4] code manuals.

The current model of VVER-1000/V-320 consists of reactor, four primary loops, pressurizer (PRZ) with pilot operated relief valves (PORV), emergency core cooling system (ECCS) and secondary system including steam generators (SG), main steam lines (MSL), main steam header (MSH), etc. Detailed model description is presented in the report [5].

The reactor is modelled by thermal-fluid objects (TFO), designated with “PV-” prefix and by heat conduction objects (HCO), which are named with “HPV-” prefix. Downcomer is modelled with four axial channels (one for each loop). Each channel is represented by two TFOs named PV-DC-x1 and PV-DC-x2 (hereinafter “x” is a loop number identifier). Lower plenum of reactor is modeled by three TFOs named PV-LP-1 ÷ PV-LP-3. Other six TFOs PV-UP-1 ÷ PV-UP-6 represent the upper plenum of reactor. Initially reactor core was represented by 2 channels.

But for purposes of applying ATHLET-CD the original 2-channel core was extended to 5-channel core. Principle of the core splitting into 5 channels (rings) is shown on the cartogram of VVER-1000 (see Fig. 1, a). Fuel assembles of different rings are shown in Fig. 1, b with different colors. Core splitting was performed according to the recommendations of the code developer. Influence of core nodalisation on the results of calculations is undetermined still and it is planned to perform such analisis in the future researches.

Fuel assembles of extended core are modeled by five TFOs: PV-COR-1 ÷ PV-COR-5 which represent five radial rings (see Fig. 2, b). PV-REF simulates reactor core bypass (reflector). Nodalization schemes of original and updated models of reactor are presented in Fig. 2.

Characteristics of the extended 5-channel core are presented in Table 1.

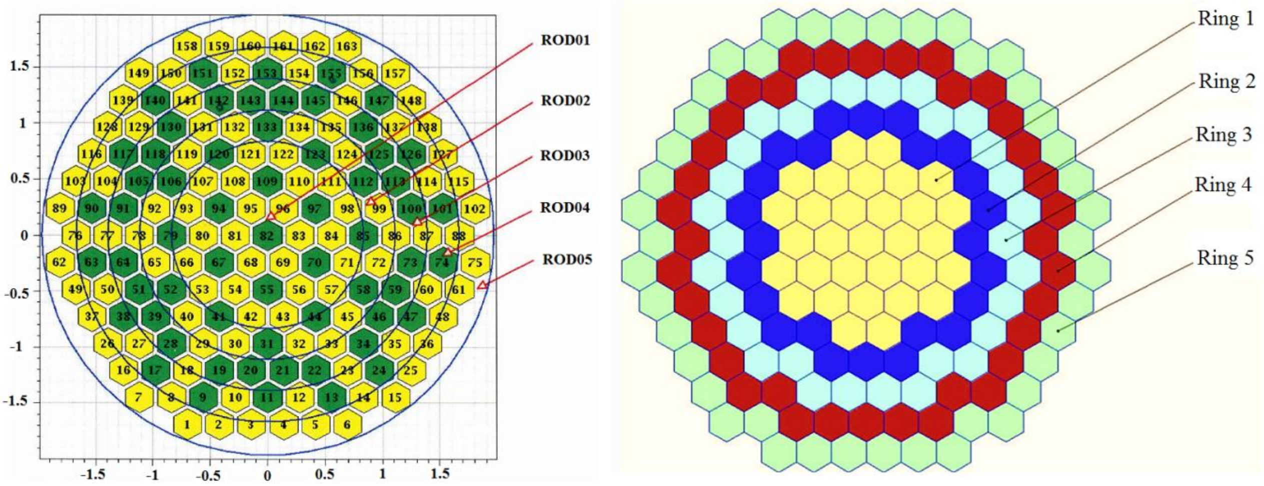

a) *b)*

Fig. 1. Visualisation of core splitting into 5 channels (*a* – cartogram of VVER-1000; *b* – rings of 5-channel core)

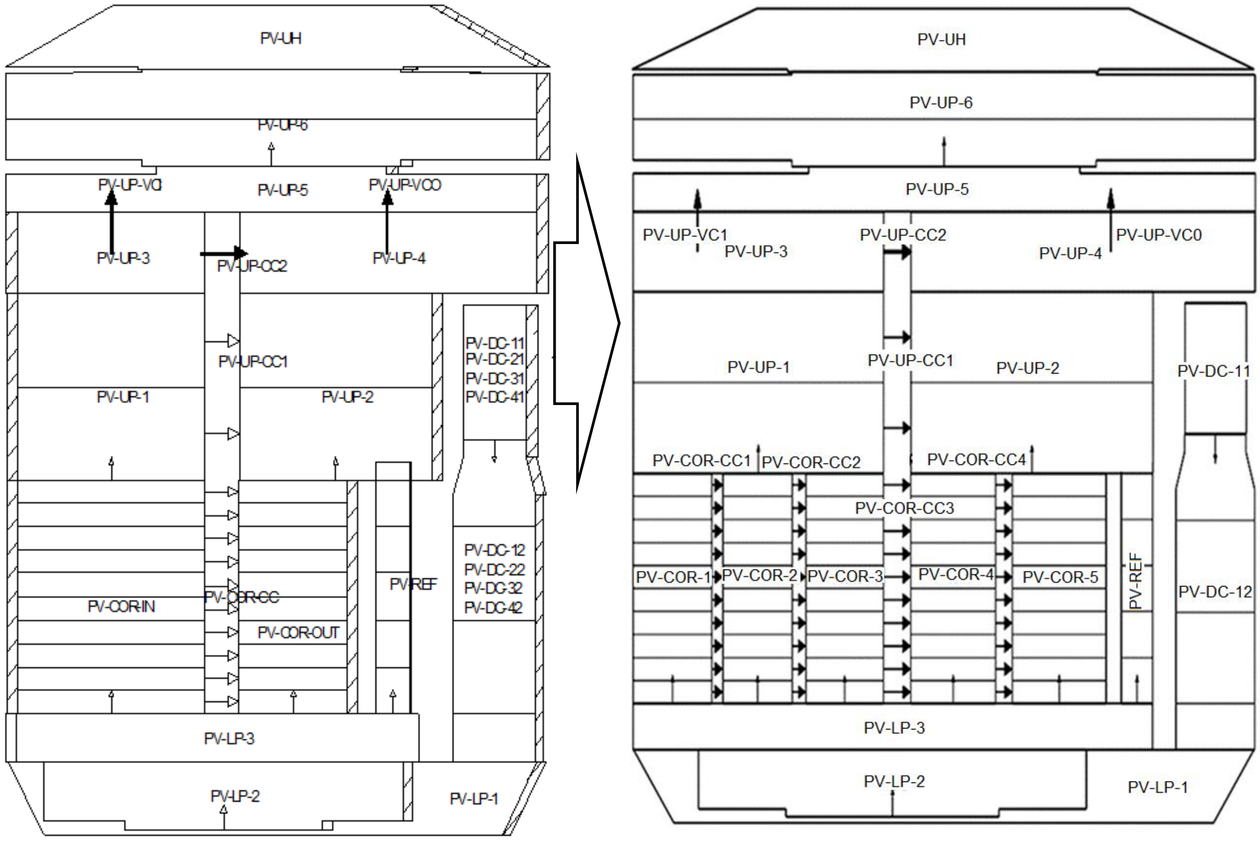

a) *b)*

Fig. 2. Nodalization schemes of reactor (*a* – original model; *b* – updated model for ATHLET-CD)

Table 1. Characteristics of the extended 5-channel core

Region #	TFO/ROD name	Number of fuel assemblies	Number of fuel rods	Number of control elements	Number of control rods	Radius of the core area, m
1	PV-COR-1/ ROD01	31	9672	7	126	0.804
2	PV-COR-2/ ROD03	24	7488	12	216	1.072
3	PV-COR-3/ ROD03	30	9360	24	432	1.3407
4	PV-COR-4/ ROD04	36	11232	18	324	1.6089
5	PV-COR-5/ ROD05	42	13104	0	0	1.743

3.2. Implementation of ATHLET-CD modules

This subsection provides short description of implemented input deck (ID) changes for performing of ATHLET-CD calculations.

3.2.1. ECORE

ECORE module allows to simulate core heatup, cladding oxidation and core degradation. For purposes of applying ATHLET-CD the 2-channel original core model was extended to 5-channel core by adding correspondent TFOs (PV-COR-x), cross-connections (PV-COR-CCx) and modifying of TOPOLOGY and GCSM. Also the model of core bypass (PV-REF) with corresponding HCOs was updated. The list of HCOs presented in the ID was supplemented by model of lower grid plate (HCO GRIDPLATE). HCOs of reactor core were replaced by special ECORE module elements (named ROD0x) which simulate fuel pins. Core splitting to five radial regions is presented in Fig. 1.

3.2.2. FIPREM

FIPREM – module defining release of fission products and aerosols from the fuel rods. The following release groups were chosen for determining of release from the fuel rods: Xe, Kr, I, Cs, Te, Sr, Sb, U, AgST, Cd and In.

3.2.3. SOPHAEROS

SOPHAEROS module defines transport and deposition of fission products and aerosols determined in FIPREM. As the flow path of fission products and aerosols next TFOs with corresponding HCOs were chosen (see Fig. 3):

- TFOs: PV-UP-1 → P4-HL → P0-SURGE → P0-PRESS;
- HCOs: HPV-UPS1 → HP4-HL → HP0-SURGE → HP0-PRESS.

The following physical models for transport and deposition of fission products and aerosols were used:

- EDDYIMP: aerosols eddy impaction;
- BENDIMP: aerosols bend impaction;
- DIFFUSIO: aerosols diffusiophoresis;
- BROWN: aerosols Brownian coagulation;
- MECRES: aerosols mechanical resuspension.

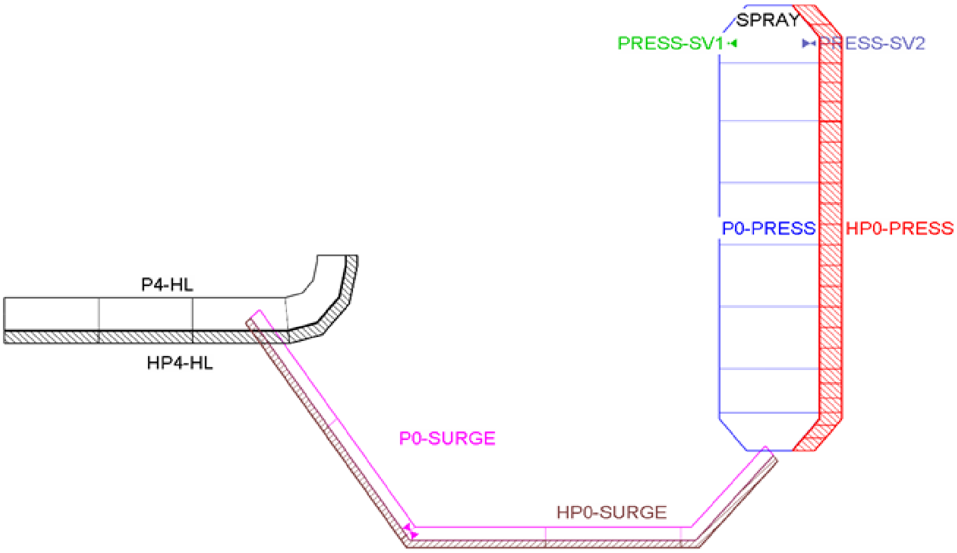

Fig. 3. Flow path of fission products and aerosols

4. APPLICATION OF ATHLET-CD FOR SEVERE ACCIDENT ANALYSIS

To evaluate the model the test calculation of total station blackout with stuck open of one PRZ PORV was performed. Initial and boundary conditions selected for analysis as well as discussion of the main analysis results are provided below.

4.1. Initial conditions

Initial conditions comprise of parameters values which define the initial NPP state prior to initiating event occurrence. Table 2 provides the design (data from the reports [6] and [7]) and calculated (reached during steady-state) values that were used as initial conditions for scenario calculation.

Table 2. Initial conditions used for accident analysis

#	Description	Design value	Calculated value
1	Reactor thermal power, MW	3000±60 [7, Table 6.2.2-1]	3000
2	Reactor outlet pressure (absolute), kgf/cm^2	158…162 [7, Table 6.2.2-1]	160.9
3	Maximal reactor inlet coolant temperature, °C	289 [7, Table 6.2.2-1]	290.3
4	Reactor coolant flow rate, m^3/h	84800^{+4000}_{-4800} [6, Table 2.1-28]	85512
5	Reactor bypass flow, %	3,0 [6, Table 2.1-30]	3.0
6	PRZ level, m	8770±150 [7, Table 6.2.2-1]	8.65
7	SG pressure (absolute), kgf/cm^2	60…64 [7, Table 6.2.2-1]	62.5…63.1
8	SG level (narrow range), m	0.270±0.05 [7, Table 6.2.2-1]	0.275
9	SG steam production, t/h	1470±103 [6, Table 2.5-1]	1460
10	SG feedwater temperature, °C	220±5 [6, Table 2.5-1]	218

4.2. Boundary conditions

The main assumptions which were applied for the computational analysis are listed below:

- loss of house loads power supply with a failure of diesel-generators actuation (total station blackout) was assumed;
- operators actions were not considered;
- PRZ control PORV failure to open was assumed. PRZ main PORV (double-valve) stuck opened after first opening;
- BRU-A (steam dump valve to atmosphere) are operable only one hour after beginning of initiating event. After batteries discharge (one hour) BRU-A stay in current position;
- the reactor power, primary and secondary pressure, SG and pressurizer levels, as well as MSH pressure are maintained automatically by correspondent controllers at nominal values.

4.3. Calculation results

Total station blackout (SBO) leads to a trip of main NPP equipment and reactor scram actuation. The heat removal from the reactor core is provided by natural circulation of primary circuit coolant with boiling of SG water and dumping steam via BRU-As. During the first hour after SBO occurrence the batteries of reliable power supply system discharge and BRU-A stuck at their current position.

Loss of SG feedwater supply with continuous steam dumping through BRU-A leads to the emptying of SG and degradation of the heat removal from the primary circuit. This leads to RCS pressure increase up to the PRZ control PORV operation setpoint.

According to the scenario PRZ control PORV failure to open was assumed. So, the RCS pressure increases up to the PRZ main PORV (double-valve) opening which remains fully open after its first actuation. Stuck of main PORV in open position results in uncompensated loss of coolant, decrease of level in the core and further fuel damage.

Calculation was stopped after core melt relocation and temporary termination of core degradation due to water injection from hydroaccumulators (HA) into reactor. Plots of the main calculation results are shown in Fig. 4–12.

The calculation results confirmed capabilities of the model and code to simulate such SA phenomena as core heating and melting, melt relocation, fission products release, their transport and deposition. Operable systems are triggered according to their settings. Analysis of the calculation results confirm physical behavior of the parameters of reactor facility.

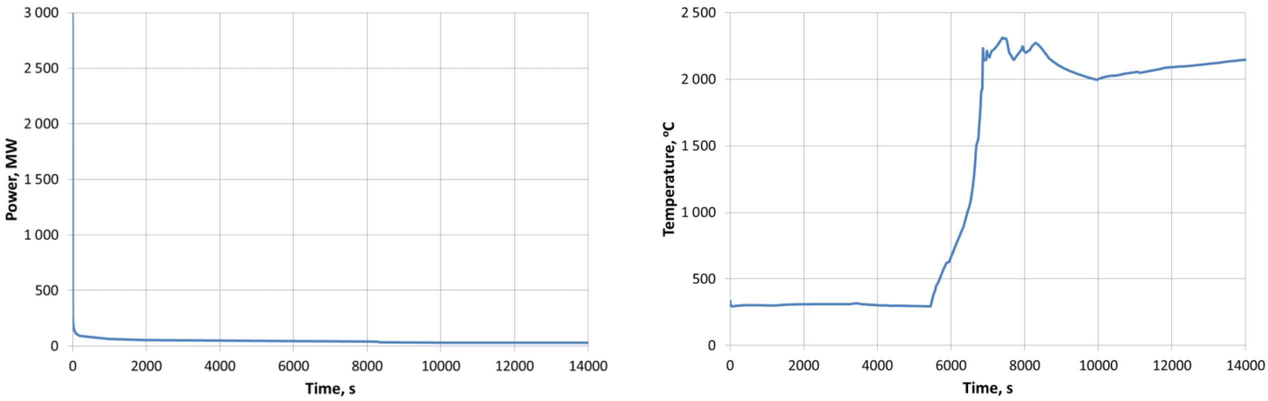

a) *b)*

Fig. 4. Core power (*a*) and maximum cladding temperature (*b*)

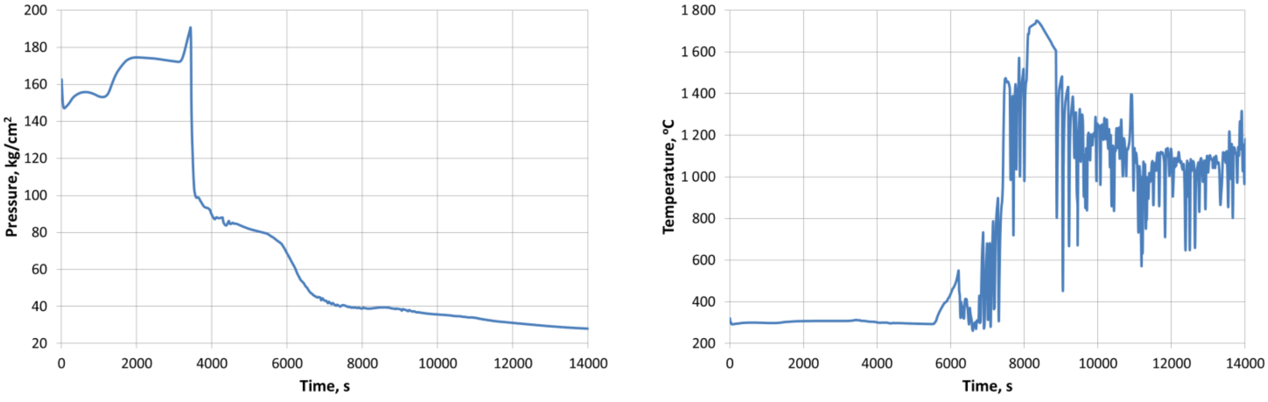

a) *b)*

Fig. 5. RCS pressure (*a*) and reactor outlet temperature (*b*)

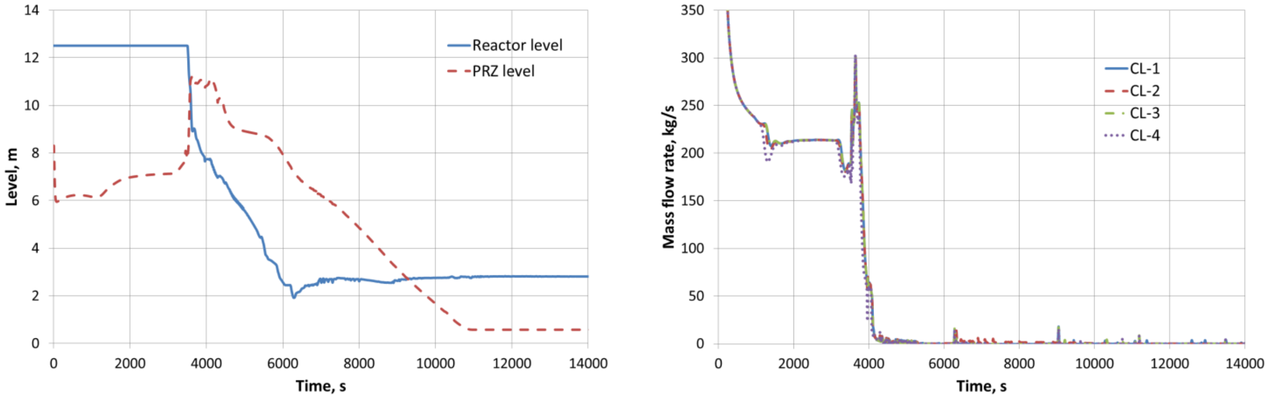

a) *b)*

Fig. 6. Reactor and pressurizer collapsed level (*a*) and fragment of mass flow rate at RCPs outlet (*b*)

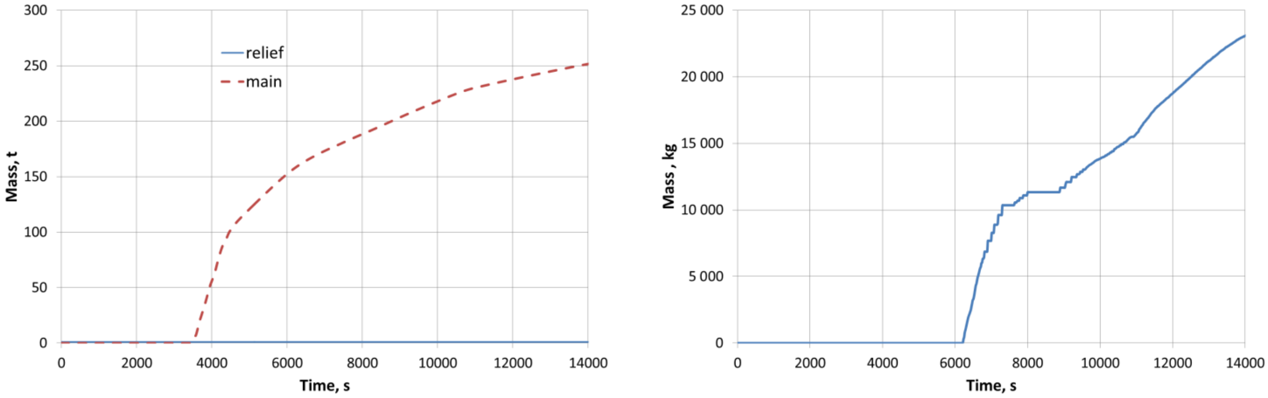

a) *b)*

Fig. 7. Integrated mass released through the PRZ PORVs (*a*) and integrated HA mass flow rate (*b*)

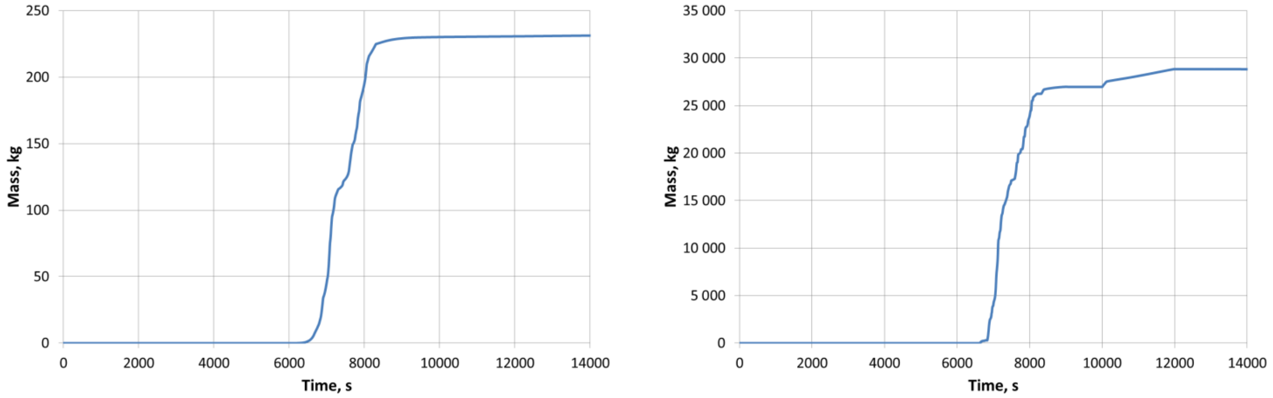

a) *b)*

Fig. 8. Total mass of hydrogen generated in the core (*a*) and total mass of molten material in core (*b*)

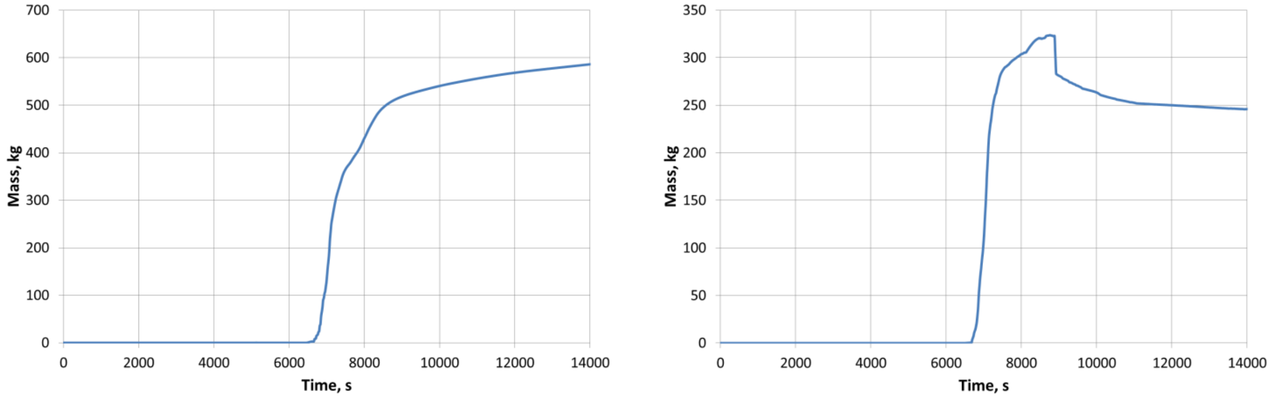

a) *b)*

Fig. 9. Mass of fission products released from the core (*a*) and total mass of deposits (*b*)

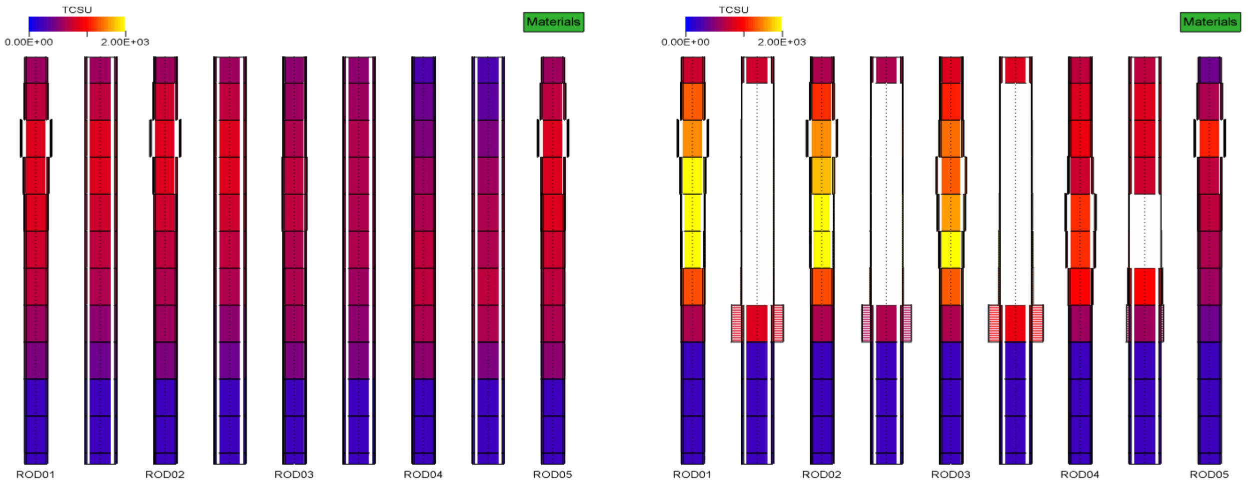

a) *b)*

Fig. 10. Average cladding and melt/crust surface temperature (*a* – 6500 s; *b* – 7000 s)

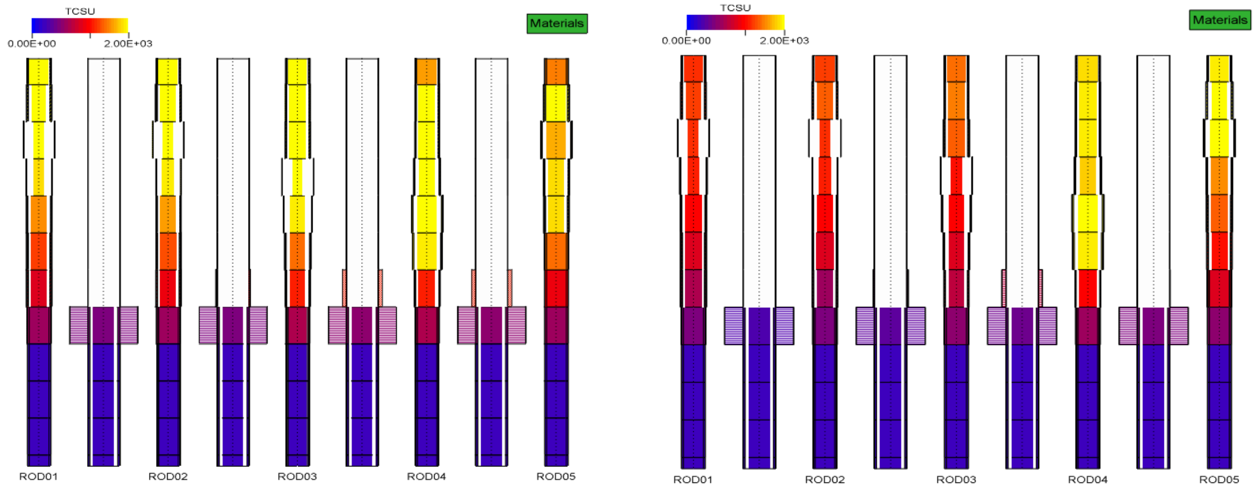

a) *b)*

Fig. 11. Average cladding and melt/crust surface temperature (*a* – 8000 s; *b* – 10000 s)

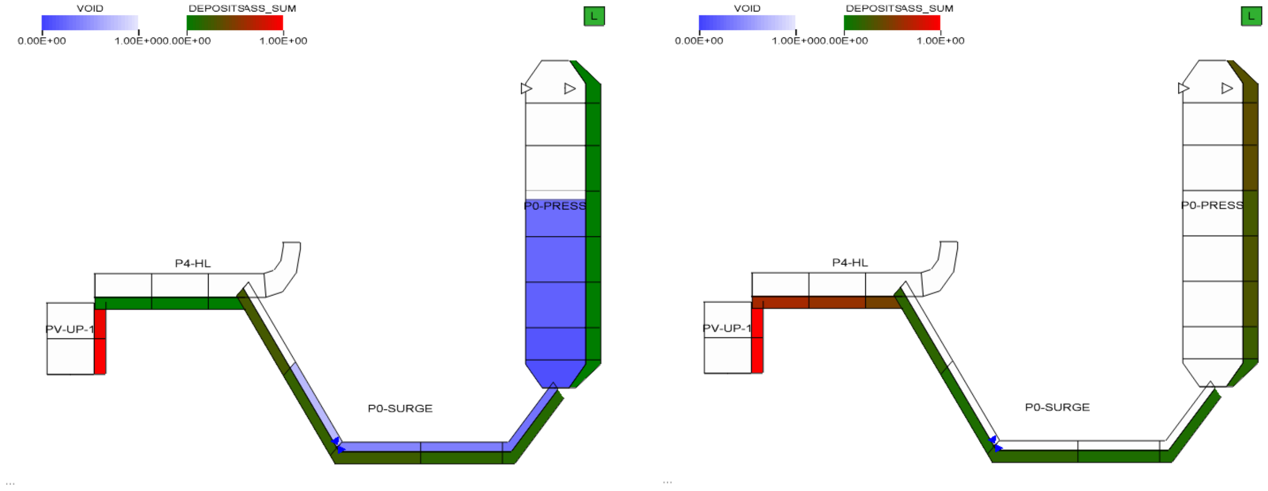

a) *b)*

Fig. 12. Volumetric vapor fraction and relative mass of deposits (*a* – 7000 s; *b* – 14000 s)

5. CONCLUSIONS

As the reuslt of this work the model of VVER-1000/V-320 reactor facility for ATHLET-CD 3.0A was developed and tested at SBO scenario caclulation with stuck open PRZ PORV.

The calculation results confirmed capabilities of the model and code to simulate such SA phenomena as core heating and melting, melt relocation, fission products release, their transport and deposition.

Use of alternative up-to-date thermal-hydraulic code ATHLET-CD 3.0A for SSTC NRS expert review calculations ensures greater independence of regulatory assessments and provides higher confidence in analysis results adequacy.

Further work will be aimed at extending the model with additional ATHLET-CD modules, performing of calculations of other scenarios and comparing the results with the ones obtained with application of MELCOR code.

REFERENCES

1. Lerchl, G., Austregesilo, H., Schöffel P., von der Cron, D., Weyermann, F. *ATHLET Mod 3.0 Cycle A. User's Manual*, 2012. GRS-P-1/Vol. 1, Rev. 6.
2. *ATHLET Mod 3.0 Cycle A. Program Overview*, 2012. GRS.
3. Austregesilo H., Bals C., Hora A., Lerchl G., Romstedt P., Schöffel P., Von der Cron D., Weyermann F. *ATHLET Mod 3.0 Cycle A. Models and Methods*, 2012. GRS-P-1/Vol. 4, Rev. 3.
4. Austregesilo, H., Bals, C., Hollands, T., Köllein, C., Luther, W., Schubert, J.-D., Trambauer, K. Weber, S. *ATHLET-CD Mod 3.0 Cycle A. User's Manual*, 2013. GRS-P-4/Vol. 1.
5. AT6-10.100.OD1. *Report on providing services on stage 1 "Calculating model of NSSS for WWER-1000 (code ATHLET)* [Zvit z nadannia poslug po etapu 1 “Rozrahunkova model YAPVU WWER-1000 (cod ATHLET)”], Kiev, 2006 (Ukr).
6. ER37-2006.310.OD (3). Zaporizhzhya NPP. Unit 5. *Safety Analysis Report. Analysis of beyond design basis accidents. NSSS data base for purposes of BDBA* [Zaporogskaya AES. Energoblok 5. Otchet po analizu bezopasnosty. Analiz zaproektnih avariy. Baza danih po YAPPU dla tseley AZPA], Kiev, 2008 (Rus).
7. ZNPP Unit №5. *Tehcnical Specification*. 05.GT.00.RG.01-2014 (Rus).

CYSENI 2017, May 26-27, Kaunas, Lithuania
ISSN 1822-7554, www.cyseni.com

MODELLING OF POOL HEAT-UP EXPERIMENT USING ANSYS FLUENT

A. Graževičius
Lithuanian Energy Institute
Breslaujos g. 3, LT-44403 Kaunas – Lithuania
E-mail: audrius.grazevicius@lei.lt

ABSTRACT

The natural circulation of water phenomena are met in the circulation loops and water pools of nuclear facilities. In the first case, the natural circulation of water in piping of circulation loop could be adequately simulated using one dimensional thermal-hydraulic codes. However, the modelling of mixing (circulation) in the water pools due to establishing of natural convection flow remains still not fully solved problem. On the other hand, this phenomenon plays significant role, when it is necessary to understand the heat transfer processes in big water pools of nuclear facilities (for example in spent fuel pools and pools used to remove heat in a case of passive heat removal systems). Due to complexity of geometry, in this case the codes with 3-dimentional modelling capabilities are the most appropriate. The experimental and 3-dimentional modelling results shows that a large natural convection flow occurs above the heater rod. The comparison of CFD and experiment results, allows to gain modelling experience. This experience will be used for investigations of thermal-hydraulics processes in the spent nuclear fuel pools and passive cooling systems.

Keywords: heat transfer, natural convection flow, computational fluid dynamics (CFD), ANSYS Fluent

1. INTRODUCTION

Due to safety issues arising after Fukushima accident on March 11 of 2011, new passive cooling systems become more important in safety systems of Nuclear Power Plant (NPP). The advanced nuclear reactors are design with new passive cooling systems. These systems mostly consist of large pools of water at atmospheric pressure. Due to large amount of water and good thermal properties, pools can remove large amounts of heat from the core and spent nuclear fuel. The natural circulation of water phenomena is met in these pools or cooling loops. Therefore, reliable computational fluid dynamics (CFD) modelling is needed to postulate accident scenarios of old and newly designed safety cooling systems and to understand the significant role of natural circulation phenomena in nuclear facilities.

In the past, many researchers for investigations of the natural circulation of water phenomena in nuclear facilities were using Lumped Parameters codes such as ATHLET, MELCOR, RELAP5, COCOSYS, ASTEC, TRACE and etc. Nowadays, for investigations often are used CFD codes. Investigation of cooling ability of a new spent fuel pool (SFP) passive cooling system of CAP1400 using ANSYS Fluent (a passive pressure water reactor) was performed byYe et al. (2013) [1]. The results of this analysis indicate that water in SFP never boils, even in a severe accident. Wang et al. (2011) have used CFD to investigate the SFP of the Chinshan NPP [2]. Their results shows that the uncovering of the fuel occurs in 2.7 days. Chen et al. (2014) have created CFD methodology for investigation of the transient thermal-hydraulic analysis of SFP cooling in the Maanshan NPP [3]. Investigation of cooling capability to remove decay heat at the Koushen NPP in Taiwan, using CFD, was performed by Hung et al. (2013) [4].

However, the previous studies on SFP safety have focused on safety evaluation, but no attention for validation of CFD on experiments was made. Tsao et al. (2013) perfomed investigation of passive air cooling capacity for SFP [5]. Results of simulations and experiments shows that the arrangement of opening and height of backplane significantly influence the temperature distribution in SFP. Validation of CFD and investigation of thermal-hydraulic safety of spent fuel bundle installed in a mast assembly was performed by Kim et al. (2016) [6].

For ANSYS Fluent validation and investigation of natural circulation of water phenomena, the volumetric scaling ratio of water tank, which is 1/910 the size of the passive auxiliary feedwater system condensing heat removal assessment loop (PASCAL), was chosen [7].

2. DESCRIPTION OF THE EXPERIMENTAL FACILITY

The experimental facility consists of a pool of water with heater rod and 2D particle image velocimetry measurement equipment. Fig. 1 shows a pool of water. The heater rod inside a pool, was designed to produce natural convection phenomena. The length of the pool is 300 mm, width is 60 mm and height is 650 mm. Water level is 400 mm. The back wall of the pool is made from 15 mm thick polycarbonate. Front and right walls of the pool are made from 3 mm thick Pyrex glass. 20 mm thick stainless steel is used for bottom and left walls. The heater rod, which has a diameter of 19.05 mm, is placed in horizontal position. The total length of heater rod is 160 mm: 150 mm is heating-part and 10 mm in the end of rod is non-heating-part. In the pool of water five (TF-01 ÷ TF-05) thermocouples were inserted to monitor and record the thermal changes during the experiment. These thermocouples were placed in the center of the pool, except the TF-02 thermocouple, which was placed 2 mm away from the heater rod surface. Thermal power of heater rod is 600 W. Heat loss – 310 W.

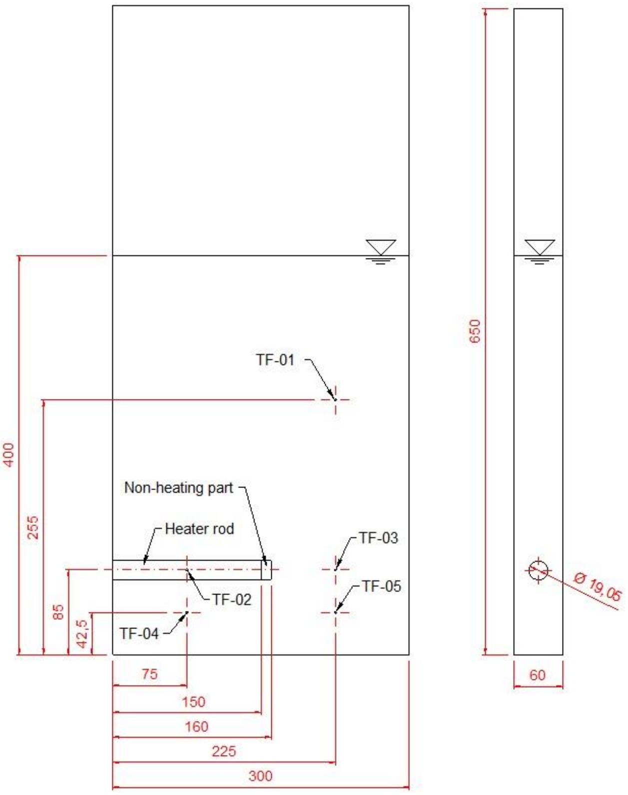

Fig. 1. Experimental facility (according to the description provided in [7])

3. COMPUTATIONAL MODEL

In this study, the natural convection of water phenomena is done with the ANSYS Fluent 17.2 academic research version using high performance computing cluster SGI Altix ICE 4800. The geometry and mesh of the pool of water were created using ICEM CFD and they are presented in Figs. 2–3. The detail parameters of the mesh are presented in Table 1. The evaluation of the mesh quality shows very high quality mesh, which consist only of hexa elements.

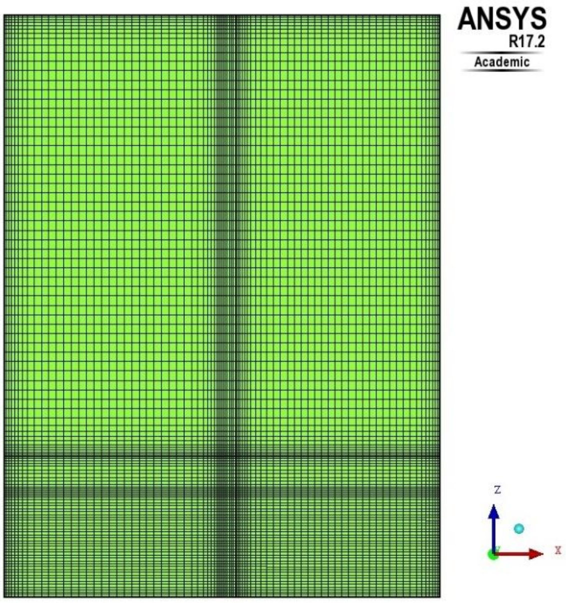

Fig. 2. Mesh of computational model

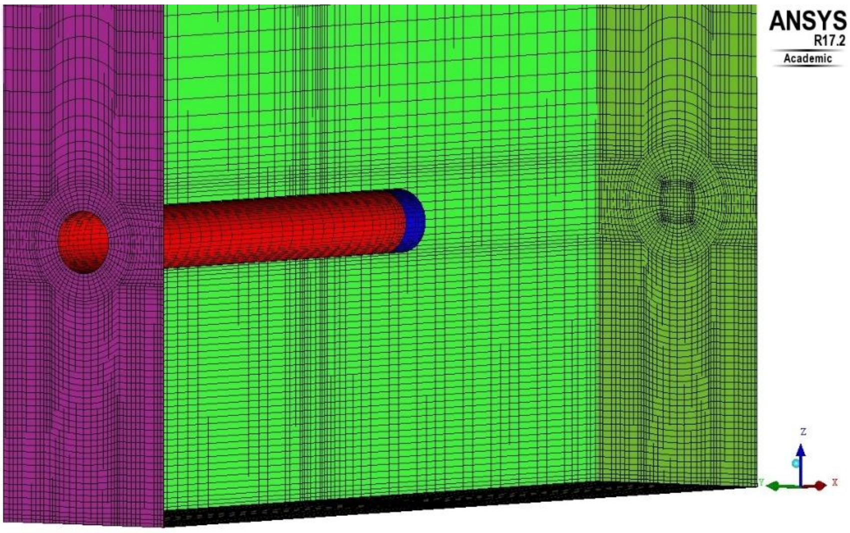

Fig. 3. Inside view of computational model

Table 1. Mesh parameters of computational model

Parameter	The obtained value	The acceptable value
Mesh size	433948 cells	–
The smallest cell size	0.9 mm	–
The biggest cell size	9.0 mm	–
Mesh quality	0.5÷1.0	> 0.3
Minimum angle of cell	> 46.6	> 20.0
Aspect ratio	< 11.6	< 100.0
Skewness	< 0.5	< 0.8
Orthonogical quality	> 0.7	> 0.1
Expansion rate	20.0%	< 20.0%

The height of computational domain is 400 mm instead of 650 mm, because air above the water is not modelled. For natural convection in closed domain Boussinesq approach, which gives faster convergence and the density of fluid is used as a function of temperature, was used. This approach treats density as constant value in all equations, except for the buoyancy term in the momentum equation [8]:

$$(\rho - \rho_0)g \approx -\rho_0 \beta (T - T_0)g; \tag{1}$$

where: ρ – fluid density, kg/m^3; ρ_0 – lightest fluid density (in this case 0 kg/m^3), kg/m^3; g – gravity, m/s^2; β – thermal expansion coefficient, 1/K; T – heat source temperature, K; T_0 – fluid temperature, K.

For modelling Pressure-Based Solver was used. This solver is default and it was used for common tasks (applicable in flows with Mach number from 0 until ~2÷3). For Pressure-Velocity Coupling, PISO scheme was used. Spatial discretization (interpolation methods) settings are presented in Table 2. Thermal properties of water and walls of the pool are presented in Table 3. Time-step size is very important parameter in transient calculations. Time-step size must be small enough to resolve transient simulations. Depending on the case, the time-step can be selected by various equations. For common flows time-step can be computed by equation (2), but in our case adaptive time stepping method is used. It means, that solver automatically adjust the best time-step for solver. The initial time-step size is 10^{-5} seconds and increases during the solution.

Table 2. Spatial discretization settings

Discretization	Scheme
Gradient	Least Squares Cell Based
Pressure	Body-Force Weighted
Momentum	First-Order Upwind
Turbulent Kinetic Energy	
Specific Dissipation Rate	
Energy	

Table 3. Thermal properties of water and walls of the pool

Properties	Water	Polycarbonate	Pyrex-glass	Stainless-steel
Density, kg/m^3	998.2	1220	2230	7850
Specific heat, j/kg·K	4182	1250	800	490
Thermal conductivity, W/m·K	0.6	0.2	1.2	14
Viscosity, kg/m·s	0.001003	–	–	–
Thermal expansion coeff., 1/K	0.000214	–	–	–
Initial water temperature, K	305.64	–	–	–
Ambient temperature, K	287,14	–	–	–

$$\Delta t = \frac{\Delta x}{V}. \tag{2}$$

where: Δx – the smallest cell size, m; V – fluid velocity, m/s.

One of the major points in CFD modelling is heat loss through the walls. If the heat loss is not described correctly, then minimal deviations can influence processes in fluid. In the analysed publication [7], there is no information about the heat loss through the walls, except total heat loss (310 W). Thus the probable heat loss through the walls is used in modelling and presented in Table 4. The walls were modeled as virtual walls.

Table 4. Heat loss through the walls

Wall	Area, m	Heat loss, W	Heat transfer coeff., W/m^2·K
Front	0.12	80.37	15.92
Back	0.12	80.37	
Left	0.024	16.07	
Right	0.024	16.07	
Bottom	0.018	12.06	
Top	0.018	105.06	138.8
	0.324	**310**	

4. RESULTS AND DISCUSION

The discussion in this chapter covers comparison of the experimental measurements and CFD modelling results. Due to heat released by heater rod, water temperature above the heater rod starts to increase. The heated water moves upward via the buoyancy force near the left wall. The heated water near the top wall is cooling and moves downward near the right wall. The natural circulation of water phenomena is formed above the heater rod. During the experiment there is no flow below the heater rod until the water temperature increases near the saturation temperature [7]. The CFD results shows, that water moves above the heater rod and below the heater rod partial thermal stratification occurs (see Figs. 5–6).

When the heating is switched on, water temperature in locations TF-01 – 03 starts to increase immediately (see Fig. 4). The temperature increases very slowly in locations TF-04 – 05 during the experiment, while in the CFD modelling it increases from the beginning of simulation. The comparison of the water velocities is presented in Fig. 7. These temperature and velocity differences arise from the unknown heat loss through the walls.

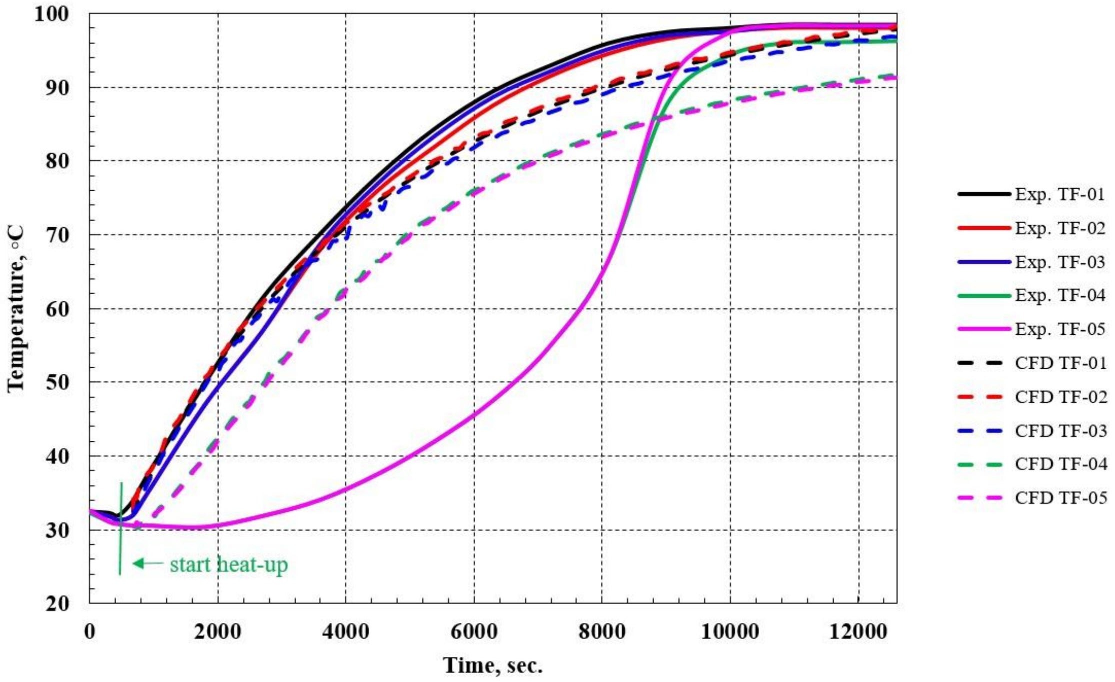

Fig. 4. Comparison of experimental and CFD temperature in locations of thermocouples

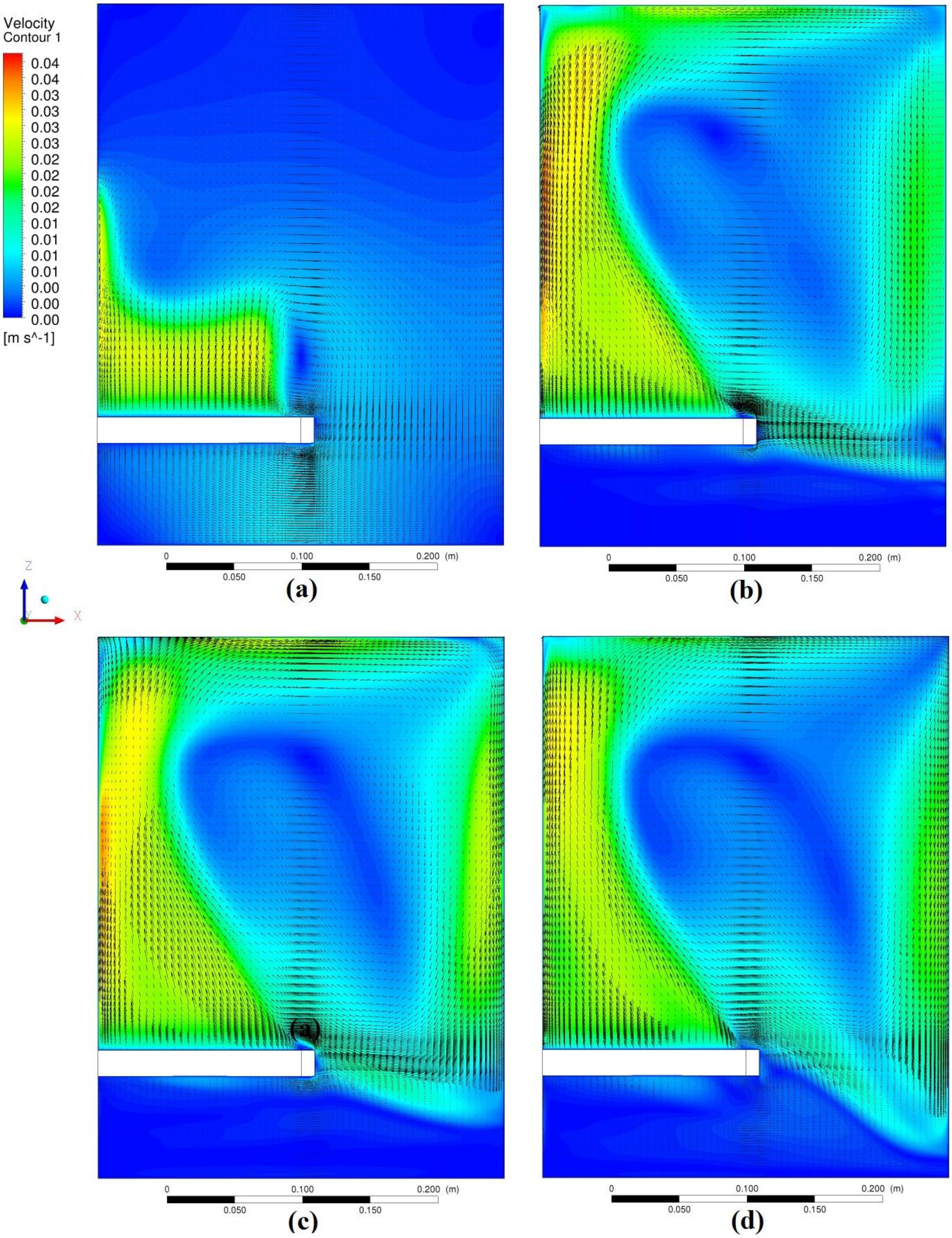

Fig. 5. Velocity contour at different time-step in the middle of CFD model: a – 15 sec; b – 1825 sec; c – 3608 sec; d – 7298 sec

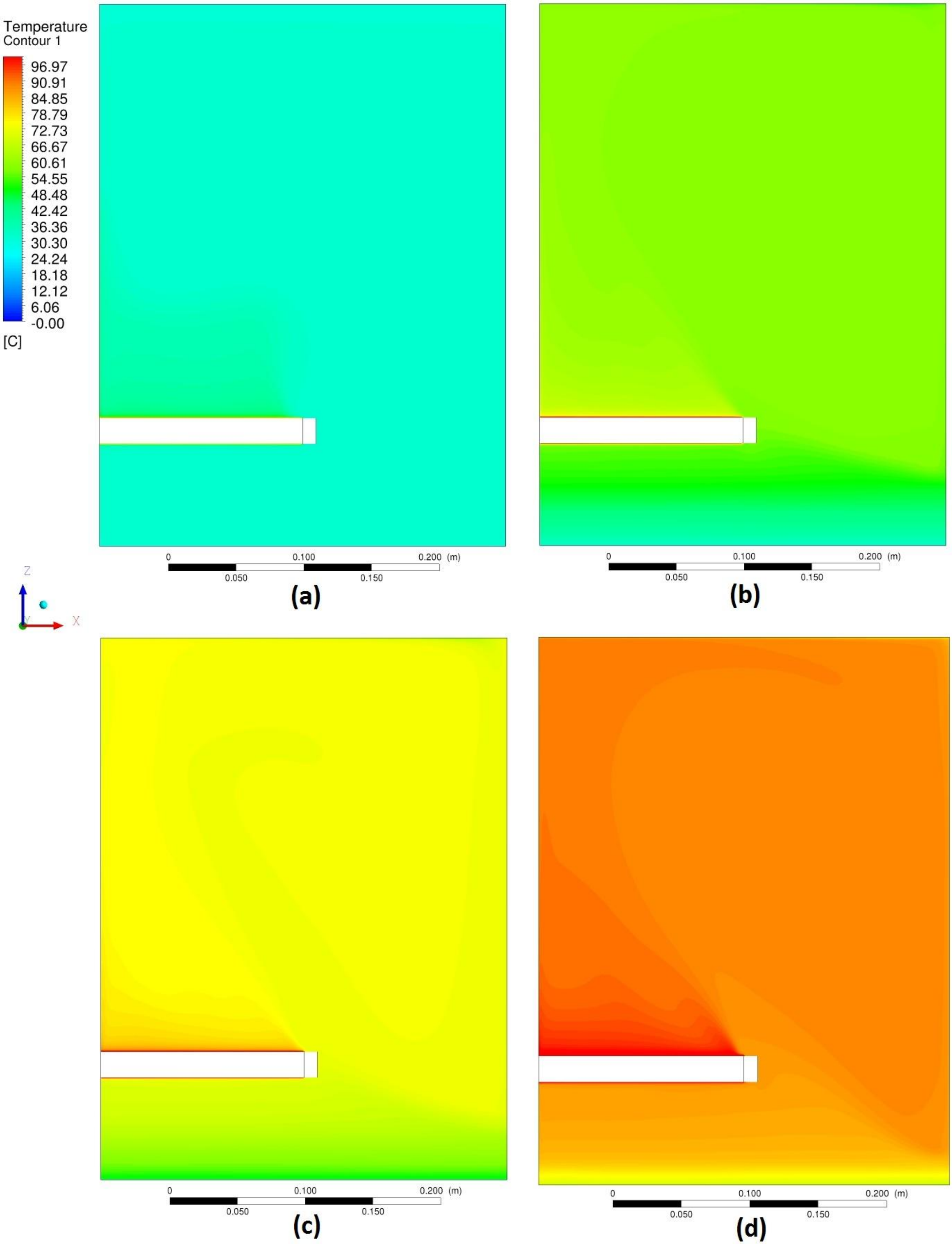

Fig. 6. Temperature contour at different time-step in the middle of CFD model: a – 15 sec; b – 1825 sec; c – 3608 sec; d – 7298 sec

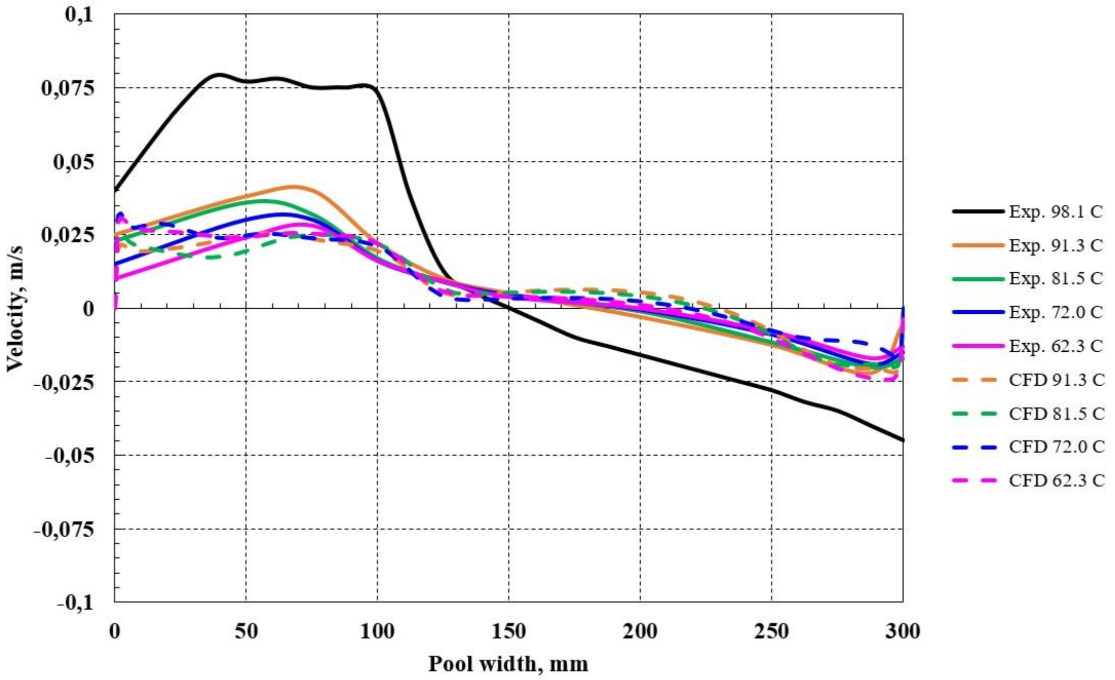

Fig. 7. Comparison of experimental and CFD velocity at h = 150 mm

5. CONCLUSION

Investigation of the natural circulation of water phenomena in the pool was performed using ANSYS Fluent. The experimental results described in publication [7], shows a large natural convection flow above the heater rod and thermal stratification until water temperature increases near the saturation temperature. The CFD results shows, that natural circulation flow above the heater rod and partial flow under the heater rod in the right side of CFD model. In order to accurately replicate this experiment using CFD, it is necessary to know heat loss through the walls. Only full replication of experiment allows to analyse large nuclear installations like SFP or reactors and as well as believe in results of modelling.

REFERENCES

1. YE, C., ZHENG, M.G., WANG, M.L., ZHANG, R.H., XIONG, Z.Q. The design and simulation of a new spent fuel pool passive cooling systems. Annals of Nuclear Energy, 2013, Vol. 58, p. 124-131.
2. WANG, J.R., LIN, H.T., TSENG, Y.S., SHIH, C.K. Application of TRACE and CFD in the spent fuel pool of Chinshan nuclear power plant. Applied Mechanic and Materials, 2012, Vol. 145, p. 78-82.
3. CHEN, S.R., LIN, W.C., FERNG, Y.M., CHIENG, C.C., PEI, B.S. Development of 3-D CFD methodology to investigate the transient thermal-hydraulic characteristics of coolant in a spent fuel pool. Nuclear Engineering and Design, 2014, Vol. 275, p. 272-280.
4. HUNG, T.C., DHIR, V.K., PEI, B.S, CHEN, Y.S. The development of a three-dimensional transient CFD model for predicting cooling ability of spent fuel pools. Applied Thermal Engineering, 2013, Vol. 50, p. 496-504.
5. TSAO, P.C., HSIEH, K.T., LEE, D.S., KIM, C.N., TSENG, Y.S., HUNG, T.C. Investigation of passive air cooling capacity for spent fuel pool. The 2013 World Congress on Advances in Nano, Biomechanics, Robotics, and Energy Research (ANBRE13), Seoul, Korea, August 25-28, 2013, p. 463-475.

6. KIM, Y.S., KIM, H.Y., BAK, J.Y., JEONG, J.J., JEON, J.Y., YUN, B. Evaluation of thermal hydraulic safety of a nuclear fuel assembly in a mast assembly of nuclear power plant. Annals of Nuclear Energy, 2016, Vol. 92, p. 136-149.
7. KIM, S., KIM, D.E., RYU, S.U., LEE, S.T., EUH, D.J. Experimental investigation on the natural convection flow in pool boiling. Nuclear Engineering and Design, 2014, Vol. 280, p. 349-361.
8. ANSYS Fluent User‘s Guide. Realise 17.2, August 2016, p. 834-838.

CYSENI 2017, May 26-27, Kaunas, Lithuania
ISSN 1822-7554, www.cyseni.com

EVALUATION OF THE POINT DEFECTS PRODUCTION IN NEUTRON IRRADIATED RBMK-1500 GRAPHITE

E. Lagzdina, D. Lingis, A. Plukis, R. Plukienė, J. Garankin, V. Remeikis
Center for Physical Sciences and Technology
Savanorių pr. 231, LT-02300 Vilnius, Lithuania
E-mail: elena.lagzdina@ftmc.lt

ABSTRACT

Graphite is used as a moderator and reflector in RBMK type reactors. Over time, the graphite is bombarded with fast neutrons, causing defects in the crystallographic structure and this leads to a wide range of effects on the physical properties of the material. The current understanding of irradiation damage in nuclear graphite is based on a point defect model. In this work MCNP, SRIM and Specter codes are used to evaluate the point defects production in the RBMK-1500 reactor graphite. The obtained results show different point defects production rates depending on the total neutron flux and neutron energy. The results are important for understanding of radionuclides mobility in irradiated graphite and optimisation of its storage in a geological disposal facility.

Keywords: RBMK-1500, graphite, DPA, MCNP, SRIM, Specter

1. INTRODUCTION

Graphite is a primary material for the gas-cooled, RBMK and HTR type nuclear reactor cores, serving as a low absorption neutron moderator and reflector which provides a high temperature, high strength structure. However, high energy neutron flux leads to the property and dimensional changes of graphite, ranging from the coefficient of thermal expansion and changes in elastic constants of the material to the dimensions of the single crystal and hence bulk material, known as radiation damage [1].

There are two graphite moderated, boiling water-cooled RBMK-1500 reactors at the Ignalina NPP site in the North-Eastern part of Lithuania [2]. Irradiated and contaminated graphite from reactor moderators and reflectors represent the greatest volume of irradiated waste materials from the RBMK type reactor [3]. The reactors in both Ignalina NPP units contain more than 3,600 t of graphite. The knowledge on the location and the chemical bond of contaminating radionuclides is a necessity for the development of methods for treatment and purification of irradiated graphite [4]. A specific problem related to irradiated graphite management is the varying content of long-lived radioisotopes, especially of ^{14}C, resulting from activation processes under neutron irradiation [3]. One of the routes for the generation of ^{14}C is via neutron activation of ^{13}C (n, γ / 0.0014 barn). ^{13}C is mainly bound in the graphite lattice. In case of the ^{13}C(n, γ)^{14}C reaction the recoil energy is high enough to dislocate the ^{14}C atom from its original lattice site. This ^{14}C atom can recombine with vacancies, stay fixed or migrate as an interstitial between the layers in the graphite matrix [4, 5]. Irradiation induced microstructural changes, such as a reduction in graphite crystallite size, point defects and preferential loss of matrix material may determine the concentration and distribution of radionuclides in irradiated graphite and their behaviour in a geological disposal facility.

Due to the scattering of the energetic neutrons by the nuclei of the carbon atoms either elastically or inelastically, the process of defects creation in the crystal matrix occurs. This leads to the changes in properties and dimensions of graphite. Fast neutrons (with a mean energy of about 2 MeV) interact with moderator transferring recoil energy to lattice atoms, which result in formation of primary knock-on atoms (PKAs). The PKA then moves through the lattice knocking other atoms out of their lattice sites creating cascades of defects, known as secondary displacement groups (SDGs). This leads to formation of point defects and defect clusters of vacancies and interstitial atoms [6]. The displacement per atom (DPA) characterizes lattice displacement events. DPA represents the number of atoms displaced from their normal lattice sites as a result of neutron irradiation. The displaced atoms can come to rest between the layers of graphite in positions, which are not original lattice sites [7]. In this case, they are called interstitial atoms. Each time an interstitial atom is formed there will be a corresponding vacant lattice site known as a vacancy. Interstitial-vacancy pair in graphite makes a Frenkel pair [8]. These point defects, interstitials and vacancies, are used to describe the damage observed in irradiated graphite. Irradiation-induced changes of material properties are measured as a function of DPA [9].

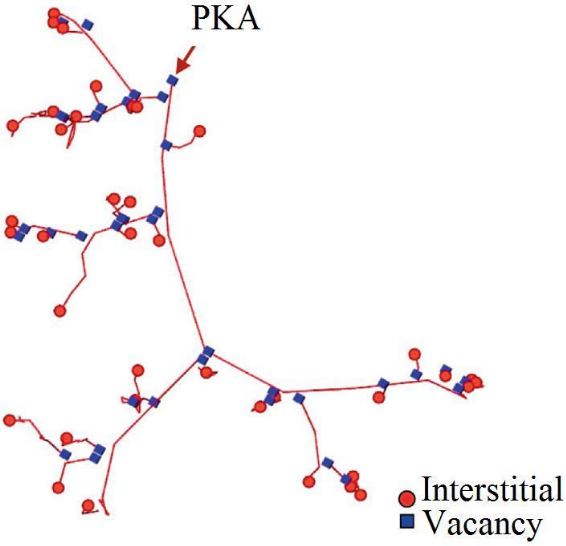

Fig. 1. The point defects cascade simulation for a PKA energy of 2.5 keV. The interstitials and vacancies are labelled as red points and blue squares, respectively. Reproduced from [7]

The aim of this work is to provide the theoretical evaluation of point defects production in neutron irradiated RBMK-1500 graphite. Neutron interaction with graphite is modelled using MCNP code, where recoil carbon ions are recorded by using PTRAC function. Recoil ion interaction with graphite matrix is modelled using SRIM code. DPA rate is calculated using MCNP and SRIM modelling results and, alternatively, by using joint MCNP and Specter modelling results.

It is hoped that the work presented here may assist not only in further understanding of the physical properties and behaviour of graphite under neutron irradiation conditions in NPP reactor core but also in irradiated graphite management using a science-based approach.

2. EXPERIMENTAL DETAILS

2.1. Modelling of neutron interaction with graphite

Neutron interactions with graphite are modelled using MCNP6 (Monte Carlo N-Particle) code [10]. Using Monte Carlo technique individual particles are tracked from the creation in a source to its death by absorption or escape. The type of particle interaction, energy of particle and other particle parameters depend on the probability distributions, which are randomly sampled using transport data. In calculations MCNP uses cross-sections from nuclear data libraries, such as ENDF, JENDL, etc. In this research ENDF-VII reaction cross-section library is used.

The object of simulation is one RBMK-1500 reactor graphite stack column with 2.4 % ^{235}U fuel enrichment and 0.41 % burnable erbium absorber as it corresponds to typical load of Unit 1 of Ignalina NPP. In this model, the density of cooling water is equal to 0.5 g/cm^3, of graphite – 1.675 g/cm^3 and temperatures of water and graphite are, respectively, 550 K and 700 K. The whole object consists of 686 cm height fuel assembly with graphite and 50 cm top and bottom graphite reflectors (see Fig. 1).

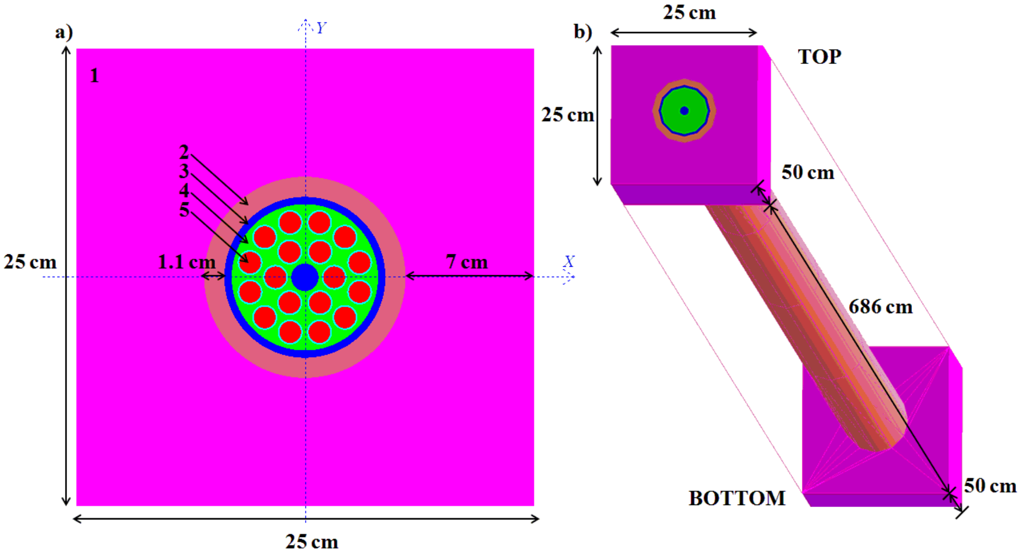

Fig. 2. Cross-sectional view of **(a)** one graphite stack column and fuel channel of RBMK-1500 reactor core with **(b)** top and bottom reflectors (1 – graphite column; 2 – graphite sleeve; 3 – fuel channel tube; 4 – coolant water; 5 – UO_2 fuel)

For simplification and acceleration of simulation, reflective surfaces are used on the side surfaces of the column. Particle track that hits a reflecting surface is reflected like in mirror and only the particles that reach the vertical surfaces of graphite column can escape. Spatial distributions of neutron and recoil ion fluxes are obtained using F4 tally and PTRAC (*Particle Track Output*) function, which is used for tracking individual ions. MCNP PTRAC card generates separate output file of user-defined events and parameters, like type of event, energy and location of particle, etc. In this case, only the bank events of carbon recoil ions are recorded within graphite stack. Parameters of these ions are used in later simulations.

MCNP outputs are calculated for 1 source particle i.e. neutron, therefore it is needed to normalize the fluxes to correspond the real fluxes of the reactor. Real flux Φ is obtained by [11]:

$$\Phi = \frac{P*\bar{\nu}}{w_f} * \frac{1}{k_{eff}} * \Phi_{F4}, \tag{1}$$

where P is the thermal power of the modelled system (one reactor RBMK-1500 graphite column with fuel assembly), $\bar{\nu}$ – average number of neutrons produced per fission, w_f – average recoverable energy per fission, k_{eff} – MCNP evaluated neutron multiplication factor of assembly, Φ_{F4} – MCNP F4 tally flux.

The evaluation of DPA is performed by using Specter code [12]. Specter is a computer code that has been developed to simplify the calculations of neutron induced damage to targets and it only needs user specified neutron energy spectrum. Specter can calculate spectral-averaged displacements, recoil PKA spectra, gas production, etc. The calculations are performed using nuclear data obtained from ENDF/B-V library. The program converts required library files according to user defined group structure and proceeds to spectral average all quantities. The code does not account for thermal effects and the simulation is performed with carbon as an element, not as a graphite matrix, hence the density of the target and lattice parameters are not considered.

2.2. Modelling of recoil ion interaction with graphite

Recoil ion interaction with graphite is performed using SRIM (*The Stopping and Range of Ions in Matter*) code [13]. SRIM is broadly used Monte Carlo based code for modelling the ion collision cascade problems, ion deposition profiles in materials and others. Both the electron energy loss and nuclear collision energy loss are considered in simulations. There are 3 computation methods in SRIM code: 1) Kinchin-Pease method; 2) Monolayer method; 3) Full-Cascades method. Using monolayer (second) method ions have to have a collision in each monolayer of the target and every collision is calculated without any approximations. This method gave no particular difference in results compared to Full-Cascades method so it isn't discussed here.

The first method provides quick statistical estimates based on Kinchin-Pease formalism. This method assumes that between specified threshold energy E_d and an upper cut-off E_c energy there is a linear relationship between the number of created displaced atoms $\nu(T)$ and the energy of primary knock-on atom E [14]:

$$\nu(T) = \begin{cases} 0\,, & for\ E < E_d \\ 1, & for\ E_d < E < 2E_d \\ \frac{T}{2E_d}, & for\ 2E_d < E < E_c. \\ \frac{E_c}{2E_d}, & for\ E \geq E_c \end{cases} \tag{2}$$

Below the threshold energy, no new displacements occur and energy above cut-off limit is treated as being dissipated in excitation and ionization of target atoms. Using this technique total number of displacements corresponds to the total number of vacancies produced. There are several modifications of the Kinchin and Pease model. Norgett, Robinson and Torrens (NRT) developed a secondary displacement model for computing the number of displacements per atom for a given energy PKA. Total number of stable Frenkel pairs produced by a PKA with kinetic energy E_{PKA} in a single cascade is given by [15]:

$$\nu = \frac{\kappa(T-Q)}{2E_d} = \frac{\kappa T}{2E_d},\ for\ T > \frac{2E_d}{\kappa}, \tag{3}$$

where Q – total energy lost to ionization, T – damage energy and κ is the displacement efficiency. Displacement efficiency parameter is a constant independent of energy and insensitive to the target or temperature. Its value is approximately 0.8 [15]. Damage energy is obtained from SRIM output by using equation [16]:

$$T = E_i^P + E_T^P, \tag{4}$$

where E_i^P is the beam energy lost to phonons and E_T^P corresponds to the target atom energy lost to phonons.

The third calculation method used, is the Full-Cascades method. Using this method, every PKA is tracked until its energy falls below threshold energy. The number of displacements in Full-Cascades technique is the sum of vacancies, interstitials and replacements. Although authors of SRIM recommend using Full-Cascade method for calculation of target damage [13], other authors criticize this method and instead recommend using Kinchin-Pease method with some additional improvements [16].

For recoil ion interaction with graphite simulation, specifically designed SRIM input file is needed. It must contain information for identification of the event and atom by atomic number. Other information is related to the input parameters of recoil ions – energy, location and direction. In this study, the lateral distance from the inner surface of graphite cylinder and the height coordinate in MCNP is treated, respectively, as the depth in target and one lateral coordinate in SRIM. For simplification of calculations, both the graphite sleeve and column are treated as single graphite unit. This input file is used by SRIM code where ion interaction with graphite is simulated by both the Kinchin-Pease and Full-Cascades methods. The obtained results are used in the calculation of DPA rate using equation:

$$R_{DPA} = \frac{N_{neutrons/s} \cdot N_{ions/neutron} \cdot N_{displacement/ion}}{N_{atoms}}, \quad (5)$$

where $N_{neutrons/s}$ corresponds to the value of neutrons obtained per second in the fuel assembly, $N_{ions/neutron}$ corresponds to the value of recoil ions per neutron, $N_{displacement/ion}$ corresponds to displacements per ion and N_{atoms} is the value of atoms in volume.

There are two major limitations of SRIM code that must be addressed. Firstly, there is no build-up of ions or damage in the target therefore every ion interacts with perfect undamaged target without the effect of previous ions. The second limitation is that the target temperature is 0 K and there are no thermal effects. This mean that thermal diffusion and thermal annealing of target damage are not taken into consideration.

3. RESULTS AND DISCUSSION

The effective neutron multiplication factor of fuel assembly with surrounding graphite evaluated by MCNP is k_{eff} = 1.03. Using this value, MCNP F4 tally results and equation (1), the neutron flux corresponding to operating reactor conditions is obtained (see Fig. 3). The portion of higher energy neutrons decreases with the distance in graphite and the lower energy neutron portion increases. The average value of total neutron flux is $\Phi = 1.87 \cdot 10^{14} n/cm^2 s$ and this value is in the good agreement with literature sources [17, 18]. Slight increase in total neutron flux near the edges of the graphite stack could be due to usage of reflecting surfaces.

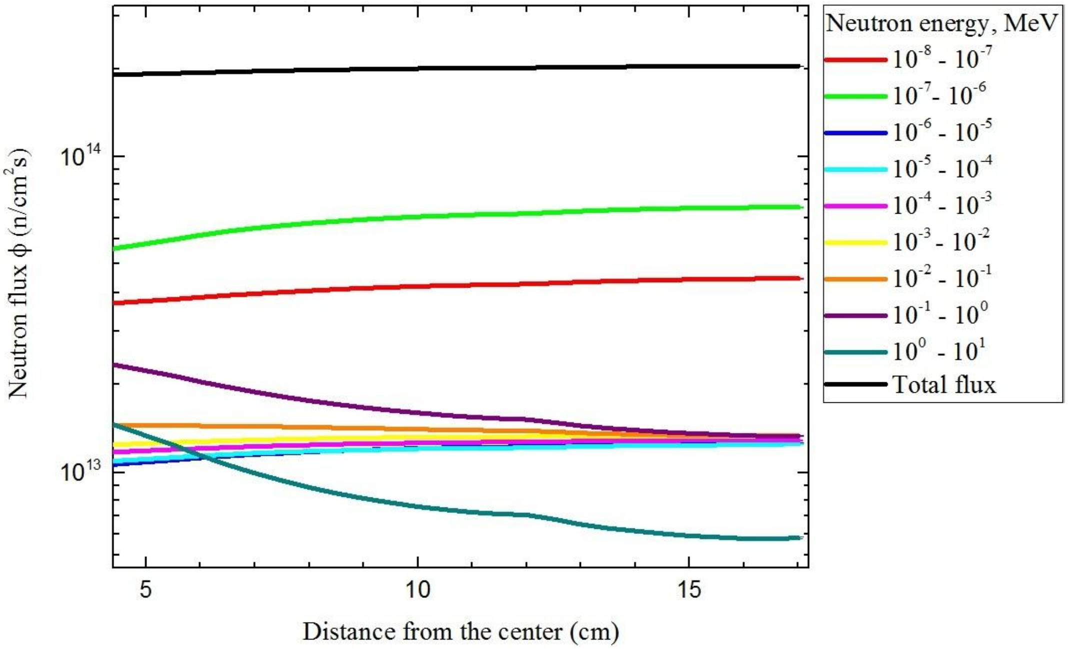

Fig. 3. Total neutron flux in graphite vs lateral distance from the centre of the fuel assembly

Using Specter code and MCNP evaluated neutron flux the distribution of DPA rate in graphite stack is determined (see Fig. 4.). The results show that higher neutron energy results in an increase of point defects formation. This is in good agreement with increased displacement cross section [19]. By using joint MCNP and Specter calculation method the DPA after one-year irradiation is evaluated as 0.80 DPA (or $R_{DPA} = (2.54 \pm 0.01) \cdot 10^{-8} s^{-1}$) in graphite sleeve near fuel assembly and 0.64 DPA (or $R_{DPA} = (1.99 \pm 0.01) \cdot 10^{-8} s^{-1}$) near the outer part of graphite column.

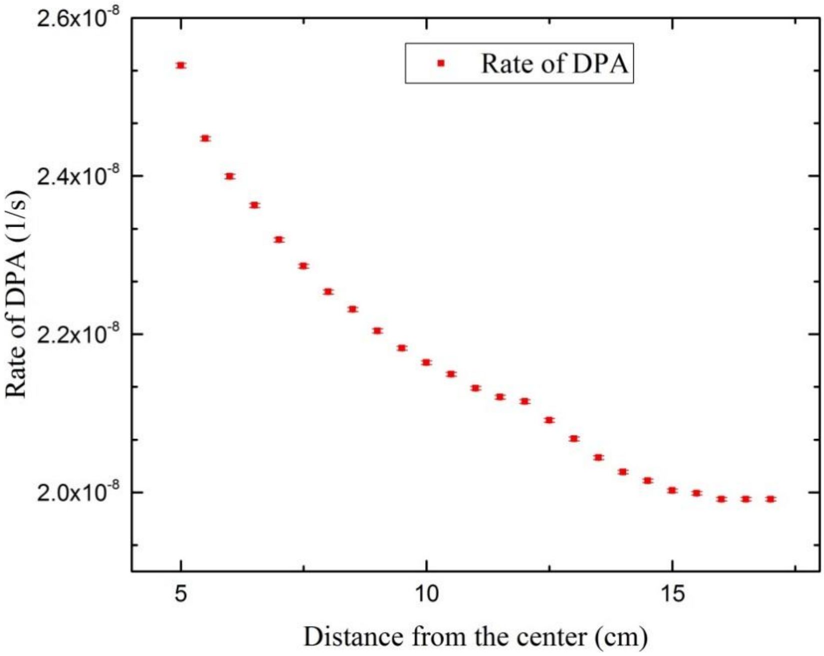

Fig. 4. The distribution of DPA in graphite

The total number of point defects versus energy of PKA evaluated by Full-Cascade and Kinchin-Pease techniques using SRIM code is shown in Fig. 5.

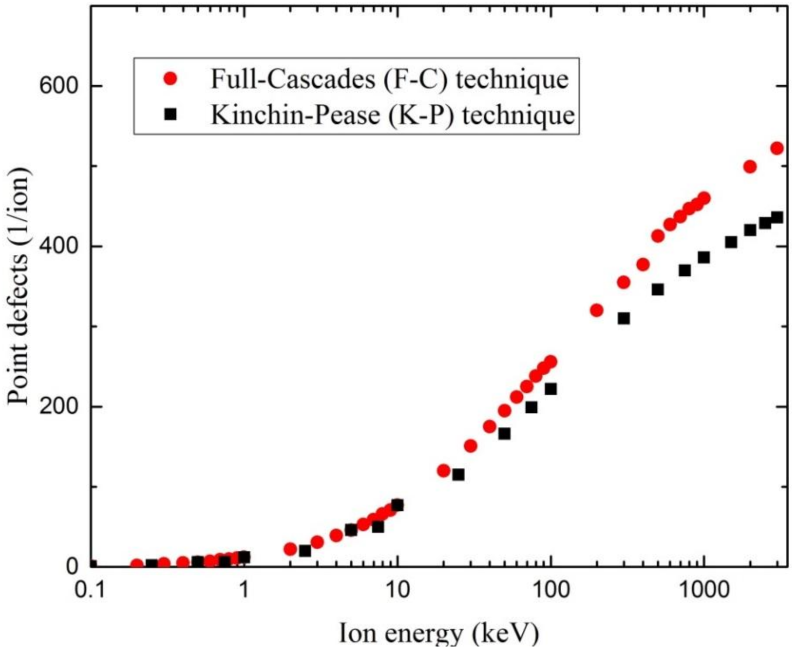

Fig. 5. The total number of displacements versus energy of PKA evaluated by using Full-Cascade and Kinchin-Pease techniques

According to SRIM modelling results, the threshold energy for PKA is near 100 eV. Below this energy, no point defects are created or their quantity is negligible. With the increase of PKA energy, more point defects are created and the difference between Full-Cascade and Kinchin-Pease methods starts to grow. When the energy of PKA is about 2 MeV, the difference is up to 13 %.

Using the MCNP PTRAC modelling results and SRIM code it is evaluated that one ion can produce around 172 vacancies as calculated by Kinchin-Pease method and 210 displacements in case of using Full-Cascade method. MCNP results show that one neutron creates around 13.8 recoil ions. Using these values and equation (5) the calculated DPA rate is $R_{KP} = (1.45 \pm 0.01) \cdot$

$10^{-8}s^{-1}$ and $R_{FC} = (1.77 \pm 0.01) \cdot 10^{-8}s^{-1}$, for Kinchin-Pease and Full-Cascades techniques respectively. According to these values the DPA values of graphite column after one-year of full power is $DPA_{KP} = 0.46$ and $DPA_{FC} = 0.56$. Rate of DPA evaluated using equations (3) and (4) is $R_{NRT} = (1.16 \pm 0.01) \cdot 10^{-8}s^{-1}$ or after one-year of full power $DPA_{NRT} = 0.37$. As reported in [20], the DPA value after one-year full power in different graphite-moderated nuclear reactors varies from 0.2 to 0.9. Results, obtained in this research show, that values calculated by Specter code is about 2 times higher than the values calculated using SRIM code. Both Kinchin-Pease and Full-Cascades techniques of SRIM code give higher DPA values than NRT model. Although values differ, all of them are in agreement with literature data. For more accurate evaluation of the DPA values additional codes could be used which consider the limitations of SRIM and Specter codes.

4. CONCLUSIONS

Neutron interaction with graphite matrix causes nuclear collisions and electronic excitation in the crystal structure, which leads to point defects formation. Results of this research show that the higher the energy of neutrons is, the more displacements are created – DPA rate in graphite sleeve near fuel assembly is calculated to be about 25% higher than near the outer part of graphite column. Due to limitations of different methods of calculation, some aspects of neutron interaction with graphite matrix may be not taken into account. Depending on the method, DPA values differ – the lowest value calculated by NRT model ($DPA_{NRT} = 0.37$) is more than 2 times smaller than value calculated using Specter code ($DPA_{Specter} = 0.80$). Although values differ, all of them fall in the range of values reported in literature, so the chosen methods are suitable for evaluation of DPA in nuclear reactor graphite. Further comparison of results obtained with experimental measurements could provide more insights into the physical properties of graphite under neutron irradiation conditions.

REFERENCES

1. MARSDEN, B. J., HAVERTY, M., BODEL, W., HALL, G. N., JONES, A. N., MUMMERY, P., TREIFI, M., Dimensional Change, Irradiation creep and Thermal/Mechanical Property Changes in Nuclear Graphite, International Materials Reviews, 2016, Volume 61, Issue 3, p. 155-182.
2. ALMENAS, K., KALIATKA, A., UŠPURAS, E., Ignalina *RBMK-1500, A Source Book*, Kaunas, Lithuania, 1998, 196 p. ISBN 9986-492-35-1.
3. Von LENSA, W., VULPIUS, D., STEINMETZ, H.-J., GIRKE, N., BOSBACH, D., THOMAUSKE, B., BANFORD, A.W., BRADBURY, D., GRAMBOW, B., GRAVE, M.J., JONES, A.N., PETIT, L., PINA, G., Treatment and Disposal of irradiated Graphite and other Carbonaceous Waste, Final Report Summary – CARBOWASTE, Project ID: 211333, Funded under: FP7-EURATOM-FISSION, 2013.
4. VULPIUS, D., BAGINSKI, K., FISCHER, C., THOMAUSKE, B., Location and chemical bond of radionuclides in neutron-irradiated nuclear graphite, Journal of Nuclear Materials, 2013, Volume 438, Issues 1-3, p. 163-177.
5. NARKŪNAS, E., ŠMAIŽYS, A., POŠKAS, P., BARTKUS, G., Modelling of the spatial distribution of the induced activities in the RBMK-1500 reactor graphite blocks and rings/sleeves, Progress in Nuclear Energy, 2016, Volume 91, p. 265-276.
6. TELLING, R., HEGGIE, M., Radiation defects in graphite, Philosophical Magazine, 2007, Volume 87, Issue 31, p. 4797-4846.
7. CHRISTIE, H.J., ROBINSON, M., ROACH, D.L., ROSS, D.K., SUAREZ-MARTINEZ, I., MARKS, N.A., Simulating radiation damage cascades in graphite, Carbon, 2015, Volume 81, p. 105-114.

8. EWELS, C. P., TELLING, R. H., EL-BARBARY, A. A., HEGGIE, M. I., BRIDDON, P. R., Metastable Frenkel Pair Defect in Graphite: Source of Wigner Energy?, Physical Review Letters, 2003, Volume 91, Issue 2, p. 025505-1-025505-4.
9. IWAMOTO, Y., NIITA, K., SAWAI, T., RONNINGEN, R.M., BAUMANN, T. P., Development of displacement damage model in PHITS and comparison with other codes in a high-energy region. SATIF-11 2013. Proceedings of 11th Meeting of the Task Force on Shielding Aspects of Accelerators, Targets and Irradiation Facilities, Tsukuba, Japan, 2012 September 11-13.
10. GOORLEY, T., JAMES, M., BOOTH, T., BROWN, F., BULL, J., COX, L. J., DURKEE, J., ELSON, J., FENSIN, M., FORSTER, R. A., HENDRICKS, J., HUGHES, H. G., JOHNS, R., KIEDROWSKI, B., MARTZ, R., MASHNIK, S., MCKINNEY, G., PELOWITZ, D., PRAEL,. R., SWEEZY, J., WATERS, L., WILCOX, T., ZUKAITIS, T., Initial MCNP6 Release Overview, Nuclear Technology, 2012, Volume 180, Number 3, p. 298-315.
11. RAVNIK, M., Calculation of Power Density with MCNP in TRIGA reactor, International Conference Nuclear Energy for New Europe, 2006, Portorož, Slovenia, September 18-21, 2006.
12. GREENWOOD, L.R., SMITHER, R. K., SPECTER: Neutron damage calculations for materials irradiations, Technical Report ANL/FPP/TM-197, Argonne National Laboratory, IL, USA, 1985.
13. ZIEGLER, J. F., ZIEGLER, M. D., BIERSACK, J. P., SRIM - The stopping and range of ions in matter (2010), Nuclear Instruments and Methods in Physics Research Section B: Beam Interactions with Materials and Atoms, 2010, Volume 268, Issue 11-12, p. 1818-1823.
14. KINCHIN, G. H., PEASE, R. S., The Displacement of Atoms in Solids by Radiation, Reports on Progress in Physics, 1955, Volume 18, Issue 1, p. 1-51.
15. NORGETT, M.J., ROBINSON, M.T., TORRENS, I.M., A proposed method of calculating displacement dose rates, Nuclear engineering and design, 1975, Volume 33, Issue 1, p. 50-54.
16. STOLLER, R.E., TOLOCZKO, M.B., WAS, G.S., CERTAIN, A.G., DWARAKNATH, S., GARNER, F.A., On the use of SRIM for computing radiation damage exposure, Nuclear Instruments and Methods in Physics Research B: Beam Interactions with Materials and Atoms, 2013, Volume 310, p. 75-80.
17. ANCIUS, D., RIDIKAS, D., REMEIKIS, V., PLUKIS, A., PLUKIENE, R., COMETTO, M., Evaluation of the activity of irradiated graphite in the Ignalina Nuclear Power Plant RBMK-1500 reactor, NUKLEONIKA, 2005, Volume 50, Issue 3, p. 113-120.
18. NARKŪNAS, E., ŠMAIŽYS, A., POŠKAS, P., Reaktoriaus RBMK-1500 konstrukcinių elementų neutroninės aktyvacijos skaitinis vertinimas. 3. Kuro kanalų neutroninės aktyvacijos vertinias naudojant sumodeliuotus neutronų srautus, Energetika, 2009, T. 55. Nr. 4, p. 200-208.
19. KONNO, C., Differences among KERMA or DPA data calculated from JENDL-4.0, ENDF/B-VII.1, JEFF-3.2 and FENDL-3.1b with NJOY, Technical Meeting (F4-TM-52919), IAEA Headquarters, Vienna, Austria, 2016 June 13-16.
20. WINDES, W., BURCHELL, T., BRATTON, R., Graphite Technology Development Plan, Technical Report INL/EXT-07-13165 Idaho National Labs, 2007, http://dx.doi.org/10.2172/968671.

CYSENI 2017, May 26-27, Kaunas, Lithuania
ISSN 1822-7554, www.cyseni.com

REMEDIATION OF PETROLEUM HYDROCARBONS CONTAMINATED SOIL USING WATER VAPOR PLASMA

D. Gimžauskaitė, A. Tamošiūnas, V. Snapkauskienė, P. Valatkevičius, V. Valinčius
Lithuanian Energy Institute
Laboratory of Plasma Processing
Breslaujos str. 3, LT-44403 Kaunas – Lithuania
E-mail: Dovile.Gimzauskaite@lei.lt

ABSTRACT

Expanding industrialization and urbanization leads to increasing environmental pollution, among this generally inconspicuous soil pollution. Soil contamination can be caused by variety of pollutants, but the most common is petroleum hydrocarbons, heavy metals, pesticides. The investigation of appropriate soil remediation techniques constantly continues. Water vapor plasma technology potentially can be an innovative solution for efficient pollutants removal from soils mainly because of possibility to form one of the most reactive species – hydroxyl radicals (·OH), as well as (·O) and (·H) radicals. On the account of that, the purpose of this paper was to investigate water vapor plasma suitability to treat soils contaminated by petroleum hydrocarbons. Hereby, elemental composition changes in soil were expected during interaction between water vapor plasma and polluted soil. In order to confirm this statement, contaminated soil was investigated before and after reaction using high-performance physical research methods: scanning electron microscopy (SEM), energy dispersive X-ray spectroscopy (EDS). Furthermore, during the reaction, measurements were performed using gas analyser. SEM data showed that contaminated soil interaction with water vapor plasma led to structural transformations of soil. Results obtained with EDS revealed that carbon content was ~ 35 times higher above the average value (~0.5 %) inherent in uncontaminated soil. Moreover, after the soil treatment EDS results confirmed that the carbon content was reduced significantly from ~18% to ~1%. Additionally, measurements taken with gas analyser indicated water vapor plasma ability to convert pollutants into useful product – syngas (H_2+CO) and thus remediate contaminated soil.

Keywords: water vapor plasma, petroleum hydrocarbons, soil remediation

1. INTRODUCTION

Petroleum-based products still represent a major source of energy for daily life and industrial activity. During exploration, production, refining, transportation and storage of oil and its products (e.g. gasoline, diesel, kerosene, lubricating oil, greases), leakages are frequent [1, 2] and most importantly it causes pollution of soil, groundwater, surface water, poses serious threat to ecosystems, living beings [3]. In view of this, petroleum hydrocarbons, as common environmental contaminants, require remediation of polluted areas.

Consequently, various soil treatment methods based on biological, physical, chemical and thermal processes have been used for remediation purposes [4, 5]. Nevertheless, all these methods have limiting factors, for example landfilling (as a physical method) was one of the first and simplest decontamination method of polluted soils, but over time it became avoidable, mainly because of contradiction to ecological approach. Moreover, the main drawback for the biological method is the long treatment time, as well as required certain conditions for the growth of microorganisms [6]. Other techniques suffer from weak points, such as chemical reagents usage, high energy consumption [7]. Furthermore, according to Fernández et al. [8] in order to demonstrate treatment efficiency, it is necessary to ensure that remediation process does not produce any toxic intermediate products and avoids undesired environmental and ecological effects. Therefore, optimization of existing treatment methods and new technologies are still needed. Taking that into account, application of plasma technologies for soil treatment provokes great interest. Recently non-thermal plasmas (corona, dielectric barrier discharge (DBD [7, 9–12]) were applied for this purpose.

Investigations have shown that non-thermal plasma technologies could be applied for treatment of various soil pollutants (e.g. hydrocarbons). However, the records about remediation of petroleum hydrocarbons contaminated soil using thermal water vapor plasma technology were not found. On the account of that, the purpose of this paper was to investigate water vapor plasma suitability to treat soils contaminated by petroleum hydrocarbons. Thus, broadening studies carried out in the field of soil treatment with thermal plasma.

2. METHODOLOGY

The experimental plasma system used in this work consists of a linear direct current (DC) plasma torch, a plasma-chemical reactor (Fig. 1), a soil supply system, electrical power source, measurement and cooling systems, as well as a gas supply and overheating systems. The plasma system was operating under atmospheric pressure. Water vapor was generated using 5 bar of pressure water steam generator GAK-50 [13]. The power of the plasma torch was 64.8 kW and water vapor flow rate was 4.1 g/s. The operating temperature of proposed plasma system was ~ 2800 K.

Moreover, in the time of water vapor plasma formation, high energy electrons were generated and it allowed the creation of a highly reactive species – hydroxyl radicals (·OH), as well as (·O) and (·H) radicals. These species hold the potential of degrading nearly all types of organic contaminants into harmless products [13, 14].

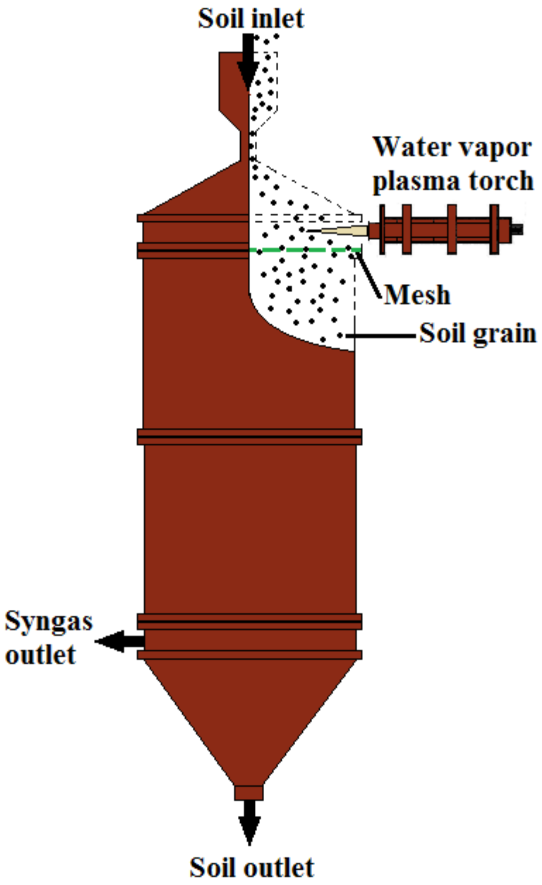

Fig. 1. A simplified scheme of plasma-chemical reactor

Performing this investigation, elemental composition changes in soil were expected. In order to confirm this statement, contaminated soil was investigated before and after reaction using high-performance physical research methods. Surface morphology of untreated (polluted) and plasma treated soil was investigated by the scanning electron (SEM, Hitachi S-3400N) microscope. The elemental composition of soil specimens was analysed by energy dispersive X-ray spectroscopy

(EDS, Bruker Quad 5040). Moreover, during the interaction between polluted soil and water vapor plasma, obtained gas concentrations were measured using multi-component gas analyser (MRU, SWG 300).

3. RESULTS AND DISCUSSION

Fig. 2 illustrates soil color changes before and after interaction with water vapor plasma. Before treatment soil contained humus (because of humic compounds in the soil, it usually are black, or brown.). After plasma treatment soil became light brown (inherent to silicon dioxide (SiO_2)) with a reddish tint (peculiarity of trivalent ferric compounds) and non-humic.


a) b)

Fig. 2. Contaminated soil by petroleum hydrocarbons: a) before treatment; b) after plasma treatment

3.1. SEM analysis of contaminated soil

Fig. 3 includes scanning electron microscope (SEM) surface views of untreated (polluted by petroleum hydrocarbons) and plasma-treated soil. Untreated soil (Fig. 3 a), c) has non-uniform, relatively rough surface and larger particles compared to treated soil (Fig. 3 b), d). Surface of treated soil seems to be relatively smooth, soil fraction has become finer. Moreover, after soil interaction with water vapor plasma, inconsiderable amount of bubbles were formed. It can be inferred from the literature [15] that bubbles coresponds to fly ash (FA). Generally fly ash is produced when carbon rich sediments are burned of at least ~1723 K [15], whereas during the experiment temperature reached ~ 2800 K.

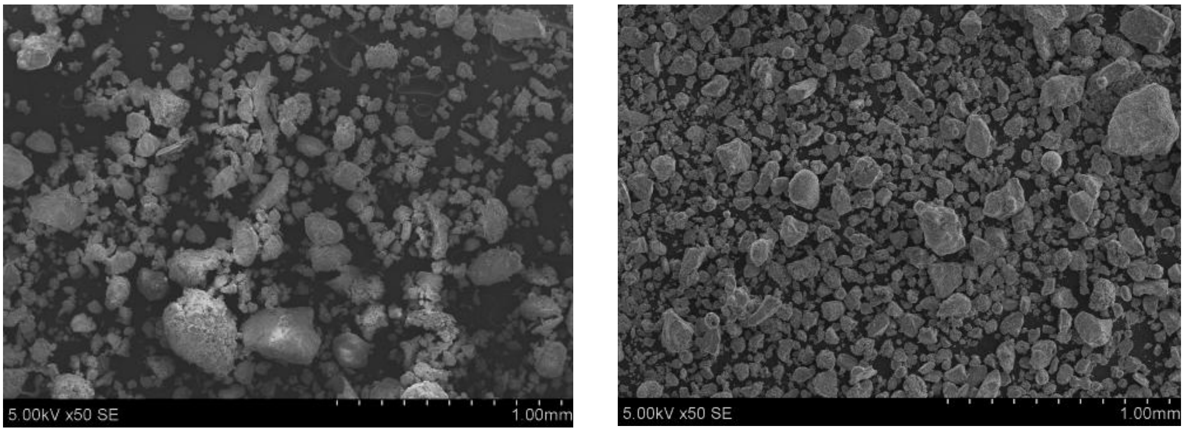

a) b)

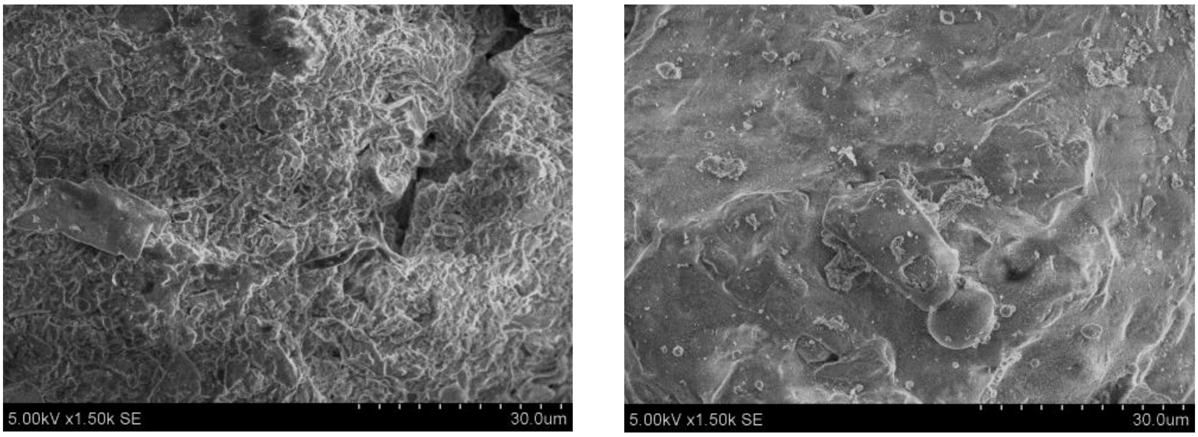

c) d)

Fig. 3. SEM surface views of contaminated soil by petroleum hydrocarbons: a), c) – untreated soil; b), d) – plasma-treated soil

3.2. EDS analysis of contaminated soil

Table 1 shows elemental composition in soil before and after interaction with water vapor plasma. It is noteworthy that elemental composition of untreated soil is close to the average theoretical quantities, except carbon concentration varies significantly (recorded ~18% instead of the average 0.5%). Furthermore, after soil treatment with water vapor plasma, it was observed that carbon content notably decreased from ~18% to ~1% and became close to average value (0.5%). These results leads to the assumption that during the reaction conversion of carbon compounds (petroleum hydrocarbons) took place. Additionaly, it was found that O, Si, Al, Fe, P, S, K, Ca, Mg, Na content after the treatment changed slightly.

Table 1. Elemental composition of soil

Element	Theoretical concentration, %*	Untreated soil concentration, at. %	Treated soil concentration, at. %
C	0.5	17.93	1.12
O	50	60.01	63.41
Al	7	2.33	4.45
Si	25	14.55	22.00
K	2	1.14	1.11
Ca	3	1.50	4.46
Mg	2	0.82	0.80
Fe	4	1.10	1.26
Na	2	0.23	0.59
P	0.1	0.21	0.65
S	0.2	0.17	0.15

* – the mean values taken from [16].

3.3. Gas analyser results

In consideration of gas concentration changes during interaction between contaminated soil and water vapor plasma (Fig. 4), noticeable decrease in oxygen was recorded, while at the same time syngas (H_2 + CO) was formed. In this context, up to 39.8% of the hydrogen and 12.69% of the CO were extracted. Also formation of CO_2 (up to 11.72%) and small amounts of NO, NO_2, SO_2, C_3H_8 (which concentration reaches the maximum value of 0.155%, 0.016%, 0.032%, 0.13%, respectively) were observed. The remaining concentration part coresponds to atmospheric N_2, which a gas analyzer does not capture.

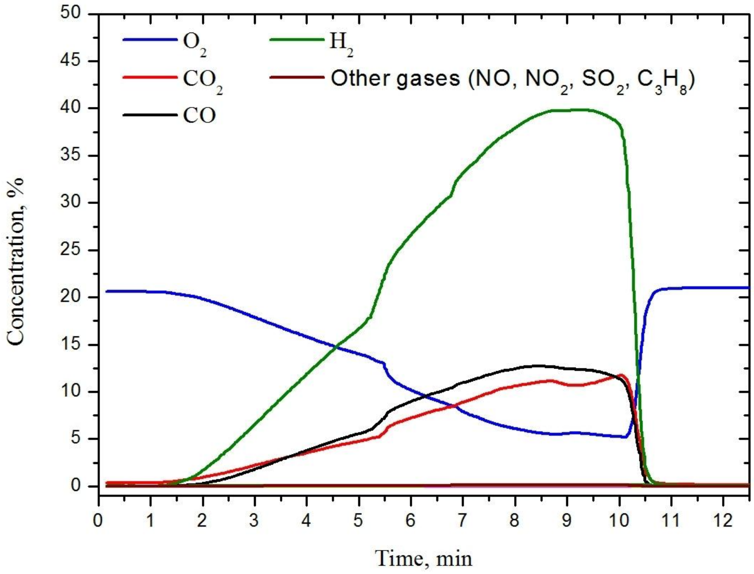

Fig. 4. Gas concentrations extracted during interaction between soil and water vapor plasma

Produced mixture of gases can be used for heating or energy generation. Also syngas is a feedstock for synthesis of industrial products such as ammonia, methanol, natural gas (SNG-methane (CH_4)), or liquid biofuels such as synthetic diesel (via Fischer-Tropsch synthesis) [17, 18].

4. CONCLUSIONS

Scanning electron microscope (SEM) data showed that contaminated soil interaction with water vapor plasma led to structural transformations of soil.

Measurements performed by energy dispersive X–ray spectroscopy (EDS) revealed that carbon content in the polluted soil was ~ 35 times higher above the average value (~0.5%) inherent in uncontaminated soil. However, measurements performed after soil interaction with water vapor plasma indicated that carbon concentration decreased from ~18% to ~1%.

Moreover, EDS showed that soil consisted of elements such as: C, O, Si, Al, Fe, P, S, K, Ca, Mg, Na. Though, content of minerals after the treatment changed slightly.

Furthermore, measurements taken with gas analyser indicated water vapor plasma ability to convert pollutants into useful product – syngas (H_2 + CO) and thus remediate contaminated soil. Hence, during plasma treatment process, volatile petroleum hydrocarbons were decomposed into C, H atoms and reacted with water vapor plasma (containing ·OH, ·O and ·H radicals) Thus, gaseous compounds (mainly syngas) were formed.

Acknowledgements. The authors are grateful to public agency "Soil Remediation Technologies" for cooperation during investigation. as well as, the authors are thankful to Dr. D. Milčius, the Head of Center for Hydrogen Energy Technologies, for the experimental facilities used to perform this work, dr. S. Tučkutė and PhD student M. Urbonavičius for the help to perform structural characterization of resultant materials.

Research was supported by Lithuanian Energy Institute and public agency "Soil Remediation Technologies".

REFERENCES

1. GUARINO, C., SPADA, V., SCIARRILLO, R. Assessment of three approaches of bioremediation (Natural Attenuation, Landfarming and Bioagumentation e Assistited Landfarming) for a petroleum hydrocarbons contaminated soil. *Chemosphere,* 2017, Vol. 170, p. 10-16.

2. BALDAN, E., BASAGLIA, M., FONTANA, F., SHAPLEIGH, JAMES P., CASELLA, S. Development, assessment and evaluation of a biopile for hydrocarbons soil remediation. *International Biodeterioration & Biodegradation,* 2015, Vol. 98, p. 66-72.
3. TIWARI, B., MANICKAM, N., KUMARI, S., TIWARI, A. Biodegradation and dissolution of polyaromatic hydrocarbons by Stenotrophomonas sp. *Bioresource Technology*, 2016, Vol. 216, p. 1102-1105.
4. SMITH, M.J, FLOWERS, T.H, DUNCAN, H.J, ALDER, J. Effects of polycyclic aromatic hydrocarbons on germination and subsequent growth of grasses and legumes in freshly contaminated soil and soil with aged PAHs residues. *Environmental Pollution*, 2006, Vol. 141, p. 519-525.
5. OKOH, A.I, Trejo-Hernandez, M.R. Remediation of petroleum hydrocarbon polluted systems: Exploiting the bioremediation strategies. *African Journal of Biotechnology,* 2006, Vol. 5, No. 25, p. 2520-2525.
6. BOULAKRADECHEA, Oualid M., AKRETCHEA, Eddine D., CAMESELLEB C., HAMIDIA N. Enhanced electrokinetic remediation of hydrophobic organics contaminated soils by the combination of non-ionic and ionic surfactants. *Electrochimica Acta,* 2015, Vol. 174, p. 1057-1066.
7. REDOLFI, M., MAKHLOUFI, C., OGNIER, S., CAVADIAS, S. Oxidation of kerosene components in a soil matrix by a dielectric barrier discharge reactor. *Process Safety and Environmental Protection,* 2010, Vol. 88, p. 207-212.
8. FERNANDEZ, M.D., PRO, J., ALONSO, C., ARAGONESE, P., TARAZONA, J.V. Terrestrial microcosms in a feasibility study on the remediation of diesel-contaminated soils. *Ecotoxicology and Environmental Safety*, 2011, Vol. 74, p. 2133-2140.
9. AGGELOPOULOS, C.A., SVARNAS, P., KLAPA, M.I., TSAKIROGLOU, C.D. Dielectric barrier discharge plasma used as a means for the remediation of soils contaminated by non-aqueous phase liquids. *Chemical Engineering Journal*, 2015, Vol. 270, p. 428-436.
10. WANG, T.C., QU, G., LI, J., LIANG, D. Evaluation of the potential of soil remediation by direct multi-channel pulsed corona discharge in soil. *Journal of Hazardous Materials,* 2014, Vol. 264, p. 169-175.
11. LI, R., LIU, Y., CHENG, W., ZHANG, W., XUE, G., OGNIER, S. Study on remediation of phenanthrene contaminated soil by pulsed dielectric barrier discharge plasma: The role of active species. *Chemical Engineering Journal,* 2016, Vol. 296, p. 132-140.
12. ZHANG, H., MA, D., QUI, R., TANG, Y., DU, C. Non-thermal plasma technology for organic contaminated soil remediation: A review. *Chemical Engineering Journal,* 2017, Vol. 313, p. 157-170.
13. TAMOŠIŪNAS, A., VALATKEVIČIUS, P., GRIGAITIENĖ, V., VALINČIUS, V. Water Vapor Plasma Torch: Design, Characteristics and Applications. *World Academy of Science, Engineering and Technology,* 2012, Vol. 6, p. 10-13.
14. CHENG, M., ZENG, G., HUANG, D., LAI C., Xu, P., ZHANG, C., LIU, Y. Hydroxyl radicals based advanced oxidation processes (AOPs) for remediation of soils contaminated with organic compounds: A review. *Chemical Engineering Journal*, 2016, Vol. 284, p. 582-598.
15. SNELLINGS, R., MERTENS, G., ELSEN, J. Supplementary Cementitious Materials. *Reviews in Mineralogy & Geochemistry*, 2012, Vol. 74, p. 211-278.
16. MOTUZAS, Algirdas J., BUIVYDAITĖ, Vanda V., VAISVALAVIČIUS, R., ŠLEINYS, Regimantas A. (2009) *Dirvotyra.* Vilnius: ENCIKLOPEDIJA, 2009. 336p. ISBN 978-9986-433-49-1.
17. PERES, Ana P.G., LUNELLIA, Betania H., FLLHO, Rubens M. Application of Biomass to Hydrogen and Syngas Production. *Chemical engineering transactions,* 2013, Vol. 32, p. 589-594.
18. *Linc Energy*. *Syngas in the Modern Energy Mix 04 UCG Series*. United States [referred on the 1st of March in 2017 y.] Link to the internet: <http://www.lincenergy.com/data/info_sheets/Syngas_in_the_Modern_Energy_Mix.pdf>.

TWO-STAGE TECHNOLOGY FOR TREATMENT OF WASTE WITH HIGH CONTENT OF ORGANIC

A. Liavonchyk, V. Sauchyn, H. Dalholenka, D. Skamarokhau, I. Khvedchyn, N. Sabirau
A. V. Luikov Heat and Mass Transfer Institute, National Academy of Sciences of Belarus
P. Brovka str. 15, 220072 Minsk – Belarus
E-mail: v.sauchyn@gmail.com, ita1661@gmail.com

ABSTRACT

Investigation of modified technology for thermal processing of organic waste is based on analysis of different methods described in literature and results of experimental research of thermal conversion and plasma pyrolysis carried out in A. V. Luikov Heat and Mass Transfer Institute.
The proposed technology consists of two stages: the first one is thermal conversion with temperature 400–500 °C. As a result, organic part of waste is decomposed and light hydrocarbons are produced; solid residues with high content of carbon has extended surface. So, material is preheated, mixed and volatile hydrocarbons are in gas phase. The second stage is high temperature (1000–1200 °C) processing of products from the first stage. Additional oxygen is supplied for carbon to carbon monoxide conversion. As a result, all hydrocarbons are converted to syngas that consists of hydrogen and carbon monoxide. This gas has high caloricity and can be used as fuel in power installation. Inorganic part is vitrified and suitable for long term storage.

Keywords: pyrolysis, plasma gasification, rubber treatment, wood treatment

1. INTRODUCTION

Today there is a huge problem of environmental pollution with wastes. A significant part of the wastes has predominant organic part. Incineration and pyrolysis are widely used for its processing. High temperature processing, namely plasma gasification, is an alternative method to produce syn-gas as a final product.

Among the key technical problems in the development of plasma gasification technologies, uniform mixing of the oxidant and the material being processed should be noted. To optimize the process, the idea of two-stage pyrolysis-plasma processing was proposed. Firstly, material enters the pyrolysis reactor, where it is divided into a vapor mixture and a carbon residue, which are then processed separately. This greatly simplifies the process control, gives an opportunity to work with materials of different fractions and to obtain useful co-products with little change in the technology.

Plasma waste gasification is studied by a number of companies and institutes all over the world. Some of them are working with a single plasma reactor, where the wastes are fully treated (Alter NRG). Others work in combined cycle of pyrolysis and plasma gasification (Europlasma, Plasco).

Alter NRG process is based on conbination of plasma torches and plasma cupola. Plasma torches are located at the bottom of the gasifier. A bed coke is created within the cupola using metallurgical coke (about 4% added to municipal solid wastes, MSW) to absorb and retain the heat energy from the plasma torches. Coke also supports MSW feed and provides stable regime and gas composition [1,2].

PLASGAS recator is used for plasma gasification research in Institute of Plasma Physics (IPP), Czech Republic. This inclined reactor is combined with hybrid water-argon plasma torch. Results of the researches carried out with the facility are described in [3, 4].

Europlasma process assumes use of a stoker grate auto-thermal gasifier for pyrolysis at a temperature of 850 °C. Then vapourized fraction is cleaned with a plasma torch at 1200 °C. Slag, metals and minerals are vitrified and melted into the inert material which can be then reused in the construction [2, 5].

Plasco process includes MSW conversion into crude syngas with the recycled heat in the conversion chamber, then the obtained syngas is cleaned and cracked with the plasma torches. Plasma heat is also used to vitrify the solid and to convert any remaining compounds and fixed carbon into crude syngas, which is sent back to the conversion chamber [2, 6].

Plasma technologies are also used for hazardous wastes treatment. Some technologies provide utilization with commercial product obtaining, other ones are used for complete destruction. The most valuable are described in [7]. Economic justification for plasma MSW treatment is given in [8].

In our work we studied process of two-stage gasification of two model materials: wood saw and rubber chips. The main difference between them is oxygen containing. Both of the materials are non-toxic and available and their ecologically safe treatment is a real challenge.

2. METHODOLOGY

Taking into account the experience gained by carrying out a one-step organic material gasification of directly exposed to the plasma torch [3, 4, 9, 10], a two-stage processing technology was proposed. It was supposed that such a technique will optimize the recycling process, increase the amount of recyclable fractions and will enable a more balanced approach to the issue of the selection of the final product.

Basic concepts, models, balances and computations for rubber pyrolysis in screw reactor are described in [11]. Reactor STR-10 was used as a screw reactor for low temperature (450–600 °C) pyrolysis. The process is described in details in [12]. The second step is the high temperature product conversion in a plasma reactor. A significant advantage of this method is the ability to recycle the material of a much larger particle size than with the direct one-stage gasification.

According to the scheme (Fig. 1) the material is loaded into the dozer (1) and then fed into the screw reactor (2). The material is heated in the reactor by controlled electrical heaters. Due to the temperature material decomposes and releases organic vapors. Degradation process results in separation of the reaction mixture. Loosened solid fraction is periodically discharged into the solid residue bunker (3). The vaporized fraction is fed into a plasma reactor CM-2 (4) for further conversion into the syn-gas.

Reactor CM2 [10] is connected to the outlet pipe to perform high-temperature stage. CM2 is a cylindrical reactor with internal volume of about 20 liters. Inside there is a crucible made of refractory steel. The gas temperature in the interior volume of the crucible is about 2000 K (on the axis). During reaction the gas goes up along the walls of the crucible and exhausts between the lid and the crucible, then goes down through the gap between the wall and the outer wall of the crucible, and finally are discharged through the exhaust tube.

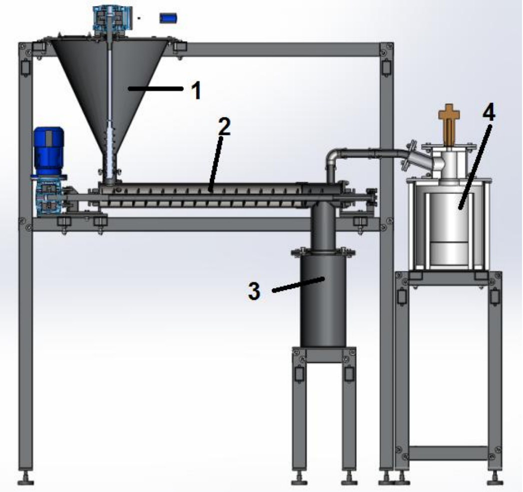

Fig. 1. Scheme of the facility: 1 – dozer; 2 – screw pyrolysis reactor STR-10; 3 – solid residue bunker; 4 – plasma reactor CM-2

Plasma torch “Pluton” is used as a source of plasma. Power range is 12–30 kW, rate of plasma gas (air) is 0.8–4 g/s.

Generally process can be described as follows. Low-temperature pyrolysis results in material decomposition into the vaporized fraction and a solid residue. The vaporized fraction at this stage is supplied in the plasma reactor and the solid residue is collected in the bunker. Each of these two products may be further gasified.

Thermodynamic calculations were carried out in CHEMCAD 6.3. The model was based on the basis of Gibbs energy minimum.

Gas analyses were performed on the gas chromatograph Agilent 7890A GC. Several (2–4) samples of exhaust gas were taken during the experiment and the average concentrations were calculated. The samples were cleaned from water and soot by filters and cooler.

3. RESULTS AND DISCUSSION

For the treatment process study two materials were selected as model ones: wood saw and rubber chips. Only vaporized fraction is subjected to the high temperature processing. The results of thermodynamic calculations and experiments for wood saw in comparison with published data [3, 13, 14] are shown in Table 1. Lower heating value (LHV) of gas is estimated on the basis of concentrations of combustible gases.

Table 1. Results of calculations and experiments for wood gasification in comparison with published data

	Wood saw		**[3]**	**[13]**	**[14]**
	Calculated, % vol.	**Experiment, % vol.**	**Experiment, % vol.**	**Experiment, % vol.**	**Experiment, % vol.**
H_2	36.5	29.8	44.8	29.4	18.8
CH_4	0	0	0.9	0	3
CO_2	3.7	5.8	15	7.9	10.3
CO	36	34.2	39.2	25.8	29
N_2	23.8	30	0	36.1	38.9
Others	0	0.2	0.1	0.8	0
Total	100	100	100	100	100
LHV, MJ/m^3	8.5	7.5	10.1	6.4	6.8

Results of wood saw pyrolysis in STR-10 are described in [15]. Based on the results of CHNS analysis of the solid residue approximate elemental ratio for the evaporation phase was determined as C:H:O = 21:56:12.

In the experiments, the material and the plasma gas flow rate was selected to get the excess of oxygen of 1–1,05. Moreover, the air flow through the plasma torch was 2.88 kg/h, flow rate of nitrogen in the screw reactor 0,61 kg/h, material feed rate 3.2 kg/h, the residence time of the material in screw reactor – 15 minutes, the reactor temperature 500 °C.

Experiment results of wood processing correlate with the calculation. It should be noted that a small amount of soot is formed. Apparently, it is the carbon dust carried from the screw reactor and carbon produced in the plasma unit.

Experiments with rubber chips of 5 mm size were carried out. On the basis of results published in [12] approximate elemental ratio for vapourized phase was determined as C:H = 4:5. Sulphur was not taken into account. Rubber does not contain oxygen in its structure as opposed to wood. The results showed that feeding the vaporized fraction of rubber in plasma mixing unit leads to active non-uniform hydrocarbons combustion with a large amount of soot forming. The reason for this is the poor mixing of the material and an oxidizing agent. The result is a large amount of the ballast nitrogen from the plasma gas and carbon black. On the basis of experiments it was proposed to supply water or steam in the screw reactor.

Water feed rate was chosen from 0 to 2.5 kg per 1 kg of vapourized fraction of material. During the experiments material feed rate was 1.5–2.6 kg/h, average mass fraction of vapourized was 62%. Water was added in a hot zone at the beginning of the screw reactor, thus steam and vapourized fraction of the material were mixed uniformly while it was going along the facility. Results presented in this work were selected for the regimes when ratio of oxygen from water and air from the plasma torch to carbon from the vapourized fraction is 1.0–1.2. Regimes with the lack of oxygen are not presented. Conversion of vaporized fraction is estimated in the range of 45–88% depending on the regime.

Experiments showed that addition of steam to the screw reactor provides positive effect on the process. In particular, the amount of soot decreases, the transition duct between the reactors clogs less, indicating more complete evaporation and coking decrease.

Clearly, there is a discrepancy between the experimental and calculated data. It can be explained by the fact that material feeding into the plasma reactor is mixed and heated non-uniformly with air from the plasma torch and hence no equilibrium is established. This leads to the formation of soot and larger amount of water than estimated. Regimes when oxygen for carbon conversion is feeded only in water and the plasma forming gas is nitrogen demonstrates more complete material conversion. In Fig. 2 volume concentrations of H_2, CO and CH_4 and LHV (MJ/m^3) are presented in dependence of water specific feed rate per 1 kg of vapourized fraction of material and specific power per kilo of total mass of gas mixture, including water, transport gas and plasma forming gas. Unfortunately, there is no available data concerning tire plasma gasification, but we can compare it with data for polyethilene (PE) and plastics gasification from [3] as in all these cases there are hydrocarbons without oxygen (Table 2).

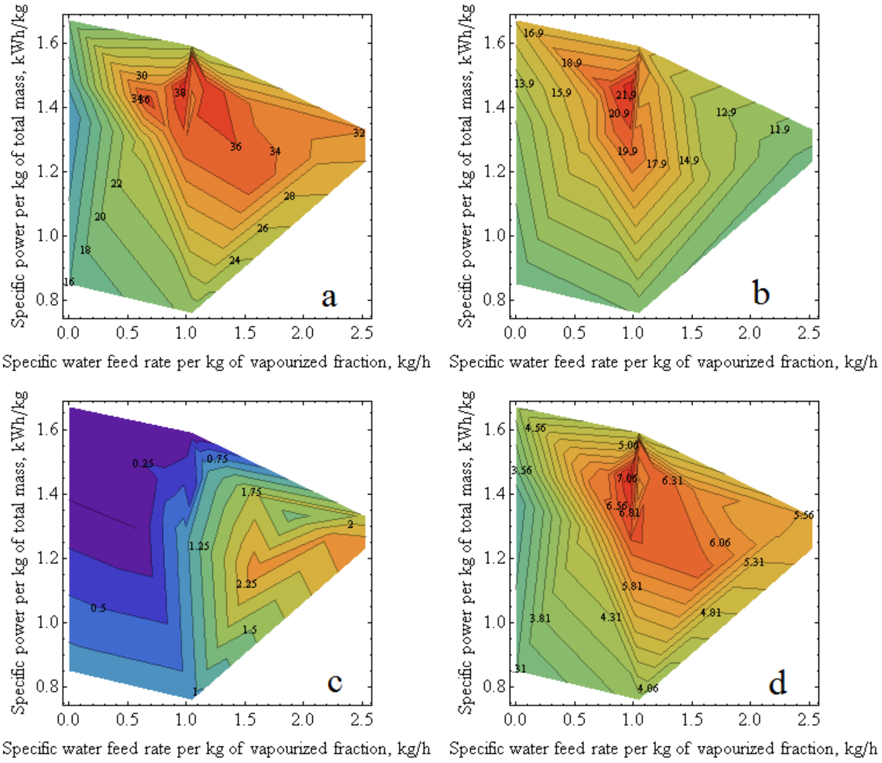

Fig. 2. Concentrations of H_2 (a), CO (b), CH_4 (c) and LHV (d) of produced syngas

Table 2. Results of calculations and experiments for rubber chips gasification in comparison with published data

	Rubber without steam		**Rubber with steam**		**PE1 [3]**	**PE2 [3]**	**Plastics [3]**
	Calc., % vol.	**Exp., % vol.**	**Calc., % vol.**	**Exp., % vol.**	**Exp., % vol.**	**Exp., % vol.**	**Exp., % vol.**
H_2	17.4	17.2	46.4	37.9	29.9	35.3	41.6
CH_4	0	0.2	0	0.5	0	0.1	0
CO_2	0.6	5	3	4.1	27.1	21.7	7.4
CO	23.5	16.4	21.4	21.3	41.3	41.5	49.7
N_2	56.4	59.1	29.1	34.5	0	0	0
Others	2.1	2.1	0.1	1.7	1.7	1.4	1.3
Total	100	100	100	100	100	100	100
LHV, MJ/m^3	4.8	4.0	7.7	7.0	8.4	9.1	10.8

On the basis of the results it is possible to select the optimal orerating regime for nesessary gas composition. In our facility we use air or nitrogen as a plasma forming gas, but it is supposed that use of water steam or CO_2 would provide less amount of ballast nitrogen and increase LHV. In comparison with data from [3], where steam plasma torch was used, CO_2 and O_2 were added into the reactor, LHV was lower, but difference in the gas media during the process must be noted.

4. CONCLUSIONS

Thermodynamic calculations for the vaporized phase of wood saw and rubber chips with and without steam were carried out. Comparison of the calculations with experimental data showed good agreement for the wood and greater divergence for rubber. It should be noted that in the case of rubber the problem of mixing the material and oxidizing agent was not fully solved.

However, now it can be said that this method is quite attractive for recycling, since it provides the complete destruction of the complex molecules that facilitates purification of the resulting product, reduces emissions as compared with conventional combustion, and can be used for a wide range of materials. Optimal parameters for the process can be found on the basis of experimental results. In comparion with the single-stage gasification the method has more flexibility in management, is less dependent on the particle size of the material, controlled more accurately. Comparison with published data for wood saw showed good LHV for the syngas. It is difficult to compare results for rubber chips with plastics and PE because of different gases used for the process and different materials. But in general it is supposed that use of steam and CO_2 instead of air and nitrogen can give us similar results despite of completely different technologies.

Experimental studies of the two-stage gasification of organic materials have shown the effectiveness of this method in comparison with the one-step plasma gasification, especially for non-dispersive materials.

REFERENCES

1. *Typical plasma facility*. Alter NRG [referred on the 12th of January in 2017 y.]. Link to the internet <http://www.alternrg.com/waste_to_energy/typical_plasma_facility/>
2. DUCHARME, C. *Technical and economic analysis of Plasma-assisted Waste-to-Energy processes. M.S. Degree in Earth Resources Engineering Theses.* Columbia University, 2010. 79 p.
3. SHAUKAT, S. *Progress in Biomass and Bioenergy Production.* InTech, 2011. 456 p. ISBN 978-953-307-491-7.

4. HRABOVSKY, M., KONRAD, M., KOPECKY, V., HLINA, M., KAVKA, T., CHUMAK, O., VAN OOST, G., BEECKMAN, E., DEFOORT, B. Pyrolysis of wood in arc plasma for syngas production. *High Temperature Material Processes*, 2006, Vol. 10, No. 4, p. 557-570.
5. *Europlasma Torch & Processes*. Europlasma Group [referred on the 12th of January in 2017 y.]. Link to the internet <http://www.europlasma.com/en/torch-a-process.html>
6. *The Plasco Process*. Plasco Energy Group [referred on the 12th of January in 2017 y.]. Link to the internet <http://plascotechnologies.com/our-technology/patented-technology/>
7. HEBERLEIN, J., MURPHY, A., Thermal plasma waste treatment. *Journal of Physics D: Applied Physics*, 2008, No. 41, p. 1-20.
8. YOUNG, G. *Municipal Solid Waste to Energy Conversion Processes. Economic, technical and renewable comparisons*. Hoboken, New Jersey: John Wiley & Sons, 2010. 384 p. ISBN 978-0-470-53967-5.
9. LIAVONCHYK, A., SAUCHYN, V., DALGOLENKA, H. Wood gasification in electric arc plasma reactor in air and nitrogen media (in Russian). *Proceedings of the National Academy of Sciences of Belarus. Series of Physical-Technical Sciences*, 2014, No 2, p. 79-82.
10. LIAVONCHYK, A. SAUCHYN, V., KHVEDCHYN, I. Wooden waste processing with thermal plasma. ISPC-22. Proceedings of 22 International symposium on plasma chemistry. Belgium, Antwerp. 2015 July 5-10.
11. DONAHUE, W., BRANDT, J. *Pyrolysis: Types, Processes, Industrial Sources and Products.* New York: Nova Science Publishers, 2009. 563 p. ISBN: 978-1-60741-669-2.
12. LOZHECHNIK, A., SAUCHYN, V. Pyrolysis of rubber in a screw reactor. *Journal of Engineering Physics and Thermophysics*, 2016, Vol. 89, Issue 6, p. 1482-1486.
13. BRATCEV, A., KUZNETSOV, V., POPOV, V., UFIMTSEV, A. Plasma gasification of biomass by example of wooden wastes (in Russian). *High temperature (Teplofizika Vysokikh Temperatur)*, 2011, Vol. 49, No. 2, p. 251-255.
14. ZHELEZNAYA, T., GELETUHA, G. Review of modern technologies of biomass gasification (in Russian). *Industrial heat engineering*, 2006, Vol. 28, No. 2, p. 61-75
15. LIAVONCHYK, A., KHVEDCHYN, I. SAUCHYN, V., DALGOLENKA, H., LOZHACHNIK, A. Wooden saw pyrolysis in screw reactor. EUBCE-2016. Proceedings of 24th European Biomass Conference and Exhibition. Amsterdam. 2016 June 6-9.

THE EFFECT OF HEAT TREATMENT ON THE STRUCTURE OF ALUMINA COATINGS

Airingas Šuopys, Liutauras Marcinauskas
Department of Physics, Kaunas University of Technology
Studentų str. 50, LT-51368 Kaunas – Lithuania
E-mail: airingas.suopys@ktu.edu

Liutauras Marcinauskas, Mindaugas Milieška, Romualdas Kėželis, Mindaugas Aikas
Lithuanian Energy Institute, Plasma Processing Laboratory
Breslaujos str. 3, LT-44403 Kaunas – Lithuania
E-mail: liutauras@mail.lei.lt

Jose Rodriguez
PSA – Plataforma Solar de Almeria, CIEMAT – Centro de Investigiones Energéticas,
Medioambientales y Tecnológicas,
Apartado 22, E-04200 Tabernas, Almería, Spain

ABSTRACT

The alumina coatings were fabricated on the stainless-steel substrates by atmospheric plasma spraying. The coatings were deposited using air and hydrogen gasses at an identical spray parameters. The coatings were later heated up to 850 ^{o}C and cooled to a 450 ^{o}C temperature. 3 sets of samples were examined which were heat treated for 1, 10 and 20 cycles. The change of surface morphology and structure of different number heat treated samples were investigated using scanning electron microscopy. The variation of elemental composition in the coatings was determined by energy-dispersive X-ray spectroscopy. The phase composition changes in a non-treated and treated samples were defined using X-ray diffraction. The X-ray diffraction measurements demonstrated that the as-sprayed coatings are composed of α-Al_2O_3, γ- Al_2O_3, and β- Al_2O_3 phases. The increase of the heat treatment cycles from 1 to 20 slightly affect the elemental composition and phase composition of the coatings.

Keywords: Alumina, plasma spraying, heat treatment, morphology, phase composition

1. INTRODUCTION

Ceramic coatings (Al_2O_3, ZrO_2, TiO_2) are widely-used in many fields, from military and medicine to aerospace industry. Coated materials exhibit superior mechanical, chemical and physical properties [1]. One of the reason why coatings are extremely popular today, is that a thin layer of material applied on a base substrate can significantly improve features of a certain item without changing the internal structure. These ceramic coatings can also be used as thermal barriers because of their high heat resistance, also to reduce the corrosion for various components [2, 3]. One of the most widely used ceramic coating today is alumina because of its low cost, inherent attrition and corrosive resistance, excellent dielectric and thermal shock resistance. These properties allowed the construction of special surface protection of metallic components operating under severe running conditions [4, 5]. Alumina coatings can be produced by a variety of techniques, such as chemical vapor deposition, physical vapor deposition, electrodeposition [6], thermal spray, etc.

Atmospheric plasma spray is an industrially well-accepted thermal spray technique and one of the most popular method to form alumina and its composite coatings [7]. Alumina coatings consists mainly of two phases: α-Al_2O_3 and γ-Al_2O_3. These phases differ in various properties like hardness, porosity, thermal and electrical conductivity and crystal lattice. The phase composition of alumina coating is possible to control by changing the critical plasma spraying parameter (CPSP) [8].

Authors demonstrated that increase of CPSP values increases the quantity of γ-Al_2O_3 in the coating. This parameter could be increased by increasing voltage and current, or decreasing carrier gas flow rate. Also, one of the easier ways to increase the content of gamma phase is to lower the spray distance [9]. The melted particles are not able to cool down much with lower distance between plasmatron exit and the sample, since a higher temperature is needed to form gamma phase. As well as it is possible to change phase composition of the coating by using different feedstock powders [10]. The smaller are the powder particles, the less power is needed to fully melt them, that's way gamma phase can form more easily. It is also possible to use agglomerated nanoparticles as feedstock powder, this can change not only phase composition but also structure of the coating from lamellar of partially-melted structure to three-dimensional network structure of partially-melted and fully-melted regions. This variation of structure and composition directly affects porosity, hardness, roughness, wear rate resistance of the coating. Also, it should be mentioned that the powder preparation technique and nature have a strong influence on the phase composition of the coating [11].

The structure of coatings can be modified not only during the deposition process, but also after coating is formed, using a heat treatment [12]. The temperature, process duration and surrounding atmosphere are the most important factors. It is extremely important to apply sufficient temperature in order achieve desired phase composition and consequently mechanical properties (as well as select suitable atmosphere) because of ongoing chemical reactions during the heat treatment process. These reactions could potentially reduce or improve the quality of the coatings.

The aim of the present research is to determine the influence of heat treatment on the structure, phase and elemental composition of alumina coatings, as well as investigate the impact of the number of heat treatment cycles applied to the samples.

2. METHODOLOGY

The coatings were sprayed on stainless steel substrates at atmospheric pressure using a direct current plasma torch. The plasma torch used in this experiment was developed at the Lithuanian Energy Institute [17]. The steel substrates (dimensions of 50 × 10 × 2 mm) were polished and chemically cleaned before starting the deposition process. The substrates were placed on the water-cooled sample holder. Air was used as both the primary gas (total flow rate of 5.62 g/s) and the powder carrier gas (flow rate of 0.6 g/s). The hydrogen (0.1055 g/s) was used as secondary gas to increase the plasma temperature. The composition of Al_2O_3 powders were: Al_2O_3 – 98.50 at, %, P_2O_5 – 0.50 at. %, Na_2O – 0.41 at.%, Si_2O – 0.33 at.%, CaO – 0.15 at.%, Fe_2O_3 – 0.1 at.%, and others. The powders were of a non-regular shape with various sizes from 64 μm to 140 μm. The specific surface area of the powders was 0.06 m^2/g. The feedstock powders were grinded and sieved using a 140 μm size grid and were dried for 12h at ~330 K before starting the deposition process. The size of the particles was selected no more than 140 μm, so that the particles could fully melt during the spraying process. The deposition duration was 30 s. The plasma torch was moving in the x-axis direction forward and back during the deposition, in order to avoid overheating the sample and ensure simmilar structure of the coating for all of the samples. The spraying distance was kept at 70 mm. The coatings were deposited at a torch power of 41.8 kW. Average plasma temperature in the injection place of the powders was 3344 ±50 K. Meanwhile, the mean plasma temperature and velocity at nozzle outlet was 3300 ±50 K and 1400 ±25 m/s. The mean temperature of the plasma jet at the exhaust of the plasma torch was calculated from the heat balance corresponding to plasma enthalpy. Detailed description of the methodology of the plasma temperature and velocity calculation is given in Ref. [17], [18].

The surface morphology of the Al_2O_3 coatings was characterized by scanning electron microscopy (SEM) using a model Hitachi S-3400N. The elemental composition of coatings was analysed by energy dispersive X-ray spectroscopy (EDS). The measurements were performed from 1.05 mm^2 surface area at 3 different points. The surface roughness was investigated by a portable profilometer "Mitutoyo Surftest SJ-210", measuring each sample 5 times on different locations in a lengh of 4 mm, and the mean values were presented. The coatings structure was analysed by X-ray diffraction (XRD) (DRON-UM1 with standard Bragg–Brentano focusing geometry) in a 5–70° range using the CuK$_\alpha$ (λ = 0.154059 nm) radiation. To create the thermal shock on the samples, high concentration solar furnace SF40 was used. Briefly, it is a 40 kW power furnace reaching a peak concentration exceeding 7000 kW/m^2 (7000 suns) in a focus of 12 cm in diameter [13]. It basically consists of a 100 m^2 reflecting surface flat heliostat, a parabolic concentrator with a projecting area of 56.5 m^2, slats shutter or attenuator, and test table with three axis movement. The working principle is as follows: the heliostat tracks the sun and reflects the collimated sun rays horizontal and parallel – without concentration – to the optical axis of the parabolic concentrator, which in turn reflects and concentrates the sunlight on a focal area where the test setup is installed. The solar flux can be controlled by adjusting the opening of the shutter and hence controls the temperature in the test table [14–15]. The sample was placed on the test table. The thermocouple (K-type) was connected to the sample from the bottom of the substrate. The heating of the sample was carried out up to 800 °C. When the maximum heating temperature was reached, the heating was stopped for 1 min and reinitiated again. The sample sides were shielded with high-temperature resistant material in order to achieve only direct heating on the coating and to keep the measurements of thermocouple accurate.

3. RESULTS AND DISCUSSION

Four different samples were used for this experiment: sample one (No. 1) indicate a non-treated coating, the second sample (No. 2) was heat treated once, for sample No. 3, 10 heat cycles were applied and for the 4th sample the number of heat cycles was increased up to 20.

Fig. 1 shows the temperature variation for each sample during the heat treatment process. As it is seen from the Fig. 1, the 2nd sample was heated only once, up to 800 ^{o}C and cooled down in the same atmosphere. For the 3rd sample 10 heat cycles were applied. It can be seen, that there are slight variations in temperatures for each cycle, but these variations are quite low and does not influence on the treatment procedure of the samples. Sample No. 4 had 20 heat treatment cycles, which can be seen from the graph, also the variation of temperatures during these cycles is a bit higher compared to sample No. 3.

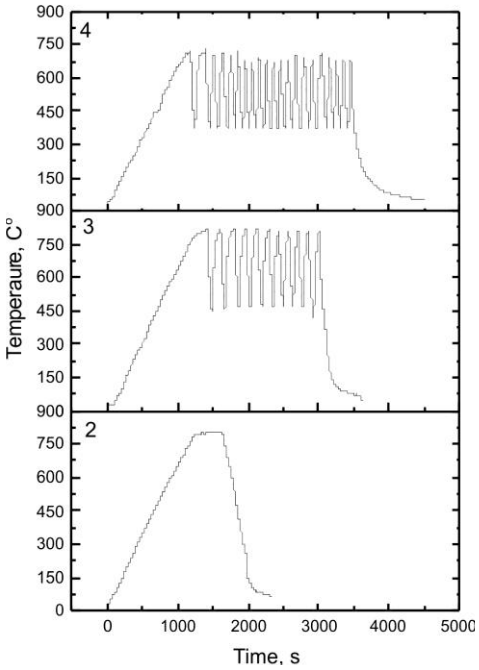

Fig. 1. Variation of the surface temperature during the heat treatment

Table 1. Elemental composition of the coatings

Sample no **Element**	**No. 1**		**No. 2**		**No. 3**		**No. 4**	
	wt, %	**at, %**	**wt, %**	**at, %**	**wt, %**	**at, %**	**wt, %**	**at, %**
Aluminium	42.2	33.2	43.2	34.1	42.8	34.4	39.8	31.5
Oxygen	47.6	62.9	45.0	61.1	44.7	60.6	47.8	63.6
Chromium	2.1	0.9	3.5	1.5	3.2	1.3	2.9	1.2
Iron	8.0	3.0	8.0	3.1	9.1	3.6	8.9	3.4
Phosphorus	0.1	0.1	0.3	0.2	0.2	0.2	0.5	0.4

The Table 1 shows the percentage values by weight (wt) and the number of atoms (at) of main elements found in the coatings. These values were determined by examining every sample 3 times with x-ray energy dispersion spectroscopy (EDS) and the mean values are shown in the Table 1. It is observed, that non-treated coating has a quite high amount of aluminium, 42.2% by weight and 33.2% by the number of atoms. By using heat treatment once we increase the amount of Al to 43.2 wt % and 31.5 at %, but strangely enough with continuous increase of the heat cycles applied to 20, the amount of aluminium decreases to 39.9 wt % and 31.5 at %. We can state that, during the heat treatment some part of aluminium is lost to the surroundings of the sample. In the case for oxygen in our coating, we observed rather different tendencies, in the untreated sample we detected a rather high amount of oxygen 47.6 wt % and 62.9 at%. The heat treatment decreases quantity of oxygen to 45.0 wt % and 61.1 at %. The increase of the number of treatment cycles slightly reduces the amount of oxygen in the coatings. However, the content of oxygen in the coating slightly increases up to 63.6 at %, when the 20 treatment cycles were used. It should be mentioned that the oxygen concentration becomes even higher than in the non-treated coating. So, it indicates that with enough heat cycles applied to an alumina coating the oxygen concentration could be increased. The increase of the oxygen is due to the chemical reactions (between the coating and atmosphere air) during the treatment process. The small amount of other elements in the coatings such as chromium, iron and phosphorus were observed (Table 1).

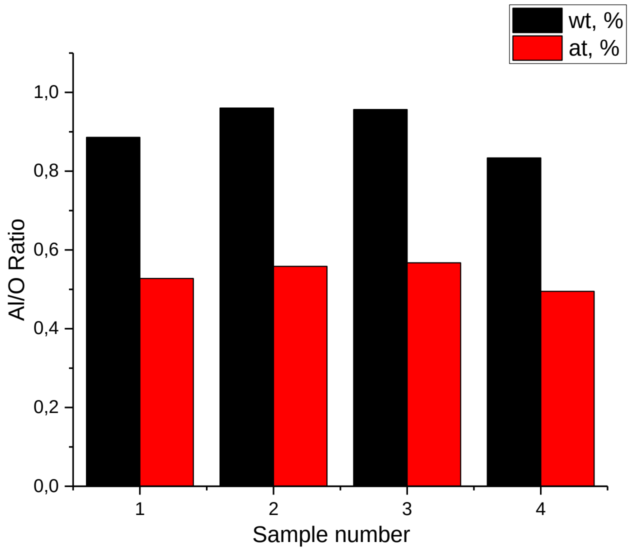

Fig. 2. The variation of Al/O ratio in the non-treated and heat treated coatings

The ratio of aluminium and oxygen in different samples are shown in the Fig. 2. It was observed that the increase of treatment cycles up to 10, increases the amount of aluminium and decreases the oxygen fraction in the coating. It leads to the increases (from 0.87 to 0.96) of Al/O ratio. However, after 20 cycles applied to the coating we observed an increase of oxygen and decrease of the Al in the sample, and the Al/O ratio significantly decreased. This could happen due to the oxidation reactions during the heat treatment. These reactions could happen not only with aluminium, but also with other elements found in the coating and new forms of oxides (FeO, CrO and many others) could be created.

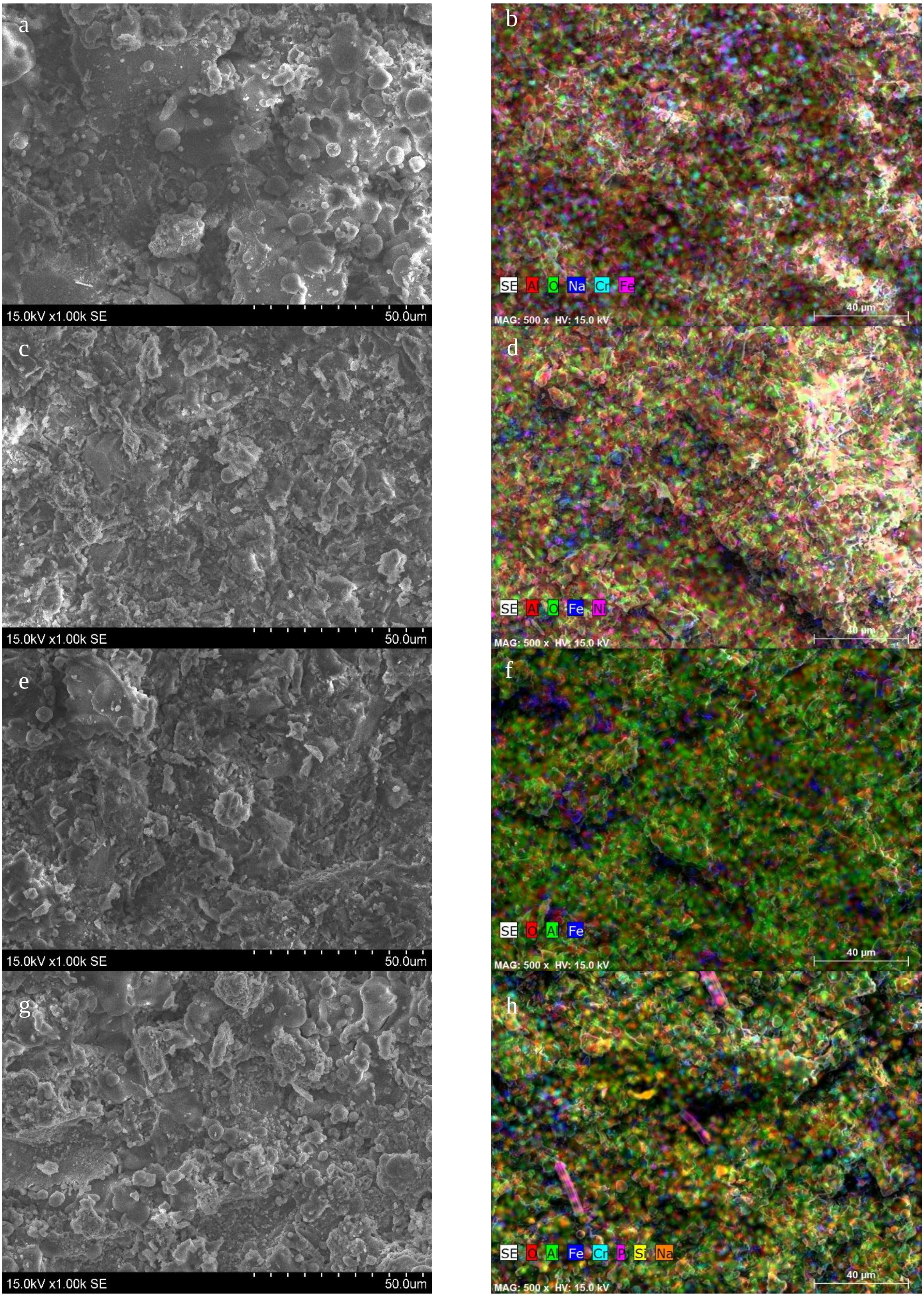

Fig. 3. The surface morphology of the plasma sprayed coatings (a, b) No. 1; (c, d) No. 2; (e, f) No. 3; (g, h) No. 4

The surface morphology of the coatings made by scanning electron microscope (left), and elements distribution on the surface of the coatings (mapping (right)) are given in Fig. 3. From the picture of formed coating at 1000 times magnification, we notice some unmelt particles and some rather larger ones. It is also easy to observe the lamellar structure of the coating. This structure is inhered for the plasma spray coating forming technique, because the melted particles are sprayed on a substrate at high speed and flattens on the surface and starts to cool down, thus creating this structure. After heat treatment we can see that there are a lot less unmelt particles, also the particles are quite smaller, what makes the surface of the coating smoother. This happens because during the heat treatment particles are partly melted once again, forming a smaller structure, with the increase of heat cycles the surface becomes smoother, because the particles are more and more melted. From the elemental mapping of coating we can state that aluminium and oxygen are evenly spread across the samples, and that the mechanical and chemical properties of the coating are about the same around the whole area of the samples. Also, there are some small amounts of phosphorus, iron or chromium, that comes from the feedstock powder, but these elements are more concentrated in a local surface areas.

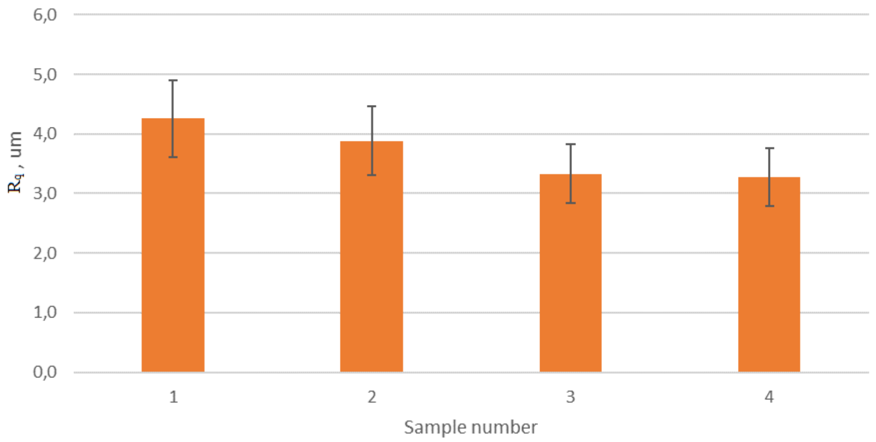

Fig. 4. Surface roughness of the coatings

The surface roughness measurements reveals, that heating of the sample decreases its roughness (Fig. 4). The untreated sample exibited the highest roughness 4.3 µm, but after one heat cycles the mean square roughness (R_q) decresed to 3.9 µm. Furthermore, continous increase of the heat cycles to 20 applied proceeded to decrease the surface roughness to 3.3 µm. It was calculated, that the mean square roughness of the samples decreases by 23%, with 20 heat cycles applied, compared with the untreaded sample.

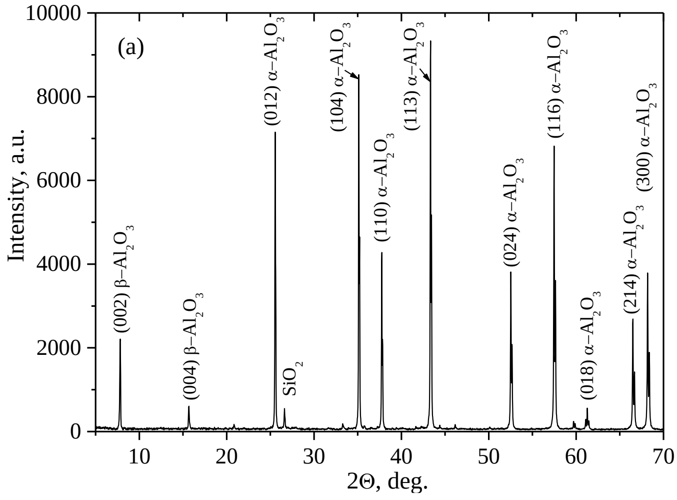

Fig. 5. The XRD pattern of the Al_2O_3 powders

Fig. 5 contains XRD spectra of alumina powders used in this experiment. Some of the same peaks can be observed as in alumina coatings, but their intensities are considerably lower, since the powder consists of mainly α-Al_2O_3.

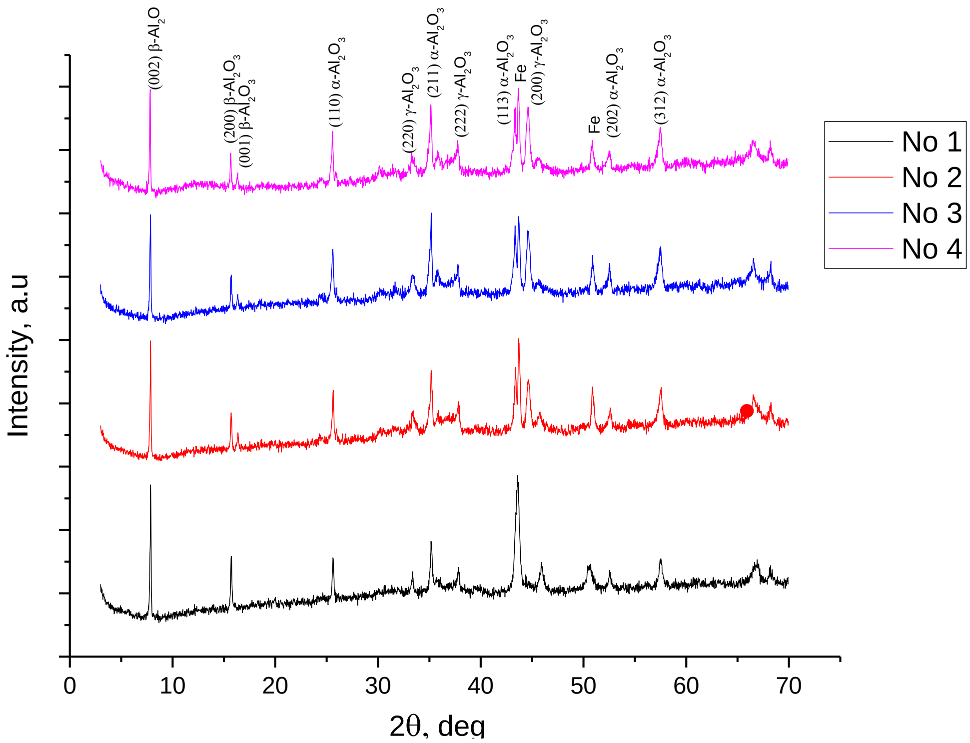

Fig. 6. The XRD patterns of the non-treated and heat treated coatings

As we can see from the Fig. 6, the nature of XRD spectra of the films remained similar, allthough the coatings consisted not only from alpha, but also gamma alumina, the main reason for this is, that during the formation of the coatings, the feedstock powder is heated to high temperatures, and fully melted alpha phase particles transforms into gamma phase. However, the characteristic peaks intensities vary with the increase of the heat treatment cycles. The high intensity peak at 2teta = 7.8°, is attributed to sodium aluminium oxide (card No. 32-1033) with the β-alumina (002), orientation, that comes from the feedstock powder. The peak at 2teta = 15.5° is attributed to (200) β-Al_2O_3 phase. The intensity of this peak is reduced with the increase of the treatment cycles (Fig. 2). A new peak at 2teta = 16.25° indicating the existence of (001) β-Al_2O_3 appeared after treatment. It should be noted that the intensity remained almost the same for the different number of treatment cycles. Peak at 2teta = 25.59° indicate an existence of (110) α-Al_2O_3 phase in the coatings [8, 11]. The intensity of the peak slightly increases with the increase of the number of cycles. The slight increase was observed for the (211), (202) and (312) α-Al_2O_3 phase peaks [12]. The variation of the peaks intensities is insignificant and it indicates that the amount of α phase and type of orientation of alumina crystals are independent on the number of heat cycles applied to the samples. The (113) α-Al_2O_3 peaks intensity was the highest in the non-treated sample, but after heat treatment, the intensity was reduced almost twice. A new peak at 2teta = 44.6° attributed to (200) γ-Al_2O_3 was observed after treatment [18]. As we can see from the Fig. 2, increasing the number of heat cycles increases the intensity of this peak. Such result indicates that with each cycle applied to the coatings, more crystaline gamma phase is formed. The low intensity peaks at 2teta = 33.2° and 2teta = 37.8° related to the (220) and (222) γ-Al_2O_3 peaks [9]. The slight increase of gamma phase peaks intensity was observed with the increase of the number of cycles. All coatings have a peak at 2teta = 43.6° Attributed to substrate. This peak is overlapping with the (113) α-Al_2O_3 peak for the non-treated coating (fig.6). However, even after one cycle of treatment those peaks were separated.

4. CONCLUSION

The Al_2O_3 coatings were deposited and the influence of the heat cycles number on the elemental composition and structure was investigated. SEM and EDS maps photographs reveals, that the increase of heat cycles reduces the surface roughness, and changes the elemental composition, although elemental distribution is not affected by it at all. In all samples aluminium and oxygen were widely spread across the film area, with small concentrations of other elements. The heat treatment initiates the change of aluminium and oxygen ratio in the coatings. The increase of heat cycles increases aluminium and oxygen ratio however this increase was observed only up to 10 cycles, the further increase of cycles numbers decreases Al/O ratio. The initial Al_2O_3 powders mainly consisted from α-Al_2O_3 phase, but sprayed and heat treated coatings contained three phases of alumina: alpha, beta and gamma. The phase composition of the sprayed coatings can be manipulated by using heat treatment. The XRD spectra showed, that the increase in the number of heat cycles increases the amount of γ-Al_2O_3 phase and consequently decreases α-Al_2O_3 phase.

REFERENCES

1. B. ZHANG, L. WEI, L. GAO, H. GUO, H. XU, Microstructural characterization of PS-PVD ceramic thermal barrier coatings with quasi-columnar structures, *Surface and Coatings Technology*, Vol. 311, 2017, P. 199-205.
2. D. ZHANG, Z. ZHAO, B. WANG, S. LI, Investigation of a new type of composite ceramics for thermal barrier coatings, *Materials & Design*, Vol. 112, 2016, P. 27-33.
3. S. DEHGAHI, R. AMINI, M. ALIZADEH, Microstructure and corrosion resistance of Ni-Al_2O_3-SiC nanocomposite coatings produced by electrodeposition technique, *Journal of Alloys and Compounds,* Vol. 692, 2017, P. 622-628.
4. L. PAWŁOWSKI, The relationship between structure and dielectric properties in plasma-sprayed alumina coatings, *Surface and Coatings Technology*, Vol. 35, 1988, P. 285-298
5. C. LI, G. YANG, Relationship between particle erosion and lamellar microstructure for plasma-sprayed alumina coatings, *Wear,* Vol. 260, 2006, P. 1166-1172.
6. S.W. JIANG, L. YANG, J.N. PANG, H. LIN, Z.Q. WANG, Electrodeposition of Ni-Al2O3 composite coatings with combined addition of SDS and HPB surfactants, *Surface and Coatings Technology*, Vol. 286, 2016, P. 197-205.
7. S. GOEL, S. BJÖRKLUND, N. CURRY, U. WIKLUND, SV. JOSHI, Axial suspension plasma spraying of Al_2O_3 coatings for superior tribological properties, *Surface and Coatings Technology,* Available online 2017.
8. S. YUGESWARAN, V. SELVARAJAN, K.P. SREEKUMAR, Influence of critical plasma spraying parameter (CPSP) on plasma sprayed Alumina–Titania composite coatings, *Ceramics International*, Vol. 36, 2010, P. 141-149.
9. E.P. SONG, J. AHN, S. LEE, N.J. KIM, Effects of critical plasma spray parameter and spray distance on wear resistance of Al_2O_3–8 wt.%TiO_2 coatings plasma-sprayed with nanopowders, *Surface and Coatings Technology*, Vol. 202, P. 3625-3632.
10. Y. YANG, Y. WANG, W. TIAN, J. ZHANG, Influence of composite powders' microstructure on the microstructure and properties of Al_2O_3–TiO_2 coatings fabricated by plasma spraying, *Materials & Design (1980-2015*), Vol. 65, 2015, P. 814-822.
11. S. JIANSIRISOMBOON, K.J.D. MACKENZIE, S.G. ROERTS Low pressure plasma-sprayed Al_2O_3 and Al_2O_3/SiC nanocomposite coatings from different feedstock powders, *Journal of the European Ceramic Society,* 23 (2003) P. 961-976.

12. K. OISHI, D. AKAI, M. ISHIDA, Integration of crystalline orientated γ-Al_2O3 films and complementary metal–oxide–semiconductor circuits on Si (100) substrate, *Solid-State Electronics*, Vol 103, 2015, P. 110-114.
13. F.A.C. OLIVEIRA, J.C. FERNANDES, J. RODRÍGUEZ. Temperature uniformity improvement in a solar furnace by indirect heating. Solar Energy 140 (2016) 141-150.
14. B. LI, F.A.C. OLIVEIRA, J. RODRIGUEZ, J.C. FERNANDES, L.G. ROSA. Numerical and experimental study on improving temperature uniformity of solar furnaces for materials processing. Solar Energy 115 (2015) 95-108.
15. J. RODRIGUEZ, New PSA High Concentration Solar Furnace SF40. SolarPACES 2015. AIP Conf. Proc. 1734, 070028-1–070028-11; doi: 10.1063/1.4949175.
16. K. BRINKIENĖ, R. KĖŽELIS, V. MEČIUS, L. PRANEVIČIUS, in *Advances in heat transfer engineering* (Eds: B. Sunden, J. Vilemas), New York, 2003, p. 629-636.
17. V. VALINČIUS, P. VALATKEVIČIUS, V. VALINČIŪTĖ, L. MARCINAUSKAS, *Plasma Sources Sci. Technol.* 2004, p. 199.
18. H. MISAN, A.M. AMINUDDIN, S. RAMESH, Facile preparation and characterizations of Potential Low-cost Nanostructured Materials for Energy Gas Storage, *The Electrochemical Society*, 2010, p. 57-65.

CYSENI 2017, May 25-26, Kaunas, Lithuania
ISSN 1822-7554, www.cyseni.com

INVESTIGATION OF THE MAGNETRON SYSTEM CONDITION AND ITS MAGNETIC PROPERTIES

A. Stankevičiūtė, A. Iljinas
Kaunas University of Technology
Studentų str. 50, LT-51368 Kaunas – Lithuania
E-mail: atigla@gmail.com

Fariza Kalyk
Abai Kazakh National Pedagogical University
Tole bi 86, 050012 Almaty - Kazakhstan

ABSTRACT

Magnetrons are commonly used in thin film deposition for: micro mechanics and electronics, solar cells, hydrogen fuel cells, for investigations in alternative energetics and its manufacturing. During the exploiting, the parameters of the magnetic system are changing due to mechanical and thermal impact on it. The configuration of magnetic field induction of three "Kurt J. Lesker" magnetrons were investigated in the magnetron sputtering system with non-magnetic and magnetic targets. By using magnetic probe sensor, we measured the magnetic flux dependence between two variables: distance from the edges of the magnetrons and different heights, where the range of the heights above targets were from 5 mm to 30 mm. Additionally, we collected the information that is based on magnetic field induction probability of different materials which were used in this experiment. In the respect to the results which were obtained, the 3rd magnetron had the strongest magnetic field and flux by the reason of its high values of the magnetic field induction (90.8 mT). Despite the fact that titanium had the same magnetic properties as the magnetron without any target. When we used the magnetic material (nickel), the magnetic flux increased to 97.7 mT. Considering that lines of the magnetic field had the same direction and position, therefore, the values of the magnetic field induction differed at various measuring points. As concerning, we investigated the glow discharge voltage dependency on the magnetic field.

Keywords: Magnetron sputtering, magnetic field induction, glow discharge

1. INTRODUCTION

A thin film can be described as a solid or a liquid layer on the primary substrate [1]. According to the Wagendristel [1], the thickness of the thin film can vary from 1 µm to less than it. Thin film technology engages an important role in recent scientific and technological developments due to various applications in which they can be used. For instance, in optics, thin films can be applied as antireflection coatings [2], solar cells [3], coatings which possess gloss [4] and colour [5], interference filters [6]. Furthermore, it includes applications in optical storage devices (CD-RW, DVD-RW) [7], optical waveguides [8] and photosensitive film technologies [9]. Likewise, they have wide attention in chemistry, magnetics, medicine, mechanics, electricity and alternative energetics by the reason of perspectives in the fabrication of diffusion barriers [10], coatings to protect system from corrosion [11], gas [12], liquid flow [13] and acoustic wave [14] sensors. There are thin films which provide adhesion [14] as well there are friction reduction coatings [15], magnetic storage [16] and Superconducting Quantum Interference (Squids) [17] devices, Piezoelectric Micro Power Generators (PMPG) [18] and etc.

Despite the fact that there are plenty techniques of physical thin film deposition, magnetron sputtering is commonly used due to large deposition rates and to the fact that substrate does not need to be at the high temperature [19]. This technique is useful for growing oxides, not to mention it helps to deposit metals at high temperature. Describing briefly, magnetron sputtering is a physical deposition method where atoms are sputtered from the surface. Firstly, energetic particles (ions) are accelerated from a plasma which produces magnetic field, then, they eject and start to bombard the surface. Afterwards, material starts to sputter and produces the layer on the primary substrate [20].

The main aim of experiment was to investigate the condition of magnetron system because the magnetic parameters can change due to frequent usage of the system.

2. METHODOLOGY

The magnetic field induction was measured on three different “Kurt J. Lesker” magnetrons in the magnetron sputtering system. The apparatus has nominal 700 W direct current and 300 W radio frequency sputtering powers. It can work at 110°C temperature because of the Currie temperature of used magnets and from 1 to 50 m Torr pressure. The flow rate of water at 25 °C is 0.170 m^3/h and the maximum water pressure of the system is 340 kPa [21].

In this experiment, nickel and titanium targets were used. The thickness of targets was 5 mm and diameter – 76.2 mm.

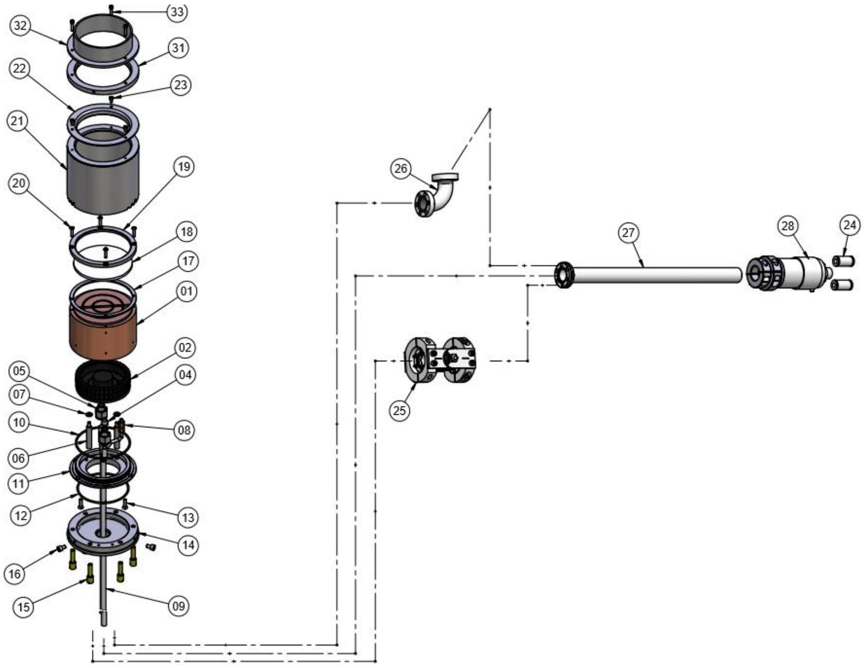

Fig. 1. A scheme of magnetron system [21]

Detailed visual scheme of magnetron system is described in (Fig. 1). The structure consists of 30 parts: 1 – cooling machine, 2 – magnetic assembly, 4 – ferrule, 5 – fitting, 6 – standoff tool, 7 – washer, 8 – wire assembly, 9 – tubing, 10, 12 – O-rings, 11 – insulator, 13, 15, 16, 20, 23, 33 – screws, 14 – cathode body, 17 – hold down ring, 18 – target, 19 – target hold down ring, 21, 22 – dark space shields, 24 - connector tube, 25 – mount, 26 – right angle assembly, 27 – tube extension assembly, 28 – bayonet connector assembly, 31 – gas distribution ring, 32 – chimney [21].

The magnetic field induction was measured with a magnetic probe Hall effect sensor (measurement error ± 6 %) on 6 different heights which varied from 5 mm to 30 mm. To investigate the glow discharge of nickel target, the magnetron sputtering vacuum system was used with oxygen pressure of 1 Pa.

3. RESULTS AND DISCUSSION

3.1. Effects of the magnetic field induction due to different magnetrons and targets

From the both edges of magnetron, magnetic field lines start to flow from the north poles to the south pole which is in the middle of mechanism. The movement of the magnetic field is circular, consequently the highest values of the magnetic field induction in all three magnetrons are in quarter of the all magnetron. Afterwards, the magnetic field induction starts to decrease until the middle point of the magnetron and then it starts to increase as previous. This is shown in (Fig. 2).

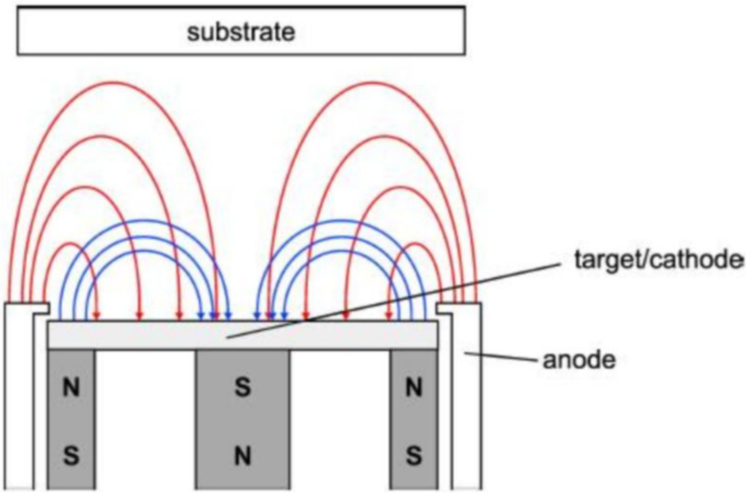

Fig. 2. A schematic view of magnetic field lines on magnetron [22]

Behaviour of the magnetic field of three magnetrons without any targets is presented in (Figs. 3–5). Evidently, the 3rd magnetron has the strongest magnetic flux (90.8 mT) at the lowest height (5 mm) by the virtue of the most potent Lorentz force of the magnet. For the reason that, on the higher point, the particles have less power to attract, that is why magnetic field induction starts to decrease from 90.8 mT (at 5 mm height) to 11.8 mT (30 mm height). The same probability is in another two magnetrons. In the 1st magnetron, the magnetic flux is getting lower from 55.4 mT (at 5 mm height) to 8.2 mT (30 mm height), in the 2nd – from 56.4 mT (at 5 mm height) to 5.4 mT (30 mm height).

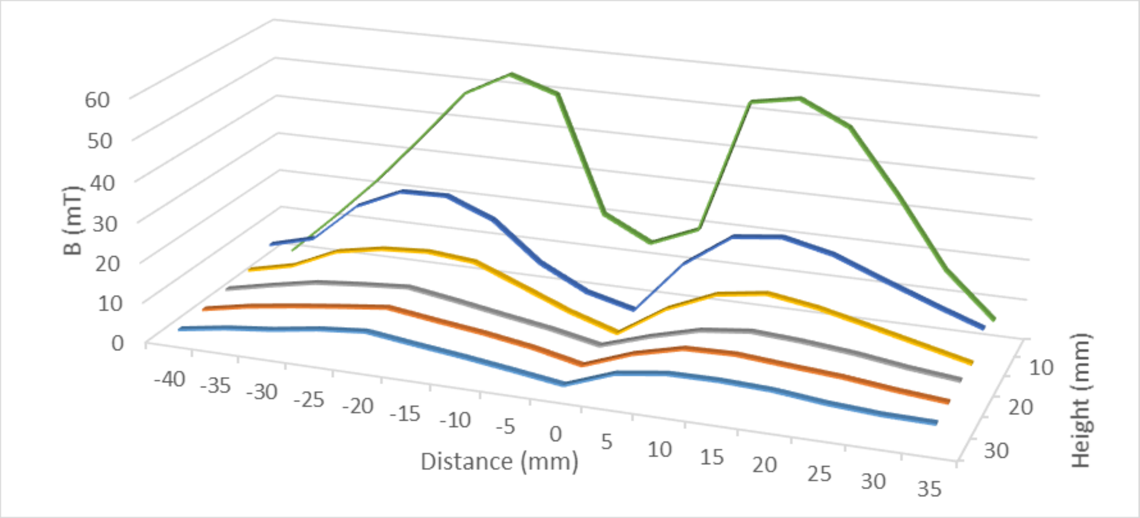

Fig. 3. The magnetic field induction dependence on the distance of 1st magnetron without a target and different heights

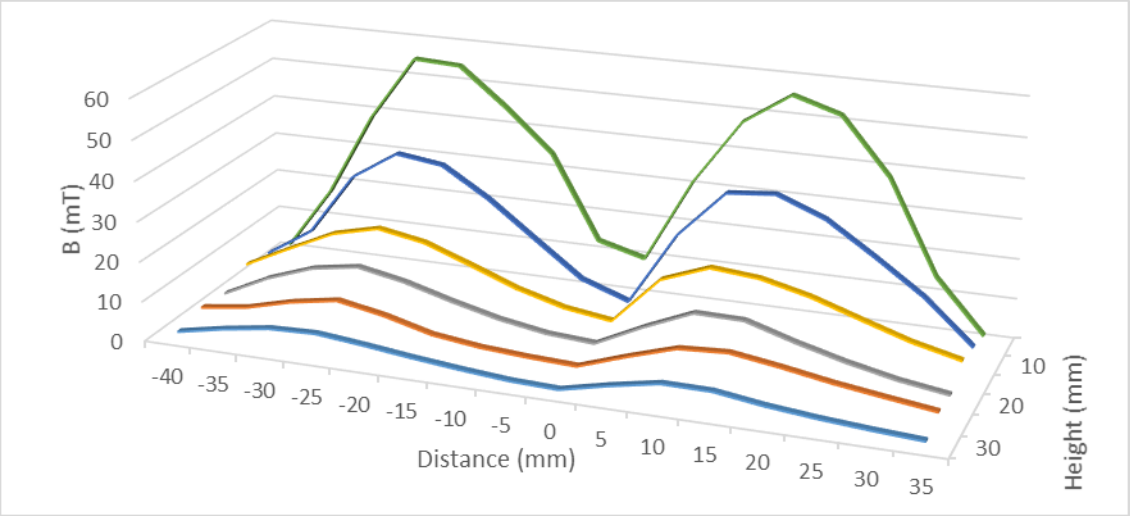

Fig. 4. The magnetic field induction dependence on the distance of 2nd magnetron without a target and different heights

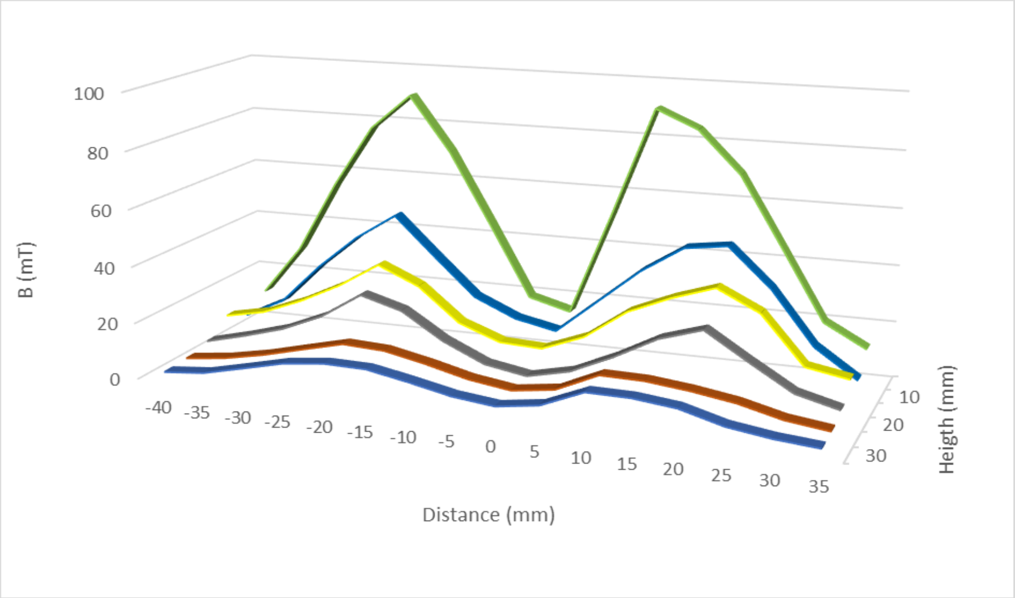

Fig. 5. The magnetic field induction dependence on the distance of 3rd magnetron without a target and different heights

Nickel is one of the most commonly used ferromagnetic material by its unique magnetic properties to magnetize other materials. It is used in various types of magnets and in different magnetic alloys. Nevertheless, titanium is a very weak magnetic material in the applied magnetic field. In (Fig. 6), the magnetic flux of titanium target and without the target is practically the same. For instance, the highest range is about 50.5 mT and 49.1 mT at the 5 mm height. Considering that nickel is a strong magnetic material, the magnetic field induction starts to increase rapidly as a result of 97.7 mT value at the 5 mm height.

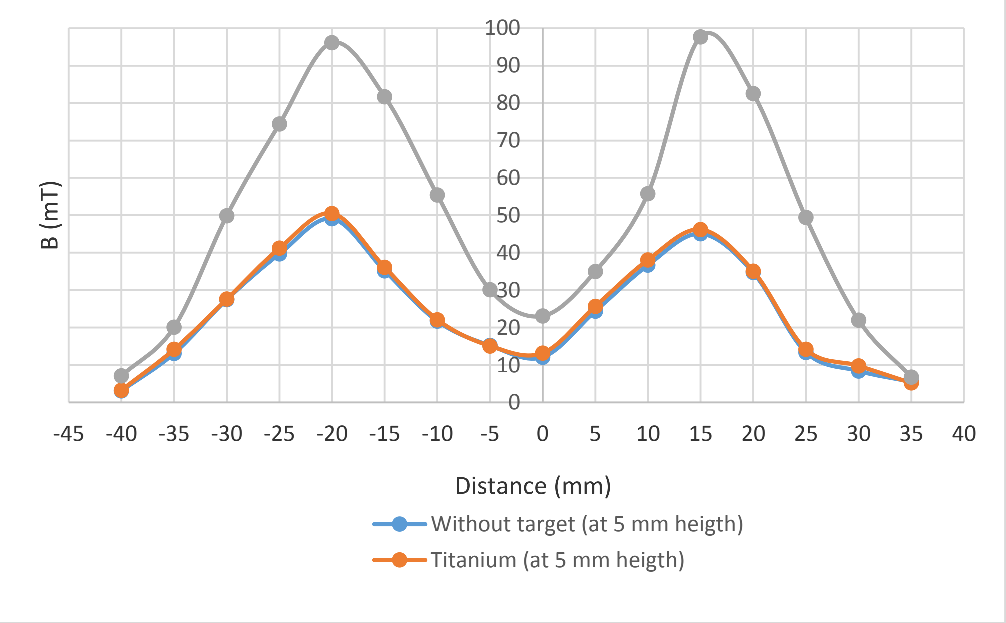

Fig. 6. The magnetic field induction dependence on the distance of 3rd magnetron without, with nickel and titanium targets at 5 mm height

3.2. Glow discharge in case of nickel target

Admitting that there are no possible changes in a movement of magnetic field lines due to energetic particles which are ejected from the magnetron source. Even thought, plasma impacts the trajectories of charged particles. Putting nickel target on magnetron and changing its position from 1st to the 3rd cathodes, we obtained that all three magnetrons have different voltage of glow discharge with valve and without it. Indubitably, 1st cathode had glow discharge voltage with valve

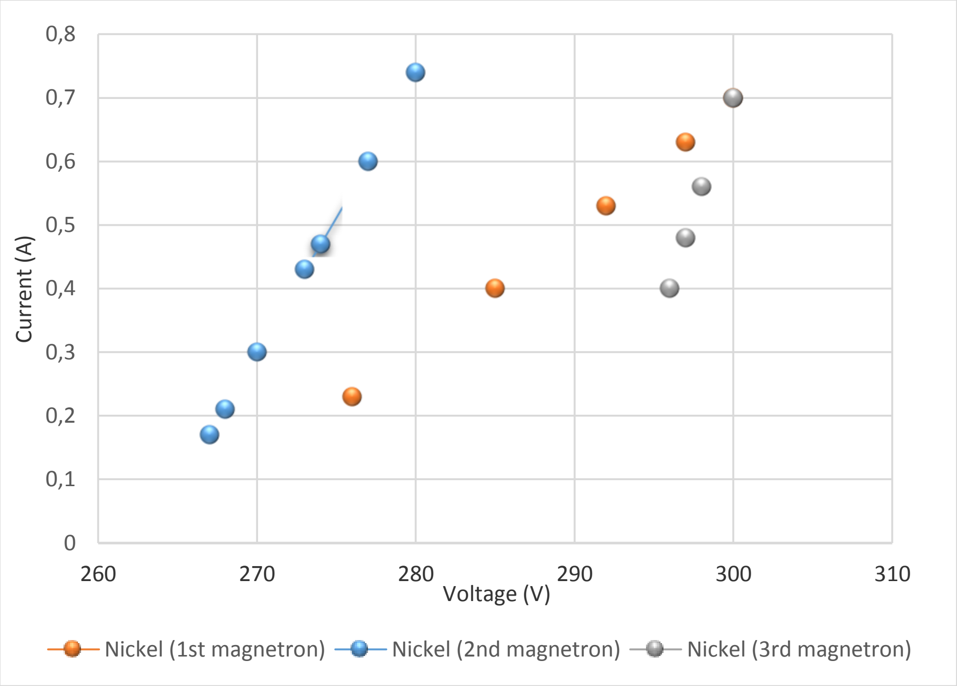

Fig. 7. The current dependence on applied voltage on three different magnetrons with nickel target

of 340 V and without it: 287 V. In 2nd magnetron, glow discharge voltage with valve was 320 V, without it was 270 V and in 3rd, voltage of glow discharge with valve became 330 V and without it, it decreased till 292 V. Despite the fact that the mobility of charged particles has an influence to the current value. In (Fig. 7), electrical current is increasing to the applied voltage as a result of accelerated ions in plasma as they move into the generated magnetic field. For example, in 1st cathode, we changed voltage range from 276 V to 300 V and the current increased from 0.23 A to 0.74 A. 2nd magnetron's current varied from 0.17 A to 0.74 A at the range of 268–280 V and 3rd target had current with values from 0.4 A to 0.7 A with voltage from 296 V till 300 V. In general case, glow discharge appears at the particular voltage because of its magnetic field.

4. CONCLUSION

To summarize results, glow discharge starts at particular point of the applied voltage at all three different magnetrons in which the current probability of voltage is increasing linearly. The phenomenon occurs because of the movement of energetic ions and its magnetic field. By using nickel and titanium targets, 3rd magnetron distinguished with the strongest magnetic flux values (90.8 mT) due to its intense magnetic properties. We obtained that at range from 5 mm to 30 mm height, magnetic flux is decreasing from 55.4 mT (at 5 mm height) to 8.2 mT (30 mm height) in 1st magnetron, from 56.4 mT (at 5 mm height) to 5.4 mT (30 mm height) in the 2nd and from 90.8 mT (at 5 mm height) to 11.8 mT (30 mm height) in the 3rd cathode by the influence of Lorentz force to ejected ions.

5. REFERENCES

1. Wagendristel, A.; Wang, Y. *An introduction to physics and technology of thin films.* Singapore: World Scientific, 1994. 41 p. ISBN 9810216165.
2. LI, Xiao, YU, Xinhong, HAN, Yanchun. Polymer thin films for antireflection coatings. *Journal of Materials Chemistry C*, 2013, vol. 1, no. 12, p. 2266-2285.
3. YU, Ze, PERERA, Ishanie R., DAENEKE, Torben, MAKUTA, Satoshi, TACHIBANA, Yasuhiro, JASIENIAK, Jacek J., MISHRA, Amaresh, BÄUERLE, Peter, SPICCIA, Leone and BACH, Udo. Indium tin oxide as a semiconductor material in efficient p-type dye-sensitized solar cells. *NPG Asia Materials*, 2016, vol. 8, p. e305-1-7.
4. LI, Jianhua, WANG, Jian, ZHANG, Letao and ZHANG, Shengdoing. Nanocrystalline SnO_2 thin films prepared by anodization of sputtered Sn thin films. *Journal of Vacuum Science & Technology A*, 2015, vol. 33, p. 031508.
5. SHEKHAH, Osama, CADIAU, Amandine, EDDAOUDI, Mohamed. Fabrication and non-covalent modification of highly oriented thin films of a zeolite-like metal–organic framework (ZMOF) with rho topology. *CrystEngComm*, 2015, vol. 17, no. 2, p. 290-294.
6. LO, Pei-Hsuan, LUO, Guo-Lun, LEE, Chih-Chun and FANG, Weileun. Nanoporous anodic aluminum oxide as a promising material for the electrostatically-controlled thin film interference filter. *Journal of Micromechanics and Microengineering*, 2015, vol. 25, no. 2, p. 025001.
7. AOUKAR, M., SZKUTNIK, P.D., JOURDE, D., PELISSIER, B., NOÉ, P. and VALLÉE, C. Control of carbon content in amorphous GeTe films deposited by plasma enhanced chemical vapor deposition (PE-MOCVD) for phase-change random access memory applications. *Journal of Physics D: Applied Physics*, 2015, vol. 48, no. 26, p. 265203.
8. PANDEY, R. K., MISHRA, Swati, KARMAKAR, Avik, SHARMA, M.P. and BAJPAI, P.K. Synthesis and Characterization of TiO_2 Thin Films for Optoelectronic Applications. *Journal of Pure Applied and Industrial Physics*, 2015, vol. 5, no. 10, p. 289-297.
9. OKUBO, Takashi, KANDA, Kensuke, FUJITA, Takyuki and MAENAKA, Kazusuke. Integration of Pb(Zr, Ti)O_3 thin films with photo-sensitive polymer. In: 2015 Joint IEEE

International Symposium on the Applications of Ferroelectric (ISAF), International Symposium on Integrated Functionalities (ISIF), and Piezoelectric Force Microscopy Workshop (PFM). *IEEE*, 2015. p. 178-181.

10. JEON, Chan-Wook, CHEON, Taehoon, KIM, Hangil, KWON, Min-Su and KIM, Soo-Hyun. Controlled formation of $MoSe_2$ by MoNx thin film as a diffusion barrier against Se during selenization annealing for CIGS solar cell. *Journal of Alloys and Compounds*, 2015, vol. 644, p. 317-323.
11. MORALES, Jorge Mario Herrera, SOURIAU, Jean-Charles, SIMON, Gilles. Corrosion Protection of Silicon Micro Systems with Ultra-Thin Barrier Films for Miniaturized Medical Devices. *ECS Transactions*, 2015, vol. 69, no. 26, p. 9-26.
12. JIAO, Zheng, WU, Minghong, GU, Jianzhong and QIN, Zheng. Preparation and gas-sensing characteristics of nanocrystalline spinel zinc ferrite thin films. *IEEE sensors journal*, 2003, vol. 3, no. 4, p. 435-438.
13. KUONI, Andreas, HOLZHERR, Raphaël, BOILLAT, Marc and DE ROOIJ, Nico F. Polyimide membrane with ZnO piezoelectric thin film pressure transducers as a differential pressure liquid flow sensor. *Journal of micromechanics and microengineering*, 2003, vol. 13, no. 4, p. S103.
14. RAPP, Michael; STAHL, Ullrich. Method for producing surface acoustic wave sensors and such a surface acoustic wave sensor. U.S. Patent No. 6,640,613, 2003.
15. BLACKWOOD, William, et al. Friction reducing coatings. U.S. Patent Application No. 15/230,016, 2016.
16. ZHOU, Wenliang, DENG, Hongmei, YANG, Pingxiong and CHU, Junhao. Designing tunable band-gap and magnetization at room-temperature in Pb $(Ti_{1-x}M_x)O_{3-\delta}$ (M = Ni and Pd) thin films. *Materials Letters*, 2016, vol. 185, p. 323-326.
17. BURTON, Matthew C., BEEBE, Melissa R., YANG, Kaida, LUKASZEW, Rosa A., VALENTE-FELICIANO, Anne-Marie and REECE, Charles. Superconducting NbTiN thin films for superconducting radio frequency accelerator cavity applications. *Journal of Vacuum Science & Technology A*, 2016, vol. 34, no. 2, p. 021518.
18. CHOI, W. J., JEON, Y., JEONG, J.-H., SOOD, E. and KIM, S.G. Energy harvesting MEMS device based on thin film piezoelectric cantilevers. *Journal of Electroceramics*, 2006, vol. 17, no. 2-4, p. 543-548.
19. R. A. Levy. *Microelectronic Materials and Processes*. NATO ASI Series: Springer, 1989. ISBN 978-0-7923-0154-7.
20. DEPLA, Diederik; MAHIEU, Stijn; GREENE, Joseph. Sputter deposition processes. *Handbook of deposition technologies for films and coatings: science, applications and technology*, 2010, 253-296 p. ISBN 9780815520313.
21. Kurt. J. Lesker company Circular Sputtering Source Torus 3 HV: Installation and Operation Manual. 2008.
22. *MAGNETRON SPUTTERING PRINCIPLE: Surface Physics Group* [interactive]. 2017 [referred 2nd of February, 2017]. Link to the internet: http://physics.mff.cuni.cz/kfpp/povrchy/method/magsputt-principles

CYSENI 2017, May 25-26, Kaunas, Lithuania
ISSN 1822-7554, www.cyseni.com

INVESTIGATION OF ARGON-ACETYLENE PLASMA USING OPTICAL EMISSION SPECTROMETRY

Vilius Dovydaitis, Liutauras Marcinauskas, Marius Černauskas
Department of Physics, Kaunas University of Technology
Studentų str. 50, LT-51368 Kaunas – Lithuania
E-mail: vilius.dovydaitis@ktu.edu

Mindaugas Milieška, Mindaugas Aikas
Lithuanian Energy Institute, Plasma Processing Laboratory
Breslaujos str. 3, LT-44403 Kaunas – Lithuania

Marius Černauskas
Vilnius University, Saulėtekio str. 9, LT-10222 Vilnius, Lithuania

ABSTRACT

Plasma jet technology was used to form carbon coatings from argon-acetylene gas at atmospheric pressure. Dominant particles in the argon-acetylene plasma were determined by optical emission spectrometry method. The results were obtained by changing the acetylene flow (from 16 ml/min to 85 ml/min) while maintaining two different argon flows (7.2 l/min and 9.2 l/min) at two distances (5 mm and 8 mm). Spectral analysis revealed that C_2 and CH species were dominant particles in the argon-acetylene plasma. It should be mentioned that H_2 particles might be present in the spectra, but it was hard to distinguish due to overlapping spectral lines. The results showed that the increase of the argon flow rate and distance decreases the intensity of C_2 and CH emission lines in argon-acetylene plasma. The influence of plasma composition on carbon films morphology, elemental composition and structure was investigated using scanning electron microscopy, energy-dispersive X-ray spectroscopy and Raman spectroscopy.

Keywords: argon-acetylene, plasma, carbon, optical emission spectroscopy, plasma jet.

1. INTRODUCTION

In recent years carbon based materials and coatings found numerous industrial and scientific applications due to variety of allotropic forms which provides different and exceptional mechanical, optical and electrical properties. One of the most promising carbon forms is amorphous carbon. Amorphous carbon excels in combining diamond and graphite properties. Depending on its structure, C=C sp^2 and C-C sp^3 bonds concentration in the material it is possible to achieve desirable set of properties [1-3].

Conventional synthesis methods of amorphous carbon coatings such as plasma-enhanced chemical vapor deposition (PECVD) or other similar methods requires vacuum to be at least 100 Pa or even less pressure [2]. Such plasma technology requires expensive equipment. The geometry of the vacuum chamber limits the size of treated sample [3]. Furthermore, the growth rates of the carbon films using vacuum based methods are usually relatively low. There is a different approach to overcome all those existing problems. Atmospheric pressure plasma jet (APPJ) technology could be successfully implemented in thin coating deposition field. It is a simple method which requires relatively cheap equipment and provides high deposition rates [4, 5]. It has been reported that amorphous diamond like carbon films with a high content of sp^3 sites were deposited using APPJ technique. Authors used Ar/CH_4 gas mixture and achieved relatively high deposition rates (21.31 nm/min) [5]. A. H. R. Castro et al. [6] deposited a polymeric-like carbon films from argon/air/acetylene gas mixture using APPJ. Authors demonstrated that the deposition rate of 330 nm/min could be achieved.

Acetylene and methane gases containing plasmas are the most widely used in the formation of various carbon films. It is very important to know the plasma composition when various hydrocarbon plasmas are used for the growth of thin carbon films because dominant plasma particles determine the film’s elemental composition and properties. It was demonstrated that C_2, CH, H, and H_2 species are dominate in hydrocarbons plasmas [5, 7, 8]. C_2 dimers are responsible for the graphite-like carbon growth, while the CH and H particles lead to the amorphous diamond-like carbon formation [8]. Optical emission spectrometry (OES) is widely used in plasma diagnostic. OES measurements are simple, fast and also non-invasive. This technique allows to analyze the plasma composition and determine the dominant plasma particles [9]. Intensity of optical emission lines is strongly dependent on the distance from the plasma torch. Increased distance causes rapid decrease in the intensity of characteristic lines [6]. Another important parameter is hydrocarbon gas flow rate. According to A. Yanguas-Gil et al. [8] investigation of APPJ plasmas, increase of acetylene gas flow rate does not affect CH/C_2 the intensity ratio of optical emision line. However, when the methane gas was used the increased CH_4 flow rate deacreased the CH/C_2 optical emision line intensity ratio which shows that the concentration of CH radicals in plasma was increased.

There are quite a few studies on argon-acetylene plasma investigations at atmospheric pressure. Therefore, the aim of this work is to investigate the influence of acetylene gas flow on the plasma composition and effect of plasma composition on the surface morphology and the structure of carbon films.

2. EXPERIMENTAL METHODS

Argon-acetylene plasma analysis was studied in the 350–650 nm range using an acousto-optic emission spectrometer IFU AOS4. The spectrometer has a solid state monochromator/grating (spectral resolution 0.05 nm at 250 nm and 0.5 nm at 800 nm). The optical lens collimator of 5 mm diameter and 2 m long optical fiber was used to focus the axial centre of the plasma jet. The fiber directs emission from plasma into the optical interface located at the entrance pinhole of the grating spectrometer. Three spectral cycle measurements for each plasma composition were done in the 350–650 nm range using scanning resolution of 0.2 nm. Measurements were done at 5 mm and 8 mm distance from the axial centre of the plasma jet changing acetylene (C_2H_2) flow rate from 16.2 ml/min to 84.2 ml/min, while argon flow rate was constant 7.2 l/min or 9.2 l/min. The ratios of argon-acetylene gas flow rates (Ar/C_2H_2) when argon flow rate was 7.2 l/min were 85, 106, 141, 186 ,280, 445. When argon flow rate was fixed at 9.2 l/min argon-acetylene gas flow rates were 109, 136, 180, 238, 357, 569.

The amorphous carbon films were deposited on silicon substrates at atmospheric pressure from argon-acetylene gas by plasma jet chemical vapour deposition [10]. A thin 3 nm nickel layers as a catalyst layer [11] was deposited on Si substrate. Argon (Ar) was the plasma working gas, with regular flow rates of 7.2 l/min or 9.2 l/min. Acetylene (C_2H_2) gas was used as carbon source with 25.7 ml/min flow rate. The substrates were chemically cleaned by acetone and for 30 s in the argon plasma to fully remove organic waste and any acetone leftovers before starting the formation process. The distance between the plasma torch nozzle exit and the samples was 5 mm or 8 mm in order to achieve plasma temperature of approximately 800–1000 ^{o}C at the substrate surface which are favourable for carbon nanostructure formation [12]. Plasma flow temperature at substrate surface was measured with chromel-aliumel (X-A) thermocouple. Relatively short deposition duration of 60 s was chosen because of high deposition rates achieved in previous work [10].

Surface morphology was characterized by scanning electron microscopy (SEM) model Hitachi S-3400N. The bonding structure of carbon films was analysed by Raman scattering (RS) spectrometer (Renishaw's InVia 90V727). RS was investigated using Ar ion laser (514 nm, spot size ~10 μm, in the 1000–2000 cm^{-1} range) as an excitation source. The RS spectra were fitted by Lorentzian shape lines in the spectral range of (1000–1800) cm^{-1}. The energy-dispersive spectrometry (EDS, Bruker AXS Microanalysis GmbH) analysis was used to determine the elemental composition of formed carbon films. The initial substrate composition was nickel (2.6 at.%), oxygen (6.0 at.%), carbon (1.4 at.%) and silicon (90.0 at.%).

3. RESULTS AND DISCUSSION

Fig. 1 shows an optical emission spectra of argon-acetylene plasma obtained at different Ar and C_2H_2 gas flows when measurement distance was 8 mm. The characteristic emission lines of argon-acetylene plasma were marked in Fig. 1 A. The main emission lines of C_2 dimer in argon-acetylene plasma belong to C_2 Swan band. They occurred due to electronic transition $D^3\Pi_g – A^3\Pi_u$. Different emission lines (516.4 nm, 473.7 nm and 563.4 nm) appear because of vibrational transitions (Δv = 0; +1; -1). CH emission lines at 431.2 nm are result of $A^2\Delta – X^2\Pi$ electronical transition [14-16]. H_2 emission line at 473 nm occurred because of the transition $Q^1\Pi_g – B^1\Sigma_u^+$ (Δv = 0) [17, 18].

Despite the changes in argon-acetylene gas mixture composition, emission lines corresponding to CH (431.2 nm), C_2 (473.7 nm, 516.4 nm and 563.4 nm) and H_2 (473.0 nm) species were observed in all the measurements. The bands corresponding for H_2 (473.0 nm) and C_2 (473.7 nm) were hard to distinguish because the overlapping of lines. Ar-C_2H_2 gas flow variation resulted in changes of emission lines intensities. As it is seen in Fig. 1, increased argon flow from 7.2 l/min to 9.2 l/min resulted in overall decrease of emission lines. This happened because acetylene was responsible for CH, C_2, H_2 emission lines and argon-acetylene gas flow ratio increased from 85–445 to 109–569, when the argon flow increased from 7.2 l/min to 9.2 l/min.

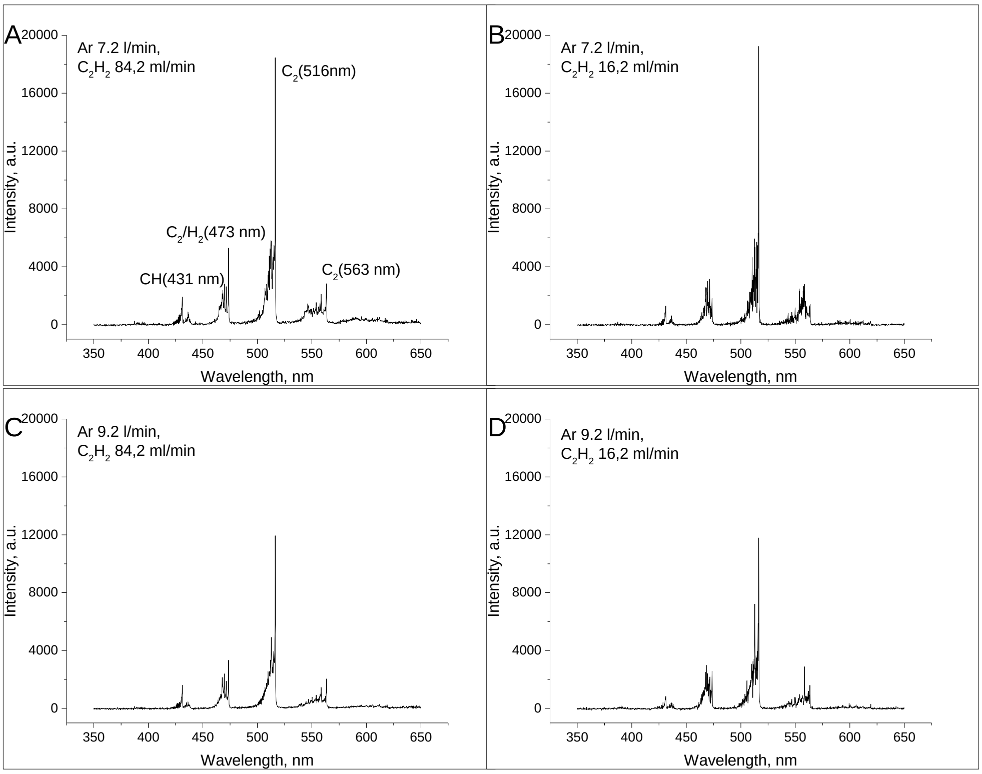

Fig. 1. The optical emission spectra of argon-acetylene plasma obtained at different Ar and C_2H_2 gas flows at 8 mm distance

As it is seen in Fig. 2, the relation between optical emission intensity and acetylene flow was complicated. At all acetylene flows, 516 nm C_2 emission line had the highest intensity. It reached its maximum values when acetylene flow was 51 ml/min and 38.6 ml/min when argon flow was 7.2 l/min and 9.2 l/min, respectively. The highest intensity values of CH radical’s emission lines were observed when acetylene flows were 38.6 ml/min (Fig. 2 A) and 25.7 ml/min (Fig. 2 B). The increase of the C_2H_2 flow rate slightly decreased the CH lines intensities (Fig. 2 A). Meanwhile, when Ar flow rate was 9.2 l/min (Fig. 2 B), the intensity of CH emission line started to decrease with increasing C_2H_2 flow rate after reaching its maximum value, until C_2H_2 flow rate reached 51 ml/min, the further increase of C_2H_2 flow had no influence on the intensity of CH line. C_2 (563 nm) and C_2/H_2 (473 nm) emission lines behaved similarly when argon flow was 9.2 l/min. They rapidly reached their maximum values and then with increasing acetylene flow started to decrease in intensity. It showed that there was an optimal gas composition at which gas mixture was at its most excited state. The highest concentration of CH and H_2 particles in plasma was at 25.7 ml/min, while the highest concentration of C_2 dimers was obtained when acetylene flow was 38.6 ml/min. The relation between optical emission intensity and acetylene flow got complicated (Fig. 2 A) when 7.2 l /min argon flow was used and did not follow the same pattern as in previous example. In this case, C_2/H_2 line intensity function had two peaks at 25.7 and 67.7 ml/min. Other optical emission lines had their maximums shifted to higher acetylene flows. Gas flow fluctuations might have been the reason why intensity behaviour differed when changing argon flow.

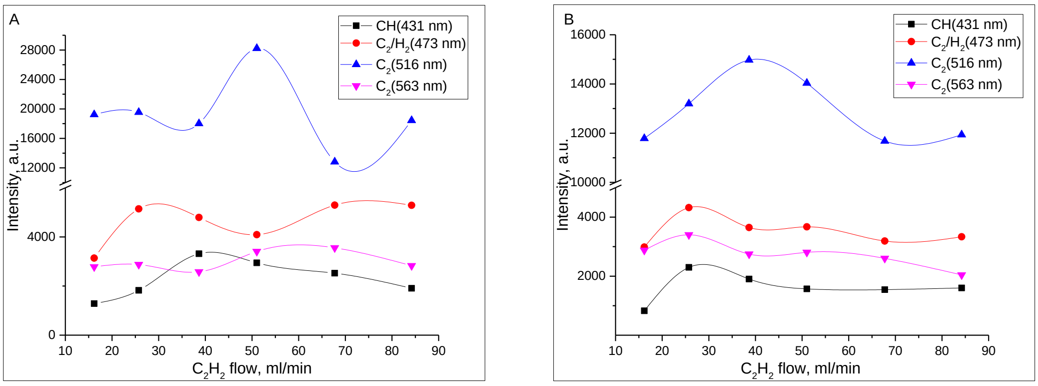

Fig. 2. Optical emission intensity of CH, C_2 and H_2 as function of acetylene flow when argon flow was: A – 7.2 l/min; B – 9.2 l/min

Optical emission spectra of Ar-C_2H_2 plasma were obtained at 5 mm distance. Argon flow rate remained constant 7.2 l/min while acetylene flow rate changed from 26.4 ml/min to 66 ml/min. In Fig. 3 C_2 (516 nm) and CH (431 nm) emission line intensity ratio (C_2/CH) dependency of acetylene flow rate was presented. The increase of C_2H_2 flow rate resulted in linear increase of C_2/CH ratio with the exception of one point at 33 ml/min C_2H_2 flow rate. This exception occurred due to gas flow fluctuation.

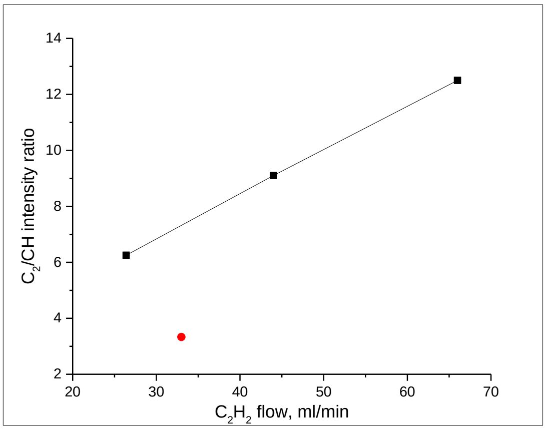

Fig. 3. Variation of the C_2/CH ratio on acetylene flow rate at 5 mm distance

It was decided to form carbon coating using 25.7 ml/min acetylene flow and 7.2 l/min argon flow because at those parameters C_2/H_2 line intensity was relatively high. This means that H_2 concentration in plasma should be higher and carbon C=C sp^2 sites etching should be improved resulting in higher C-C sp^3 content in carbon films [1, 8, 14]. According to data presented in Fig. 3 lower acetylene flow leads to increased relative concentration of CH particles in plasma. Coatings were deposited at 5 mm and 8 mm distance from the nozzle. The surface morphology SEM images of carbon films deposited at 5 mm and 8 mm distance are presented in Fig. 4.

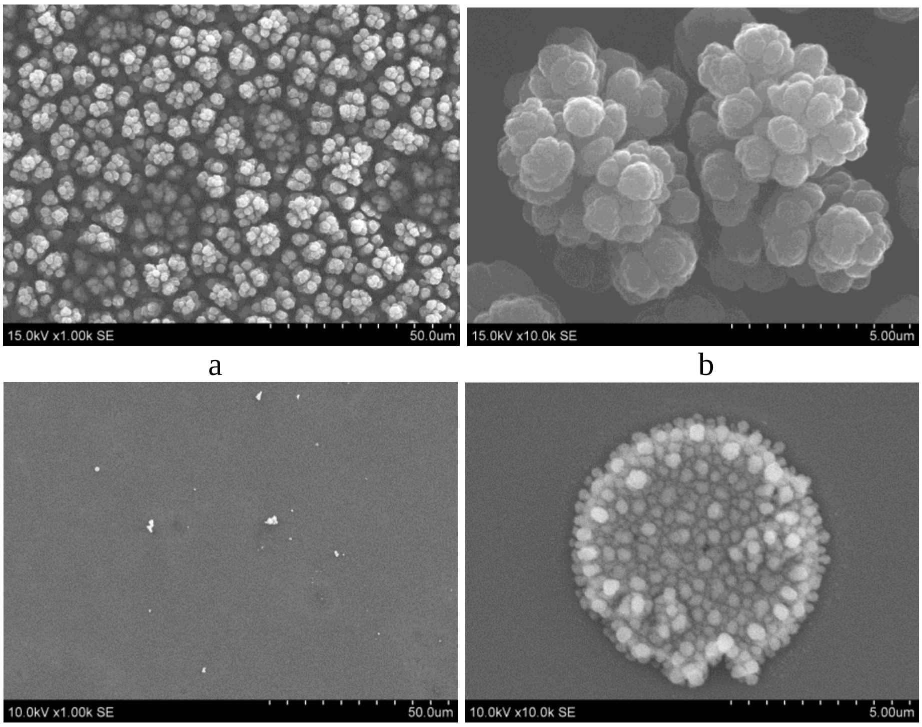

a b

c d

Fig. 4. Surface morphology of carbon films deposited at (a, b) 5 mm and (c, d) 8 mm distance

The coating deposited at 5 mm distance had rough, inhomogeneous and porous surface. SEM images showed that the film had columnar structure and high surface area (Fig.4. a-b). EDS analysis results showed that the coating consists of 86.90 at.% of carbon and 13.10 at.% of oxygen.

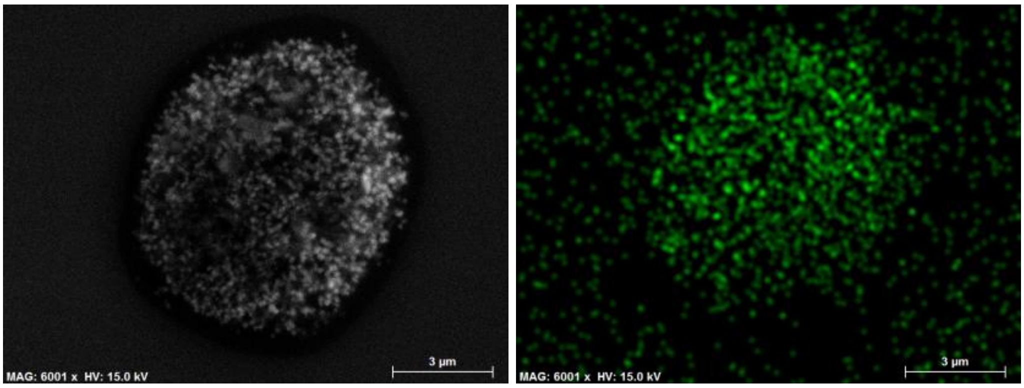

Fig. 5. SEM and EDS carbon mapping images at 6000 magnification

Film's deposited at 8 mm distance surface images are presented in Fig. 4 c-d. Continuous coating deposition failed at this distance. However, individual micro-structures of various forms can be observed on the surface (Fig. 4 d). They were scattered chaotically across the silicon substrate. Elemental analysis of the coating at 100 times magnification mainly showed only silicon signal (95.77 at.%) and a small content of carbon (0.46 at.%), oxygen (1.87 at.%) and nickel(1.90 at.%).

However, if the elemental composition of individual particles were measured using greater magnification, the carbon content drastically increased. An example is shown in Fig. 5. EDS mapping results shows that the structure mainly consists of carbon and the carbon content increased up to 24 at.%. This proved that an individual structures were formed from carbon.

The Raman spectra of carbon coatings are presented in Fig. 6. D and G peaks of carbon coating deposited at 5 mm distance were positioned at 1340 cm^{-1} and 1600 cm^{-1}, respectively. D and G bands were relatively narrow and separated. Their full width at half maximum (FWHM) were 195 cm^{-1} and 64 cm^{-1}. Intensity ratio of D and G peaks (I_D/I_G) was 0.76. Raman spectrum of structure grown at 8 mm distance had similar features like in previous spectrum. D band position shifted to higher values by 19 cm^{-1} (from 1340 cm^{-1} to 1359 cm^{-1}), FWHM of D peak remained almost the same 194 cm^{-1} (Fig. 6). The position of G peak slightly shifted to higher values (1602 cm^{-1}) and G peak became broader by 14 cm^{-1} (FWHM$_G$ = 78 cm^{-1}). Also, I_D/I_G ratio increased from 0.76 to 1.01. The increase in FWHM of G peak and I_D/I_G ratio showed that disorder in the structure had increased. RS results showed that coatings consist of the mixture of amorphous carbon and nanocrystalline graphite [1, 5]. Therefore, relative content of amorphous carbon in microstructures should be higher than in the coating produced at 5 mm distance. Graphite like features of RS spectrum well agreed with OES results because as shown in Fig. 2 dominant species in formation plasma were C_2 dimers which corresponded to carbon C=C sp^2 sites formation [8, 14].

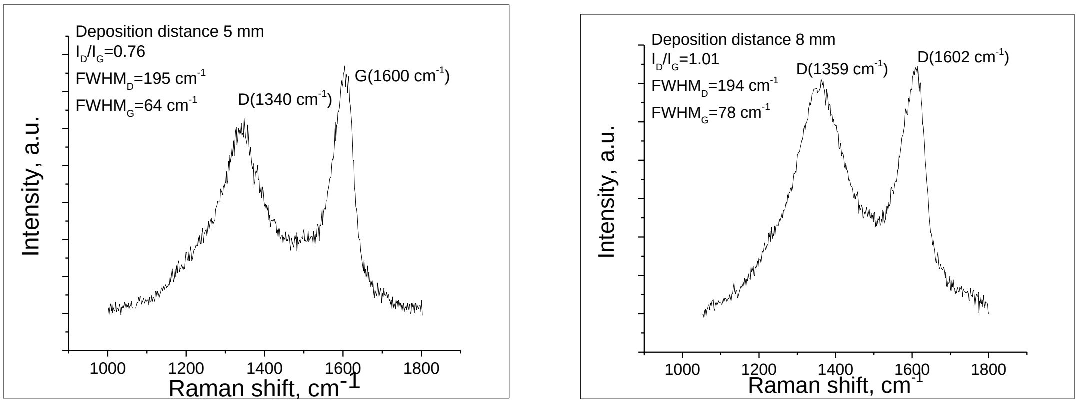

Fig. 6. Raman spectra of carbon films deposited at 5 mm and 8 mm distances

The results of Raman spectroscopy agreed with EDS analysis results and proved that structures were made from carbon. The increase of the deposition distance from 5 mm to 8 mm resulted in decrease of the substrate surface temperature. It was obtained that the temperature decreased from approximately 925 ^{o}C down to 765 ^{o}C. This might have reduced chemical reaction speed and nucleation probability of carbon films. Therefore the growth of continuous film was replaced by formation of local nucleation centres. Also, increased distance from the nozzle to the substrate allowed plasma particles to mix more with ambient air which might have led to decreased flux of excited particles.

4. CONCLUSIONS

OES analysis revealed that the dominant particles in Ar-C_2H_2 plasma are CH, C_2 and H_2. Overall intensities of emission lines decreased when argon flow rate increased from 7.2 l/min to 9.2 l/min. Optical emission line (516 nm) corresponding for C_2 dimer was the most intense independently of argon-acetylene gas mixture composition. The highest intensities of C_2 emission lines were reached at 51 ml/min and 38.6 ml/min acetylene flow rates when argon flow rates were 7.2 l/min and 9.2 l/min respectively. Carbon films deposited at 5 mm and 8 mm distances demonstrated a different surface morphology. Columnar structure was obtained at 5 mm distance while individual and scattered structures were formed at 8 mm distance. Elemental composition analysis revealed that in both cases coating and microstructures mainly consists of carbon. Raman spectroscopy results confirmed that the film and structures were made from carbon. Raman spectra shapes and positions of D and G peaks indicated that the nanocrystalline graphite carbon clusters with some addition of amorphous carbon were formed.

REFERENCES

1. ROBERTSON J. Diamond-like amorphous carbon. *Materials Science and Engineering: R: Report*, 2002, Vol. 37, No 4, p. 129-281.
2. SAKURAI, T., NOBORISAKA, M., HIRAKO, T., SHIRAKURA, A., & SUZUKI, T. Hardness and surface roughness of hydrogenated amorphous carbon films synthesized by atmospheric pressure plasma enhanced CVD method with various pulse frequencies. *Surface and Coatings Technology*, 2013,Vol. 215, p. 460-464.
3. LADWIG, A. M., KOCH, R. D., WENSKI, E. G., & HICKS, R. F. (2009). Atmospheric plasma deposition of diamond-like carbon coatings. *Diamond and Related Materials*, 2009, Vol. 18, No. 9, p. 1129-1133.
4. *Cornell university library*. Departament de Física Aplicada i Óptica, Universitat de Barcelona, 2015- [referred on the 28th of September in 2015 y.]. Link to the internet < https://arxiv.org/ftp/arxiv/papers/1509/1509.08512.pdf>
5. MARCINAUSKAS, L., VALINČIUS, V., & GRIGONIS, A. Deposition and structure characterization of carbon films prepared at atmospheric pressure by plasma jet. *Surface and Coatings Technology*, 2011, Vol. 205, p.71-74.
6. SOHBATZADEH, F., SAFARI, R., ETAATI, G. R., ASADI, E., MIRZANEJHAD, S., HOSSEINNEJAD, M. T., ... & BAGHERI, H. Characterization of diamond-like carbon thin film synthesized by RF atmospheric pressure plasma Ar/CH4 jet. *Superlattices and Microstructures*, 2016, Vol. 89, p. 231-241.
7. CASTRO, A. H. R., KODAIRA, F. V., PRYSIAZHNYI, V., MOTA, R. P., & KOSTOV, K. G. Deposition of thin films using argon/acetylene atmospheric pressure plasma jet. *Surface and Coatings Technology*, 2016, Vol. 312, p. 13-18.
8. YANGUAS-GIL, A., FOCKE, K., BENEDIKT, J., & VON KEUDELL, A. Optical and electrical characterization of an atmospheric pressure microplasma jet for Ar⁄ CH4 and Ar⁄ C2H2 mixtures. *Journal of applied physics*, 2007, Vol. *101*, No. 10, 103307.
9. LARIJANI, M. M., LE NORMAND, F., & CRÉGUT, O. An optical emission spectroscopy study of the plasma generated in the DC HF CVD nucleation of diamond. *Applied Surface Science*, 2007, Vol. 253, No. 8, p. 4051-4059.
10. MARCINAUSKAS, L., SILINSKAS, M., & GRIGONIS, A. Influence of standoff distance on the structure and properties of carbon coatings deposited by atmospheric plasma jet. *Applied Surface Science*, 2011, Vol. 257, No. 7, p. 2694-2699.
11. MALESEVIC, A., CHEN, H., HAUFFMAN, T., VANHULSEL, A., TERRYN, H. AND VAN HAESENDONCK, C. Study of the catalyst evolution during annealing preceding the growth of carbon nanotubes by microwave plasma-enhanced chemical vapour deposition. *Nanotechnology*, 2007, Vol. 18, No. 45, p.455602.
12. AKSAK, M., KIR, S. AND SELAMET, Y. Effect of the growth temperature on carbon nanotubes grown by thermal chemical vapor deposition method. Journal of Optoelectronics and Advanced Materials, 2009, Vol. 1, p. 281-284.
13. KOLPAKOVÁ, A., KUDRNA, P., & TICHÝ, M. Study of plasma system by OES (optical emission spectroscopy). In Proc. of 20th Annual Conference of Doctoral Students. Prague. 2011, Vol. 2, p. 180-185.

14. VIZIREANU, S., STOICA, S. D., LUCULESCU, C., NISTOR, L. C., MITU, B., & DINESCU, G. Plasma techniques for nanostructured carbon materials synthesis. A case study: carbon nanowall growth by low pressure expanding RF plasma. *Plasma Sources Science and Technology*, 2010, Vol. 19, No. 3, 034016.
15. LEE, S., YOON, S. H., KIM, J. K., & KIM, D. G. Hydrogenated Amorphous Carbon Films Prepared by Filtered Vacuum Arc Method with Various C2H2 Pressures. *Japanese Journal of Applied Physics*, 2011, Vol. 50(1S1), p. 01AH01.
16. DONG, M., LU, J., YAO, S., ZHONG, Z., LI, J., LI, J. and LU, W. Experimental study on the characteristics of molecular emission spectroscopy for the analysis of solid materials containing C and N. *Optics express*, 2011, Vol. 19, No.18, p. 17021-17029.
17. KOBASHI, K. Diamond films: chemical vapor deposition for oriented and heteroepitaxial growth. Amsterdam: Elsevier, 2010. 348 p. ISBN 0080525571.
18. Mindaugas, M., Marcinauskas, L., Valatkevičius, P., Grigaitienė, V. Investigation of the Ar-C2H2 and Ar-H2-C2H2 plasma using optical emission spectrometry. Radiation interaction with material and its use in technologies 2012: 4th international conference. Kaunas. 2012 May 14-17.

CYSENI 2017, May 25-26, Kaunas, Lithuania
ISSN 1822-7554, www.cyseni.com

REFRACTION OF MICROWAVES IN AN INHOMOGENEOUS GAS-METAL ROTATING PLASMA

Yu.V. Kovtun, Y.V. Siusko, A.I. Skibenko, E.I. Skibenko
National Science Center "Kharkov Institute of Physics and Technology"
1, Akademicheskaya St., Kharkov, 61108 – Ukraine
E-mail: Ykovtun@kipt.kharkov.ua, Zhenya-syusko@kipt.kharkov.ua

ABSTRACT

The development of researches in plasma physics and the progress attained in this domain are determined to a great extent by the development of methods for the measurement of plasma parameters. In current investigations uses different plasma diagnostics methods: probe (electric and magnetic probes), spectrometric, microwave, laser, corpuscular methods. Among them the most used are microwave methods, including the methods based on the refraction of microwaves in the plasma. By using the refraction it is possible to determine the plasma density distribution. An essential requirement for application of this technique is the use of narrow microwave rays supposing the fulfillment of the condition for geometric optics. On the other hand, the rays, which are sent from the horn, propagate through the plasma and traverse different plasma layers, can be used for the plasma diagnostics. So, to extend possibilities of microwave-based diagnostics plasma it is reasonable to consider the opportunity of using the refraction microwaves in peripheral layers of the plasma column.

The paper analytically, numerically and experimentally studied the possibility of using refraction microwave rays to measure the density in different plasma layers. Microwave ray trajectories are calculated in the geometrical optics approximation. Performed calculations the angle of deflection of the ray from the angle of its incidence onto the inhomogeneous plasma using some model functions of plasma density distribution. In the experiments the scattering of microwaves at an angle of ~60º and ~120º was observed. The average plasma density were also measured in the peripheral plasma layer when the plasma density exceeds the critical value and the through microwave probing is impossible by means of a microwave interferometer with inclined microwave rays.

Keywords: microwave rays, plasma diagnostics, refraction, microwave methods, geometrical optics.

1. INTRODUCTION

Experimental investigations of the plasma in crossed electric and magnetic fields (**E**×**B**) are interesting for wide range of physical and applied problems concerning the laboratory, fusion and space plasmas. One of these problems is the research into the multicomponent gas-metal rotating plasma, which is generated in the cross-field **E**×**B** devices, e.g., in the reflex discharge (Penning discharge) [1]. Among the methods of plasma diagnostics, the microwave techniques have gained wide recognition [2–5], including the methods based on microwave refraction in plasma [6–11]. In those methods, the dependences of the refraction angle on the plasma parameters at the plasma probing by an ordinary wave and on the magnetic field strength in the case of extraordinary wave are analyzed [9, 10]. By using the refraction it is possible to determine the plasma density distribution. An important condition for this method to be applicable is the usage of narrow microwave rays that satisfy the geometrical optics criteria. When the plasma probing is performed by microwave rays that are inclined with respect to the plasma boundary, the deviations of the rays from the initial direction and their path lengths in plasma depend on the entrance angle and the plasma parameters (see Fig. 1a). The deviation angle of the ray radius vector from its orientation at the ray entrance into plasma can be determined by the formula [9]:

$$\theta(\Psi) = 2R\sin\Psi \int_{r_0}^{R} \frac{dr}{r^2\sqrt{n^2(r) - \frac{R^2}{r^2}\sin^2\Psi}}, \qquad (1)$$

where R is the cylinder radius, r the current coordinate, Ψ the angle between the ray propagation direction and the cylinder radius at the point, where the ray strikes the plasma cylinder, n the refractive index, r_0 is the turn point of a ray trajectory, which is determined from the condition

$$\frac{R^2}{r_0^2}\sin^2\Psi = n^2(r), \tag{2}$$

Equation (1) assumes the form of Abel equation and has the inversion

$$r = R\cdot\exp\left[-\frac{1}{\pi}\int_{\rho n}^{1}\frac{\theta(\Psi)dS}{\sqrt{S^2-\rho^2 n^2}}\right], \tag{3}$$

where $\rho = r/R$, $S = \sin\psi$. This equation determines (in an implicit form) the dependence of n on r. Thus, the experimental determination of the point of ray emergence as a function of the angle of incidence enables us to find the radial dependence of the refractive index. These measurements call for wide-range variations in the angle of horn antenna inclination relative to the plasma, and this is not always feasible in practice. On the other hand, the rays propagating from the horn diverge and cross various plasma layers, so that they can be used for the diagnostics of the latter (see fig. 1b). This is especially useful if the transmission probing is impossible, when the plasma density exceeds the critical value.

So, for extending the capabilities of the microwave diagnostics of the multicomponent gas-metal rotating plasma, it is reasonable to consider the possibility of using the electromagnetic wave refraction in the peripheral plasma column layers.

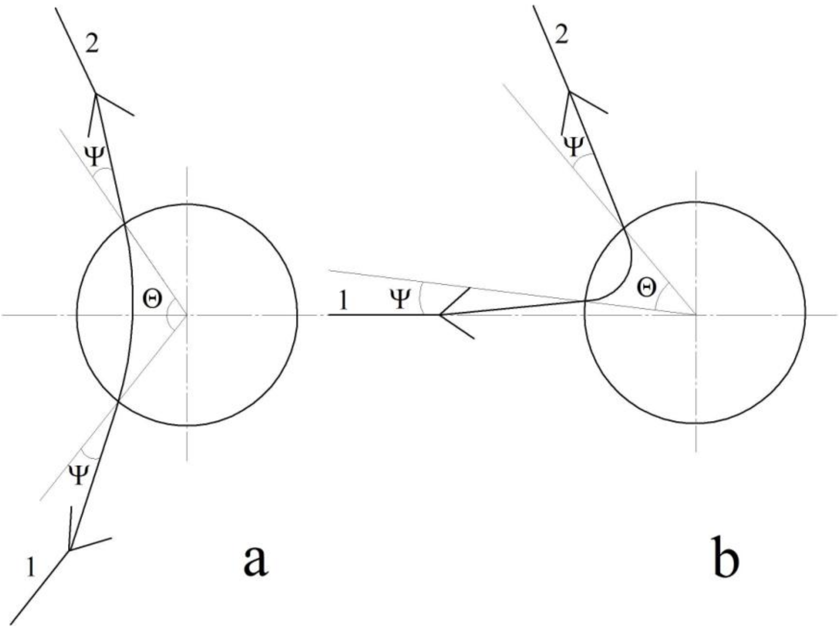

Fig. 1. Refraction of microwave ray in a plasma cylinder. Transmitting (1) and receiving (2) horn antennas. (a and b see text)

2. EXPERIMENTAL INSTALLATION AND DIAGNOSTIC TECHNIQUES

Experiments on microwave refraction in inhomogeneous gas-metal rotating plasma were carried out on the device MAKET [1]. In the device a high-power impulse reflex discharge was realized. The discharge stainless steel chamber had the following dimensions: the internal diameter of 0.2 m and the length of 2 m. The plasma was produced by discharging a capacitor bank between the cold cathodes and the anode (the wall of the vacuum chamber). The gas-metal plasma was produced in the mixture of the igniter gas and the sputtered cathode material. The cathodes were made from a composite material, namely, copper, onto which zirconium (Zr) was deposited by the vacuum-arc method. More detailed description of the experimental facility can be found in ref. [1]. The experiments were carried out at the following initial conditions: the magnetic field of mirror configuration $B \leq 0.45$ T; the discharge voltage and current: $U \leq 4.2$ kV and $I \leq 1.8$ kA, respectively; Ar was used as an ignition gas at a pressure between 0.6 and 3 Pa.

In the experiments, we have used two receiving horn antennas, which were turned, relative to the radiating horn antenna by a fixed angle equal to $\varphi_1 = 60^\circ$ and $\varphi_2 = 120^\circ$. Taking into account the horn antenna aperture , the angle of microwave radiation reception amounts to $\varphi_1 \approx 60^\circ \pm 9^\circ$ and $\varphi_2 \approx 120^\circ \pm 9^\circ$, respectively.The horn antennas were installed at diagnostic ports, the design of which does not allow variations in the angles of antenna inclination relative to the plasma. Therefore, precomputations were made to estimate the ray deflection angle versus the angle of ray incidence on the inhomogeneous plasma for a number of model plasma density distribution functions. The computation data have shown the possibility in principle to use in the given case the phenomenon of microwave refraction for plasma diagnostics. A more detailed discussion of the results will be given below.

The mean plasma density was measured experimentally with the aid of two microwave interferometers simultaneously. The plasma density across the plasma column was measured by the first interferometer. The plasma density in the cross section different from the normal one ($\varphi = 0$) was measured by the second interferometer with the horn antennas spaced by the angle of $\varphi_1 = 60^\circ$. Simultaneously with the interferometer measurements the scattered microwave signal was registered. The plasma cylinder was probed using an ordinary wave (O-wave) at the frequency $f = 37$ GHz.

3. MICROWAVE RAY TRAJECTORIES IN THE PLASMA CYLINDER

The deflection angle φ of the microwave ray is dependent not only on the angle of the ray incidence ψ and the plasma electron density, but also on the plasma density profile. Therefore, calculations were carried out for a number of model functions of plasma density distributions. For calculations we take the density distribution in the form of $N_p(r) = N_p(0) \cdot F(r)$. The calculation results obtained for the microwave ray trajectory in the plasma cylinder are represented in Fig. 2. In view of the above, calculations were made for the deflection angle φ of the microwave ray as a function of the angle ψ of the ray incidence on the inhomogeneous plasma. The calculation data are presented in Figs. 3 and 4. As it is obvious from Figs. 3 and 4, at certain $N_p(0)/N_{cr.}$ values a part of the rays may enter the receiving horn antennas. The calculations show (see Fig. 3) that with the parabolic plasma density profile at $N_p(0)/N_{cr.} < 1$, the microwave ray comes to the second receiving horn antenna deflected relative to the radiating antenna by the angle $\varphi_2 \approx 120^\circ \pm 9^\circ$. At $N_p(0)/N_{cr.} > 1$ the microwave ray comes to the first receiving antenna ($\varphi_1 \approx 60^\circ \pm 9^\circ$). Hence it follows that at the given initial conditions and density variations with time, e.g., density increase (see Fig. 4) , the microwave signal is first registered by the second receiving antenna $\varphi_2 \approx 120^\circ \pm 9^\circ$ (there is no signal in the first antenna). Later on, at $N_p(0)/N_{cr.} > 1$ the signal is registered by the first receiving antenna $\varphi_1 \approx 60^\circ \pm 9^\circ$ (no signal in the second antenna), and in the case of $1.75 > N_p(0)/N_{cr}$ there is no signal in the both antennas. At plasma decay, a similar pattern is to be observed, but in the reverse sequence. The obtained calculation data demonstrate the possibility in principle to use in the given case the phenomenon of microwave refraction for plasma diagnostics.

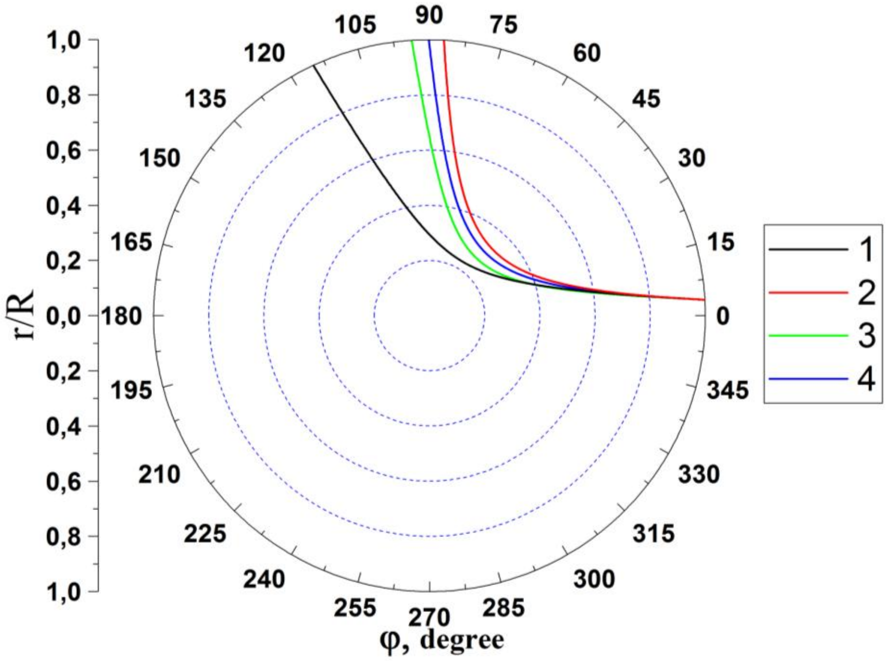

Fig. 2. Microwave ray trajectory in the plasma cylinder ($N_p(0)/N_{cr.} = 1$; $\psi = 6.31^{\circ}$). Density profile $N_p(r) = N_p(0)\cdot F(r)$: 1 – $F(r) = (1-(r/R))$; 2 – $F(r) = (1-(r/R)^2)$; 3 – $F(r) = \cos(1-(r\pi/2R)^2$;
4 – $F(r) = J(2.405r/R)$

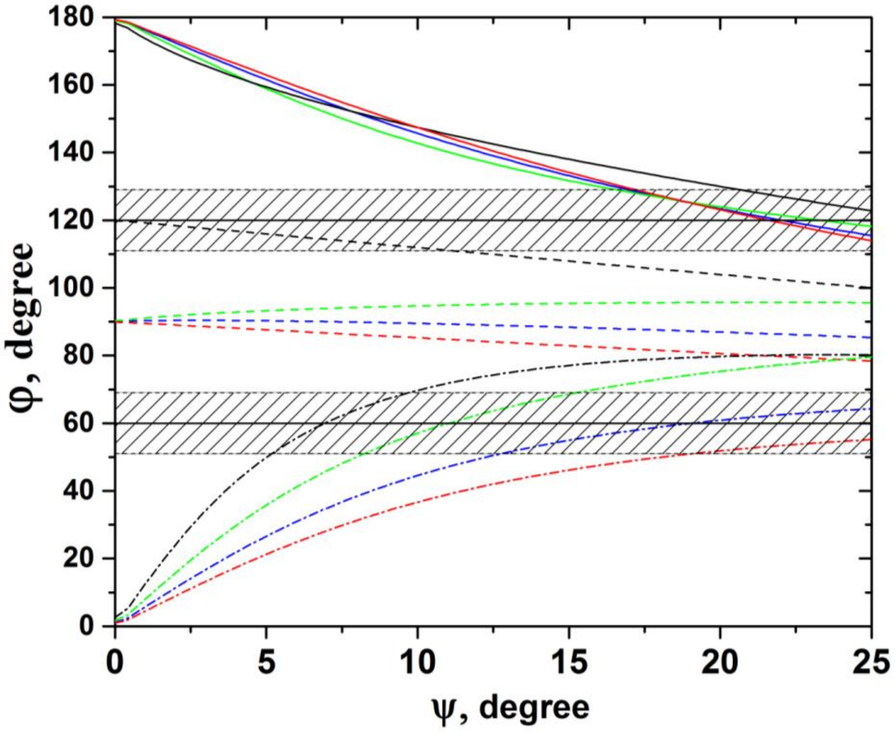

Fig. 3. Deflection angle φ of the ray versus the angle ψ of ray incidence on the inhomogeneous plasma. Density profile $N_p(r) = N_p(0)\cdot F(r)$: black $F(r) = (1-(r/R))$; red $F(r) = (1-(r/R)^2)$; green $F(r) = \cos(1-(r\pi/2R)^2$; blue $F(r) = J(2.405r/R)$. Solid line $N_p(0)/N_{cr.} = 0.5$; dotted line $N_p(0)/N_{cr.} = 1$; dashed-dot line $N_p(0)/N_{cr.} = 1.5$

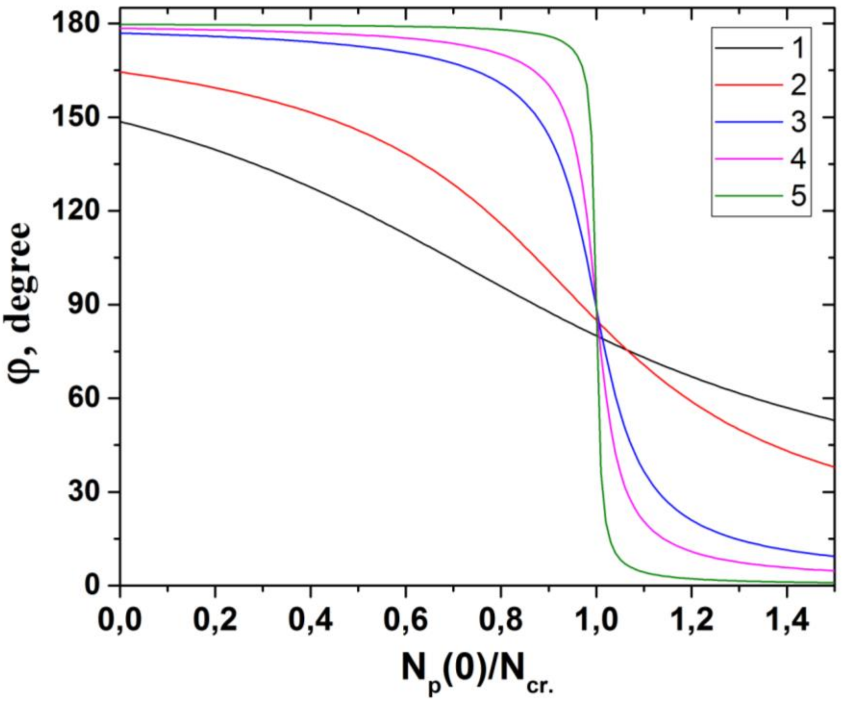

Fig. 4. Deflection angle φ of the ray in the inhomogeneous plasma versus $N_p(0)/N_{cr.}$ values for different angles ψ of ray incidence (density profile is $N_p(r) = N_p(0)(1-(r/R)^2)$). 1 – ψ = 21.39°; 2 – ψ = 10.55°; 3 – ψ = 2.1°; 4 – ψ = 1.05°; 5 – ψ = 0.21°.

4. EXPERIMENTAL RESULTS AND DISCUSSION

4.1. Refraction of microwaves in an inhomogeneous plasma

The previous investigations of the plasma generated in a high-power pulsed discharge [1] have demonstrated that the time dynamics of the mean gas-metal plasma density can be divided by convention into three stages. The first stage presents the plasma creation and its density increase up to $N_p = 1.7\cdot10^{13}$ cm^{-3}. The second stage is the plasma existence with the density attaining $N_p \sim 10^{14}$ cm^{-3} and more. The third stage presents the plasma density decrease and decay.

In the present experiments, we have registered the microwave scatter at angles $\varphi_1 \approx 60^\circ \pm 9^\circ$ and $\varphi_2 \approx 120^\circ \pm 9^\circ$. Fig. 5 shows the curves signals scattered by the angles angles $\varphi_1 \approx 60^\circ \pm 9^\circ$ and $\varphi_2 \approx 120^\circ \pm 9^\circ$ with simultaneous registration of the signals. In the given case the following time sequence of events is observed (see Fig. 5): (i) the signal is registered on the second antenna ($\varphi_2 \approx 120^\circ \pm 9^\circ$); (ii) the signal is registered on the first antenna ($\varphi_1 \approx 60^\circ \pm 9^\circ$), there is no signal on the second antenna, the signal is not registered by both antennas; (iii) the signal is registered on the first antenna ($\varphi_1 \approx 60^\circ \pm 9^\circ$), no signal on the second antenna, the signal is registered by both antennas. Actually, taking into account the time behavior of the plasma density, the observed pattern has appeared to be similar to that resulting from the analysis of the calculation data (see Figs. 3 and 4). This testifies that the approximations chosen for the calculations prove able to describe to some extent the experimental data. The presence in the two oscillograms of the region that shows no scatter signal is evidently indicative of the considerable size of the layer having the density $N_p \geq 1.7\cdot10^{13}$ cm^{-3}. The analysis of the calculation data (see Figs. 3 and 4) and the experimental data (see Fig. 5) shows that the occurrence of the signal scattered by the angle $\varphi_1 \approx 60^\circ \pm 9^\circ$ at the plasma density $N_p \geq N_{cr}$, and the signal scattered by $\varphi_2 \approx 120^\circ \pm 9^\circ$ at $N_p < N_{cr.}$ is connected with the microwave ray refraction in the inhomogeneous plasma.

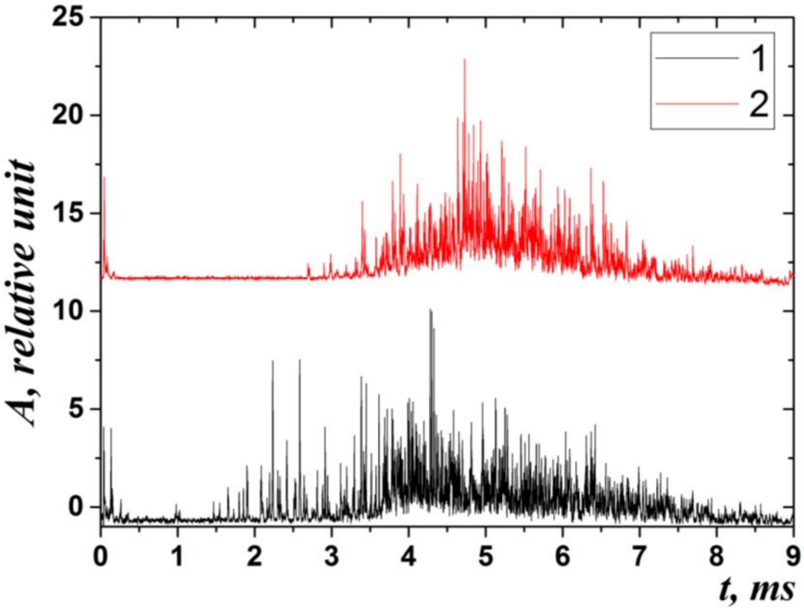

Fig. 5. Time dependence of the signals scattered by the angles $\varphi_1 \approx 60^\circ \pm 9^\circ$ (1) and $\varphi_2 \approx 120^\circ \pm 9^\circ$ (2). ($U_{dis.}$ = 3.7 kV; p = 1.16 Pa)

4.2. Interferometry of plasma with the use of the microwave ray refraction

The phase shift between the waves passed through the reference and measuring channels of an interferometer [11] equals

$$\Delta\Phi(t) = \varphi_0 - \varphi_p(t), \tag{4}$$

where φ_0 is the phase in the reference channel, and $\varphi_p(t)$ the phase in the measuring one. The phase in the reference channel always remains constant and is equal to

$$\varphi_0 = \frac{\omega}{c}L = 2\pi\frac{L}{\lambda_0}. \tag{5}$$

In the measuring channel, the phase changes depend on the plasma density:

$$\varphi_p(t) = \frac{2\pi}{\lambda_0}\int_0^L n(l,t)dl, \tag{6}$$

where λ_0 is the length of a microwave probing in vacuum, L the size of the researched plasma (the optical path length), and $n(l,t)$ the index of wave refraction at the given point l (coordinate along the microwave ray trajectory) of plasma. The ray trajectory length in plasma depends on the entrance angle and the plasma parameters (density, density profile, electron effective collision frequencies). In the case of cylindrical symmetry, the phase change in the measuring channel can be presented in the form

$$\varphi_p(t) = \frac{2\pi}{\lambda_0}2\int_{r_0}^{R}\frac{n^2(r,t)rdr}{\sqrt{n^2(r,t)r^2 - R^2\sin^2\Psi}}. \tag{7}$$

The mean plasma density was measured experimentally with the aid of two microwave interferometers simultaneously. The results obtained from the oscillograms processing are represented in Fig. 6. As is seen from the graph the time dependences of the phase shift for the transverse plasma column probing (see Fig. 6a curve 1) and for the cross section different from the normal one are not similar (see Fig. 6a, curve 2). Conventionally, the curves of the phase shift as a function of time can be divided into two parts. The first part (t ≤ 4 ms) is characterized by the presence of the plasma layer with $N_p \geq N_{cr.}$. Consequently, for the transverse probing of the plasma column the microwave signal cutoff is observed and the phase shift is absent. In the case of the plasma probing in the cross section different from the normal one the inclined rays pass through the plasma layers with $N_p < N_{cr.}$ and the phase shift is recorded (see Fig. 6a, curve 2). In the second part (t > 4 ms) the plasma density is $N_p < N_{cr.}$ For the two cases of the plasma probing the phase shift is observed. However, if the plasma probing is performed in the cross section different from the normal one the phase shift is ~2 times more compared to the transverse probing.

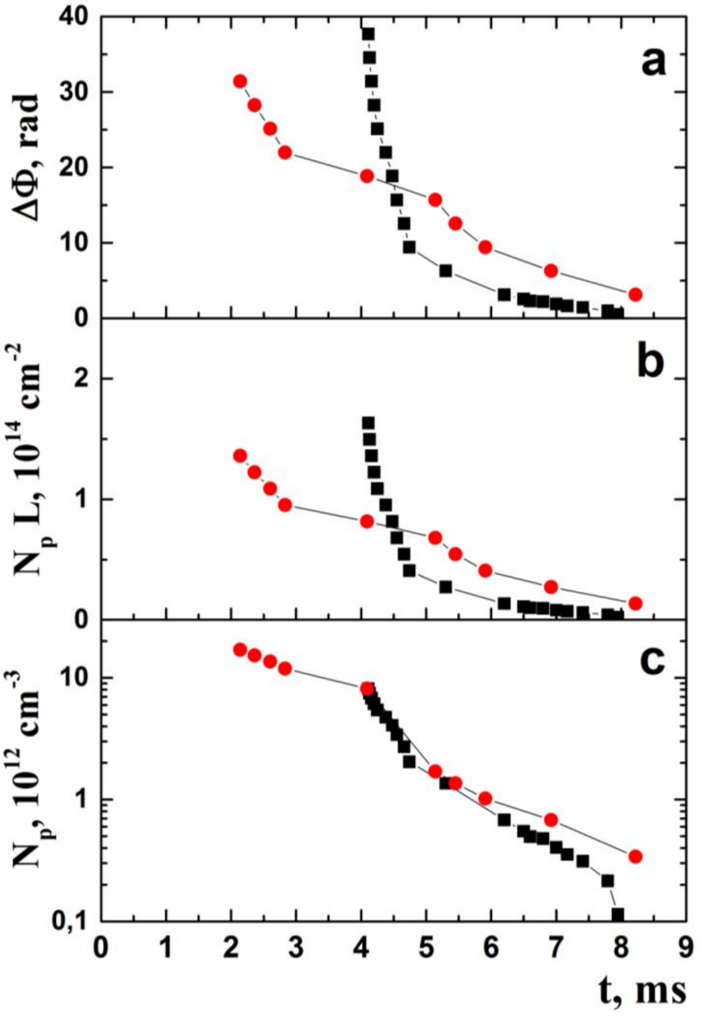

Fig. 6. Time dependence of the phase shift (a), product of N_pL (b) and average plasma density (c): 1 – (■) φ ≈ 0°; 2 – (●) φ_1 = 60°

Unlike the transverse probing of the plasma column, if the plasma probing is performed in the cross section different from the normal one, the ray trajectory in the plasma, and the quantity L respectively, can be significantly changed. Therefore, to analyze the time dependence of the plasma density let us represent the plasma density in the form of a product N_pL (t ≤ 4 ms) (see Fig. 6 b). It is seen from the graph that with $N_p \geq N_{cr.}$ (t ≤ 4 ms) the plasma probing in the cross section different from the normal one (see Fig. 6 b, curve 2) gives the plasma density value in the peripheral plasma region while in the case of transverse probing it is impossible to determine the average plasma density. With the decreased plasma density $N_p < N_{cr.}$ (t > 4 ms) the measured quantity N_pL in the cross section different from the normal one (see Fig. 6 b, curve 2) is higher than for the probing in the transversal cross section (see Fig. 6 b, curve 1). This related with the difference in the quantity *L* for the normal plasma probing and for the probing different from the normal one. Given L has been estimated the average plasma density presented in Fig. 6 c.

5. CONCLUSIONS

Calculations have been made to determine the dependence of the deflection angle of the microwave ray, φ, on the angle of its incidence, ψ, onto the inhomogeneous plasma. The calculation data have shown that a part of microwave rays may enter the horn antenna installed at a fixed angle with respect to the plasma.

The present experiments have registered the microwave scatter at angles of ~ 60º and ~ 120º. The analysis of the calculation data and the experimental data shows that the occurrancy of the signal scattered by the angle $\varphi_1 \approx 60^\circ \pm 9^\circ$ at the plasma density $N_p \geq N_{cr}$, and the signal scattered by $\varphi_2 \approx 120^\circ \pm 9^\circ$ at $N_p < N_{cr.}$ is related with the microwave ray refraction in the inhomogeneous plasma.

The investigation results show a possibility in principle of using the plasma interferometry with inclined microwave rays for diagnostics of multicomponent gas-metal plasma in crossed E×B fields. This method is suitable for determining the average plasma density in the peripheral plasma layer when the plasma density exceeds the critical value and the through probing is impossible.

Thus, the present studies have demonstrated the possibility in principle of using the phenomenon of microwave refraction for diagnostics of multicomponent gas-metal rotating plasma.

REFERENCES

1. KOVTUN, YU. Features of Dense Plasma Formation in the Reflex Discharge on Gas-Metal Mixes. *Problems of Atomic Science and Technology. Series: Plasma Electronics and New Methods of Acceleration*, 2013, No. 4(86), p. 38-43.
2. HEALD, M. A.; WHARTON, C.B. *Plasma Diagnostics With Microwaves*. New York: John Willey & Sons, 1965. 452 p.
3. GOLANT, V. E. *Microwave Methods of Plasma Diagnostics*. Nauka, Moscow, 1968. 328 p.
4. HARTFUSS, H.-J.; GEIST T. *Fusion Plasma Diagnostics with mm-Waves: An Introduction*. Weinheim: Wiley-VCH Verlag GmbHCo, 2013. 408 p.
5. MAZZUCATO, E. *Electromagnetic Waves for Thermonuclear Fusion Research*. Singapore: World Scientific Publishing Co. Pte. Ltd., 2014. 204 p.
6. SHMOYS, J., Proposed Diagnostic Method for Cylindrical Plasmas. *J. Appl. Phys.* 1961, Vol. 32, No. 4, p. 689-695.
7. DUSHIN, L., KONONENKO V., SIZONENKO, V., et al. Determining the plasma density distribution by the microwave ray refraction. *Zh. Tekh. Fiz.* 1966, Vol. 36, No. 2, p. 304-312 (in Russian).
8. DUSHIN, L., KONONENKO, V., SKIBENKO, A. Investigation of spatial plasma density distribution by the refraction of a microwave ray with several frequency components. *Zh. Tekh. Fiz.*, 1966, Vol. 36, No. 10, p. 1842-1850 (in Russian).
9. NEMOV, V., SIZONENKO, V., STEPANOV, K. Technical Methods of determining the density and temperature distribution of a plasma using electromagnetic waves. *Nucl. Fusion*, 1969, Vol. 9, No. 3, p. 243-251.
10. DUSHIN, L., SKIBENKO, A., FOMIN, I.P. Refraction of the Extraordinary Wave in a Cross Section of an Anisotropy Plasma Cylinder. *Sov. Phys.-Tech. Phys.* 1972, Vol. 16, No. 8, p. 1291-1295.
11. SKIBENKO, A., PINOS, I., KOVTUN, YU., SKIBENKO, E., SYUS'KO, E. Application Of Microwave Ray Refraction in Inhomogeneous Plasma Interferometer. *Ukr. J. Phys*, 2016. Vol. 61, No. 8, p.715-721.

CYSENI 2017, May 25-26, Kaunas, Lithuania
ISSN 1822-7554, www.cyseni.com

INVESTIGATION OF THE BIOFUEL DRYING INTENSIFICATION BY EXPERIMENTS IMITATING THE FURNACE OPERATIONAL PROCESSES

Lina Vorotinskienė, Nerijus Striūgas
Lithuanian Energy Institute
Laboratory of Combustion Processes
Breslaujos st. 3, LT-44403 Kaunas – Lithuania
E-mail: lina.vorotinskiene@lei.lt

ABSTRACT

In many countries the fossil fuels are being replaced by the biofuels due to ecological reasons. In nowadays more than 40% of solid biofuels are used for the district heating and the demand of biofuel is growing, what causes the increase of biofuel price. As the residual wet biomass from lumbering is cheaper than stored dry biomass, residual wet biomass is more often supplied to the heating plants due to economic reasons. One of the important property of the biofuel is the moisture content as it effects the heating value of the biofuel and the combustion process too. The moisture content of the residual biofuel from the urban districts and forests could reach more than 60 wt.% and if fed into a furnace with moving grates, such biofuel only starts to combust when dried till 30 wt.%. As the biofuel should be dried to appropriate moist content, the use of wet biofuel requires investments in the technological process of biofuel combustion such as fuel drying in bunker before feeding on grates or the actual length of grates in furnace should be increased.

The aim of this work is to investigate the possibilities of the biofuel drying intensification process by the experiments performed on the rig, which imitates the processes occurring in the furnace systems. In order to perform experiments with biofuels, the experimental rig was designed, assembled and the research methods were formulated. The biofuels used for experiments were in high moisture content (60 wt.%) – the wood chips, the residuals from urban districts and the residuals from lumbering/harvest. In order to reach the moisture content of (60 wt.%) the biofuel was continuously soaked in the special container for 16 hours. To investigate the possibilities of biofuel drying intensification three setups of increasing affection to biofuel drying were generated, where the biofuel was exposed to: a) the heated air, which simulated the furnace primary air inlet, b) heated air and the steam, which simulated the recirculation of the gases in the furnace. It was found that the intensity of biofuel drying is affected by the biofuel granulometry and the furnace operating parameters, such as air temperature and moisture content of the drying air.

Keywords: biofuel, furnace, moisture content, drying.

1. INTRODUCTION

The European Union (EU) seeks to increase the use of renewable resources for heat and power production until 2020 [1]. As the member state, Lithuania is also committed to seek for this aim, thus in general fossil fuel is replaced by biofuel. In view of renewable resources, the biomass is the main source to produce heat. In this case, more than 40% of solid biofuels are used for district heating. Growing demand on biofuels cause increase of the biofuel price in the market and the heat producers are impelled to buy an inferior quality, moist biofuel for economical purposes. The moisture content of low quality biofuel varies from 40 to 65 wt.% [2]. Mostly, the solid biofuel such as wood chips are fired in a 5–10 MW moving grate furnace equipped with water boiler and a flue gas condensing economizer. Such moving grate furnaces are to sufficiently resist to changes in the quality of biofuel, but the fluctuations of fuel moisture content complicate the furnace continuous operation and automatic control [3]. The moisture content is important parameter of biofuel as it affects efficiency of combustion process. Combusting the moist biofuel, there is produced less amount of heat than using a dry biofuel, as a part of emitted heat is consumed for water evaporation [4]. When the moist biofuel enters the furnace, it falls to the burning bed of wood on the grate and the process of biofuel drying takes place. As the moisture content of fuel reaches around 30 wt.%, the combustion begins [5]. In order to avoid the drying stage on the grates or noxious emissions into the environment due to incomplete combustion of fuel, the biofuels could be dried to a certain moisture content before it enter the furnace. Many types of drying systems have been developed for drying the biomass, for example, the most common are the drum dryers, in other words rotary dryers [6]. Drum dryers are common in the market due to its simple design, though these devices require high-grade energy for efficient work and as well the moisture content of drying material is difficult to control [7]. The highest process efficiency is achieved when the biofuel dryer is designed together with the biofuel furnace, thus avoiding the dried biofuels storing [3], which must be installed in an indoor, sealed and dry place. The mentioned dryers mostly use a heat of flue gas for drying process, thus no addition heat source is needed.

Another method to ensure stable operation of furnace with moist biofuel presented Niedermayr et al. [8]. Method is based on an innovative fuel feeding system: a crane and a sensor-equipped gripper, featuring different sensors, such as ultrasound, moisture, and image recognition with a camera. The sensor-equipped gripper analyses fuel in the hopper and feeds fuel of the required moisture with the required feeding rate according the boiler operating regime. According to authors [8], this approach helps to avoid fluctuations of the boiler operation regime due to differing moisture content, as well as to reduce CO_2 emissions, though the feeding system is only a lab scale and tested in a thermal power plant with a capacity below 500 kW.

This work presents the investigation of regularities of ongoing moisture content variations in drying zone affecting the biofuel layer with hot air (simulation of the primary air) and with mixture of hot air and water vapor (simulation of recirculation gas).

2. MATERIALS AND METHOD

For investigations two different experiments were performed: the first experiment was conducted to determine the differences of water evaporation from biofuel with surface and internal moisture between the fuel with only internal moisture. The second experiment was performed in order to investigate the effect of primary air and recirculation gas to the biofuel layer in the furnace drying zone.

2.1. The methodology for experimental investigation of biomass drying

A freshly cut and chopped wood (alder) with moisture content up to 46 wt.% and partly dried wood chips with moisture content around 28 wt.% were used for the first experiment. The partly dried wood chips were soaked in a barrel with water for 16 hours and after it samples were pulled out of the barrel and drained. After soaking moisture content of the chips reached around 46 wt.%. Before and after the experiment, the moisture content of wood chips was measured manually by drying the samples in an oven. The prepared samples were placed into an electrically heated furnace (Fig. 1).

Using the electrically heated horizontal tubular furnace Nabertherm RS 80/500/13 *1*, mass loss of biomass samples was determined during drying process. A special frame with moving tray was mounted on the top of furnace and a digital scale Kern EW 420-3NM (accuracy ± 0,003 g) *4* was placed on the tray. The digital scale was connected to computer *10* and mass loss data was collected over software Kern BC2006. A special rod with bracket of stainless steel mesh *5* with K-type thermocouple *7* for measurement of sample center temperature, was attached to measurement point at scale bottom. The center temperature values were collected by data logger PICO TC-08. Air flow of 11 l/min, controlled by the flow meter (3) was maintained from the bottom of tube *2* into the furnace when the heating temperature reached the desired level (200 ^{o}C). The sample was placed in the bracket and fed into heating tube through open end when the mass readings become steady. When mass loss of sample was no more observed, bracket with sample was extracted from heating tube and obtained data was analysed.

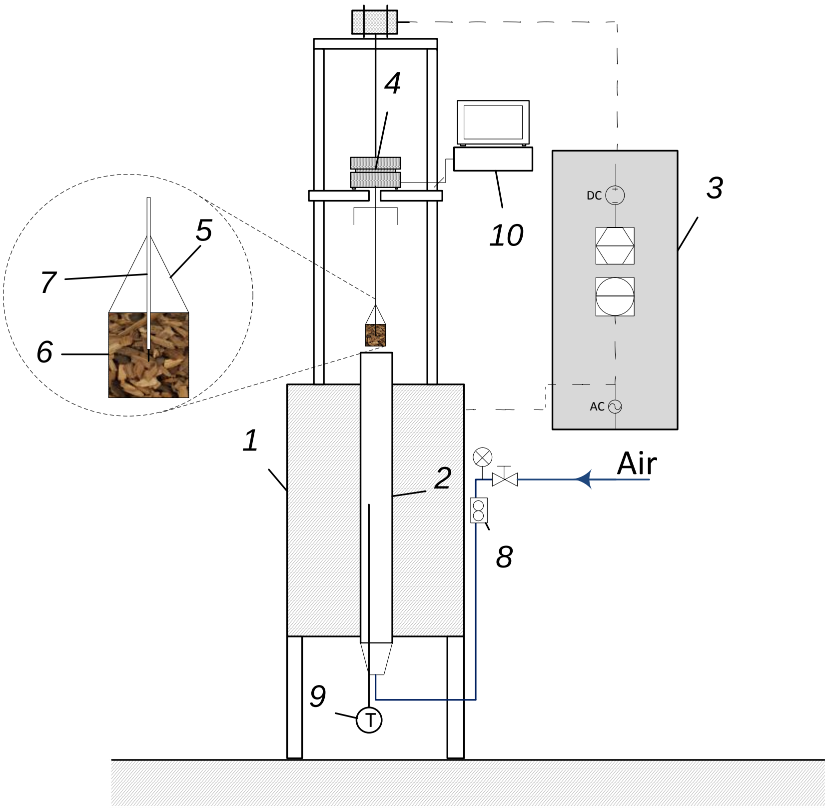

Fig. 1. Biomass mass loss rig: 1 – electrically heated horizontal tubular furnace Nabertherm RS 80/500/13; 2 – tube; 3 – controlled by the flow meter; 4 – digital scale Kern EW 420-3NM; 5 – sample bag with thermocouple; 6 – sample; 7 – sample basket holder; 8 – rotameter air flow detection; 9 – thermocouple air flow measurement; 10 – computer data collection and storage

2.2. The methodology for experimental investigation of moisture content variation in biomass layer during drying process

The second series of experiments was performed in order to determine the effect of primary air and recirculation products to biofuel drying process. Primary air, as well as the recirculation products, is supplied to the furnace through the grate, get saturated with moisture while permeating the layer of biofuel and thereby desiccates it. In order to find out the effect of properties of primary air and recirculation products to drying process, an experimental biofuel drying rig was designed and installed in the lab (Fig. 2). For the experiments the operation parameters were selected to match those of a real 6 MW furnace.

The experimental biofuel drying rig consists of the following main parts: electrical heaters, a steam generator and a drying chamber. Ambient air used for experiments passes through a compressor, a control valve *1* and a rotameter *2* and is preheated as it enters an air duct. The flow rate of drying air is 23.76 m^3/h. This flow rate is selected to reproduce the real processes in a furnace related to biofuel combustion. For air heating, two heating coils *3* are installed in the air duct with the maximum electrical power of 4000 W. In order to achieve precisely the desired temperature of the air supplied to the grate, the power of the heating coils was reduced by a transformer. The air preheated to the desired temperature is supplied through the duct to the drying chamber *4*. Air enters the drying chamber through a steel mesh *5*. The steel mesh consists of two layers so that small particles of biofuel do not drop into the air duct. The holes of the first mesh, through which preheated air flows, have the diameter of 10 mm, and those of the second one have the diameter of 1 mm. Five k-type thermocouples *6* are installed inside the experimental setup for temperature measurements at various points. In the front wall of the drying chamber, an observation opening *7* was installed, to observe the process and reduce the risk of biofuel ignition. The thermocouples are connected to the data acquisition device *8* PICO TC-08. The data of these temperature sensors gives better understand in what points of the biofuel layer drying is more intense and where it goes on slowly.

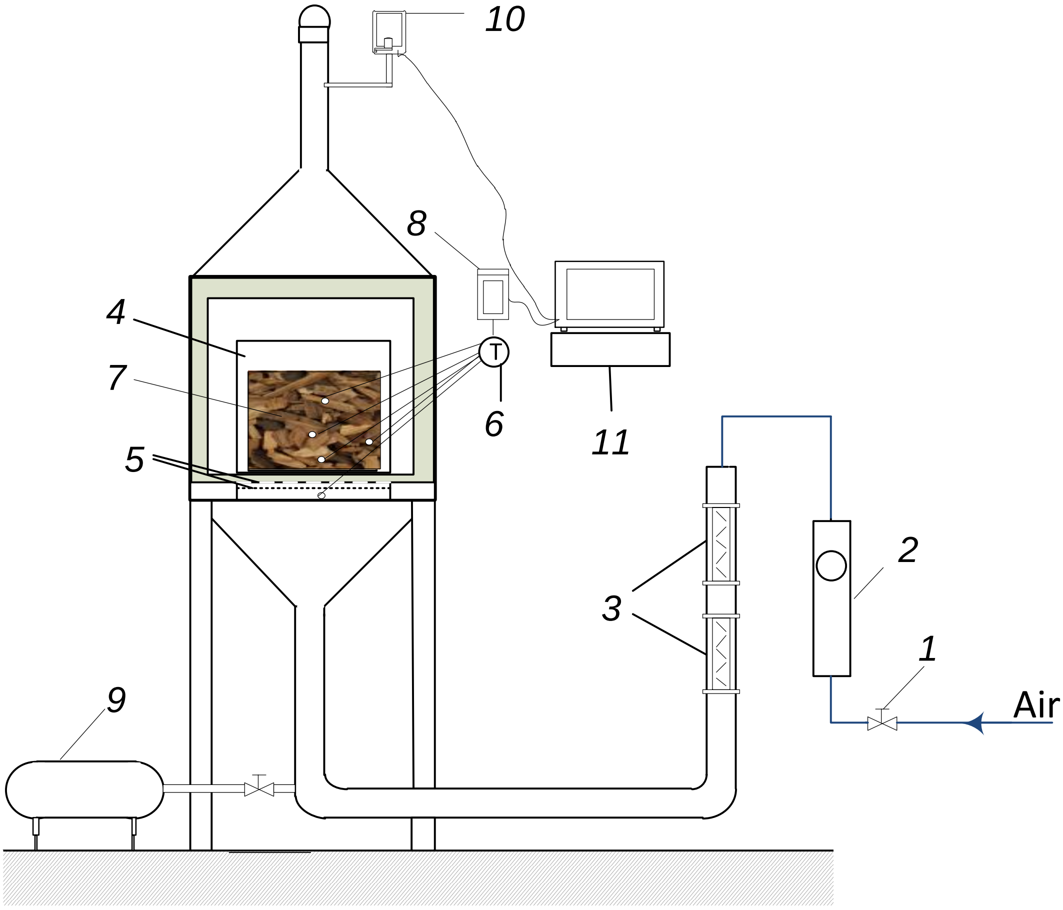

Fig. 2. Biomass drying rig: 1 – control valve; 2 – rotameter; 3 – heating coils; 4 – biomass drying chamber; 5 – steel mesh; 6 – k-type thermocouples; 7 – observation opening; 8 – data acquisition device; 9 – steam generator ; 10 – Testo 454 with a connected RH sensor; 11 – computer data collection and storage

For experiments using steam, a steam generator *9* was installed in the setup. Steam flow rate was adjusted by a valve.

In the beginning of a biomass drying experiment, the entire system was preheated. Air heats to the temperature required for the experiment by flowing around 2 heating coils. During experiments, biofuel was dried in the temperatures of 50 ^{o}C, 100 ^{o}C, 150 ^{o}C, 200 ^{o}C. The temperature of preheated air was measured before flowing through the grate and controlled by the heating coils. After stabilization of the parameters of the unloaded experimental setup, i.e., the selected air flow rate and temperature, the drying chamber (40×33×26.5 cm) was loaded with a 23 cm deep layer of biomass. When using steam in experiments, the supplied steam flow rate was constant in all experiments at 17 g/m^3. The readings of thermocouples were collected and processed using the software of PICO TC-08. The average moisture content of biofuel was estimated by measuring the air humidity at the outflow. Air humidity was measured by a measurement unit Testo 454 with a connected relative humidity (RH) sensor 10 (accuracy, 2% RH of + 2 to + 98% RH). The humidity analyser and the PICO TC-08 unit processing the readings of the thermocouples were connected to a computer *11* for data collection and analysis.

2.2.1. Used samples

For the second experiment were used three kinds of biomass: mix of deciduous tree branches chips with leaves, mix of spines with chips of coniferous tree branches and mix of bark chips with chips of different trees branches. The main characteristics of used samples are presented in Table 1.

Table 1. The characteristics of used samples

Parameter	**Chips of broad-leaved tree branches with leaves**	**Chips of conifer branches with needles**	**Chips of various species of tree branches with bark**
HHV, (kJ/kg)	18630	19785	18998
LVH, (kJ/kg)	17328	18609	17652
Moisture content, %	33	14	36
Ash, %	4.50	7.60	3.50
Carbon, %	49.13	48.53	48.60
Hydrogen, %	5.97	5.39	5.80
Nitrogen, %	0.52	0.79	0.60
Sulfur, %	< 0.01	< 0.01	< 0.01
Oxygen (diff.), %	44.37	45.28	49.99

Before starting the experiments in the biomass drying rig, the samples were soaked up to 60 wt.% to correspond moisture content of biomass which is supplied to heating plants during cold season. The special stainless steel bracket was fulfilled with the wood chips and the bracket inserted into the barrel with water to soak for 16 hours. After it, the bracket was pulled out and leaved to dry for 2 hours.

Another important parameter of biofuel is its particle size, so it was determined using 8 meshes with different fraction and fraction distribution of wood chips presented in Fig. 3.

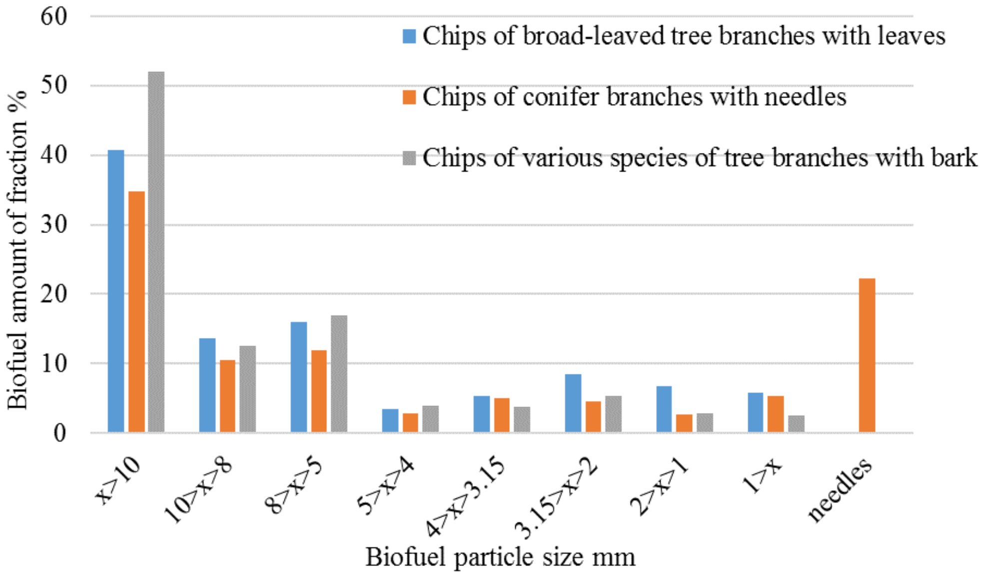

Fig. 3. Fraction distribution of biofuel

3. RESULTS AND DISCUSION

3.1. Biomass mass loss during drying

Supplied biofuel to the heating plants is stored outdoors and affected fuel by weather (rain, snow and etc.) is undried before enters the furnace. The fuel stored outdoors mostly is unusually wet and moisture content reaches up to 60 wt.% or more. Even the existing furnaces are designed to combust the moist fuel, however supplying fuel with moisture content of 60 wt.% into the furnace, it is necessary to intensify the drying process on the grates. Intensification of biofuel drying process in drying zone causes more intensive the biofuel combustion, which could result in a length reduction of the furnace.

Water in biomass occurs in three forms as surface, capillary and bound water. In order to determine the difference of these forms evaporation, the experiment of biomass mass loss during drying at 200 °C temperature was performed. Results shows that a dehydration process starts immediately after sample placement (Fig. 4). According to the changes of sample temperature and no longer observed mass loss, an evaporation process of the wood chips ends after 95 minutes.

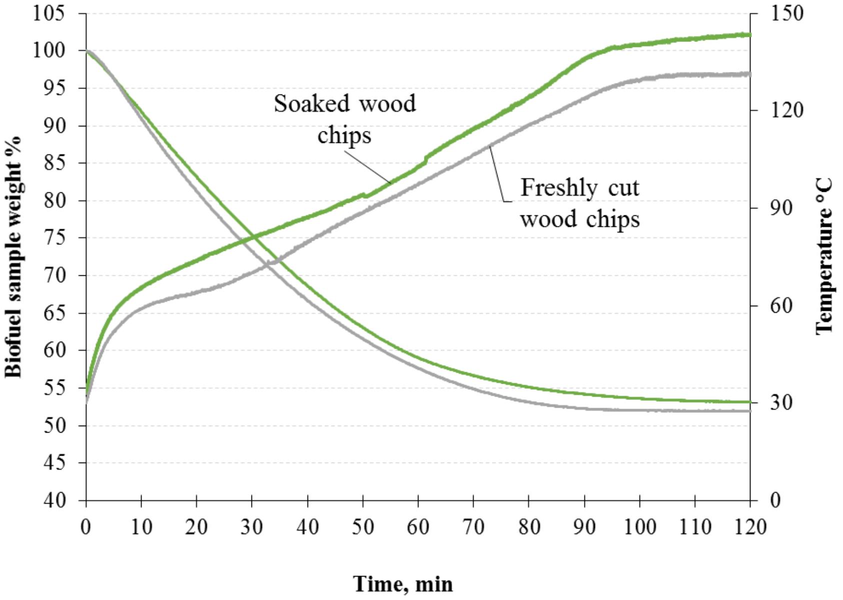

Fig. 4. Freshly cut wood chips and soaked wood chips weight loss over time

Besides results revealed that dehydration of the wood chips does not depend on moisture type (internal or surface). Also results showed that parameters of the soaked samples for 16 hours correspond to fuel stored outdoors, which later is supplied to the furnace.

3.2. Influence of primary air supply to changes of moisture content in a biofuel layer

Particle size distribution of the tree bark samples used for experiments can be very different and this might influence significantly the shapes of the drying curves, therefore, each experiment was repeated five times. The first experiments were performed using preheated air only. Fig. 5 shows the changes of biofuel moisture content with changing temperature of the supplied air. In the chart, the moisture content is normalized to the maximum value. The results of the experiments show that the drying intensity grows as the supplied air temperature grows. In drying layers of all three samples, the intensity was lowest at 50 ^{o}C temperature of the supplied air and highest at 200 ^{o}C. The experiment at the temperature of the supplied air of 50 ^{o}C showed that the moisture content initially present in the conifer chips with needles decreases by only 6% in 90 minutes, and this decrease is even lower, by only 5%, in case of broad-leaved tree branches with leaves and tree branches with bark. In case of repeating the experiments with the supplied air temperature of 200 ^{o}C before entering the grate, drying of the biofuel samples intensified. After 90 minutes, the moisture content in chips of broad-leaved branches with leaves decreases by 24%, for chips of various wood types with bark – by 18%, and for the chips of conifers with needles, the moisture content decreases by even 30%.

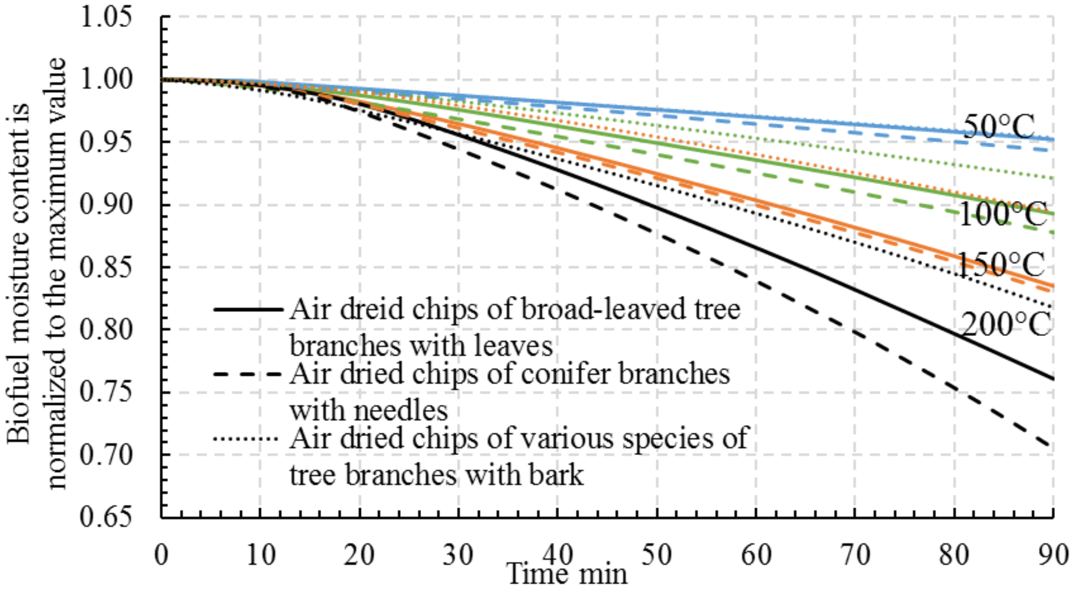

Fig. 5. Average moisture content of the biofuel when changing the primary air temperature

The curves in Fig. 5 show that drying is most intense in the chips of conifers with needles. Chips of conifer branches with needles (containing 22% of needles) (Fig. 3) have largest content of fine (8 > x mm) particles by fractional composition, therefore, the total surface area of the sample is largest. Larger total surface area leads to more intense heat transfer and faster drying of biofuel. This is confirmed by experimental results of drying chips of tree branches with bark. The biofuel sample consisting of chips of tree branches with bark contained the highest amount of coarse particles (x > 10), 52% by mass, and least amount of fine (8 > x) particles, therefore, drying was not as intense as in cases of other analysed biofuel samples.

3.3. Influence of primary air supply and recirculation products to changes in moisture content in a biofuel layer

Flue gas recirculation is installed in the currently operating biofuel boilers. Recirculation means returning flue gas back into the combustion chamber. The biofuel boilers are designed in a way where the recirculation products are supplied into the combustion chamber through the bottom of the grate. In order to intensify biofuel drying in the drying zone of the grate, it is necessary to research not only the influence of primary air to biofuel drying, but the influence of recirculation products as well. Experiments were performed where biofuel samples were dried using air–water mixture, imitating the influence of recirculation products. The obtained experimental results have shown that drying intensity of biofuel layer depends significantly on the temperature of recirculation products and biofuel properties.

Humidity of flue gas was measured during experiments with air-water mixture. The temperatures of air–water mixture were set equal (50 °C, 100 °C, 150 °C and 200 °C) to those of previous experiments where biofuel was dried with preheated air only. The measurement results are shown in Fig. 6. Analysis of the obtained measurement results in Fig. 6a revealed that drying of chips of broad-leaved tree branches with leaves on the grate slows down when water vapour is injected in the process. Biofuel drying in the drying chamber slows down by

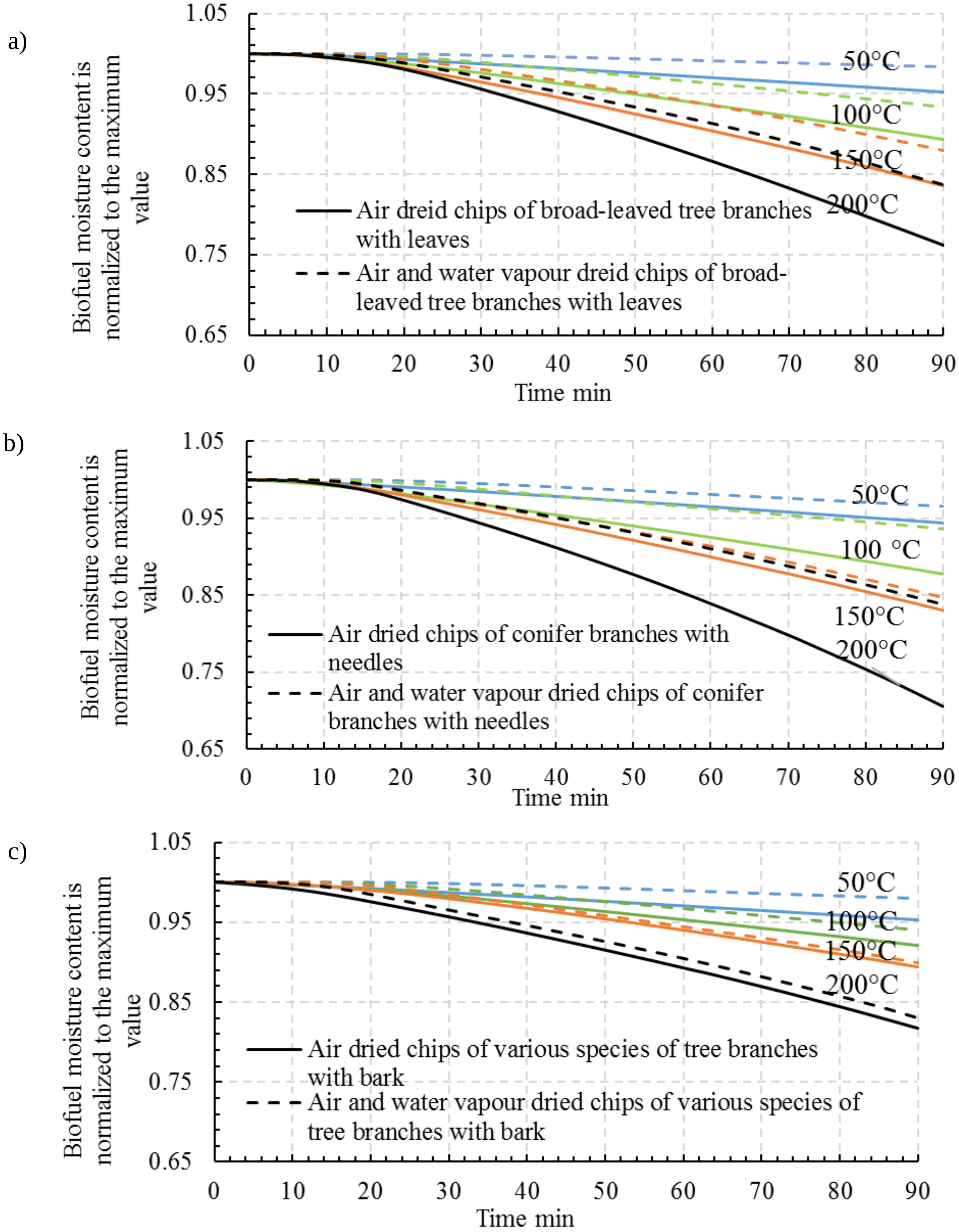

Fig. 6. Changes in biofuel sample moisture content when injecting water vapour: a) chips of broad-leaved tree branches with leaves; b) chips of conifer branches with needles; c) chips of tree branches with bark

5% on average at all the researched temperatures when water vapour is injected. The chart in Fig. 6a shows the trend of larger difference between the average moisture content of the biofuel sample at higher temperature of the supplied drying agent. After 90 minutes of drying chips of broad-leaved tree branches with leaves by air heated to the temperature of 150 °C or by mixture of air and water vapour heated to 200 °C, the residual moisture content of the sample is approximately 17%. Taking into account the obtained results, in case of combustion of moisture-rich chips of broad leaved tree branches with leaves, amount of recirculation products in the drying zone of the combustion chamber must be kept at minimum or its supply must be prevented at all, if possible.

Measurement results of drying chips of conifer branches with needles in Fig. 6b additionally confirm that the recirculation products slow down the drying process on the grate. When drying biofuel with working agents of 50 °C temperature, the drying process goes on slowly and the residual moisture content differs by only a few percent. Comparison of the obtained results show that when drying the biofuel sample by air at the temperature of 100 °C, the average moisture content of the sample after 90 minutes decreases by 11%, and when drying the same sample with air-water vapour mixture, the moisture content decreases by only 7%. It can also be seen from the chart in Fig. 6b that the difference in drying rate is minimal when drying the chips of conifer branches with needles by preheated air or by air-water vapour mixture at the temperature of 150 °C. At the working temperature of air–water vapour mixture of 200°C, the drying rate remains the same as at the temperature of 150 °C.

Intensity of drying process was experimentally analysed with three types of biofuel. As mentioned in Section 3.2, the drying process is slowest for chips of tree branches with bark, due to its fractional composition. Injection of water vapour into the drying process of chips of tree branches with bark slows down the drying process even more (Fig. 6c). The obtained results can be explained as follows: the more humid is the drying agent, the sooner is the condensation point attained and humidity condenses more promptly on the biofuel surfaces. Evaporation of condensed moisture on the surfaces of particles in a biofuel sample consumes additional energy. Therefore, when drying a sample by either preheated air or a mixture of air and water vapour, drying intensity of the biofuel layer differs only slightly when the temperature is increased to 150 °C.

During the primary experiments imitating the influence of the primary air supply and recirculation products to biofuel drying, only the effect of convective processes to drying process was established. The biofuel layer in the combustion chamber on the grate is also affected by radiation from incandescent inner surfaces of the combustion chamber, therefore, the further plans are to analyse the effect of radiation to drying of the biofuel layer.

4. CONCLUSIONS

1. Moisture removal from chips of freshly felled wood and dried soaked wood chips was observed by analysing biofuel mass loss at the temperature of 200 °C with supplied 11 l/min air flow. Moisture removal rate was the same from the sample containing 46% of inner moisture and from the sample containing 18% of surface and 28% of inner moisture.
2. Experimental analysis of drying was carried out with three different types of biofuel. The obtained results have shown that the biofuel granulometry influences its drying intensity. The finer is the biofuel fraction, the higher is its drying rate on the grate. During analysis, drying rate of chips of conifer branches with needles was highest, because this biofuel sample contains largest fraction of fine particles, compared to the other two samples.
3. Experiments of drying were carried out with four temperatures of drying air: 50 °C, 100 °C, 150 °C and 200 °C. Analysis of the obtained results imply that increasing temperature of drying air leads to higher drying rate of biofuel layer on the grate.
4. Experiments with air and water vapour mixture were performed in order to estimate the influence of recirculation products to biofuel drying process in the combustion chamber. Experimental results have shown that the recirculation products slow down the drying process of the biofuel layer on the grate regardless of the type of biofuel supplied to the combustion chamber.

5. REFERENCES

1. European Commission. Reneweble energy. http//ec.europa.eu/energy/renewables/index_en.htm (accessed December 2, 2013).
2. Myllymaa, Tiina, et al. "Wood Chip Drying in Fixed Beds: Drying Kinetics and Economics of Drying at a Municipal Combined Heat and Power Plant Site." Drying Technology 33.2 (2015): 205-215.
3. Yrjölä, Jukka, and Jaakko J. Saastamoinen. "Modelling and practical operation results of a dryer for wood chips." Drying technology 20.6 (2002): 1077-1099.
4. Slepikas, Osvaldas, and Audrius Cereska. "Biofuels drying process efficiency research/Biokuro dziovinimo proceso efektyvumo tyrimai." Science-Future of Lithuania 5.6 (2013): 609-614.
5. Bauer, Robert, et al. "Modelling of grate combustion in a medium scale biomass furnace for control purposes." biomass and bioenergy 34.4 (2010): 417-427.
6. Liu, Yuping, et al. "Novel fluidized bed dryer for biomass drying." Fuel Processing Technology 122 (2014): 170-175.
7. Bengtsson, Peter. "Experimental analysis of low-temperature bed drying of wooden biomass particles." Drying Technology 26.5 (2008): 602-610.
8. Niedermayr, Florian. "Design of a scalable and robust woodchip handling control system."//SDEWES2015-1012.

CYSENI 2017, May 25-26, Kaunas, Lithuania
ISSN 1822-7554, www.cyseni.com

CALCULATION AND COMPARATIVE ANALYSIS OF THE MEAN ENERGY EXPENDED PER ION PAIR BY ELECTRONS IN WATER AND HYDROXYL RADICAL

Yu. V. Kovtun
National Science Center "Kharkov Institute of Physics and Technology"
1, Akademicheskaya St., Kharkov, 61108 – Ukraine
E-mail: Ykovtun@kipt.kharkov.ua

ABSTRACT

Researches of physical and chemical processes occurring in water during the interaction with particles (electrons, ions, photons, etc.) is interesting for a wide range of physical and applied problems in astrophysics, radiation physics, chemistry, medicine and biology, plasma physics, and other branches of science and technology. One of the directions, which invokes a considerable interest in low-temperature plasma physics and its application technologies, includes researches of electric discharges in the liquid and above its surface. While developing any technology, in which electric discharges in a liquid and above its surface will be used, the determination of the main channels of energy expenditure and, accordingly, the total amount of energy expenditure comprises an important task. One of the main channels of energy expenditures are those for ionization by an electron impact, or the so-called ionization cost. The cost of ionization by an electron impact is usually assumed to be a certain mean value of energy spent by an electron for the formation of an ion-electron pair in the substance.

There are different models for calculating the ionization cost, which may be conditionally divided into two basic approaches. In the first approach, the ionization cost value is estimated from the consideration of elementary processes associated with the passage of a monoenergetic electron flow (beam) through the medium. This approach is fully justified when the ionization of the medium is mainly contributed by the primary electron flow (beam). In the second approach, the ionization cost involves the elementary processes occurring in the plasma, where the electrons have the energy distribution function. In any case, there is always the necessity of knowing both the threshold energy values and the cross sections for the elementary processes, which, in turn, have an effect on the finite ionization cost. Irrespective of the model used, the ionization cost calculation always presents an approximation to the real value.

So, in view of the above, it is of interest to calculate and compare the costs of H_2O and OH ionization by electron impact on the basis of two models; the more so, as the calculations of OH ionization costs are absent in the literature. We here consider in detail the both approaches, and using them as the base, carry out numerical calculations.

The present OH ionization cost calculations, based on two models, with the use of the same initial data sets, and the comparison with H_2O ionization cost have shown a somewhat higher W value for H_2O than for OH. The calculation in the framework of the model considering the passage of a monoenergetic electron flow (beam) of energy 15 to 1000 eV through the medium, has demonstrated that for electron energy of 1000 eV the ionization cost for H_2O and OH makes 25.26 eV and 21.65 eV, respectively. We have considered the model taking into account the Maxwell and electron energy distribution functions at temperatures ranging from 3 to 100 eV. At the electron temperature T_e=100 eV, the calculation has shown the W values to be 16.85 eV and 14.5 eV for H_2O and OH, respectively.

Keywords: plasma, cost of ionization, hydroxyl radical, electron impact, water molecule

CYSENI 2017, May 25-26, Kaunas, Lithuania
ISSN 1822-7554, www.cyseni.com

FLAME CHEMILUMINESCENCE AND RADICALS EMISSION RESEARCH DURING COMBUSTION OF SINGLE BIOMASS PARTICLE

M. Sadeckas, N. Striūgas
Lithuanian Energy Institute
Breslaujos str. 3, LT-44403 Kaunas – Lithuania
E-mail: Marius.Sadeckas@lei.lt, Nerijus.Striugas@lei.lt

ABSTRACT

During last decade, the use of biomass for energy production became very important. With increase of biomass usage, the quality of the feedstock for energy production becomes worse. During thermal degradation of biomass various chemical transformation occurs and due to change of fuel properties it is hardly to forecast the whole combustion process. The biggest challenges occurring during combustion is related with an ash issues. Flame and combustion monitoring using chemiluminescence method has received a lot of attention for combustion sensing and diagnostic applications in various fields. For example: flame monitoring in furnaces, combustion optimization, monitoring emitted radicals and to find flame stabilization methods. The main radiative species of radicals in typical hydrocarbon-air flames are CH·, OH·, C2·, CO_2·. Chemiluminescence from these radicals provides information about certain element concentration during combustion process. In various reaction zones emission of radicals are different and can be indicated as important combustion parameters. It is used on purpose to find the ways how to improve combustion performance and furnace or combustor lifetime. The aim of this investigation is the chemiluminescence phenomenon of the main radicals during combustion of single biomass particle by means of atomic spectroscopy method and ICCD camera (based on digital charge-coupled device). In this work, few solid fuel types mainly wood and straw are comparing during combustion. Using atomic spectroscopy method, flame is monitoring and emitted photons at selected wavelength are recorded by Andor program. The results of experimental investigation are summarized and shown as radiant intensity at selected wavelengths. The dependencies of emission intensities on burning regime were determined. Results shows, that when fuel is changing during combustion it is possible to predict the emissions of radicals of different fuels and adjust appropriate regime of combustion.

Keywords: chemiluminescence, biomass, combustion, radicals, spectroscopy, flame monitoring

1. INTRODUCTION

Expanding the use of biomass bioenergy inevitably faces with the deterioration of the characteristics of bio-fuels [1], which directly influences the combustion process and formation various compounds. Burning poor performance biofuels resultes an ash slagging problems [1]. Fly ash deposit on the heat transfer surfaces of the boiler, furnace masonry walls. These things negatively influence the boiler work.

Also, the combustion of biomass mixtures with straw or other agricultural crops, containing additional components such as alkali chloride, causes corrosion of boiler surfaces. Humidity, mineral impurities, biomass particle size are of the main characteristics of biofuels which determines the quality of combustion and combustion equipment work. The potassium content in biofuels is one of the main factors that influence the formation ash and plaque. Chemiluminescence method is used to determine the emission intensity of potassium, sodium, calcium elementsions during combustion of straw, wood, sludge [2].

For example potassium largest exuding intensity is seen at the beginning of combustion, then this value proportionally decreas [3]. Lack of data based on regularities occuring during biofuel thermal decomposition encourages re-searchers to engage in the global experimental and numerical studies. In this work the solid biofuel combustion process optimization, covering the flame in the radicals of the chemiluminescent radiation pattern tests, depending on the combustion conditions, aerodynamic parameters, flame-shaped, excited radical emission intensity levels for assessing the potential for combustion process control limits. The research was based on spectroscopic analysis of the flame. Atomic spectroscopy and high-sensitivity ICCD camera can explore the main radicals in the flame of chemiluminescent radiation pattern, depending on the combustion conditions and fuel parameters.

Chemical excitation, luminescence (glowing, luminescence) by flame is named chemiluminescent phenomenon, which is found in the visible and ultraviolet spectral region. In hydrocarbon flame are four main emitting radicals: OH^-, CH^-, C_2^-, CO_2^-. Visible and ultraviolet wavelength region of the flame spectrum caused by the movement of electrons. The intensive radiation peaks of OH^- radicals usually occur at 283 nm and 306–315 nm. CH^- radicals are found to 390 nm and 431 nm wavelength range. C_2^- radiation intensity maximum value gets at 469–473 nm and 510–516 nm. The main reactions of radicals formation [4]:

$CH^- + O_2 = CO + OH^-$;
$C2 + OH^- = CO + CH^-$;
$C2H + O = CO + CH^-$;
$C + CH^- = C_2^- + H$.

Studies have shown that OH^-, CH^-, CO_2^- intensity is directly dependent on airflow. Monitoring of flame chemiluminescent characteristics is widely used in combustion diagnostics. In particular, OH * and CH * radicals radiant intensity is used to measure the quantity of heat emitted during combustion. In various areas of research flame luminous intensity is measured using multiple photomultiplier or optical fiber cables – fiber. Using these signals are evaluated exuding heat or its relative size. Use of photomultiplier can not provide the broader features, such as the unequal distribution of fuels and processes in recirculation zones [5]. Flame radicals (i.e., OH^-,CH^- , C_2^-) are acting as intermediates which are involved in chemical and thermal reactions during combustion. Early studies have shown that the effect of flame characteristics (including radicals) is relative to the construction of furnaces, burner and fuel-air ratio during combustion. For example, based on the information about the radiating flame radicals, we can draw conclusions on the air-fuel ratio of qualitative justice. Previous studies have also demonstrated that there is a close link between the flame radicals and NOx emissions [6].

Tests were carried out using a Bunsen burner and ICCD camera with interference OH^- and CH^- filters. It was summed up and collected 50 images of the flame with 20 microseconds exposure time. Pictures accumulated and added up in order to obtain a higher contrast. The different fuel and air ratio were set to perform tests and record OH^- and CH^- emission intensity and the results were summarized. Using a certain frequency of sound waves were obtained results of the flame pulsation or part of the flame extension or abruption of the main part of the torch [7].

Chemiluminescence method for capturing the emission of flame has been proposed as an alternative to stoichiometric surveillance and fire control. Mainly this method is used in methane and natural gas flame tests at different fuel-air mixture ratio. Monitoring of the syngas flame is less tested and there are not many studies. The authors in their work explores the possibility of using chemiluminescence based approach and stoichiometry calculations, perform flame emission analysis. This has been used in different amounts of hydrogen enriched fuel mixture. The described results and conclusions show that the OH^- / CH^- ratio, which has been widely used as the best option for methane may not be adequate to monitor the flames with a high hydrogen content of a number of operational (running) intervals. Therefore OH^-/ CO_2^- ratio is proposed to use as a preferable option in flame emission analysis research [8].

More tightening ecological requirements of the combustion of various fuels, occur the need to test the use of biodiesel in gas turbines as an alternative fuel. A comparison was made of treated, untreated diesel fuel and burn-ing Kerosene swirl-type burner. Burning biodiesel mixture of saturated waste gases generated higher NOx concen-tration, but with a lower oxygen content and CO emissions. Also, in the mixture are organic components, which have a catalytic effect, which enables increasing formation of radicals along the flame zone. In this way formed rapid NOx. These compounds also affect the OH^- radicals in the changing oxygen content of the fuel. As the temperature rises, together forming nitrogen oxides [9].

In hydrocarbon flames OH^-, CH^- and C_2^- chemiluminescence emission electron states can be related to the chemical reaction rate, heat release rate and equivalence ratio. OH^- and CH^- radicals chemiluminescence phenomenon were used to detect the flame in gas turbines. Also chemiluminescence relationship between radicals CH^-/OH^- and C_2^-/OH^- was used to determine the local equivalent ratio of laminar and turbulent type of flames [10].

The rational use of fuel in gas combustion processes require efficient combustion control devices, which should have sufficiently fast response time. Typical task points will be: emission of pollutants, the gas temperature or the concentration of soot particles. To achieve the desired results, the most important factors is the use of sensors and their type, properly selected mounting location in the combustion system. Despite the currently existing wide spectrum of diagnostic tools that can provide useful information recording flame, these measures have sub-stantial drawbacks. Practical use of sophisticated sensors is limited at extremely and unstable environmental circumstances due to the high cost of optical equipment and other aspects. In this case, simpler is an optical tech-nique that uses flame emitted radiation, known as chemiluminescence, it has been widely used for combustion diagnostics. When combustion conditions and the chemical process change, it instantly affects emissions and the light that reaches the sensor. CH^- and C_2^- radical chemiluminescence leaves a mark in the reaction zone.

During the experiment, produced a flame images are ICCD camera, in which is the latest generation photo sensors with the option to customize them to the combustion monitoring, control and development of new engineering projects of burners. Digital camera acts as a light-sensitive sensor array. Each pixel signal is an electronic response to the spectral energy distribution. Currently, there are opportunities to capture and view multiple wavelengths emitted by the elements. However, in order to capture a specific radical, OH^-, CH^- or Na^+, K^+, Ca^+ elements ion's radiation intensity either interference filters are used. They miss only a certain length of the spectrum waves with a small margin of error.

Various types of coal, biofuels, peat or mud have significantly more K and Na content compared to wood. During combustion is usually formed of several zones with different temperatures in combustion chamber when changing fuel quality indicators. In the high-temperature combustion zones distinguished by higher amounts of KCl, but the intensity of NaCl when increasing temperature decreas [12].

Furthermore potassium concentrations of emissions during combustion were investigated when high concen-trations peak suddenly appears in the beginning of the combustion within 15–25 seconds. Later K concentration gradually decreasing and remains unchanged. However, by repeating the experiment with the higher 30 mg, 40 mg, 50 mg amount of wood pellets, potassium characterizig peak occurs later because complete combustion of the particles need longer time [13].

Otherwise, was detected in the case of few "green biofuels" samples. One was taken directly from the stored biofuels. A second, rinsed, fresh sample of biofuel was heated in deionized water and then dried. To prepare demineralized sample, biofuel was soaked few hours in HCl solution until the filtrate is free of Cl ions and then dried. Potassium saturated sample is prepared in demineralized sample admixing potassium acetate and deionized water followed by drying.

The results show that saturated potassium and biofuel raw samples combustion K^+ concentration peaks were 5–20 the time intervals, in other samples of potassium concentration was very low [14].

Spectroscopic method can be analyzed by using a laser. Laser-induced spectroscopic breakdown used to quantitatively potassium loss measured at two different environmental circumstances [15].

So chemiliumenescence method is already widely used in flame monitoring combustion of methane, natural gas and synthetic gas mixtures with different fuel - air relationship. However, currently spread use of biofuels in the energy sector, there is a need chemiliumenescence method to adjust the flame monitoring and control equipment together. In this area there are not many experiments conducted investigating radical emission flame. Therefore, the following will be examined biofuel particles of combustion of the main radical emission intensity in the experiment of the particle-granules of ignition to complete combustion.

2. EXPERIMENT

2.1. Laboratory stand and devices

Laboratory stand (Fig. 1) have been used to make an experiment. During combustion are generated radicals. ICCD camera Andor Istar DH734-18U-E3 spectroscopy system are used to capture the radiation intensity of emitted radicals

Laboratory stand consists of CH_4 flat flame burner. Combustion air and natural gas is mixed in the combustion chamber, where later the flame evenly distributed through the cellular plate. On this plate is burned biofuel pellet. Several different types of biofuel samples were used: furniture wood pellets, straw pellets and biofuel wood pellet.

Since the start of combustion ICCD camera recorded pellets ignition and process of combustion. Time and flame frame rate are fixed, so the experiment recorded 50 shots, filming duration of 138.3 seconds. Each flame frame is recorded every 2.8 seconds.

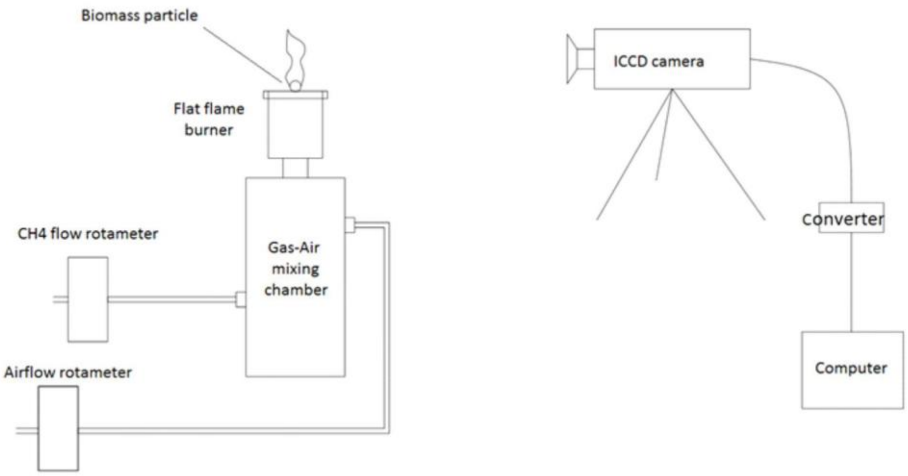

Fig. 1. The principled stand scheme

2.2. Interference filters

Interference filters are used to record major hydrocarbon radicals and other elements emitted during combus-tion process. These filters are designed to spend only a certain wavelength.

Table 1. Interference filters and their wavelength

Filter	OH	CH	K	Na	Ca
Wavelength, nm	310 ± 2 nm	387 ±1 nm	770 ± 2 nm	590 ± 2 nm	620 ± 2 nm

Table 2. The main chemical elements and it‘s concentration in biofuel

	K, mg/kg	Na, mg/kg	Ca mg/kg
Wheat straw pellet	4273	0.7	1689
Wood pellet	519	11.7	1776
Wooden grain	985	5.4	1739

3. RESULTS AND DISCUSSION

3.1. OH^-, CH^- radicals and K^+, Ca^+, Na^+ ion's flame radiation intensity images during combustion

Observing the OH^- radical emission intensity of CH_4 gas (Fig. 2. a) it was determined that flames maintain the homogeneous combustion conditions, i.e. a constant fuel-air mixture ratio, the intensity of OH^- radical radiation does not change. During wooden grain (Fig. 2. d) combustion intensity of OH^- radical emission is higher than during straw pellet combustion (Fig. 2. b). Pictures of Fig. 2 in a, b and d, in time periods from 27.6 to 38.7 seconds show higher intensity because it is the middle of combustion process, when temperature is increasing.

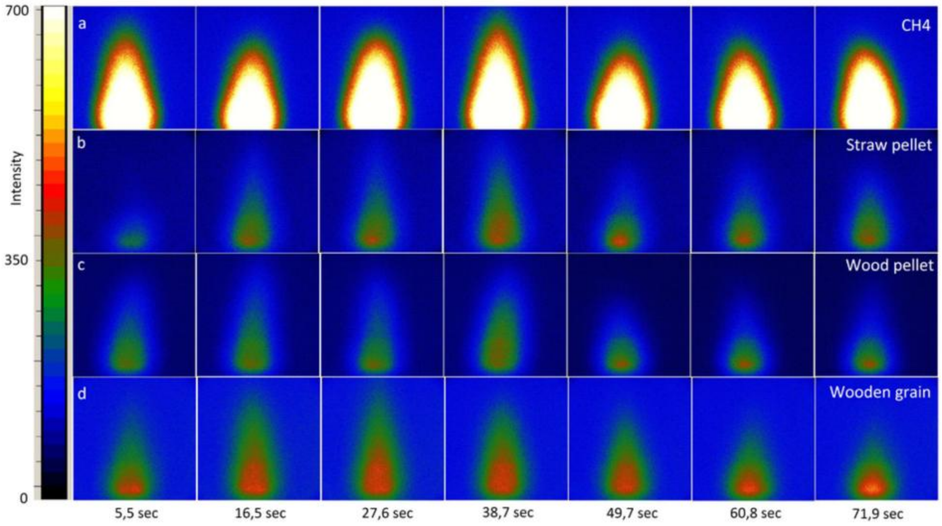

Fig. 2. OH^- radical radiation in (a) CH_4; (b) wheat straw pellet; (c) wood pellet; (d) wooden grain during combustion

Otherwise, CH^- intensity is higher during wooden grain (Fig. 3. d) combustion compared with that of wood pellet (Fig. 3. c). The most intensive radiation of CH^- during wooden grain combustion was recorded at time between 16.5 and 27.6 seconds, while starting from 38.7 second intensity of the combustion process decrea. Also, it depends on form of pellet, it‘s wight and shape. Also, it depends on form of pellet, it’s weight and shape.

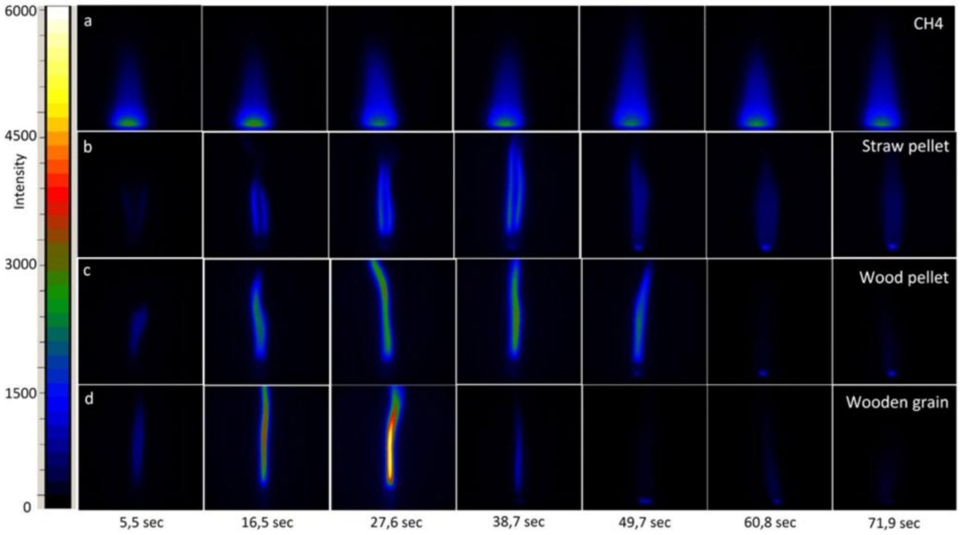

Fig. 3. CH radical radiation in (a) CH_4; (b) wheat straw pellet; (c) wood pellet; (d) wooden grain during combustion

Calcium element ion’s radiation intensity during combustion process in wooden grain (Fig. 4. d) is higher than burning straw pellet (Fig. 4. b). The highest and quickly increased intensity of radiation recorded in wooden grain (Fig. 4. d) combustion process between 16.5 to 27.6 seconds of burning time. Therefore, it is possible to predict that the high-est amount of calcium concentration is in wooden grain. It was found that during wood pellet (Fig. 4. a) combustion process, calcium intensity concentration is more stable compared with wooden grain. In (Fig. 4) flame form consists of two peaks with high intensity.

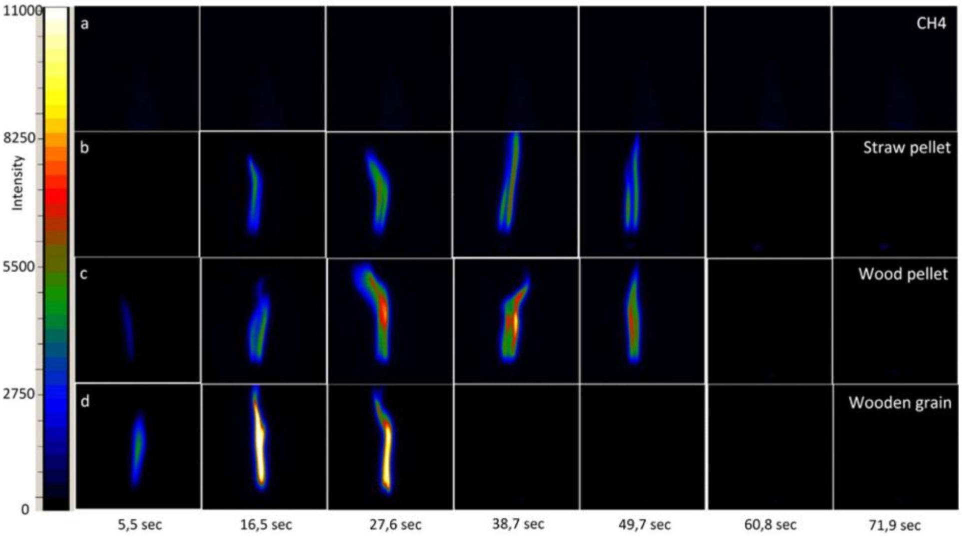

Fig. 4. Calcium element ion’s radiation intensity in (a) wheat straw pellet; (b) wood pellet; (c) wooden grain during combustion

Potassium element ion’s radiation intensity (Fig. 5.) is different compared with calcium and is more intensive at the end of combustion. The most intensive flame was recorded in straw pellet (Fig. 5. b) combustion process, starting from the middle of combustion time 49.7 to 71.9 seconds. It happens because wheat straw is organic and contain a lot of mineral elements. The less intensity is recoded in wood pellet (Fig. 5. c) combustion process. (Fig. 5. b, c, d) show that radiation emission during all combustion process. CH_4 (Fig. 5. a) combustion does not exhibit intensive flame from 5.5 to 71.9 seconds, because in CH_4 flame there is no potassium element or it’s particle.

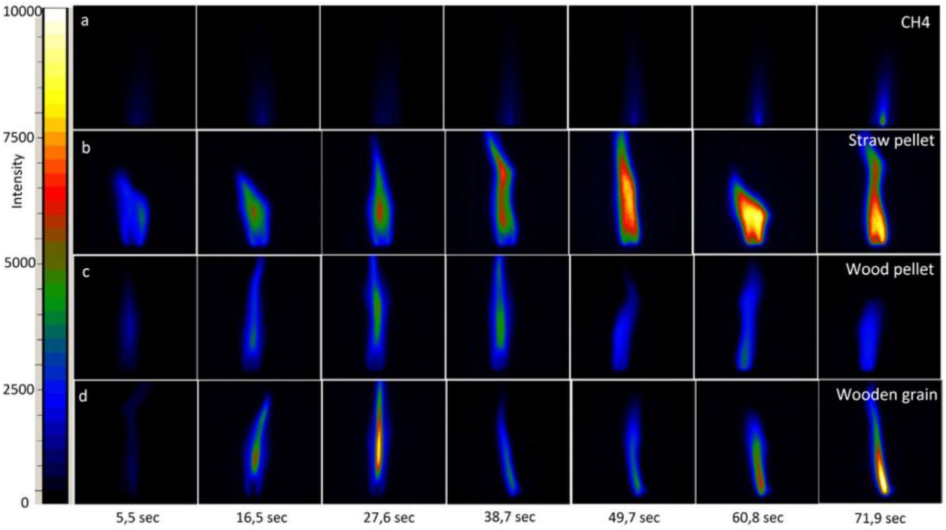

Fig. 5. Potassium element ion’s radiation intensity in (a) wheat straw pellet; (b) wood pellet; (c) wooden straw during com-bustion

Sodium element ion’s radiation intensity is the highest during wooden grain (Fig. 6. d) combustion process at the beginning of burning, at the time between 16.5 and 27.6 seconds. The lowest intensity of flame is detected in wood pellet (Fig. 6. c) combustion process. Radiation intensity trend in Fig. 6. c and d flame pictures is very similar and is very low at the end. The highest flame intensity of sraw pellet (Fig. 6. b) is set at the middle of combustion process. The flame form consists of two peaks (Fig. 6. b), because of pellet form. Combustion process starts at the corners of pellet, where is very thin material layer and more flamable than the centre of pellet.

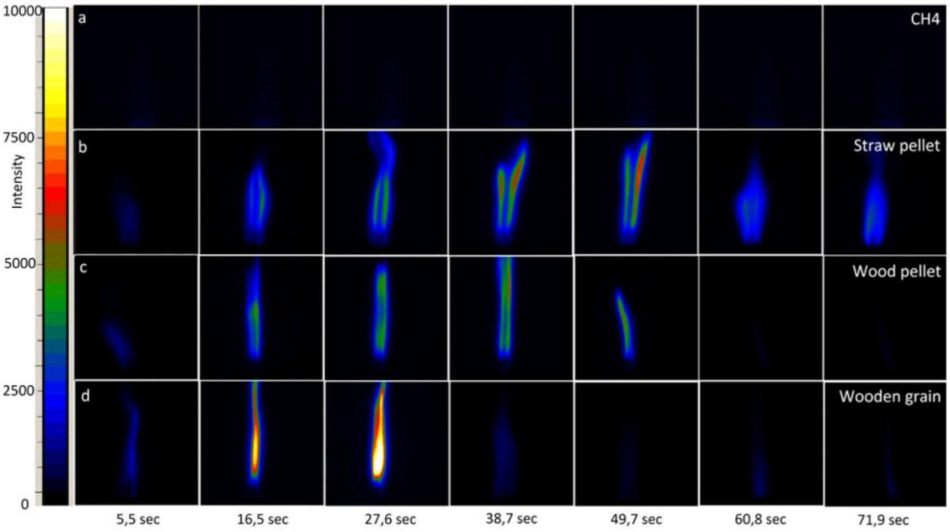

Fig. 6. Sodium element ion’s radiation intensity in (a) wheat straw pellet; (b) wood pellet; (c) wooden grain during combustion

3.2. Release of potassium, calcium and sodium species during combustion of various type biomass

The most intensive radiation of sodium was detected during burning of wooden grain, and the smallest one during burning of simple wood (Fig. 7.). Three biomass types were compared (Fig. 8.) aconcerning the amount of potassium, the highest intensity of radiation was recorded in straw pellet, and the lowest in wooden grain. It was observed potassium emissions in straw during combustion remains constant. This phenomenon occurs because the straw is the agrocultural biomass type and have mineral im-purities, trace elements. The most intensive radiation of calcium was detected during burning of wooden grain, and the smallest one during burning of wheat straw (Fig. 9.).

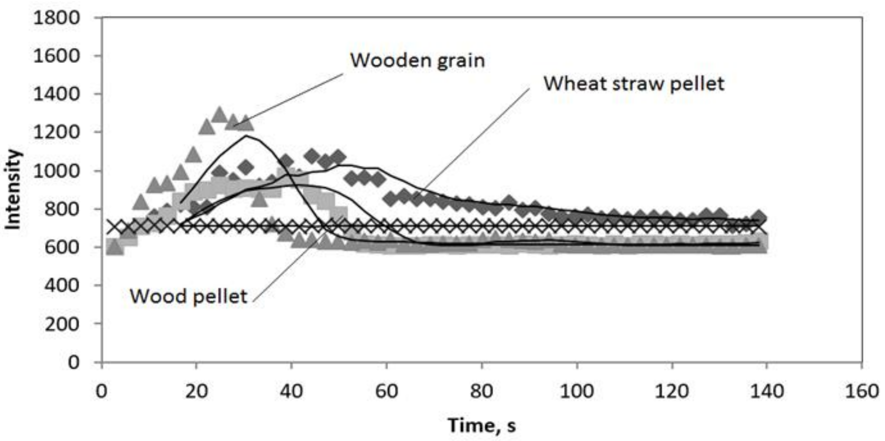

Fig. 7. Na element ion’s radiation intensity during combustion

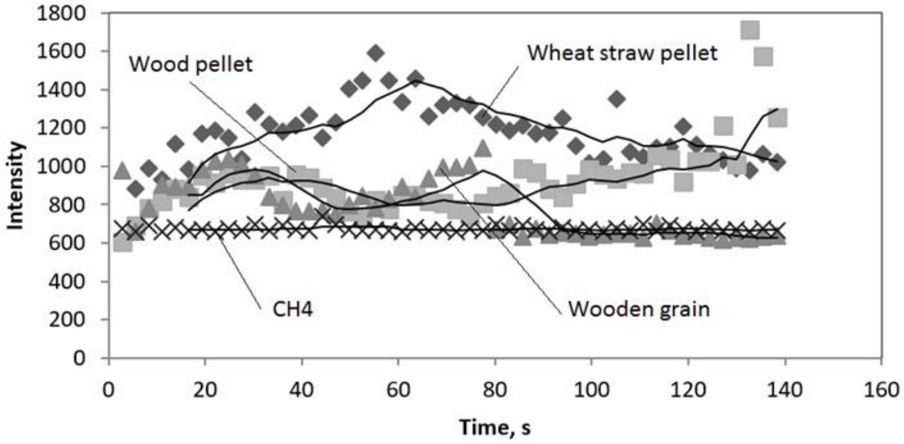

Fig. 8. K element ion’s radiation intensity during combustion

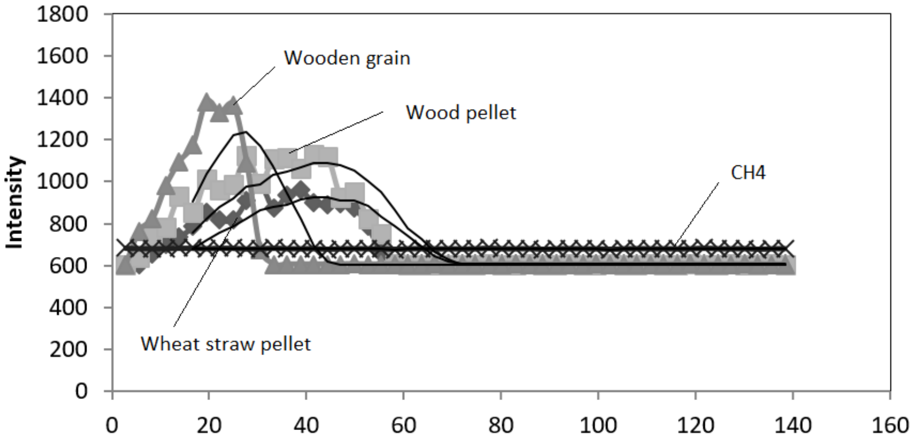

Time, s

Fig. 9. Ca element ion’s radiation intensity during combustion

4. CONCLUSIONS AND SUMMARY OF RESULTS

The investigation of several types of biofuel combustion process was made and the following conclusions were made about the substances contained in the biofuel radiation patterns. During the combustion process of CH_4 gas at constant fuel-air ratio, the emission intensity of main hydrocarbon group of radicals CH^- and OH^- was maintained over time. From the images it can be concluded that sodium and calcium ion‘s intense radiation occurs at the beginning of combustion, from 0 s to 70 s time interval. Potassium ion‘s radiation is more constant during combustion of wood and wooden grain, but in wheat straw radiation is higher.

At the end of the combustion process intensity decrease until completely disappears or becomes minimal. There are other important elements: Na, Ca, K when burning logging waste, bark or straw fuel. For ash, rich in that elements occur boiler surfaces corrosion in the furnace space. So, knowing and predicting emitted elements volume and intensity during combustion, it is possible to carry out the combustion process optimization, flame control and combustion quality.

5. REFERENCES

1. S. Vrubliauskas, E. P. (2010). Biomasės ir iškastinio kuro mišinių deginimo ypatumai. Energetika, 56, 247-253.
2. Mason, P. E., Darvell, L. I., Jones, J. M., Pourkashanian, M., & Williams, A. (2015). Single particle flame-combustion studies on solid biomass fuels. Fuel, 151, 21-30.
3. Mason, P. E., Darvell, L. I., Jones, J. M., & Williams, A. (2016). Observations on the release of gas-phase potassium during the combustion of single particles of biomass. Fuel, 182, 110-117.
4. R. W. Schefer. (1997). Flame sheet imaging using CH chemiluminescence. Combustion Science and Technology, 126(1-6), 255-279.
5. Daniel Guyot, Felix Guethe, Bruno Schuermans, Arnaud Lacarelle, Christian Oliver Paschereit. (2010). CH*/OH* chemiluminescence response of an atmospheric premixed flame under varying operating conditions. [ASME Turbo Expo 2010] ASME Turbo Expo 2010.
6. Nan Li, Gang Lu, Xinli Li & Yong Yan. (2016). Prediction of NOx emissions from a biomass fired combustion process based on flame radical imaging and deep learning techniques. Combustion Science and Technology, 188(2), 233-246.
7. Li, J., Durox, D., Richecoeur, F., & Schuller, T. (2015). Analysis of chemiluminescence, density and heat release rate fluctuations in acoustically perturbed laminar premixed flames. Combustion and Flame, 162(10), 3934-3945.
8. García-Armingol, T., & Ballester, J. (2014). Flame chemiluminescence in premixed combustion of hydrogen-enriched fuels. International Journal of Hydrogen Energy, 39(21), 11299-11307.
9. Kurji, H., Valera-Medina, A., Runyon, J., Giles, A., Pugh, D., Marsh, R., et al. (2016). Combustion characteristics of biodiesel saturated with pyrolysis oil for power generation in gas turbines. Renewable Energy, 99, 443-451.
10. T. S. CHENG, C.-Y. WU, Y.-H. LI & Y.-C. CHAO. (2006). Chemiluminescence measurements of local equivalence ratio in a partially premixed flame. Combustion Science and Technology, 178(10-11), 1821-1841.
11. Trindade, T., Ferreira, A., & Fernandes, E. (2014). Characterization of combustion chemiluminescence: An image processing approach. Procedia Technology, 17, 194-201.
12. Kim, S. S., Kang, Y. S., Lee, H. D., Kim, J. K., & Hong, S. C. (2012). Release of potassium and sodium species during combustion of various rank coals, biomass, sludge and peats. Journal of Industrial and Engineering Chemistry, 18(6), 2199-2203.
13. Zhang, Z., Song, Q., Alwahabi, Z. T., Yao, Q., & Nathan, G. J. (2015). Temporal release of potassium from pinewood particles during combustion. Combustion and Flame, 162(2), 496-505.
14. Jones, J. M., Darvell, L. I., Bridgeman, T. G., Pourkashanian, M., & Williams, A. (2007). An Investigation of the thermal and catalytic behaviour of potassium in biomass combustion. Proceedings of the Combustion Institute, 31(2), 1955-1963.
15. Fatehi, H., He, Y., Wang, Z., Li, Z. S., Bai, X. S., Aldén, M., et al. (2015). LIBS measurements and numerical studies of potassium release during biomass gasification. Proceedings of the Combustion Institute, 35(2), 2389-2396.

CYSENI 2017, May 25-26, Kaunas, Lithuania
ISSN 1822-7554, www.cyseni.com

THE COMBINED HEAT AND MASS TRANSIT PROCESSES OF WATER DEROPLETS IN BIOFUEL TECHNOLOGIES

V. Ramanauskas
UAB "Enerstena"
Raktažolių 21, LT-52181 Kaunas – Lithuania

M. Maziukiene, G. Miliauskas
Kaunas University of Technologies
Studentų 56, LT-51424 Kaunas, Lithuania
E-mail: monika.maziukiene@ktu.lt

ABSTRACT

Liquid spraying has long been used at industrial technologies. The researches of heat and mass transfer in sprayed droplets liquid flows are promoted by the need to define an optimal operating conditions of combined transfer processes. In modern biofuel combustion technologies water spraying is applied. During biofuel combustion process humid flue gases forms. In order to increase the effectiveness and to reduce the thermal nature pollution, heat from removed humid flue gases of biofuel is recovered in condensing economizers.In the contact type condensing economizers for heat recovery from removed biofuel flue gases water is directly sprayed to the gas flow and humidity is condensed out on droplets. In recuperative type economizers water is sprayed at the upper part in economizer in order to improve hydrodynamics of condensate film and flue gas flow.Water spraying is used to humidify air, that is supplied into furnace and to control biofuel combustion process, to clean flue gases from solid particle and to regulate parameters of flue gases that is supplied into condensing economizer.Therefore, for biofuel technologies it is important to know the water droplets transfer processes in a wide boundary conditions range.

In this work the phase transformations of warming droplets in humid gases is modelled.Water droplets heat and mass combined processes are connected by phase transformation regime cycle on droplet surface.This cycle is formed from condensation, transit evaporation and equilibrium evaporation regimes $\tau \equiv 0 \div \tau_{co} \div \tau_{pf} \div \tau_{f}$.The main attention is focused on transit phase transformation condensation and evaporation regimes. In two phase flow the droplet movement is defined by Reynolds number. Phase transformation regimes on droplet surface are distinguished according to this surface temperature variation, which is defined according to heat flux balance model on a droplet surface. Then droplet surface temperature is defined according to iterative numerical scheme.The combined heat flux inside droplet is described according to combined heat transfer model in semi-transparent sphere. The heat flux supplied for a droplet by convection is described according to Newton‘s law, while for convection heat flow description inside droplet the modified Fourier‘s law is applied. Furrier number time scale was applied to summarize the modelling results.The transfer processes interaction is taken into account with the Stefan‘s hydrodynamic flow, with droplet slipping in gases and with radiation impact.

The factors defining phase transformation cycle of water droplets sprayed in biofuel flue gases are: flue gases temperature and humidity, water temperature and droplets dispersity, as well its heating process. These factors influence for water droplets phase transformations at biofuel combustion technologies is presentedThe defining factor of heat transfer is droplet slipping intensity, when heat is recovered from relatively low temperature flue gases. When flue gases temperature rises, the radiation impact increases and radiation as well as droplet slipping factors are equivalent in high temperature flue gases. Droplets heat and mass transfer parameters function $\overline{P}(Fo)$ distributions are universal in aspect of droplets dispersity in "c" heat transfer case.This allows to optimize the numerical modelling of water droplets heat and mass transfer, when droplet is sprayed in biofuel flue gases. It is enough to simulate the phase transformation cycle of freely chosen diameter and according to its results it is possible to define the universal functions $\overline{P}_{\text{"}c\text{"}}(Fo)$ for the desirable droplets dispersity. These functions can be easily transformed into individual functions$P(\tau)$ based on individual parameters P_0 and a_0 / R_0^2. At the combined droplet heating case, the phase transformation cycle will be individual for each droplet.

Keywords: biofuel technologies, water spraying, droplets, phase transformation, heat recovery

CYSENI 2017, May 25-26, Kaunas, Lithuania
ISSN 1822-7554, www.cyseni.com

AN INVESTIGATION OF THE BALANCE PRINCIPLE IMPLEMENTED BY A NON-INVASIVE INTRACRANIAL PRESSURE MEASUREMENT METHOD BY MEANS OF A COMPUTATIONAL MODELING

Edgaras Misiulis, Algis Džiugys
Lithuanian Energy Institute
Laboratory of Combustion Processes
Breslaujos st. 3, LT-44403 Kaunas – Lithuania
E-mail: edgaras.misiulis@lei.lt, algis.dziugys@lei.lt

ABSTRACT

Clinically safe and accurate measurement of intracranial pressure (ICP) is crucial for the secondary brain damage prevention. There are two ICP measurement method groups: invasive and non-invasive. Invasive methods are clinically unsafe, therefore, safer non-invasive methods are being developed worldwide. One of the non-invasive ICP measurement methods implements balance principle, which states, that if the blood flow velocity is equal between intracranial ophthalmic artery (IOA) segment and extracranial ophthalmic artery (EOA) segment, then the acting pressures ICP on IOA and external pressure (Pe) on EOA are also equal.

In order to investigate an application of a balance principle for a non-invasive ICP measurement a computational model incorporating a fluid-structure interaction (FSI) module was created. Computational model was used to simulate the non-invasive ICP measurement method by taking into account a time-dependent behavior of a deformable ophthalmic artery (OA) and its interaction with a pulsatile blood flow.

It was found, that extra balance pressure term incorporating the hydrodynamic pressure drop ΔABP, which is evaluated between axial center of the IOA and EOA, has to be added into the balance equation and the corrections on a difference between the velocity of blood flow in the IOA and EOA have to be made, due to a difference in blood flow rate in IOA and EOA.

Keywords: intracranial pressure, non-invasive, balance principle, ophthalmic artery, fluid-structure interaction

1. INTRODUCTION

Abnormal intracranial pressure (ICP), which can cause secondary brain damage, can be induced by a traumatic brain injury or due to a chronic illness [1]. Generally, prevention of secondary brain damage in severe cases is crucial for saving patients' lives or otherwise for non-compromising social welfare. Prevention of secondary brain damage mainly consists of several procedures, which includes ICP monitoring and a clinical surgery if needed in order to maintain ICP in normal limits; for a patient in a supine position normal ICP limits are 7–15 mmHg [2].

ICP monitoring can be performed in two distinct ways: invasively and noninvasively. Invasive methods have only proven to be accurate in short term, due to the need of calibration – a zero drift is a common problem, also an implementation of invasive methods requires qualified neurosurgeons and inherit a clinical unsafety, due to possible infections [3]. Noninvasive methods are clinically safe and thus are being widely developed [4].

One of the noninvasive ICP measurement methods implements a balance principle and a unique OA morphological property [5]; assessed clinical research on human OA shows that in general OA crosses several different segments: intracranial ophthalmic artery segment (IOA), which is inside the skull, optic canal segment (OC) and extracranial segment (EOA), which is in the eye socket [6].

OA is a first major bifurcation of ICA and supplies oxygenated blood to the eye [6]. Blood flow and arterial blood pressure (ABP), which is a pressure inside arteries (stretches them), is generated by a heart and further transferred via circulatory system, thus also reaching OA. IOA segment is inherently affected by ICP, which is the outside pressure of artery (contracts it), while EOA is basically unaffected by any additional outside pressure [7]. So the basic idea is to artificially add Pe on the EOA segment by a specifically designed head mask so that the comparative evaluation of ICP could be performed.

Head mask and measurement device consists of several equipment in which the most vital are external air pump, inflatable cushion, rigid chamber, ultrasound device and a signal processing unit. During ICP measurement the air is regularly pumped (approximately increasing Pe by 2 mmHg on every 10 heart pulses) to the inflatable cushion of which part of a surface surrounds the eye while other part is enclosed by a rigid chamber. Measurements of blood flow velocity in IOA and EOA segments are performed by ultrasound waves generated by Two Depth Transcranial Dopler (TDTD) device that is mounted on a head mask's rigid chamber while being enveloped by the cushion. It is oriented towards OA in the most optimum manner. Recorded signals representing a relative blood flow velocity profile, thus only the maximum velocity profile values are used to minimize any noise induced errors, are transferred to a signal processing unit where further data operations are made to obtain ICP value, given the assumptions of balance principle holds [8].

Balance principle states that ICP = Pe, if the blood flow velocity in IOA and EOA is also equal. Actually, as only the relative blood flow velocity could be measured using ultrasound, due to the fact that obtained signal intensity is dependent on the angle of incident ultrasound beam and a blood flow direction, and there can be inherited IOA and EOA cross-sectional area differences, the way to eliminate these accuracy influencing phenomena is to divide systolic and diastolic values of velocities for IOA and EOA separately. Commonly, more sophisticated methods use similar divisions etc.: pulsatility index (PI), resistivity index (RI) or any other comparative index [9, 10]. For example RI is calculated as follows:

$$RI = \frac{u_{sys} - u_{dias}}{u_{dias}} \tag{1}$$

The following assumptions are still to be made:

- OA mechanical properties are similar across its length (artery length is around 30 mm);
- Pressures acting in OA segments will deform them uniformly;
- By taking maximum and minimum blood flow velocity values at IOA and EOA error of time lag or shift of values in time will be eliminated.

Clinical assessments shows, that approximately similar PI, RI value at different segments corresponds to the condition, when ICP = Pe [11].

A theoretical one dimensional model of blood flow in an arteries using finite element method was implemented by [12]. Authors [6] employed an open source software CMGUI (www.cmiss.org/cmgui) to digitize centerline of the ophthalmic artery and a few other major arteries (ICA, ACA, MCA) using key nodes and a one-dimensional cubic Hermite mesh from a Computed Tomography Angiography (CTA) image. Although in their study patient-specific case was investigated, although for simplicity artery wall was assumed as rigid.

[13] investigated two different mechanical models for artery tissue behavior: model HI – homogeneous, single-layer, isotropic model and model HA – non-homogeneous, single-layer, fiber-reinforced anisotropic model, although ABP was neglected.

The aim of the study was to develop numerical model incorporating OA and acting pressures and asses the use of RI for an evaluation of noninvasive ICP.

2. COMPUTATIONAL METHOD

Numerical model comprising of a pulsating blood flow, deformable straight OA and the blood flow-OA wall interaction was developed using COMSOL 5.1 to assess the use of RI for a noninvasive ICP evaluation. Following assumptions were made:

- Blood flow in OA is laminar and starts as a fully developed flow;
- Blood is treated as a homogenous, incompressible Newtonian fluid;

- OA wall is treated as a non-homogenous and anisotropic, due to a layered artery structure and also as a nearly incompressible material.

Time-dependent 3D fluid-structure interaction (FSI) numerical simulations that included inertial terms were performed with a developed numerical model. One simulation covered 60 heartbeat pulses. Initial heartbeat pulse was used to change the state of a system from initial to one that could be regarded as a diastolic state. ICP was applied on the outside wall surface of IOA segment. Values of ICP was (0; 10; 20; 30) mmHg depending on a simulation, while afterwards it was prescribed to remain constant according to eq. (11). Pe was applied on the outside wall surface of EOA segment according to eq. (12) within limits of (0, 38) mmHg.

Laminar inflow and outflow pressures were prescribed on the OA inlet and OA outlet, respectively, in accordance with an assumption that a provided waveform of a blood flow velocity in the IOA segment Fig. 1 is similar to the waveform of ABP and only the absolute values differ. It is important to prescribe the absolute ABP, because OA wall mechanical behavior is dependent on it, ABP limits were (40; 80) mmHg.

The initial heartbeat pulse was used to increase the ABP from 0 to 80 mmHg at the OA inlet and also increase the pressure on the OA outlet with a defined function $P_{out}(t)$ to form a hydrodynamic pressure drop between the OA inlet and the OA outlet at the distance L_{exit}. Formed pressure drop generated a diastolic velocity inside OA, and in further periods the pressure at the inlet boundary varied according to a function $P_{in}(t)$, while outlet pressure was held constant P_{dist} at specific distance L_{exit}, thus generating a similar blood flow velocity waveform compared with a provided experimental data.

The end surfaces of OA vessel walls were prescribed to be immovable and OA could only expand and contract, no twisting or bending was permitted. OA mechanical wall behavior was described by a fiber-reinforced double layer model.

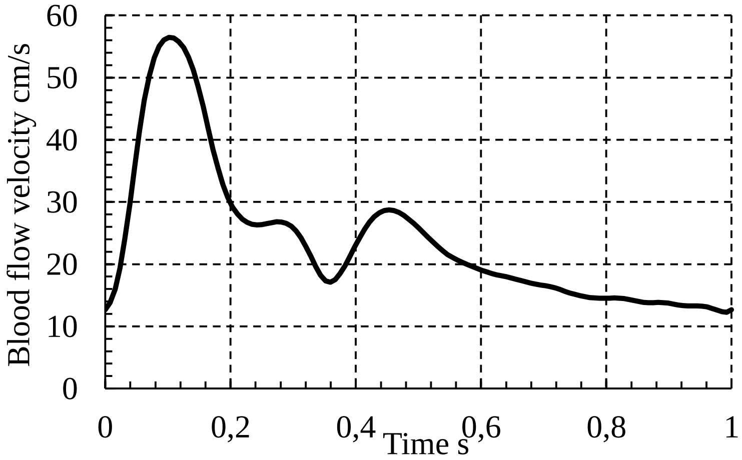

Fig. 1. Mean blood flow velocity waveform in OA obtained through clinical measurements from “VITTAMED” (mean from 25 measurements) and implemented in our simulations

2.1. Navier-Stokes equations for blood flow domain

For an incompressible blood flow Navier-Stokes equations is as follows:

$$\rho_{\text{blood}}\nabla\cdot\mathbf{v}=0 \tag{1}$$

and

$$\rho_{\text{blood}}\frac{\partial\mathbf{v}}{\partial t}+\rho_{\text{blood}}(\mathbf{v}\cdot\nabla)\mathbf{v}=\nabla\cdot[-p_{blood}\mathrm{I}+\mu_{\text{blood}}(\nabla\mathbf{v}+(\nabla\mathbf{v})^{T})] \tag{2}$$

The conservation of mass is represented by the continuity equation (1), while the conservation of momentum by equation (2).

2.2. Fiber-reinforced double layer model for OA wall mechanical behavior

Fiber-reinforced double layer is a non-homogeneous, anisotropic material model based on the Fung's material model [14]. Fung's material model implements only the exponential function for the high loading regimes while the fiber-reinforced double-layer model also describes the low loading regimes by implementing the isotropic ground structure. Isotropic ground structure is described by neo-Hookean material model, while anisotropic part comes from double-layer that represents the layered structure of arterial collagen.

For a material with two families of fibers strain energy is described in the following form:

$$W_s(I_1, I_4, I_6) = W_g(I_1) + W_f(I_4, I_6) + W_{vol} \qquad (3)$$

were $W_g(I_1)$ captures isotropy of ground structure and $W_f(I_4, I_6)$ captures anisotropy of fiber structure, while W_{vol} defines the volumetric strain energy density and resolves nearly incompressibility, I_6 represents the square of the stretch in the direction of the second family of fibers.

Fiber-reinforced double layer strain energy density function is as follows:

$$W_s = \frac{1}{2}\mu(I_1 - 3) + \frac{k_1}{2k_2}\sum_{i=4,6}\left\{e^{k_2(I_i-1)^2} - 1\right\} + \frac{\kappa}{2}(J_{el} - 1)^2 \qquad (4)$$

where μ, k_1, k_2 are positive material constants, κ is initial bulk modulus and μ is the shear modulus. When exhibited to small stresses the material response is isotropic. If stresses are large, then exponential term takes effect, which means that artery fibers are extended and gives stiffening effect to the material. For each layer the form of strain-energy function is the same but the material constants and fiber orientations are different.

The associated Cauchy stress tensor is as follows:

$$\boldsymbol{\sigma} = -p\boldsymbol{I} + \mu\boldsymbol{B} + 2k_1(I_4 - 1)e^{k_2(I_4-1)^2\boldsymbol{m}\otimes\boldsymbol{m}} + 2k_1(I_6 - 1)e^{k_2(I_6-1)^2\boldsymbol{m}'\otimes\boldsymbol{m}'} \qquad (5)$$

were $\boldsymbol{B} = \boldsymbol{F}\boldsymbol{F}^T$ is the left Cauchy-Green tensor, $\boldsymbol{M}$ is a family of collagen fibers preferred direction, and $\boldsymbol{m}' = \boldsymbol{F}\boldsymbol{M}'$, $\boldsymbol{m} = \boldsymbol{F}\boldsymbol{M}$. Fiber-reinforced double layer model was successfully used by [15] by modeling arterial tissue behavior. Used OA wall properties are given in Table 1.

Table 1. ICA Adventitia and Intima-Media mean dissected vessel wall parameters for fiber-reinforced double layer model provided by [16]

ICA and OA* parameters	**Adventitia**	**Intima-Media**
Isotropic, c_{10}, kPa	28.3	17.6
Anisotropic, k_1, kPa	112.1	21.3
Anisotropic, k_2	100.6	17.3
Fiber angle, β, deg	31.8	9.8

2.2.1. Local coordinate system for a fiber orientation

In case artery can be considered as a straight tube, geometry of vessel wall then can be described by a cylindrical coordinate system consisting of three unit vectors $\boldsymbol{\alpha}, \boldsymbol{\theta}, \mathbf{R}$ prescribing axial, tangential and radial directions, respectively. This model assumes that collagen fibers are laying helically with respect to the circumferential direction. In the non-deformed configuration, the fiber orientation in local frame are defined by two unit vectors $\mathbf{f}_x$ and $\mathbf{f}_y$ that are in constant angles

$\pm\gamma$ with circumferential direction, and they lie in a plane that is normal to the surface of a tube, which is composed of $\boldsymbol{\theta}, \mathbf{R}$ tangential and radial directions. In this case unit vectors $\mathbf{f}_{\boldsymbol{a}}$ and $\mathbf{f}_{\boldsymbol{t}}$ with respect to cylindrical coordinate system $(\boldsymbol{\alpha}, \boldsymbol{\theta}, \mathbf{R})$ are as follows:

$$\mathbf{f}_{\boldsymbol{a}} = (0, \cos\gamma, \sin\gamma) \tag{6}$$

$$\mathbf{f}_{\boldsymbol{t}} = (0, \cos\gamma, -\sin\gamma) \tag{7}$$

2.3. Fluid-structure interaction method

A boundary between OA and blood is treated as a fluid-structure interface. Arbitrary Lagrangian-Eulerian (ALE) formulation is used to describe deformations of blood domain mesh [17]. OA wall is formulated by Lagrangian description on a material reference frame while blood domain is formulated by Eulerian description on a spatial reference frame. Blood flow velocity **v** is obtained by solving Navier-Stokes equations. Total stress **f** applied by blood on OA wall is calculated as follows:

$$\mathbf{f} = \mathbf{n} \cdot \left\{-p_{blood}\mathrm{I} + \left(\mu_{\mathrm{blood}}(\nabla\mathbf{v} + (\nabla\mathbf{v})^{T})\right)\right\} \tag{8}$$

where p_{blood} is the applied blood pressure, μ_{blood} is the dynamic blood viscosity, **n** is the outward normal to the boundary, I is the identity matrix. The transformation of the stress have to be made, due to calculations of blood flow velocity and OA wall performed in different configurations, by $\mathbf{F} = \mathbf{f} \cdot dv/dV$, where dv is a scale factor of mesh element for a spatial reference frame and dV for a material reference frame. Blood domain boundaries are affected by OA wall acting as a moving wall through structural velocities calculated by $(\partial\mathbf{u}_{\mathrm{wall}})/\partial t$, where $\mathbf{u}_{\mathrm{wall}}$ is displacement of OA wall.

2.4. Basic model parameters

Parameters presented in Table 2, describing blood flow, OA wall and other values were used throughout all numerical simulations. All velocity values were obtained from clinical measurements performed by “VITTAMED” organization.

Table 2. Basic parameters

Blood flow parameters	**Parameter**	**Value**	**Units**
dynamic viscosity [18]	μ_{blood}	0.003675	$\mathrm{kg \cdot m^{-1} \cdot s^{-1}}$
density [19]	ρ_{blood}	1060	$\mathrm{kg \cdot m^{-3}}$
OA parameters	**Parameter**	**Value**	**Units**
density [20]	ρ_{OA}	1100	$\mathrm{kg \cdot m^{-3}}$
initial lumen diameter	d_{lumen}	1.3	mm
initial outer diameter [21]	d_{outer}	1.477	mm
full length [22]	L_{OA}	25.783	mm
IOA length [22]	L_{IOA}	4.116	mm
Optic canal length [23]	L_{OC}	12	mm
EOA length [22]	L_{EOA}	9.667	mm
wall thickness [24]	h_w	0.177	mm
Other parameters	**Parameter**	**Value**	**Units**
Heart beat period [25]	T	1	s
Initialization time	t_{init}	1	s
Time when $Pe =$ const	t_c	2	s
Time of Pe loop	t_P	3	s

Systolic velocity	u_{sys}	56.48	cm/s
Mean systolic velocity	$u_{sys_{mean}}$	28.24	cm/s
Diastolic velocity	u_{dias}	12.28	cm/s
Mean diastolic velocity	$u_{dias_{mean}}$	6.14	cm/s
Systolic pressure [26]	P_{sys}	120	mmHg
Diastolic pressure [26]	P_{dias}	80	mmHg
ICP step	s_{ICP}	10	mmHg
Amplitude of ICP	A_{ICP}	Depends on current model nr. m_c	mmHg
Amplitude of Pe	A_{Pe}	50	mmHg
Pe step	s_{Pe}	2	mmHg
ABP(t) interpolated experimental values in IOA	P_{IOA}		mmHg
ABP at distance L_{exit}	P_{dist}	70.15	mmHg
Exit distance	L_{exit}	25.63	cm

Exit distance L_{exit} was calculated as follows:

$$L_{exit} = \frac{d_{lumen}^2 (P_{sys} - P_{dias})}{32\mu_{blood}(u_{sys_{mean}} - u_{dias_{mean}})} \tag{9}$$

ABP at distance L_{exit} was obtained through following equation:

$$P_{dist} = P_{sys} - \frac{u_{sys_{mean}}(P_{sys} - P_{dias})}{(u_{sys_{mean}} - u_{dias_{mean}})} \tag{10}$$

2.5. Model geometry and boundary conditions

OA model consisted of blood domain Ω_{blood} and two layered OA wall domains Ω_{media} and $\Omega_{adventitia}$ Fig. 2.

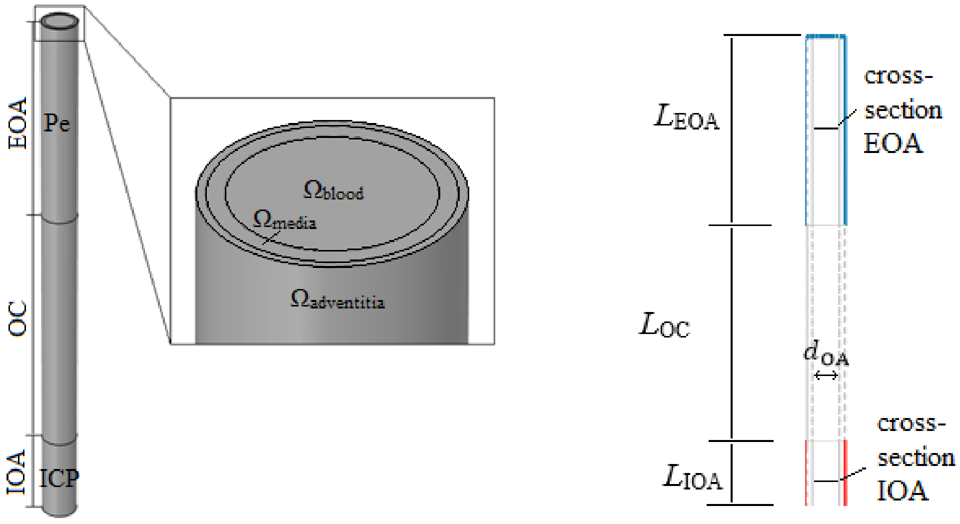

Fig. 2. Model geometry showing IOA, OC, EOA segments, blood and OA media and adventitia layer domains, boundaries of acting pressures Pe and ICP together with a cross-section scheme of OA and planes where data for evaluations was collected

Model boundary functions were prescribed as time dependent functions. Laminar inflow and outflow boundary conditions conserve the inlet and outlet diameters and the laminar blood flow profiles at the specified inflow and outflow lengths, while hydrodynamic pressure drop is calculated accordingly.

ICP was prescribed as a pressure function $ICP(t)$ acting on the surface of an outside IOA wall segment as follows:

$$ICP(t) = A_{ICP} \begin{cases} \dfrac{t}{t_{init}}, & t < t_{init} \\ 1, & t \geq t_{init} \end{cases} \tag{11}$$

Pe was prescribed as a pressure function $Pe(t)$ acting on the surface of an outside EOA wall segment as following:

$$Pe = \begin{cases} Pe_b, & t > t_{init} \\ 0, & t \leq t_{init} \end{cases} \tag{12}$$

where Pe_b was prescribed as follows:

$$Pe_b = s_{Pe} \begin{cases} \dfrac{t - \text{floor}\left(\dfrac{t}{t_P}\right) t_P}{T} + \text{floor}\left(\dfrac{t}{t_P}\right) - 1, & t - \text{floor}\left(\dfrac{t}{t_P}\right) t_P < T \\ \text{ceil}\left(\dfrac{t - t_P}{t_P}\right), & t - \text{floor}\left(\dfrac{t}{t_P}\right) t_P \geq T \end{cases} \tag{13}$$

Laminar inflow pressure function $P_{in}(t)$ acting on the surface of OA blood domain inlet was prescribed as follows:

$$P_{in} = \begin{cases} \dfrac{P_{dias} t}{t_{init}}, & t < t_{init} \\ P_{IOA}, & t \geq t_{init} \end{cases} \tag{14}$$

Laminar outflow pressure function $P_{out}(t)$ acting on the surface of OA blood domain outlet was prescribed as follows:

$$P_{out} = \begin{cases} \dfrac{P_{dist} t}{t_{init}}, & t < t_{init} \\ P_{dist}, & t \geq t_{init} \end{cases} \tag{15}$$

2.6. Solver properties

Parallel sparse direct linear system solver PARDISO in conjunction with a nonlinear fully coupled damped-Newton method was used together with the generalized-α time-dependent solver for numerical simulations. Damping factor for a nonlinear Newton method was set to be constant and equal 1 and the Jacobian update was set to minimal (reuse the Jacobian for several nonlinear systems whenever deemed possible). Absolute tolerance for all variables: pressure, auxiliary pressure, displacement field, velocity field, spatial coordinates was set to be $5\cdot10^{-4}$, while the maximum time step was 0.004 s. At times when gradients were high, to resolve study on such tolerances, time step decreased up to a value of 10^{-6} s.

3. RESULTS AND DISCUSSION

RI values obtained at IOA and EOA cross-sections as shown in Fig. 2 with ICP limits of (0; 30) mmHg and Pe limits of (0; 38) mmHg are depicted in Fig. 3. A linear increase of RI_{IOA} values with an increase in Pe is related to the systolic and diastolic blood flow velocity ratio change. Evaluation of these velocities showed that both systolic and diastolic values of blood flow velocity were decreasing with an increase in Pe, although decrease in diastolic blood flow value was relatively higher compared with a systolic blood flow velocity. As blood flow rate is assumed to be constant so the increase in Pe, which only acts on the outside wall surface of EOA segment also affects the cross-sectional area of IOA segment, pushed some of the blood flow volume into the connecting volume. By the same reasoning increase in ICP also increases RI in EOA segment to a lesser extent, due to a smaller blood volume being pushed. [8] have performed a numerical simulations of the axisymmetric elastic OA and obtained the pulsatility index (PI) variations. PI is related to the RI except that the denominator is the pulse mean blood flow velocity. They have found the nonlinear behavior pattern of PI as we have found in the RI, although following numerical simulation used different material model, three-dimensional geometry, included pressure drop and time-dependent behavior.

The affection of ICP and Pe on their respectively affected IOA and EOA segments are nonlinear. This can be explained by a nonlinear change in cross-sectional area due to the acting outside pressure e. g.: let‘s assume that when ICP was 0 mmHg the cross-sectional area was 1 at systole and was 0.5 at diastole of some relative units, in which the ratio would be equal to 2. When ICP became 20 mmHg, due to a nonlinear mechanical behavior of OA wall, cross-sectional area at systole could have become 0.6, while at diastole 0.4, in which same ratio would become 1.5 leading to a nonlinear RI behavior.

Finally, the correspondence between RI_{IOA} and RI_{EOA} intersection and the ICP value, thus accuracy of predicting ICP via RI was increasing with the increase in ICP. This is true to current model configuration, and comes from the same nonlinear OA wall mechanical behavior. Additionally, the assumption of a constant blood flow rate in a deformable tube is not correct at all time moments, as some part of fluid container by some minor margin may increase its volume more compared with a directly connected container that increases the fluid flow rate.

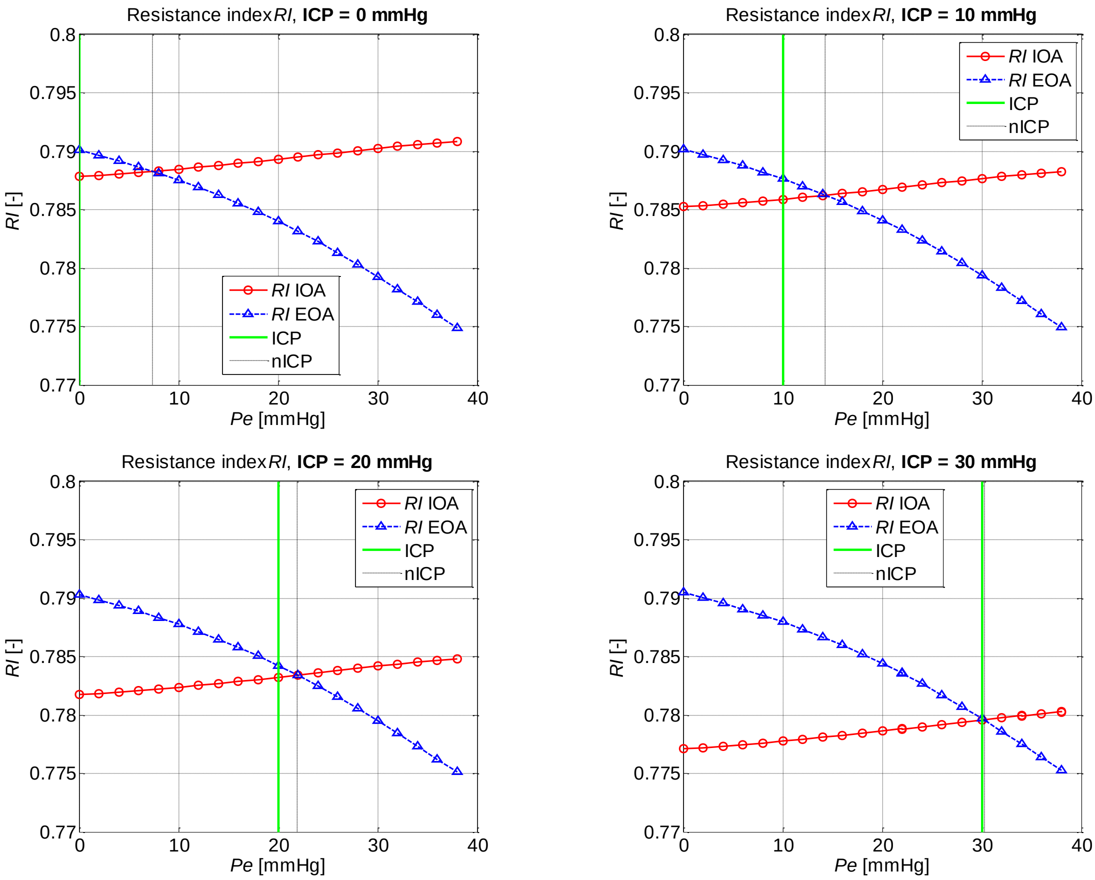

Fig. 3. RI values obtained by developed OA computational model simulations. ICP limits (0; 30) mmHg, Pe limits (0; 38) mmHg

4. CONCLUSIONS

If mechanical forces acting on IOA and EOA segments are similar and if all assumptions of the balance principle are valid, the nonlinear mechanical behavior of OA wall enables clinicians to accuratelly determine ICP for a patient *in vivo*. The hydrodynamic pressure drop ΔABP between IOA and EOA segments must be introduced into the balance equation as follows: $ABP - ICP = ABP + \Delta ABP - Pe$. In order to increase accuracy *in vivo*, further research of how much acting ICP pushes additional blood volume to the EOA segment and how much acting Pe pushes additional blood volume to the IOA segment is needed. And finally, to even further increase noninavsive ICP measurement accuracy, the blood flow rate, due to OA wall dynamics, must be evaluated in both segments and in accordance the RI value corrections must be performed.

REFERENCES

1. D. P. ASIEDU, K. LEE, G. MILLS, AND E. E. KAUFMANN, “A review of non-invasive methods of monitoring intracranial pressure,” J Neurol Res., vol. 4, no. 1, pp. 1–6, 2014.
2. L. A. STEINER AND P. J. D. ANDREWS, “Monitoring the injured brain: ICP and CBF,” Br. J. Anaesth., vol. 97, no. 1, pp. 26–38, 2006.
3. S. R. DASHTI, H. BAHARVAHDAT, R. F. SPETZLER, E. SAUVAGEAU, S. W. CHANG, M. F. STIEFEL, M. S. PARK, AND N. C. BAMBAKIDIS, “Operative intracranial infection following craniotomy,” Neurosurg. Focus, vol. 24, no. 6, p. E10, Jun. 2008.
4. L. C. PADAYACHY, “Non-invasive intracranial pressure assessment,” Child’s Nerv. Syst., vol. 32, no. 9, pp. 1587–1597, Sep. 2016.
5. A. RAGAUSKAS, G. DAUBARIS, AND A. DZIUGYS, “Method and apparatus for determining the pressure inside the brain,” 1999.
6. H. HO, C. MCGHEE, AND P. HUNTER, “Numerical analysis for the blood flow in a patient-specific ophthalmic artery,” Med. Eng. Phys., vol. 34, no. 1, pp. 123–127, Jan. 2012.
7. G. RODRÍGUEZ-BOTO, M. RIVERO-GARVÍA, R. GUTIÉRREZ-GONZÁLEZ, AND J. MÁRQUEZ-RIVAS, “Basic concepts about brain pathophysiology and intracranial pressure monitoring,” Neurología, vol. 30, no. 1, pp. 16–22, 2015.
8. A. RAGAUSKAS, G. DAUBARIS, A. DZIUGYS, V. AZELIS, AND V. GEDRIMAS, “Innovative non-invasive method for absolute intracranial pressure measurement without calibration,” Acta Neurochir. Suppl., vol. 95, no. 95, pp. 357–61, 2005.
9. R. CHOMSKIS, D. GEDIMINAS, R. GIANSIRACUSA, M. MOEHRING, V. PETKUS, A. RAGAUSKAS, E. A. SAXON, S. SWEDENBURG, AND R. ZAKELIS, “Method and apparatus for determining the absolute value of intracranial pressure.” Google Patents, 2011.
10. A. RAGAUSKAS, V. PETKUS, R. CHOMSKIS, R. ZAKELIS, G. DAUBARIS, M. MOEHRING, E. A. SAXON, R. GIANSIRACUSA, S. SWEDENBURG, AND R. RAISUTIS, “Method and apparatus for determining the absolute value of intracranial pressure.” Google Patents, 2013.
11. A. RAGAUSKAS, V. MATIJOSAITIS AND R. ZAKELIS, “Clinical assessment of noninvasive intracranial pressure absolute value measurement method,” Neurology, vol. 78, p. 1684–1691, 2012.
12. T. TEKORIUS, “Investigation of mathematical model of blood vessel,” Biomedicininė inžinerija, pp. 44–47, 1997.
13. F. AURICCHIO, M. CONTI, A. FERRARA, S. MORGANTI AND A. REALI, “Patient-specific finite element analysis of carotid artery stenting: a focus on vessel modeling,” International Journal for Numerical Methods in Biomedical Engineering, 2012.
14. G. A. HOLZAPFEL AND R. W. OGDEN, “Constitutive modelling of arteries,” Proc. R. Soc. A Math. Phys. Eng. Sci., vol. 466, no. 2118, pp. 1551–1597, Jun. 2010.

15. G. A. HOLZAPFEL, J. A. NIESTRAWSKA, R. W. OGDEN, A. J. REINISCH, AND A. J. SCHRIEFL, “Modelling non-symmetric collagen fibre dispersion in arterial walls,” J. R. Soc. Interface, vol. 12, no. 106, pp. 20150188–20150188, Apr. 2015.
16. G. SOMMER AND G. A. HOLZAPFEL, “3D constitutive modeling of the biaxial mechanical response of intact and layer-dissected human carotid arteries,” Journal of the Mechanical Behavior of Biomedical Materials, vol. 5, pp. 116–128, 2012.
17. A. M. BENSELAMA AND J. MONNIER, “Navier-Stokes ALE free surface flow with generalized Navier slip conditions. Droplet impact and attempt using Comsol Multiphysics 3.2” 2007.
18. W. R. MILNOR, “Cardiovascular Physiology, 1st ed,”, New York, NY: Oxford University Press, 1990.
19. J. D. CUTNELL AND K. JOHNSON, “Physics: Fourth Edition,” Wiley, p.308, 1998.
20. E. KUHL, R. MASS, G. HIMPEL, A. MENZEL, “Computational modeling of arterial wall growth: Attempts towards patient-specific simulations based on computer tomography,” Biomechanical Modeling in Mechanobiology, 2006.
21. K. AMBARKI, P. HALLBERG, G. JÓHANNESSON, C. LINDÉN, L. ZARRINKOOB, A. WÅHLIN, R. BIRGANDER, J. MALM, AND A. EKLUND, “Blood flow of ophthalmic artery in healthy individuals determined by phase-contrast magnetic resonance imaging,” Investig. Opthalmology Vis. Sci., vol. 54, no. 4, p. 2738, Apr. 2013.
22. S. S. HAYREH, “Orbital vascular anatomy,” Eye, vol. 20, no. 10, pp. 1130–1144, Oct. 2006.
23. X. LIU, C. ZHOU, G. ZHANG, Y. LIN, AND S. LI, “CT anatomic measurement of the optic canal and its clinical significance,” Zhonghua Er Bi Yan Hou Ke Za Zhi, vol. 35, no. 4, pp. 275–7, 2000.
24. J. F. POLAK, M. J. PENCINA, A. MEISNER, K. M. PENCINA, L. S. BROWN, P. A. WOLF, AND R. B. D’AGOSTINO, “Associations of carotid artery intima-media thickness (IMT) with risk factors and prevalent cardiovascular disease: comparison of mean common carotid artery IMT with maximum internal carotid artery IMT.,” J. Ultrasound Med., vol. 29, no. 12, pp. 1759–68, Dec. 2010.
25. D. W. HOLDSWORTH, C. J. D. NORLEY, R. FRAYNE, D. A. STEINMAN, AND B. K. RUTT, “Characterization of common carotid artery blood-flow waveforms in normal human subjects,” Physiol. Meas., vol. 20, no. 3, p. 219, 1999.
26. B. WIZNER, B. GRYGLEWSKA, J. GASOWSKI, J. KOCEMBA, AND T. GRODZICKI, “Normal blood pressure values as perceived by normotensive and hypertensive subjects,” J. Hum. Hypertens., vol. 17, no. 2, pp. 87–91, Feb. 2003.

CYSENI 2017, May 25-26, Kaunas, Lithuania
ISSN 1822-7554, www.cyseni.com

INVESTIGATION OF PULSATING FLOW IN OPEN-TYPE MICROCAVITY

P. Vilkinis, N. Pedišius
Lithuanian Energy Institute
Breslaujos str. 3, LT-44403 – Lithuania
E-mail: paulius.vilkinis@lei.lt

ABSTRACT

Microchannels with variable cross-sections and microcavities has become an attractive area of research due to their integration into micro-pumps, micro-reactors, micro heat sinks, microelectromechanical systems and also their usage in cell isolation and sorting devices and in many others. For optimizing microfluidic applications it is very important to fully understand flow behaviour in microchannel cavities at different flow conditions. In this study, micro particle image velocimetry system (micro-PIV) is used to investigate water flow in a single open-type micro cavity located in a straight rectangular cross-section microchannel with an aspect ratio of 4. Flow velocity structure along microcavity cross-section is investigated under wide range of Reynolds (Re) (50–400) and Womersley (Wo) (0.4–40) numbers. Velocity profiles at axis of cavity and across primary vortex are investigated. All results are compared with a stationary flow. Change of location of vortex centre and velocity distribution around vortex is investigated for every flow condition. Results indicate that flow field in microcavity is two-dimensional and velocity distribution highly depends on Reynolds and Womersley numbers.

Keywords: microfluidics, microcavity, micro particle image velocimetry, micro fluid dynamics

1. INTRODUCTION

There is a growing interest towards evaluation of fluid flow patterns in microchannels because of increasing demand of microfluidic devices in technological and biomedical applications. The usage of a micro scale device not only reduce the application size but also minimize the consumption of a costly reagent, facilitate the control of fluid flow, simplify the analysis and in most cases, reduce the cost of application. Conventional and micro scale open-type cavities ($L/h < 9–10$, where L – cavity length and h – cavity depth) [1] are widely used for cell docking and positioning [2–6], mixing [7] and heat transfer enhancement [8, 9].

In the open-type cavity fluid flow the recirculation is generated. Flow over these cavities is related to a complex interaction between vortices in the cavity and the external flow. Faure et al. [10] have investigated these phenomena by changing the relative length L/h_1 of a rectangular cavity in a flat channel from 0.5 to 2 for Re_L ranging from 1.15×10^3 to 10.67×10^3. The structure of the vortices generated in the cavity had depended on the relative length of the cavity and Re_{Dh}, moreover, flow three-dimensionality and vortex instability in the cavity had developed. The interaction of the recirculation flow in the cavity with the main flow is of interest in addressing transfer-process intensity [11] and flow-induced instabilities, followed by undesirable acoustic noise. The latter phenomenon received a considerable attention in the investigation of flows in channels with closed side branches, where resonance phenomenon occurs, causing increased flow pulsations and acoustic noise [12, 13]. Fishler [14] et al. experimentally and numerically investigated flow structure in cylindrical microcavities at low Re numbers. Attached, single vortex and two- and three-vortex recirculating vortex systems are classified using non-dimensional parameters. Similar investigations of rectangular microcavities at low Re numbers and wide aspect ratio interval are presented by Shen et al. [15]. Only single vortex is formed in cavity. Re number and aspect ratio of cavity show significant effect on flow structure in cavity. In our previous work [16] similar geometry microcavity in square cross-section microchannel was investigated. The results indicated signs of transverse flows in microcavity, as well as, early transition to turbulent flow regime in the case of high flow pulsation frequency.

It can be seen that microcavities of various shapes are widely investigated. However, in most cases, studies are performed only at low Re number interval. Also, there is a lack of studies on pulsatile flow conditions. In this study flow in rectangular microchannel cavity of aspect ratio L/h = 0.5, is analyzed at medium range Re number interval (50–400) at stationary and pulsatile (0.1–10 Hz) flow conditions.

2. EXPERIMENTAL SETUP

The micro-PIV equipment supplied by Dantec Dynamics consists of a double pulsed Nd:YAG laser with the laser control unit LPU 450. Particle pictures are captured with FlowSense EO CCD camera, providing a maximum image field of 2048×2048 pixels, with pixel size of 7.4 μm. For image magnification, the camera is mounted on Leica DM ILM inverted microscope. Objectives with magnification of 10x and numerical aperture of 0.4 is used in experiments. The microscope is equipped with dichroic mirror used to filter out background noise and only florescent light from excited tracer particles can reach the camera. 1 μm in diameter fluorescent particles provided by Invitrogen are used in experiments. The working fluid is deionized water. Tracer particles are excited by green (λ_{exc} = 532 nm) laser light and red (λ_{em} = 575 nm) florescent light is emitted, which is collected by CCD camera after filtered out by dichroic mirror.

The flow is created by microfluidic flow control system OB1 MK3 provided by Elveflow. Up to 2000 mbar pressure can be maintained in microchannel. Stationary, as well as various pulsatile shape (sinus, triangle, square, etc.) flow can be created.

DynamicStudio®? software provided by DantecDynamics®? is used for system controlling, data acquisition and picture analysis. Particle pictures are captured at 15 Hz with time delay between two frames varying from 10000 to 50 μs depending on a flow rate. Data is analyzed using Adaptive correlation and Adaptive PIV methods with interrogation windows size of 16×32 pixels. Various filters are applied to pictures before analysis to increase signal-to-noise ratio.

Experiments were performed in a microchannel that was manufactured in a transparent polymer chip. The scheme of used microchannel with single open-type microcavity is presented in Fig. 1a. Microchannel is of a rectangular cross-section shape with dimensions of 2×0.5 mm^2. Channel is 90 mm long. Microcavity is located at 60 mm from inlet port. The cross section of cavity is rectangular to a depth of 0.75 mm. The bottom of cavity is rounded at radius r = 0.25 mm. The total height of cavity is 1 mm. Measurements were performed at different locations along the microcavity cross-section. 7 measurements were taken at relative distances from side wall of cavity equal to 0.15, 0.25, 0.35, 0.5, 0.65, 0,75 and 0.85. Locations of analyzed velocity profiles across axis of cavity and center of primary vortex are shown in Fig. 1 b.

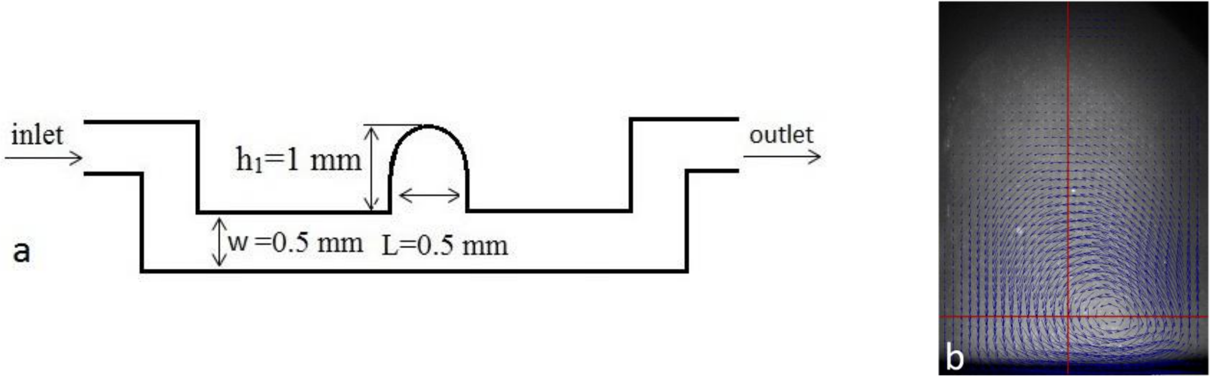

Fig. 1. a) scheme of a microchannel; b) locations of investigated velocity profiles is cavity in flow field

3. RESULTS AND DISCUSSION

3.1. Velocity profiles in mid-depth plane

Velocity profiles across cavity axis (y/h_1) in middle plane at different flow conditions are presented in Fig. 2. The vertical coordinates are the normalized velocities v/v_0, where v – is the velocity module in the cavity and v_0 – mean velocity in the channel. The horizontal coordinates are the depth of cavity, where $y/h_1 = 0$ indicates the lid of the cavity, and $y/h_1 = 1$ – the bottom of the cavity. The minimum at $y/h_1 \sim 0.05–0.12$ corresponds to the center of vortex. The center of vortex shifts toward the lid of the cavity with the increasing Re number in the channel. This displacement remains the same for all Wo numbers at low Re numbers. In the case of Re = 400, the slight shift toward the lid of cavity with increasing Wo is observed. The high velocity peak at $y/h_1 \sim 0.28$ indicates the maximum velocity of flow above center of vortex. At low Re number (Fig 2a) velocity above center of vortex depends on Wo number. Maximum velocity decreases as Wo increases and smallest velocity value is observed at stationary flow. In the case of Re = 100 (Fig. 2b), significant relation between peak velocity and Wo number is no longer observable. At Re = 200 (Fig. 2c) the decrease of relative velocity is obtained only for low Wo number. While increasing Re (Fig. 2d), the velocity slightly decreases at higher Wo numbers. In many cases minor velocity increase is observed at the bottom of the cavity. It indicates the beginning of formation of secondary vortex, but Re number is too low in all cases for structure of vortex to be visible.

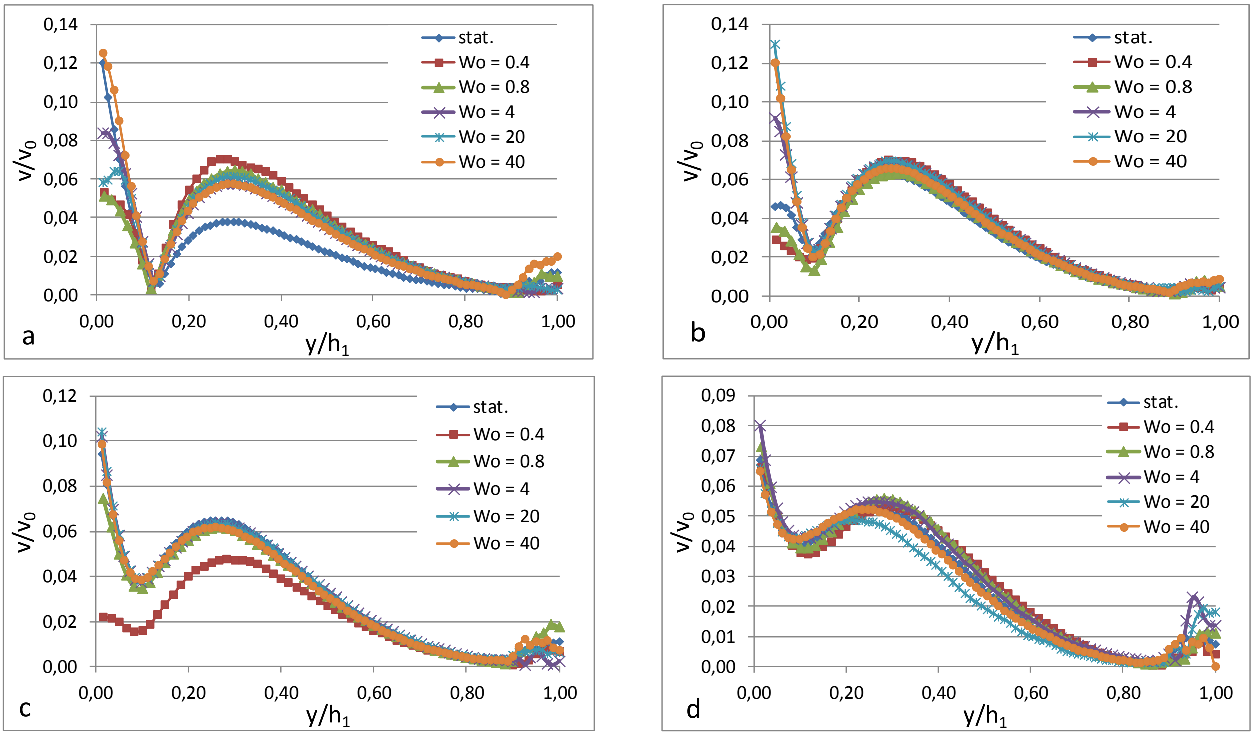

Fig. 2. Relative velocity profiles across cavity axis in the middle plane at different flow conditions: a) – Re = 50; b) Re = 100; c) Re = 200; d) Re = 400

The relative velocity profiles across the center of vortex provide additional information about velocity distribution in horizontal plane (Fig. 3). Velocity peak on left side, near trailing wall of cavity, presents a velocity at which the fluid is leaving cavity and merges with a flow in the channel. In the same manner, velocity on the right side, near the leading wall, is directed towards the bottom of the cavity and represents the velocity at which fluid is entering the cavity. The velocity magnitude near trailing and leading walls, as well as ratio between these velocities depends on both – Re and Wo numbers. For the low Re number (Fig 3a) relative velocity is smallest for a stationary flow. As Wo increases, the velocity near trailing edge decreases. However, no relation between velocity and Wo number is observed near leading wall. In the case of Re = 100 (Fig. 3b), velocity near trailing wall is the same as in the whole range of Wo. While increasing the Re number (Fig 3c) lowest velocity across the center of cavity is observed at lowest Wo number compared to higher Wo numbers. When Re = 400, velocity near leading wall decreases with increasing Wo in a range from 0.8 to 40. In the case of Wo = 0.4, velocity is smallest compared to higher Wo numbers. In the cases of Re = 100–400 (Fig 3 b, c and d) no apparent velocity dependence on Wo number is observed.

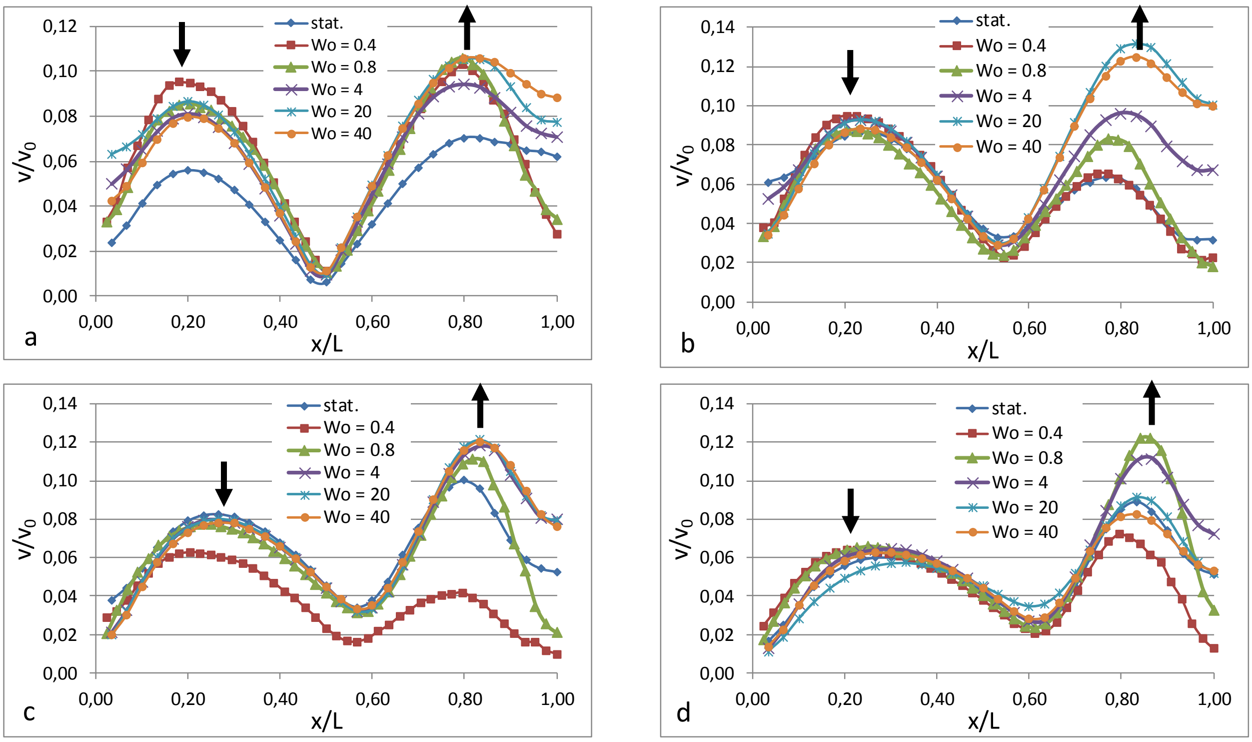

Fig. 3. Relative velocity profiles across centre of vortex at different flow conditions: a) Re = 50; b) Re = 100; c) Re = 200; d) Re = 400

In Fig. 4, ratio between maximum velocity near trailing wall (v_{tr}) and leading wall (v_{ld}), strongly depends on Re and Wo numbers. In most cases (Wo = 0.4–20 and stationary flow) sharp peak is observed at Re = 100 and is higher at low Wo numbers. Increasing Re v_{tr}/ v_{ld} tends to decrease. In the case of Wo = 40, the ratio depends almost linearly on Re number with slight minimum at Re = 200.

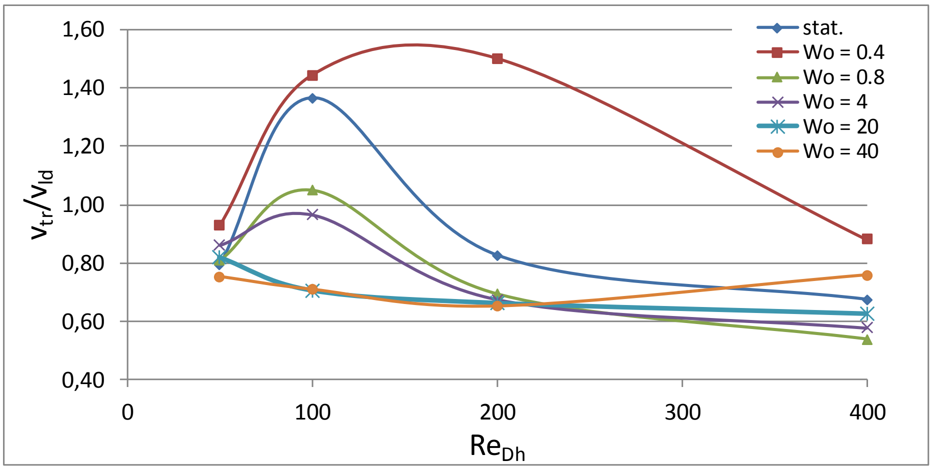

Fig. 4. The ratio between the velocity near trailing and leading walls relation on Re number at different Wo numbers

The location of a center of vortex in Fig 3 is indicated by minimum velocity value at x/L ~ 0.5–0.6. The location of a vortex center depends on Re number and shifts towards the leading wall of cavity as the Re number increases. Also, velocity in the vicinity of vortex center tends to increase with Wo and Re numbers.

3.2. Spatial velocity profiles

Since measurements were performed at different planes of cavity across all the cross-section, spatial velocity profiles can be created. Seven different velocity profiles were obtained and combined to a one three-dimensional velocity profile for each flow regime. These profiles provide information about velocity distribution in a transverse direction. Regardless of a two-dimensional nature of a single velocity profile, sudden changes between two adjacent velocity profiles can be explained as a transverse flow between these two plains. In Fig. 5, velocity profiles across cavity axis are presented at different flow conditions. It should be noted that velocity gradients between the bottom and the lid of the cavity are very large. It is impossible to measure the flow field in entire cavity using one acquisition frame rate. Since our investigation focuses on flow structure in cavity, velocity near boundary between flow in channel and cavity may be inaccurate in locations y/h_1 ~ 0.02–0.05.

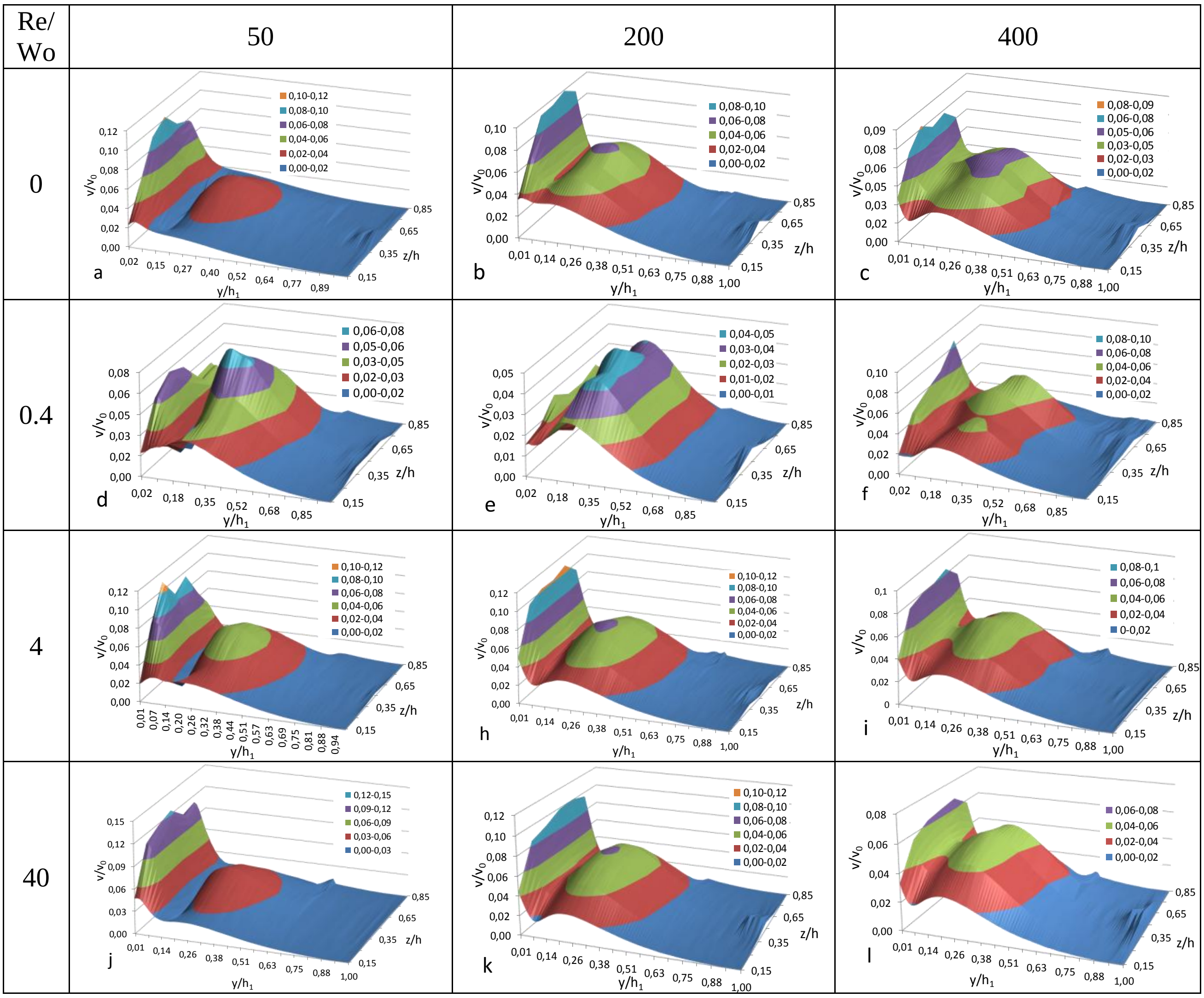

Fig. 5. Spatial velocity profiles across cavity axis at different flow conditions

Conical velocity distribution above centre of vortex is observed at Re = 50 for all Wo numbers. Velocity peak is located at the middle plane of the cavity. In the case of Re = 200 the cone is extended between side walls of the cavity, but velocity maximum is still located in the middle plane. At higher Re number some irregularities in velocity distribution can be observed (Fig. 5f). Also, the zone of maximum velocity is developed in vicinity around middle plane covering several measurement planes.

Re/ Wo	50	200	400
0	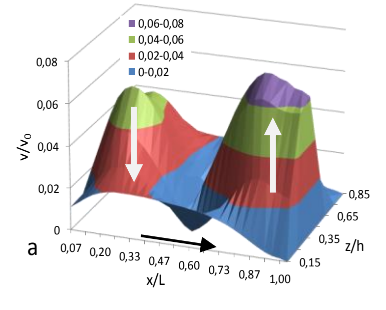	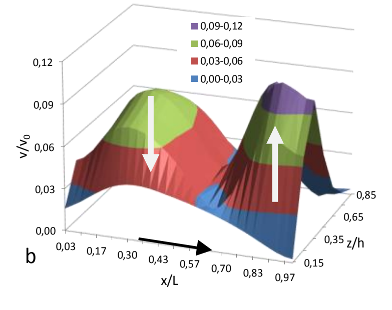	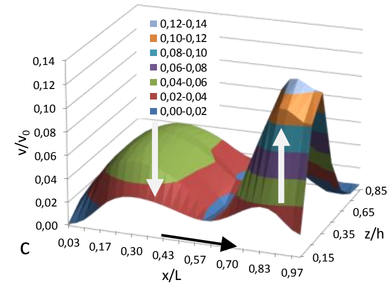
0.4	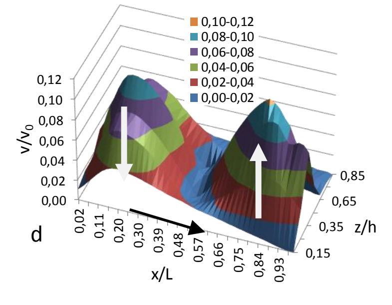	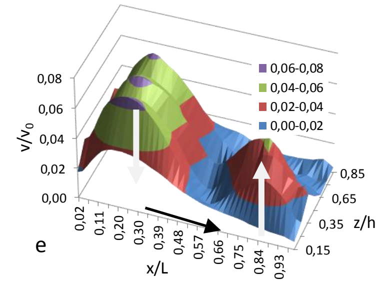	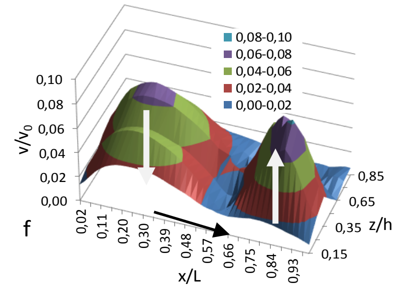
4	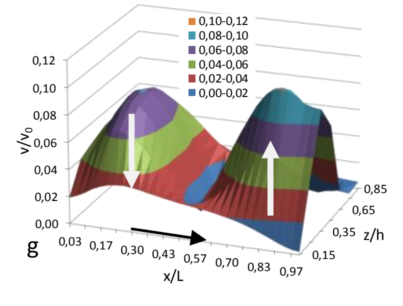	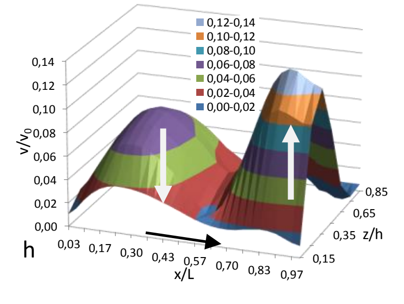	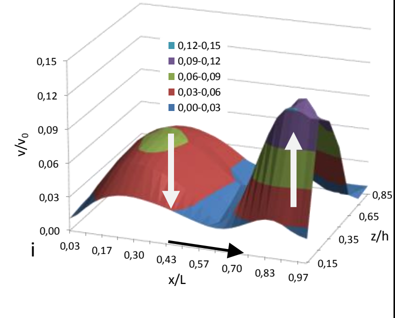
40	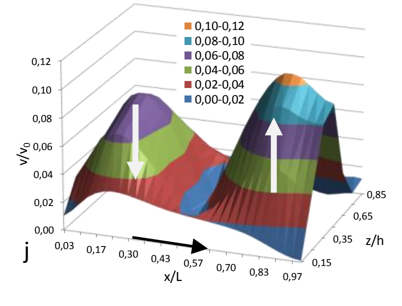	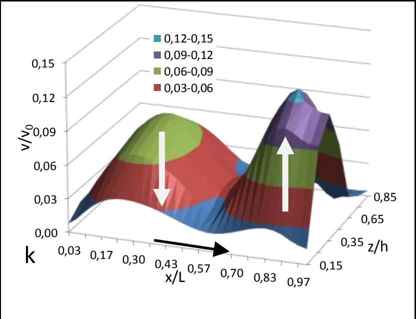	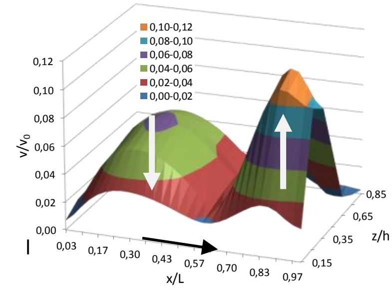

Fig. 6. Spatial velocity profiles across centre of cavity at different flow conditions

Spatial velocity profiles across center of vortex are presented in Fig. 6. White arrows indicate flow direction near cavity walls and black arrows indicates flow direction in channel. Changing flow regime, velocity distribution near trailing and leading walls changes uniformly. Exceptional is the case of Wo = 0.4 at all investigated Res. At Re = 50 (Fig. 6d) profile has sharp velocity peak near trailing wall in the middle measurement plane. Receding from this plane, velocity suddenly decreases. In the case of Re = 200 (Fig. 6e) velocity near trailing wall is greater than near leading wall across the cross-section. Also near trailing wall several velocity peaks are observed, one in the middle measurement plane and others – near side walls. Slightly velocity decreases between peaks are noticed. Velocity profile for Re = 400 (Fig. 6f) shows similar results to Re = 50 case with strong velocity peak in middle plane and comparable velocities near trailing and leading edges.

In the previous work [16], with narrower microchannel with same type of cavity (aspect ratio equals to 1) investigated, spatial velocity profiles revealed three-dimensional flow nature in cavity at a wide range of Re and Wo numbers. It is noted that channel's aspect ratio in current study is 4. Considering to symmetrical velocity profiles in the axial plane of cavity and across the center of vortex, the flow can be classified as two-dimensional. The side walls are far enough from each other and their influence to flow structure is absence or very low.

4. CONCLUSIONS

In this article, flow structure in rectangular cross-section open-type cavity under pulsatile flow conditions was investigated under a wide range of Re and Wo numbers. Flow in microchannel was mainly laminar. All pulsatile flow results were compared to stationary flow under same Re number. Velocity profiles in the axis of cavity and across vortex center were investigated. Measurements were performed at different planes of cavity and spatial velocity profiles were created.

Velocity distribution in the cavity axis in the middle plane depends on Re number. Influence of flow pulsation can be observed only at low Re number and velocity above center of vortex is decreasing with Wo number increasing. Location of vortex center depends on Re number and shifts towards leading wall as Re increases. Relative velocity distribution near leading and trailing walls depends on both Re and Wo and approaches asymptotical value as they increase. Spatial velocity profiles provide information about two-dimensional flow nature in cavity and symmetrical velocity distribution in respect of middle plane of cavity. These results can provide useful information for microfluidic based devices.

REFERENCES

1. CHARWAT A. An investigation of separated flows-Part I: The pressure field. Journal of the Aerospace Sciences 28(6), 13 (1961).
2. KHABIRY M, CHUNG B.G., HANCOCK M.J., SOUNDARARAJAN H.C., DU Y., CROPEK D., LEE W.G., KHADEMHOSSEINI A. Cell docking in double grooves in a microfluidic channel. *Small*, 2009, Vol. 5, No. 10, p. 1186–1194.
3. MANBACHI A, SHRIVASTAVA S, CIOFFI M, CHUNG B.G., MORETTI M., DEMIRCI U., YLIPERTTULA M., KHADEMHOSSEINI A. Microcirculation within grooved substrates regulates cell positioning and cell docking inside microfluidic channels. *Lab on a chip*, 2008, Vol. 8, No. 5, p. 747–754.
4. HUR S.C., MACH A.J., CARLO D.D. *Biomicrofluidics*, 2011, Vol. 5, No. 2, 022206.
5. JUNG J-Y, OH H-S., KWAK H-Y. Forved convective heat transfer of nanofluidc in microchannels. *International journal of heat and mass transfer*, 2009, Vol.52, No. 1, p. 466–472.
6. NILSSON J., EVANDER M., HAMMASSTROM B., LAURELL T. Review of cell and particle trapping in microfluidic systems. *Analytica Chimica Acta*, 2009, Vol. 649, No. 2, p. 141–157.
7. ANDERSON P.D., GALAKTIONOV S.O. PETERS G. W.M., VOSSE VAN DE F.N., MEIJER H.E.H. Chaotic fluid mixing in non-quasi-static time-periodic cavity flows. Heat and fluid flow. *International journal of heat and fluid flow*, 2000, Vol. 21, No. 2, p. 176–185.

8. HERMAN C., KANG E. Heat transfer enhancement in a grooved channel with curved vanes. *Heat and mass transfer*, 2002, Vol. 45, No. 18, p. 3741–3757.
9. VELAZQUEZ A., ARIAS J.R., MENDEZ B. Laminar heat transfer enhancement downstream of a backward facing step by using a pulsating flow. *International journal of heat and mass transfer*, 2008, Vol. 51, No. 7, p. 176–185.
10. FAURE T.M., ADRIANOS P., LUSSEYRAN F., PASTUR L. Visualizations of the flow inside an open cavity at medium range Reynolds numbers. *Experiments in fluids*, 2007, Vol. 42, No. 2, p. 169–184.
11. BEVES C., BARBER T., LEONARDI E. An investigation of flow over a two-dimensional circular cavity. *15th Australasian fluid mechanics conference, The university of Sydney*, 2004.
12. DEQUAND S., HULSHOFF S., HIRSCHBERG A. Self-sustained oscillations in a closed side branch system. *Journal of sound and vibration,* 2003, Vol. 265, No. 2, p. 359–386.
13. TONON D., WILLEMS J., HIRSCHBERG A. Flow-induced pulsations in pipe systems with closed side branches: study of the effectiveness of detuning as remedial measure. *20th international congress on acoustics*, Sydney, Australia, 2010
14. FISHLER R., MULLIGAN M.K., SZNITMAN J. Mapping low-Reynolds-number microcavity flows using microfluidics screening devices. *Microfluidics and nanofluidics,* 2013, Vol. 15, No. 4, p. 491–500.
15. SHEN F., XIAO P., LIU Z. Microparticle image velocimetry (μPIV) study of microcavity flow at low Reynolds number. *Microfluidics and nanofluidics*, 2015, Vol. 19, No. 2, p. 403–417.
16. VILKINIS P., VALANTINAVIČIUS M., PEDIŠIUS N. Investigation of fluid flow structure in open type cavity under stationary and pulsatile flow conditions. *Energetika,* 2016, Vol. 62, No. 1–2, p. 37–44.

CYSENI 2017, May 25-26, Kaunas, Lithuania
ISSN 1822-7554, www.cyseni.com

INFLUENCE OF pH ON THE HYDROXIDE IMPURITIES IN CHEMICALLY DEPOSITED CdS THIN FILM

M. Üürike, N. Maticiuc, O. Volobujeva, N. Spalatu, J. Hiie
Department of Materials and Environmental Technologies, School of Engineering, Tallinn University of Technology
Ehitajate tee 5, 19086 – Estonia
E-mail: marvin.uurike@ttu.ee

ABSTRACT

High quality CdS thin films are of great interest in the thin film photovoltaic community. CdS impurities like oxygen and hydroxide impact the electrical, optical and structural properties of CdS film, which may cut the performance of CdTe, CIGS or CZTS devices. One of the possibilities to control the hydroxide content in CdS lattice is the pH modification of the deposition solution. In the present work we study the effect of solution pH on the hydroxide content in CdS thin film, as well as their structural and optical properties. We noticed that a change in the pH from 8.7 to 10.4 gives raise to major variations in CdS properties measured by X-ray diffraction, UV-vis spectroscopy, energy-dispersive X-ray spectroscopy, and scanning electron microscopy. At low pH values (8.7 and 9.5) CdS films are dense and uniformly cover the glass substrates. The grain size of these films increases from 126 nm to 148 nm while the rate of film growth is doubled for CdS film deposited at 9.5 pH. At higher pH value (10.0 and 10.4) the films become porous and have an increased grain size from 153 nm to 300 nm. The crystalline structure of CdS thin film obtained at 8.7–10.4 pH changed from (002) hexagonal to (111) cubic, respectively. The influence of CdS films deposited at different pH values on the device performance is shown for CdS-CdTe solar cells. Due to less hydroxide impurities and larger CdS grains at higher pH values of deposition solution the photovoltaic parameters of CdS-CdTe solar cells were improved and the efficiency was raised from 5.1% up to 7.6%;

Keywords: CdS, pH, OH impurities, thin film solar cell.

1. INTRODUCTION

Cadmium sulfide (CdS) has proven to be one of the most important semiconductor materials for the industry of different optoelectronic devices such as optical sensors, light-emitting diodes, transistors and photovoltaic panels [1]. CdS thin films are deposited by several physical and chemical methods: sputtering [2], vacuum evaporation [3], electrodeposition [4], spray pyrolysis [5], and chemical bath deposition (CBD) [6]. Among them CBD is most widely used in industry as the simplest, fastest, cost effective and promising method to obtain uniform, dense and large area CdS thin films [7, 8].

Due to the aqueous environment the chemically deposited CdS film may contain a significant amount of oxygen and hydrogen compounds which influence the growth mechanism and the film properties. This is directly connected to the fact that CBD CdS thin film is obtained from an alkaline solution with a pH value around 10, where the hydroxide mechanism of CdS formation is commonly accepted [8, 9, 10]. The hydroxide ions participate in the decomposition of thiourea with S^{2-} release so that CdS formation occurs preferentially on the surface of hydroxide rather than nucleating separately in the solution. In this sense, the inclusion of $Cd(OH)_2$ in chemically deposited CdS was widely presumed [11, 12, 13], however, its thermal instability [14] and impact on the properties of CdS film were underestimated.

Such unstable thermal activity of hydroxide species generates uncontrollable properties of CBD CdS thin films already at low temperatures [8, 15]. As the OH incorporates on sulfur site in the CdS lattice [16], it acts as a donor dopant which dramatically changes the electrical, structural and optical properties of CBD CdS thin films already in the deposition process [17]. There is a possibility to remove these OH-containing impurities by means of a post deposition thermal annealing at temperatures up to 450 °C, but the CdS properties will be also affected [15, 16, 18].

As an alternative, in this article we investigate the possibility to control the incorporation of OH impurities into CdS lattice during the deposition process. In this sense we prepare CdS thin films by CBD method at pH values of solution below and above the usual value (pH 10) [8]: 8.7, 9.5, 10.0 and 10.4 pH. In addition, we study crystallography, morphology, elemental composition, and optical properties of CdS thin films by means of X-ray diffraction (XRD), scanning electron microscopy (SEM), energy-dispersive X-ray analysis (EDX) and UV-vis-NIR spectrometry. CBD CdS thin films deposited at different pH values are used in CdTe solar cells and the effect of solution pH on solar cell parameters is discussed.

2. EXPERIMENTAL DETAILS

Polycrystalline CdS films were deposited on 25 mm × 25 mm soda-lime glass substrates by CBD technique. The plates were properly cleaned and immersed in the chemical bath which consisted in 200 ml water solution of 1 mM $CdSO_4$, 10 mM thiourea and 30 mM $(NH_4)_2SO_4$. The value of solution pH was changed from 8.7 up to 10.4 by means of NH_4OH concentration in the solution (10 mM, 75 mM, 0.25 M and 0.7 M). The pH values were measured at room temperature. The temperature and agitation speed of the reaction solution were 85 °C and 500 rpm, respectively. One deposition lasted for 10 min, but for thicker CdS films the process was repeated. After deposition a vacuum drying at 120 °C was applied to remove most of the secondary phases of water, hydroxides and organic impurities. This drying was the last stage of preparation for the so-called as-deposited CdS layers.

Surface morphology of CdS films was examined by high resolution SEM apparatus (Zeiss Merlin) at an operating voltage of 0.9 kV. The elemental composition of films was determined by means of EDX analysis, using the Bruker EDX-XFlash 6/30 detector with the PB-ZAF standard less mode with a measurement error of ~1.0 at. %. Crystallographic investigations were performed using the XRD technique. The measurements were made in the Bragg–Brentano (θ–2θ) geometry by the Rigaku Ultima IV diffractometer with Cu-Kα radiation. Crystallite size, lattice constant and interplanar distance were computed by the PDXL software (Version1.4.0.3) on the Rigaku system. The crystallite size was calculated using the Debye–Scherrer method and a Scherrer's constant of 0.94. The optical characteristics were measured in the wavelength range of 200–1500 nm on the Jasco V-670 UV–vis–NIR spectrophotometer equipped with an integrating sphere. Total optical transmission and reflection spectra were used to determine the transmittance of CdS and the optical thickness. Based on the Tauc relation (1), the values of bandgap have been estimated from the $(\alpha h\nu)^2$ versus hν dependence, by taking the intercept of the extrapolation to zero absorption on the hν axis.

$$(\alpha h\nu) = A\left(h\nu - E_g\right)^n \quad (1),$$

here α is the absorption coefficient given by $\alpha = 2.303 \log(T/d)$ (d here is film thickness and T is transmission), $h\nu$ is the photon energy, and the exponent n denotes the nature of the transition (n = ½ for direct allowed transitions).

For solar cell fabrication in superstrate configuration we deposited CBD CdS buffer layer onto transparent conductive oxide (FTO) from solution with different pH values (pH 8.7, pH 9.5, pH 10.0). Following CdS deposition, CdTe absorber layers were deposited by close spaced sublimation (CSS) technique at 450 °C in a high vacuum of 10^{-6} torr. The next step was the classical $CdCl_2:O_2$ activation treatment [19], after which the solar cells were finished by sputtering of Au back contact. Performance of the CdS–CdTe solar cells was characterized by current-voltage (J–V) and external quantum efficiency (EQE) measurements under AM1.5 (room temperature, 100 mW/cm^2) conditions.

3. RESULTS AND DISCUSSION

3.1. Properties of CBD CdS thin films

SEM surface images of CBD CdS thin films are presented in Fig. 1. Almost all CBD CdS films cover uniformly the underlying glass substrate after 60 minutes deposition, an exception being the case of 10.4 pH (Fig. 1). At such a high pH value the CdS grains do not manage to coalesce and to cover uniformly the underlying glass substrate. Even by increasing the deposition time from 1 to 2 hours (not shown here) we obtained CdS films composed of large separated grains that do not cover completely the glass substrate.

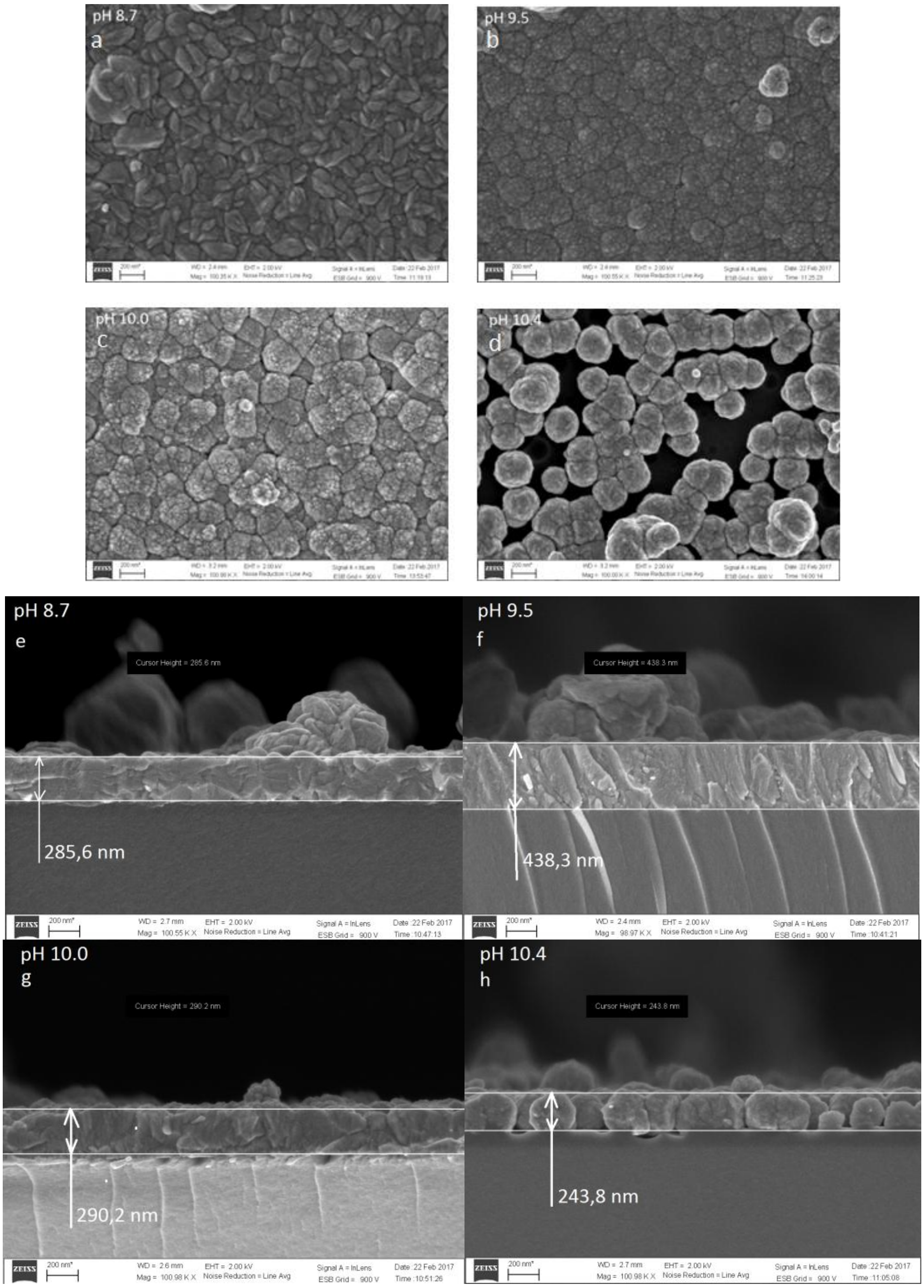

Fig. 1. SEM surface view (a–d) and cross sectional image (e–h) of CdS thin film deposited for one hour at different pH values: a, e) 8.7 pH; b, f) 9.5 pH; c, g) 10.0 pH; d, h) 10.4 pH

The thickness is almost the same for all the experiments except for the film obtained at 9.5 pH which is twice thicker in comparison to other CdS films (Table 1). When the value of solution pH increases from 8.7 to 10.4 we observe an increase in the grain size of CdS thin films from 126 nm up to 300 nm (Table 1). At the same time the grains shape is changed from asymmetrical with distinguishable corners to spherical grains (Fig. 1), respectively.

Table 1. Thickness, grain size and elemental composition of CBD CdS thin films deposited at different pH values

pH	**8.7**	**9.5**	**10.0**	**10.4**
Thickness, nm	285	438	290	243
Grain size, nm	180	180	245	300
[Cd], at.%	51.5	49.6	52.2	52.4
[S], at.%	40.8	41.2	41.9	43.4
[O], at.%	7.7	9.2	5.9	4.2

When analyzing the elemental composition of CdS thin film, a special attention was paid to the oxygen-containing species in the CdS thin film as a function of solution pH. A special interest in the oxygen content is connected to the aim of our investigation – to study how the pH of solution influences the presence of hydroxide impurities which will be suggested by the oxygen content [9]. As the pH value is raised from 8.7 up to 10.4 CdS films are similarly Cd-rich whereas atomic concentration of oxygen decreases from 7.7 at.% down to 4.2 at.% (Table 1). Similarly to the previously discussed microstructural properties, the CdS thin film deposited at 9.5 pH represents an exception of the tendency and shows the highest content of oxygen impurities (9.2 at%). We suppose that at this solution pH, the mechanism of CdS growth is faster and a larger amount of hydroxide species are incorporated from the deposition solution.

Nevertheless, the presence of hydroxide impurities incorporated in CdS film is decreased with increasing pH value of the deposition solution. This incorporation, which was previously thoroughly analyzed by X-ray photoelectron spectroscopy [16], is supported here by our XRD analysis data (Fig. 2) that indicate to an increase of the interplanar distance (Table 2). Besides that, with increasing value of pH, the crystalline structure of CdS thin film changes from multiple orientation to single orientation with improvement of crystallinity at 9.5 and 10.0 pH. Higher value of pH (10.4) in the deposition solution brings back the disperse structure of CBD CdS thin film described by decreased crystallinity, multiple orientation structure and very small size of crystallites. All these characteristics suggest that 10.4 is a too high pH value for deposition of CdS thin film for application in superstrate solar cells. Moreover, if at low pH values of solution (8.7 pH and 9.5 pH) the deposited CdS thin films have a hexagonal structure, at values higher than 10.0 pH the crystalline structure of CdS re-orientates itself to cubic structure (Table 2).

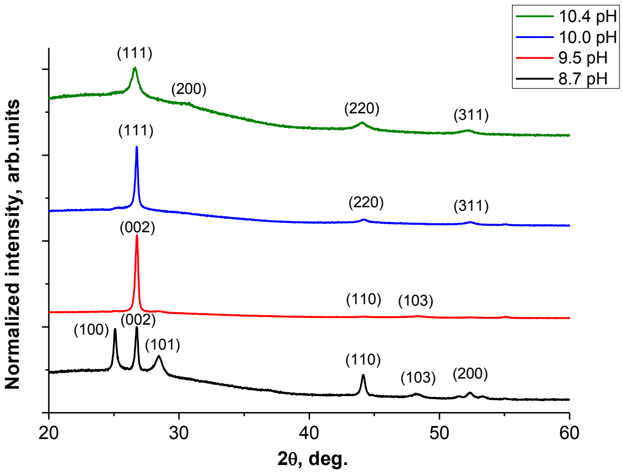

Fig. 2. XRD patterns of CBD CdS thin films deposited at different values of solution pH

Taking into account that the incorporated hydroxide impurity in CdS is bound to Cd and that crystalline lattice of $Cd(OH)_2$ is hexagonal [11], we believe that the high presence of hydroxide impurities reorganize the crystalline lattice of CdS towards hexagonal structure. On the other hand, when our CBD CdS thin films contain less hydroxide impurities the CdS lattice re-arrange itself into a stable cubic structure (Table 2).

Table 2. Interplanar distance (d), crystallite size (s), and lattice parameters (a, c) calculated for the main peak of CdS thin films deposited at different pH values

pH	**Main peak**	**2θ, deg.**	**d, Å**	**s, nm**	**a, Å**	**c, Å**
8.7	(002)	26.752	3.329	39.2	4.10	6.66
9.5	(002)	26.760	3.328	36.0	4.08	6.65
10.0	(111)	26.742	3.331	45.2	5.77	–
10.4	(111)	26.662	3.341	6.1	5.88	–

The optical band gap values of CBD CdS thin films confirm that the characteristics of $Cd(OH)_2$ dictate properties of CdS. The general trend of band gap value is a decrease from 2.43 eV to 2.31 eV corresponding to a raise in the value of solution pH from 8.7 up to 10.4. Such a decrease of band gap is in close connection to previously presented EDX data that indicate to a reduced presence of OH-containing phases at increasing values of pH. This tendency is in agreement with Yucel et al. study that indicates that the band gap of CdS is decreased when a higher pH is applied in the deposition process [20]. Again, CdS thin films with a higher content of hydroxide impurities have a higher band gap and vice versa (Fig. 3) and we connect it to the high band gap of incorporated $Cd(OH)_2$ [21]. Still, in our case the band gap values are lower due to less concentrated solution, higher Cd/S rate and lower pH values in our CBD process compared to Yucel et al. work.

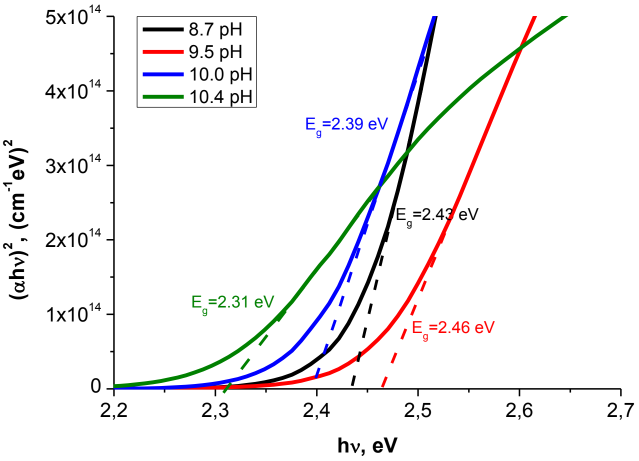

Fig. 3. Tauc's plots and band gap values of CBD CdS thin film deposited at different pH values of solution

Our intention to control the content of hydroxide species by changing the value of pH was successful. We were able to decrease the oxygen concentration from 7.7 at% down to 4.2 at% when raising the value of solution pH from 8.7 up to 10.4. However, the CdS film obtained at 10.4 pH is also described by poorest substrate coverage and uniformity of the layer. Such microstructure of this CdS film makes its application as a buffer layer almost impossible. Therefore, for solar cell application we used only CdS thin films deposited at three pH values: 8.7, 9.5, and 10.

3.2. Properties of CdS/CdTe solar cells

Fig. 4a shows the current-voltage (J–V) characteristics of CdS–CdTe solar cells with identically thick CdS films (~100 nm) obtained at different values of solution pH: 8.7, 9.5, and 10.0. The photoelectric performance of these solar cells is shown in Table 3.

The highest performance is shown by the solar cell with CdS film deposited at 10.0 pH. An important reason of this improvement might be the lowest concentration of oxygen containing species, larger grains of CdS, and less interface defects between this CdS film and CdTe absorber. These interface defects are probably more numerous in the case of CdS deposited at lower pH values. In result, solar cell with CdS deposited at 8.7 pH show lowest solar cell parameters (Table 3) due to smallest grain size of CdS film (Table 1). When compared to the cells with CdS deposited at pH 9.5 and 10.0, the grain size of only 180 nm for CdS deposited at 8.7 pH implies a faster interdiffusion at the CdS/CdTe junction interface in the process of $CdCl_2$ treatment. This interdiffusion appears to be accelerated also by the relatively high oxygen content in this CBD CdS film.

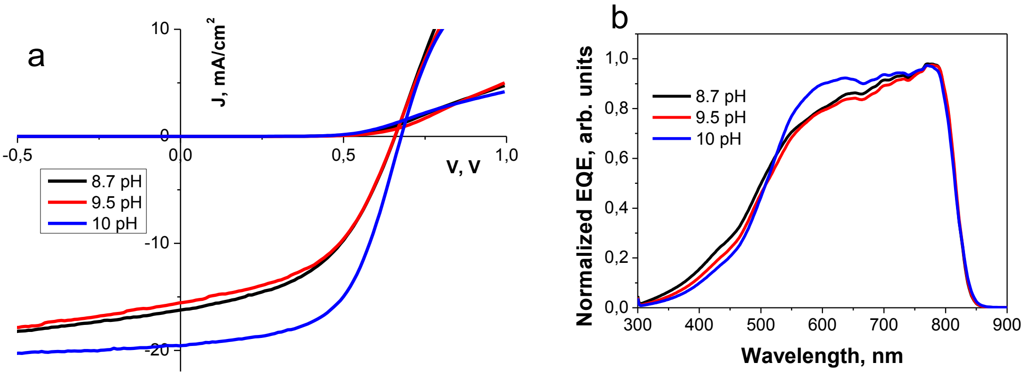

Fig. 4. J-V (a) and EQE (b) characteristics of CdS-CdTe solar cells with CBD CdS obtained at different values of solution pH (8.7, 9.5 and 10.0)

Table 3. Photovoltaic parameters of CdS-CdTe solar cells with CBD CdS film obtained at different values of solution pH (8.7, 9.5, and 10.0)

pH of CdS CBD solution	**V_{OC}, V**	**J_{SC}, mA/cm^2**	**FF, %**	**η, %**
8.7	660	16.1	48	5.1
9.5	660	15.5	49	5.0
10.0	680	19.5	57	7.6

These conclusions are supported by simultaneous changes of the EQE dependencies (Fig. 4b) in the wavelength region of 300-700 nm. The solar cells with CdS deposited at 8.7 and 9.5 pH exhibit slightly higher EQE response in the mentioned wavelength region probably because of the thinning of CdS as a result of intermixing at the CdTe-CdS interface [18]. Although this enhancement is beneficial for window transmission, non-uniform CdS consumption may lead to the formation of parallel junctions between the absorber and FTO front contact, and hence to the reduction of solar-cell performance (Table 3). Based on these arguments it is clear that solar cell that uses CdS with larger grains obtained at pH value of 10.0 exhibits the best EQE response implying better collection efficiency.

4. CONCLUSIONS

In this paper CBD CdS thin films were obtained at different values of solution pH (8.7, 9.5, 10.0 and 10.4) that generate changes in microstructural, crystallographic and optical properties of CdS thin films. First of all the coverage and uniformity of the film is damaged at higher pH values whereas the grain size is increased from 180 nm to 300 nm. In addition, with increasing value of solution pH the crystalline structure of CdS thin films is transformed from hexagonal with (002) orientation toward cubic with (111) orientation. The most important result of the present work is that we managed to decrease the amount of oxygen impurities in CBD CdS thin films from 7.7 at.% to 4.2 at.% by means of increasing pH values from 8.7 up to 10.4. Such an approach allowed us to diminish the content of hydroxide impurities in CBD CdS thin films. However, CdS films with the lowest content of hydroxide impurities have the poorest microstructure in terms of bad substrate coverage and non-uniformity of the film. In solar cell application, by using CBD CdS films deposited at different pH values we managed to increase the solar cell efficiency from 5.1 % up to 7.6 %. Such an improvement of CdS-CdTe solar cell parameters are due to larger grain size of CdS film as well as decreased amount of oxygen containing species at higher pH values.

ACKNOWLEDGEMENTS

This work was financially supported by the Estonian Ministry of Education and Research [projects IUTI9-4, IUT19-28 and PUT1495]; the Estonian Centre of excellence in Research [Project TK141].

REFERENCES

1. LUQUE A., HEGEDUS S., *Handbook of Photovoltaic Science and Engineering, 2nd edition*, Chichester, UK: John Wiley & Sons Ltd, 2010.
2. LIANG G.X., FAN P., ZHENG Z.H., LUO J.T., ZHANG D.P., CHEN C.M., CAO P.J., Room-temperature preparation and properties of cadmium sulfide thin films by ion-beamsputteringdeposition, *Applied Surface Science*, 2013, Vol. 273, p. 491–495.
3. GHOSH B., DAS M., BANERJEE P., DAS S., Fabrication of vacuum-evaporated SnS/CdS heterojunction for PV applications, *Sol. Energy Mater. Sol. Cells*, 2008, Vol. 92, p. 1099–1104.
4. BARANSKI A.S., FAWCETT W.R., MCDONALD A.C., The mechanism of electrodeposition of cadmium sulphide on inert metals from dimethylsulphoxide solution, *Journal of Electroanalytical Chemistry and Interfacial Electrochemistry*, 1984, Vol. 160, p. 271–287.
5. YADAV A.A., BAROTE M.A., MASUMDAR E.U., Studies on nanocrystalline cadmium sulphide (CdS) thin films deposited by spray pyrolysis, *Solid State Science*, 2010, Vol. 12, p. 1173–1177.
6. ISAIAH O., OLADEJI L.C., Optimization of chemical bath deposited cadmium sulfid thin films, *J. Elecrochem. Soc.*, 1997, Vol. 144, p. 2342–2346.
7. SOUNDESWARAN S., SENTHIL KUMAR O., DHANASEKARAN R., Effect of ammonium sulphate on chemical bath deposition of CdS thin films, *Materials Letters*, 2004, Vol. 58, p. 2381–2385.
8. HODES G., *Chemical Solution Deposition of Semiconductor Films*, New York: Marcel Dekker Inc, 2003.
9. ORTEGA-BORGES R., LINCOT D., Mechanism of chemical bath deposition of cadmium sulfide thin films in the ammonia-thiourea system, *J. Electrochem. Soc.*, 1993, Vol. 140, p. 3464–3473.
10. KAUR I., PANDYA D.K., CHOPRA K.L, Growth kinetics and polymorphism of chemically deposited CdS films, *J. Elecrochem. Soc.*, 1980, Vol. 127, p. 943–948.
11. KYLNER A., ROCKETT A., STOLY L., Oxygen in solution growth CdS films for thin film solar cells, *Solid State Phenom.*, 1996, Vol. 51–52, p. 533–540.
12. KOZHEVNIKOVA N.S., REMPEL A.A., HERGERT F., MAGERL A., Structural study of the initial growth of nanocrystalline CdS thin films in a chemical bath, *Thin Solid Films*, 2009, Vol. 517, p. 2586–2589.
13. LEE S., LEE E.S., KIM T.Y., CHO J.S., EO Y.J., YUN J.H., CHO A., Effect of annealing treatment on CdS/GIGS thin film solat cells depending on different CdS deposition temperatures, *Sol. Energy Mater. Sol. Cells*, 2015, Vol. 141, p. 299–308.
14. LOW M.J.D., KAMEL A.M., The thermal decomposition of cadmium hydroxide, *J. Phys. Chem.*, 1965, Vol. 69, p. 450–457.

15. MATICIUC N., KATERSKI A., DANILSON M., KRUNKS M., HIIE J., XPS study of OH impurity in solution processed CdS this films, *Sol. Energy Mater. Sol. Cells*, 2017, Vol. 160, p. 211–216.
16. MATICIUC N., HIIE J., MIKLI V., POTLOG T., VALDNA V., Structural and optical properties of cadmium sulfide thin films modified by hydrogen anneaing, *Materials Science in Semiconductor Processing*, 2014, Vol. 26, p. 169–174.
17. MATICIUC N., HIIE J., POTLOG T., VALDNA V., GAVRILOV A., Influence of annealing in H_2 atmosphere on the electrical properties of thin film CdS, *Mater. Res. Soc. Symp. Proc.*, 2011, Vol. 1324.
18. MATICIUC N., SPALATU N., MIKLI V., HIIE J., Impact of CdS annealing atmosphere on the performace of CdS-CdTe solar cell, *Applied Surface Science*, 2015, Vol. 350, p. 14–18.
19. SPALATU N., HIIE J., VALDNA V., CARAMAN M., MATICIUC N., MIKLI V., POTLOG T., KRUNKS M., LUGHI V., Properties of the $CdCl_2$ air-annealed CSS CdTe thin films. *Energy Procedia,* 2014, Vol. 44, p. 85–95.
20. YÜCEL E., SAHIN O., Effect of pH on the structural, optical and nanomechanical properties of CdS thin films grown by chemical bath deposition, *Ceramics International*, 2016, Vol. 42, p. 6399–6407.
21. SAHIN B., BAYANSAL F., CAKMAK H.M., KAHRAMAN S., CETINKARA H.A., Effect of heat treatment on the properties of $Cd(OH)_2$ and CdO films grown by chemical bath deposition, *Philosophical Magazine Letters*, 2013, Vol. 93, p. 101–108.

CYSENI 2017, May 25-26, Kaunas, Lithuania
ISSN 1822-7554, www.cyseni.com

PHOTOCATALYTIC PROPERTIES OF TIO2 DEPOSITED ON NON-EXPANDED POLYSTYRENE BEADS

Š. Varnagiris, D. Girdzevičius, M. Urbonavičius, D. Milčius
Lithuanian Energy Institute
Breslaujos st. 3, LT-44403 Kaunas – Lithuania
E-mail: Sarunas.Varnagiris@lei.lt

S. Sakalauskaitė
Vytautas Magnus University
K. Donelaičio st. 58, LT-44248 Kaunas – Lithuania

ABSTRACT

Titanium dioxide (TiO_2) is widely researched and used material because of its photocatalytic and other attractive properties. However, formation of TiO_2 on thermally non-stable substrates is still challenging. Photocatalytic properties of TiO_2 films deposited on non-expanded polystyrene (PS) beads using magnetron sputtering technique were investigated. Prior to magnetron sputtering, plasma pre-treatment was used. PS beads were transferred directly under the magnetron without extraction to atmosphere after plasma pre-treatment. Photocatalytic TiO_2 properties were tested by investigating bleaching of the Methylene Blue (MB) in aqueous solution (15 mg/L). Also viability experiments of *Escherichia coli* (E. coli) bacteria under UV-B light irradiation were performed. Significant degradation of MB solution was observed during MB bleaching experiment. Two-phase E. coli bacteria inactivation process was observed during viability experiments. UV irradiation alone can damage outer E. coli bacteria membrane (lipopolysacchride), while combination of TiO_2 and UV can break down both lipopolysacchride and peptidoglycan outer membranes. Moreover, combination of TiO_2 and UV decompose approximately 94% of intact and 100% of ethylenediaminetetraacetic acid (EDTA) treated E. coli bacteria after 45 min. TiO_2 films on PS beads were characterised using combination of scanning electron microscope (SEM) and X-ray photoelectron spectroscope (XPS) analysis techniques. XPS results confirmed formation of TiO_2 compound. SEM results showed that PS beads were coated by TiO_2 films.

Keywords: Photocatalysis, titanium dioxide, polystyrene beads, Escherichia coli, magnetron sputtering

1. INTRODUCTION

Photocatalytic decomposition of organic pollutants or bacterias has attracted much attention in recent years. One of the most promising photocatalyst is TiO_2 because of its high photocatalytic activity, photo-stability and non-toxicity. Since 1927 pioneering work on water photolysis by Honda and Fujishima [1] multitude researches focusing on TiO_2 photocatalytic properties and applications were done. However TiO_2 has relatively wide band gap (3.0–3.2 eV). Therefore UV irradiation or additives is required for various TiO_2 applications [2, 3]. UV light itself can cause damage to the structure or functionality of the living cells. On the other hand, using UV light with photo-catalytic TiO_2 materials antibacterial treatment efficiency can be increased up to several times [4–6]. When TiO_2 is irradiated with UV light (photonic energy equal to, or greater than, its band gap energy 3.2 eV) pair of the electron-hole is generated (Eq. (1)). The electron reduces oxygen to the superoxide ion or anion radicals (Eq. (2)) while generated holes reacts with hydroxyl ions and adsorbs water to form free radicals (Eq. (3)). These created highly reactive oxygen species (ROS) react with bacterias or pollutants and promote their inactivation (Eq. (4), (5)). The most important oxidant species that is responsible for bacteria inactivation is $OH^{\bullet}$ radical [7–10].

$$TiO_2 + hv \rightarrow TiO_2 + e^- + h^+ \quad (1)$$

$$e^- + O_2 \rightarrow O_2^- / HO_2 \quad (2)$$

$$h^{+} + OH^{-} \rightarrow OH^{\bullet} \tag{3}$$

$$Bacteria(B) + OH^{\bullet} \rightarrow B_{ox}(oxidized) \tag{4}$$

$$B_{ox} \rightarrow radical\_chain\_reactions \tag{5}$$

Such TiO_2 photocatalytic properties could be very attractive for food packing, medicine, water cleaning or other areas where bacteria inactivation is required [11–13]. However different application requires different preparation of TiO_2. For example, water cleaning requires substrates in order to avoid the use of titanium powder, which has to be separated from the water in a slurry system after the photocatalytic reaction. Moreover buoyant substrates are required which could be easily photoilluminated [14, 15]. One of suitable materials for TiO_2 substrates could be non-expanded polystyrene (PS) beads. These beads are buoyant, relatively cheap and easily manufactured [16, 17]. Also, PS beads are spherical material with arround 1–3 mm dimensions (surface area: 12.5–113 mm^2).

In order to use PS beads as TiO_2 substrates, coatings should be formed on the surface of PS beads. Sol-gel is The most frequently used method to form TiO_2 coatings [18, 19]. However this method involves relatively high temperature (about 200 ^{o}C), while PS glass transition temperature is about 95 ^{o}C. Because of this PS beads undergo structural changes. [20–22] showed that magnetron sputtering (MS) could be suitable method to form films on the surface of polymers. MS involves low temperature (less than 100 ^{o}C) plasma during deposition process. Therefore polymers are not overheated and do not undergo structural changes.

In present work MS was used in order to form TiO_2 films on the surface of PS beads. These beads were used for photocatalysis experiments: methylene blue (MB) degradation in aqueous solution, and *Escherichia coli* (E. coli) bacteria decomposition.

2. METHODOLOGY

2.1. TiO_2 film synthesis

TiO_2 films were deposited on the non-expanded polystyrene (PS) beads using modified physical vapour deposition system manufactured by Kurt J. Lesker company. In order to increase free surface energy of PS beads and to obtain better adhesion between beads and TiO_2 films argon plasma pre-treatment was used [23, 24]. Gas pressure during plasma pre-treatment was set to 1×10^{-1} mbar. Plasma was generated using 400 V supplied by pulsed DC power source (combination of Advanced Energy MDX-1K and Sparcle-20 units). Plasma pre-treatment time was 40 s. Distance between sample surface and high temperature stainless steel (made from Alloy 600) cathode was 40 mm. PS beads were rotated by 180 degree after plasma activation. Beads were placed directly under the magnetron. Titanium disk (76 mm diameter, 99.99% purity, Kurt J.Lesker Company) was used as a primary cathode material. Distance between Ti magnetron and polystyrene sample was 70 mm. During reactive magnetron sputtering process total gas pressure was 6×10^{-3} mbar. Ar-O_2 gas mixture with nominal ratio 1:5.5 was used during TiO_2 films formation (both 99.999% purity, AGA Company). Reactive sputtering was conducted with 0.7 A (power 240 W). Total deposition time was 9 hours. PS beads were thoroughly mixed after every three hours in order to avoid deposition of TiO_2 films just on one side of beads.

2.2. TiO_2 film characterisation

Microstructure and elemental composition of TiO_2 films deposited on PS beads were analysed by Scanning Electron Microscope (Hitachi S-3400N). Chemical state of the magnetron sputtered films was analysed with X-ray photoelectron spectrometer (PHI Versaprobe 5000) using monochromated 1486.6 eV Al radiation; 25 W beam power; 100 μm beam size; and 45°

measurement angle. Observed spectra were shifted using anthropogenic carbon C 1 s peak at 284.8 eV. XPS spectra processing and analysis was done using Multipak software and NIST Standard Reference Database [25].

2.3. Photocatalytic TiO_2 properties testing

Photocatalytic TiO_2 properties were tested by investigating bleaching of the Methylene Blue (MB; made by Reachem Slovakia s.r.o.) in aqueous solution under UV-B irradiation. 1 g of PS beads with TiO_2 films were poured into the petri dish kept in dark for 24 hours. The UV-B exposure experiment was started straight after 10 ml of 15 mg/L concentration aqueous MB solution was syringed above the beads and top of the petri dish was covered by 500 μm thick fused silica disc to minimize evaporation of MB solution.

UV-B light was produced using medical lamp manufactured by Philips (PL-S 9W/01/2p 1CT) with aluminium reflector positioned 30 mm above the UV-B lamp. The distance between UV-B lamp and TiO_2 coating was 200 mm. UV-B lamp power declared by the manufacturer is roughly 1 W after 9 W nominal conversion to narrow wavelength UV-B radiation (305–315 nm).

UV-VIS spectrophotometer (Jasco V-650) was used for measuring of MB concentration changes. All measurements were repeated regularly at 1 hour intervals with 1.5 ml volume. MB solution was syringed back to the petri dish with the sample immediately after the spectroscopic analysis (approximately 2 minutes).

TiO_2 photocatalytic properties also were evaluated by observing inactivation of with *Escherichia coli* (*E. coli*) bacteria. Night culture of *E. coli* DH5α bacteria was grown by introducing several bacterial colonies into 10 ml of sterile Luria Bertani Broth (LB medium) and leaving them to grow for 16–18 hours in Environmental Shaker – Incubator ES-20 (250 rpm, 37 °C). Bacterial suspension was used to grow 100 ml of day culture suspension to optical density equal to 1. This suspension was divided into three parts: one third of the suspension was poured above TiO_2 coated EPS and placed in the dark (this suspension was used to obtain reference viability values); one third was used for exposition to UV-B light without any contact with TiO_2; and the last part of suspension was used to pour above TiO_2 coated EPS and exposed to UV-B light. UV-B light source as well as the distance between sample (thermostated at 37 °C) and the light were the same as in MB bleaching tests. Two types of E. coli bacteria were used: intact and ethylenediaminetetraacetic acid (EDTA) treated E. coli bacteria. Inactivation process took 45 min. After experiment the viability of *E .coli* cells was evaluated as a number of colonies after 18 hours of incubation. The number of colonies was evaluated manually by marking each calculated colony.

3. RESULTS AND DISCUSSION

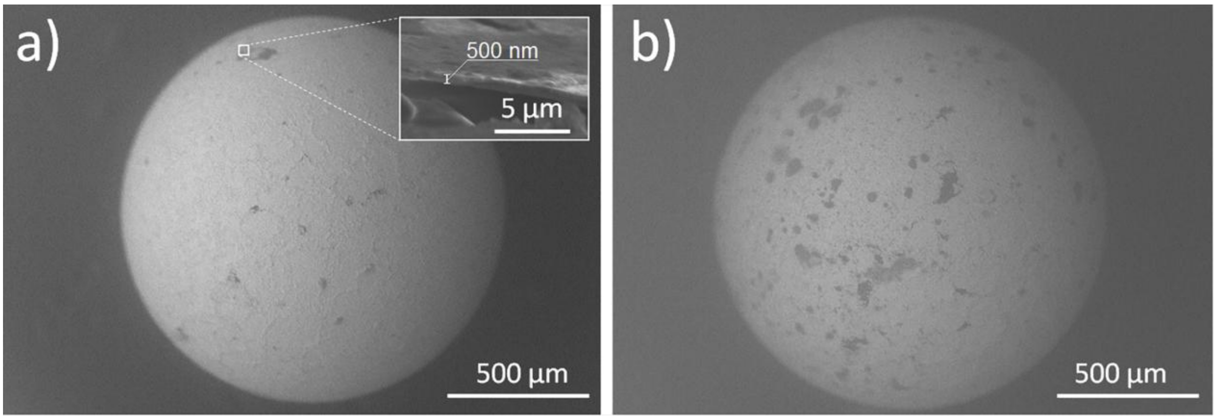

Fig. 1. SEM views of PS bead: a) after TiO_2 deposition; b) after MB decomposition experiment

Surface morphology of PS bead with deposited TiO_2 film could be seen in Fig. 1a. PS bead was covered with TiO_2 film. However, small parts without TiO_2 film were observed. These uncovered parts could appear due to several processes: shadowing effect during deposition process or friction between beads when they were stored after TiO_2 deposition. Cross-cutting measurement showed approximately 500 nm thickness of deposited TiO_2 film. However, TiO_2 film thickness varied from approximately 100 nm to 1100 nm. Thickness of deposited TiO_2 film depends on deposition parameters and mixing of PS beads. Surface morphology of PS beads was done after MB decomposition experiment (Fig. 1b). Results showed that some parts of TiO_2 film are lost and TiO_2 film itself has more cracks. This loss of TiO_2 film could be related with detaching of weakly bonded TiO_2 film when residual of MB solution is rinsed from the sample after MB decomposition experiment. Moreover, absorption of MB solution could initiate aggregation and sedimentation of MB solution on the surface of PS beads [26–28]. As a consequence, bonds between TiO_2 and PS beads could become weaker.

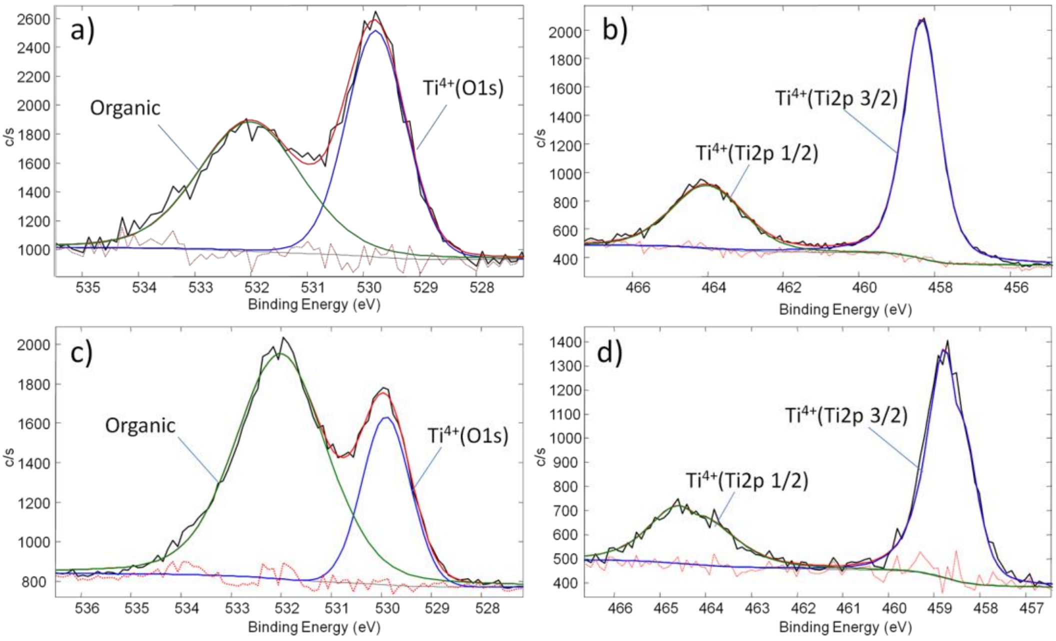

Fig. 2. XPS fitting results: a) O1s peak of deposited TiO_2 film; b) Ti2p peak of deposited TiO_2 film; c) O1s peak after MB degradation experiment; d) Ti2p peak after MB degradation experiment

Results of XPS analysis are shown in Fig. 2. Ti2p 3/2 peak was observed at 458.7 eV, separation between Ti2p 3/2 and Ti2p 1/2 is 5.7 eV (Fig. 2b). These two results are inherent for TiO_2 compound and confirm its formation on the surface of PS beads. However, the difference between binding energies of anatase and rutile phases is just 0.1 eV. Therefore it is not possible to reliably evaluate their ratio. Also is could be seen that O1s peak (Fig. 2a) consist of two parts: TiO_2 and organic. Area measurements performed that TiO_2 part covers 51.1% while organic part covers 48.9% of O1s peak. This observed organic (which include compounds such as C-O/C-OH, H_2O, etc.) could be adsorbed with humidity from atmosphere. All these compounds have very similar binding energy, therefore it is hard to identify separate compounds. Measurements of Ti2p after MB degradation showed that TiO_2 remain stable and do not form any other compound. However intensities of Ti2p peak decreased compared to Ti2p peak before MB decomposition measurement. This decreace could be related to several processes. First of all some parts of TiO_2 could be decomposed during MB degradation experiment. However this part is relatively small. Secondly, agglomeration and sedimentation of MB solution of the surface of PS beads could have influence in decrease of TiO_2 peak intensities. These agglomeration and sedimentation processes also have influence in increase in organic part of O1s peak [27, 28]. O1s peak showed change of Organic/TiO_2 ratio (TiO_2 – 26.4%, Organic – 73.6%). This increase of organic amount confirms that additional amount humidity was observed on the surface of PS beads during MB decomposition measurement.

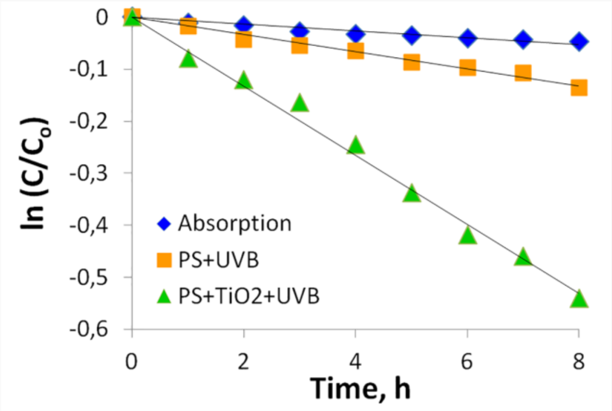

Fig. 3. MB aqueous solution bleaching in the dark (absorption), pure PS beads with UV-B irradiation (PS + UVB); PS with TiO_2 under UV-B irradiation (PS + TiO_2 + UVB)

Aqueous MB solution bleaching experiment results are shown in Fig. 3. First of all absorption of MB solution into PS beads with TiO_2 was evaluated. Beads were mixed with MB solution end kept in the dark for 8 hours. Measurement showed that absorption of MB solution into PS beads with TiO_2 film is relatively negligible. UV-B irradiation influence of MB bleaching was estimated using PS beads without TiO_2. Results showed that exposure to UV-B light initiates MB molecule degradation (first order reaction constant $k = 4.6\times10^{-6}$ s^{-1}). Bleaching of MB solution measurement using PS beads with TiO_2 films under UV-B irradiation showed significant degradation which is more than 4 times higher (first order reaction constant $k = 1.95\times10^{-5}$ s^{-1}) compared to single UV-B irradiation.

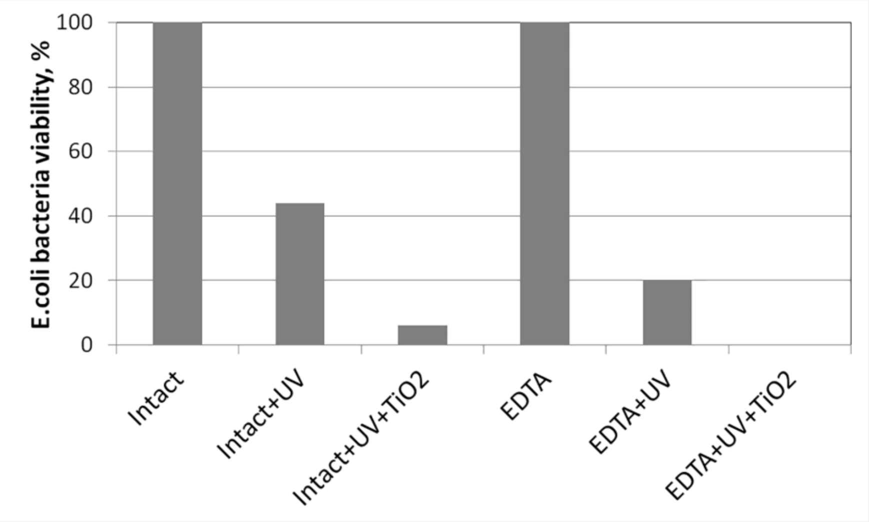

Fig. 5. Viability of intact and EDTA treated E. coli bacteria: untreated (Intact / EDTA), under UV-B irradiation (Intact + UV / EDTA + UV); under UV-B with TiO_2 coated PS beads (EDTA + UV + TiO_2)

E. coli viability test was performed with intact and EDTA treated bacteria under UV-B irradiation and combination of TiO_2 (PS beads with TiO_2 films) and UV-B (Fig. 5) after 45 min of treatment time. Results showed that UV-B alone can make damage for both intact and EDTA treated bacteria after 45 min of treatment (bacteria viability 44% and 20% respectively). Combination of UV-B and TiO_2 can increase decomposition of E. coli bacteria more than 7 times (bacteria viability 6% for intact and 0% for EDTA treated bacteria). This result indicates that there are two mechanisms of E. coli bacteria inactivation. E. coli consist of inner (phospholipid chains and proteins) and outer (lipopolysacchride (LPS), phospholipid layer and peptidoglycan (PP)) membranes [29]. P. Liu [4] demonstrated that UV-B alone or TiO_2 under daylight irradiation could destroy LPS but were not able to break down peptidoglycan. Therefore further inactivation of E. coli bacteria by UV-B irradiation or TiO_2 alone is limited by inability to damage PP layer. On the other hand combination of UV-B irradiation and TiO_2 could create highly reactive oxygen species [30, 31] (see Introduction part) which able to break down PP layer. This additional decomposition invokes reduction of E. coli bacteria viability [11, 32, 33]. The higher decomposition ratio of EDTA treated bacteria is related to EDTA mechanism. Using such method, bonds of LPS layer becomes weaker. Therefore it is easier to treat PP layer using UV-B or combined UV-B with TiO_2.

O. Akhavan in his previous works [34–36] demonstrated that bacteria could start to proliferate when viability is highly than 10%. In common, such decomposition (when viability is still more than 10 %) is useless for practical purpose. Our results showed that 45 min decomposition of E. coli bacteria using UV-B with TiO_2 deposited on PS beads could be suitable mechanism for practical purpose. On the other hand, further experiments for photocatalysis stability (cycling) are also required.

4. CONCLUSIONS

TiO_2 film was deposited on the surface of PS beads using magnetron sputtering technique. XPS measurement confirms formation of TiO_2. SEM views showed that thickness of TiO_2 is about 500 nm. However, TiO_2 film thickness varied from approximately 100 nm to 1100 nm. MB solution bleaching experiment showed high decomposition ratio (first order reaction constant $k = 1.95\times10^{-5}\ s^{-1}$) using combined UV-B and TiO_2 treatment. However increase of organic compounds as well as detachment of TiO_2 film was observed after MB decomposition. E. coli bacteria inactivation experiments showed that two-step mechanism initiate decomposition process: UV-B irradiation alone can damage outer E. coli bacteria membrane (lipopolysacchride), while combination of TiO_2 and UV can break down both lipopolysacchride and peptidoglycan outer membranes. Such mechanism invokes just 6% viability of E. coli bacteria, which is sufficient for practical purposes.

5. AKNOWLEDGEMENTS

This work was financially supported by The European Social Fund under project with SFMIS code: VP1-3.1-SMM-10-V-02-019.

REFERENCES

[1] A. Fujishima, K. Honda, Electrochemical photolysis of water at a semiconductor electrode, Nature. 238 (1972) 37–38. doi:10.1038/238037a0.
[2] H. Saleem, A. Habib, Study of band gap reduction of TiO2 thin films with variation in GO contents and use of TiO2/Graphene composite in hybrid solar cell, J. Alloys Compd. 679 (2016) 177–183. doi:10.1016/j.jallcom.2016.03.240.
[3] I. Dobrosz-Gómez, M. Gómez-García, S.M. López Zamora, E. Gilpavas, J. Bojarska, M. Kozanecki, J.M. Rynkowski, Transition metal loaded TiO2 for phenol photo-degradation, Comptes Rendus Chim. 18 (2015) 1170–1182. doi:10.1016/j.crci.2015.03.006.
[4] P. Liu, W. Duan, Q. Wang, X. Li, The damage of outer membrane of Escherichia coli in the presence of TiO2 combined with UV light, Colloids Surfaces B Biointerfaces. 78 (2010) 171–176. doi:10.1016/j.colsurfb.2010.02.024.
[5] R.H. West, M.S. Celnik, O.R. Inderwildi, M. Kraft, G.J.O. Beran, W.H. Green, Toward a Comprehensive Model of the Synthesis of TiO2 Particles from TiCl4, J. Ind. Eng. Chem. 46 (2007) 6147–6156. doi:10.1021/ie0706414.

[6] M. Casarin, C. Maccato, a Vittadini, Molecular Chemisorption on TiO 2 (110): A Local Point of View, J. Phys. Chem. B. 102 (1998) 10745–10752. doi:10.1021/jp981377i.

[7] U. Khan, N. Benabderrazik, A.J. Bourdelais, D.G. Baden, K. Rein, P.R. Gardinali, L. Arroyo, K.E. O'Shea, UV and solar TiO2 photocatalysis of brevetoxins (PbTxs), Toxicon. 55 (2010) 1008–1016. doi:10.1016/j.toxicon.2009.11.014.

[8] A.K. Benabbou, Z. Derriche, C. Felix, P. Lejeune, C. Guillard, Photocatalytic inactivation of Escherischia coli. Effect of concentration of TiO2 and microorganism, nature, and intensity of UV irradiation, Appl. Catal. B Environ. 76 (2007) 257–263. doi:10.1016/j.apcatb.2007.05.026.

[9] J. Schneider, M. Matsuoka, M. Takeuchi, J. Zhang, Y. Horiuchi, M. Anpo, D.W. Bahnemann, Understanding TiO 2 Photocatalysis : Mechanisms and Materials, Chem. Rev. 114 (2014) 9919–9986. doi:10.1021/cr5001892.

[10] S.G. Kumar, L.G. Devi, Review on modified TiO2 photocatalysis under UV/visible light: Selected results and related mechanisms on interfacial charge carrier transfer dynamics, J. Phys. Chem. A. 115 (2011) 13211–13241. doi:10.1021/jp204364a.

[11] I. Altin, M. Sökmen, Preparation of TiO2-polystyrene photocatalyst from waste material and its usability for removal of various pollutants, Appl. Catal. B Environ. 144 (2014) 694–701. doi:10.1016/j.apcatb.2013.06.014.

[12] E. V. Loddo, G. Marci, G. Palmisano, Extruded expanded polystyrene sheets coated by TiO 2 as new photocatalytic materials for foodstuffs packaging, Appl. Surf. Sci. 261 (2012) 783–788. doi:10.1016/j.apsusc.2012.08.100.

[13] M. Birnie, M. Gillott, S. Riffat, The immobilization of titanium dioxide on organic polymers, for a cost effective and energy efficient means of improving indoor air quality, Int. J. Green Energy. 3 (2006) 101–114. doi:10.1080/01971520500439567.

[14] L. Wang, J. Zhang, C. Li, H. Zhu, W. Wang, T. Wang, Synthesis, Characterization and Photocatalytic Activity of TiO2 Film/Bi2O3 Microgrid Heterojunction, J. Mater. Sci. Technol. 27 (2011) 59–63. doi:http://dx.doi.org/10.1016/S1005-0302(11)60026-1.

[15] C. Li, B. Wang, H. Cui, J. Zhai, Q. Li, Preparation and characterization of buoyant nitrogen-doped TiO2 composites supported by fly ash cenospheres for photocatalytic applications, J. Mater. Sci. Technol. 29 (2013) 835–840. doi:10.1016/j.jmst.2013.04.027.

[16] M.. Fabiyi, R.. Skelton, Photocatalytic mineralisation of methylene blue using buoyant TiO2-coated polystyrene beads, J. Photochem. Photobiol. A Chem. 132 (2000) 121–128. doi:10.1016/S1010-6030(99)00250-6.

[17] D. Raps, N. Hossieny, C.B. Park, V. Altstädt, Past and present developments in polymer bead foams and bead foaming technology, Polym. (United Kingdom). 56 (2015) 5–19. doi:10.1016/j.polymer.2014.10.078.

[18] S.M. Gupta, M. Tripathi, A review on the synthesis of TiO2 nanoparticles by solution route, Cent. Eur. J. Chem. 10 (2012) 279–294. doi:10.2478/s11532-011-0155-y.

[19] J. Tian, Z. Zhao, A. Kumar, R.I. Boughton, H. Liu, Recent progress in design, synthesis, and applications of one-dimensional TiO2 nanostructured surface heterostructures: a review, Chem. Soc. Rev. 43 (2014) DOI: 10.1039/C4CS00180J. doi:10.1039/C4CS00180J.

[20] Y. Horie, K. Daizaka, H. Mukae, S. Guo, T. Nomiyama, Enhancement of photocurrent by columnar Nb-doped TiO2 compact layer in dye sensitized solar cells with low temperature process of dc sputtering, Electrochim. Acta. 187 (2016) 348–357. doi:10.1016/j.electacta.2015.11.054.

[21] C.G. Kuo, C.Y. Hsu, S.S. Wang, D.C. Wen, Photocatalytic characteristics of TiO2 films deposited by magnetron sputtering on polycarbonate at room temperature, Appl. Surf. Sci. 258 (2012) 6952–6957. doi:10.1016/j.apsusc.2012.03.142.

[22] D. Hegemann, Plasma Polymer Deposition and Coatings on Polymers, 2014. doi:10.1016/B978-0-08-096532-1.00426-X.

[23] Y. Sasai, N. Matsuzaki, S. Kondo, M. Kuzuya, Introduction of carboxyl group onto

polystyrene surface using plasma techniques, Surf. Coatings Technol. 202 (2008) 5724–5727. doi:10.1016/j.surfcoat.2008.06.085.

[24] A. Vesel, Modification of polystyrene with a highly reactive cold oxygen plasma, Surf. Coatings Technol. 205 (2010) 490–497. doi:10.1016/j.surfcoat.2010.07.016.

[25] NIST X-ray Photoelectron Spectroscopy Database, NIST Standard Reference Database 20, Version 4.1, (n.d.). http://srdata.nist.gov/xps/Default.aspx (accessed December 20, 2016).

[26] Y. Lv, L. Yu, X. Zhang, J. Yao, R. Zou, Z. Dai, P-doped TiO2 nanoparticles film coated on ground glass substrate and the repeated photodegradation of dye under solar light irradiation, Appl. Surf. Sci. 257 (2011) 5715–5719. doi:10.1016/j.apsusc.2011.01.082.

[27] M.A. Elsayed, M. Gobara, Enhancement removal of tartrazine dye using HCl-doped polyaniline and TiO2-decorated PANI particles, Mater. Res. Express. 3 (2016) 1–16. doi:10.1088/2053-1591/3/8/085301.

[28] E.M. Saggioro, A.S. Oliveira, T. Pavesi, M.J. Tototzintle, M.I. Maldonado, F.V. Correia, J.C. Moreira, Solar CPC pilot plant photocatalytic degradation of indigo carmine dye in waters and wastewaters using supported-TiO2: Influence of photodegradation parameters, Int. J. Photoenergy. 2015 (2015). doi:10.1155/2015/656153.

[29] C. Raetz, Biochemistry Of Endotoxins, Annu. Rev. Biochem. 59 (1990) 129–170. doi:10.1146/annurev.biochem.59.1.129.

[30] P. Chen, F. Wang, Z.-F. Chen, Q. Zhang, Y. Su, L. Shen, K. Yao, Y. Liu, Z. Cai, W. Lv, G. Liu, Study on the photocatalytic mechanism and detoxicity of gemfibrozil by a sunlight-driven TiO2/carbon dots photocatalyst: The significant roles of reactive oxygen species, Appl. Catal. B Environ. 204 (2017) 250–259. doi:10.1016/j.apcatb.2016.11.040.

[31] M. Pelaez, P. Falaras, V. Likodimos, K. O’Shea, A.A. de la Cruz, P.S.M. Dunlop, J.A. Byrne, D.D. Dionysiou, Use of selected scavengers for the determination of NF-TiO2 reactive oxygen species during the degradation of microcystin-LR under visible light irradiation, J. Mol. Catal. A Chem. 425 (2016) 183–189. doi:10.1016/j.molcata.2016.09.035.

[32] C. Karunakaran, V. Rajeswari, P. Gomathisankar, Optical, electrical, photocatalytic, and bactericidal properties of microwave synthesized nanocrystalline Ag-ZnO and ZnO, Solid State Sci. 13 (2011) 923–928. doi:10.1016/j.solidstatesciences.2011.02.016.

[33] X. Hu, G. Li, J.C. Yu, Design, fabrication, and modification of nanostructured semiconductor materials for environmental and energy applications, Langmuir. 26 (2010) 3031–3039. doi:10.1021/la902142b.

[34] O. Akhavan, M. Abdolahad, Y. Abdi, S. Mohajerzadeh, Synthesis of titania/carbon nanotube heterojunction arrays for photoinactivation of E. coli in visible light irradiation, Carbon N. Y. 47 (2009) 3280–3287. doi:10.1016/j.carbon.2009.07.046.

[35] O. Akhavan, Lasting antibacterial activities of Ag-TiO2/Ag/a-TiO2 nanocomposite thin film photocatalysts under solar light irradiation, J. Colloid Interface Sci. 336 (2009) 117–124. doi:10.1016/j.jcis.2009.03.018.

[36] O. Akhavan, E. Ghaderi, Photocatalytic reduction of graphene oxide nanosheets on TiO2 thin film for photoinactivation of bacteria in solar light irradiation, J. Phys. Chem. C. 113 (2009) 20214–20220. doi:10.1021/jp906325q.

CYSENI 2017, May 25-26, Kaunas, Lithuania
ISSN 1822-7554, www.cyseni.com

A COMPARATIVE STUDY ON PHYSICAL PROPERTIES OF AL-DOPED ZINC OXIDE THIN FILMS DEPOSITED FROM ZINC ACETATE AND ZINC ACETYLACETONATE SOLUTIONS BY SPRAY PYROLYSIS

J. S. Eensalu, M. Krunks, I. Gromyko, A. Katerski, A. Mere
Tallinn University of Technology
Ehitajate tee 5, EE-19086 Tallinn – Estonia
E-mail: jako.eensalu@gmail.com

ABSTRACT

Doped zinc oxide is a suitable candidate for replacing indium tin oxide (ITO), one of the most popular transparent conductive oxides (TCO) as a cheaper and non-toxic alternative. In this paper we present a comparative study on highly transparent and electrically conductive aluminium-doped ZnO (AZO) thin films deposited by pneumatic spray pyrolysis (PSP) of a zinc acetate based solution and a zinc acetylacetonate based solution on soda lime glass. The structural, optical and electrical properties of the films were studied depending on aluminium content in the precursor solution and substrate temperature during deposition (T_s). The solvent was composed of isopropanol, water and acetic acid in the volume ratio 30:19:1. The solution used to prepare AZO thin films contained 0.2 M zinc acetate ($Zn(ac)_2$) or 0.2 M zinc acetylacetonate ($Zn(acac)_2$) between 0 and 15 at% [Al]/[Zn] using aluminium acetylacetonate ($Al(acac)_3$) as dopant. Solution spray rate was fixed at 3 ml/min. Substrate temperature was varied from 275 ^oC to 450 ^oC. Phase composition and crystal structure were studied by X-ray diffraction analysis (XRD). Transmittance, reflectance spectra, band gap and film thickness were determined by UV-VIS-NIR spectroscopy. Electrical resistivity, mobility and charge carrier density were measured by four point probe Hall measurements in ambient conditions.

According to XRD, AZO films are highly c-axis oriented up to 2-3 at% [Al]/[Zn] in the spray solution, depending on the zinc precursor. Crystallite size is 25-30 nm for AZO films deposited at T_s 400 ^oC. AZO films deposited from $Zn(ac)_2$ show higher/larger average crystallite size vs films deposited from $Zn(acac)_2$. AZO films grown at T_s 450 ^oC from $Zn(acac)_2$ solution containing 7.5 at% [Al]/[Zn] exhibit lower crystallinity as a mixture of ZnO, $Zn_6Al_2O_3$ and Al_2O_3 phases forms. All AZO films exhibited 80% average optical transmittance in the spectrum 400-800 nm wavelength range. Film thickness was 530 ±130 nm. Band gap in AZO films deposited from $Zn(ac)_2$ was 3,30-3,42 eV. Band gap in $Zn(acac)_2$ counterparts ranged from 3.32 eV in undoped to 3.58 eV in highly doped AZO films due to formation of secondary Al_2O_3 phase. Charge carrier mobility was 0,1-10 $cm^2V^{-1}s^{-1}$. The lowest electrical resistivity (0.40 Ωcm) and highest charge carrier concentration ($2*10^{19}$ cm^{-3}) were obtained at T_s 400 ^oC for films deposited from zinc acetate and zinc acetylacetonate solutions with [Al]/[Zn] of 3-7.5 at% and 7.5 at%, respectively. Zinc acetate was determined to produce AZO films with higher crystallinity and more stable band gap containing less secondary phases.

Keywords: AZO, Al-doped ZnO, pneumatic spray pyrolysis, thin films

CYSENI 2017, May 25-26, Kaunas, Lithuania
ISSN 1822-7554, www.cyseni.com

LUMINESCENCE OF X-RAY INDUCED RADIATION DEFECTS IN MODIFIED LITHIUM ORTHOSILICATE PEBBLES WITH ADDITIONS OF TITANIUM DIOXIDE

J. Cipa, G. Kizane, A. Supe, A. Zolotarjovs
University of Latvia
1 Jelgavas street, Riga, LV-1004 – Latvia
E-mail: janis.cipa@gmail.com

A. Zarins
Daugavpils University
Parades street 1a, Daugavpils, LV-5401 – Latvia

L. Baumane
Latvian Institute of Organic Synthesis
Aizkraukles 21, Riga, LV-1006 – Latvia

ABSTRACT

Modified lithium orthosilicate (Li_4SiO_4) pebbles with additions of titanium dioxide (TiO_2) are designed as a possible tritium breeder ceramic for the helium cooled pebble bed (HCPB) test blanket module (TBM).Due to the additions of TiO_2, lithium metatitanate (Li_2TiO_3) is obtained as a secondary phase in the modified Li_4SiO_4 pebbles. In combining of these two phases – Li_4SiO_4 and Li_2TiO_3, it is anticipated to obtain a modified tritium breeding ceramic with improved mechanical properties, without losing the benefit of the high lithium density, melting temperature and good tritium release behaviour.

Under the operation conditions of the HCPB TBM, the modified Li_4SiO_4 pebbles will be exposed to an intense neutron flux, a high temperature and a magnetic field. Under such conditions radiation-induced defects (RD) and radiolysis products (RP) can be induced in the tritium breeder pebblesand could play a crucial role in tritium diffusion and release processes. Previous researches confirmed that in the modfied pebbles both phase - Li_4SiO_4 and Li_2TiO_3, are separated by grain boundries and thus it is anticipated that the formation mechanisms and the structure of the accumulated RD and RP will be similar to single phase ceramics.

In order, to evaluate the formation of RD, the modified Li_4SiO_4 pebbles with 10, 20 and 30 mol% Li_2TiO_3were analysed by X-ray induced luminescence (XRL) technique and compared with the reference Li_4SiO_4 pebbles. After XRL measurements the accumulated RD were also analysed by thermally stimulated luminescence (TSL) and electron spin resonance (ESR) spectrometry.

XRL spectra of the modified Li_4SiO_4 pebbles consist of several bands with maxima at around 430, 490, 690, 700 and 800 nm. The XRL band with a peak at 490 nm could be associated with intrinsic defects in Li_4SiO_4 matrix whereas all the other maxima at lower photon energies are the result of the addition of TiO_2. For XRL kinetics measurements of the modified pebbles a trend of decreasing intensity was detected as X-ray irradiation time increases which could be associated whit recombination of defects present in the sample. After XRL measurements, detected signals for ESR spectra of the modified Li_4SiO_4 pebbles consists of at least three first derivative signals with g-factors 2.019 ±0.001, 2.003 ±0.001and 1.93 ±0.01 and most likely could be associated with E' centres (SiO_3^{3-} or TiO_3^{3-}), oxygen related defects and Ti^{3+} centres, respectively. The TSL technique confirmed that the accumulated RD recombine 400-773 K temperature.However, all above mentioned results also clearly confirm the necessity to further study the radiation-induced effects in the modified Li_4SiO_4 pebbles with additions of TiO_2.

Keywords: Lithium orthosilicate, Titanium dioxide, X-ray induced luminescence, XRL, Thermally stimulated luminescence, TSL, Electron spin resonance, ESR.

THERMAL NEUTRON DETECTION USING THIN PEN FILM DOPED WITH HIGH CROSS SECTION MATERIALS

J. Garankin, A. Plukis, E. Lagzdina
Center for Physical Sciences and Technology
Savanorių pr. 231, LT-02300 Vilnius – Lithuania
E-mail: Jevgenij.garankin@ftmc.lt

ABSTRACT

Poly(ethylene 2,6-naphthalate) (PEN) is promising as the new plastic scintillator, which emits deep-blue photons. Its photoluminescence emission peak (434–436 nm), and the decay time is of the order of 3 ns as well as it is resistant to a harsh environment. PEN has bigger oxygen barer than PET (polyethylene terephthalate). This material density (1.36 g/cm^3) is higher than typical organic scintillator and it emits a high number of photons per incident radiation event, up to 10500 photons per incident. In addition, it has 10% energy resolution in the 1 MeV energy region. In this study, thin PEN film with high neutron cross section dopants was used for the thermal neutron detection. 100 μm iron boride (FeB), 500 nm lithium tetraborate ($Li_2B_4O_7$) and lithium metaborate ($LiBO_2$) layers were coated on 125 μm PEN films. The iron boride layer was coated using prepared paste and the lithium based layer was coated using physical vapor deposition process.

The experimental setup was prepared for measurements. Detector dimensions 20×20 mm, photomultiplier (PMT) cathode window diameter is 20 mm and multiplication cascade has 10 dynodes. Detector film was loaded on a photomultiplier photocathode window using a liquid optical contact. Scintillator detector was covered with cadmium and lead. Reaction particles from the boron neutron and lithium neutron reaction were detected by scintillation in PEN, PMT pulses were registered and spectra were analyzed. Neutron flow was generated by ^{239}PuBe and ^{238}PuBe sources. Sources total neutron activity was 4.5×10^7 n/s. The neutron dose rate was about 300 μSv/h and the gamma dose rate was about 20 μSv/h. To decrease fast neutron energy the neutron source was surrounded by paraffin and polyethylene granules. ^{238}Pu source was used as α particles source to calibrate detector. The experiment model was prepared for simulation and the energy deposition in the film samples was calculated by MCNP6 code taking into account losses in the source and air gap for the alpha particle source and incomplete energy deposition for the electrons.

It was found that a small quantity of particles from the thermal neutron reaction could be detected in the strong neutron, gamma ray and recoil proton background. The PEN film detector with 100 μm thickness FeB layer showed that ionized particles form thermal neutron and ^{10}B reaction could be registered in strong background conditions. Otherwise, the detector with thin lithium based layer showed that ionized particles form thermal neutron and ^{6}Li could not be registered in same conditions.

Keywords: scintillation, irradiation detection, neutrons

CYSENI 2017, May 25-26, Kaunas, Lithuania
ISSN 1822-7554, www.cyseni.com

NUMERICAL INVESTIGATION OF J-INTEGRAL

R. Janulionis
Lithuanian Energy Institute
Breslaujos str. 3, LT-44403 Kaunas – Lithuania
E-mail: remigijus.janulionis@lei.lt

ABSTRACT

During Nuclear Power Plant (NPP) operation, degradation effects like corrosion, fatigue, and in-service degradation of fracture toughness, may significantly impact component integrity. Therefore while estimating structural integrity analysis it is important to evaluate the influence of the ageing on material degradation. When the metal is ageing under certain conditions the crack can appear and this finally could lead to the failure of construction. To evaluate the resistance to failure of the constructions with cracks usually the fracture criterions are used. For the ductile materials J-integral is used as a fracture parameter. Calculated J-integral value of the component with crack is compared with critical J-integral value of the material. Critical J-integral values are usually determined experimentally. There are two objectives of this work: create the methodology for critical J-integral determination using numerical methods; using created methodology evaluate the ageing influence to the critical J-integral.

In accordance with the objectives of the work the modelling of the J-integral of steel P91 was performed. Numerically simulation results were compared with experiment. For this purpose, the Finite Element (FE) method was used as numerical method and ABAQUS v6.11 as FE code.

Keywords: finite element method, J-integral, ageing

1. INTRODUCTION

Structural integrity of steel without and with cracks after long-term service is one of the most important factors to the safety and reliability of engineering components and also for prediction of their lifetime. During operation of steel components, degradation effects, such as corrosion, fatigue, and in-service degradation of fracture toughness, may significantly impact component integrity. Due to an ageing the degradation of material properties results in increased susceptibility to cracking under load and environmental conditions. Quantitative understanding of material fracture mechanism is a subject of modelling and experimental research in lifetime evaluation of structures. Analysis of structural integrity of the engineering structures shows that small cracks in the body of structures can be a cause of failure. It is important to know the limit when a crack starts to grow. One factor that can help an engineer to determine this limit is the critical J-integral [1]. Critical J-integral is used as a fracture parameter for ductile materials. Calculated J-integral value of the component with crack is compared with critical J-integral value of the material. And then it can be decided if construction with cracks is safe to be in operation. J-integral depends on the size and location of the crack, geometry, the magnitude of load, environment, i.e. temperature and etc. Usually critical J-integral is determined by an experiment, whereas the procedures are described in standards such as ASTM, ISO, etc. However, it is not always possible to conduct an experiment. Therefore, alternative methods for determination of critical values of fracture parameter are necessary. Finite element method (FEM) and boundary element method (BEM) are the most widely used techniques for evaluating J-integral.

A number of papers can be found on fracture parameters calculation using FEM [2, 3]. Jun-Young and all [4] presents sophisticated crack growth modelling technique which is used for critical J-integral determination. However this technique requires damage analysis to be added in the model and another three material constants have to be found. Also calculation results appear to be sensitive to mesh size. Overall it makes this technique complicated.

The influence of ageing of steel on the static mechanical properties is also important for the prognosis of J-integral. Cumino and all [5] carried out ageing research of the high chromium ferritic steels and estimated the following: about 10% maximum reduction of the tensile properties after 1,000 hours of exposure; constant values of ductility; and a strong reduction of the impact properties during the first 3,000 hours of exposure with an increase of brittle fracture. This means that ageing of the steel can potentially have influence on its fracture toughness.

The aim of this research is numerically determine J-integral and compare the results with experiment. Also, investigate the influence of ageing on J-integral of steel P91. The finite element method was applied for simulation. The J-integral was investigated for as received and aged steel P91. The experimental and numerical results were compared.

2. METHODOLOGY

The idea of numerical investigation of J-integral is numerically simulate the experiment according to actual procedures/instructions used for experiment conduction. For this purpose instructions described in ASTM E1820 standard [6] were used. The computer code ABAQUS v6.11 [7] has been chosen for numerical simulation. ABAQUS uses finite element method (FEM) for numerical simulation. ASTM E1820 instructions for critical stress intensity factor determination are presented in the following section.

2.1. Instructions for critical J-integral determination

According to ASTM E1820, to determine the value of J-integral it is necessary to develop so called J-R curve which consist of J-integral values at a series of measured specimen crack extensions. The actual result after the experiment is data points which later are used for J-R curve construction. However not all points are good to be used for J-R curve but the points which are in the area limited by 0.15 mm and 1.5 mm exclusion lines and by J_{limit} line. To draw an exclusion line in the first place it is necessary to determine a construction line which is calculated by the following equation:

$$J = 2\sigma_Y \Delta a \tag{1}$$

where σ_Y – effective yield strength (the average of yield strength R_p and ultimate strength R_m) of the material, MPa; $\triangle a$ – crack extension, mm.

The exclusion lines are just the parallel lines to the construction line with offset of 0.15 mm and 1.5 mm. J_{limit} is calculated by equation:

$$J_{limit} = b_0 \sigma_Y / 7.5 \tag{2}$$

where b_0 – uncracked ligament of the specimen, mm.

Using selected data points power law regression line can be constructed using a method of least squares. Also the offset line has to be determined. The offset line, the same as exclusion lines, is the line parallel to the construction line with offset of 0.2 mm. This line is used to determine the conditional J_Q value which is determined at the intersection of regression line with offset line. After J_Q is determined and if effective yield strength, specimen size and J_Q meet ASTM E1820 conditions it is possible to state that $J_Q = J_{IC}$.

2.2. Material and specimen

Test specimens were manufactured from commercial 30 mm thick P91steel plate. Thermal ageing of the specimens were carried out in electric furnace at 650 °C for 11000 h.

The tests of mechanical properties and fracture toughness were carried out using Instron Model 8801 servo-hydraulic testing machine with capacity of ±100 kN axial force. Tensile tests were performed according to EN ISO 6892-1:2009 [8] standard recommendations. Mechanical properties of steel are shown in Table 1. Here $R_{p0.2}$ – yield stress at 0.2% plastic strain, MPa; R_m – tensile strength, MPa; E – Young's modulus, GPa. According to presented results the ageing effect to mechanical properties of steel P91 is noticeable. However, actual drop of parameters is not significant and the biggest change of value was detected for tensile strength and it was up to 4.2%.

Table 1. Averaged mechanical properties of P91 steel

Ageing time at 650 °C, h	**$R_{p0.2}$, MPa**	**R_m, MPa**	**E, GPa**
0	513	666	214
11000	487	637	209

J-integral was determined in accordance with ASTM E1820 [6] using compact tension C(T) specimens. Experimentally determined J-integral values are later presented in section 3.

2.3. Numerical model

3D finite element model of Compact Tension (CT) specimen was prepared for J-integral modelling. The mesh of the models is shown in Fig. 1. The dimensions of FE models are the same as dimension of CT specimen used in the experimental testing, which was a standard CT specimen described in ASTM E1820 [6] with W = 50 mm and with side grooves. FE model was meshed with C3D20R elements [7]. These elements are quadratic brick shape and have 20 nodes.

The length of fatigue crack in FE models were the same as in CT specimen used in experiment and it was equal to a_1 = 2.78 mm (see Fig. 1).

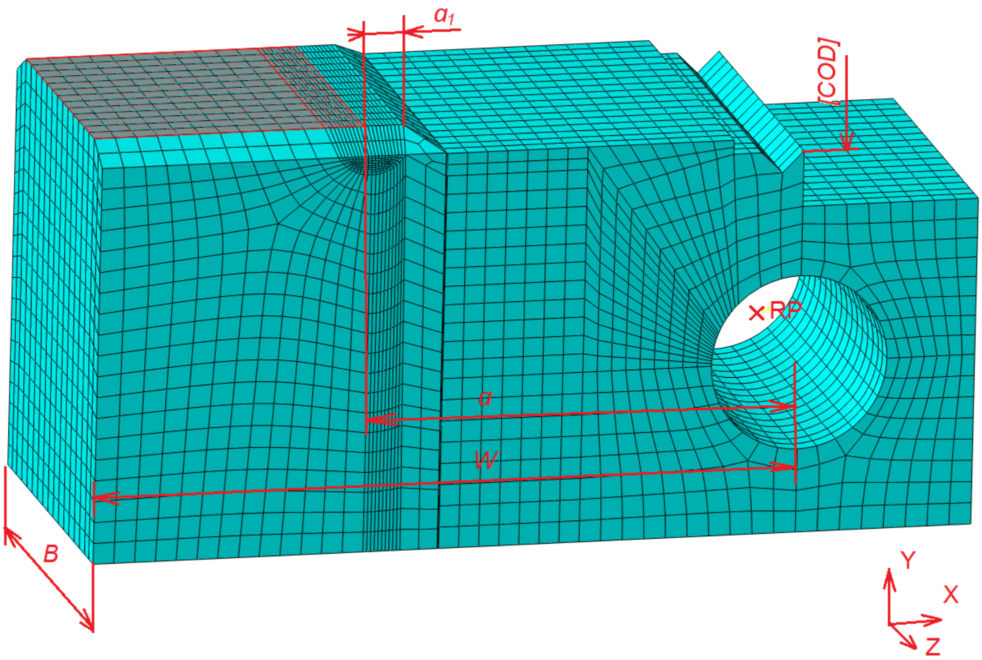

Fig. 1. Finite element mesh of CT specimen

As the specimen is symmetric about the XZ plane only half of the model was created. The symmetry boundary conditions were applied to the red coloured surface showed in Fig. 1. Also additional boundary conditions were added to the Reference Points (RP) placed at the centre of the hole used for pin in experiment. The displacements of RP were restricted in two directions, i.e. along the X and Z axes. However, the displacement was added along Y axis and was used as load.

As calculation results the following parameters were received: reaction force at the RP where displacement was added, crack opening displacement [COD] was measured at the edge point were extensometer was attached in experiment, and J-integral at crack tip. The calculated J-integral values were averaged along the crack front.

3. CALCULATION RESULTS

Comparison of CT specimen simulation result with experiment is presented in Fig. 2. The figure presents load versus crack opening displacement curves for experiment and FE simulation of as received and aged steel. As it can be seen the simulation results quite well match the experiment. Up to the peak of experimentally determined curve simulation result does not deviate more than 4% for all cases. However, results start to deviate more when the load starts to drop. This deviation occurs due to the fact that the drop of the load appears due to the growth of the crack and the actual crack growth is not directly modelled in numerical simulation.

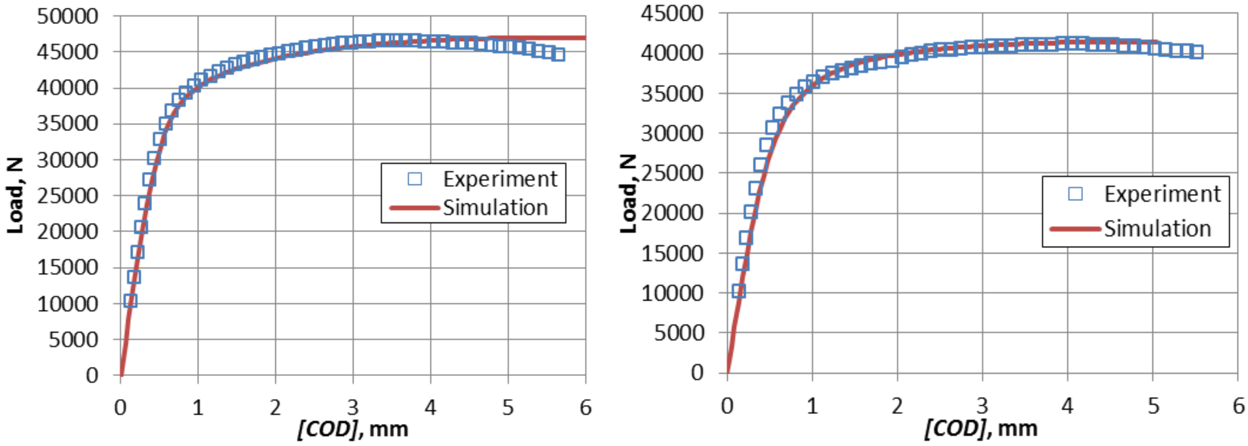

a) b)

Fig. 2. Simulation results of load vs COD compared with experiment: a) as received material; b) aged at 650 °C for 11000 h

According to methodology presented in section 2.1 it is necessary to construct J-R curve for J-integral determination. For this reason the crack extension should be measured during the tension of CT specimen. However, for the FE models presented in the section 2.3 the direct crack extension is not simulated. Therefore neither direct crack length measurement nor the elastic compliance measurement method suggested in ASTM code can be used. In this article the crack growth was determined from of the crack opening displacement and load ratio dependency on crack extension. In 1977 Sullivan and Crooker [9] have presented the crack opening displacement technique for crack length measurement. The authors suggest to use the polynomial function $a/W = f\,(E,\ B,\ [COD],\ P)$ they determined where E is Young's modulus, Pa; B – specimen thickness, m; $[COD]$ – crack opening displacement, m; P – load, N. However the function that authors recommend is only good to be used for materials which produce linear load vs COD trace.

For crack length extension of steel P91 the quadratic polynomial expression of experimentally determined curve $EB[COD]/P$ versus a/W, which is shown in Fig. 3, has been found. Found polynomial expression is presented below:

$$\frac{EB[COD]}{P} = -32051\left(\frac{a}{w}\right)^2 + 57864\left(\frac{a}{w}\right) - 23118 \tag{3}$$

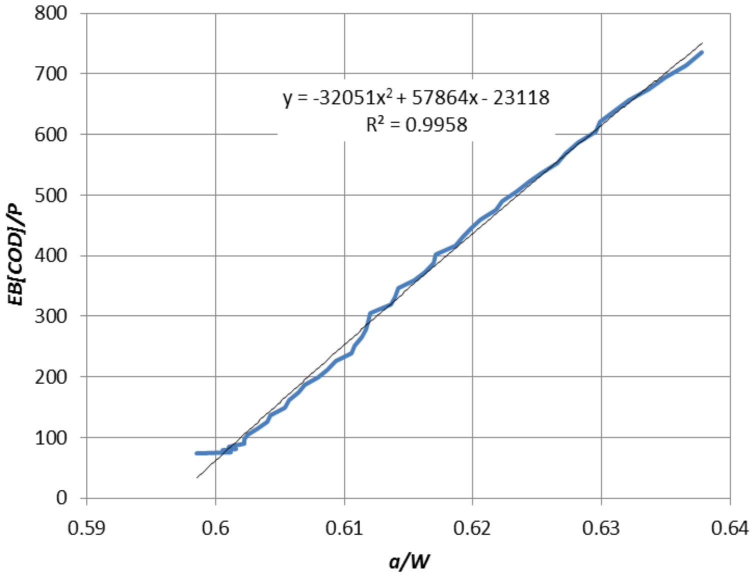

Fig. 3. *EB[COD] / P* versus *a / W*

Fig. 4 represents calculated J-R curves of not aged steel P91. J_Q values are determined at intersection points of curve and offset line. The ASTM E1820 indicates that for qualification of J_Q as elastic plastic fracture toughness J_{IC}, $J_{IC} = J_Q \leq \min(b_0\sigma_y / 10; B\sigma_y / 10)$. Applying this criterion determined J_Q values could be qualified as J_{IC}.

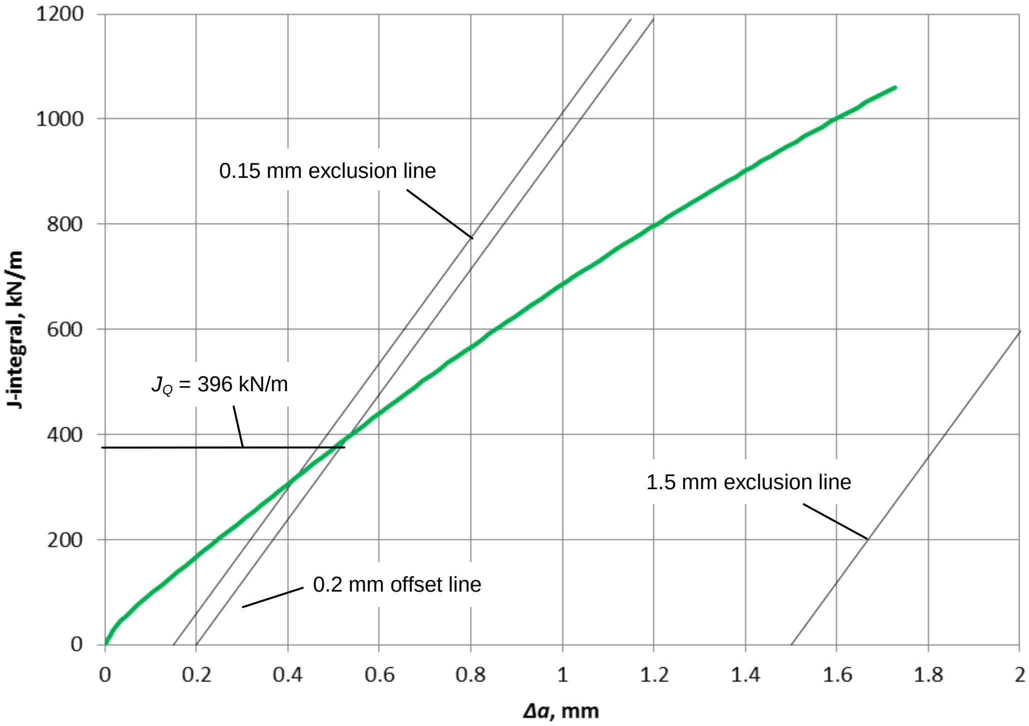

Fig. 4. Simulated J-R curve of as received steel P91

The comparison of experimentally determined and numerically modeled J-integral results for as received and aged steel are presented in Table 2. According to the data simulated J_Q values are smaller than experimentally determined for as received as well as for aged material. However, the drop of J_Q value by units using numerical simulation was determined close to experimental testing. It is necessary to note that J_Q determination procedure is quite complicated and the literature research revieled that J_Q values determined by different research institutions distribute in quite big interval between 290 kN/m [10] and 425 kN/m [11]. This show that my numerically determined J_Q values by using presented methodology are not necesseraly incorect. Further development and comparison with larger number of experiments needs to be done for validation of presented methodology.

Table 2. Numerical simulation and experimental results of J_Q determination

Ageing time at 650 °C, h	**J_Q, kN/m**		**Deviation from experiment,%**
	Experiment	**Simulation**	
–	475	396	17
11000	432	311	28
The drop of value by units	77	85	–

4. CONCLUSIONS

The numerical investigations of the Compact Tension (CT) specimen were carried out for the estimation of J-R curve for the ferritic-martensitic class steel (P91). The finite element method was used for the numerical investigation using the ABAQUS/Standard code. The values of J-integral were determined using finite element analysis simulating the experiment according to instructions described in ASTM E1820 standard. The numerical investigation results have been compared with the experimental test.

The quadratic polynomial expression for crack extension calculation for steel P91 was suggested on experimentally determined curve *EB[COD]/P* versus *a/W*.

Numerically simulated J_Q values are smaller than experimentally determined for as received as well as for aged material. However, simulated J_Q are still in the range of values determined in the literature, i.e. between 290–425 kN/m. Further development and comparison with larger number of experiments needs to be done for validation of presented methodology.

REFERENCES

1. ANDERSEN, T.L. *Fracture Mechanics. Fundamentals and Applications*. Boca Raton, Ann Arbor, Boston: CRC Press Inc, 1991. 793 p. ISBN 0-8493-4277-5.
2. ZARE, A., KOSARI, E. S. M., ASADI, I., BIGHAM, A., BIGHAM, Y. Finite Element Method Analysis of Stress Intensity Factor in Different Edge Crack Positions, and Predicting their Correlation using Neural Network method. *Research Journal of Recent Sciences*, 2014, Vol. 3(2), pp. 69-73.
3. LIKEB, A., GUBELJAK, N., MATVIENKO, Y. Stress Intensity Factor and Limit Load Solutions for New Pipe-Ring Specimen with Axial Cracks. *Procedia Material Science*, 2014, Vol. 3, pp. 1941-1946.
4. JUN-YOUNG, J., YUN-JAE, K., SA-YONG, L., JIN-WEON, K. Extracting ductile fracture toughness from small punch test data using numerical modeling. *International Journal of Pressure Vessels and Piping*, 2016, pp. 1-16.
5. CUMINO, G., DI CUONZO, S., DI GIANFRANCESCO, A., TASSA, O. Advanced high chromium ferritic steels for boiler components operating at high temperature. *Latin American Applied Research*, 2002, Vol. 32(3), pp. 229-235.
6. ASTM E1820-15a. *Standard Test Method for Measurement of Fracture Toughness*. ASTM International, West Conshohocken, PA, 2014. www.astm.org.
7. ABAQUS/Standard User’s Manual, Version 6.11.
8. ISO 6892-1:2009, Metallic materials – Tensile testing – Part 1: Method of test at room temperature.

9. SULIVAN, A. M., CROOKER, T. W. A crack-opening-displacement technique for crack length measurement in fatigue crack growth rate testing – development and evaluation. *Engineering Fracture Mechanics*, 1977, Vol. 9, pp. 159-166.
10. SASIKALA, G., RAY, S.K. Evaluation of quasistatic fracture toughness of a modified 9Cr-1Mo (P91) steel. *Materials Science and Engineering A*, 2008, Vol. 479, pp. 105-111.
11. KONOPÍK, P., VIEHRIG, H-W. Fracture toughness characterisation of the martensitic chromium steel P91. COMAT 2012. 2nd International conference on recent trends in structural materials. Czech Republic, 2012 11 21-22.

CYSENI 2017, May 25-26, Kaunas, Lithuania
ISSN 1822-7554, www.cyseni.com

IMPROVEMENT OF IMAGING ALGORITHMS TO INCREASE THE RELIABILITY OF ULTRASONIC INSPECTION RESULTS FOR NPP EQUIPMENT

D.R. Zhydyk, Ya.P. Cherniak, O.P. Shugailo
State Scientific and Technical Center for Nuclear and Radiation Safety
35-37 V. Stusa Street, 03142 – Ukraine
E-mails: dr_zhydyk@sstc.com.ua, yp_chernyak@sstc.com.ua, ap_shugaylo@sstc.com.ua

ABSTRACT

In order to check the quality of materials and confirm the operational reliability of NPP (Nuclear Power Plant) equipment, various nondestructive inspection methods, particularly ultrasonic inspection (USI), are used. The methods and tools currently used to display the USI results do not ensure adequate representativeness. The main issue is complex data processing. As a result, the displayed results partially lose their representativeness. In this connection, activities are underway to improve imaging methods to increase the reliability of USI results for NPP equipment.

The data imaging and filtering algorithms were analyzed to improve the imaging methods. Software for display of scanned defects was developed based on the Ray Casting algorithm. A group of tools was created to study the structure of defects and evaluate their sizes to allow generation of 3D images of USI scans along with systems for automatic scan of the inspection area.

To confirm the reliability of the imaging algorithm, the software code was preliminary verified, in particular, by display of all defects for an open test sample.

The preliminary verification indicates that this imaging algorithm is an effective method for analyzing the structure and defects of materials. The correlation coefficient shows linear dependence and correlation between the measured and made defect sizes.

Keywords: USI of NPP equipment, 3D visualization

1. INTRODUCTION

Various nondestructive inspection methods, particularly ultrasonic inspection (USI), are used to check the quality of materials and confirm the operational reliability of NPP equipment. The methods and tools currently used to display the USI results do not ensure adequate representativeness. The main issue is complex data processing that requires searching of ways to improve imaging methods to increase reliability and representativeness of USI results for NPP equipment. The objective of work is creation of new methodology for visualization of USI results in order to improve quality and representativity of test's results.

The data imaging and filtering algorithms were analyzed to improve the imaging methods. Software for display of scanned defects was developed based on the Ray Casting algorithm. A group of tools was created to study the structure of defects and evaluate their sizes to allow generation of 3D images of USI scans along with systems for automatic scan of the inspection area. Imaging examples used today are presented below.

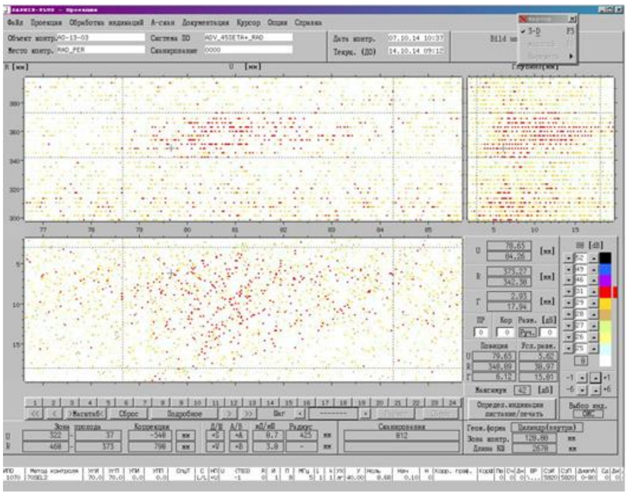

Fig. 1. Example for imaging of scanned defect. GSK converter. Ultrasonic wave entry angle 45°

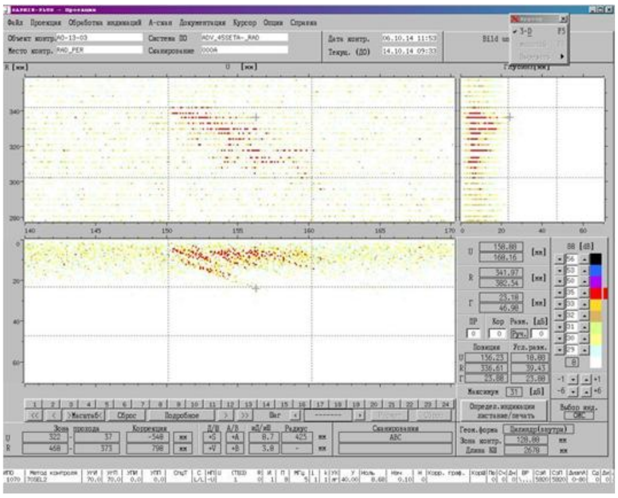

Fig. 2. Example for imaging of scanned defect. GSK converter. Ultrasonic wave entry angle 45°

2. RAY CASTING ALGORITHM

To generate three-dimensional images of USI scans, the Ray Casting algorithm was applied based on modeling interaction of rays with a virtual surface. It is used to image three-dimensional objects in two-dimensional space, considering interaction of rays from the observer to the light source. The ray can reflect, refract or pass thorugh voxel (element of space that indicates the value in cells of regular space lattice, tops of which are points with measurements performed). The algorithm does not consider the new path of a reflected ray. Depending on the type of interaction and intensity of interactions regarding this ray, the screen is filled with a certain color.

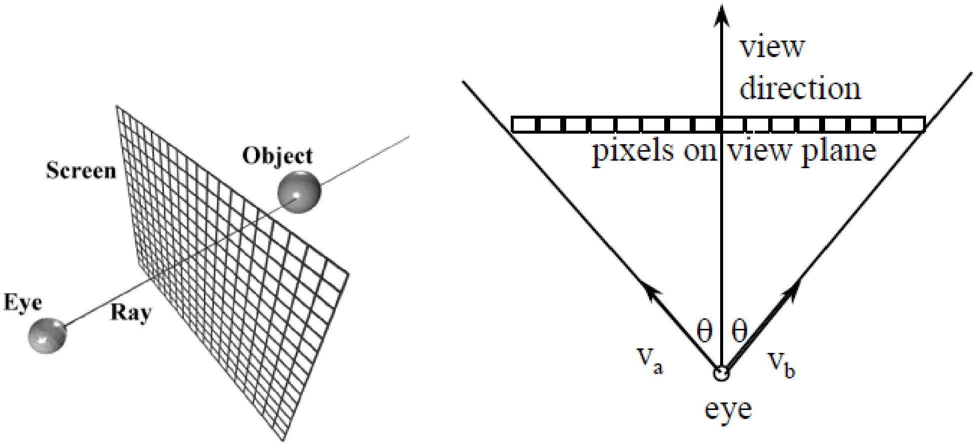

Fig. 2. Ray generation

Procedure for measuring the size of defects lies in determining the distance between points of the defect. Calibration shall be performed to perform each specific measurement. Calibration is based on determining voxel size in pixels. Voxel size depends on breakdown of lattice, in the nodes of which measurements are performed. After calibration measurement of voxel, one get interaction factor for size in mm and pixels. According to interaction factor, one receives defect sizes in milimeters.

Below are results of comparing proposed imaging method with existing imaging methods of USI visalisation (Transmmiter – GSK, ultrasonic waves entering angle 45°, control method – echo-pulse, frequency range: 0.3–10 MHz). Currently for visualisation of USI results the Raster Algorithm is used.

The figures below presents generated image recevied during verification of software code.

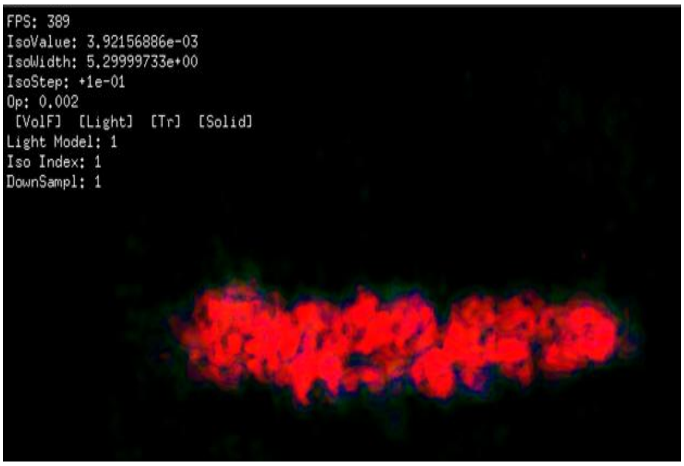

```
FPS: 389
IsoValue: 3.92156886e-03
IsoWidth: 5.29999733e+00
IsoStep: +1e-01
Op: 0.002
 [VolF]  [Light]  [Tr]  [Solid]
Light Model: 1
Iso Index: 1
DownSampl: 1
```

Fig. 3.1. Defect D5 of test sample No. A0-13/01 RayCasting Algorithm

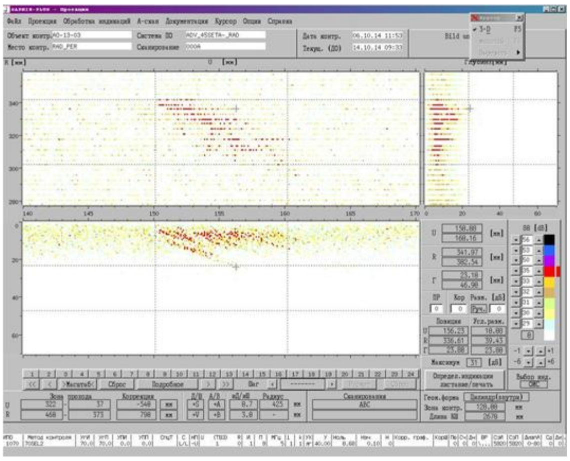

Fig. 3.2. Defect D5 of test sample No. A0-13/01 Raster represent Algorithm

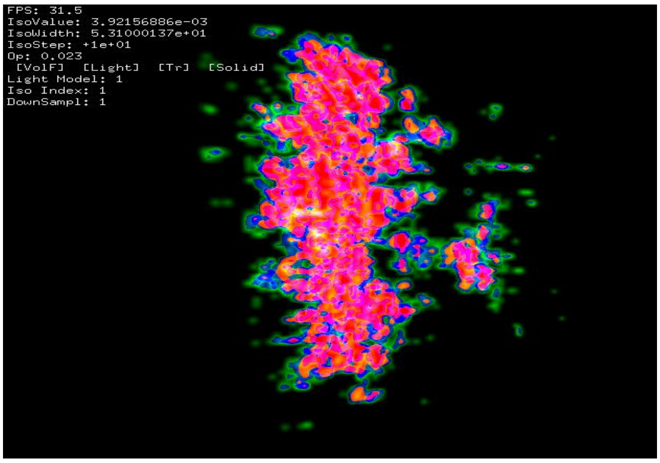

```
FPS: 31.5
IsoValue: 3.92156886e-03
IsoWidth: 5.31000137e+01
IsoStep: +1e+01
Op: 0.023
 [VolF]  [Light]  [Tr]  [Solid]
Light Model: 1
Iso Index: 1
DownSampl: 1
```

Fig. 3.3. Defect D6 of test sample No. A0-13/01 RayCasting Algorithm

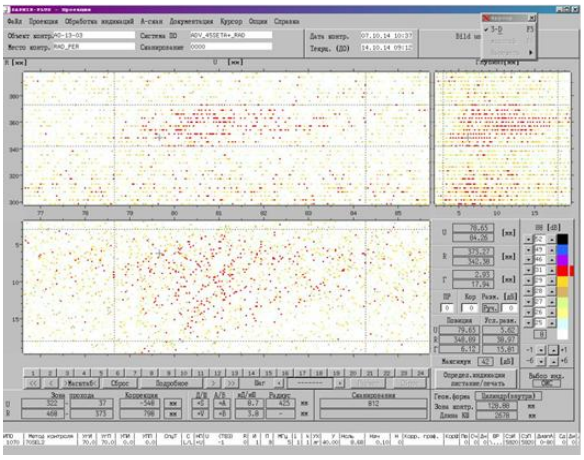

Fig. 3.4. Defect D6 of test sample No. A0-13/01 Raster represent Algorithm

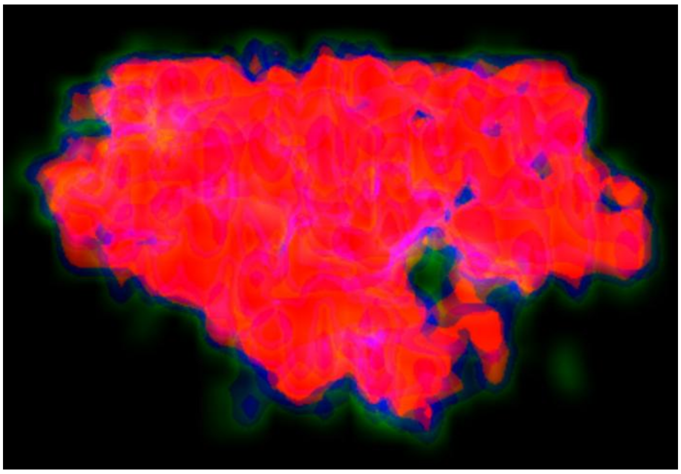

Fig. 3.5. Defect D1 of test sample No. A0-13/01 RayCasting Algorithm

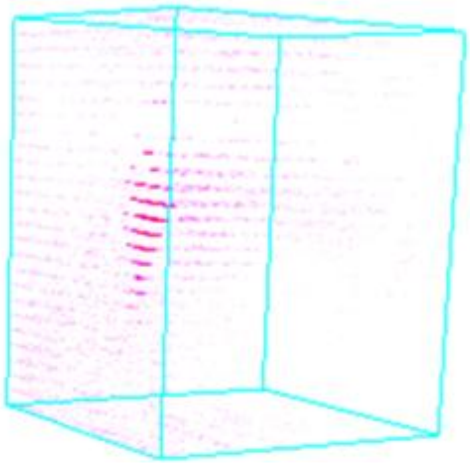

Fig. 3.6. Defect D1 of test sample No. A0-13/01 PyRasterCube Algorithm

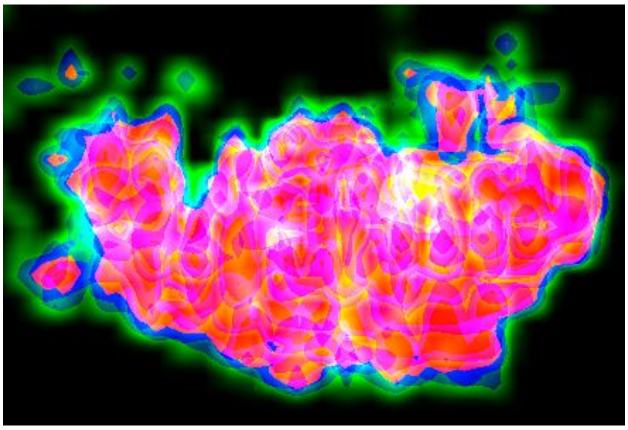

Fig. 3.7. Defect D4 of test sample No. A0-13/01 RayCasting Algorithm

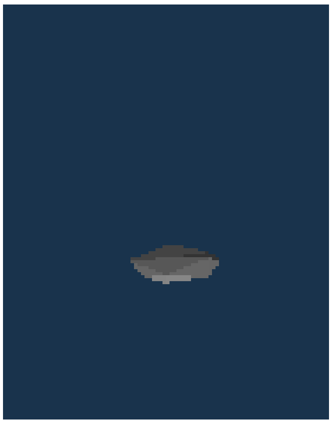

Fig. 3.8. Defect D4 of test sample No. A0-13/01 MarshingCubes Algorithm

Advantages of the method

- Fast response speed 200 FPS when performing manipulations
- Low sensitivity to noise
- Small amounits of memory required for processing
- Large number of freeness degree for research

Disadvantages of the method:

- Ignoring of repeately scattered rays
- Low quality of display of surfaces with high transparency.

3. VERIFICATION

To confirm the accuracy of received imaging, it is necessary to verify the method. Ray Casting was selected as the most adequate imaging algorithm. Using data obtained by non-destructive testing of an open test sample No. A0-13/01 applying ultrasonic method, the methods were verified by comparing the calculated parameters with passport data of a test sample.

Open test sample No. A0-13/01 is an imitation of a fragment of reactor pressure vessel cylindrical part with welding made of steel similar to acoustic properties of material of VVER-1000 RPV base metal. On the surfase of test sample No. A0-13/01, there is a two-layer anticorrosive cladding of 11 ±2 mm thick. Articficial discontinuities simulating crack-like defects were factored into the test sample.

The verification was divided into two key stages. The first stage included visual comparison of obtained imaging and form and orientation of produced defects. The second stage included comparison of parameters of measured and produced defects and determination of the correlation coefficient. Fig. 4 presents schematic view of an open test sample.

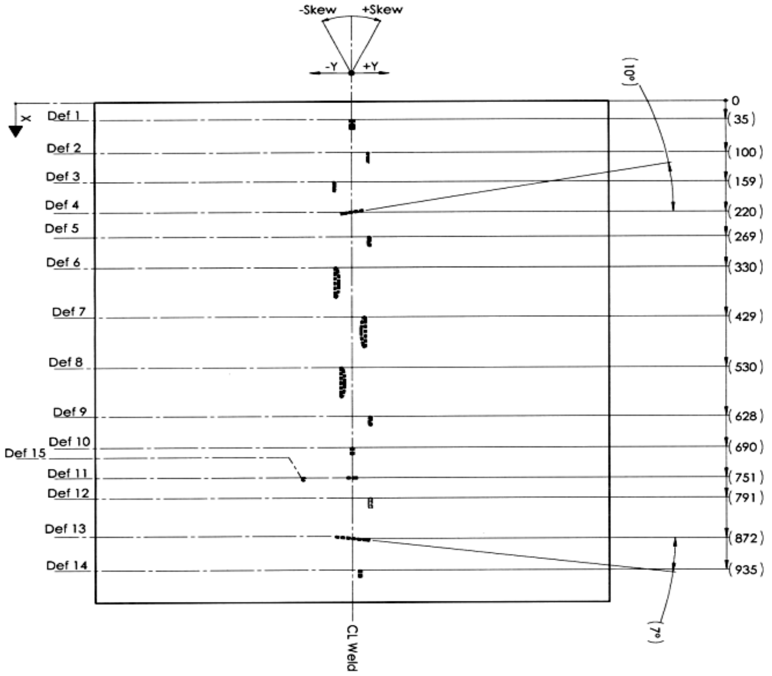

Fig. 4. Open test sample № A0-13/01

3.1. Visual comparison (Stage 1)

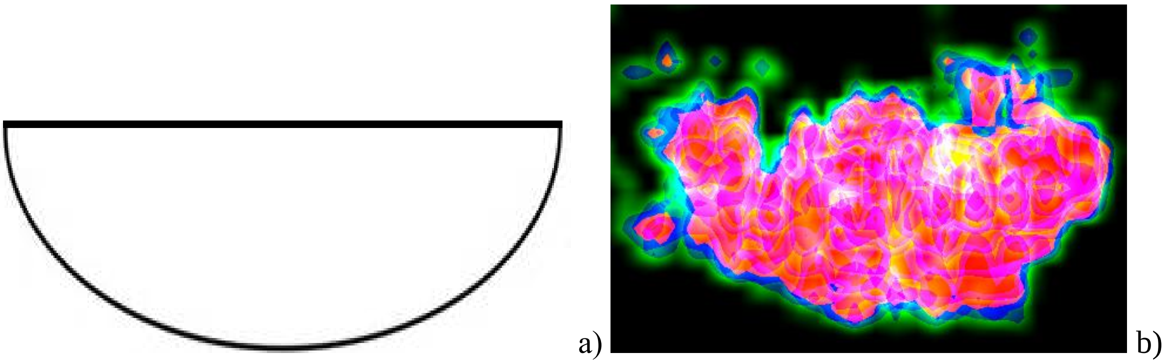

Fig. 5. a) Schematic view of D4 defect: minor semi-axis – 8 mm, major semi-axis – 20 mm (Passport data); b) Imaging of D4 defect

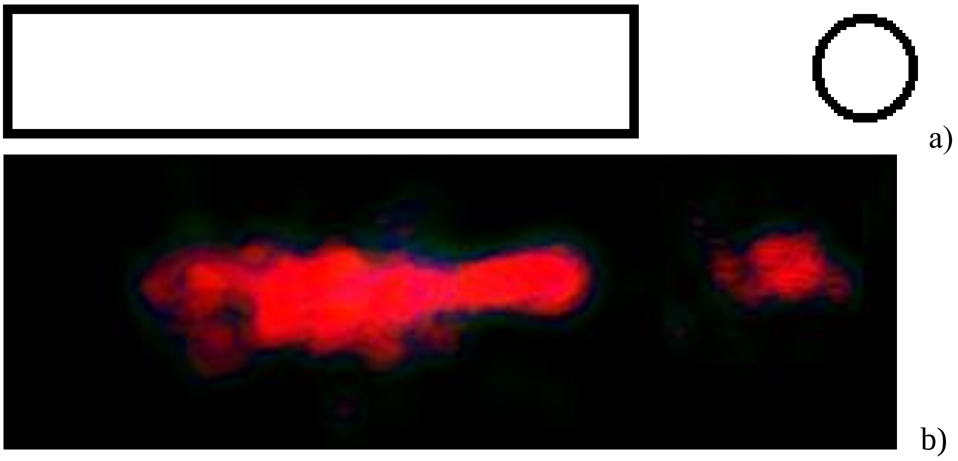

Fig. 6. a) Schematic view of D10 defect: length of rectangle – 15 mm (Passport data); b) Imaging of D10 defect

3.2. Correlation of defined and real parameters of defects (Stage 2)

Stage 2 is divided into two key phases. The first is to compare measured and produced parameters of defect, and then calculation of their correlation.
The equation for the correlation coefficient is as follows:

$$r_{XY} = \frac{COV_{XY}}{\sigma_X \sigma_Y} = \frac{\sum (X - \bar{X})(Y - \bar{Y})}{\sqrt{\sum (X - \bar{X})^2 \sum (Y - \bar{Y})^2}} \tag{1}$$

where X and Y are values of a specific measurement, and $\bar{X}$ and $\bar{Y}$ are calculated by formulas 2 and 3 correspondently:

$$\bar{X} = \frac{1}{n}\sum_{t=1}^{n} X_t \tag{2}$$

$$\bar{Y} = \frac{1}{n}\sum_{t=1}^{n} Y_t \tag{3}$$

where n is a number of measurements and X_t is a value of a particular measurement.

Correlation coefficient varies from -1 to +1, if:

$r_{xy} = 1$ – numerical values of X sampling are linearly dependent and completely correlate with Y sampling values.

$r_{xy} = 0$ – there is no correlation between X and Y sampling values.

$r_{xy} = -1$ – numerical values of X are linearly dependent and anticorrelated with Y sampling values.

Table 1. Correlation of measures and produced parameters

	Length	**Height**
Average	1.9	1.4
Maximum	6.2	3
Minimum	0.3	0
Standard deviation	3.052	1.432
Correlation	0.993	0.989

4. RESULTS

The new methodology for visualization of USI results is presented in the paper. Verification results showed that this imaging algorithm can be considered as efficient method for studying the structure of materials and defects. The correlation coefficient indicates the linear dependence and correlation of measured and produced sizes of defects.

It is planned to continue studies in the following areas:

- Improvement of filtering methods;
- Transition to cloud calculation;
- Improvement of graphical interface, etc.

REFERENCES

1. *F´abio F. Bernardon, Christian A. Pagot, Jo˜ao L. D. Comba Cl´audio T. Silva*, “GPU-based Tiled Ray Casting using Depth Peeling”.
2. *Eric Heitz* (2010), “Adaptive GPU Ray Casting Based on Spectral Analysis, Stefan Suwelack. Medical Imaging and Augmented Reality 5th International Workshop”, MIAR 2010.
3. *M. Durst* (1988), “Letters: Additional Reference to Marching Cubes”, Computer Graphics, vol. 22, no. 2, pp.72-73.
4. *Herasimov, V.G., Ostanin, Yu.Ya., Pokrovskii, A.D.* (2008), “Non-Destructive Testing of Quality Applying Ultrasonic Methods”, Moscow, Energy, 215 p.

CYSENI 2017, May 25-26, Kaunas, Lithuania
ISSN 1822-7554, www.cyseni.com

TECHNOLOGY FOR PRODUCTION OF PHOSPHORUS CONTAINING FERTILIZERS FROM CENTRAL KYZYLKUM PHOSPHORITE

A. J. Allamuratova, A. U. Erkaev
Tashkent chemical technological institute
32, Navoi Street, 100011 – Uzbekistan
E-mail: ahmed_ram@mail.ru

A. M. Reymov
Institute of General and Inorganic Chemistry of the Academy of Sciences of Uzbekistan
77a, Mirzo-Ulugbek Street, 100170 – Uzbekistan
E-mail: ahmed_ram@mail.ru

ABSTRACT

We have studied process of the high calcareous containing phosphorites from Central Kyzylkum (17% P_2O_5) treatment by circulating solution of ammonium and calcium nitrates to obtain phosphorite concentrate. At that yield of P_2O_5 into the phosphorite concentrate is 55–65%, the calcium module is reduced by 0.18–0.56 from the overall initial one.

Obtained concentrate depending on the experience condition contents 18.27–19.60% of P_2O_5 and 44.66–48.42% of CaO. Alongside with washed and calcined concentrate in technological cycle liquid suspended fertilizers with content 2–4% P_2O_5 and 12–14% N are obtained simultaneously. Subsequent the process of decomposition of phosphorite concentrate with nitric acid and ammonization of nitrogen acid slurry has been investigated. In a result of experimental studies nitrogen-phosphorus-calcium fertilizers have been prepared with the following composition: 17.3–21.34% N, 12.7–16.36 P_2O_5 and 25.1–27.86% CaO. At the second stages the technology concentrated phosphorus containing fertilizers with composition: 0.91–2.7% N, 27.13–30.61 P_2O_5 and 37.34–39.34% CaO. In both variants fertilizers are obtained with advanced content of acceptable forms of phosphorus and calcium.

The phase composition of the obtained fertilizers was determined by radiographic and infrared spectrometry analysis. It was defined that nitrogen-phosphorus fertilizers consist of dicalcium phosphate, indecomposable fluorine-and hydroxyapatites, ammonium and calcium nitrates, and phosphorus containing fertilizers consist of various forms of calcium phosphates, indecomposable fluorine-and hydroxyapatites, as well as small quantity of ammonium and calcium nitrate salts.

Thus we have presented the possibility of treatment of low-grade phosphorites from Central Kyzylkum into concentrated phosphates and complex fertilizers. The manufacturing scheme has been proposed and the material balance of the fertilizers production has been calculated.

Keywords: phosphorite, concentrate, nitric acid, nitrogen-phosphorus-calcium fertilizers.

1. INTRODUCTION

Central Kyzylkum phosphorite has not analogs on quality in Commonwealth of Independent States and is in the top ten of deposits in the world. Resources of the phosphorites raw material (PRM) are estimated in quantity 43.5 mil ton of 100% of P_2O_5 that provides needs of Uzbekistan agriculture in phosphorus fertilizers more than by 100 years. It is necessary noted that Kyzylkum phosphorites on content of main component are applied to low-grade ore. Considerable quantity of carbonate compounds (calcium module is $CaO:P_2O_5 = 2.85$), clay minerals, organic matters and chlorine are contented in them [1, 2]. That’s why at Kyzylkum phosphorite combine stages of raw thermic benefication and washing up it out of chlorine have been realize. In results in concentrated phosphorite obtained P_2O_5 reaches up to 26%, but due to complicacy of benefication technology and large heat-and-power engineering expenditure, cost of washed and calcined concentrate and phosphorus fertilizers are rised significantly. Moreover, productivity of combine limited, i.e. it does not increase 760 thousand ton (197.6 thousand тon 100% of P_2O_5) per year. Annual need of agriculture of Republic of Uzbekistan in phosphorus fertilizers makes 525.21 thousand ton 100% of P_2O_5.

Issue of inexpensive phosphorus containing fertilizers based on local raw material can be solved by implication into sphere processing of low-grade phosphorites by nitric acid. In a case chemical energy of nitric acid is used to disclose phosphate raw material as well as NO_3^- anions in form of nutrient is left in finished product. In addition the approach is less difficult for quantity of raw material than sulfuric processing, owing to low solubility impurities R_2O_3 in the resulting extract [3].

In this connection, we had been investigated the processing of high calcareous phosphate rock from Central Kyzylkum phosphorite (17% P_2O_5) by recirculating solutions of ammonium nitrate and calcium to obtain the phosphorite concentrate. By nitric acid decomposition of the phosphorite concentrate liquid nitrogen-calcium and concentrated phosphorus fertilizer obtained with prolonged action. The aim presented study is to explore chemical composition phosphorus containing products prepared by nitric acid treatment of the Central Kyzylkum phosphorite.

2. METHODOLOGY

In the experiments, the following salts used are phosphate powder from Central Kyzylkum, calcium nitrate and ammonium nitrate, nitric acid and ammonia gas. The chemical and dispersed composition of the initial raw material is shown in Table 1 and 2 below.

Table 1. The chemical composition of the ordinary powder from Central Kyzylkum phosphorite

Components content, weight. %							**CaO: P_2O_5**	**$P_2O_{5accep.}$: P_2O_{5total}**
P_2O_5	**CAO**	**Al_2O_3**	**Fe_2O_3**	**MgO**	**F**	**CO_2**		
17.10	46.30	1.33	1.09	1.78	1.87	15.90	2.71	18.49

Table 2. Dispersed composition of phosphorite powder

Size grade, mm	**Fraction outlet, %**
-2+0.5	–
-0.5+0.315	1.9
-0.315+0.16	8.6
-0.16+0.1	20.3
-0.1+0.063	37.7
-0.063+0.05	16.2
-0.05	15.3
Starting mass	100

Processing unenriched phosphate rock by circulating solution (CS) of ammonium and calcium nitrate was conducted in a temperature-controlled cylindrical reactor with volume of 200 ml equipped by a paddle stirrer for 60 minutes at 30 °C. After completion of the processing of the resulting suspension settled for 4–6 minutes, then the slurry was separated from the upper part of the thickened mass. Condensed mass was filtered and the precipitate is dried at a temperature of 100 °C. The phosphorite concentrate dried and the resulting suspension with the main components was analyzed by known methods [4]. The results are summarized in Table 3 and 4.

When preparation the phosphate fertilizers, the phosphorite concentrate (18.27–19.60% of P_2O_5 and 44.66–48.42% of CaO) was decomposed by nitric acid (HNO_3) at a rate of 100% from the stoichiometry on calcium oxide. The process temperature is maintained at a level of 40 °C for 30 minutes. The resulting dense nitric acid pulp was repulped by recycle solution of ammonium and calcium nitrate (RSACN) previously prepared at L:S = 1:3. Further the slurry was ammoniated with ammonia gas to various pH values (4.4, 5.1, 6.2 and 7.0). The solid phase was separated from the liquid subsequently washing with water circulating at a ratio L: S = 1: 2, the wet cake was dried at a temperature 95–100 °C for 4 hours and analyzed according to known methods.

3. RESULTS AND DISCUSSIONS

From the data obtained (Table 3) that the interaction of the phosphate powder with solutions of nitrate salts depending on the N_{amm}: N_{nit} (ratio of ammonia nitrogen (N_{amm}) to nitrate nitrogen ($N_{nit.}$)) is activated (transfer of unassimilable P_2O_5 forms in plants as an acceptable (P_2O_{5accep}.) form) raw material phosphate [5–7]. The ratio of P_2O_{5accep}. : P_2O_{5total}. on Trilon B and by 2% of citric acid in the dried samples of the solid phase is 44.97–48.32 and 36.45–41.56%, respectively, which exceeds several times higher than the ratio P_2O_{5accep}. : P_2O_{5total} in the initial phosphorite powder – 18.49% and 12.7% relatively.

Table 3. Effect of initial ratio of CS:PRM and N_{amm}:N_{nit} on composition of dried phosphorite concentrate

Starting ratio of CS:PRM	N_{amm}:N_{nit}	Chemical composition of the dried product, %							$\frac{CaO}{P_2O_5}$
		P_2O_{5total}	P_2O_{5accep} on 2% of citric acid	P_2O_{5accep} by 0.2 M Trilon B	CaO_{total}	CaO_{accep}	CaO_{water}	N	
3:1	0.8	19.37	9.36	8.05	48.42	31.81	3.06	0.64	2.50
	0.5	18.56	8.94	7.50	46.77	31.08	3.64	0.69	2.52
	0.2	18.27	8.77	7.33	46.58	31.10	4.47	0.80	2.55
4.5:1	0.8	19.41	9.17	7.77	47.36	29.55	2.78	0.53	2.44
	0.5	18.67	8.72	7.18	46.11	29.01	3.36	0.65	2.47
	0.2	18.27	8.49	6.96	45.67	28.98	4.04	0.76	2.50
6:1	0.8	19.60	9.05	7.39	46.65	28.37	2.56	0.41	2.38
	0.5	18.84	8.5	6.95	45.21	27.6	3.16	0.62	2.40
	0.2	18.30	8.23	6.67	44.66	27.36	3.76	0.71	2.44

At low values of CS:PRM = 3:1 in the same conditions $P_2O_{5accep.}$ and $CaO_{accep.}$ are 2–3% higher than the CS:PRM = 6:1. This is due to the fact that with increasing ratio of CS:PRM amount of transfers of acceptable CaO and P_2O_5 in the liquid phase increased. With increasing ratio of N_{amm}:N_{nit} in the circulating solutions total concentration of P_2O_5 is increased to 18.27–19.6%, and the calcium module is reduced to 2.38 (that is 2.71 from starting).

Chemical analysis shows the composition of the liquid phase (Table 4.) that with increasing initial ratio CS: PRM (3:1 to 6:1) in suspension the nitrogen content varied in a range of 14.7–14.74% and 8.96–9.31%, respectively at N_{amm}:N_{nit} equal to 0.8 and 0.2, and P_2O_{5total} content decreased from 2.26 to 0.95% and from 2.14 to 0.72%, respectively. With carrying out this process, one part of the liquid phase returns to the initial step of treating the phosphate raw material and the rest of one is used as a liquid fertilizer containing suspended nutrients (N + P_2O_5 + CaO) – 22.1–29.77%.

Table 4. Effect initial ratio of CS:PRM and N_{amm}:N_{nit} on the composition separated liquid phase

Starting ratio of CS:PRM	N_{amm}:N_{nit}	P_2O_{5total}, %	CaO_{total}, %	N, %
3:1	0.8	2.26	9.20	14.72
	0.5	2.16	13.85	11.76
	0.2	2.14	18.67	8.96
4,5:1	0.8	1.52	7.85	14.72
	0.5	1.50	12.10	11.80
	0.2	1.43	16.51	9.22
6:1	0.8	0.95	6.41	14.74
	0.5	0.80	10.53	11.95
	0.2	0.72	14.30	9.31

Thus, based on the experiments showed the possibility of complex processing of low-grade phosphate from Central Kyzylkum allowing in the same production cycle produce phosphorite concentrate and liquid suspended fertilizer containing nutrients (N + P_2O_5 + CaO) – 22.1–29.77%.

Then we studied the process of nitric acid's extract ammoniation obtained by decomposition of the pretreated phosphate rock by circulating solutions of calcium and ammonium nitrate, and carried out technological research of the process of obtaining phosphorus-containing and liquid suspended fertilizer from products of nitric acid's extract ammonization of phosphate based on Central Kyzylkum (Table 5).

Table 5. Composition phosphorus containing fertilizers obtaining on the laboratory facility

№	**pH pulp**	**Components content, weight, %**						**$P_2O_{5accep.}$: P_2O_{5total} on 2% of citric acid, %**	**P_2O_{5accep}: P_2O_{5total} by 0.2 M Trilon B, %**	**CaO_{accep}: CaO_{5total} on 2% of citric acid, %**
		P_2O_{5total}	**P_2O_{5accep} by 0.2M Trilon B, %**	**$P_2O_{5accep.}$on 2% of citric acid, %**	**CaO_{total}**	**$CaO_{accep.}$**	**N_{total}**			
1	4.4	28.55	22.36	23.65	38.54	33.04	1.44	78.34	82.83	85.73
2	5.1	28.01	22.07	23.28	39.5	33.97	2.01	78.79	83.11	86.00
3	6.2	27.11	21.56	22.71	38.78	33.44	2.20	79.53	83.77	86.23
4	7.0	27.85	22.60	23.42	40.38	34.85	2.56	81.15	84.09	86.30

It should be noted that the implementation of the process of obtaining phosphorus-containing fertilizers, the liquid phase is formed, which is composed mainly of calcium and ammonium nitrate. They may be recommended to use as a liquid nitrogen-calcium fertilizer that can be applied successfully during the foliar treatment of cotton and grain crops.

The results of laboratory experiments have allowed to develop the basic technological processing scheme on treatment of phosphate from Central Kyzylkum to phosphorus and suspended liquid fertilizer (Fig. 1). According to the flow sheet high calcareous phosphate powder from the hopper (1) through the feeder (2) enters the repulpator (3) where processed by circulating solution of calcium and ammonium nitrate further thickened part of the slurry is separated in the settlers (4) and (5) and sent to the decomposition reactor (8). Here it is fed simultaneously the nitric acid through

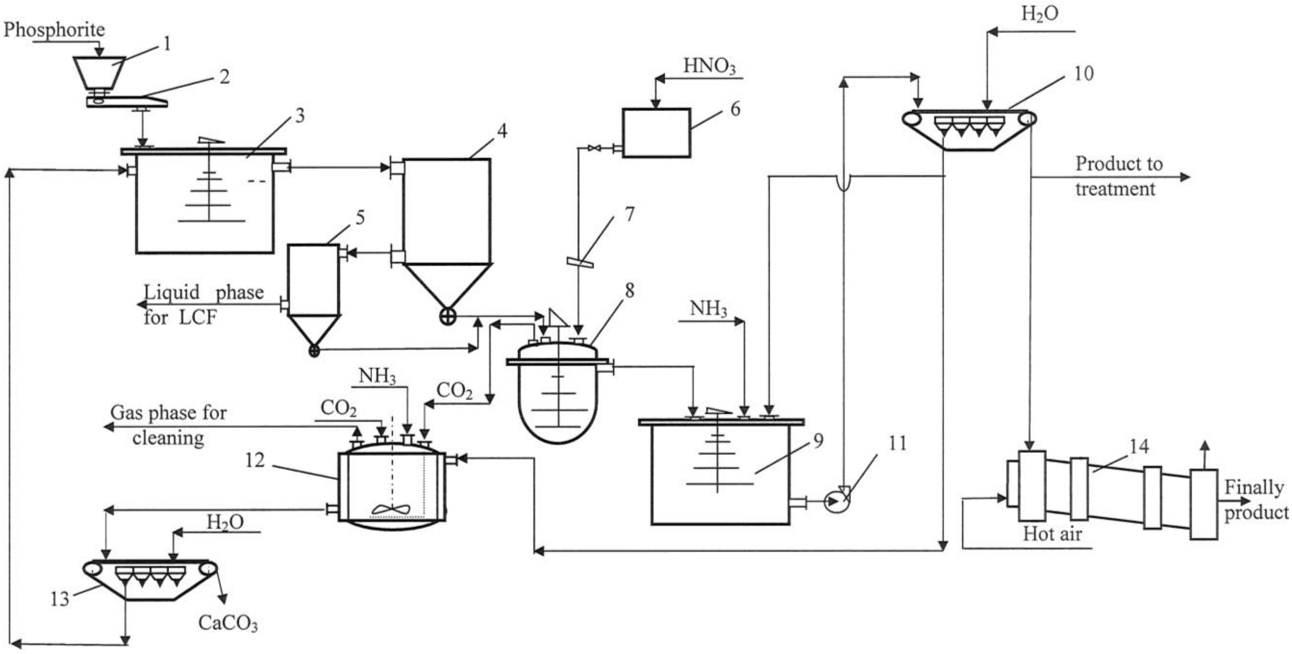

Fig. 1. Flow sheet for the processing of high calcareous phosphorite from Central Kyzylkum.
1 – phosphate feed hopper; 2 – dispenser; 3 – repulpator; 4 – settler stage 1; 5 – settler stage 2;
6 – pressure tank of nitric acid; 7 – slit feeder; 8 – reactor; 9 – repulpator- ammonizator;
10, 13 – band vacuum filter; 11 – pump; 12 – converter; 14 – drum-dryer

a slit batcher (7) of the pressure tank (6). The clarified part of the solution is used as a liquid complex fertilizer (LCF).

Nitrogen-calcium-phosphate slurry formed in the reactor, is fed in repulpator - ammonizator (9) and mixed with circulating ammonium and calcium nitrate solution further ammoniated by gaseous ammonia to a pH of 4.5–5.0. The resulting slurry by pump (11) is pumped to a vacuum belt filter (10) for separating the ammonium and calcium nitrate solution from the solid phase. After washing the filter cake solid phase is sent to the dryer drum (14) for single phosphorous and other types of fertilizers. One part of the filtrate is circulated in the repulping and ammoniation stage of nitric acid slurry as working solution and the second portion is directed to the converter (12) for the conversion of calcium nitrate with carbon dioxide in the presence of ammonia. Suspension from the converter is supplied to the vacuum belt filter (13) for separating the calcium carbonate generated from the liquid phase, latter is used as a circulating solution for pretreatment high calcareous phosphorite or after evaporation can be used for complex fertilizers generation.

Fig. 2 provides a block diagram and the material balance of nitric acid processing 1000 kg high calcareous phosphorite from Central Kyzylkum, which is calculated based on the laboratory researches.

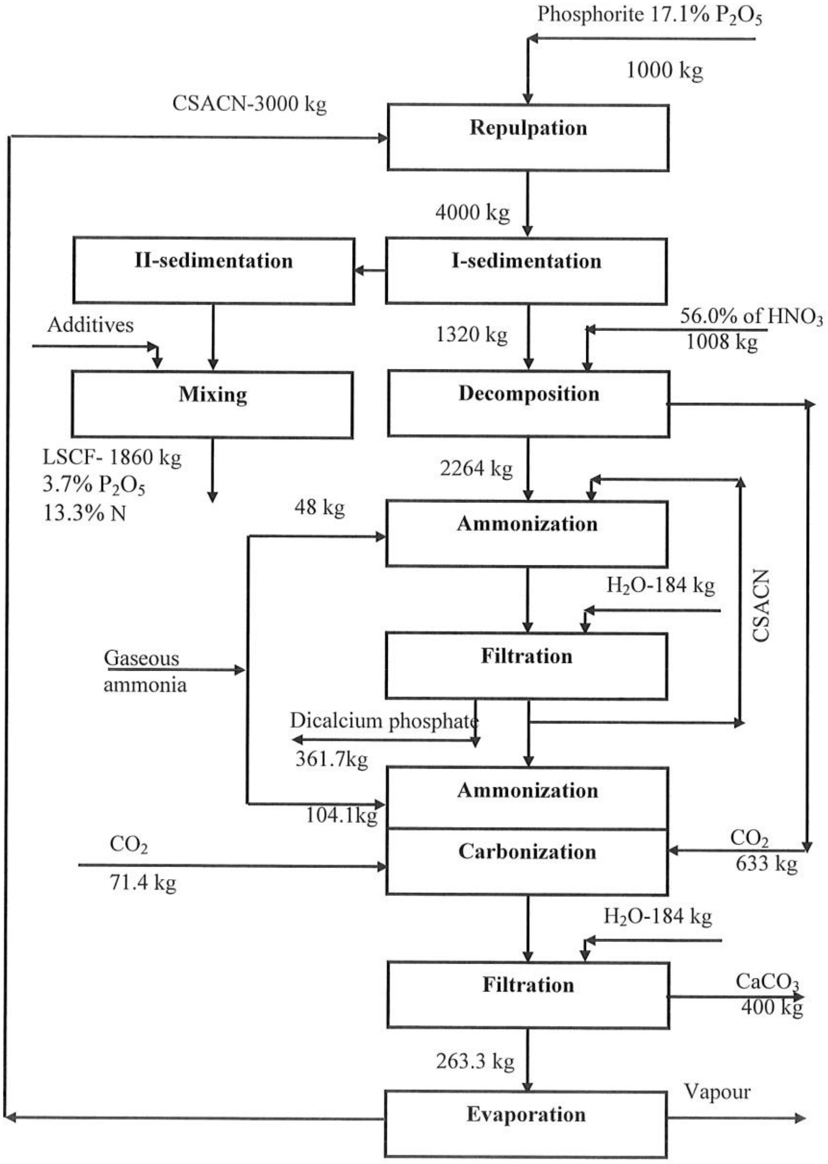

Fig. 2. Block diagram of nitric acid and the material balance of processing 1000 kg of high calcareous phosphorite from Central Kyzylkum

4. CONCLUSION

To sum up, based on the conducted experiments studied the process of processing low-grade phosphate rock from the Central Kyzylkum on liquid nitrogen- calcium and solid concentrated phosphorus fertilizer. The technological scheme and material balance of production had been calculated.

REFERENCES

1. BEGLOV B.M., NAMAZOV Sh.S. *Phosphorites from Central Kyzylkum and their processing*. Tashkent: Fan, 2013, 460 p. 660-0-63185.
2. CEZART NORBERT V. Industrial chloride removal of phosphorite ore at wet enrichment in extreme condition of Kyzylkum desert. *Mining bulletin of Uzbekistan*. 2008, No 4, p. 54-58.
3. NABIEV M.N. *Nitric acid processing phosphates*. Tashkent: Fan, 1976, 366 p. 40306-43827-76.
4. VINNIK M.M., ERBANOVA L.N., ZAITSEV P.M. *Methods of analysis of phosphate rock, phosphate and compound fertilizers, feed phosphates*. Moscow: Chemistry, 1975, 218 p. 5-02-029255-9.
5. ALLAMURATOVA A.J., ERKAEV A.U., TOIROV Z.K. Phosphate concentrate of ordinary phosphorite flour from the Central Kyzylkum. *Chemistry and Chemical technology*, 2009, No. 4, p. 16-20.
6. ALLAMURATOVA A.J., ERKAEV A.U. Enrichment high calcareous phosphate from the Central Kyzylkum with solutions of nitrate salts. *Bulletin of Academy of Sciences of Uzbekistan*, 2010, No. 5, p. 57-60.
7. ALLAMURATOVA A.J., ERKAEV A.U., TOIROV Z.K., REYMOV A.M. Technological studies produce phosphate fertilizers of nitric acid extract of phosphate from the Central Kyzylkum. *Chemical Industry*, 2011. Vol. 88, No. 3, p. 109-114.

CYSENI 2017, May 25-26, Kaunas, Lithuania
ISSN 1822-7554, www.cyseni.com

PECULIARITIES OF F$^-$ IONS LEACHING FROM WASTE SILICA GEL IN STATIC AND DYNAMIC CONDITIONS

V. Rudelis, T. Dambrauskas, K. Baltakys
Kaunas University of Technology
Radvilenu st. 19, Kaunas LT-50254 – Lithuania
E-mail: valdas.rudelis@ktu.edu; v.rudelis@lifosa.com

ABSTRACT

In this work the elution of F$^-$ ions from waste silica gel to the liquid medium was performed under static and dynamic conditions. It was determined that dried (50 °C, 48 h) waste silica gel from aluminum fluoride production mainly consists of silicon dioxide (79.01%) and other compounds containing 10.02–5.67% F$^-$ and 2.14–2.48% Al^{3+} ions. It was found that under static elution conditions (water-to-solid ratio was 100) it is possible to decrease the amount of F$^-$ ions in waste silica gel till 5 wt.% . In addition, under this conditions $AlF_3 \cdot 3H_2O$ remained stable. Meanwhile, the elution conditions affects the stability of $AlF_3 \cdot 3H_2O$ and removable of F$^-$ ions. It was determined that under dynamic conditions not all fluorine ions transferred to the liquid phase due to the adsorption properties of silica gel. The data of hydrothermal synthesis showed, that waste silica gel can be used for the production of calcium silicates hydrates. It was estimated that in CaO–waste silica gel–H_2O mixture when the molar ratio of CaO/SiO_2 = 2.5 after 16 h of isothermal curing at 200 °C dibasic calcium fluoride silicate hydrate – cuspidine ($Ca_4(Si_2O_7)(F,OH)_2$), which contain F$^-$ ions and hydrogarnet ($Ca_3Al_2O_6(H_2O)_6$) were formed. The previous results were confirmed by instrumental and chemical analysis.

Keywords: waste silica gel, fluoride ions, leaching, hydrothermal synthesis

1. INTRODUCTION

Solid wastes are the useless solid materials generated from combined residential, industrial and commercial activities in a given area [1, 2]. It can be categorized according to its origin (domestic, industrial, commercial, construction or institutional); according to its contents (organic material, glass, metal, plastic paper etc.); or according to hazard potential (toxic, non-toxin, flammable, radioactive, infectious etc.) [3, 4]. For a long time it has been disposed of without really paying attention to the harmful effect of chemical substances on environment and human. Nowadays waste management is regulated by national and international laws, it is efforts are made to reduce impact on environment [5–7]. However, more secure means of storage do not reduce the amount of emissions.

Solving waste disposal problem, it is possible to choose from three different waste treatment directions: waste recycling, incineration of waste in specialized companies, waste storage in specially equipped and controlled landfills [8].

Landfill is one of the simplest and the most popular solution for waste utilization problem. However, landfills occupy relatively large areas, they are concentrated sources of air, ground water and primer pollution [5–8]. According to the waste management hierarchy, landfilling is the least preferable option and should be limited to the necessary minimum.

In order to reduce this problem, it is necessary to change the approach and consider waste as potential raw material for the techno genic production. The priority direction is considered to be secondary waste utilization. For this reason waste is sorted, recycled and this helps to reduce environmental pollution and save material resources. So far secondary utilization of waste and techno genic raw materials is limited and it can be associated with very unstable chemical and mineral composition of industrial waste [6, 7].

Aluminium fluoride is used in many industrial processes: in the preparation of white enamels, as an anti-reflection coating in complex optical systems, as a constituent in welding fluxes, and in the preparation of fluorine containing glasses [9, 10].

Generally production of aluminium fluoride is based on its property to form relatively stable supersaturated solutions [10, 11]. The steadiness of these solutions can be explained by good hydratation of the molecules of aluminium fluoride in water solutions. As the concentration and temperature of these solutions increase, steadiness decreases. When a steady supersaturated aluminium fluoride solution is formed, dispersive silica gel can be separated from it. During the production process of AlF_3, a large amount of silica gel contaminated with F^- ions as a by-product is obtained: 0.4 t of silica gel is generated by producing 1 t of aluminium fluoride. The main process reaction can be described by the following reaction:

$$H_2SiF_6 + 2Al(OH)_3 \rightarrow 2AlF_3 + SiO_2 \cdot nH_2O + H_2O + Q\ .$$

As a result in Lithuania 2016 years, JSC “Lifosa” produced 4.3 thousand tonnes of silica gel waste [10]. The use of waste silica gel is limited due to the harmful and aggressive premises, containing fluorine. At the moment silica gel is not widely used or recycled, but is stored on the landfill.

This is why the issue of its utilization is so relevant. Dispose or neutralisation of harmful premises in the waste silica gel would allow to use this material for the production of binders, building materials or in other industries [12, 13].

The aim of this work was to investigate the possibility of fluoride ions leaching from waste silica gel into liquid medium.

2. MATERIALS AND METHODS

Waste silica gel, i.e., a waste product of AlF_3 production in the chemical plant of “Lifosa” (Kedainiai, Lithuania) (with moisture content 60–65%), $S_a = 964\ m^2/kg$);

Calcium oxide, which has been produced by burning calcium hydroxide (“Stanchem”, Poland, purity 97%) at 550 °C for 60 minutes, with the quantity of free CaO equal to 98.41% ;

The hydrothermal synthesis of calcium silicate hydrates by using waste silica gel was performed in the mixture with molar ratio of C/S (CaO/SiO_2) was equal to 2.5. Homogenized raw materials were mixed with distilled water to obtain water/solid ratio of the suspension equal to 10. The hydrothermal synthesis has been carried out in unstirred suspensions in 25 ml volume PTFE cells, which were placed in a stainless steel autoclave (“Parr instruments”, Germany), under saturated steam pressure at 200 °C temperature for 16 hours by applying extra argon gas (10 bar). Temperature was reached within 2 h. After hydrothermal treatment, the suspensions were filtered off, the products rinsed with acetone to prevent carbonization of materials, dried at 50 °C ±5 temperature for 24 h, and sieved through a sieve with an 80 μm mesh.

Standard method of SiO_2 chemical analysis. 1 g of the sample was mixed with sodium and potassium carbonate mixture (5 or 6 g) and put in a platinum crucible. The crucible was placed into a furnace and melted at 900–1000 °C temperature for 1 h. After fusion, crucible was placed into a 200 cm^3 porcelain plate with distilled water in order to solidify the melt on the crucible wall when it was cooling down. Later, crucible was put into a porcelain plate, a large amount of 10% HCl was added and mixed until CO_2 gas was not released from solution. After that, the crucible was removed from the porcelain plate and this plate was heating on the sand bath until solution was evaporated. Subsequently, the formed residue was powdered with a glass stick, poured a few drops of concentrated HCl acid and the porcelain plate was left to cool down. After 30 min, hot distilled water was added into porcelain plate in order to dissolve of chlorides. Then, the solution with residue of SiO_2 was filtrated through ash-free filter and rinsed with distilled water to eliminate chloride ions (the amount of chloride ions was proofed by adding one drop of clean filtrate and a drop of 1% $AgNO_3$ solution on a glass). The obtained filtrate was used for the second chemical analysis of SiO_2 and finally, both filtrate papers were put in the crucibles and heated at 1000 °C for 1 h. The amount of SiO_2 was calculated by using equation:

$$SiO_2 = \frac{a_1 \cdot 100}{a}, \% \tag{1}$$

where a_1 is the mass of heated residue after experiment, g; a is the initial mass of the sample, g.

Standard method of Al_2O_3 chemical analysis. Al_2O_3 was determined in the obtained filtrate after SiO_2 separation. This solution was poured into 250 cm^3 of volumetric flask, diluted with distilled water to the indicated level and mixed. After that, 50 cm^3 of filtrate was poured into a 300 cm^3 of glass and heated until boiling. Then, 1.5 g of NH_4Cl, 3–4 drops of HNO_3 ($\rho = 1400$ kg/m^3), also 3–4 drops of methyl orange indicator were added and the amount of 10% ammonium added till the solution in the glass changed into yellow. Subsequently, formed precipitates were filtrated and rinsed with hot solution of 2% NH_4NO_3. The obtained filtrate was used for the second chemical analysis of Al_2O_3 and finally, both filtrate papers were put in the crucibles and heated at 1000 °C for 20 min. The amount of Al_2O_3 was calculated by using equation:

$$Al_2O_3 = \frac{a \cdot 100}{m}, \% \tag{2}$$

where a is the mass of heated residue after experiment, g; m is the initial mass of the sample, g.

The determination of fluoride. 1 g of sample was put into a platinum plate and mixed with 10 g of sodium and potassium hydroxides mixture (5 g of NaOH and 7 g of KOH). After that, platinum plate was put in the sand bath and heated approximately 40 min. During heating the mixture was often mixed with platinum spatula. After fusion, the platinum plate was turned around that the melt would solidify on the internal walls. Then, the 150 cm^3 of distilled water was added and the platinum plate was put into a boiling water bath for melting salts. After that, 15 g of chemically pure $(NH_4)_2CO_3$ powder was added, which melt by mixing with platinum spatula and plate was held in the boiling water bath until solution was evaporated to dry salt. Subsequently, salt was poured with 150 cm^3 of distilled water and melted by mixing in the boiling water bath. Later, hot solution with precipitates was poured into a 250 cm^3 flask, which was resistant for the variations of temperature. The solution in the flask was cooled down and diluted with water to the indicated level. After that, the solution was filtrated and concentrations of fluoride ions in solution were measured by using a Metler Toledo T70 potentiometer. The error of the selective electrode for F_{-} ions is 1 ppm (0.0001%).

Fluoride leaching. F^- ions leaching from waste silica gel to the aqueous phase was done under static and dynamic conditions. Leaching in static conditions was done by keeping the suspensions at 25 °C for 24 h when water-to-solid (w/s) ratio was 100. Leaching of F^- ions under dynamic conditions by using the continuous distilled water (25 °C) flow, which was applied on waste silica gel till the water-to-solid (w/s) ratio reached the value of 100.

The X-ray diffraction analysis (XRD) of compounds was performed on the D8 Advance diffractometer (Bruker AXS, Karlsruhe, Germany) operating at the tube voltage of 40 kV and tube current of 40 mA. The X-ray beam was filtered with Ni 0.02 mm filter to select the CuKα wavelength. Diffraction patterns were recorded in a Bragg-Brentano geometry using a fast counting detector Bruker LynxEye based on silicon strip technology. The specimens were scanned over the range 3–70 ° (2θ) at a scanning speed of 6 ° min^{-1} using a coupled two theta/theta scan type.

The X-ray Fluorescence spectroscopy (XRF) was performed on a Bruker X-ray S8 Tiger WD spectrometer equipped with a Rh tube with energy of up to 60 keV. Powder samples were measured in Helium atmosphere and data were analysed with Spectra Plus Quant Express standard less software.

3. RESULTS AND DISCUSSION

In the first stage of the investigation, the chemical analysis of aluminium fluoride production waste – waste silica gel (SGW) (raw sample and an additional dried for 48 hours at 50 °C in the dryer sample) samples was performed.

It was obtained that SGW-1 consists of 79.01% silicon dioxide, 10.02% F^-, and 1.08% Al_2O_3 (Table 1). Meanwhile, by changing thechnological parameters of AlF_3 production (SGW-2 sample), it's possible to reduce fluorine quantity till 5.67% F^-. It should be noted that the latter value is almost equal to data obtained in raw SGW sample (5.28% F^-). While almost the same tendency was observed by applying XRF: it was determined that SGW-1 contains 36.2% of silica, which is equivalent to 78.9% of SiO_2 (Table 2). Moreover, 2.48% of Al^{3+} ions and traces of other elements are also present in mentioned compound. It was determined that XRF method is not suitable for fluorine ions measurement in waste silica gel samples.

Table 1. Chemical composition of AlF_3 production waste determined by chemical analysis

Name of sample	First experiment			Second experiment			Average,%		
	Concentration,%			Concentration,%					
	SiO_2	**F^-**	**Al_2O_3**	**SiO_2**	**F^-**	**Al_2O_3**	**SiO_2**	**F^-**	**Al_2O_3**
Raw SGW	–	5.28* (211.13 ppm)	–	–	5.28* (211.00 ppm)	–	–	5.28	–
SGW-1 dried at 48h 50 °C	78.42	10.01* (400.82 ppm)	1.23	79.6	10.03* (401.3 ppm)	0.93	79.01	10.02	1.08
SGW-2 dried at 48h 50 °C	80.6	5.67* (226.79 ppm)	1.17	81.2	5.67* (226.81 ppm)	1.12	80.9	5.67	1.13

Table 2. Chemical composition of AlF_3 production waste determined by XRF analysis

Name of sample	Concentration,%						
	Si	**Al**	**F**	**Cl**	**Ca**	**Fe**	**Total**
SGW-1 dried at 48h 50 °C	36.2	2.48	0.795	0.0799	0.0297	0.0220	39.6
SGW-2 dried at 48h 50 °C	38.6	2.14	0.455	–	0.0876	0.0242	41.4

XRD analysis data showed that the main compound containing fluoride ions in waste silica gel is $AlF_3{\cdot}3H_2O$ (*d*-spacing: 0.545, 0.386, 0.329, 0.244 nm) (Fig. 1). It should be noted that mineralogical composition of SGW-2 sample differs from SGW-1 sample because, diffraction maximums characteristic to aluminium hydroxide $Al(OH)_3$ (*d*-spacing: 0.485; 0.437; 0.432; 0.245; 0.239 nm) and aluminium fluoride hydroxide hydrate $AlF_{1.5}(OH)_{1.5}{\cdot}0.375H_2O$ (*d*-spacing: 0.568; 0.296; 0.284; 0.189; 0.174 nm) were observed on the XRD pattern (Fig. 1, b). Furthermore, the silicon dioxide is amorphous because a broad peak in the angle of diffraction that varied from 18 to 26° was observed. The diffraction maximums of compounds containing other aluminium components (due to a small quantity) were not identified on the XRD pattern.

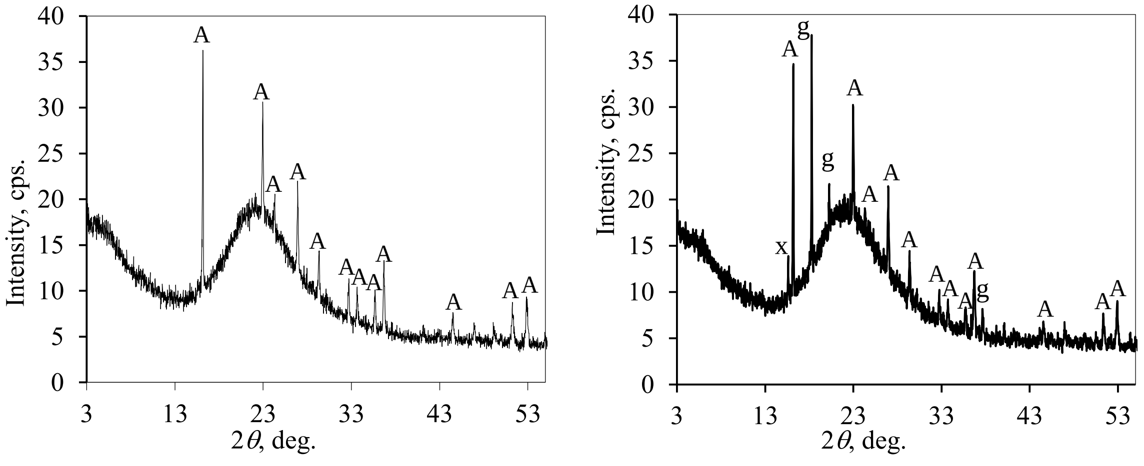

a

b

Fig. 1. XRD patterns of dried SGW-1 (a) and SGW-2 samples (b). Indexes: A – $AlF_3{\cdot}3H_2O$; g – $Al(OH)_3$; x – $AlF_{1.5}(OH)_{1.5}{\cdot}0.375H_2O$

In the next stage of investigation the possibility of F^- ion elution from SGW-1 to a liquid medium was examined. The water-soluble fluoride compounds presented on the AlF_3 production waste surface could be removed by using hot water. Extraction with hot water promotes release of hydrogen fluoride and reconstruction of active silanol groups on the surface of waste silica gel:

$$\equiv Si - F + H_2O \rightarrow \equiv Si - OH + HF$$

It was obtained that the mineralogical composition of SGW-1 slightly varies during elution at 25 °C for 1 h when the ratio of w/s = 100: the intensity of diffraction peaks characteristic to $AlF_3{\cdot}3H_2O$ decreased by 3.1 times (Fig. 2.).

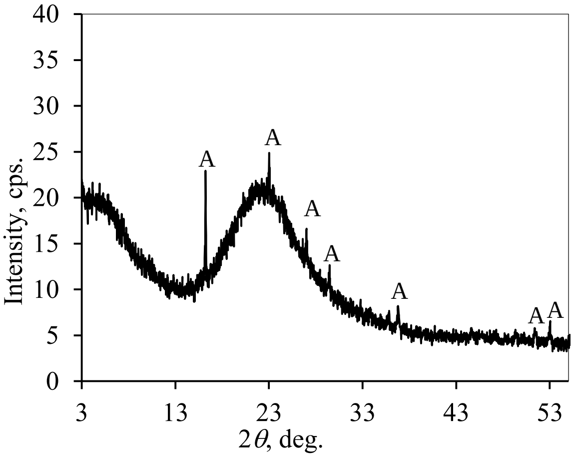

Fig. 2. XRD patterns of SGW-1 samples after 24 h of leaching under static conditions. Indexes: A – $AlF_3{\cdot}3H_2O$

Thus, it is clearly seen that a high concentration of F^- ions is still present in the structure of SGW-1, which can be explained by the strong adsorption properties of this compound. For this reason, in order to reduce the adsorption properties of SGW and the mobility of F^- ions, in the next stage of this research, the leaching of F^- ions was performed under dynamic conditions.

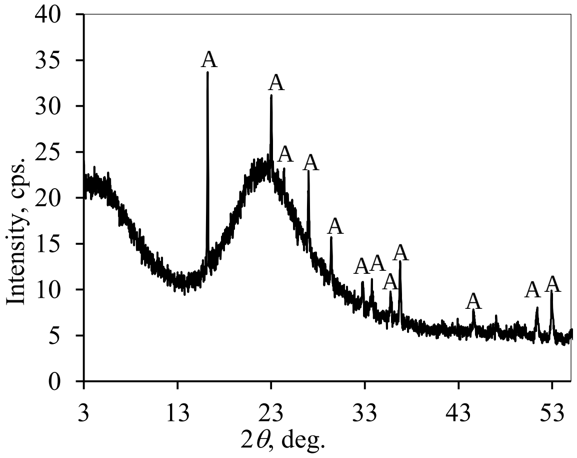

Fig. 3. XRD patterns of waste silica gel samples after leaching under dynamic conditions at 25 °C. Indexes: A – $AlF_3·3H_2O$

It was examined that the change in leaching conditions had an effect on the stability of $AlF_3·3H_2O$: the intensity of diffraction peaks characteristic to $AlF_3·3H_2O$ decreased by 1.23 times (Fig. 3). The XRD results were verified by the chemical analysis.

It should be noted that the higher w/s ratio during leaching process due to the principle of the technology is impossible and economically useless.

Summarizing the above mentioned results, it can be stated that fluoride ions removal into the liquid medium depends on such factors as dissociation, solubility, w/s ratio and adsorption properties of the waste silica gel. However, even if all of these factors were in control during the leaching, still a high amount of F^- ions will be present in this compound, resulting in limited application possibilities. For this reason, in the next experimental stage the application of SGW to the formation of calcium silicate hydrate under hydrothermal synthesis conditions was performed.

Hydrothermal synthesis includes the various techniques of crystallizing substances from high-temperature aqueous solutions at high vapour pressures. It is presumed that during hydrothermal synthesis F^- ions in the SGW will be combined into stable compounds, and this material could be used in binders and in the building materials industry. Only fragmentary data on the removal of fluoride ions from the limited solubility of solid materials and waste during hydrothermal synthesis are published in the literature.

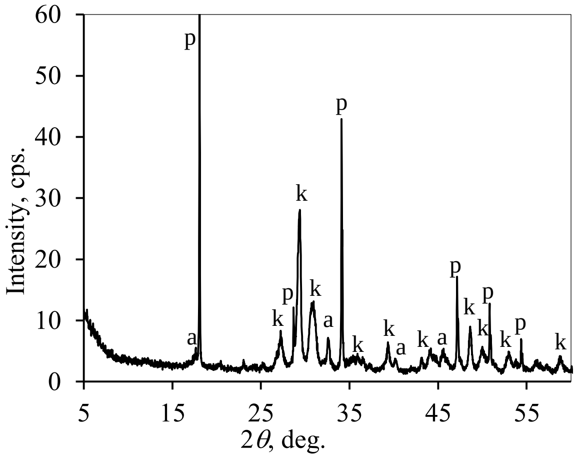

Fig. 4. XRD patterns of synthesis product. Indexes: A – $AlF_3·3H_2O$

It was determined that in $CaO–SGW–H_2O$ system when the molar ratio of CaO/SiO_2 = 2.5 after 16 h of isothermal curing at 200 °C, cuspidine (*d*-spacing: 0.306, 0.290, 0.287 nm) was formed (Fig. 4). Also together with this compound, hydrogarnet (*d*-spacing: 0.276, 0.226, 0.200 nm) was also identified on XRD patterns.). It should be noted that under these synthesis conditions, the basic reflections (*d*-spacing: 0.493; 0.193; 0.179 nm) of partially unreacted portlandite was observed on X-ray diffraction pattern.

4. CONCLUSIONS

The chemical and mineralogical composition of waste silica gel samples depends on technological parameters of AlF_3 production. It was determined that waste silica gel mainly consists of silicon dioxide (79.01–80.90%) and other compounds containing 10.02–5.67% F^- and 2.14–2.48% Al^{3+} ions. It was found that under static and dynamic elution conditions at 25 °C temperature is impossible to remove all fluorine ions into liquid medium.

It was determined that SGW can be used as raw material for the hydrothermal synthesis of calcium silicate hydrates, because a stable compound – cuspidine, was formed.

ACKNOWLEDGEMENT

This research was partially supported by JSC “Lifosa”.

REFERENCES

1. JESWANI, H. K., AZAPAGIC, A. Assessing the environmental sustainability of energy recovery from municipal solid waste in the UK. Waste management. 2016, Vol. 50, p. 346-363.
2. BAHRAMI, A., SOLTANI, N., PECH-CANUL, M.I., GUTIÉRREZ, C. A. Development of metal-matrix composites from industrial/agricultural waste materials and their derivatives. Critical Reviews in Environmental Science and Technology. 2015, Vol. 3389, p. 1-66.
3. APRILIA, A., TEZUKA, T., SPAARGAREN, G. Inorganic and Hazardous Solid Waste Management: Current Status and Challenges for Indonesia. Procedia Environmental Sciences. 2013, Vol. 17, p. 640-647.
4. SPRUOGIS A., JASKELEVIČIUS B. *Waste and its management.* Vilnius: *Technics.* 2006.
5. Natural resources and environmental safety 2015. Vilnius. Department of Statistics to the Government of the Republic of Lithuania. 2016. *https://osp.stat.gov.lt/services-portlet/pub-edition-file?id=24700*
6. USEPA. Integrating Pollution Prevention - Getting Started. Pollution Prevention. 2010. P. 1- 121.
7. Europen Contributions to the Commission Consultation on the EU Waste Management Targets Review. 2013.
8. GORSEVSKI, P. V., DONEVSKA, K. R., MITROVSKI, C. D., FRIZADO, J. P. Integrating multi-criteria evaluation techniques with geographic information systems for landfill site selection: A case study using ordered weighted average. Waste Management. 2012, Vol. 32, Iss. 2, p. 287-296.
9. KARLSTRÖM, J. Reactor Model for Production of Aluminum Fluoride. 1970. No. 1966.
10. Internal documents of JCC “Lifosa”.
11. DREVETON, A. Economic aspects of utilizing fluosilicic acid as raw material for the manufacture of hydrofluoric acid and aluminium fluoride. Procedia Engineering. 2014. Vol. 83, p. 279-285.
12. ILJINA A., BALTAKYS K., BANKAUSKAITE A., EISINAS A., KITRYS S. The stability of formed CaF_2 and its influence on the thermal behavior of C-S-H in CaO-silica gel waste-H_2O system. Journal of Thermal Analysis and Calorimetry. 2017, Vol. 127, Iss. 1, p. 221-228.
13. BALTAKYS K., ILJINA I., BANKAUSKAITE A. Thermal properties and application of silica gel waste contaminated with F^- ions for C-S-H synthesis. Journal of thermal analysis and calorimetry. 2015, Vol. 121, Iss. 1, p. 145-154.

CYSENI 2017, May 25-26, Kaunas, Lithuania
ISSN 1822-7554, www.cyseni.com

INFLUENCE OF pH ON THE HYDROXIDE IMPURITIES IN CHEMICALLY DEPOSITED CdS THIN FILM

M. Üürike, N. Maticiuc, O. Volobujeva, N. Spalatu, J. Hiie
Department of Materials and Environmental Technologies, School of Engineering, Tallinn University of Technology
Ehitajate tee 5, 19086 – Estonia
E-mail: marvin.uurike@ttu.ee

ABSTRACT

High quality CdS thin films are of great interest in the thin film photovoltaic community. CdS impurities like oxygen and hydroxide impact the electrical, optical and structural properties of CdS film, which may cut the performance of CdTe, CIGS or CZTS devices. One of the possibilities to control the hydroxide content in CdS lattice is the pH modification of the deposition solution. In the present work we study the effect of solution pH on the hydroxide content in CdS thin film, as well as their structural and optical properties. We noticed that a change in the pH from 8.7 to 10.4 gives raise to major variations in CdS properties measured by X-ray diffraction, UV-vis spectroscopy, energy-dispersive X-ray spectroscopy, and scanning electron microscopy. At low pH values (8.7 and 9.5) CdS films are dense and uniformly cover the glass substrates. The grain size of these films increases from 126 nm to 148 nm while the rate of film growth is doubled for CdS film deposited at 9.5 pH. At higher pH value (10.0 and 10.4) the films become porous and have an increased grain size from 153 nm to 300 nm. The crystalline structure of CdS thin film obtained at 8.7–10.4 pH changed from (002) hexagonal to (111) cubic, respectively. The influence of CdS films deposited at different pH values on the device performance is shown for CdS-CdTe solar cells. Due to less hydroxide impurities and larger CdS grains at higher pH values of deposition solution the photovoltaic parameters of CdS-CdTe solar cells were improved and the efficiency was raised from 5.1% up to 7.6%;

Keywords: CdS, pH, OH impurities, thin film solar cell.

1. INTRODUCTION

Cadmium sulfide (CdS) has proven to be one of the most important semiconductor materials for the industry of different optoelectronic devices such as optical sensors, light-emitting diodes, transistors and photovoltaic panels [1]. CdS thin films are deposited by several physical and chemical methods: sputtering [2], vacuum evaporation [3], electrodeposition [4], spray pyrolysis [5], and chemical bath deposition (CBD) [6]. Among them CBD is most widely used in industry as the simplest, fastest, cost effective and promising method to obtain uniform, dense and large area CdS thin films [7, 8].

Due to the aqueous environment the chemically deposited CdS film may contain a significant amount of oxygen and hydrogen compounds which influence the growth mechanism and the film properties. This is directly connected to the fact that CBD CdS thin film is obtained from an alkaline solution with a pH value around 10, where the hydroxide mechanism of CdS formation is commonly accepted [8, 9, 10]. The hydroxide ions participate in the decomposition of thiourea with S^{2-} release so that CdS formation occurs preferentially on the surface of hydroxide rather than nucleating separately in the solution. In this sense, the inclusion of $Cd(OH)_2$ in chemically deposited CdS was widely presumed [11, 12, 13], however, its thermal instability [14] and impact on the properties of CdS film were underestimated.

Such unstable thermal activity of hydroxide species generates uncontrollable properties of CBD CdS thin films already at low temperatures [8, 15]. As the OH incorporates on sulfur site in the CdS lattice [16], it acts as a donor dopant which dramatically changes the electrical, structural and optical properties of CBD CdS thin films already in the deposition process [17]. There is a possibility to remove these OH-containing impurities by means of a post deposition thermal annealing at temperatures up to 450 ^{o}C, but the CdS properties will be also affected [15, 16, 18].

As an alternative, in this article we investigate the possibility to control the incorporation of OH impurities into CdS lattice during the deposition process. In this sense we prepare CdS thin films by CBD method at pH values of solution below and above the usual value (pH 10) [8]: 8.7, 9.5, 10.0 and 10.4 pH. In addition, we study crystallography, morphology, elemental composition, and optical properties of CdS thin films by means of X-ray diffraction (XRD), scanning electron microscopy (SEM), energy-dispersive X-ray analysis (EDX) and UV-vis-NIR spectrometry. CBD CdS thin films deposited at different pH values are used in CdTe solar cells and the effect of solution pH on solar cell parameters is discussed.

2. EXPERIMENTAL DETAILS

Polycrystalline CdS films were deposited on 25 mm × 25 mm soda-lime glass substrates by CBD technique. The plates were properly cleaned and immersed in the chemical bath which consisted in 200 ml water solution of 1 mM $CdSO_4$, 10 mM thiourea and 30 mM $(NH_4)_2SO_4$. The value of solution pH was changed from 8.7 up to 10.4 by means of NH_4OH concentration in the solution (10 mM, 75 mM, 0.25 M and 0.7 M). The pH values were measured at room temperature. The temperature and agitation speed of the reaction solution were 85 ^{o}C and 500 rpm, respectively. One deposition lasted for 10 min, but for thicker CdS films the process was repeated. After deposition a vacuum drying at 120 ^{o}C was applied to remove most of the secondary phases of water, hydroxides and organic impurities. This drying was the last stage of preparation for the so-called as-deposited CdS layers.

Surface morphology of CdS films was examined by high resolution SEM apparatus (Zeiss Merlin) at an operating voltage of 0.9 kV. The elemental composition of films was determined by means of EDX analysis, using the Bruker EDX-XFlash 6/30 detector with the PB-ZAF standard less mode with a measurement error of ~1.0 at. %. Crystallographic investigations were performed using the XRD technique. The measurements were made in the Bragg–Brentano (θ–2θ) geometry by the Rigaku Ultima IV diffractometer with Cu-Kα radiation. Crystallite size, lattice constant and interplanar distance were computed by the PDXL software (Version1.4.0.3) on the Rigaku system. The crystallite size was calculated using the Debye–Scherrer method and a Scherrer’s constant of 0.94. The optical characteristics were measured in the wavelength range of 200–1500 nm on the Jasco V-670 UV–vis–NIR spectrophotometer equipped with an integrating sphere. Total optical transmission and reflection spectra were used to determine the transmittance of CdS and the optical thickness. Based on the Tauc relation (1), the values of bandgap have been estimated from the $(\alpha h\nu)^2$ versus hν dependence, by taking the intercept of the extrapolation to zero absorption on the hν axis.

$$(\alpha h\nu) = A\left(h\nu - E_g\right)^n \qquad (1),$$

here α is the absorption coefficient given by $\alpha = 2.303 \log(T/d)$ (d here is film thickness and T is transmission), $h\nu$ is the photon energy, and the exponent n denotes the nature of the transition ($n = ½$ for direct allowed transitions).

For solar cell fabrication in superstrate configuration we deposited CBD CdS buffer layer onto transparent conductive oxide (FTO) from solution with different pH values (pH 8.7, pH 9.5, pH 10.0). Following CdS deposition, CdTe absorber layers were deposited by close spaced sublimation (CSS) technique at 450 ^{o}C in a high vacuum of 10^{-6} torr. The next step was the classical $CdCl_2:O_2$ activation treatment [19], after which the solar cells were finished by sputtering of Au back contact. Performance of the CdS–CdTe solar cells was characterized by current-voltage (J–V) and external quantum efficiency (EQE) measurements under AM1.5 (room temperature, 100 mW/cm^2) conditions.

3. RESULTS AND DISCUSSION

3.1. Properties of CBD CdS thin films

SEM surface images of CBD CdS thin films are presented in Fig. 1. Almost all CBD CdS films cover uniformly the underlying glass substrate after 60 minutes deposition, an exception being the case of 10.4 pH (Fig. 1). At such a high pH value the CdS grains do not manage to coalesce and to cover uniformly the underlying glass substrate. Even by increasing the deposition time from 1 to 2 hours (not shown here) we obtained CdS films composed of large separated grains that do not cover completely the glass substrate.

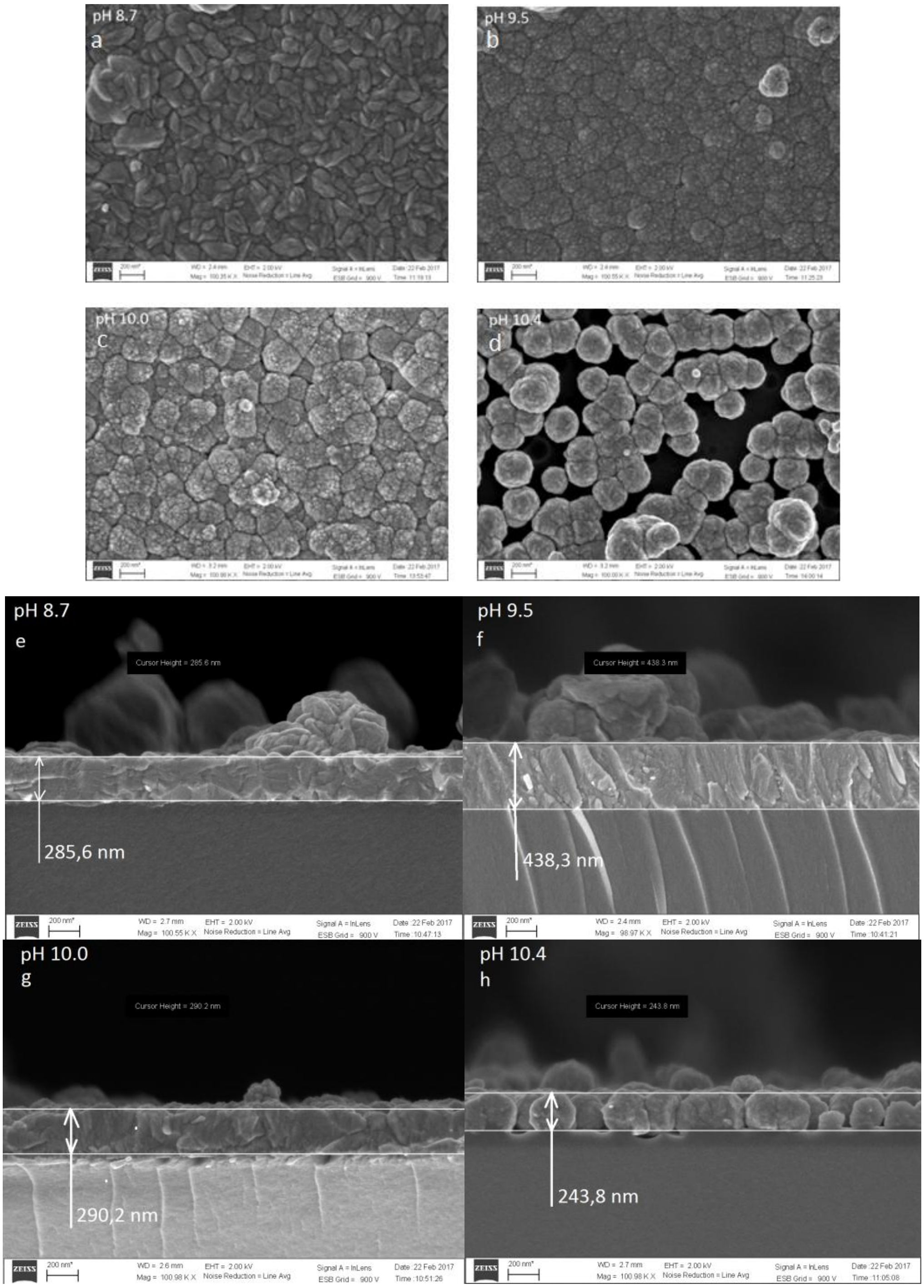

Fig. 1. SEM surface view (a–d) and cross sectional image (e–h) of CdS thin film deposited for one hour at different pH values: a, e) 8.7 pH; b, f) 9.5 pH; c, g) 10.0 pH; d, h) 10.4 pH

The thickness is almost the same for all the experiments except for the film obtained at 9.5 pH which is twice thicker in comparison to other CdS films (Table 1). When the value of solution pH increases from 8.7 to 10.4 we observe an increase in the grain size of CdS thin films from 126 nm up to 300 nm (Table 1). At the same time the grains shape is changed from asymmetrical with distinguishable corners to spherical grains (Fig. 1), respectively.

Table 1. Thickness, grain size and elemental composition of CBD CdS thin films deposited at different pH values

pH	**8.7**	**9.5**	**10.0**	**10.4**
Thickness, nm	285	438	290	243
Grain size, nm	180	180	245	300
[Cd], at.%	51.5	49.6	52.2	52.4
[S], at.%	40.8	41.2	41.9	43.4
[O], at.%	7.7	9.2	5.9	4.2

When analyzing the elemental composition of CdS thin film, a special attention was paid to the oxygen-containing species in the CdS thin film as a function of solution pH. A special interest in the oxygen content is connected to the aim of our investigation – to study how the pH of solution influences the presence of hydroxide impurities which will be suggested by the oxygen content [9]. As the pH value is raised from 8.7 up to 10.4 CdS films are similarly Cd-rich whereas atomic concentration of oxygen decreases from 7.7 at.% down to 4.2 at.% (Table 1). Similarly to the previously discussed microstructural properties, the CdS thin film deposited at 9.5 pH represents an exception of the tendency and shows the highest content of oxygen impurities (9.2 at%). We suppose that at this solution pH, the mechanism of CdS growth is faster and a larger amount of hydroxide species are incorporated from the deposition solution.

Nevertheless, the presence of hydroxide impurities incorporated in CdS film is decreased with increasing pH value of the deposition solution. This incorporation, which was previously thoroughly analyzed by X-ray photoelectron spectroscopy [16], is supported here by our XRD analysis data (Fig. 2) that indicate to an increase of the interplanar distance (Table 2). Besides that, with increasing value of pH, the crystalline structure of CdS thin film changes from multiple orientation to single orientation with improvement of crystallinity at 9.5 and 10.0 pH. Higher value of pH (10.4) in the deposition solution brings back the disperse structure of CBD CdS thin film described by decreased crystallinity, multiple orientation structure and very small size of crystallites. All these characteristics suggest that 10.4 is a too high pH value for deposition of CdS thin film for application in superstrate solar cells. Moreover, if at low pH values of solution (8.7 pH and 9.5 pH) the deposited CdS thin films have a hexagonal structure, at values higher than 10.0 pH the crystalline structure of CdS re-orientates itself to cubic structure (Table 2).

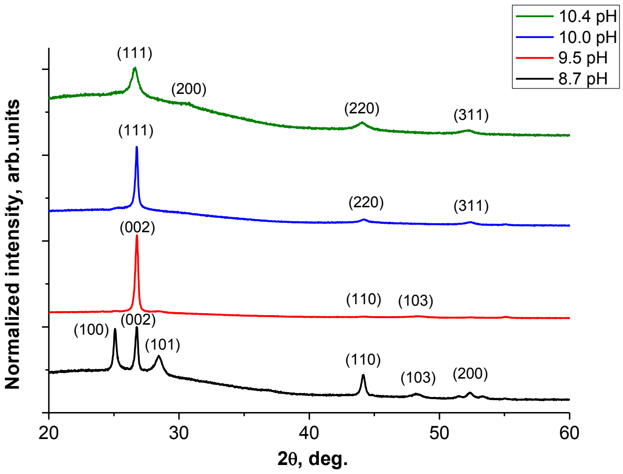

Fig. 2. XRD patterns of CBD CdS thin films deposited at different values of solution pH

Taking into account that the incorporated hydroxide impurity in CdS is bound to Cd and that crystalline lattice of $Cd(OH)_2$ is hexagonal [11], we believe that the high presence of hydroxide impurities reorganize the crystalline lattice of CdS towards hexagonal structure. On the other hand, when our CBD CdS thin films contain less hydroxide impurities the CdS lattice re-arrange itself into a stable cubic structure (Table 2).

Table 2. Interplanar distance (d), crystallite size (s), and lattice parameters (a, c) calculated for the main peak of CdS thin films deposited at different pH values

pH	**Main peak**	**2θ, deg.**	**d, Å**	**s, nm**	**a, Å**	**c, Å**
8.7	(002)	26.752	3.329	39.2	4.10	6.66
9.5	(002)	26.760	3.328	36.0	4.08	6.65
10.0	(111)	26.742	3.331	45.2	5.77	–
10.4	(111)	26.662	3.341	6.1	5.88	–

The optical band gap values of CBD CdS thin films confirm that the characteristics of $Cd(OH)_2$ dictate properties of CdS. The general trend of band gap value is a decrease from 2.43 eV to 2.31 eV corresponding to a raise in the value of solution pH from 8.7 up to 10.4. Such a decrease of band gap is in close connection to previously presented EDX data that indicate to a reduced presence of OH-containing phases at increasing values of pH. This tendency is in agreement with Yucel et al. study that indicates that the band gap of CdS is decreased when a higher pH is applied in the deposition process [20]. Again, CdS thin films with a higher content of hydroxide impurities have a higher band gap and vice versa (Fig. 3) and we connect it to the high band gap of incorporated $Cd(OH)_2$ [21]. Still, in our case the band gap values are lower due to less concentrated solution, higher Cd/S rate and lower pH values in our CBD process compared to Yucel et al. work.

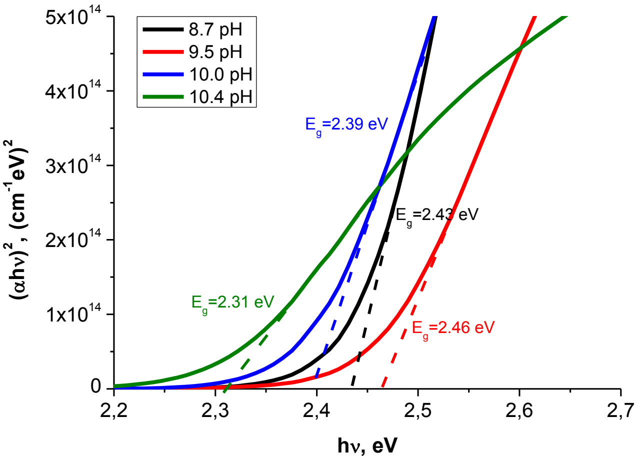

Fig. 3. Tauc's plots and band gap values of CBD CdS thin film deposited at different pH values of solution

Our intention to control the content of hydroxide species by changing the value of pH was successful. We were able to decrease the oxygen concentration from 7.7 at% down to 4.2 at% when raising the value of solution pH from 8.7 up to 10.4. However, the CdS film obtained at 10.4 pH is also described by poorest substrate coverage and uniformity of the layer. Such microstructure of this CdS film makes its application as a buffer layer almost impossible. Therefore, for solar cell application we used only CdS thin films deposited at three pH values: 8.7, 9.5, and 10.

3.2. Properties of CdS/CdTe solar cells

Fig. 4a shows the current-voltage (J–V) characteristics of CdS–CdTe solar cells with identically thick CdS films (~100 nm) obtained at different values of solution pH: 8.7, 9.5, and 10.0. The photoelectric performance of these solar cells is shown in Table 3.

The highest performance is shown by the solar cell with CdS film deposited at 10.0 pH. An important reason of this improvement might be the lowest concentration of oxygen containing species, larger grains of CdS, and less interface defects between this CdS film and CdTe absorber. These interface defects are probably more numerous in the case of CdS deposited at lower pH values. In result, solar cell with CdS deposited at 8.7 pH show lowest solar cell parameters (Table 3) due to smallest grain size of CdS film (Table 1). When compared to the cells with CdS deposited at pH 9.5 and 10.0, the grain size of only 180 nm for CdS deposited at 8.7 pH implies a faster interdiffusion at the CdS/CdTe junction interface in the process of $CdCl_2$ treatment. This interdiffusion appears to be accelerated also by the relatively high oxygen content in this CBD CdS film.

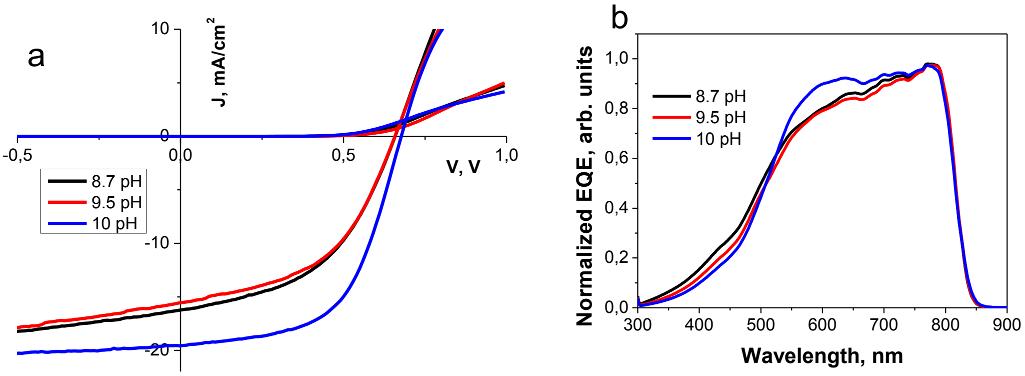

Fig. 4. J-V (a) and EQE (b) characteristics of CdS-CdTe solar cells with CBD CdS obtained at different values of solution pH (8.7, 9.5 and 10.0)

Table 3. Photovoltaic parameters of CdS-CdTe solar cells with CBD CdS film obtained at different values of solution pH (8.7, 9.5, and 10.0)

pH of CdS CBD solution	V_{OC}, V	J_{SC}, mA/cm^2	FF, %	η, %
8.7	660	16.1	48	5.1
9.5	660	15.5	49	5.0
10.0	680	19.5	57	7.6

These conclusions are supported by simultaneous changes of the EQE dependencies (Fig. 4b) in the wavelength region of 300-700 nm. The solar cells with CdS deposited at 8.7 and 9.5 pH exhibit slightly higher EQE response in the mentioned wavelength region probably because of the thinning of CdS as a result of intermixing at the CdTe-CdS interface [18]. Although this enhancement is beneficial for window transmission, non-uniform CdS consumption may lead to the formation of parallel junctions between the absorber and FTO front contact, and hence to the reduction of solar-cell performance (Table 3). Based on these arguments it is clear that solar cell that uses CdS with larger grains obtained at pH value of 10.0 exhibits the best EQE response implying better collection efficiency.

4. CONCLUSIONS

In this paper CBD CdS thin films were obtained at different values of solution pH (8.7, 9.5, 10.0 and 10.4) that generate changes in microstructural, crystallographic and optical properties of CdS thin films. First of all the coverage and uniformity of the film is damaged at higher pH values whereas the grain size is increased from 180 nm to 300 nm. In addition, with increasing value of solution pH the crystalline structure of CdS thin films is transformed from hexagonal with (002) orientation toward cubic with (111) orientation. The most important result of the present work is that we managed to decrease the amount of oxygen impurities in CBD CdS thin films from 7.7 at.% to 4.2 at.% by means of increasing pH values from 8.7 up to 10.4. Such an approach allowed us to diminish the content of hydroxide impurities in CBD CdS thin films. However, CdS films with the lowest content of hydroxide impurities have the poorest microstructure in terms of bad substrate coverage and non-uniformity of the film. In solar cell application, by using CBD CdS films deposited at different pH values we managed to increase the solar cell efficiency from 5.1 % up to 7.6 %. Such an improvement of CdS-CdTe solar cell parameters are due to larger grain size of CdS film as well as decreased amount of oxygen containing species at higher pH values.

ACKNOWLEDGEMENTS

This work was financially supported by the Estonian Ministry of Education and Research [projects IUTI9-4, IUT19-28 and PUT1495]; the Estonian Centre of excellence in Research [Project TK141].

REFERENCES

1. LUQUE A., HEGEDUS S., *Handbook of Photovoltaic Science and Engineering, 2nd edition,* Chichester, UK: John Wiley & Sons Ltd, 2010.
2. LIANG G.X., FAN P., ZHENG Z.H., LUO J.T., ZHANG D.P., CHEN C.M., CAO P.J., Room-temperature preparation and properties of cadmium sulfide thin films by ion-beamsputteringdeposition, *Applied Surface Science*, 2013, Vol. 273, p. 491–495.
3. GHOSH B., DAS M., BANERJEE P., DAS S., Fabrication of vacuum-evaporated SnS/CdS heterojunction for PV applications, *Sol. Energy Mater. Sol. Cells*, 2008, Vol. 92, p. 1099–1104.
4. BARANSKI A.S., FAWCETT W.R., MCDONALD A.C., The mechanism of electrodeposition of cadmium sulphide on inert metals from dimethylsulphoxide solution, *Journal of Electroanalytical Chemistry and Interfacial Electrochemistry*, 1984, Vol. 160, p. 271–287.
5. YADAV A.A., BAROTE M.A., MASUMDAR E.U., Studies on nanocrystalline cadmium sulphide (CdS) thin films deposited by spray pyrolysis, *Solid State Science,* 2010, Vol. 12, p. 1173–1177.
6. ISAIAH O., OLADEJI L.C., Optimization of chemical bath deposited cadmium sulfid thin films, *J. Elecrochem. Soc.*, 1997, Vol. 144, p. 2342–2346.
7. SOUNDESWARAN S., SENTHIL KUMAR O., DHANASEKARAN R., Effect of ammonium sulphate on chemical bath deposition of CdS thin films, *Materials Letters*, 2004, Vol. 58, p. 2381–2385.
8. HODES G., *Chemical Solution Deposition of Semiconductor Films,* New York: Marcel Dekker Inc, 2003.
9. ORTEGA-BORGES R., LINCOT D., Mechanism of chemical bath deposition of cadmium sulfide thin films in the ammonia-thiourea system, *J. Electrochem. Soc.,* 1993, Vol. 140, p. 3464–3473.
10. KAUR I., PANDYA D.K., CHOPRA K.L, Growth kinetics and polymorphism of chemically deposited CdS films, *J. Elecrochem. Soc.*, 1980, Vol. 127, p. 943–948.
11. KYLNER A., ROCKETT A., STOLY L., Oxygen in solution growth CdS films for thin film solar cells, *Solid State Phenom.,* 1996, Vol. 51–52, p. 533–540.
12. KOZHEVNIKOVA N.S., REMPEL A.A., HERGERT F., MAGERL A., Structural study of the initial growth of nanocrystalline CdS thin films in a chemical bath, *Thin Solid Films,* 2009, Vol. 517, p. 2586–2589.
13. LEE S., LEE E.S., KIM T.Y., CHO J.S., EO Y.J., YUN J.H., CHO A., Effect of annealing treatment on CdS/GIGS thin film solat cells depending on different CdS deposition temperatures, *Sol. Energy Mater. Sol. Cells*, 2015, Vol. 141, p. 299–308.
14. LOW M.J.D., KAMEL A.M., The thermal decomposition of cadmium hydroxide, *J. Phys. Chem.,* 1965, Vol. 69, p. 450–457.

15. MATICIUC N., KATERSKI A., DANILSON M., KRUNKS M., HIIE J., XPS study of OH impurity in solution processed CdS this films, *Sol. Energy Mater. Sol. Cells*, 2017, Vol. 160, p. 211–216.
16. MATICIUC N., HIIE J., MIKLI V., POTLOG T., VALDNA V., Structural and optical properties of cadmium sulfide thin films modified by hydrogen anneaing, *Materials Science in Semiconductor Processing*, 2014, Vol. 26, p. 169–174.
17. MATICIUC N., HIIE J., POTLOG T., VALDNA V., GAVRILOV A., Influence of annealing in H_2 atmosphere on the electrical properties of thin film CdS, *Mater. Res. Soc. Symp. Proc.*, 2011, Vol. 1324.
18. MATICIUC N., SPALATU N., MIKLI V., HIIE J., Impact of CdS annealing atmosphere on the performace of CdS-CdTe solar cell, *Applied Surface Science*, 2015, Vol. 350, p. 14–18.
19. SPALATU N., HIIE J., VALDNA V., CARAMAN M., MATICIUC N., MIKLI V., POTLOG T., KRUNKS M., LUGHI V., Properties of the $CdCl_2$ air-annealed CSS CdTe thin films. *Energy Procedia*, 2014, Vol. 44, p. 85–95.
20. YÜCEL E., SAHIN O., Effect of pH on the structural, optical and nanomechanical properties of CdS thin films grown by chemical bath deposition, *Ceramics International*, 2016, Vol. 42, p. 6399–6407.
21. SAHIN B., BAYANSAL F., CAKMAK H.M., KAHRAMAN S., CETINKARA H.A., Effect of heat treatment on the properties of $Cd(OH)_2$ and CdO films grown by chemical bath deposition, *Philosophical Magazine Letters*, 2013, Vol. 93, p. 101–108.

CYSENI 2017, May 25-26, Kaunas, Lithuania
ISSN 1822-7554, www.cyseni.com

PHOTOCATALYTIC PROPERTIES OF TIO2 DEPOSITED ON NON-EXPANDED POLYSTYRENE BEADS

Š. Varnagiris, D. Girdzevičius, M. Urbonavičius, D. Milčius
Lithuanian Energy Institute
Breslaujos st. 3, LT-44403 Kaunas – Lithuania
E-mail: Sarunas.Varnagiris@lei.lt

S. Sakalauskaitė
Vytautas Magnus University
K. Donelaičio st. 58, LT-44248 Kaunas – Lithuania

ABSTRACT

Titanium dioxide (TiO_2) is widely researched and used material because of its photocatalytic and other attractive properties. However, formation of TiO_2 on thermally non-stable substrates is still challenging. Photocatalytic properties of TiO_2 films deposited on non-expanded polystyrene (PS) beads using magnetron sputtering technique were investigated. Prior to magnetron sputtering, plasma pre-treatment was used. PS beads were transferred directly under the magnetron without extraction to atmosphere after plasma pre-treatment. Photocatalytic TiO_2 properties were tested by investigating bleaching of the Methylene Blue (MB) in aqueous solution (15 mg/L). Also viability experiments of *Escherichia coli* (E. coli) bacteria under UV-B light irradiation were performed. Significant degradation of MB solution was observed during MB bleaching experiment. Two-phase E. coli bacteria inactivation process was observed during viability experiments. UV irradiation alone can damage outer E. coli bacteria membrane (lipopolysacchride), while combination of TiO_2 and UV can break down both lipopolysacchride and peptidoglycan outer membranes. Moreover, combination of TiO_2 and UV decompose approximately 94% of intact and 100% of ethylenediaminetetraacetic acid (EDTA) treated E. coli bacteria after 45 min. TiO_2 films on PS beads were characterised using combination of scanning electron microscope (SEM) and X-ray photoelectron spectroscope (XPS) analysis techniques. XPS results confirmed formation of TiO_2 compound. SEM results showed that PS beads were coated by TiO_2 films.

Keywords: Photocatalysis, titanium dioxide, polystyrene beads, Escherichia coli, magnetron sputtering

1. INTRODUCTION

Photocatalytic decomposition of organic pollutants or bacterias has attracted much attention in recent years. One of the most promising photocatalyst is TiO_2 because of its high photocatalytic activity, photo-stability and non-toxicity. Since 1927 pioneering work on water photolysis by Honda and Fujishima [1] multitude researches focusing on TiO_2 photocatalytic properties and applications were done. However TiO_2 has relatively wide band gap (3.0–3.2 eV). Therefore UV irradiation or additives is required for various TiO_2 applications [2, 3]. UV light itself can cause damage to the structure or functionality of the living cells. On the other hand, using UV light with photo-catalytic TiO_2 materials antibacterial treatment efficiency can be increased up to several times [4–6]. When TiO_2 is irradiated with UV light (photonic energy equal to, or greater than, its band gap energy 3.2 eV) pair of the electron-hole is generated (Eq. (1)). The electron reduces oxygen to the superoxide ion or anion radicals (Eq. (2)) while generated holes reacts with hydroxyl ions and adsorbs water to form free radicals (Eq. (3)). These created highly reactive oxygen species (ROS) react with bacterias or pollutants and promote their inactivation (Eq. (4), (5)). The most important oxidant species that is responsible for bacteria inactivation is $OH^{\bullet}$ radical [7–10].

$$TiO_2 + hv \rightarrow TiO_2 + e^- + h^+ \tag{1}$$

$$e^- + O_2 \rightarrow O_2^- / HO_2 \tag{2}$$

$$h^{+} + OH^{-} \rightarrow OH^{\bullet} \tag{3}$$

$$Bacteria\,(B) + OH^{\bullet} \rightarrow B_{ox}(oxidized) \tag{4}$$

$$B_{ox} \rightarrow radical\_chain\_reactions \tag{5}$$

Such TiO_2 photocatalytic properties could be very attractive for food packing, medicine, water cleaning or other areas where bacteria inactivation is required [11–13]. However different application requires different preparation of TiO_2. For example, water cleaning requires substrates in order to avoid the use of titanium powder, which has to be separated from the water in a slurry system after the photocatalytic reaction. Moreover buoyant substrates are required which could be easily photoilluminated [14, 15]. One of suitable materials for TiO_2 substrates could be non-expanded polystyrene (PS) beads. These beads are buoyant, relatively cheap and easily manufactured [16, 17]. Also, PS beads are spherical material with arround 1–3 mm dimensions (surface area: 12.5–113 mm^2).

In order to use PS beads as TiO_2 substrates, coatings should be formed on the surface of PS beads. Sol-gel is The most frequently used method to form TiO_2 coatings [18, 19]. However this method involves relatively high temperature (about 200 ^{o}C), while PS glass transition temperature is about 95 ^{o}C. Because of this PS beads undergo structural changes. [20–22] showed that magnetron sputtering (MS) could be suitable method to form films on the surface of polymers. MS involves low temperature (less than 100 ^{o}C) plasma during deposition process. Therefore polymers are not overheated and do not undergo structural changes.

In present work MS was used in order to form TiO_2 films on the surface of PS beads. These beads were used for photocatalysis experiments: methylene blue (MB) degradation in aqueous solution, and *Escherichia coli* (E. coli) bacteria decomposition.

2. METHODOLOGY

2.1. TiO_2 film synthesis

TiO_2 films were deposited on the non-expanded polystyrene (PS) beads using modified physical vapour deposition system manufactured by Kurt J. Lesker company. In order to increase free surface energy of PS beads and to obtain better adhesion between beads and TiO_2 films argon plasma pre-treatment was used [23, 24]. Gas pressure during plasma pre-treatment was set to 1×10^{-1} mbar. Plasma was generated using 400 V supplied by pulsed DC power source (combination of Advanced Energy MDX-1K and Sparcle-20 units). Plasma pre-treatment time was 40 s. Distance between sample surface and high temperature stainless steel (made from Alloy 600) cathode was 40 mm. PS beads were rotated by 180 degree after plasma activation. Beads were placed directly under the magnetron. Titanium disk (76 mm diameter, 99.99% purity, Kurt J.Lesker Company) was used as a primary cathode material. Distance between Ti magnetron and polystyrene sample was 70 mm. During reactive magnetron sputtering process total gas pressure was 6×10^{-3} mbar. Ar-O_2 gas mixture with nominal ratio 1:5.5 was used during TiO_2 films formation (both 99.999% purity, AGA Company). Reactive sputtering was conducted with 0.7 A (power 240 W). Total deposition time was 9 hours. PS beads were thoroughly mixed after every three hours in order to avoid deposition of TiO_2 films just on one side of beads.

2.2. TiO_2 film characterisation

Microstructure and elemental composition of TiO_2 films deposited on PS beads were analysed by Scanning Electron Microscope (Hitachi S-3400N). Chemical state of the magnetron sputtered films was analysed with X-ray photoelectron spectrometer (PHI Versaprobe 5000) using monochromated 1486.6 eV Al radiation; 25 W beam power; 100 μm beam size; and 45°

measurement angle. Observed spectra were shifted using anthropogenic carbon C 1 s peak at 284.8 eV. XPS spectra processing and analysis was done using Multipak software and NIST Standard Reference Database [25].

2.3. Photocatalytic TiO_2 properties testing

Photocatalytic TiO_2 properties were tested by investigating bleaching of the Methylene Blue (MB; made by Reachem Slovakia s.r.o.) in aqueous solution under UV-B irradiation. 1 g of PS beads with TiO_2 films were poured into the petri dish kept in dark for 24 hours. The UV-B exposure experiment was started straight after 10 ml of 15 mg/L concentration aqueous MB solution was syringed above the beads and top of the petri dish was covered by 500 μm thick fused silica disc to minimize evaporation of MB solution.

UV-B light was produced using medical lamp manufactured by Philips (PL-S 9W/01/2p 1CT) with aluminium reflector positioned 30 mm above the UV-B lamp. The distance between UV-B lamp and TiO_2 coating was 200 mm. UV-B lamp power declared by the manufacturer is roughly 1 W after 9 W nominal conversion to narrow wavelength UV-B radiation (305–315 nm).

UV-VIS spectrophotometer (Jasco V-650) was used for measuring of MB concentration changes. All measurements were repeated regularly at 1 hour intervals with 1.5 ml volume. MB solution was syringed back to the petri dish with the sample immediately after the spectroscopic analysis (approximately 2 minutes).

TiO_2 photocatalytic properties also were evaluated by observing inactivation of with *Escherichia coli* (*E. coli*) bacteria. Night culture of *E. coli* DH5α bacteria was grown by introducing several bacterial colonies into 10 ml of sterile Luria Bertani Broth (LB medium) and leaving them to grow for 16–18 hours in Environmental Shaker – Incubator ES-20 (250 rpm, 37 °C). Bacterial suspension was used to grow 100 ml of day culture suspension to optical density equal to 1. This suspension was divided into three parts: one third of the suspension was poured above TiO_2 coated EPS and placed in the dark (this suspension was used to obtain reference viability values); one third was used for exposition to UV-B light without any contact with TiO_2; and the last part of suspension was used to pour above TiO_2 coated EPS and exposed to UV-B light. UV-B light source as well as the distance between sample (thermostated at 37 °C) and the light were the same as in MB bleaching tests. Two types of E. coli bacteria were used: intact and ethylenediaminetetraacetic acid (EDTA) treated E. coli bacteria. Inactivation process took 45 min. After experiment the viability of *E .coli* cells was evaluated as a number of colonies after 18 hours of incubation. The number of colonies was evaluated manually by marking each calculated colony.

3. RESULTS AND DISCUSSION

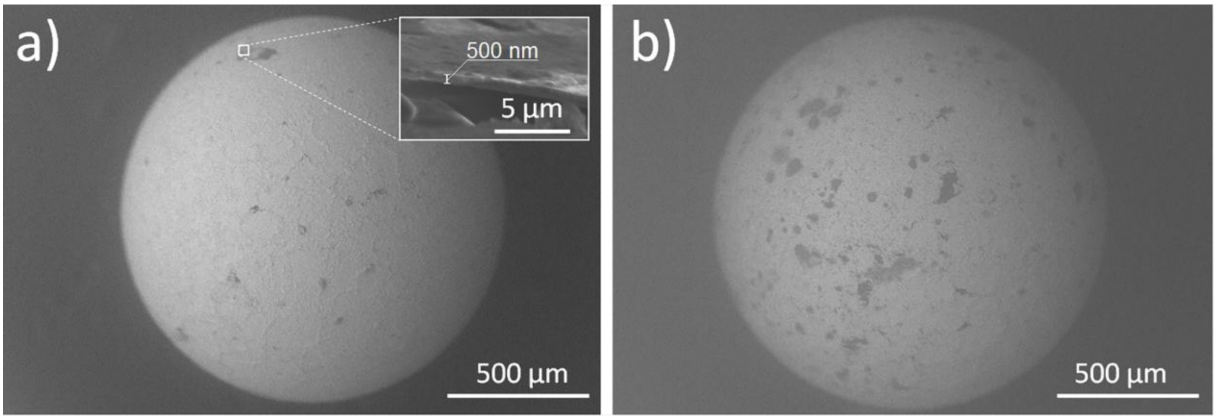

Fig. 1. SEM views of PS bead: a) after TiO_2 deposition; b) after MB decomposition experiment

Surface morphology of PS bead with deposited TiO_2 film could be seen in Fig. 1a. PS bead was covered with TiO_2 film. However, small parts without TiO_2 film were observed. These uncovered parts could appear due to several processes: shadowing effect during deposition process or friction between beads when they were stored after TiO_2 deposition. Cross-cutting measurement showed approximately 500 nm thickness of deposited TiO_2 film. However, TiO_2 film thickness varied from approximately 100 nm to 1100 nm. Thickness of deposited TiO_2 film depends on deposition parameters and mixing of PS beads. Surface morphology of PS beads was done after MB decomposition experiment (Fig. 1b). Results showed that some parts of TiO_2 film are lost and TiO_2 film itself has more cracks. This loss of TiO_2 film could be related with detaching of weakly bonded TiO_2 film when residual of MB solution is rinsed from the sample after MB decomposition experiment. Moreover, absorption of MB solution could initiate aggregation and sedimentation of MB solution on the surface of PS beads [26–28]. As a consequence, bonds between TiO_2 and PS beads could become weaker.

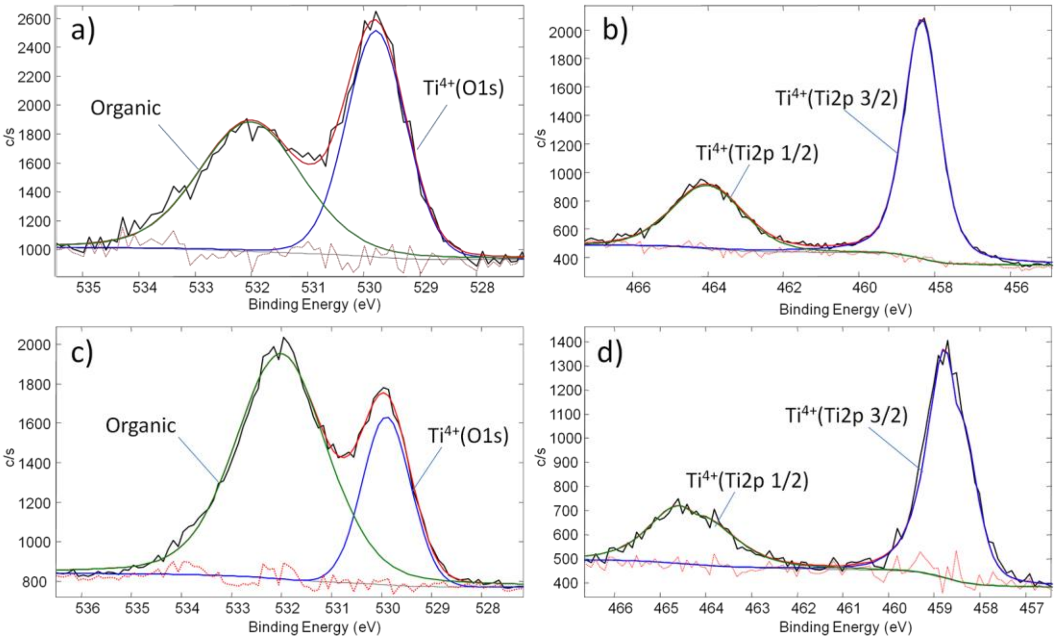

Fig. 2. XPS fitting results: a) O1s peak of deposited TiO_2 film; b) Ti2p peak of deposited TiO_2 film; c) O1s peak after MB degradation experiment; d) Ti2p peak after MB degradation experiment

Results of XPS analysis are shown in Fig. 2. Ti2p 3/2 peak was observed at 458.7 eV, separation between Ti2p 3/2 and Ti2p 1/2 is 5.7 eV (Fig. 2b). These two results are inherent for TiO_2 compound and confirm its formation on the surface of PS beads. However, the difference between binding energies of anatase and rutile phases is just 0.1 eV. Therefore it is not possible to reliably evaluate their ratio. Also is could be seen that O1s peak (Fig. 2a) consist of two parts: TiO_2 and organic. Area measurements performed that TiO_2 part covers 51.1% while organic part covers 48.9% of O1s peak. This observed organic (which include compounds such as C-O/C-OH, H_2O, etc.) could be adsorbed with humidity from atmosphere. All these compounds have very similar binding energy, therefore it is hard to identify separate compounds. Measurements of Ti2p after MB degradation showed that TiO_2 remain stable and do not form any other compound. However intensities of Ti2p peak decreased compared to Ti2p peak before MB decomposition measurement. This decreace could be related to several processes. First of all some parts of TiO_2 could be decomposed during MB degradation experiment. However this part is relatively small. Secondly, agglomeration and sedimentation of MB solution of the surface of PS beads could have influence in decrease of TiO_2 peak intensities. These agglomeration and sedimentation processes also have influence in increase in organic part of O1s peak [27, 28]. O1s peak showed change of Organic/TiO_2 ratio (TiO_2 – 26.4%, Organic – 73.6%). This increase of organic amount confirms that additional amount humidity was observed on the surface of PS beads during MB decomposition measurement.

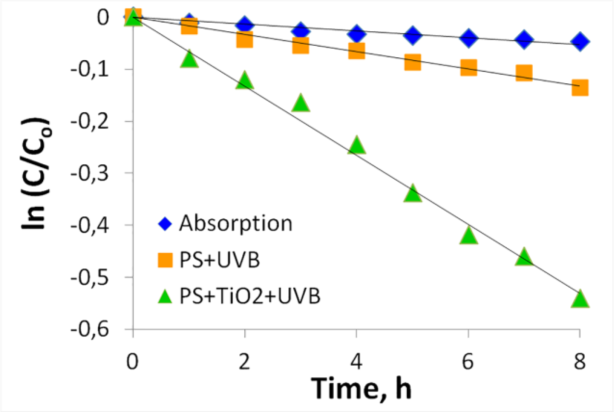

Fig. 3. MB aqueous solution bleaching in the dark (absorption), pure PS beads with UV-B irradiation (PS + UVB); PS with TiO_2 under UV-B irradiation (PS + TiO_2 + UVB)

Aqueous MB solution bleaching experiment results are shown in Fig. 3. First of all absorption of MB solution into PS beads with TiO_2 was evaluated. Beads were mixed with MB solution end kept in the dark for 8 hours. Measurement showed that absorption of MB solution into PS beads with TiO_2 film is relatively negligible. UV-B irradiation influence of MB bleaching was estimated using PS beads without TiO_2. Results showed that exposure to UV-B light initiates MB molecule degradation (first order reaction constant $k = 4.6\times10^{-6}$ s^{-1}). Bleaching of MB solution measurement using PS beads with TiO_2 films under UV-B irradiation showed significant degradation which is more than 4 times higher (first order reaction constant $k = 1.95\times10^{-5}$ s^{-1}) compared to single UV-B irradiation.

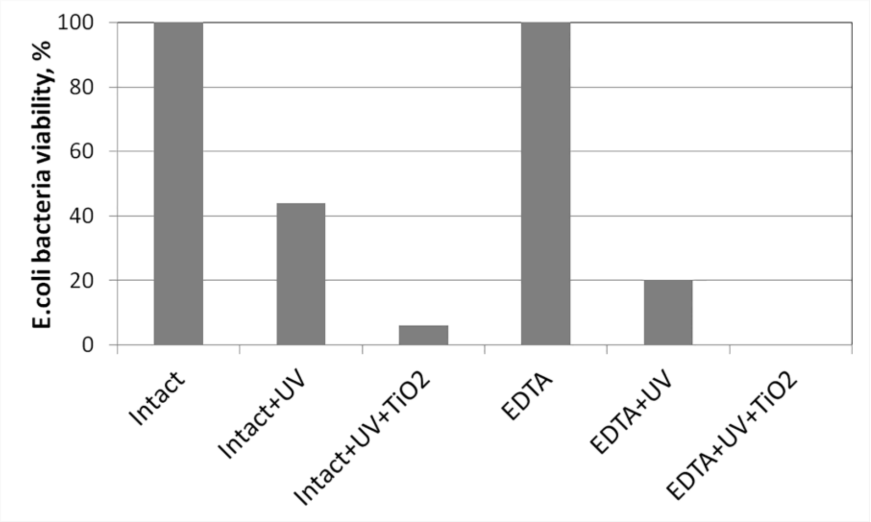

Fig. 5. Viability of intact and EDTA treated E. coli bacteria: untreated (Intact / EDTA), under UV-B irradiation (Intact + UV / EDTA + UV); under UV-B with TiO_2 coated PS beads (EDTA + UV + TiO_2)

E. coli viability test was performed with intact and EDTA treated bacteria under UV-B irradiation and combination of TiO_2 (PS beads with TiO_2 films) and UV-B (Fig. 5) after 45 min of treatment time. Results showed that UV-B alone can make damage for both intact and EDTA treated bacteria after 45 min of treatment (bacteria viability 44% and 20% respectively). Combination of UV-B and TiO_2 can increase decomposition of E. coli bacteria more than 7 times (bacteria viability 6% for intact and 0% for EDTA treated bacteria). This result indicates that there are two mechanisms of E. coli bacteria inactivation. E. coli consist of inner (phospholipid chains and proteins) and outer (lipopolysacchride (LPS), phospholipid layer and peptidoglycan (PP)) membranes [29]. P. Liu [4] demonstrated that UV-B alone or TiO_2 under daylight irradiation could destroy LPS but were not able to break down peptidoglycan. Therefore further inactivation of E. coli bacteria by UV-B irradiation or TiO_2 alone is limited by inability to damage PP layer. On the other hand combination of UV-B irradiation and TiO_2 could create highly reactive oxygen species [30, 31] (see Introduction part) which able to break down PP layer. This additional decomposition invokes reduction of E. coli bacteria viability [11, 32, 33]. The higher decomposition ratio of EDTA treated bacteria is related to EDTA mechanism. Using such method, bonds of LPS layer becomes weaker. Therefore it is easier to treat PP layer using UV-B or combined UV-B with TiO_2.

O. Akhavan in his previous works [34–36] demonstrated that bacteria could start to proliferate when viability is highly than 10%. In common, such decomposition (when viability is still more than 10 %) is useless for practical purpose. Our results showed that 45 min decomposition of E. coli bacteria using UV-B with TiO_2 deposited on PS beads could be suitable mechanism for practical purpose. On the other hand, further experiments for photocatalysis stability (cycling) are also required.

4. CONCLUSIONS

TiO_2 film was deposited on the surface of PS beads using magnetron sputtering technique. XPS measurement confirms formation of TiO_2. SEM views showed that thickness of TiO_2 is about 500 nm. However, TiO_2 film thickness varied from approximately 100 nm to 1100 nm. MB solution bleaching experiment showed high decomposition ratio (first order reaction constant $k = 1.95\times10^{-5}\ s^{-1}$) using combined UV-B and TiO_2 treatment. However increase of organic compounds as well as detachment of TiO_2 film was observed after MB decomposition. E. coli bacteria inactivation experiments showed that two-step mechanism initiate decomposition process: UV-B irradiation alone can damage outer E. coli bacteria membrane (lipopolysacchride), while combination of TiO_2 and UV can break down both lipopolysacchride and peptidoglycan outer membranes. Such mechanism invokes just 6% viability of E. coli bacteria, which is sufficient for practical purposes.

5. AKNOWLEDGEMENTS

This work was financially supported by The European Social Fund under project with SFMIS code: VP1-3.1-SMM-10-V-02-019.

REFERENCES

[1] A. Fujishima, K. Honda, Electrochemical photolysis of water at a semiconductor electrode, Nature. 238 (1972) 37–38. doi:10.1038/238037a0.

[2] H. Saleem, A. Habib, Study of band gap reduction of TiO2 thin films with variation in GO contents and use of TiO2/Graphene composite in hybrid solar cell, J. Alloys Compd. 679 (2016) 177–183. doi:10.1016/j.jallcom.2016.03.240.

[3] I. Dobrosz-Gómez, M. Gómez-García, S.M. López Zamora, E. Gilpavas, J. Bojarska, M. Kozanecki, J.M. Rynkowski, Transition metal loaded TiO2 for phenol photo-degradation, Comptes Rendus Chim. 18 (2015) 1170–1182. doi:10.1016/j.crci.2015.03.006.

[4] P. Liu, W. Duan, Q. Wang, X. Li, The damage of outer membrane of Escherichia coli in the presence of TiO2 combined with UV light, Colloids Surfaces B Biointerfaces. 78 (2010) 171–176. doi:10.1016/j.colsurfb.2010.02.024.

[5] R.H. West, M.S. Celnik, O.R. Inderwildi, M. Kraft, G.J.O. Beran, W.H. Green, Toward a Comprehensive Model of the Synthesis of TiO2 Particles from TiCl4, J. Ind. Eng. Chem. 46 (2007) 6147–6156. doi:10.1021/ie0706414.

[6] M. Casarin, C. Maccato, a Vittadini, Molecular Chemisorption on TiO 2 (110): A Local Point of View, J. Phys. Chem. B. 102 (1998) 10745–10752. doi:10.1021/jp981377i.

[7] U. Khan, N. Benabderrazik, A.J. Bourdelais, D.G. Baden, K. Rein, P.R. Gardinali, L. Arroyo, K.E. O'Shea, UV and solar TiO2 photocatalysis of brevetoxins (PbTxs), Toxicon. 55 (2010) 1008–1016. doi:10.1016/j.toxicon.2009.11.014.

[8] A.K. Benabbou, Z. Derriche, C. Felix, P. Lejeune, C. Guillard, Photocatalytic inactivation of Escherischia coli. Effect of concentration of TiO2 and microorganism, nature, and intensity of UV irradiation, Appl. Catal. B Environ. 76 (2007) 257–263. doi:10.1016/j.apcatb.2007.05.026.

[9] J. Schneider, M. Matsuoka, M. Takeuchi, J. Zhang, Y. Horiuchi, M. Anpo, D.W. Bahnemann, Understanding TiO 2 Photocatalysis : Mechanisms and Materials, Chem. Rev. 114 (2014) 9919–9986. doi:10.1021/cr5001892.

[10] S.G. Kumar, L.G. Devi, Review on modified TiO2 photocatalysis under UV/visible light: Selected results and related mechanisms on interfacial charge carrier transfer dynamics, J. Phys. Chem. A. 115 (2011) 13211–13241. doi:10.1021/jp204364a.

[11] I. Altin, M. Sökmen, Preparation of TiO2-polystyrene photocatalyst from waste material and its usability for removal of various pollutants, Appl. Catal. B Environ. 144 (2014) 694–701. doi:10.1016/j.apcatb.2013.06.014.

[12] E. V. Loddo, G. Marci, G. Palmisano, Extruded expanded polystyrene sheets coated by TiO 2 as new photocatalytic materials for foodstuffs packaging, Appl. Surf. Sci. 261 (2012) 783–788. doi:10.1016/j.apsusc.2012.08.100.

[13] M. Birnie, M. Gillott, S. Riffat, The immobilization of titanium dioxide on organic polymers, for a cost effective and energy efficient means of improving indoor air quality, Int. J. Green Energy. 3 (2006) 101–114. doi:10.1080/01971520500439567.

[14] L. Wang, J. Zhang, C. Li, H. Zhu, W. Wang, T. Wang, Synthesis, Characterization and Photocatalytic Activity of TiO2 Film/Bi2O3 Microgrid Heterojunction, J. Mater. Sci. Technol. 27 (2011) 59–63. doi:http://dx.doi.org/10.1016/S1005-0302(11)60026-1.

[15] C. Li, B. Wang, H. Cui, J. Zhai, Q. Li, Preparation and characterization of buoyant nitrogen-doped TiO2 composites supported by fly ash cenospheres for photocatalytic applications, J. Mater. Sci. Technol. 29 (2013) 835–840. doi:10.1016/j.jmst.2013.04.027.

[16] M.. Fabiyi, R.. Skelton, Photocatalytic mineralisation of methylene blue using buoyant TiO2-coated polystyrene beads, J. Photochem. Photobiol. A Chem. 132 (2000) 121–128. doi:10.1016/S1010-6030(99)00250-6.

[17] D. Raps, N. Hossieny, C.B. Park, V. Altstädt, Past and present developments in polymer bead foams and bead foaming technology, Polym. (United Kingdom). 56 (2015) 5–19. doi:10.1016/j.polymer.2014.10.078.

[18] S.M. Gupta, M. Tripathi, A review on the synthesis of TiO2 nanoparticles by solution route, Cent. Eur. J. Chem. 10 (2012) 279–294. doi:10.2478/s11532-011-0155-y.

[19] J. Tian, Z. Zhao, A. Kumar, R.I. Boughton, H. Liu, Recent progress in design, synthesis, and applications of one-dimensional TiO2 nanostructured surface heterostructures: a review, Chem. Soc. Rev. 43 (2014) DOI: 10.1039/C4CS00180J. doi:10.1039/C4CS00180J.

[20] Y. Horie, K. Daizaka, H. Mukae, S. Guo, T. Nomiyama, Enhancement of photocurrent by columnar Nb-doped TiO2 compact layer in dye sensitized solar cells with low temperature process of dc sputtering, Electrochim. Acta. 187 (2016) 348–357. doi:10.1016/j.electacta.2015.11.054.

[21] C.G. Kuo, C.Y. Hsu, S.S. Wang, D.C. Wen, Photocatalytic characteristics of TiO2 films deposited by magnetron sputtering on polycarbonate at room temperature, Appl. Surf. Sci. 258 (2012) 6952–6957. doi:10.1016/j.apsusc.2012.03.142.

[22] D. Hegemann, Plasma Polymer Deposition and Coatings on Polymers, 2014. doi:10.1016/B978-0-08-096532-1.00426-X.

[23] Y. Sasai, N. Matsuzaki, S. Kondo, M. Kuzuya, Introduction of carboxyl group onto

polystyrene surface using plasma techniques, Surf. Coatings Technol. 202 (2008) 5724–5727. doi:10.1016/j.surfcoat.2008.06.085.

[24] A. Vesel, Modification of polystyrene with a highly reactive cold oxygen plasma, Surf. Coatings Technol. 205 (2010) 490–497. doi:10.1016/j.surfcoat.2010.07.016.

[25] NIST X-ray Photoelectron Spectroscopy Database, NIST Standard Reference Database 20, Version 4.1, (n.d.). http://srdata.nist.gov/xps/Default.aspx (accessed December 20, 2016).

[26] Y. Lv, L. Yu, X. Zhang, J. Yao, R. Zou, Z. Dai, P-doped TiO2 nanoparticles film coated on ground glass substrate and the repeated photodegradation of dye under solar light irradiation, Appl. Surf. Sci. 257 (2011) 5715–5719. doi:10.1016/j.apsusc.2011.01.082.

[27] M.A. Elsayed, M. Gobara, Enhancement removal of tartrazine dye using HCl-doped polyaniline and TiO2-decorated PANI particles, Mater. Res. Express. 3 (2016) 1–16. doi:10.1088/2053-1591/3/8/085301.

[28] E.M. Saggioro, A.S. Oliveira, T. Pavesi, M.J. Tototzintle, M.I. Maldonado, F.V. Correia, J.C. Moreira, Solar CPC pilot plant photocatalytic degradation of indigo carmine dye in waters and wastewaters using supported-TiO2: Influence of photodegradation parameters, Int. J. Photoenergy. 2015 (2015). doi:10.1155/2015/656153.

[29] C. Raetz, Biochemistry Of Endotoxins, Annu. Rev. Biochem. 59 (1990) 129–170. doi:10.1146/annurev.biochem.59.1.129.

[30] P. Chen, F. Wang, Z.-F. Chen, Q. Zhang, Y. Su, L. Shen, K. Yao, Y. Liu, Z. Cai, W. Lv, G. Liu, Study on the photocatalytic mechanism and detoxicity of gemfibrozil by a sunlight-driven TiO2/carbon dots photocatalyst: The significant roles of reactive oxygen species, Appl. Catal. B Environ. 204 (2017) 250–259. doi:10.1016/j.apcatb.2016.11.040.

[31] M. Pelaez, P. Falaras, V. Likodimos, K. O’Shea, A.A. de la Cruz, P.S.M. Dunlop, J.A. Byrne, D.D. Dionysiou, Use of selected scavengers for the determination of NF-TiO2 reactive oxygen species during the degradation of microcystin-LR under visible light irradiation, J. Mol. Catal. A Chem. 425 (2016) 183–189. doi:10.1016/j.molcata.2016.09.035.

[32] C. Karunakaran, V. Rajeswari, P. Gomathisankar, Optical, electrical, photocatalytic, and bactericidal properties of microwave synthesized nanocrystalline Ag-ZnO and ZnO, Solid State Sci. 13 (2011) 923–928. doi:10.1016/j.solidstatesciences.2011.02.016.

[33] X. Hu, G. Li, J.C. Yu, Design, fabrication, and modification of nanostructured semiconductor materials for environmental and energy applications, Langmuir. 26 (2010) 3031–3039. doi:10.1021/la902142b.

[34] O. Akhavan, M. Abdolahad, Y. Abdi, S. Mohajerzadeh, Synthesis of titania/carbon nanotube heterojunction arrays for photoinactivation of E. coli in visible light irradiation, Carbon N. Y. 47 (2009) 3280–3287. doi:10.1016/j.carbon.2009.07.046.

[35] O. Akhavan, Lasting antibacterial activities of Ag-TiO2/Ag/a-TiO2 nanocomposite thin film photocatalysts under solar light irradiation, J. Colloid Interface Sci. 336 (2009) 117–124. doi:10.1016/j.jcis.2009.03.018.

[36] O. Akhavan, E. Ghaderi, Photocatalytic reduction of graphene oxide nanosheets on TiO2 thin film for photoinactivation of bacteria in solar light irradiation, J. Phys. Chem. C. 113 (2009) 20214–20220. doi:10.1021/jp906325q.

CYSENI 2017, May 25-26, Kaunas, Lithuania
ISSN 1822-7554, www.cyseni.com

A COMPARATIVE STUDY ON PHYSICAL PROPERTIES OF AL-DOPED ZINC OXIDE THIN FILMS DEPOSITED FROM ZINC ACETATE AND ZINC ACETYLACETONATE SOLUTIONS BY SPRAY PYROLYSIS

J. S. Eensalu, M. Krunks, I. Gromyko, A. Katerski, A. Mere
Tallinn University of Technology
Ehitajate tee 5, EE-19086 Tallinn – Estonia
E-mail: jako.eensalu@gmail.com

ABSTRACT

Doped zinc oxide is a suitable candidate for replacing indium tin oxide (ITO), one of the most popular transparent conductive oxides (TCO) as a cheaper and non-toxic alternative. In this paper we present a comparative study on highly transparent and electrically conductive aluminium-doped ZnO (AZO) thin films deposited by pneumatic spray pyrolysis (PSP) of a zinc acetate based solution and a zinc acetylacetonate based solution on soda lime glass. The structural, optical and electrical properties of the films were studied depending on aluminium content in the precursor solution and substrate temperature during deposition (T_s). The solvent was composed of isopropanol, water and acetic acid in the volume ratio 30:19:1. The solution used to prepare AZO thin films contained 0.2 M zinc acetate ($Zn(ac)_2$) or 0.2 M zinc acetylacetonate ($Zn(acac)_2$) between 0 and 15 at% [Al]/[Zn] using aluminium acetylacetonate ($Al(acac)_3$) as dopant. Solution spray rate was fixed at 3 ml/min. Substrate temperature was varied from 275 ^{o}C to 450 ^{o}C. Phase composition and crystal structure were studied by X-ray diffraction analysis (XRD). Transmittance, reflectance spectra, band gap and film thickness were determined by UV-VIS-NIR spectroscopy. Electrical resistivity, mobility and charge carrier density were measured by four point probe Hall measurements in ambient conditions.

According to XRD, AZO films are highly c-axis oriented up to 2-3 at% [Al]/[Zn] in the spray solution, depending on the zinc precursor. Crystallite size is 25-30 nm for AZO films deposited at T_s 400 ^{o}C. AZO films deposited from $Zn(ac)_2$ show higher/larger average crystallite size vs films deposited from $Zn(acac)_2$. AZO films grown at T_s 450 ^{o}C from $Zn(acac)_2$ solution containing 7.5 at% [Al]/[Zn] exhibit lower crystallinity as a mixture of ZnO, $Zn_6Al_2O_3$ and Al_2O_3 phases forms. All AZO films exhibited 80% average optical transmittance in the spectrum 400-800 nm wavelength range. Film thickness was 530 ±130 nm. Band gap in AZO films deposited from $Zn(ac)_2$ was 3,30-3,42 eV. Band gap in $Zn(acac)_2$ counterparts ranged from 3.32 eV in undoped to 3.58 eV in highly doped AZO films due to formation of secondary Al_2O_3 phase. Charge carrier mobility was 0,1-10 $cm^2V^{-1}s^{-1}$. The lowest electrical resistivity (0.40 Ωcm) and highest charge carrier concentration ($2*10^{19}$ cm^{-3}) were obtained at T_s 400 ^{o}C for films deposited from zinc acetate and zinc acetylacetonate solutions with [Al]/[Zn] of 3-7.5 at% and 7.5 at%, respectively. Zinc acetate was determined to produce AZO films with higher crystallinity and more stable band gap containing less secondary phases.

Keywords: AZO, Al-doped ZnO, pneumatic spray pyrolysis, thin films

CYSENI 2017, May 25-26, Kaunas, Lithuania
ISSN 1822-7554, www.cyseni.com

LUMINESCENCE OF X-RAY INDUCED RADIATION DEFECTS IN MODIFIED LITHIUM ORTHOSILICATE PEBBLES WITH ADDITIONS OF TITANIUM DIOXIDE

J. Cipa, G. Kizane, A. Supe, A. Zolotarjovs
University of Latvia
1 Jelgavas street, Riga, LV-1004 – Latvia
E-mail: janis.cipa@gmail.com

A. Zarins
Daugavpils University
Parades street 1a, Daugavpils, LV-5401 – Latvia

L. Baumane
Latvian Institute of Organic Synthesis
Aizkraukles 21, Riga, LV-1006 – Latvia

ABSTRACT

Modified lithium orthosilicate (Li_4SiO_4) pebbles with additions of titanium dioxide (TiO_2) are designed as a possible tritium breeder ceramic for the helium cooled pebble bed (HCPB) test blanket module (TBM).Due to the additions of TiO_2, lithium metatitanate (Li_2TiO_3) is obtained as a secondary phase in the modified Li_4SiO_4 pebbles. In combining of these two phases – Li_4SiO_4 and Li_2TiO_3, it is anticipated to obtain a modified tritium breeding ceramic with improved mechanical properties, without losing the benefit of the high lithium density, melting temperature and good tritium release behaviour.

Under the operation conditions of the HCPB TBM, the modified Li_4SiO_4 pebbles will be exposed to an intense neutron flux, a high temperature and a magnetic field. Under such conditions radiation-induced defects (RD) and radiolysis products (RP) can be induced in the tritium breeder pebblesand could play a crucial role in tritium diffusion and release processes. Previous researches confirmed that in the modfied pebbles both phase - Li_4SiO_4 and Li_2TiO_3, are separated by grain boundries and thus it is anticipated that the formation mechanisms and the structure of the accumulated RD and RP will be similar to single phase ceramics.

In order, to evaluate the formation of RD, the modified Li_4SiO_4 pebbles with 10, 20 and 30 mol% Li_2TiO_3were analysed by X-ray induced luminescence (XRL) technique and compared with the reference Li_4SiO_4 pebbles. After XRL measurements the accumulated RD were also analysed by thermally stimulated luminescence (TSL) and electron spin resonance (ESR) spectrometry.

XRL spectra of the modified Li_4SiO_4 pebbles consist of several bands with maxima at around 430, 490, 690, 700 and 800 nm. The XRL band with a peak at 490 nm could be associated with intrinsic defects in Li_4SiO_4 matrix whereas all the other maxima at lower photon energies are the result of the addition of TiO_2. For XRL kinetics measurements of the modified pebbles a trend of decreasing intensity was detected as X-ray irradiation time increases which could be associated whit recombination of defects present in the sample. After XRL measurements, detected signals for ESR spectra of the modified Li_4SiO_4 pebbles consists of at least three first derivative signals with g-factors 2.019 ±0.001, 2.003 ±0.001and 1.93 ±0.01 and most likely could be associated with E' centres (SiO_3^{3-} or TiO_3^{3-}), oxygen related defects and Ti^{3+} centres, respectively. The TSL technique confirmed that the accumulated RD recombine 400-773 K temperature.However, all above mentioned results also clearly confirm the necessity to further study the radiation-induced effects in the modified Li_4SiO_4 pebbles with additions of TiO_2.

Keywords: Lithium orthosilicate, Titanium dioxide, X-ray induced luminescence, XRL, Thermally stimulated luminescence, TSL, Electron spin resonance, ESR.

THERMAL NEUTRON DETECTION USING THIN PEN FILM DOPED WITH HIGH CROSS SECTION MATERIALS

J. Garankin, A. Plukis, E. Lagzdina
Center for Physical Sciences and Technology
Savanorių pr. 231, LT-02300 Vilnius – Lithuania
E-mail: Jevgenij.garankin@ftmc.lt

ABSTRACT

Poly(ethylene 2,6-naphthalate) (PEN) is promising as the new plastic scintillator, which emits deep-blue photons. Its photoluminescence emission peak (434–436 nm), and the decay time is of the order of 3 ns as well as it is resistant to a harsh environment. PEN has bigger oxygen barer than PET (polyethylene terephthalate). This material density (1.36 g/cm^3) is higher than typical organic scintillator and it emits a high number of photons per incident radiation event, up to 10500 photons per incident. In addition, it has 10% energy resolution in the 1 MeV energy region. In this study, thin PEN film with high neutron cross section dopants was used for the thermal neutron detection. 100 μm iron boride (FeB), 500 nm lithium tetraborate ($Li_2B_4O_7$) and lithium metaborate ($LiBO_2$) layers were coated on 125 μm PEN films. The iron boride layer was coated using prepared paste and the lithium based layer was coated using physical vapor deposition process.

The experimental setup was prepared for measurements. Detector dimensions 20×20 mm, photomultiplier (PMT) cathode window diameter is 20 mm and multiplication cascade has 10 dynodes. Detector film was loaded on a photomultiplier photocathode window using a liquid optical contact. Scintillator detector was covered with cadmium and lead. Reaction particles from the boron neutron and lithium neutron reaction were detected by scintillation in PEN, PMT pulses were registered and spectra were analyzed. Neutron flow was generated by ^{239}PuBe and ^{238}PuBe sources. Sources total neutron activity was 4.5×10^7 n/s. The neutron dose rate was about 300 μSv/h and the gamma dose rate was about 20 μSv/h. To decrease fast neutron energy the neutron source was surrounded by paraffin and polyethylene granules. ^{238}Pu source was used as α particles source to calibrate detector. The experiment model was prepared for simulation and the energy deposition in the film samples was calculated by MCNP6 code taking into account losses in the source and air gap for the alpha particle source and incomplete energy deposition for the electrons.

It was found that a small quantity of particles from the thermal neutron reaction could be detected in the strong neutron, gamma ray and recoil proton background. The PEN film detector with 100 μm thickness FeB layer showed that ionized particles form thermal neutron and ^{10}B reaction could be registered in strong background conditions. Otherwise, the detector with thin lithium based layer showed that ionized particles form thermal neutron and ^{6}Li could not be registered in same conditions.

Keywords: scintillation, irradiation detection, neutrons

NUMERICAL INVESTIGATION OF J-INTEGRAL

R. Janulionis
Lithuanian Energy Institute
Breslaujos str. 3, LT-44403 Kaunas – Lithuania
E-mail: remigijus.janulionis@lei.lt

ABSTRACT

During Nuclear Power Plant (NPP) operation, degradation effects like corrosion, fatigue, and in-service degradation of fracture toughness, may significantly impact component integrity. Therefore while estimating structural integrity analysis it is important to evaluate the influence of the ageing on material degradation. When the metal is ageing under certain conditions the crack can appear and this finally could lead to the failure of construction. To evaluate the resistance to failure of the constructions with cracks usually the fracture criterions are used. For the ductile materials J-integral is used as a fracture parameter. Calculated J-integral value of the component with crack is compared with critical J-integral value of the material. Critical J-integral values are usually determined experimentally. There are two objectives of this work: create the methodology for critical J-integral determination using numerical methods; using created methodology evaluate the ageing influence to the critical J-integral.

In accordance with the objectives of the work the modelling of the J-integral of steel P91 was performed. Numerically simulation results were compared with experiment. For this purpose, the Finite Element (FE) method was used as numerical method and ABAQUS v6.11 as FE code.

Keywords: finite element method, J-integral, ageing

1. INTRODUCTION

Structural integrity of steel without and with cracks after long-term service is one of the most important factors to the safety and reliability of engineering components and also for prediction of their lifetime. During operation of steel components, degradation effects, such as corrosion, fatigue, and in-service degradation of fracture toughness, may significantly impact component integrity. Due to an ageing the degradation of material properties results in increased susceptibility to cracking under load and environmental conditions. Quantitative understanding of material fracture mechanism is a subject of modelling and experimental research in lifetime evaluation of structures. Analysis of structural integrity of the engineering structures shows that small cracks in the body of structures can be a cause of failure. It is important to know the limit when a crack starts to grow. One factor that can help an engineer to determine this limit is the critical J-integral [1]. Critical J-integral is used as a fracture parameter for ductile materials. Calculated J-integral value of the component with crack is compared with critical J-integral value of the material. And then it can be decided if construction with cracks is safe to be in operation. J-integral depends on the size and location of the crack, geometry, the magnitude of load, environment, i.e. temperature and etc. Usually critical J-integral is determined by an experiment, whereas the procedures are described in standards such as ASTM, ISO, etc. However, it is not always possible to conduct an experiment. Therefore, alternative methods for determination of critical values of fracture parameter are necessary. Finite element method (FEM) and boundary element method (BEM) are the most widely used techniques for evaluating J-integral.

A number of papers can be found on fracture parameters calculation using FEM [2, 3]. Jun-Young and all [4] presents sophisticated crack growth modelling technique which is used for critical J-integral determination. However this technique requires damage analysis to be added in the model and another three material constants have to be found. Also calculation results appear to be sensitive to mesh size. Overall it makes this technique complicated.

The influence of ageing of steel on the static mechanical properties is also important for the prognosis of J-integral. Cumino and all [5] carried out ageing research of the high chromium ferritic steels and estimated the following: about 10% maximum reduction of the tensile properties after 1,000 hours of exposure; constant values of ductility; and a strong reduction of the impact properties during the first 3,000 hours of exposure with an increase of brittle fracture. This means that ageing of the steel can potentially have influence on its fracture toughness.

The aim of this research is numerically determine J-integral and compare the results with experiment. Also, investigate the influence of ageing on J-integral of steel P91. The finite element method was applied for simulation. The J-integral was investigated for as received and aged steel P91. The experimental and numerical results were compared.

2. METHODOLOGY

The idea of numerical investigation of J-integral is numerically simulate the experiment according to actual procedures/instructions used for experiment conduction. For this purpose instructions described in ASTM E1820 standard [6] were used. The computer code ABAQUS v6.11 [7] has been chosen for numerical simulation. ABAQUS uses finite element method (FEM) for numerical simulation. ASTM E1820 instructions for critical stress intensity factor determination are presented in the following section.

2.1. Instructions for critical J-integral determination

According to ASTM E1820, to determine the value of J-integral it is necessary to develop so called J-R curve which consist of J-integral values at a series of measured specimen crack extensions. The actual result after the experiment is data points which later are used for J-R curve construction. However not all points are good to be used for J-R curve but the points which are in the area limited by 0.15 mm and 1.5 mm exclusion lines and by J_{limit} line. To draw an exclusion line in the first place it is necessary to determine a construction line which is calculated by the following equation:

$$J = 2\sigma_Y \Delta a \tag{1}$$

where σ_Y – effective yield strength (the average of yield strength R_p and ultimate strength R_m) of the material, MPa; $\triangle a$ – crack extension, mm.

The exclusion lines are just the parallel lines to the construction line with offset of 0.15 mm and 1.5 mm. J_{limit} is calculated by equation:

$$J_{limit} = b_0 \sigma_Y / 7.5 \tag{2}$$

where b_0 – uncracked ligament of the specimen, mm.

Using selected data points power law regression line can be constructed using a method of least squares. Also the offset line has to be determined. The offset line, the same as exclusion lines, is the line parallel to the construction line with offset of 0.2 mm. This line is used to determine the conditional J_Q value which is determined at the intersection of regression line with offset line. After J_Q is determined and if effective yield strength, specimen size and J_Q meet ASTM E1820 conditions it is possible to state that $J_Q = J_{IC}$.

2.2. Material and specimen

Test specimens were manufactured from commercial 30 mm thick P91steel plate. Thermal ageing of the specimens were carried out in electric furnace at 650 °C for 11000 h.

The tests of mechanical properties and fracture toughness were carried out using Instron Model 8801 servo-hydraulic testing machine with capacity of ±100 kN axial force. Tensile tests were performed according to EN ISO 6892-1:2009 [8] standard recommendations. Mechanical properties of steel are shown in Table 1. Here $R_{p0.2}$ – yield stress at 0.2% plastic strain, MPa; R_m – tensile strength, MPa; E – Young's modulus, GPa. According to presented results the ageing effect to mechanical properties of steel P91 is noticeable. However, actual drop of parameters is not significant and the biggest change of value was detected for tensile strength and it was up to 4.2%.

Table 1. Averaged mechanical properties of P91 steel

Ageing time at 650 °C, h	**$R_{p0.2}$, MPa**	**R_m, MPa**	**E, GPa**
0	513	666	214
11000	487	637	209

J-integral was determined in accordance with ASTM E1820 [6] using compact tension C(T) specimens. Experimentally determined J-integral values are later presented in section 3.

2.3. Numerical model

3D finite element model of Compact Tension (CT) specimen was prepared for J-integral modelling. The mesh of the models is shown in Fig. 1. The dimensions of FE models are the same as dimension of CT specimen used in the experimental testing, which was a standard CT specimen described in ASTM E1820 [6] with W = 50 mm and with side grooves. FE model was meshed with C3D20R elements [7]. These elements are quadratic brick shape and have 20 nodes.

The length of fatigue crack in FE models were the same as in CT specimen used in experiment and it was equal to a_1 = 2.78 mm (see Fig. 1).

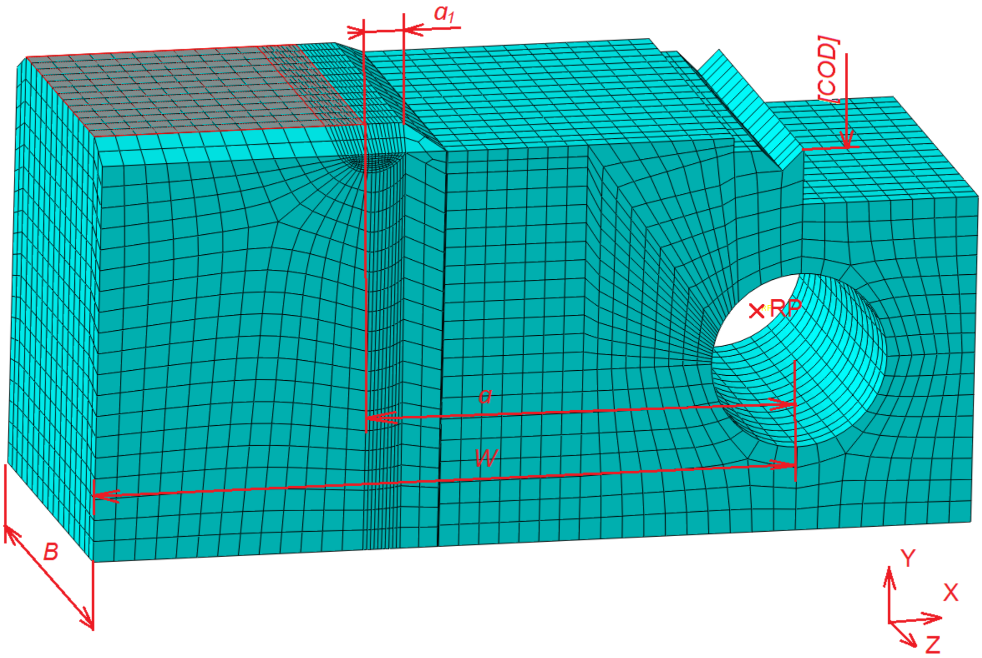

Fig. 1. Finite element mesh of CT specimen

As the specimen is symmetric about the XZ plane only half of the model was created. The symmetry boundary conditions were applied to the red coloured surface showed in Fig. 1. Also additional boundary conditions were added to the Reference Points (RP) placed at the centre of the hole used for pin in experiment. The displacements of RP were restricted in two directions, i.e. along the X and Z axes. However, the displacement was added along Y axis and was used as load.

As calculation results the following parameters were received: reaction force at the RP where displacement was added, crack opening displacement [COD] was measured at the edge point were extensometer was attached in experiment, and J-integral at crack tip. The calculated J-integral values were averaged along the crack front.

3. CALCULATION RESULTS

Comparison of CT specimen simulation result with experiment is presented in Fig. 2. The figure presents load versus crack opening displacement curves for experiment and FE simulation of as received and aged steel. As it can be seen the simulation results quite well match the experiment. Up to the peak of experimentally determined curve simulation result does not deviate more than 4% for all cases. However, results start to deviate more when the load starts to drop. This deviation occurs due to the fact that the drop of the load appears due to the growth of the crack and the actual crack growth is not directly modelled in numerical simulation.

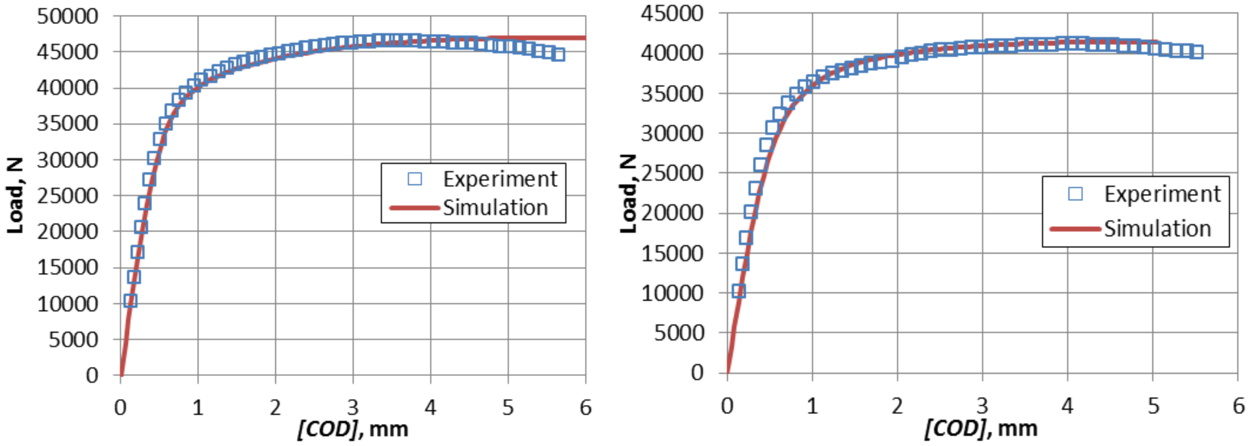

a) b)

Fig. 2. Simulation results of load vs COD compared with experiment: a) as received material; b) aged at 650 °C for 11000 h

According to methodology presented in section 2.1 it is necessary to construct J-R curve for J-integral determination. For this reason the crack extension should be measured during the tension of CT specimen. However, for the FE models presented in the section 2.3 the direct crack extension is not simulated. Therefore neither direct crack length measurement nor the elastic compliance measurement method suggested in ASTM code can be used. In this article the crack growth was determined from of the crack opening displacement and load ratio dependency on crack extension. In 1977 Sullivan and Crooker [9] have presented the crack opening displacement technique for crack length measurement. The authors suggest to use the polynomial function *a/W = f (E, B, [COD], P)* they determined where *E* is Young's modulus, Pa; *B* – specimen thickness, m; *[COD]* – crack opening displacement, m; *P* – load, N. However the function that authors recommend is only good to be used for materials which produce linear load vs COD trace.

For crack length extension of steel P91 the quadratic polynomial expression of experimentally determined curve *EB[COD]/P* versus *a/W*, which is shown in Fig. 3, has been found. Found polynomial expression is presented below:

$$\frac{EB[COD]}{P} = -32051\left(\frac{a}{w}\right)^2 + 57864\left(\frac{a}{w}\right) - 23118 \tag{3}$$

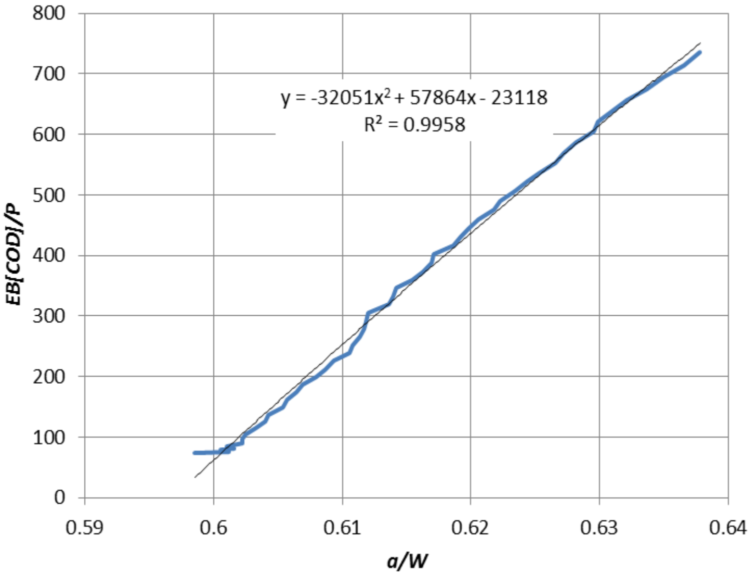

Fig. 3. *EB[COD] / P* versus *a / W*

Fig. 4 represents calculated J-R curves of not aged steel P91. J_Q values are determined at intersection points of curve and offset line. The ASTM E1820 indicates that for qualification of J_Q as elastic plastic fracture toughness J_{IC}, $J_{IC} = J_Q \leq \min(b_0\sigma_y / 10; B\sigma_y / 10)$. Applying this criterion determined J_Q values could be qualified as J_{IC}.

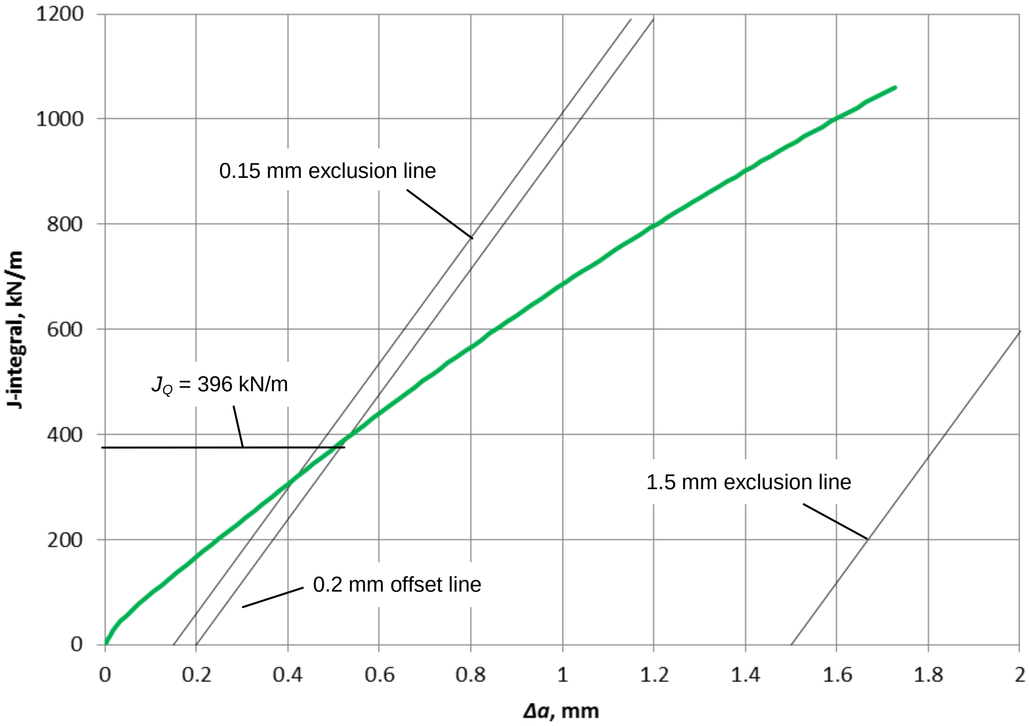

Fig. 4. Simulated J-R curve of as received steel P91

The comparison of experimentally determined and numerically modeled J-integral results for as received and aged steel are presented in Table 2. According to the data simulated J_Q values are smaller than experimentally determined for as received as well as for aged material. However, the drop of J_Q value by units using numerical simulation was determined close to experimental testing. It is necessary to note that J_Q determination procedure is quite complicated and the literature research revieled that J_Q values determined by different research institutions distribute in quite big interval between 290 kN/m [10] and 425 kN/m [11]. This show that my numerically determined J_Q values by using presented methodology are not necesseraly incorect. Further development and comparison with larger number of experiments needs to be done for validation of presented methodology.

Table 2. Numerical simulation and experimental results of J_Q determination

Ageing time at 650 °C, h	**J_Q, kN/m**		**Deviation from experiment,%**
	Experiment	**Simulation**	
–	475	396	17
11000	432	311	28
The drop of value by units	77	85	–

4. CONCLUSIONS

The numerical investigations of the Compact Tension (CT) specimen were carried out for the estimation of J-R curve for the ferritic-martensitic class steel (P91). The finite element method was used for the numerical investigation using the ABAQUS/Standard code. The values of J-integral were determined using finite element analysis simulating the experiment according to instructions described in ASTM E1820 standard. The numerical investigation results have been compared with the experimental test.

The quadratic polynomial expression for crack extension calculation for steel P91 was suggested on experimentally determined curve *EB[COD]/P* versus *a/W*.

Numerically simulated J_Q values are smaller than experimentally determined for as received as well as for aged material. However, simulated J_Q are still in the range of values determined in the literature, i.e. between 290–425 kN/m. Further development and comparison with larger number of experiments needs to be done for validation of presented methodology.

REFERENCES

1. ANDERSEN, T.L. *Fracture Mechanics. Fundamentals and Applications*. Boca Raton, Ann Arbor, Boston: CRC Press Inc, 1991. 793 p. ISBN 0-8493-4277-5.
2. ZARE, A., KOSARI, E. S. M., ASADI, I., BIGHAM, A., BIGHAM, Y. Finite Element Method Analysis of Stress Intensity Factor in Different Edge Crack Positions, and Predicting their Correlation using Neural Network method. *Research Journal of Recent Sciences*, 2014, Vol. 3(2), pp. 69-73.
3. LIKEB, A., GUBELJAK, N., MATVIENKO, Y. Stress Intensity Factor and Limit Load Solutions for New Pipe-Ring Specimen with Axial Cracks. *Procedia Material Science*, 2014, Vol. 3, pp. 1941-1946.
4. JUN-YOUNG, J., YUN-JAE, K., SA-YONG, L., JIN-WEON, K. Extracting ductile fracture toughness from small punch test data using numerical modeling. *International Journal of Pressure Vessels and Piping*, 2016, pp. 1-16.
5. CUMINO, G., DI CUONZO, S., DI GIANFRANCESCO, A., TASSA, O. Advanced high chromium ferritic steels for boiler components operating at high temperature. *Latin American Applied Research*, 2002, Vol. 32(3), pp. 229-235.
6. ASTM E1820-15a. *Standard Test Method for Measurement of Fracture Toughness*. ASTM International, West Conshohocken, PA, 2014. www.astm.org.
7. ABAQUS/Standard User's Manual, Version 6.11.
8. ISO 6892-1:2009, Metallic materials – Tensile testing – Part 1: Method of test at room temperature.

9. SULIVAN, A. M., CROOKER, T. W. A crack-opening-displacement technique for crack length measurement in fatigue crack growth rate testing – development and evaluation. *Engineering Fracture Mechanics*, 1977, Vol. 9, pp. 159-166.
10. SASIKALA, G., RAY, S.K. Evaluation of quasistatic fracture toughness of a modified 9Cr-1Mo (P91) steel. *Materials Science and Engineering A*, 2008, Vol. 479, pp. 105-111.
11. KONOPÍK, P., VIEHRIG, H-W. Fracture toughness characterisation of the martensitic chromium steel P91. COMAT 2012. 2nd International conference on recent trends in structural materials. Czech Republic, 2012 11 21-22.

IMPROVEMENT OF IMAGING ALGORITHMS TO INCREASE THE RELIABILITY OF ULTRASONIC INSPECTION RESULTS FOR NPP EQUIPMENT

D.R. Zhydyk, Ya.P. Cherniak, O.P. Shugailo
State Scientific and Technical Center for Nuclear and Radiation Safety
35-37 V. Stusa Street, 03142 – Ukraine
E-mails: dr_zhydyk@sstc.com.ua, yp_chernyak@sstc.com.ua, ap_shugaylo@sstc.com.ua

ABSTRACT

In order to check the quality of materials and confirm the operational reliability of NPP (Nuclear Power Plant) equipment, various nondestructive inspection methods, particularly ultrasonic inspection (USI), are used. The methods and tools currently used to display the USI results do not ensure adequate representativeness. The main issue is complex data processing. As a result, the displayed results partially lose their representativeness. In this connection, activities are underway to improve imaging methods to increase the reliability of USI results for NPP equipment.

The data imaging and filtering algorithms were analyzed to improve the imaging methods. Software for display of scanned defects was developed based on the Ray Casting algorithm. A group of tools was created to study the structure of defects and evaluate their sizes to allow generation of 3D images of USI scans along with systems for automatic scan of the inspection area.

To confirm the reliability of the imaging algorithm, the software code was preliminary verified, in particular, by display of all defects for an open test sample.

The preliminary verification indicates that this imaging algorithm is an effective method for analyzing the structure and defects of materials. The correlation coefficient shows linear dependence and correlation between the measured and made defect sizes.

Keywords: USI of NPP equipment, 3D visualization

1. INTRODUCTION

Various nondestructive inspection methods, particularly ultrasonic inspection (USI), are used to check the quality of materials and confirm the operational reliability of NPP equipment. The methods and tools currently used to display the USI results do not ensure adequate representativeness. The main issue is complex data processing that requires searching of ways to improve imaging methods to increase reliability and representativeness of USI results for NPP equipment. The objective of work is creation of new methodology for visualization of USI results in order to improve quality and representativity of test's results.

The data imaging and filtering algorithms were analyzed to improve the imaging methods. Software for display of scanned defects was developed based on the Ray Casting algorithm. A group of tools was created to study the structure of defects and evaluate their sizes to allow generation of 3D images of USI scans along with systems for automatic scan of the inspection area. Imaging examples used today are presented below.

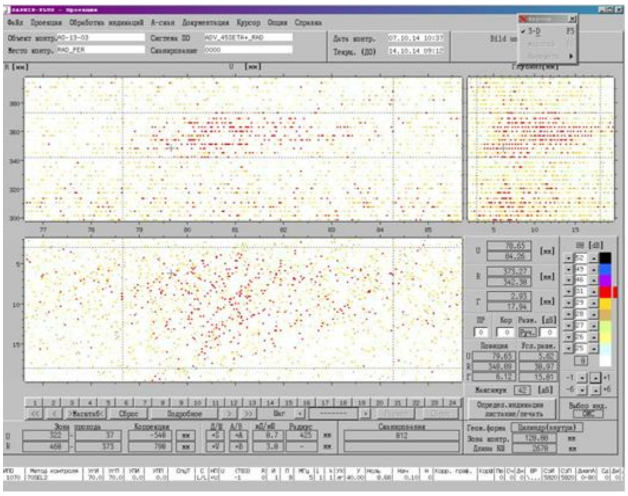

Fig. 1. Example for imaging of scanned defect. GSK converter. Ultrasonic wave entry angle 45°

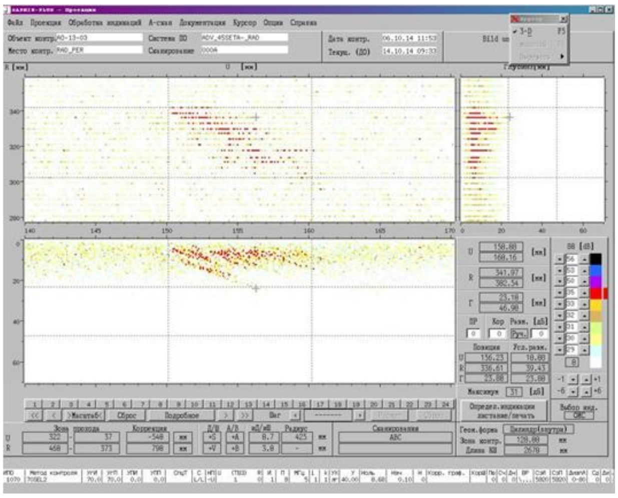

Fig. 2. Example for imaging of scanned defect. GSK converter. Ultrasonic wave entry angle 45°

2. RAY CASTING ALGORITHM

To generate three-dimensional images of USI scans, the Ray Casting algorithm was applied based on modeling interaction of rays with a virtual surface. It is used to image three-dimensional objects in two-dimensional space, considering interaction of rays from the observer to the light source. The ray can reflect, refract or pass thorugh voxel (element of space that indicates the value in cells of regular space lattice, tops of which are points with measurements performed). The algorithm does not consider the new path of a reflected ray. Depending on the type of interaction and intensity of interactions regarding this ray, the screen is filled with a certain color.

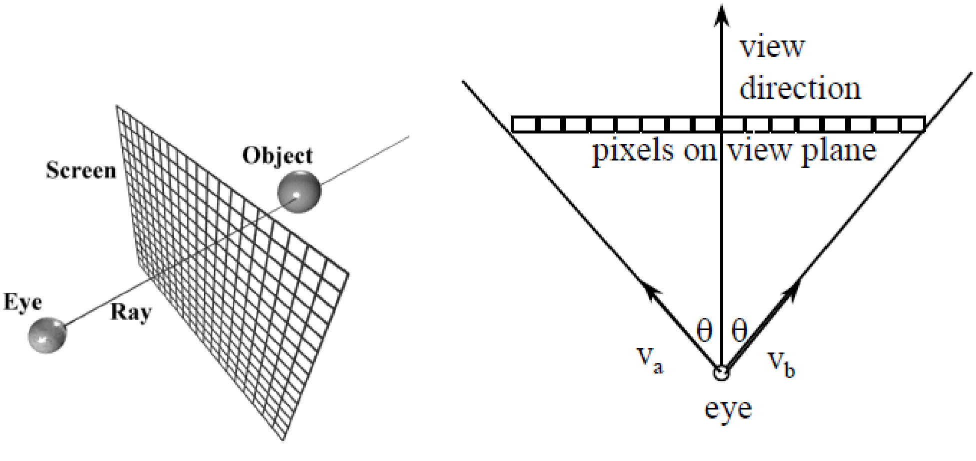

Fig. 2. Ray generation

Procedure for measuring the size of defects lies in determining the distance between points of the defect. Calibration shall be performed to perform each specific measurement. Calibration is based on determining voxel size in pixels. Voxel size depends on breakdown of lattice, in the nodes of which measurements are performed. After calibration measurement of voxel, one get interaction factor for size in mm and pixels. According to interaction factor, one receives defect sizes in milimeters.

Below are results of comparing proposed imaging method with existing imaging methods of USI visalisation (Transmmiter – GSK, ultrasonic waves entering angle 45°, control method – echo-pulse, frequency range: 0.3–10 MHz). Currently for visualisation of USI results the Raster Algorithm is used.

The figures below presents generated image recevied during verification of software code.

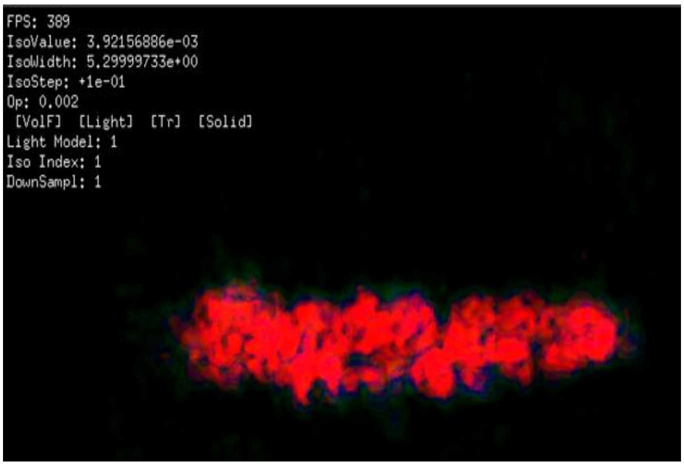

```
FPS: 389
IsoValue: 3.92156886e-03
IsoWidth: 5.29999733e+00
IsoStep: +1e-01
Op: 0.002
 [VolF]  [Light]  [Tr]  [Solid]
Light Model: 1
Iso Index: 1
DownSampl: 1
```

Fig. 3.1. Defect D5 of test sample No. A0-13/01 RayCasting Algorithm

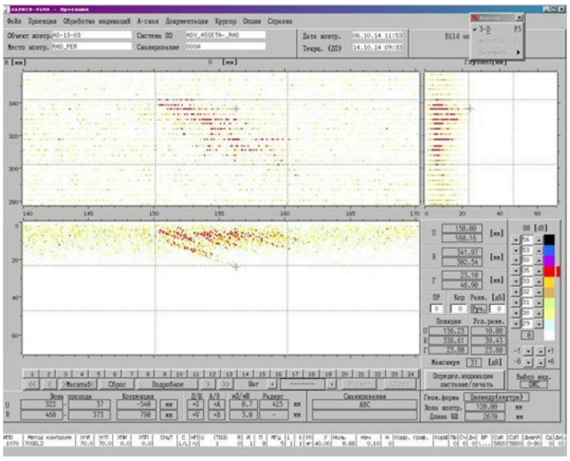

Fig. 3.2. Defect D5 of test sample No. A0-13/01 Raster represent Algorithm

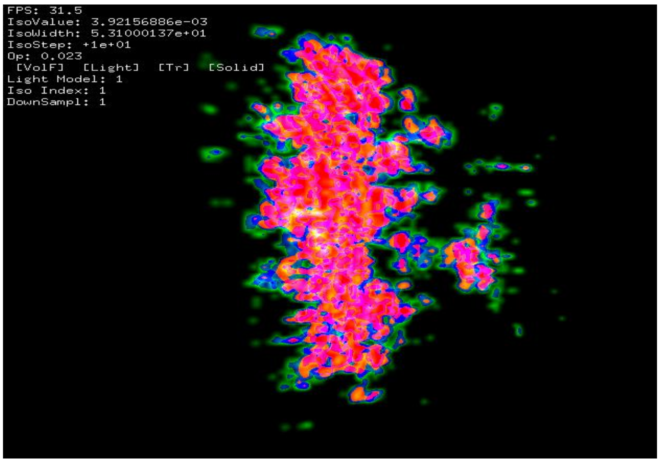

```
FPS: 31.5
IsoValue: 3.92156886e-03
IsoWidth: 5.31000137e+01
IsoStep: +1e+01
Op: 0.023
 [VolF]  [Light]  [Tr]  [Solid]
Light Model: 1
Iso Index: 1
DownSampl: 1
```

Fig. 3.3. Defect D6 of test sample No. A0-13/01 RayCasting Algorithm

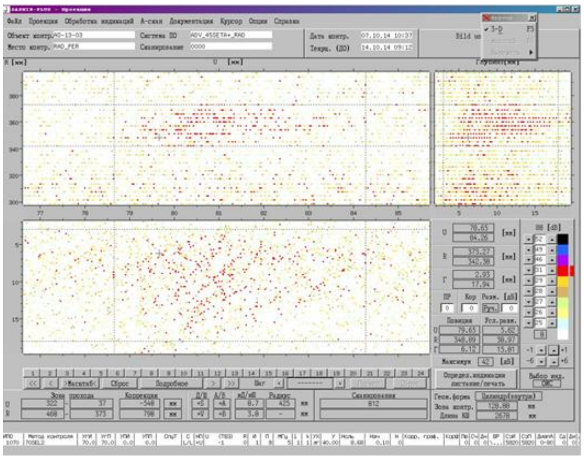

Fig. 3.4. Defect D6 of test sample No. A0-13/01 Raster represent Algorithm

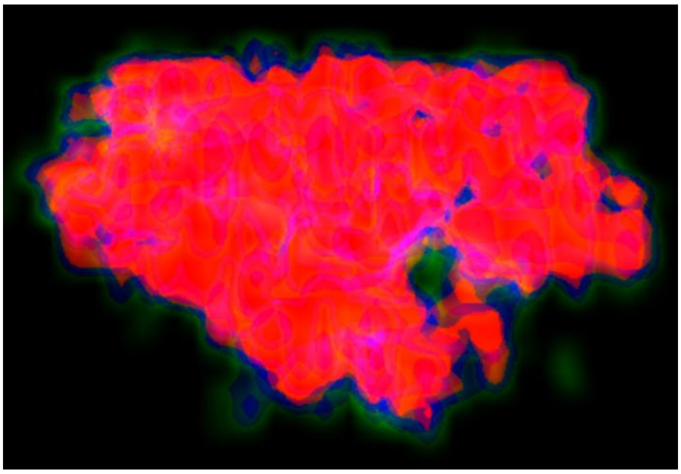

Fig. 3.5. Defect D1 of test sample No. A0-13/01 RayCasting Algorithm

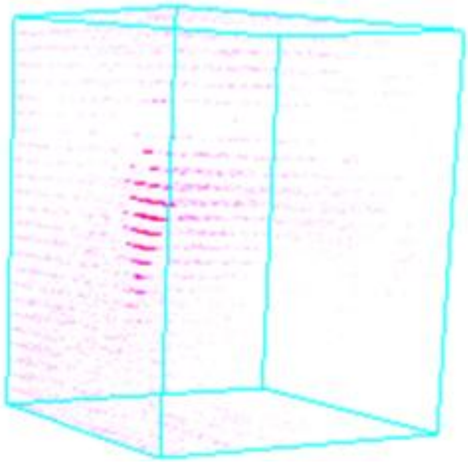

Fig. 3.6. Defect D1 of test sample No. A0-13/01 PyRasterCube Algorithm

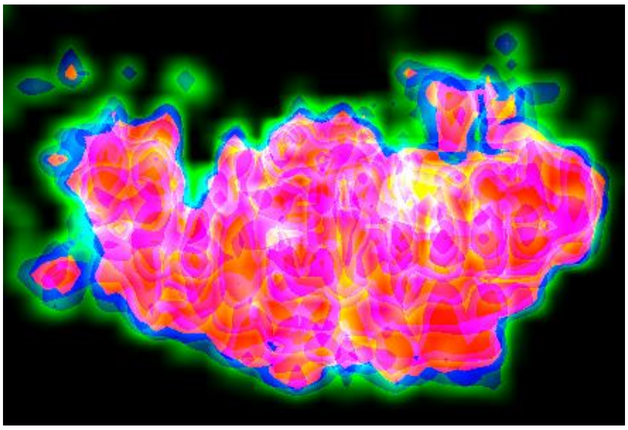

Fig. 3.7. Defect D4 of test sample No. A0-13/01 RayCasting Algorithm

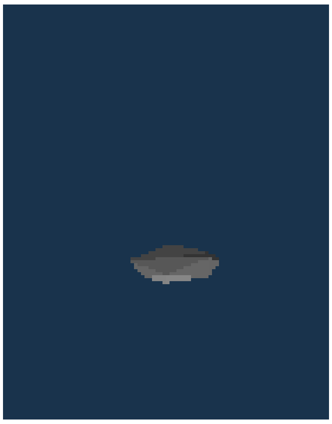

Fig. 3.8. Defect D4 of test sample No. A0-13/01 MarshingCubes Algorithm

Advantages of the method

- Fast response speed 200 FPS when performing manipulations
- Low sensitivity to noise
- Small amounits of memory required for processing
- Large number of freeness degree for research

Disadvantages of the method:

- Ignoring of repeately scattered rays
- Low quality of display of surfaces with high transparency.

3. VERIFICATION

To confirm the accuracy of received imaging, it is necessary to verify the method. Ray Casting was selected as the most adequate imaging algorithm. Using data obtained by non-destructive testing of an open test sample No. A0-13/01 applying ultrasonic method, the methods were verified by comparing the calculated parameters with passport data of a test sample.

Open test sample No. A0-13/01 is an imitation of a fragment of reactor pressure vessel cylindrical part with welding made of steel similar to acoustic properties of material of VVER-1000 RPV base metal. On the surfase of test sample No. A0-13/01, there is a two-layer anticorrosive cladding of 11 ±2 mm thick. Articficial discontinuities simulating crack-like defects were factored into the test sample.

The verification was divided into two key stages. The first stage included visual comparison of obtained imaging and form and orientation of produced defects. The second stage included comparison of parameters of measured and produced defects and determination of the correlation coefficient. Fig. 4 presents schematic view of an open test sample.

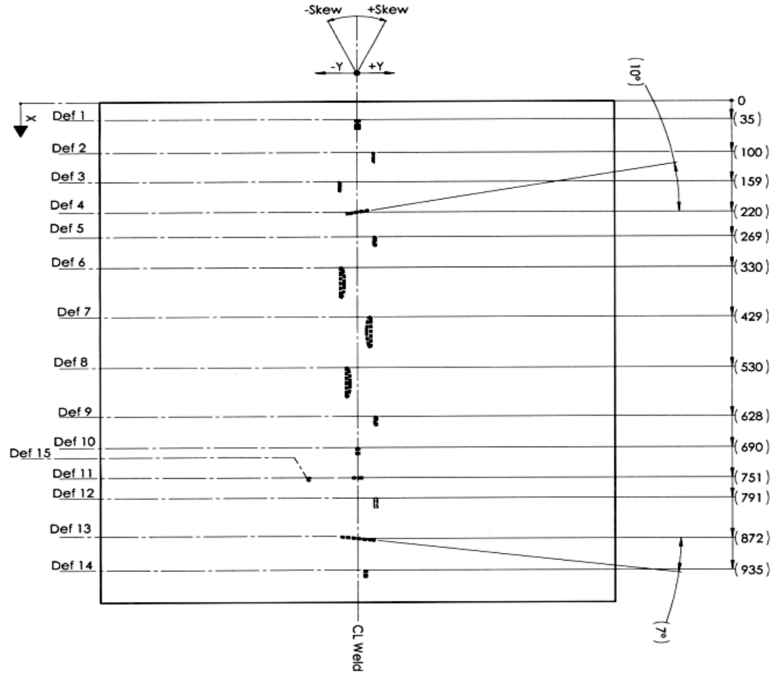

Fig. 4. Open test sample № A0-13/01

3.1. Visual comparison (Stage 1)

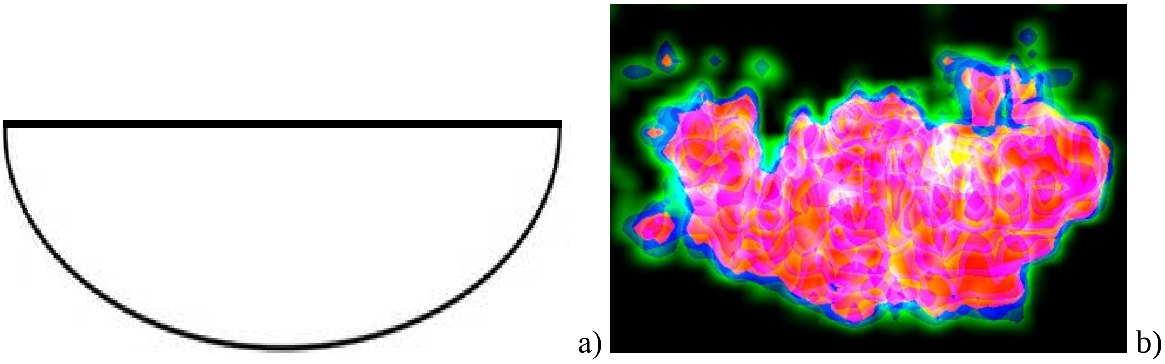

Fig. 5. a) Schematic view of D4 defect: minor semi-axis – 8 mm, major semi-axis – 20 mm (Passport data); b) Imaging of D4 defect

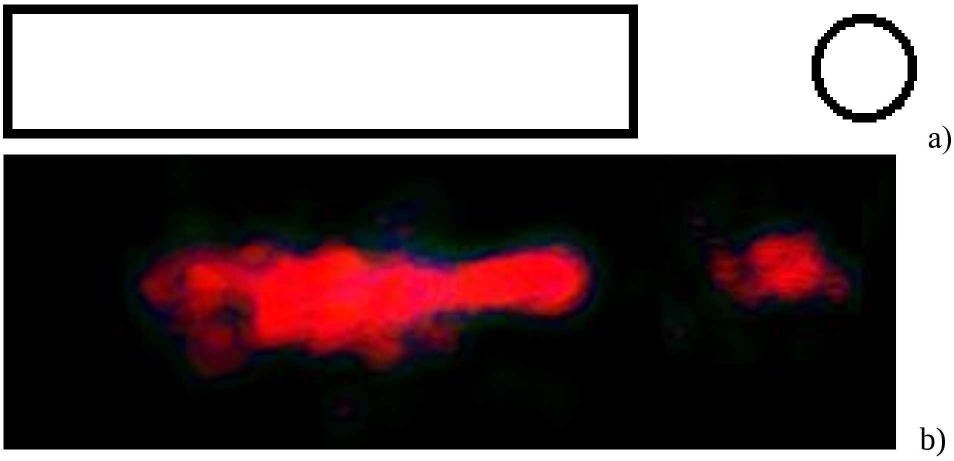

Fig. 6. a) Schematic view of D10 defect: length of rectangle – 15 mm (Passport data); b) Imaging of D10 defect

3.2. Correlation of defined and real parameters of defects (Stage 2)

Stage 2 is divided into two key phases. The first is to compare measured and produced parameters of defect, and then calculation of their correlation.
The equation for the correlation coefficient is as follows:

$$r_{XY} = \frac{COV_{XY}}{\sigma_X \sigma_Y} = \frac{\sum(X-\bar{X})(Y-\bar{Y})}{\sqrt{\sum(X-\bar{X})^2 \sum(Y-\bar{Y})^2}} \qquad (1)$$

where X and Y are values of a specific measurement, and $\bar{X}$ and $\bar{Y}$ are calculated by formulas 2 and 3 correspondently:

$$\bar{X} = \frac{1}{n}\sum_{t=1}^{n} X_t \qquad (2)$$

$$\bar{Y} = \frac{1}{n}\sum_{t=1}^{n} Y_t \qquad (3)$$

where n is a number of measurements and X_t is a value of a particular measurement.

Correlation coefficient varies from -1 to +1, if:

$r_{xy} = 1$ – numerical values of X sampling are linearly dependent and completely correlate with Y sampling values.

$r_{xy} = 0$ – there is no correlation between X and Y sampling values.

$r_{xy} = -1$ – numerical values of X are linearly dependent and anticorrelated with Y sampling values.

Table 1. Correlation of measures and produced parameters

	Length	**Height**
Average	1.9	1.4
Maximum	6.2	3
Minimum	0.3	0
Standard deviation	3.052	1.432
Correlation	0.993	0.989

4. RESULTS

The new methodology for visualization of USI results is presented in the paper. Verification results showed that this imaging algorithm can be considered as efficient method for studying the structure of materials and defects. The correlation coefficient indicates the linear dependence and correlation of measured and produced sizes of defects.

It is planned to continue studies in the following areas:

- Improvement of filtering methods;
- Transition to cloud calculation;
- Improvement of graphical interface, etc.

REFERENCES

1. *F´abio F. Bernardon, Christian A. Pagot, Jo˜ao L. D. Comba Cl´audio T. Silva*, “GPU-based Tiled Ray Casting using Depth Peeling”.
2. *Eric Heitz* (2010), “Adaptive GPU Ray Casting Based on Spectral Analysis, Stefan Suwelack. Medical Imaging and Augmented Reality 5th International Workshop”, MIAR 2010.
3. *M. Durst* (1988), “Letters: Additional Reference to Marching Cubes”, Computer Graphics, vol. 22, no. 2, pp.72-73.
4. *Herasimov, V.G., Ostanin, Yu.Ya., Pokrovskii, A.D.* (2008), “Non-Destructive Testing of Quality Applying Ultrasonic Methods”, Moscow, Energy, 215 p.

CYSENI 2017, May 25-26, Kaunas, Lithuania
ISSN 1822-7554, www.cyseni.com

TECHNOLOGY FOR PRODUCTION OF PHOSPHORUS CONTAINING FERTILIZERS FROM CENTRAL KYZYLKUM PHOSPHORITE

A. J. Allamuratova, A. U. Erkaev
Tashkent chemical technological institute
32, Navoi Street, 100011 – Uzbekistan
E-mail: ahmed_ram@mail.ru

A. M. Reymov
Institute of General and Inorganic Chemistry of the Academy of Sciences of Uzbekistan
77a, Mirzo-Ulugbek Street, 100170 – Uzbekistan
E-mail: ahmed_ram@mail.ru

ABSTRACT

We have studied process of the high calcareous containing phosphorites from Central Kyzylkum (17% P_2O_5) treatment by circulating solution of ammonium and calcium nitrates to obtain phosphorite concentrate. At that yield of P_2O_5 into the phosphorite concentrate is 55–65%, the calcium module is reduced by 0.18–0.56 from the overall initial one.

Obtained concentrate depending on the experience condition contents 18.27–19.60% of P_2O_5 and 44.66–48.42% of CaO. Alongside with washed and calcined concentrate in technological cycle liquid suspended fertilizers with content 2–4% P_2O_5 and 12–14% N are obtained simultaneously. Subsequent the process of decomposition of phosphorite concentrate with nitric acid and ammonization of nitrogen acid slurry has been investigated. In a result of experimental studies nitrogen-phosphorus-calcium fertilizers have been prepared with the following composition: 17.3–21.34% N, 12.7–16.36 P_2O_5 and 25.1–27.86% CaO. At the second stages the technology concentrated phosphorus containing fertilizers with composition: 0.91–2.7% N, 27.13–30.61 P_2O_5 and 37.34–39.34% CaO. In both variants fertilizers are obtained with advanced content of acceptable forms of phosphorus and calcium.

The phase composition of the obtained fertilizers was determined by radiographic and infrared spectrometry analysis. It was defined that nitrogen-phosphorus fertilizers consist of dicalcium phosphate, indecomposable fluorine-and hydroxyapatites, ammonium and calcium nitrates, and phosphorus containing fertilizers consist of various forms of calcium phosphates, indecomposable fluorine-and hydroxyapatites, as well as small quantity of ammonium and calcium nitrate salts.

Thus we have presented the possibility of treatment of low-grade phosphorites from Central Kyzylkum into concentrated phosphates and complex fertilizers. The manufacturing scheme has been proposed and the material balance of the fertilizers production has been calculated.

Keywords: phosphorite, concentrate, nitric acid, nitrogen-phosphorus-calcium fertilizers.

1. INTRODUCTION

Central Kyzylkum phosphorite has not analogs on quality in Commonwealth of Independent States and is in the top ten of deposits in the world. Resources of the phosphorites raw material (PRM) are estimated in quantity 43.5 mil ton of 100% of P_2O_5 that provides needs of Uzbekistan agriculture in phosphorus fertilizers more than by 100 years. It is necessary noted that Kyzylkum phosphorites on content of main component are applied to low-grade ore. Considerable quantity of carbonate compounds (calcium module is $CaO:P_2O_5 = 2.85$), clay minerals, organic matters and chlorine are contented in them [1, 2]. That’s why at Kyzylkum phosphorite combine stages of raw thermic benefication and washing up it out of chlorine have been realize. In results in concentrated phosphorite obtained P_2O_5 reaches up to 26%, but due to complicacy of benefication technology and large heat-and-power engineering expenditure, cost of washed and calcined concentrate and phosphorus fertilizers are rised significantly. Moreover, productivity of combine limited, i.e. it does not increase 760 thousand ton (197.6 thousand тon 100% of P_2O_5) per year. Annual need of agriculture of Republic of Uzbekistan in phosphorus fertilizers makes 525.21 thousand ton 100% of P_2O_5.

Issue of inexpensive phosphorus containing fertilizers based on local raw material can be solved by implication into sphere processing of low-grade phosphorites by nitric acid. In a case chemical energy of nitric acid is used to disclose phosphate raw material as well as NO_3^- anions in form of nutrient is left in finished product. In addition the approach is less difficult for quantity of raw material than sulfuric processing, owing to low solubility impurities R_2O_3 in the resulting extract [3].

In this connection, we had been investigated the processing of high calcareous phosphate rock from Central Kyzylkum phosphorite (17% P_2O_5) by recirculating solutions of ammonium nitrate and calcium to obtain the phosphorite concentrate. By nitric acid decomposition of the phosphorite concentrate liquid nitrogen-calcium and concentrated phosphorus fertilizer obtained with prolonged action. The aim presented study is to explore chemical composition phosphorus containing products prepared by nitric acid treatment of the Central Kyzylkum phosphorite.

2. METHODOLOGY

In the experiments, the following salts used are phosphate powder from Central Kyzylkum, calcium nitrate and ammonium nitrate, nitric acid and ammonia gas. The chemical and dispersed composition of the initial raw material is shown in Table 1 and 2 below.

Table 1. The chemical composition of the ordinary powder from Central Kyzylkum phosphorite

Components content, weight. %							**CaO: P_2O_5**	**P_2O_{5accep}: P_2O_{5total}**
P_2O_5	**CAO**	**Al_2O_3**	**Fe_2O_3**	**MgO**	**F**	**CO_2**		
17.10	46.30	1.33	1.09	1.78	1.87	15.90	2.71	18.49

Table 2. Dispersed composition of phosphorite powder

Size grade, mm	**Fraction outlet, %**
-2+0.5	–
-0.5+0.315	1.9
-0.315+0.16	8.6
-0.16+0.1	20.3
-0.1+0.063	37.7
-0.063+0.05	16.2
-0.05	15.3
Starting mass	100

Processing unenriched phosphate rock by circulating solution (CS) of ammonium and calcium nitrate was conducted in a temperature-controlled cylindrical reactor with volume of 200 ml equipped by a paddle stirrer for 60 minutes at 30 °C. After completion of the processing of the resulting suspension settled for 4–6 minutes, then the slurry was separated from the upper part of the thickened mass. Condensed mass was filtered and the precipitate is dried at a temperature of 100 °C. The phosphorite concentrate dried and the resulting suspension with the main components was analyzed by known methods [4]. The results are summarized in Table 3 and 4.

When preparation the phosphate fertilizers, the phosphorite concentrate (18.27–19.60% of P_2O_5 and 44.66–48.42% of CaO) was decomposed by nitric acid (HNO_3) at a rate of 100% from the stoichiometry on calcium oxide. The process temperature is maintained at a level of 40 °C for 30 minutes. The resulting dense nitric acid pulp was repulped by recycle solution of ammonium and calcium nitrate (RSACN) previously prepared at L:S = 1:3. Further the slurry was ammoniated with ammonia gas to various pH values (4.4, 5.1, 6.2 and 7.0). The solid phase was separated from the liquid subsequently washing with water circulating at a ratio L: S = 1: 2, the wet cake was dried at a temperature 95–100 °C for 4 hours and analyzed according to known methods.

3. RESULTS AND DISCUSSIONS

From the data obtained (Table 3) that the interaction of the phosphate powder with solutions of nitrate salts depending on the N_{amm}: N_{nit} (ratio of ammonia nitrogen (N_{amm}) to nitrate nitrogen ($N_{nit.}$)) is activated (transfer of unassimilable P_2O_5 forms in plants as an acceptable (P_2O_{5accep}.) form) raw material phosphate [5–7]. The ratio of P_2O_{5accep}. : P_2O_{5total}. on Trilon B and by 2% of citric acid in the dried samples of the solid phase is 44.97–48.32 and 36.45–41.56%, respectively, which exceeds several times higher than the ratio P_2O_{5accep}. : P_2O_{5total} in the initial phosphorite powder – 18.49% and 12.7% relatively.

Table 3. Effect of initial ratio of CS:PRM and N_{amm}:N_{nit} on composition of dried phosphorite concentrate

Starting ratio of CS:PRM	**N_{amm}: N_{nit}**	**Chemical composition of the dried product, %**							**$\frac{CaO}{P_2O_5}$**
		P_2O_{5total}	**P_2O_{5accep} on 2% of citric acid**	**P_2O_{5accep} by 0.2 M Trilon B**	**CaO_{total}**	**CaO_{accep}**	**CaO_{water}**	**N**	
3:1	0.8	19.37	9.36	8.05	48.42	31.81	3.06	0.64	2.50
	0.5	18.56	8.94	7.50	46.77	31.08	3.64	0.69	2.52
	0.2	18.27	8.77	7.33	46.58	31.10	4.47	0.80	2.55
4.5:1	0.8	19.41	9.17	7.77	47.36	29.55	2.78	0.53	2.44
	0.5	18.67	8.72	7.18	46.11	29.01	3.36	0.65	2.47
	0.2	18.27	8.49	6.96	45.67	28.98	4.04	0.76	2.50
6:1	0.8	19.60	9.05	7.39	46.65	28.37	2.56	0.41	2.38
	0.5	18.84	8.5	6.95	45.21	27.6	3.16	0.62	2.40
	0.2	18.30	8.23	6.67	44.66	27.36	3.76	0.71	2.44

At low values of CS:PRM = 3:1 in the same conditions $P_2O_{5accep.}$ and $CaO_{accep.}$ are 2–3% higher than the CS:PRM = 6:1. This is due to the fact that with increasing ratio of CS:PRM amount of transfers of acceptable CaO and P_2O_5 in the liquid phase increased. With increasing ratio of N_{amm}:N_{nit} in the circulating solutions total concentration of P_2O_5 is increased to 18.27–19.6%, and the calcium module is reduced to 2.38 (that is 2.71 from starting).

Chemical analysis shows the composition of the liquid phase (Table 4.) that with increasing initial ratio CS: PRM (3:1 to 6:1) in suspension the nitrogen content varied in a range of 14.7–14.74% and 8.96–9.31%, respectively at N_{amm}:N_{nit} equal to 0.8 and 0.2, and P_2O_{5total} content decreased from 2.26 to 0.95% and from 2.14 to 0.72%, respectively. With carrying out this process, one part of the liquid phase returns to the initial step of treating the phosphate raw material and the rest of one is used as a liquid fertilizer containing suspended nutrients (N + P_2O_5 + CaO) – 22.1–29.77%.

Table 4. Effect initial ratio of CS:PRM and N_{amm}:N_{nit} on the composition separated liquid phase

Starting ratio of CS:PRM	**N_{amm}:N_{nit}**	**P_2O_{5total}, %**	**CaO_{total}, %**	**N, %**
3:1	0.8	2.26	9.20	14.72
	0.5	2.16	13.85	11.76
	0.2	2.14	18.67	8.96
4,5:1	0.8	1.52	7.85	14.72
	0.5	1.50	12.10	11.80
	0.2	1.43	16.51	9.22
6:1	0.8	0.95	6.41	14.74
	0.5	0.80	10.53	11.95
	0.2	0.72	14.30	9.31

Thus, based on the experiments showed the possibility of complex processing of low-grade phosphate from Central Kyzylkum allowing in the same production cycle produce phosphorite concentrate and liquid suspended fertilizer containing nutrients (N + P_2O_5 + CaO) – 22.1–29.77%.

Then we studied the process of nitric acid's extract ammoniation obtained by decomposition of the pretreated phosphate rock by circulating solutions of calcium and ammonium nitrate, and carried out technological research of the process of obtaining phosphorus-containing and liquid suspended fertilizer from products of nitric acid's extract ammonization of phosphate based on Central Kyzylkum (Table 5).

Table 5. Composition phosphorus containing fertilizers obtaining on the laboratory facility

№	pH pulp	Components content, weight, %						$P_2O_{5accep.}$: P_2O_{5total} on 2% of citric acid, %	P_2O_{5accep}: P_2O_{5total} by 0.2 M Trilon B, %	CaO_{accep}: CaO_{5total} on 2% of citric acid, %
		P_2O_{5total}	P_2O_{5accep} by 0.2M Trilon B, %	$P_2O_{5accep.}$on 2% of citric acid, %	CaO_{total}	$CaO_{accep.}$	N_{total}			
1	4.4	28.55	22.36	23.65	38.54	33.04	1.44	78.34	82.83	85.73
2	5.1	28.01	22.07	23.28	39.5	33.97	2.01	78.79	83.11	86.00
3	6.2	27.11	21.56	22.71	38.78	33.44	2.20	79.53	83.77	86.23
4	7.0	27.85	22.60	23.42	40.38	34.85	2.56	81.15	84.09	86.30

It should be noted that the implementation of the process of obtaining phosphorus-containing fertilizers, the liquid phase is formed, which is composed mainly of calcium and ammonium nitrate. They may be recommended to use as a liquid nitrogen-calcium fertilizer that can be applied successfully during the foliar treatment of cotton and grain crops.

The results of laboratory experiments have allowed to develop the basic technological processing scheme on treatment of phosphate from Central Kyzylkum to phosphorus and suspended liquid fertilizer (Fig. 1). According to the flow sheet high calcareous phosphate powder from the hopper (1) through the feeder (2) enters the repulpator (3) where processed by circulating solution of calcium and ammonium nitrate further thickened part of the slurry is separated in the settlers (4) and (5) and sent to the decomposition reactor (8). Here it is fed simultaneously the nitric acid through

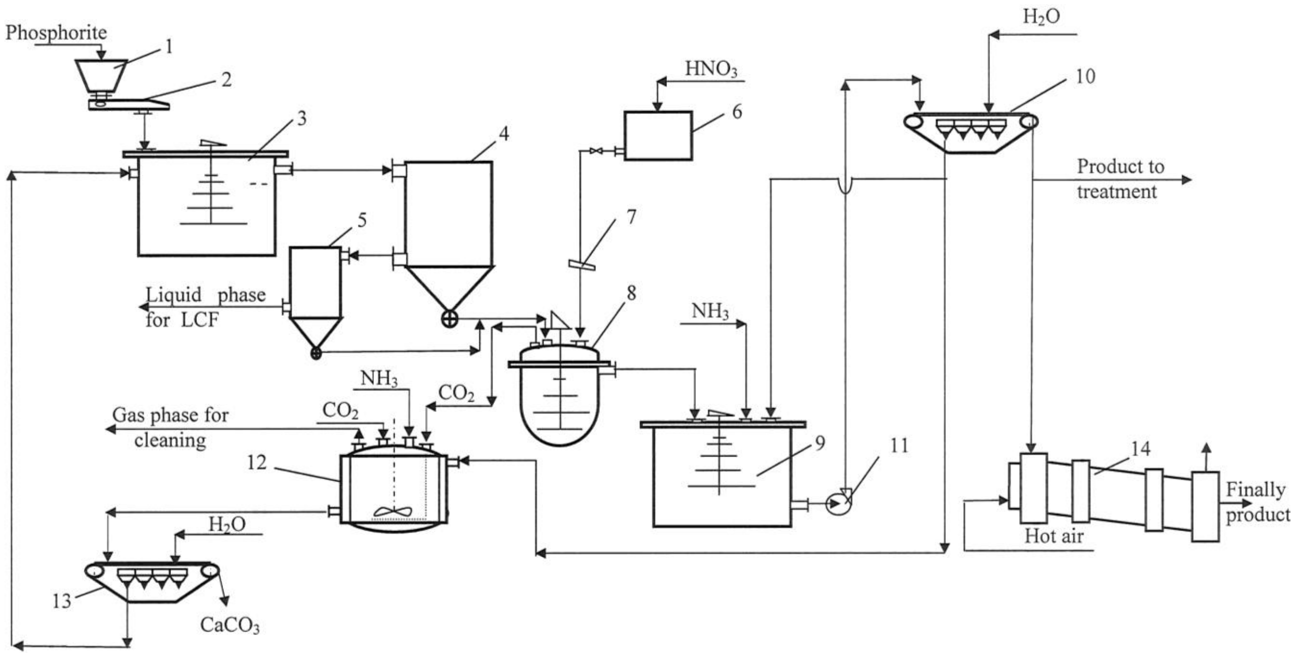

Fig. 1. Flow sheet for the processing of high calcareous phosphorite from Central Kyzylkum.
1 – phosphate feed hopper; 2 – dispenser; 3 – repulpator; 4 – settler stage 1; 5 – settler stage 2; 6 – pressure tank of nitric acid; 7 – slit feeder; 8 – reactor; 9 – repulpator- ammonizator; 10, 13 – band vacuum filter; 11 – pump; 12 – converter; 14 – drum-dryer

a slit batcher (7) of the pressure tank (6). The clarified part of the solution is used as a liquid complex fertilizer (LCF).

Nitrogen-calcium-phosphate slurry formed in the reactor, is fed in repulpator - ammonizator (9) and mixed with circulating ammonium and calcium nitrate solution further ammoniated by gaseous ammonia to a pH of 4.5–5.0. The resulting slurry by pump (11) is pumped to a vacuum belt filter (10) for separating the ammonium and calcium nitrate solution from the solid phase. After washing the filter cake solid phase is sent to the dryer drum (14) for single phosphorous and other types of fertilizers. One part of the filtrate is circulated in the repulping and ammoniation stage of nitric acid slurry as working solution and the second portion is directed to the converter (12) for the conversion of calcium nitrate with carbon dioxide in the presence of ammonia. Suspension from the converter is supplied to the vacuum belt filter (13) for separating the calcium carbonate generated from the liquid phase, latter is used as a circulating solution for pretreatment high calcareous phosphorite or after evaporation can be used for complex fertilizers generation.

Fig. 2 provides a block diagram and the material balance of nitric acid processing 1000 kg high calcareous phosphorite from Central Kyzylkum, which is calculated based on the laboratory researches.

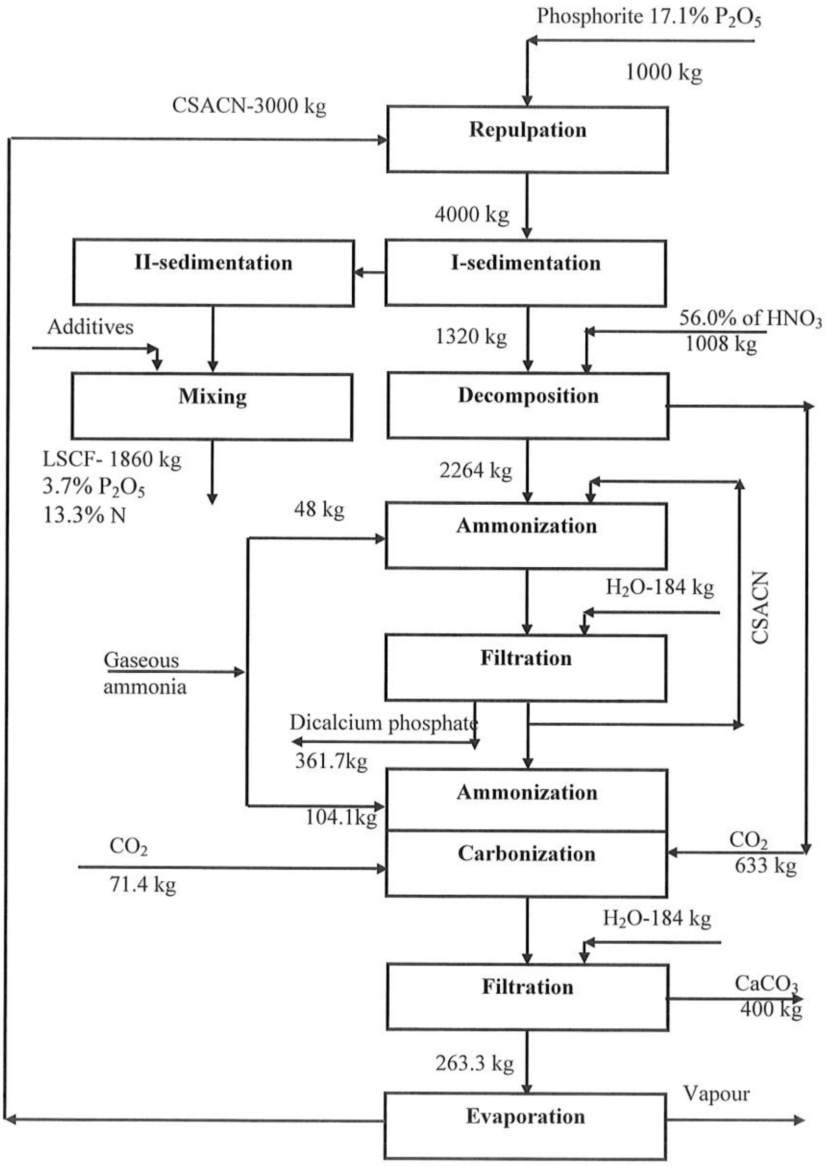

Fig. 2. Block diagram of nitric acid and the material balance of processing 1000 kg of high calcareous phosphorite from Central Kyzylkum

4. CONCLUSION

To sum up, based on the conducted experiments studied the process of processing low-grade phosphate rock from the Central Kyzylkum on liquid nitrogen- calcium and solid concentrated phosphorus fertilizer. The technological scheme and material balance of production had been calculated.

REFERENCES

1. BEGLOV B.M., NAMAZOV Sh.S. *Phosphorites from Central Kyzylkum and their processing*. Tashkent: Fan, 2013, 460 p. 660-0-63185.
2. CEZART NORBERT V. Industrial chloride removal of phosphorite ore at wet enrichment in extreme condition of Kyzylkum desert. *Mining bulletin of Uzbekistan*. 2008, No 4, p. 54-58.
3. NABIEV M.N. *Nitric acid processing phosphates*. Tashkent: Fan, 1976, 366 p. 40306-43827-76.
4. VINNIK M.M., ERBANOVA L.N., ZAITSEV P.M. *Methods of analysis of phosphate rock, phosphate and compound fertilizers, feed phosphates*. Moscow: Chemistry, 1975, 218 p. 5-02-029255-9.
5. ALLAMURATOVA A.J., ERKAEV A.U., TOIROV Z.K. Phosphate concentrate of ordinary phosphorite flour from the Central Kyzylkum. *Chemistry and Chemical technology*, 2009, No. 4, p. 16-20.
6. ALLAMURATOVA A.J., ERKAEV A.U. Enrichment high calcareous phosphate from the Central Kyzylkum with solutions of nitrate salts. *Bulletin of Academy of Sciences of Uzbekistan*, 2010, No. 5, p. 57-60.
7. ALLAMURATOVA A.J., ERKAEV A.U., TOIROV Z.K., REYMOV A.M. Technological studies produce phosphate fertilizers of nitric acid extract of phosphate from the Central Kyzylkum. *Chemical Industry*, 2011. Vol. 88, No. 3, p. 109-114.

PECULIARITIES OF F^- IONS LEACHING FROM WASTE SILICA GEL IN STATIC AND DYNAMIC CONDITIONS

V. Rudelis, T. Dambrauskas, K. Baltakys
Kaunas University of Technology
Radvilenu st. 19, Kaunas LT-50254 – Lithuania
E-mail: valdas.rudelis@ktu.edu; v.rudelis@lifosa.com

ABSTRACT

In this work the elution of F^- ions from waste silica gel to the liquid medium was performed under static and dynamic conditions. It was determined that dried (50 °C, 48 h) waste silica gel from aluminum fluoride production mainly consists of silicon dioxide (79.01%) and other compounds containing 10.02–5.67% F^- and 2.14–2.48% Al^{3+} ions. It was found that under static elution conditions (water-to-solid ratio was 100) it is possible to decrease the amount of F^- ions in waste silica gel till 5 wt.% . In addition, under this conditions $AlF_3 \cdot 3H_2O$ remained stable. Meanwhile, the elution conditions affects the stability of $AlF_3 \cdot 3H_2O$ and removable of F^- ions. It was determined that under dynamic conditions not all fluorine ions transferred to the liquid phase due to the adsorption properties of silica gel. The data of hydrothermal synthesis showed, that waste silica gel can be used for the production of calcium silicates hydrates. It was estimated that in CaO–waste silica gel–H_2O mixture when the molar ratio of CaO/SiO_2 = 2.5 after 16 h of isothermal curing at 200 °C dibasic calcium fluoride silicate hydrate – cuspidine ($Ca_4(Si_2O_7)(F,OH)_2$), which contain F^- ions and hydrogarnet ($Ca_3Al_2O_6(H_2O)_6$) were formed. The previous results were confirmed by instrumental and chemical analysis.

Keywords: waste silica gel, fluoride ions, leaching, hydrothermal synthesis

1. INTRODUCTION

Solid wastes are the useless solid materials generated from combined residential, industrial and commercial activities in a given area [1, 2]. It can be categorized according to its origin (domestic, industrial, commercial, construction or institutional); according to its contents (organic material, glass, metal, plastic paper etc.); or according to hazard potential (toxic, non-toxin, flammable, radioactive, infectious etc.) [3, 4]. For a long time it has been disposed of without really paying attention to the harmful effect of chemical substances on environment and human. Nowadays waste management is regulated by national and international laws, it is efforts are made to reduce impact on environment [5–7]. However, more secure means of storage do not reduce the amount of emissions.

Solving waste disposal problem, it is possible to choose from three different waste treatment directions: waste recycling, incineration of waste in specialized companies, waste storage in specially equipped and controlled landfills [8].

Landfill is one of the simplest and the most popular solution for waste utilization problem. However, landfills occupy relatively large areas, they are concentrated sources of air, ground water and primer pollution [5–8]. According to the waste management hierarchy, landfilling is the least preferable option and should be limited to the necessary minimum.

In order to reduce this problem, it is necessary to change the approach and consider waste as potential raw material for the techno genic production. The priority direction is considered to be secondary waste utilization. For this reason waste is sorted, recycled and this helps to reduce environmental pollution and save material resources. So far secondary utilization of waste and techno genic raw materials is limited and it can be associated with very unstable chemical and mineral composition of industrial waste [6, 7].

Aluminium fluoride is used in many industrial processes: in the preparation of white enamels, as an anti-reflection coating in complex optical systems, as a constituent in welding fluxes, and in the preparation of fluorine containing glasses [9, 10].

Generally production of aluminium fluoride is based on its property to form relatively stable supersaturated solutions [10, 11]. The steadiness of these solutions can be explained by good hydratation of the molecules of aluminium fluoride in water solutions. As the concentration and temperature of these solutions increase, steadiness decreases. When a steady supersaturated aluminium fluoride solution is formed, dispersive silica gel can be separated from it. During the production process of AlF_3, a large amount of silica gel contaminated with F^- ions as a by-product is obtained: 0.4 t of silica gel is generated by producing 1 t of aluminium fluoride. The main process reaction can be described by the following reaction:

$$H_2SiF_6 + 2Al(OH)_3 \rightarrow 2AlF_3 + SiO_2 \cdot nH_2O + H_2O + Q\,.$$

As a result in Lithuania 2016 years, JSC “Lifosa” produced 4.3 thousand tonnes of silica gel waste [10]. The use of waste silica gel is limited due to the harmful and aggressive premises, containing fluorine. At the moment silica gel is not widely used or recycled, but is stored on the landfill.

This is why the issue of its utilization is so relevant. Dispose or neutralisation of harmful premises in the waste silica gel would allow to use this material for the production of binders, building materials or in other industries [12, 13].

The aim of this work was to investigate the possibility of fluoride ions leaching from waste silica gel into liquid medium.

2. MATERIALS AND METHODS

Waste silica gel, i.e., a waste product of AlF_3 production in the chemical plant of “Lifosa” (Kedainiai, Lithuania) (with moisture content 60–65%), $S_a = 964\ m^2/kg$);

Calcium oxide, which has been produced by burning calcium hydroxide (“Stanchem”, Poland, purity 97%) at 550 °C for 60 minutes, with the quantity of free CaO equal to 98.41% ;

The hydrothermal synthesis of calcium silicate hydrates by using waste silica gel was performed in the mixture with molar ratio of C/S (CaO/SiO_2) was equal to 2.5. Homogenized raw materials were mixed with distilled water to obtain water/solid ratio of the suspension equal to 10. The hydrothermal synthesis has been carried out in unstirred suspensions in 25 ml volume PTFE cells, which were placed in a stainless steel autoclave (“Parr instruments”, Germany), under saturated steam pressure at 200 °C temperature for 16 hours by applying extra argon gas (10 bar). Temperature was reached within 2 h. After hydrothermal treatment, the suspensions were filtered off, the products rinsed with acetone to prevent carbonization of materials, dried at 50 °C ±5 temperature for 24 h, and sieved through a sieve with an 80 µm mesh.

Standard method of SiO_2 chemical analysis. 1 g of the sample was mixed with sodium and potassium carbonate mixture (5 or 6 g) and put in a platinum crucible. The crucible was placed into a furnace and melted at 900–1000 °C temperature for 1 h. After fusion, crucible was placed into a 200 cm^3 porcelain plate with distilled water in order to solidify the melt on the crucible wall when it was cooling down. Later, crucible was put into a porcelain plate, a large amount of 10% HCl was added and mixed until CO_2 gas was not released from solution. After that, the crucible was removed from the porcelain plate and this plate was heating on the sand bath until solution was evaporated. Subsequently, the formed residue was powdered with a glass stick, poured a few drops of concentrated HCl acid and the porcelain plate was left to cool down. After 30 min, hot distilled water was added into porcelain plate in order to dissolve of chlorides. Then, the solution with residue of SiO_2 was filtrated through ash-free filter and rinsed with distilled water to eliminate chloride ions (the amount of chloride ions was proofed by adding one drop of clean filtrate and a drop of 1% $AgNO_3$ solution on a glass). The obtained filtrate was used for the second chemical analysis of SiO_2 and finally, both filtrate papers were put in the crucibles and heated at 1000 °C for 1 h. The amount of SiO_2 was calculated by using equation:

$$SiO_2 = \frac{a_1 \cdot 100}{a}, \% \tag{1}$$

where a_1 is the mass of heated residue after experiment, g; a is the initial mass of the sample, g.

Standard method of Al_2O_3 chemical analysis. Al_2O_3 was determined in the obtained filtrate after SiO_2 separation. This solution was poured into 250 cm^3 of volumetric flask, diluted with distilled water to the indicated level and mixed. After that, 50 cm^3 of filtrate was poured into a 300 cm^3 of glass and heated until boiling. Then, 1.5 g of NH_4Cl, 3–4 drops of HNO_3 (ρ = 1400 kg/m^3), also 3–4 drops of methyl orange indicator were added and the amount of 10% ammonium added till the solution in the glass changed into yellow. Subsequently, formed precipitates were filtrated and rinsed with hot solution of 2% NH_4NO_3. The obtained filtrate was used for the second chemical analysis of Al_2O_3 and finally, both filtrate papers were put in the crucibles and heated at 1000 °C for 20 min. The amount of Al_2O_3 was calculated by using equation:

$$Al_2O_3 = \frac{a \cdot 100}{m}, \% \tag{2}$$

where a is the mass of heated residue after experiment, g; m is the initial mass of the sample, g.

The determination of fluoride. 1 g of sample was put into a platinum plate and mixed with 10 g of sodium and potassium hydroxides mixture (5 g of NaOH and 7 g of KOH). After that, platinum plate was put in the sand bath and heated approximately 40 min. During heating the mixture was often mixed with platinum spatula. After fusion, the platinum plate was turned around that the melt would solidify on the internal walls. Then, the 150 cm^3 of distilled water was added and the platinum plate was put into a boiling water bath for melting salts. After that, 15 g of chemically pure $(NH_4)_2CO_3$ powder was added, which melt by mixing with platinum spatula and plate was held in the boiling water bath until solution was evaporated to dry salt. Subsequently, salt was poured with 150 cm^3 of distilled water and melted by mixing in the boiling water bath. Later, hot solution with precipitates was poured into a 250 cm^3 flask, which was resistant for the variations of temperature. The solution in the flask was cooled down and diluted with water to the indicated level. After that, the solution was filtrated and concentrations of fluoride ions in solution were measured by using a Metler Toledo T70 potentiometer. The error of the selective electrode for F_{-} ions is 1 ppm (0.0001%).

Fluoride leaching. F^{-} ions leaching from waste silica gel to the aqueous phase was done under static and dynamic conditions. Leaching in static conditions was done by keeping the suspensions at 25 °C for 24 h when water-to-solid (w/s) ratio was 100. Leaching of F^{-} ions under dynamic conditions by using the continuous distilled water (25 °C) flow, which was applied on waste silica gel till the water-to-solid (w/s) ratio reached the value of 100.

The X-ray diffraction analysis (XRD) of compounds was performed on the D8 Advance diffractometer (Bruker AXS, Karlsruhe, Germany) operating at the tube voltage of 40 kV and tube current of 40 mA. The X-ray beam was filtered with Ni 0.02 mm filter to select the CuKα wavelength. Diffraction patterns were recorded in a Bragg-Brentano geometry using a fast counting detector Bruker LynxEye based on silicon strip technology. The specimens were scanned over the range 3–70 ° (2θ) at a scanning speed of 6 ° min^{-1} using a coupled two theta/theta scan type.

The X-ray Fluorescence spectroscopy (XRF) was performed on a Bruker X-ray S8 Tiger WD spectrometer equipped with a Rh tube with energy of up to 60 keV. Powder samples were measured in Helium atmosphere and data were analysed with Spectra Plus Quant Express standard less software.

3. RESULTS AND DISCUSSION

In the first stage of the investigation, the chemical analysis of aluminium fluoride production waste – waste silica gel (SGW) (raw sample and an additional dried for 48 hours at 50 °C in the dryer sample) samples was performed.

It was obtained that SGW-1 consists of 79.01% silicon dioxide, 10.02% F^-, and 1.08% Al_2O_3 (Table 1). Meanwhile, by changing thechnological parameters of AlF_3 production (SGW-2 sample), it's possible to reduce fluorine quantity till 5.67% F^-. It should be noted that the latter value is almost equal to data obtained in raw SGW sample (5.28% F^-). While almost the same tendency was observed by applying XRF: it was determined that SGW-1 contains 36.2% of silica, which is equivalent to 78.9% of SiO_2 (Table 2). Moreover, 2.48% of Al^{3+} ions and traces of other elements are also present in mentioned compound. It was determined that XRF method is not suitable for fluorine ions measurement in waste silica gel samples.

Table 1. Chemical composition of AlF_3 production waste determined by chemical analysis

Name of sample	First experiment			Second experiment			Average,%		
	Concentration,%			Concentration,%					
	SiO_2	**F^-**	**Al_2O_3**	**SiO_2**	**F^-**	**Al_2O_3**	**SiO_2**	**F^-**	**Al_2O_3**
Raw SGW	–	5.28* (211.13 ppm)	–	–	5.28* (211.00 ppm)	–	–	5.28	–
SGW-1 dried at 48h 50 °C	78.42	10.01* (400.82 ppm)	1.23	79.6	10.03* (401.3 ppm)	0.93	79.01	10.02	1.08
SGW-2 dried at 48h 50 °C	80.6	5.67* (226.79 ppm)	1.17	81.2	5.67* (226.81 ppm)	1.12	80.9	5.67	1.13

Table 2. Chemical composition of AlF_3 production waste determined by XRF analysis

Name of sample	Concentration,%						
	Si	**Al**	**F**	**Cl**	**Ca**	**Fe**	**Total**
SGW-1 dried at 48h 50 °C	36.2	2.48	0.795	0.0799	0.0297	0.0220	39.6
SGW-2 dried at 48h 50 °C	38.6	2.14	0.455	–	0.0876	0.0242	41.4

XRD analysis data showed that the main compound containing fluoride ions in waste silica gel is $AlF_3 \cdot 3H_2O$ (*d*-spacing: 0.545, 0.386, 0.329, 0.244 nm) (Fig. 1). It should be noted that mineralogical composition of SGW-2 sample differs from SGW-1 sample because, diffraction maximums characteristic to aluminium hydroxide $Al(OH)_3$ (*d*-spacing: 0.485; 0.437; 0.432; 0.245; 0.239 nm) and aluminium fluoride hydroxide hydrate $AlF_{1.5}(OH)_{1.5} \cdot 0.375H_2O$ (*d*-spacing: 0.568; 0.296; 0.284; 0.189; 0.174 nm) were observed on the XRD pattern (Fig. 1, b). Furthermore, the silicon dioxide is amorphous because a broad peak in the angle of diffraction that varied from 18 to 26° was observed. The diffraction maximums of compounds containing other aluminium components (due to a small quantity) were not identified on the XRD pattern.

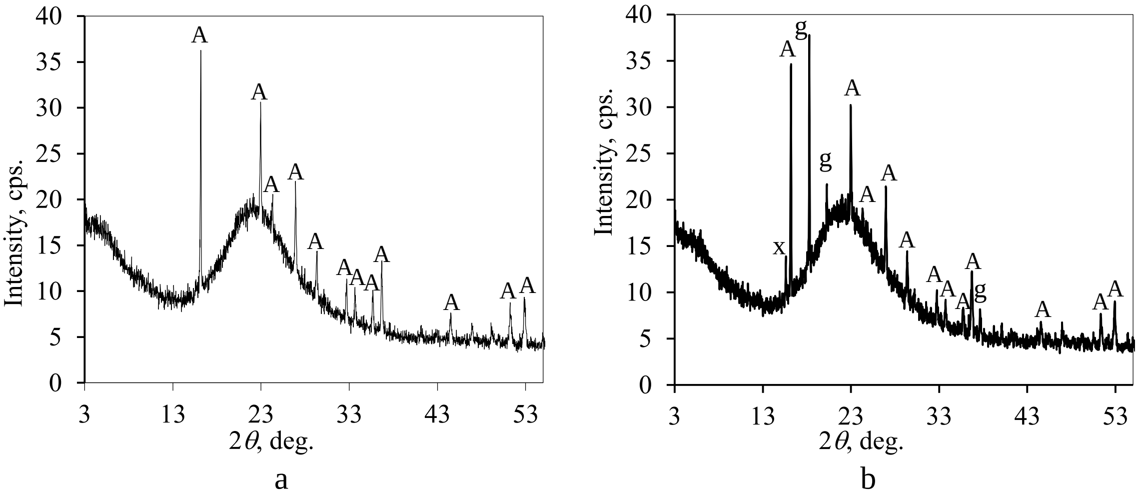

Fig. 1. XRD patterns of dried SGW-1 (a) and SGW-2 samples (b). Indexes: A – $AlF_3 \cdot 3H_2O$; g – $Al(OH)_3$; x – $AlF_{1.5}(OH)_{1.5} \cdot 0.375H_2O$

In the next stage of investigation the possibility of F^- ion elution from SGW-1 to a liquid medium was examined. The water-soluble fluoride compounds presented on the AlF_3 production waste surface could be removed by using hot water. Extraction with hot water promotes release of hydrogen fluoride and reconstruction of active silanol groups on the surface of waste silica gel:

$$\equiv Si - F + H_2O \rightarrow \equiv Si - OH + HF$$

It was obtained that the mineralogical composition of SGW-1 slightly varies during elution at 25 °C for 1 h when the ratio of w/s = 100: the intensity of diffraction peaks characteristic to $AlF_3 \cdot 3H_2O$ decreased by 3.1 times (Fig. 2.).

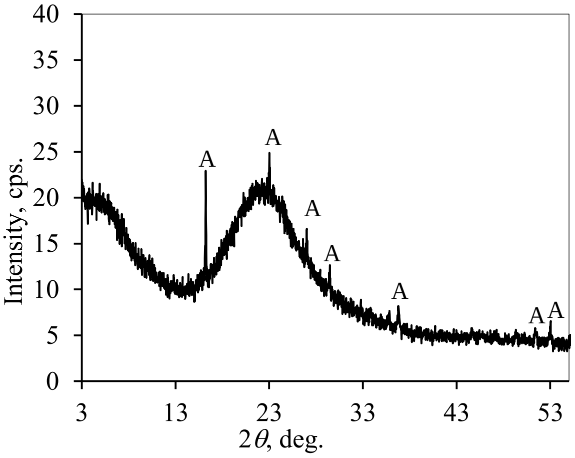

Fig. 2. XRD patterns of SGW-1 samples after 24 h of leaching under static conditions. Indexes: A – $AlF_3 \cdot 3H_2O$

Thus, it is clearly seen that a high concentration of F^- ions is still present in the structure of SGW-1, which can be explained by the strong adsorption properties of this compound. For this reason, in order to reduce the adsorption properties of SGW and the mobility of F^- ions, in the next stage of this research, the leaching of F^- ions was performed under dynamic conditions.

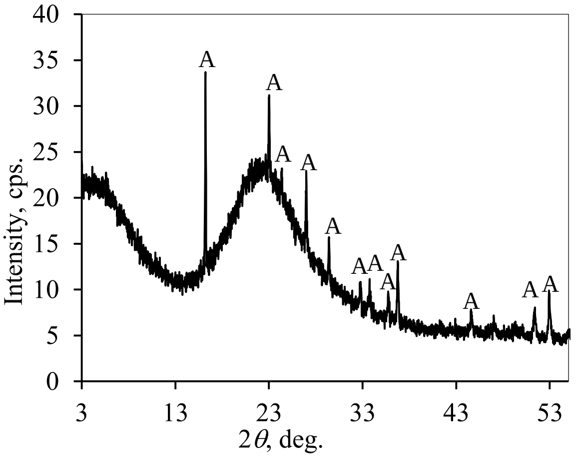

Fig. 3. XRD patterns of waste silica gel samples after leaching under dynamic conditions at 25 °C. Indexes: A – $AlF_3·3H_2O$

It was examined that the change in leaching conditions had an effect on the stability of $AlF_3·3H_2O$: the intensity of diffraction peaks characteristic to $AlF_3·3H_2O$ decreased by 1.23 times (Fig. 3). The XRD results were verified by the chemical analysis.

It should be noted that the higher w/s ratio during leaching process due to the principle of the technology is impossible and economically useless.

Summarizing the above mentioned results, it can be stated that fluoride ions removal into the liquid medium depends on such factors as dissociation, solubility, w/s ratio and adsorption properties of the waste silica gel. However, even if all of these factors were in control during the leaching, still a high amount of F^- ions will be present in this compound, resulting in limited application possibilities. For this reason, in the next experimental stage the application of SGW to the formation of calcium silicate hydrate under hydrothermal synthesis conditions was performed.

Hydrothermal synthesis includes the various techniques of crystallizing substances from high-temperature aqueous solutions at high vapour pressures. It is presumed that during hydrothermal synthesis F^- ions in the SGW will be combined into stable compounds, and this material could be used in binders and in the building materials industry. Only fragmentary data on the removal of fluoride ions from the limited solubility of solid materials and waste during hydrothermal synthesis are published in the literature.

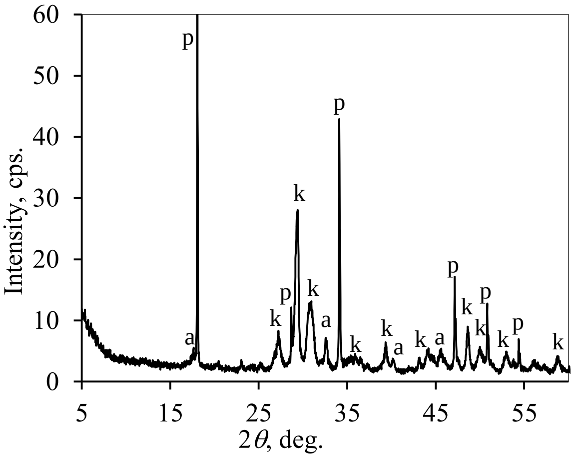

Fig. 4. XRD patterns of synthesis product. Indexes: A – $AlF_3·3H_2O$

It was determined that in CaO–SGW–H_2O system when the molar ratio of CaO/SiO_2 = 2.5 after 16 h of isothermal curing at 200 °C, cuspidine (*d*-spacing: 0.306, 0.290, 0.287 nm) was formed (Fig. 4). Also together with this compound, hydrogarnet (*d*-spacing: 0.276, 0.226, 0.200 nm) was also identified on XRD patterns.). It should be noted that under these synthesis conditions, the basic reflections (*d*-spacing: 0.493; 0.193; 0.179 nm) of partially unreacted portlandite was observed on X-ray diffraction pattern.

4. CONCLUSIONS

The chemical and mineralogical composition of waste silica gel samples depends on technological parameters of AlF_3 production. It was determined that waste silica gel mainly consists of silicon dioxide (79.01–80.90%) and other compounds containing 10.02–5.67% F^- and 2.14–2.48% Al^{3+} ions. It was found that under static and dynamic elution conditions at 25 °C temperature is impossible to remove all fluorine ions into liquid medium.

It was determined that SGW can be used as raw material for the hydrothermal synthesis of calcium silicate hydrates, because a stable compound – cuspidine, was formed.

ACKNOWLEDGEMENT

This research was partially supported by JSC "Lifosa".

REFERENCES

1. JESWANI, H. K., AZAPAGIC, A. Assessing the environmental sustainability of energy recovery from municipal solid waste in the UK. Waste management. 2016, Vol. 50, p. 346-363.
2. BAHRAMI, A., SOLTANI, N., PECH-CANUL, M.I., GUTIÉRREZ, C. A. Development of metal-matrix composites from industrial/agricultural waste materials and their derivatives. Critical Reviews in Environmental Science and Technology. 2015, Vol. 3389, p. 1-66.
3. APRILIA, A., TEZUKA, T., SPAARGAREN, G. Inorganic and Hazardous Solid Waste Management: Current Status and Challenges for Indonesia. Procedia Environmental Sciences. 2013, Vol. 17, p. 640-647.
4. SPRUOGIS A., JASKELEVIČIUS B. *Waste and its management.* Vilnius: *Technics.* 2006.
5. Natural resources and environmental safety 2015. Vilnius. Department of Statistics to the Government of the Republic of Lithuania. 2016. *https://osp.stat.gov.lt/services-portlet/pub-edition-file?id=24700*
6. USEPA. Integrating Pollution Prevention - Getting Started. Pollution Prevention. 2010. P. 1- 121.
7. Europen Contributions to the Commission Consultation on the EU Waste Management Targets Review. 2013.
8. GORSEVSKI, P. V., DONEVSKA, K. R., MITROVSKI, C. D., FRIZADO, J. P. Integrating multi-criteria evaluation techniques with geographic information systems for landfill site selection: A case study using ordered weighted average. Waste Management. 2012, Vol. 32, Iss. 2, p. 287-296.
9. KARLSTRÖM, J. Reactor Model for Production of Aluminum Fluoride. 1970. No. 1966.
10. Internal documents of JCC "Lifosa".
11. DREVETON, A. Economic aspects of utilizing fluosilicic acid as raw material for the manufacture of hydrofluoric acid and aluminium fluoride. Procedia Engineering. 2014. Vol. 83, p. 279-285.
12. ILJINA A., BALTAKYS K., BANKAUSKAITE A., EISINAS A., KITRYS S. The stability of formed CaF_2 and its influence on the thermal behavior of C-S-H in CaO-silica gel waste-H_2O system. Journal of Thermal Analysis and Calorimetry. 2017, Vol. 127, Iss. 1, p. 221-228.
13. BALTAKYS K., ILJINA I., BANKAUSKAITE A. Thermal properties and application of silica gel waste contaminated with F^- ions for C-S-H synthesis. Journal of thermal analysis and calorimetry. 2015, Vol. 121, Iss. 1, p. 145-154.

CYSENI 2017, May 25-26, Kaunas, Lithuania
ISSN 1822-7554, www.cyseni.com

THE SUM OF ACTIVE TEMPERATURES AND THEIR LONG-TERM CHANGES IN UKRAINE

L.Pysarenko
Ukrainian Hydrometeorological Institute
Nauky Av. 37, 03028 Kyiv – Ukraine
E-mail: lolinal@ukr.net

ABSTRACT

Heat is one of the main factors of growth, phenological development and harvest formation. The heat resources estimation belongs to crucial tasks of agrometeorological foundation in agricultural production. Therefore, the determination of heat resources has scientific and practical importance on climate change.

The spatial distribution features of the sum of active temperatures (SAT) has been studied for the 1961–1990 and 1991–2014 periods. Estimation of characteristics and tendency of heat resources change in period of active vegetation over the territory of Ukraine were done. The valuation of decadal (ten days) increase in SAT on different Ukrainian physico-geographical regions was done.

Analysis showed that “modern” global warming causes the increase of SAT. The threshold through 10 °C shifts in spring season and intensification in accumulation of active temperatures in the warmest months (July and August) with reaching maximum in the third decade of July (to 260 °C per decade) were revealed.

Keywords: the sum of active temperatures, heat resources, threshold, decadal increase

1. INTRODUCTION

In recent years, agrometeorological conditions have been very changeable and unstable especially in period of active vegetation (limited by spring and autumn thresholds through 10 °C) in Ukraine. In accordance with this it is necessary to take into account changes of components of agroclimatic resources in time and space during period of active vegetation and adapt the strategy of growing crops. This period is crucial because it is time of intensive growth and plants' development. Thermal conditions are one of the main components which are described through parameter as the sum of active temperatures (SAT). This integral index came from USSR [1–7] also similar index was proposed by foreign scientists.

Nowadays there are many researches dedicated to the sum of active temperatures, their distribution over the territory of Ukraine, changes during different period [8–14] and their possible variations because of climate change [14]. This parameter also is used not widely abroad and it has another ways of calculations [15]. More common is Growing degree day with a basic lower temperature 10 °C [16–17], which can be used as a characteristic of climate change if it is applied for a long period [18, 19].

Analysis of literature has shown that many researches were done about heat resources from agroclimatological aspect [8–20]. This problem was researched well, but papers don't include last ten years in which significant climate changes were observed. So, the research of the sum of active temperatures and their long-term changes including last years' data in Ukraine are very relevant. It has to demonstrate spatial and temporal features of distribution of SAT in modern climate change.

2. METHODOLOGY

For estimation of changes and tendency of heat resources in period of active vegetation were used data from 74 meteorological stations. Alpine meteorological stations in the Carpathians and Crimea were not included, because lack of meteorological data. Research contains data for period from 1961 to 2014, which has been divided into 2 parts for comparison to indicate changes: 30-year climatological standard normal (1961–1990) and “modern” period (1991–2014). Term “modern” is used for indication of period 1991–2014. Spring and autumn temperature threshold through 10° C and average decadal temperature (10 days) have been used for SAT calculations. They have been done by using formula:

$$\sum T_{ac} \geq 10^{\circ}C = \sum (T_{II,IV} \cdot N_{II,IV} + T_{III,IV} \cdot N_{III,IV} + \ldots + T_{I,X} \cdot N_{I,X}), \qquad (1)$$

where $T_{II,IV}$ – average temperature with indices: decade and month (for example: II – the second decade, IV – April); N – amount of days in certain decade of month.

For better visualization it has been built maps of distribution of SAT for two different periods and analysed characteristics of change of SAT. To reveal their features during warm season, calculations of decadal (10 days) increase were done. It is subtraction between current and previous decade.

In this paper physico-geographical regions were used: Polissia – the Northern part of Ukraine, Forest steppe or Lisosteppe – the Central part of Ukraine, Steppe – the Southern part of Ukraine, Zakarpattia – is the region which is situated on the South-West from the Carpathians.

Maps were built by using Surfer software with ASCII Grid input.

3. RESULTS

3.1. Spatial and temporal distribution of SAT

There are some changes in spatial distribution of average SAT comparing two maps (Fig. 1 and Fig. 2) of 1961–1990 and 1991–2014. It was revealed more intensification of SAT during last 25 years (1991–2014) period of research because of climate change. The difference in SAT between two periods is so big, that exaggerate or comparable with maximal values that could have impact on plants’ development [8]. If the difference between SAT is more than 100 °C it is necessary to redistribute sorts of plants in according to current conditions [9].

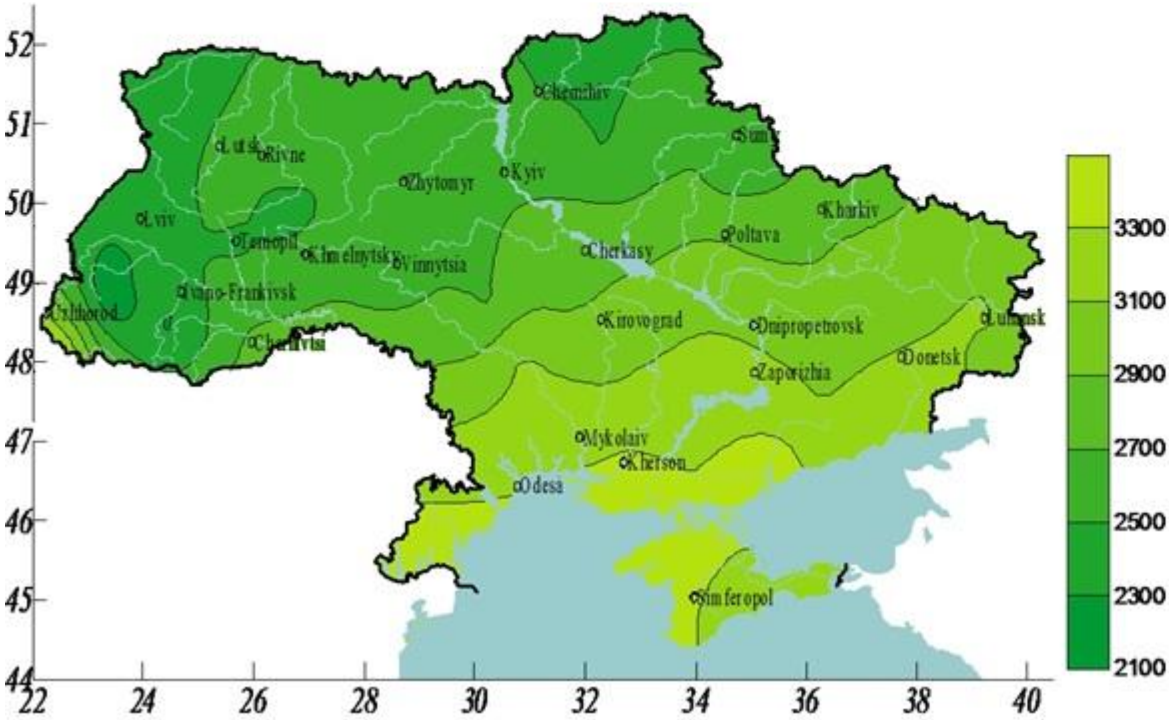

Fig. 1. Spatial distribution of average SAT of the period 1961–1990

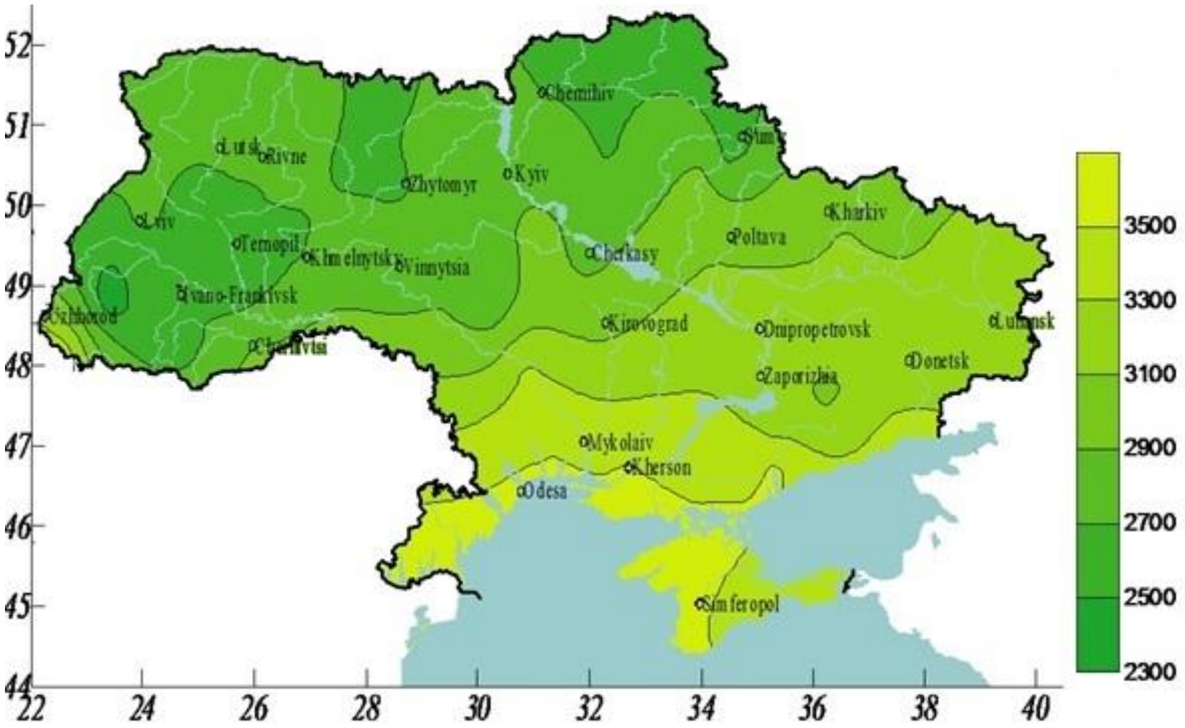

Fig. 2. Spatial distribution of average SAT of the period 1991–2014

On the Fig. 2 (1991–2014) closed isoline with the lowest value of SAT 2100 °C in the Carpathian region in contrast to the Fig. 1 (1961–1990) starts only from 2300 °C. For this area of study data from alpine meteorological stations have not been included.

In the Northern and Western parts of Polissia which were with mean values of SAT 2300–2500 °C and 2500–2700 °C for period of climatological normal (Fig. 1) and now these values have been changed: with mean 2500–2700 °C and 2700–2900 °C respectively.

There are also changes in SAT in the Central and Eastern part of Lisosteppe or Forest steppe and Steppe of the period 1991–2014 (Fig. 2). This region is characterised by temperatures 2900–3100 °C and 3100–3300 °C instead of 2700–2900 °C and 2900–3100 °C. The last mentioned zone with certain values of SAT has been expanded in compare with previous years (Fig. 1).

It has been revealed stronger intensification in SAT accumulation in the South comparing 2 periods. During 1961–1990 this part was with temperatures 3100–3300 °C, 3300 °C and more (with maximum 3450 °C).

From Fig. 3 it can be seen that maximum changes took place in the Northwestern and Western parts of Ukraine. For example, maximum changes are observed on meteorological stations Kovel and Lviv, where SAT have increased from 2412 °C and 2417 °C (1961–1990) to 2714 °C and 2734 °C (1991–2014) respectively. Also, the similar situation is the Carpathians on station Slavske and SAT are much higher nowadays – 2310 °C (1991–2014) instead of SAT with mean 2034 °C (1961–1990). Comparing 2 research periods the difference between SAT in this region ranges within 200–320 °C. Maximum differences are observed on stations Kovel (322 °C), Lviv (297 °C), Slavske (276 °C). In Northwestern and Western parts of Ukraine it can be connected with spring thresholds through 10 °C which have been shifted to more early dates.

For Zakarpattia the difference in SAT have been ranging from 130 to 180°C between 2 periods of research. In Uzhhorod they have increased from 3123 °C to 3250 °C, in Beregove – from 3213 °C to 3379 °C.

Slightly smaller changes in SAT could be seen in local areas in the North-East and South-West. They have increased from 2706 °C (meteorological station Bohoduhiv, North-East) up to 2968 °C with difference 262 °C. In this part spring temperature threshold through 10 °C has taken place earlier. In the Southeastern part, for example, on station Odesa which is situated near the Black Sea, SAT have changed on 255 °C – from 3286 °C (1961–1990) to 3541 °C (1991–2014) and autumn temperature thresholds through 10 °C have been shifted to later dates. There is range in SAT from 190 °C to 260 °C.

Calculations of SAT have shown lesser changes in the South East, Eastern and local in the Central part. For example, SAT have increased up to 116 °C (a meteorological station Kirovograd, which is located in the Central part): from 2933 °C to 3049 °C. SAT also have increased up to 100 °C (meteorological station Amvrosiivka, Eastern part): from 3171 °C to 3270 °C. Also it was revealed that on some stations SAT accumulation slightly reduced or did not change. Maximum decrease with value -46 °C was observed on station Pryshyb (the South East) (mean SAT 3240 °C in 1961–1990 and 3194 °C in 1991–2014). Also on station Cherkasy (Central part of Ukraine) SAT have reduced on 21 °C. On some stations which are on the East from the Carpathians – Ternopil, Kremenets, Chortkiv with no significant change. On these several stations (without changes in SAT or negative changes) it may be explained by microclimatological regime, but it is impossible to check on available data.

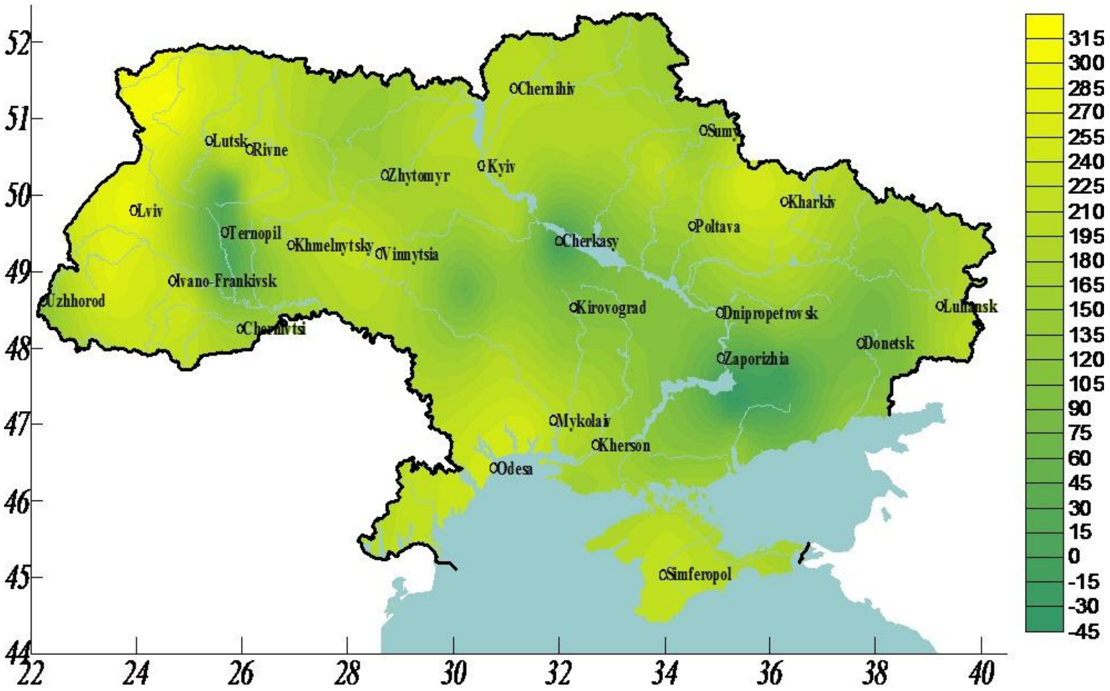

Fig. 3. Difference in SAT between period 1961–1990 and 1991–2014

3.2. The estimation of decadal (10-day) increase SAT in physico-geographical regions of Ukraine

For more detailed characteristic of heat resources it has been estimated the accumulation of SAT for every decade (10 days) during the period of active vegetation. It was made for several stations in different physico-geographical regions for 1961–1990 and 1991–2014 (Fig. 4, Fig. 5).

As we can compare these 2 periods, on meteorological station Lutsk (Polissia) the accumulation of SAT in average starts earlier on one decade now (Fig. 4, a). This process is connected with threshold shift through 10 °C in spring, but in autumn it has not changed significantly. During a 30-year climatological normal accumulation of SAT started in average in the 1-st decade of May and finished in the 3-rd decade of September, in period 1991–2014 has changed the beginning – in the 3-rd decade of April. The similar pattern is observed on stations of Northeastern part of Ukraine (also Polissia).

Last years in Lutsk there has been more intensification in decadal increase of SAT especially in summer. For example, in the 3-rd decade of July the mean SAT increase was 200 °C for 1961–1990 and 223 °C for 1991–2014. So, comparing 2 research periods the differences in mean SAT increase are range from 3 °C per decade (spring and autumn) to reaching maximum 23 °C (in summer, the 3-rd decade of July). Similar situation is typical for other stations of Polissia.

As was analysed, on meteorological station Yaremche (the Carpathians) spring threshold through 10 °C shifted on earlier dates in compare with climatological normal. The accumulation of SAT begins in average in the 1-st decade of May during the period of 1991–2014 in contrast with 1961–1990 – the 2-nd decade of May. But the end of period has not changed – the 3-rd decade of September. In “modern” period decadal increase of SAT has become more intensive it could be seen during spring and summer. The maximum difference is in the 3-rd decade of July – 20 °C with average decadal accumulation 179 °C (1961–1990) and 199 °C (1991–2014). This difference ranges in decadal SAT from 2 °C (autumn) per decade to 20 °C (summer).

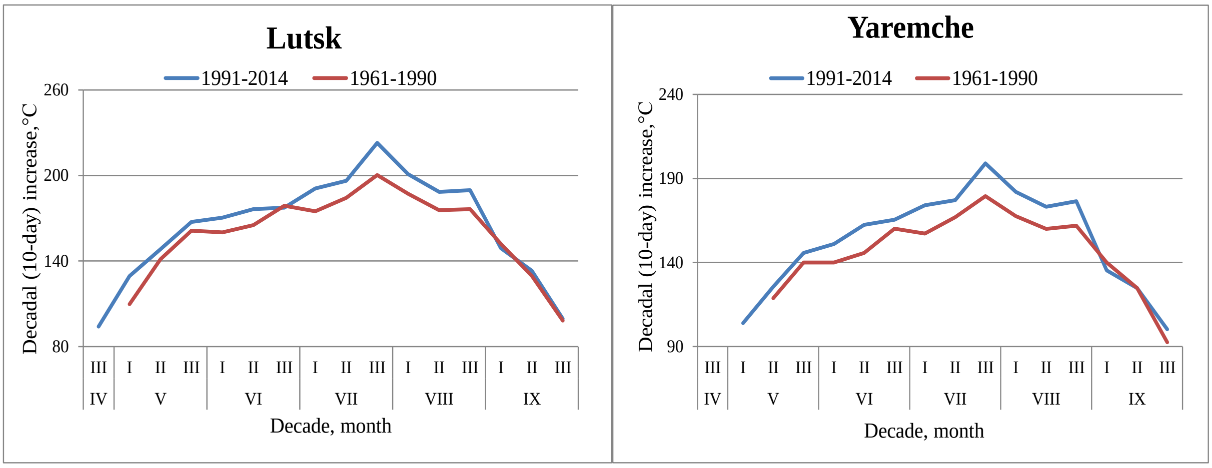

a) b)

Fig. 4. SAT accumulation for every decade (10 days) for period 1961–1990 and 1991–2014 on meteorological station Lutsk (a) (the Northwestern part of Ukraine, Polissia) and Yaremche (the Carpathians) (b)

The Central part of Ukraine (physico-geographical region Lisosteppe) is characterised by different conditions because of threshold shift through 10 °C in spring during 1991–2014 in compare with 1961–1990. For example, on station Kobelyaky (Fig. 5, a) there is no significant change in threshold. The accumulation of SAT begins in the 3-rd decade of April and stops in the 3-rd decade of September. But it is observed the decadal increase in SAT in summer in compare with climatological normal with maximum in the 3-rd decade of July – 227 °C (1961–1990) and 247 °C (1991–2014). The difference between these 2 periods changes from 2 °C (spring and autumn) to 20 °C (maximum in summer).

In the Southwestern part of Ukraine (physic-geographical region Steppe) where station Sarata is situated, it is observed that autumn threshold through 10 °C has shifted on later dates. It was revealed in analysing period 1991–2014. The modern period of active vegetation has been widened per one decade (from 1-st decade of October to 2-nd) in average comparing with climatological normal. Maximum of decadal SAT accumulation is in the 3-rd decade of July, the warmest decade. In 1961–1990 in this decade mean increase was 239 °C, in 1991–258 °C with difference 19 °C. It changes between decades 1961–1990 and 1991–2014 from 2 °C (spring and autumn) to 19 °C (summer). There are not the same changes in different parts of the Steppe. The most powerful they have been revealed in the South West, less – in the South East.

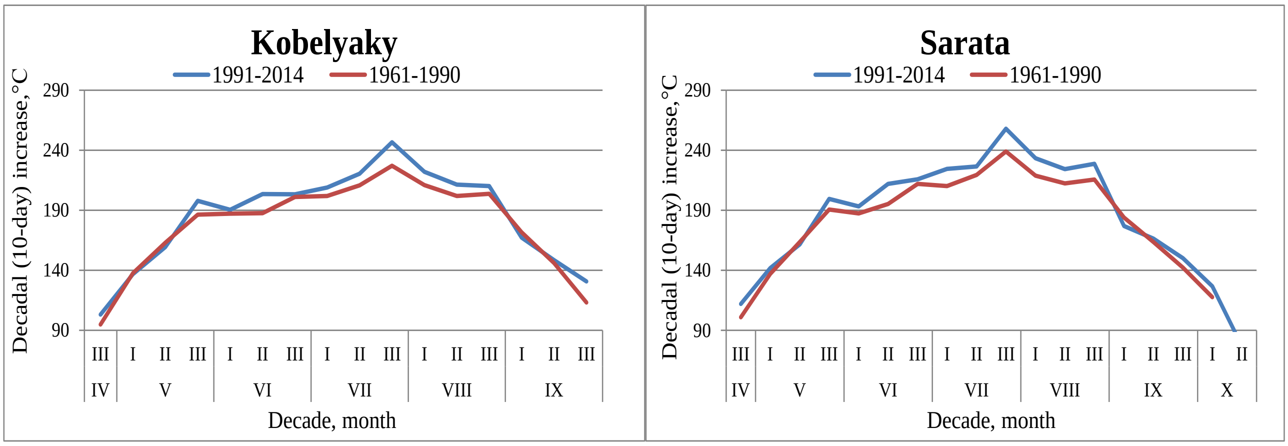

a) b)

Fig. 5. SAT accumulation for every decade (10 days) for period 1961–1990 and 1991–2014 on meteorological station Kobelyaky (a) (the Central part of Ukraine, Lisosteppe or Forest steppe) and Sarata (b) (the Southwestern part, Steppe)

4. DISCUSSIONS

Last comparison with previous results [9] for Ukraine has shown that changes of SAT in Polissia and the Carpathian region were about 150 °C, in Lisosteppe – about 130–150 °C, Steppe – about 100–150 °C. Results in this paper showed that SAT have increased. It means, that from the last researches of SAT, strong changes in climate and SAT distribution have happened.

5. CONCLUSIONS

It has been analysed and compared the features of distribution of heat resources over the territory of Ukraine between 1961–1990 and 1991–2014. As it has been revealed the SAT increased in almost all parts of the country during last period. The maximum differences in SAT between 2 periods of research are: in the North-West (Polissia) – 322 °C (station Kovel), the Carpathians – 276 °C (station Slavske), the North-East (Lisosteppe) – 262 °C (station Bohoduhiv), the South-West (Steppe) – 255 °C (station Sarata). It connected with spring and autumn threshold through 10 °C which shifted to early and later dates respectively. This process caused the expansion of period of active vegetation and also earlier accumulation of SAT in some regions.

The calculations have shown that decadal SAT accumulation starts earlier on one decade on the West (Polissia and the Carpathians), North-East (Lisosteppe) and it finishes later on the South-West comparing (Steppe) 1961–1990 and 1991–2014. Also, it has been revealed more decadal intensification especially in summer with the biggest difference in the 3-rd decade of July.

REFERENCES

1. СЕЛЯНИНОВ, Г.Т. О сельскохозяйственной оценке климата. *Труды по сельскохозяйственной метеорологии, Ленинград*, 1928, вып. 20. С. 165-177.
2. КОЛОСКОВ, П.И. *Климатический фактор сельского хозяйства и агроклиматическое районирование*. Ленинград: Гидрометеоиздат, 1974. 328 с.
3. САПОЖНИКОВА, С.А. *Агроклиматический атлас Украинской ССР*. Киев: Урожай, 1964. 36 с.
4. ДАВИТАЯ, Ф.Ф. *Агроклиматические условия освоения целинных и залежных земель*. Ленинград: Гидрометеоиздат, 1954. 130 с.
5. ШАШКО, Д.И. *Агроклиматическое районирование СССР*. Москва: Колос, 1967. 334 с.

6. ШАШКО, Д.И. *Агроклиматические ресурсы СССР*. Ленинград.: Гидрометеоиздат, 1985. 247 с.
7. ГУЛИНОВА, Н.В. *Методы агроклиматической обработки наблюдений*. Лениград: Гидрометеоиздат, 1974. 152 с.
8. LIPINSKY, V. M.; DYACHUK V.A.; BABICHENKO, V.M. *Climate of Ukraine*. Kyiv: View of Raevskogo, 2003. 343 p.
9. БАРАБАШ, М.Б; ГРЕБЕНЮК, М.П; ТАТАРЧУК, О.Г. Особливості зміни ресурсів тепла та вологи в Україні при сучасному потеплінні клімату. *Наукові праці УкрНДГМІ*, 2007, вип. 256, с. 174-186.
10. ДМИТРЕНКО, В.П.; КРУКІВСЬКА, А.В. Основи мезомасштабного агрокліматичного районування території на засадах математико-картографічного методу. *Наукові праці УкрНДГМІ*, 2005, вип. 254, с. 135-152.
11. АДАМЕНКО, Т.І.; КУЛЬБІДА, М.І.; ПРОКОПЕНКО, А.Л. *Агрокліматичний довідник по Київській області*. Кам’янець-Подільський: ПП Буйницький О.А., 2010. 184 с.
12. ЛЯШЕНКО, Г.В. Агроклиматическое районирование Украины. Научные труды УкрНДГМИ, 2008,вып. 3, с. 98-108.
13. ЛЯШЕНКО, Г.В. *Практикум з агрокліматології. Навчальний посібник*. Одеса: ОДЕКУ, 2014. 150 с.
14. МИЩЕНКО, З.А. *Агроклиматология.* Киев: КНТ,2009. 512 с.
15. ПОЛЬОВИЙ, А.М. та ін.. Зміна показників термічного режиму повітря в Україні на період до 2030 р. *Український гідрометеорологічний журнал*, 2014, вип. 14, с. 95-104.
16. LYSIAK, G. The sum of active temperatures as a method of determining the optimum harvest date of “Samption” and “Ligol” apple cultivars. *Acta Sci Pol*., 2012, Vol. 11, No. 3, p. 3-13.
17. VILLORDON, A. et al. Using Growing Degree Days, Agrometeorological Variables, Linear Regression, and Data Mining Methods to Help Improve Prediction of Sweetpotato Harvest Date in Louisiana. HortTechnology, 2009, Vol. 19, No.1, p. 133-144.
18. *Ministry of agriculture, food and rural affairs*. Field scouting: Using Growing Degree Days and Crop Heat Units. Link to the internet: <http://www.omafra.gov.on.ca/english/crops/pub811/10using.htm#gdd>
19. GRIGORIEVA, E.A.; MATZARAKIS, A. Growing degree days at the Russian far East. Link to the internet: <http://www.urbanclimate.net/matzarakis/papers/BIOMET7_Grigorieva_Matzarakis_44_49.pdf>
20. GRIGORIEVA, E.A.; MATZARAKIS, A.; DE FREITAS,C.R. Analysis of growing degree-days as a climate impact indicator in a region with extreme annual air temperature amplitude. Link to the internet: < http://www.int-res.com/articles/cr2010/42/c042p143.pdf>

CYSENI 2017, May 25-26, Kaunas, Lithuania
ISSN 1822-7554, www.cyseni.com

COHESION OF STATISTICAL DOWNSCALING METHODS AND PROJECTIONS OF METEOROLOGICAL PARAMETERS OVER LITHUANIA

V. Akstinas
Lithuanian Energy Institute
Breslaujos str. 3, LT-44403 Kaunas – Lithuania
E-mail: Vytautas.Akstinas@lei.lt

ABSTRACT

In projections of future climate variables there are so many uncertainties which related to different sources of origin. According to IPCC Fifth Assessment Report appropriately used scenarios are RCP (Representative Concentration Pathways). For constructing future climate variables the Global Climate Models (GCM) are used. These numerical models together with RCP provide the projections for investigation of future climate change, but on the other hand they are the primary source of systematic errors. There are large biases comparing GCM output data with historical observations therefore statistical downscaling (SD) methods are used for reduction of mentioned biases. Only after improvement by SD the projections of meteorological parameters are better fit for any kind of climate change impact models (hydrological, ecological, economical, social etc.).

The main objective is to evaluate how SD methods improve GCMs output according to climate change scenarios (RCPs) and impact eventual projections of temperature and precipitation over Lithuania. Evaluation of temperature and precipitation data in four climate regions of Lithuania was done. For this analysis, geographically the most dominant meteorological station was chosen from each climate region of Lithuania. Projections of mentioned meteorological parameters according to two RCP scenarios (RCP2.6 and RCP8.5) have been taken from three GCMs (GFDL-CM3, HadGEM2-ES and NorESM1-M) and processed by three statistical downscaling methods (Bias Correction with variable, Change Factor with variable and Quantile Mapping). All deviations of near future projections (2016–2035) were compared with reference period (1986–2005). Analysis of potential range of meteorological parameters according to different sources of biases (GCM, RCP and SD) will let better to know possible climate change magnitude in four climate regions of Lithuania.

Keywords: climate change, RCP, statistical downscaling, GCM

1. INTRODUCTION

After the appearance of Fifth Assessment Report (AR5) of IPCC, all research community has started to use new RCP (Representative Concentration Pathways) climate change scenarios. These scenarios were implemented according to tendencies of nowadays social-economical growth as a basis for long term climate modelling experiments [1]. The last one CMIP5 (The fifth phase of the Climate Model Intercomparison Project) experiment involve 20 climate modelling groups all over the world [2] and provide wide range output of climatic variables from atmosphere-ocean general circulation model, hereafter GCMs. These models have became increasingly important for better understanding of climate change phenomena and provide the basis for different kind of impact studies [3]. Discussion about climate change uncertainties is tending to focus on climate sensitivity, which highly depends on chosen GCM [4]. Therefore combinations of GCMs and RCP scenarios are primary source of climate change uncertainties. Atmosphere-ocean general circulation models are limited by the inherent simplifications of some processes of Earth’s climate system. Accordingly, the model outputs involve different kinds of biases comparing to the observed climate variables [5]. Uncorrected biases can lead to significant errors on impact assessments studies. Consequently, statistical downscaling of GCM outputs is necessary before GCM outputs will be used in local or regional impact analysis [6, 7]. Most statistical downscaling (SD) approaches are based on the statistical relations between large-scale GCM outputs and local scale observation datasets. The model biases directly depend how GCM simulate climate in the past and it is assumed that analogue biases can be reflected in the future [5, 8].There are many studies applied downscaling methods for corrections of climate model outputs of meteorological variables using observation data, where biases of precipitation and temperature outputs for future periods are generally reduced [5, 9, 10]. Application of SD methods corrected projections of meteorological parameters, respectively the projections of surface runoff and hydrological regime in impact assessments studies were improved [9, 11]. Also some studies analyse advantages and disadvantages of different statistical downscaling approaches [12, 13, 14]. Mentioned researches can be used for improvement of GCM outputs to a fine temporal and spatial scale [15].

In Lithuania the evaluation of different GCMs output was made according to the newest RCP scenarios [16]. The projections of hydrological regime in rivers of Nemunas River basin were evaluated according to mentioned scenarios [17]. But the potential impact of statistical downscaling methods on meteorological parameters (temperature and precipitation) is not sufficient investigated. Therefore the main task of this research is to evaluate how SD methods improve projections of GCMs output (temperature and precipitation) according to climate change scenarios (RCPs) in four climate regions of Lithuania. Investigation of potential range of meteorological parameters could indicate possible variability in climate change magnitude.

2. METHODOLOGY

2.1. Study area

Lithuania is divided into four climate regions: Seaside, Žemaičiai, Middle Lowland, South-Eastern Uplands (Fig. 1). All these regions are characterized by different climatic conditions which are caused by local topography and distance from the Baltic Sea. The study area consists of four selected meteorological stations (Klaipėda, Telšiai, Dotnuva and Vilnius) from each major climate region (CR) of Lithuania. Seaside region has marine weather type with lower temperature amplitude through the seasons and the highest number of sunshine hours. In Žemaičiai CR the topography effect is strongly expressed because Žemaičiai uplands collect greater part of moisture from the air masses. Therefore Žemaičiai CR has the highest annual precipitation comparing with other regions. Middle Lowland CR is characterized by adiabatic downhill air flow from the nearest uplands, consequently temperature slightly rises and amount of precipitation decreases. In South-Eastern Uplands CR the different kind of hills and sandy loam dominate. Such local physical geographical conditions determine strong temperature inversions and high amplitude in temperature fluctuation during the seasons [18].

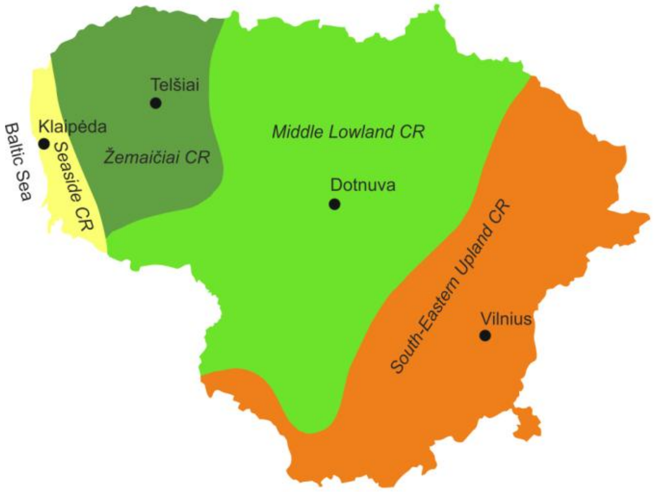

Fig. 1. Climate regions (CR) of Lithuania and location of meteorological stations (MS)

2.2. Meteorological data

Raw research data (temperature and precipitation) of historical period (1985–2005) simulations and near future (2016-2035) projections (according to RCP2.6 and RCP8.5) have been taken from NOAA (National Oceanic and Atmospheric Administration) GFDL (Geophysical Fluid Dynamics Laboratory) and WDCC (World Data Center for Climate) CERA data portals. Three GCMs (GFDL-CM3, NorESM1-M ir HadGEM2-ES) with different spatial resolution were selected from these data basis (Table 1).

Table 1. Spatial resolution of selected GCMs

No.	**GCM**	**Abbreviation**	**Grid resolution**	
			Longitude	**Latitude**
1.	GFDL-CM3	GFDL	1.5°	2°
2.	HadGEM2-ES	HAD	1.875°	1.25°
3.	NorESM1-M	NOR	2.5°	1.895°

Geographically the most dominant meteorological station (MS) of particular climate region was selected for each grid cell of different GCM (Fig. 2). The historical observations of temperature and precipitation for the period of 1985–2005 have been taken from Lithuanian Hydrometeorological Service. All historical observations are needed for correction of systematic biases of GCM output in reference period as well as biases of projections in the future.

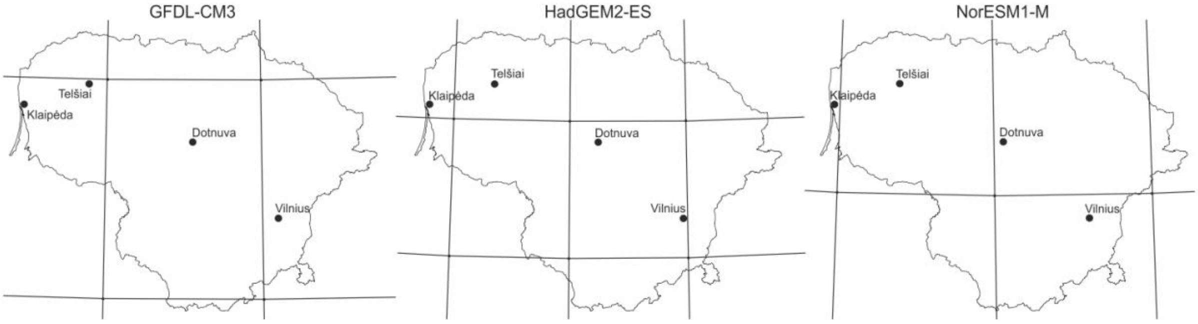

Fig. 2. Location of selected MS in the context of grid cells of various GCMs

2.3. Statistical downscaling

Projections of daily precipitation and temperature data in the period of 2016–2035 (near future) were performed by three different statistical downscaling methods – Bias Correction with variable (BC), Change Factor with variable (CF) and Quantile Mapping (QM). The major purpose of these methods is to downscale the low resolution data to a fine spatial scale for purpose to reproduce local conditions. All methods were implemented according to reference period (1986–2005). BC method corrects the projected raw daily GCM outputs in mean and variance [19, 20]:

$$P_{\mathrm{BC}}(t) = \overline{O_{\mathrm{REF}}} + \frac{\sigma_{O,\mathrm{REF}}}{\sigma_{P,\mathrm{REF}}}(P_{\mathrm{RAW}}(t) - \overline{P_{\mathrm{REF}}}) \quad (1)$$

where P_{BC} is corrected meteorological parameter of GCM output, O_{REF} is observation in the historical reference period, P_{REF} is meteorological parameter of GCM output from the historical reference period, P_{RAW} is meteorological parameter of raw GCM output for the future period. The time mean is denoted by the bar above a symbol. Equation (1) was used to represent the relationship between distribution of O_{REF} (observations in reference period) and distribution of P_{REF} (GCM simulations in reference period), therefore $\sigma_{O,\mathrm{REF}}$ and $\sigma_{P,\mathrm{REF}}$ are standard deviations of daily observations and meteorological parameter of GCM output in the reference period respectively.

CF method corrects the observed variables according to the differences between projected variables of GCM output and simulated GCM output from the historical reference period. It is described by following equation [19, 20]:

$$P_{\mathrm{CF}}(t) = \overline{P_{\mathrm{RAW}}} + \frac{\sigma_{P,\mathrm{RAW}}}{\sigma_{P,\mathrm{REF}}}\left(O_{\mathrm{REF}}(t) - \overline{P_{\mathrm{REF}}}\right) \qquad (2)$$

which was used to represent the relationship between distribution of P_{RAW} (GCM projection in the future) and distribution of P_{REF} (GCM simulations in reference period), therefore $\sigma_{P,\mathrm{RAW}}$ and $\sigma_{P,\mathrm{REF}}$ are standard deviation of GCM output of the future projections and deviation of GCM output in the reference period respectively.

QM method [21] is based on the concept of transformation h, such that

$$P_{\mathrm{Obs}} = h(P_{\mathrm{GCM\,REF}}) = ECDF_{Obs-1}(ECDF_{\mathrm{GCM\,REF}}(P_{\mathrm{GCM\,RAW}})) \qquad (3)$$

where P_{Obs} is observed meteorological parameter, $P_{\mathrm{GCM\ REF}}$ is GCM output for reference period, $P_{\mathrm{GCM\ RAW}}$ is meteorological parameter, which is projected by GCM for the future period. $ECDF_{\mathrm{Obs-1}}$ is empirical cumulative distribution function for observed period and $ECDF_{\mathrm{GCM\ REF}}$ is empirical cumulative distribution function for GCM reference period. First, all the probabilities in $ECDF_{\mathrm{Obs-1}}$ and $ECDF_{\mathrm{GCM\ REF}}$ are calculated at a fixed interval of 0.01. Then, h in each interval is estimated as the relative difference between the two different ECDFs. Interpolation between the fixed values is based on a monotonic tricubic spline interpolation. For correction of the number of wet days were estimated from the empirical probability of non-zero values in P_{Obs}. After that all RCM values below this threshold were set to zero [22]. The method was implemented by *Python* software.

3. RESULTS AND DISCUSSION

3.1. Effect of statistical downscaling methods on corrections of temperature projections

For analysis of near future temperature projections two climate change scenarios (RCP2.6 and RCP8.5) were chosen. These scenarios combine the lowest and the highest range of impact of climate change. Therefore for evaluation of differences between RCPs two case studies were selected (Fig. 3), where $\mathrm{RAW}_{\mathrm{ref}}$ – raw data of GCM output simulation in historical reference period (1985–2005), $\mathrm{RAW}_{\mathrm{fut}}$ – raw data of GCM output projections in near future (2016–2035), BC – corrected data of GCM output of near future projections according to BC method, CF – corrected data of GCM output of near future projections according to CF method, QM – corrected data of GCM output of near future projections according to QM method. The analysis showed differences between RCP2.6 and RCP8.5 in the projections of near future temperature, which were detected insignificant. Accordingly in this study the RCP2.6 was selected.

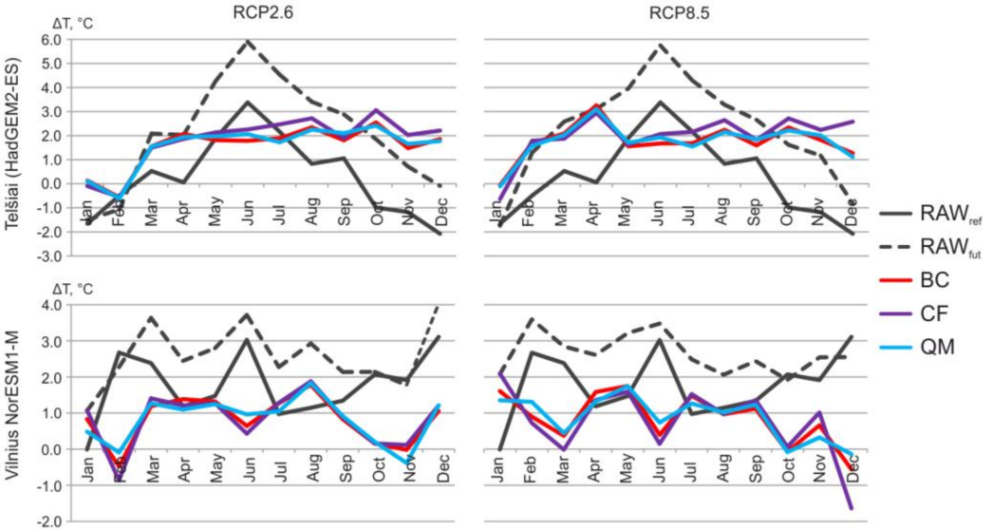

Fig. 3. Deviation of temperature simulation in reference period (RAW$_{ref}$) and projections in near future according to two RCP scenarios (RAW$_{fut}$) and three SD methods (BC, CF, QM) at two case studies (temperature of HAD model at Telšiai MS and temperature of NOR model at Vilnius MS) comparing with the observations of reference period

According to different GCMs the raw temperature simulations of historical period varied in wide range (Fig. 4). At Klaipėda MS the GFDL model simulated lower temperature in reference period comparing with historical observations, except months of May, June and December. Consequently the implementation of SD methods improve near future temperature projections relating to historical deviations, because only temperatures of May, June and December were slightly reduced and the temperature of other months were increased comparing with raw projections of GFDL output. Meteorological stations of Dotnuva and Vilnius gained similar deviations of historical simulations and near future projections as well as similar tendencies of SD corrections.

Meanwhile historical simulations and near future projections of HAD model at Klaipėda MS were significantly differed from the other MS, because HAD model simulated warming of cold months and coldness in warm months at Klaipėda MS. The situation was opposite at Telšiai, Dotnuva and Vilnius meteorological stations. Therefore it is important to use SD for corrections of GCMs output, which sometimes does not reflect local meteorological conditions. Application of SD methods for four MS provided range decrease of projected temperature in near future, because large positive deviations of the projections of near future were reduced and negative deviations were improved into positive side.

The temperatures of NOR model simulations in generally were high comparing with observations of reference period at Telšiai and Vilnius MS. Such distributions of simulated GCMs output in reference period highly influenced projections of near future according to different SD methods, whereas temperatures of all months (except January at Vilnius MS) were reduced in mentioned meteorological stations. Temperature of NOR simulations at Klaipėda MS had different identity comparing with the other meteorological stations and gained a similar character like output of HAD model. These similarities can be described by certain grid cells of NOR and HAD models, because according to both GCMs the Klaipėda MS falls within the grid cell, which mainly located over the Baltic Sea. Therefore future projections of temperature highly depend on geographical location of the MS and MS location in the grid cell of selected GCM. Due to these reasons application of statistical downscaling reducing systematic biases of GCM output and providing better fit temperature projections.

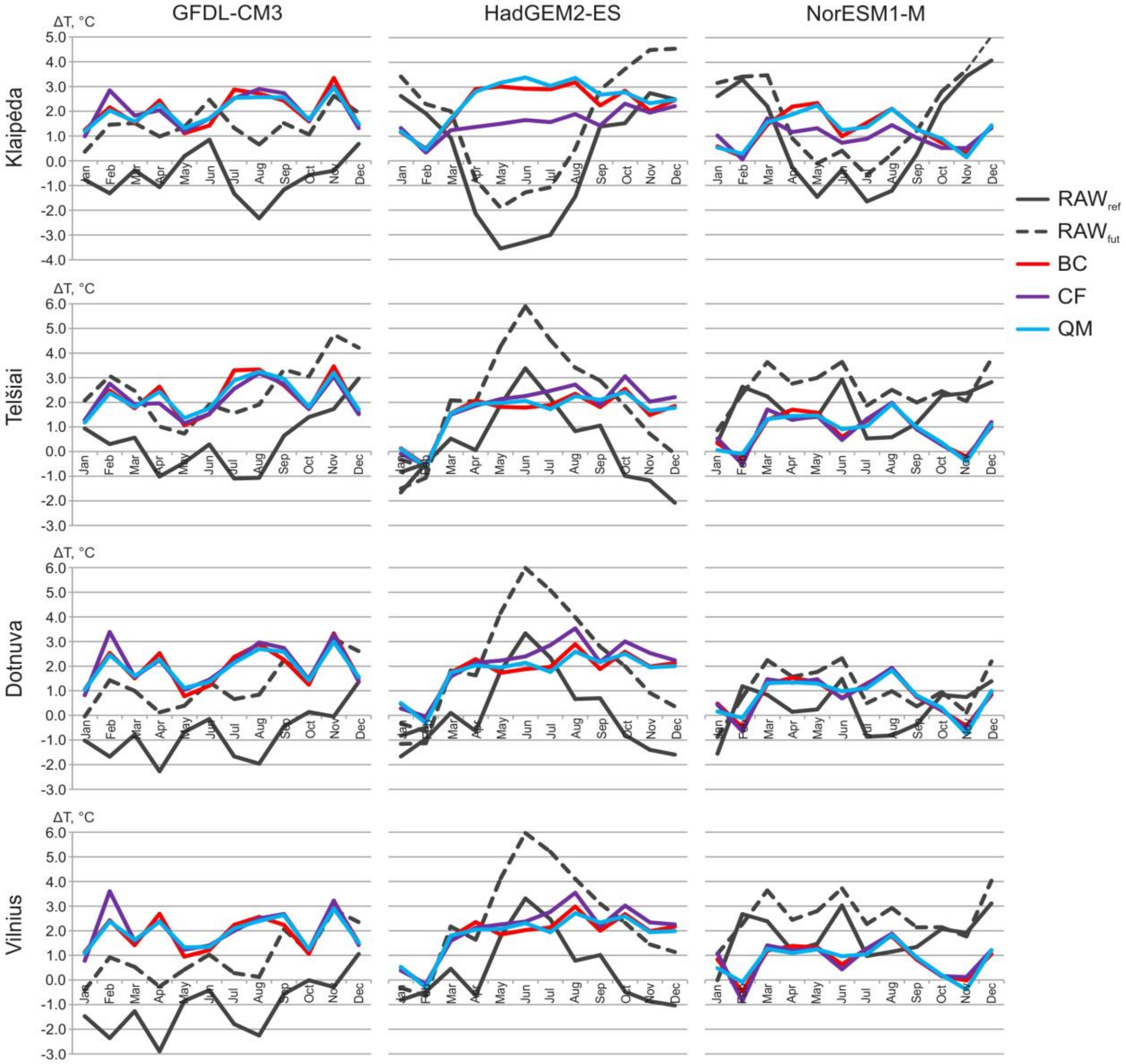

Fig. 4. Deviations of temperature simulation in reference period (RAW$_{ref}$) and projections in near future according to RCP2.6 scenario, three GCMs (RAW$_{fut}$) and three statistical downscaling methods (BC, CF, QM) comparing with observations of the reference period in four meteorological stations

Analysis of corrected temperature projections with statistical downscaling methods showed that influence of RCP scenarios on temperature projections were not so huge as influence of selected GCM and projections after SD corrections. Bias Correction and Quantile Mapping methods showed similar corrections of temperature projections in near future projections, because both methods based on correction factor from the reference period. Results of Change Factor method differed from the other only in cases of very high deviations (simulation of HAD and NOR models at Klaipėda MS), whereas this method based on differences between projected GCM output in the future and simulated GCM output in reference period. Also, selected GCMs were major uncertainty sources of projections and provided wide range of temperature amplitude.

3.2. Effect of statistical downscaling methods on corrections of precipitation projections

Projections of near future precipitation were done according to two climate change scenarios – RCP2.6 and RCP8.5. Two case studies were selected For estimation of differences (Fig. 5). The results of these scenarios showed similarities between RCP2.6 and RCP8.5, therefore for this study RCP2.6 was selected for estimation of effect of SD methods on precipitation projections as well as in analysis of the temperature projections in near future temperature.

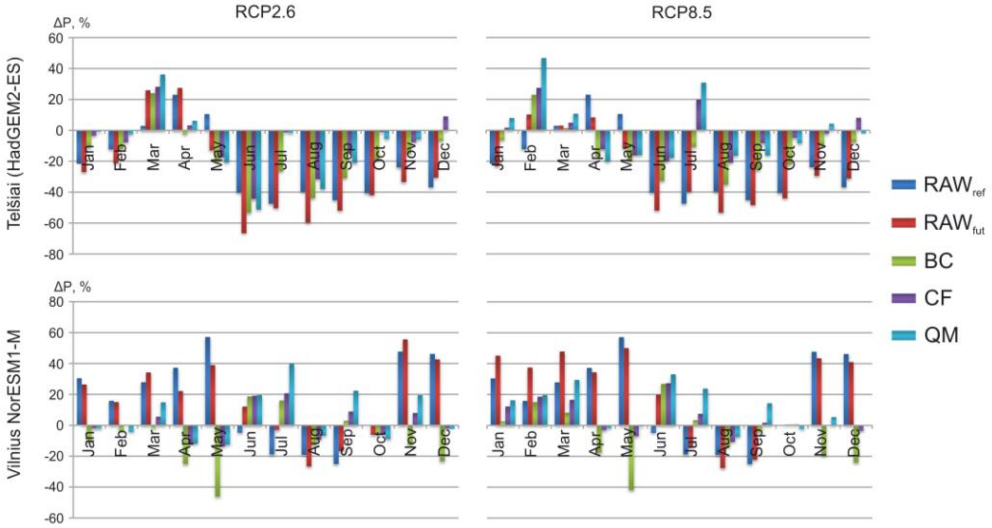

Fig. 5. Deviations of precipitation simulation in reference period (RAW$_{ref}$) projections in near future according to two RCP scenarios (RAW$_{fut}$) and three SD methods (BC, CF, QM) at two case studies (precipitation of HAD model at Telšiai MS and precipitation of NOR model at Vilnius MS) comparing with the observations of reference period

At Klaipėda MS the lowest range of precipitation projections was simulated by GFDL model (Fig. 6). Only results in few months showed higher than 40% deviations. HAD and NOR models projected very large negative deviations during the warm season and all these biases are reflected on projections according to different RCP scenarios. CF and QM methods showed the best fit corrections, i.e. changes of precipitation corrections had low amplitude than in the raw data. All GCMs mostly projected lower precipitation at Telšiai MS than in historical observations, except few months in winter and spring seasons (Fig. 6). HAD model provided high negative deviations, therefore the best fit corrections were done by the methods of CF and QM. NOR model showed the lowest deviations between corrections of different SD methods and only QM method provided extreme precipitation values in June.

Dotnuva MS from Middle Lowland climate region had particular character comparing with other meteorological stations. During the periods of January-April and November-December all GCMs simulated very high positive deviations, which in some cases exceeded 100% (1985–2005). These uncertainties of GCM output were reflected on raw precipitation projections of near future and implementation of SD methods. The application of BC method became tricky (in some cases this method can provide -100% (Fig. 6)), when differences between GCM simulation in reference period and historical observations are very large. Therefore in such condition CF or QM methods are appropriate for reduction biases of GCM output.

Fig. 6. Deviations of precipitation simulations in reference period (RAW$_{ref}$) and projections in near future according to RCP2.6 scenario, three GCMs (RAW$_{fut}$) and three statistical downscaling methods (BC, CF, QM) comparing with the observations of reference period in four meteorological stations

The best precipitation simulations of NOR model was established in meteorological station of Vilnius. Accordingly, corrections of precipitation projections of this MS fluctuate in the smallest range (Fig. 6). BC method provided the lowest projections, when QM method generated the highest values. HAD model projected the largest negative deviations during the warm season as well as in previous MS and after corrections with CF method better fit precipitation projections of near future were determined.

4. CONCLUSIONS

The importance of statistical downscaling was estimated, because systematic biases were generated depending on selected GCM. All biases appear in reference period of GCM simulations, therefore months with lower temperatures in reference period were strongly corrected upward implementing the statistical downscaling in the future projections. Otherwise months with higher temperatures in reference period were highly reduced. Primary biases are caused by location of meteorological station in the context of GCM grid. Klaipėda MS is in the grid cell of HAD and NOR models, which mostly representing marine conditions, therefore application of SD methods reduced biases and temperature better reflected local conditions.

The projections of future precipitation showed large dispersion between different GCMs. Generally meteorological stations from all climate regions indicated particular differences as well. Consequently, the raw data of GCM projections should be improved by statistical downscaling. The application of Bias Correction method (case of Dotnuva MS) is inappropriate to use when differences between GCM simulations in reference period and historical observations are very large (twice bigger than observations). Mostly the Bias Correction provided the lowest projections of precipitation, meanwhile Quantile Mapping method generated the highest values with extreme events of precipitation.

Analysis of temperature and precipitation projections and their correction by statistical downscaling methods showed various differences. Established differences between RCP scenarios were not as large as influence of selected GCMs. The statistical downscaling methods strongly improved temperature projections, however differences between SD methods were not so large. The wider scattering was obtained between results of different SD methods in corrections of precipitation projections, accordingly the methods of CF and QM were established as best fit for Lithuanian conditions.

REFERENCES

1. VAN VUUREN, D. P., EDMONDS, J., KAINUMA, M., RIAHI, K., THOMSON, A., HIBBARD, K., HURTT, G. C., KRAM, T., KREY, V., LAMARQUE, J. F., MASUI, T., MEINSHAUSEN, M., NAKICENOVIC, N., SMITH, S. J., ROSE, S. K. The representative concentration pathways: an overview. *Climatic Change*, 2011, Vol. 109, p. 5–31.
2. TAYLOR, K. E., STOUFFER, R. J., MEEHL, G. A. An overview of CMIP5 and the experiment design. *Bulletin of the American Meteorological Society*, 2012, Vol. 93, No. 4, p. 485–498.
3. RAMIREZ-VILLEGAS, J., CHALLINOR, A. J., THORNTON, P. K, JARVIS, A. Implications of regional improvement in global climate models for agricultural impact research. *Environmental Research Letters*, 2013, Vol. 8, 024018, 12 pp.
4. AHLSTROM, A., SMITH, B., LINDSTROM, J., RUMMUKAINEN, M., UVO, C. B. GCM characteristics explain the majority of uncertainty in projected 21st century terrestrial ecosystem carbon balance. *Biogeosciences*, 2013, Vol. 10, p. 1517–1528.
5. RÄTY, O., RÄISÄNEN, J., YLHÄISI, J. S. Evaluation of delta change and bias correction methods for future daily precipitation: intermodel cross-validation using ENSEMBLES simulations. *Climate Dynamics*, 2014, Vol. 42, p. 2287–2303.
6. KIDSON, J.W., THOMPSON, C.S. A comparison of statistical and model-based downscaling techniques for estimating local climate variations. *Journal of Climate*, 1998, Vol. 11, p. 735–753.
7. MURPHY, J. An evaluation of statistical and dynamical techniques for downscaling local climate. *Journal of Climate*, 1999, Vol. 12, No. 8, p. 2256–2284.
8. BOÉ, J., TERRAY, L., HABETS, F., MARTIN, E. A simple statistical-dynamical downscaling scheme based on weather types and conditional resampling. *Journal of Geophysical Research*, 2006, Vol. 111, D23106, 20 pp.

9. HAGEMANN, S., CHEN, C., HAERTER, J. O., HEINKE, J., GERTEN, D., PIANI, C. Impact of a statistical bias correction on the projected hydrological changes obtained from three GCMs and two hydrology models. *Journal of Hydrometeorology*, 2011, Vol. 12, p. 556–578.
10. VAN PELT, S. C., BEERSMA, J. J., BUISHAND, T. A., VAN DEN HURK, B. J. J. M., KABAT, P. Future changes in extreme precipitation in the Rhine basin based on global and regional climate model simulations. *Hydrology and Earth System Sciences*, 2012, Vol. 16, p. 4517–4530.
11. HUNDECHA, Y., SUNYER, M. A., LAWRENCE, D., MADSEN, H., WILLEMS, P., BÜRGER, G., KRIAUCIUNIENE, J., LOUKAS, A., MARTINKOVA, M., OSUCH, M., VASILIADES, L., VON CHRISTIERSON, B., VORMOOR, K., YÜCEL, I. Inter-comparison of statistical downscaling methods for projection of extreme flow indices across Europe. *Journal of Hydrology*, 2016, Vol. 541, p. 1273–1286.
12. FOWLER, H. J., BLENKINSOP, S., TEBALDI, C. Linking climate change modelling to impacts studies: recent advances in downscaling techniques for hydrological modelling. *International Journal of Climatology*, 2007, Vol. 27, No. 12, p. 1547–1578.
13. TEUTSCHBEIN, C., SEIBERT, J. Is bias correction of regional climate model (RCM) simulations possible for non-stationary conditions? *Hydrology and Earth System Sciences*, 2013, Vol. 17, p. 5061–5077.
14. MAURAN, D. Bias Correcting Climate Change Simulations – a Critical Review. *Current Climate Change Reports*, 2016, Vol. 2, p. 2011–220.
15. AHMED, K. F., WANG, G., SILANDER, J., WILSON, A. M., ALLEN, J. M., HORTON, R., ANYAH, R. Statistical downscaling and bias correction of climate model outputs for climate change impact assessment in the U.S. northeast. *Global and Planetary Change*, 2013, Vol. 100, p. 320–332.
16. KERŠYTĖ, D., RIMKUS, E., KAŽYS, J. Near-term and long-term climate projections for Lithuania. *Geologija. Geografija*, 2015, Vol. 1, No. 1, p. 22–35 [In Lithuanian].
17. STONEVIČIUS, E., RIMKUS, E., ŠTARAS, A., KAŽYS, J., VALIUŠKEVIČIUS, G. Climate change impact on the Nemunas River basin hydrology in the 21st century. *Boreal Environment Research*, 2017, Vol. 22, p. 49–65.
18. GALVONAITĖ, Audronė; MISIŪNIENĖ, Monika; VALIUKAS, Donatas; BUITKUVIENĖ, Marija S. *Lithuanian Climate*. Kaunas: ARX Baltica, 2007. 207 p. ISBN 978-9955-9758-2-3 [In Lithuanian].
19. HO, C. K., STEPHENSON, D. B., COLLINS, M., FERRO, C. A. T., BROWN, S. J. Calibration strategies: a source of additional uncertainty in climate change projections. *Bulletin of the American Meteorological Society*, 2012, Vol. 93, p. 21–26.
20. HAWKINS, E., OSBORNE, T. M., HOA, C. K., CHALLINOR, A. J. Calibration and bias correction of climate projections for crop modelling: An idealised case study over Europe. *Agricultural and Forest Meteorology*, 2013, Vol. 170, p. 19–31.
21. GUDMUNDSSON, L., BREMNES, J. B., HAUGEN, J. E., ENGEN-SKAUGEN, T. Technical Note: Downscaling RCM precipitation to the station scale using statistical transformations – a comparison of methods. *Hydrology and Earth System Sciences*, 2012, Vol. 16, p. 3383–3390.
22. SUNYER, M. A., HUNDECHA, Y., LAWRENCE, D., MADSEN, H., WILLEMS, P., MARTINKOVA, M., VORMOOR, K., BÜRGER, G., KRIAUČIŪNIENĖ, J., LOUKAS, A., OSUCH, M., YÜCEL I. Inter-comparison of statistical downscaling methods for projection of extreme precipitation in Europe. *Hydrology and Earth System Sciences*, 2015, Vol. 19, p. 1827–1847.

CYSENI 2017, May 25-26, Kaunas, Lithuania
ISSN 1822-7554, www.cyseni.com

CLIMATE CHANGE IMPACT ON EFFICIENCY OF USAGE ROOFTOP RAINWATER HARVESTING SYSTEMS OVER THE TERRITORY OF UKRAINE

O. Shchehlov
Ukrainian Hydrometeorological Institute
Nayki prospect 37, 03028, Kyiv – Ukraine
E-mail: aleshcheglov@gmail.com

ABSTRACT

The efficiency of the usage rooftop rainwater harvesting systems is estimated for the climate conditions of the 21st century and the end of the 20th century in Ukraine. The balance model of water storage is used. The calculations are performed on actual daily precipitation data given by Central Geophysical Observatory at 146 meteorological stations in Ukraine. Based on the average water consumption and according to the constant water collecting area the water balance has been calculated for the three periods (1970–1984, 1985–1999 and 2000–2014). The simulation has been performed for time period from April to October using constant water storage volume of 5 m^3. The investigation has shown that roof area of about 50–70 m^2 is not economically viable for water consumption greater than 0.1 m^3 day^{-1}. In this case the water storage remains empty on average 20–23 days a month in the southern and eastern regions of Ukraine, in the western region – 15–18 days, in the Ukrainian Carpathians – up to 10–12 days. The roof area of about 80–100 m^2 and daily water consumption of 0.15 m^3 day^{-1} keeps preserving water storage from drying up to 50–60% of the days of month in southern and south-eastern regions and up to 70–90% in the west. Comparison of the water supply conditions in the 21st century to 1970–1984 and 1985–1999 periods has shown a deterioration of water supply conditions in the central, south-western and north-eastern regions. Here the index that shows the number of days with water demand exceeding rainwater supply (DES) has increased by 1–3 days a month. On the contrary, in the central-eastern region it has decreased by 1–2 days a month, probably due to the increase in daily precipitation rate but not the frequency of precipitation days. The water supply conditions have improved in the north-western regions by decreasing DES index by 1–2 days a month. The biggest changes have been observed during the time period from April to June.

Keywords: daily precipitation, climate changes, rainwater harvesting systems, water demand

1. INTRODUCTION

Humanity depends on the climate system which is undergoing significant change according to the recent Intergovernmental Panel on Climate Change (IPCC) report [9]. Some of these changes are connected with precipitation. Precipitation is a part of the hydrological cycle that serves as a water source for rivers and groundwater. The precipitation regime plays a vital role in ecosystem functioning. Moreover precipitation effect on life condition of humans. Therefore the precipitation change is a key issue. As we know humanity is trying to adapt to the environmental changes by achieving success in sustainable urban development and human settlements managing, as evidenced by the existence of the program UN-Habitat. One of the technologies focused on optimizing water consumption is a rooftop rain rainwater harvesting system (RRWHS). The issue of RRWHS has been raised in several studies [1–8, 16, 21–25]. There are no articles on the effectiveness of the systems in Ukraine. Obviously that the RRWHS technology is justified in regions with sufficient precipitation amount. The territory of Ukraine is characterized by moderate annual precipitation (400–700 mm on the plains) [10]. Therefore, the effectiveness of RRWHS is not obvious. Besides, installing RRWHS also needs assessing of it’s prospects due to the climate change and climate variability. For this purpose a consideration of the recent changes as well as climate forecasts is necessary. At the present stage the end of the summer season is becoming drier in Ukraine [11]. There are reasons to believe that the redistribution of precipitation is occuring during the warm period. Moreover, a rainfall extremity growth is observed in the central regions [12]. The regional climate models forecasts reveal uneven precipitation changes over the different parts of the Earth. According to the study [13] multi-model approach shows decreasing of precipitation in southern Europe. Based on regional climate models a decrease in precipitation is predicted for most of Ukraine. In [14] investigators came to conclusion about possible changes in precipitation over Ukraine: “cold season is becoming more humid; warm period is becoming dryer; the north-western region is better provided with precipitation but southeastern region is becoming more arid”.

2. PROBLEM FORMULATION

In this study two objectives have been set. The first is to estimate the efficiency of usage RRWHS over the territory of Ukraine at present stage. The second objective is to evaluate how great may be worsening or improving the performance RRWHS according to the observed precipitation changes. It is known that Ukraine is characterised by zonal distribution of precipitation, especially during the summer season [10]. Summer is a period of high frequency of dry days. In case of using RRWHS is equally important how often precipitation occurs in a given region and what intensity it is. The best way to evaluate the efficiency of rainwater accumulation by RRWHS is a simulation method based on balance approach [16]. To accomplish this the actual data of daily precipitation is used. It is important to set the same assumptions about identity of the roof construction in all points over the country. This assumptions includes the same roof geometry and material used for roofing. The area of the roof, apparently to be close to 100 m^2, and the runoff coefficient to be around 0.7–0.85 [16]. Various combinations of these parameters lead to different results. In practise a water storage volume is about 4–6 m^3.

The next step is to define the daily water demand for a particular household. According to the statistical data for the period 1970–2001 the average family size in Ukraine is 3.2 persons [15]. In [17] the average water consumption in Ukrainian for rural households is determined as 0.12–0.185 m^3 day^{-1} per 1 person. Hence, water consumption per household might exceed 0.4–0.5 m^3 day^{-1}. In practice, the rainwater inflow is sufficient only for limited number of needs, such as flushing toilets or watering lawns [16]. Usually it is one third or quarter of the total water consumption according to [17].

The winter period is characterized mostly by snow falling [10]. This fact is not convenient for simulating the performance of RRWHS. The liquid phase of precipitation is prevail during warm period, but in March and November days with snow possible. Therefore, period from April to October has been chosen in this study. All these justification has influenced on setting the initial parameters of simulation demonstrated in Table 1.

3. DATA AND METHODOLOGY

The main idea of the simulation is to calculate daily water balance in storage which contains rainwater for domestic use. Summing up the results for different periods (i.e. months, year, decade, etc.) helps to estimate how effective was RRWHS during this time. The process of accumulation/water consumption for the particular water storage can be given by the balance equation:

$$W_t - W_{t-\Delta t} + \Delta W = 0 \tag{1}$$

where W_t is the actual water level in the storage, $W_{t-\Delta t}$ is the water level at previous day, ΔW is the change of the water level which is given by:

$$\Delta W = kS\Delta r - \Delta o - q\Delta e \tag{2}$$

where k is the runoff coefficient, S is the roof area, Δr is the water inflow (actual daily precipitation), Δo is the water outflow (daily water demand), Δe is the daily evaporation rate, q is the area of the water storage.

There are several formulas to describe evaporation rate (i.e. Meyer's, Rohwer's or Penman equation) [20]. Assuming that the area of water storage is small ($q = 1$ m^2) and it is closed from sun radiation, it is obvious that $\Delta o >> \Delta e$. To avoid sophisticated calculations equation (2) has been simplified by removing the actual daily evaporation Δe by the average assessment which is given in [18]. Depending on month it is about 3-7 mm day^{-1}.

In our simulation the water storage volume (*Wmax*) has been set as 5 m^3. Based on the limited volume of the storage, there is a condition that actual water level *W* cannot exceed *Wmax:*

$$\begin{gathered} W_t = 0 \text{ if } W_t < 0 \\ W_t = W_t \text{ if } 0 < W_t < Wmax \\ W_t = Wmax \text{ if } W_t > Wmax \end{gathered} \tag{3}$$

The balance equation (1) has been simulated at each time step (one day). The period of simulation is 1970–2014. The calculations are performed on actual daily precipitation data given by Central Geophysical Observatory at 146 meteorological stations in Ukraine. Runoff coefficient, evaporation rate for each month were set as constants (Table 1).

Table 1. List of parameters used in the simulation

Constants	Variables	Time periods
Runoff coefficient, *k* – 0.75 Area of water surface in the storage, *q* – 1 m^2 Volume of the storage, *Wmax*– 5 m^3 Evaporation rate, Δe – 3–7mm day^{-1} (depending on month)	Roof area *S*: a) 50 m^2, b) 75 m^2, c) 100 m^2 Water demand, Δo: a) 0.15 m^{3}day^{-1}, b) 0.2 m^{3}day^{-1}, c) 0.3 m^{3}day^{-1}	April–October: a) 1970–1984 – 1st period b) 1985–1999 – 2nd period c) 2000–2014 – 3rd period

The effectiveness of RRWHS can be generally expressed either as the total time of demand exceeding actual rain water supply (DES) or the total time that water supply exceeding demand (SED). In this article the DES index is considered. DES is determined as the number of days with $W_t = 0$ during the base period. For better comprehension one months was chosen as a base time period. DES index has been calculated for each month during 1970–2014.To present results for April–October averaging of monthly DES indexes has been used. Appropriate operations were used for larger periods given in Table 1. Simulation has been performed on Visual Basic code written for this study. For building maps Surfer 8 was used.

4. RESULTS AND DISCUSSIONS

According to the Table 1, 27 different simulation results have been obtained. Two of them are presented in this paper: for S = 50 m^2 and S = 100 m^2 with water demand of 0.15 m^{3}day^{-1}. The DES index has been calculated for each year of the period 1970–2014. Only 5 of the 146 stations have shown significant trends at the 95% level. There are more significant trends in particular month. To analyze the effectiveness of RRWHS it is necessary to use the data of the whole period April–October. Thus, the trends for particular months have not been taken into account. Because of existence of precipitation periodicity applying of simple linear trends is a bad approach to estimate such changes [19]. Consequently, there are no reasons to speak of the long-period changes on a given time-scale 1970–2014, but we can consider the issue in terms of climate variability. The problem is that precipitation variability reveals asynchronously over a large territories. To represent how precipitation variability influences on the effectiveness of RRWHS we considered DES index by decades for the all territory of Ukraine. For each station the average value DES_{mean} and standard deviation σ_{DES} have been calculated. For each decade the number of exceeding $DES_{mean} + \sigma_{DES}$ have been calculated (Fig. 1). The total amount of exceeding the criteria (N_{DES}) has been examined for all the territory. The simulation has shown heterogeneity of N_{DES} index during 44-yr period (1970–2014). Fig. 1 shows the result of the simple moving averaging of N_{DES} and the coefficient of variation C_V (lag is 10 years). By 1984 low values of C_V (0.9–1.0) and low values of N_{DES} index (about 15–20 stations) are observed. In general during the 1980s N_{DES} index is high (N_{DES}>30 stations) as well as the coefficient of variation (C_V > 1–0). This fact may indicate heterogeneity of this period. Low N_{DES} values and high C_V values prevail after a decade 1987–1996. 1995–2004 and the subsequent decades are characterized by C_V values of about 0.8–0.9. Therefore, a change in precipitation is less severe. The increase of N_{DES} index is observed after the decade 1998–2007. In more recent years (2002-2011 decade and later) particularly high N_{DES} values are noted (35–55 stations). This fact indicates the drying conditions in recent years.

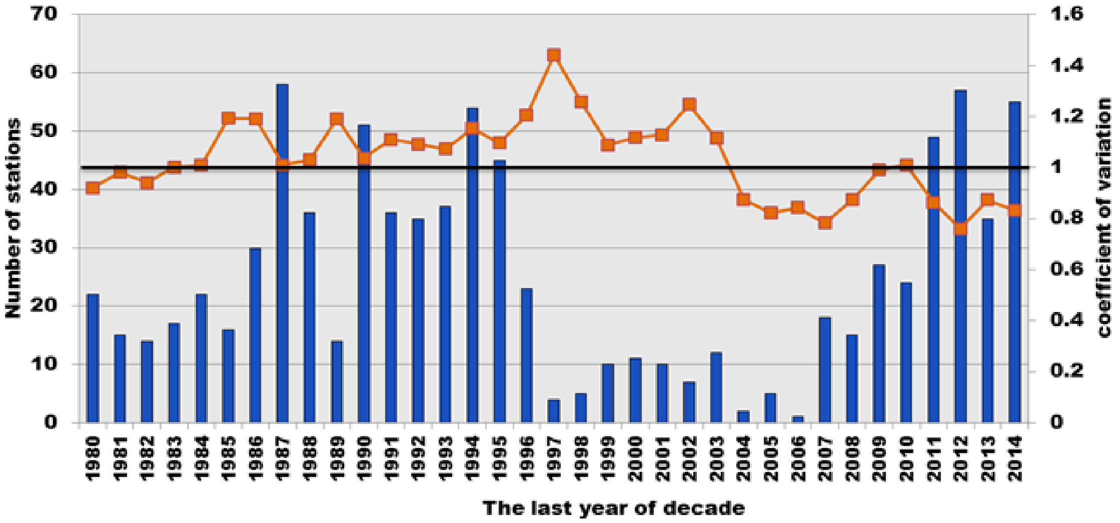

Fig. 1. Number of stations on which DES index > DES_{mean} + σ_{DES} by decades (April–October), coefficient of variation (line)

The period 1970–1984 is characterized by moderate precipitation variability and more favorable conditions for exploitation RRWHS. Moreover it is noted that in the end of the 20th century there is a tendency to worsening of rainwater supply conditions (as the high N_{DES} index combined with low C_V values have showed). Overall the 1980s and 1990s are characterized by different regimes of precipitation and variability. This time period should be considered as a transitional period. The performance of RRWHS during the transitional period is a quite interesting for our study. Thus, in the study we consider 3 periods: 1970–1984, 1985–1999 and 2000–2014 (1st, 2nd, 3rd periods respectively).

First, consider the spatial distribution of DES for the last 3rd period (2000–2014). The average monthly DES for the roof area of 50 m^2 (Fig. 2b) and 100 m^2 (Fig. 2a) are studied.

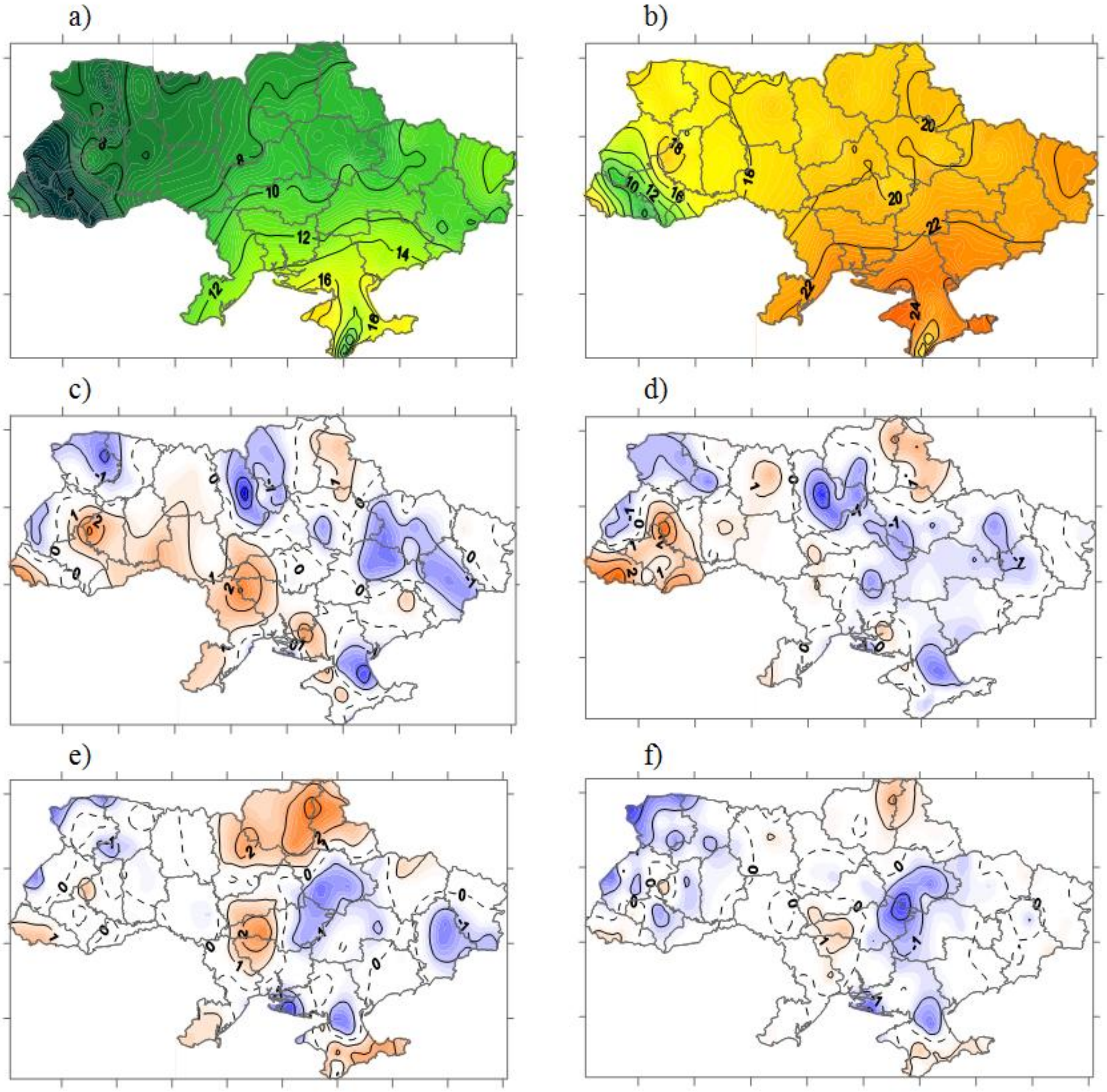

Fig. 2. Spatial distribution of DES index per month for roof area: a) S = 100 m^2, b) S = 50 m^2; DES anomalies for periods: c) 3rd minus 1st period for S = 100 m^2, e) 3rd minus 2nd for S = 100 m^2, : c) 3rd minus 1st for S = 50 m^2, e) 3rd minus 2nd for S = 50 m^2 (blue color – negative, red – positive anomaly)

Calculations have been made for the fixed water demand of 0.15 m^{3}day^{-1}. In both cases, the increase of the index is observed from the western parts of Ukraine towards the southeastern regions. Obviously, the smaller area of the roof, the lower rain water inflow to the water storage. For example, the roof area of 50 m^2 has a half days per month with a deficit of rainwater. An exception is the Carpathian Mountains region, where DES index is about 8–12 days. But even in case of a large roof area (100 m^2) with water demand of 0,15 m^{3}day^{-1} the rainwater deficit is within 8–15 days a month. Only the far western region of the country achieves DES values less than 5 days a month. A households in the Carpathians can fully meets itself water demand in case of constant daily water consumption. Obviously, the roof area of 50 m^2 is not valuable for RRWHS in the eastern and southern parts of Ukraine. It meets the water demand only for a third of the time period from April to October. Obviously, even the roof area about 100 m^2 is sufficient only to meet a limited number of water needs. Sensitivity of RRWHS performance to precipitation changes is proportional to the area of the roof. One of the possible ways to improve the performance of

RRWHS is to increase a water collection area. This can be realized by involvement surfaces of other facilities in a household. In case of roof area of 100 m^2 the simulation has shown that there is a significant frequency of days with $W = Wmax$. In the western region it ranges from 2 to 5 days a month; in the mountains it is up to 8 days a month. Thus, there is a possibility to increase the potential of RRWHS by increase the water storage volume. Assessment of the optimal volume of the water storage is a prospective objective for future studies.

Climate change impact on the efficiency of usage RRWHS is manifested through changes in precipitation regime. It is important to remember the distinction between climate changes and climate variability. As it has been described above some decades are more humid, some are less humid. In Fig. 2c–f the anomalies of DES index for respective periods (see Table 1) are depicted. In general, the changes between three periods vary in different regions. For most of the territory the changes of DES index vary between -2...2 days a month. Besides, for most of the territory changes in sign of DES anomaly are not the same for 1st and 2nd periods. Territories that demonstrates the same positive or negative anomaly (more then 1 day) are shown in Fig. 3. Saving of the anomaly sign relative to the both prior periods indicates the features of modern 2000–2014 period. These features are considered in the first approximation as climate changes. It is important to notice that regions highlighted might not show significant linear trends. But saving of negative (positive) anomalies in comparison with two previous periods (1985–1999 and 1970–1984) may indicate increasing of wet (dry) day frequency. This means improving (worsening) of the efficiency of RRWHS. There are four areas where anomalies of DES index are negative: 1) noth-western region, 2) central and eastern region. Also there are areas where anomalies are positive for both previous periods: 3) northeastern region, 4) central region, 5) southern region, 6) southwestern region, which corresponds to Transcarpathian Lowland (Fig. 3).

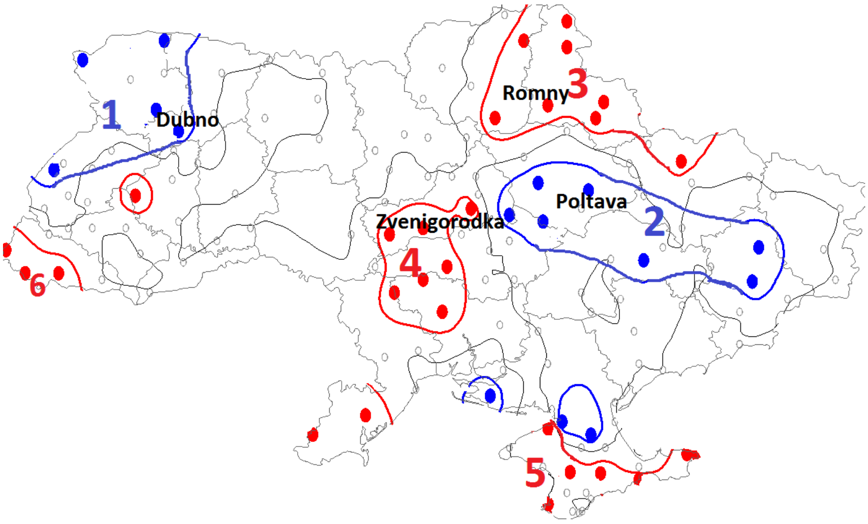

Fig. 3. Regions with the same anomaly sign for 1st and 2nd period: red borders: positive; blue borders – negative sign

Those changes discussed above are different during a year. Fig. 4 shows the monthly DES indexes and related anomalies for the stations that are typical for regions depicted in Fig. 3. Rain water supplying conditions for RRWHS during the months of the warm season are not stable. The most unfavorable conditions observed in April and May. For this period of year, water outflow exceed inflow during more than a third of time. In contrast, the best conditions are inherent for the summer season. All of the stations are characterized by a minimum of DES index in July. Moreover, the water demand in western region is almost provided by rain water during the summer. Here changes of DES index are about 1–2 days (Fig. 3b). In the 2nd period this region is characterized by anomalies of DES index of about 2–6 days a month during April-August. In the first period anomalies are less considerable in the region. In the central zone (Zvenyhorodka) a positive anomaly of DES index is marked in each months from April to September (Fig. 3a). In the eastern region the rain water supplying conditions are becoming drier in spring and improving from July to October (Fig. 3c). Given the presence of significant trends in extreme rainfall in Poltava [12] we suggest that decreasing of DES index also is caused by this factor. Northeastern region is characterized by increasing of DES index from April to June by 1–3 days a month (Fig. 3d).

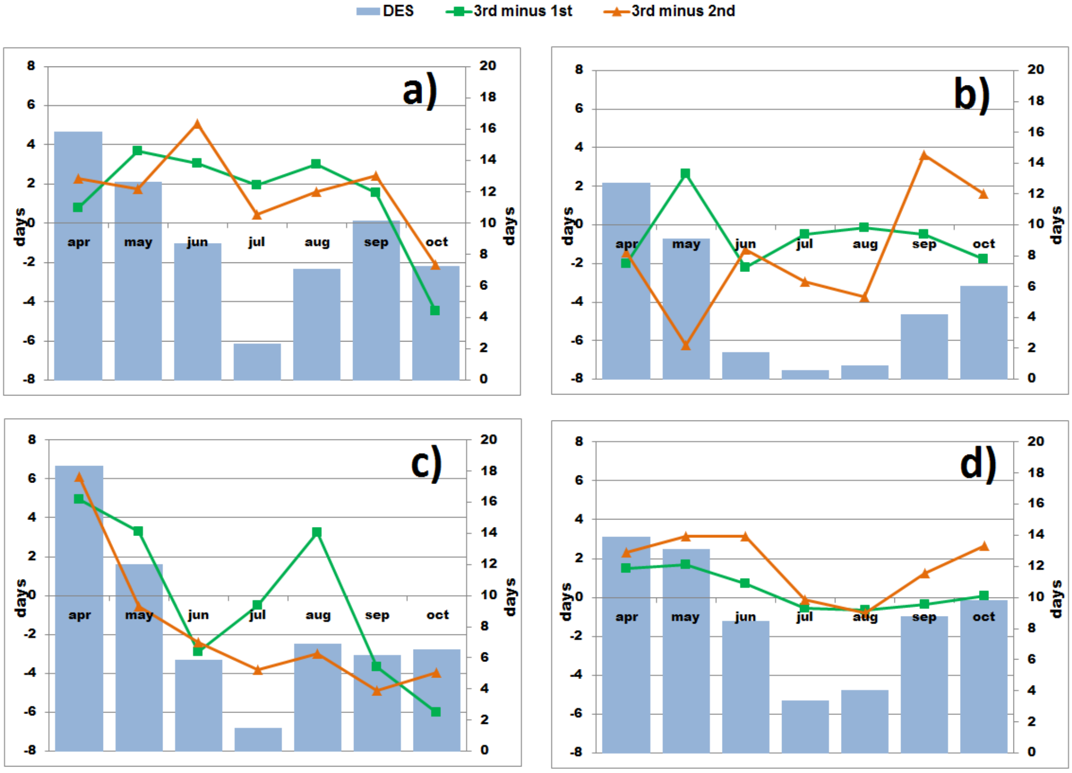

Fig. 4. DES indexes for 3rd period 2000–2014 (right axis) and anomalies: 3rd minus 1st and 3rd minus 2nd period (see Table 1) for S = 100 m^2: a) Zvenigorodka; b) Dubno; c) Poltava; d) Romny station

5. CONCLUSIONS

1) The efficiency of using RRWHS for domestic use can be represented as number of days when the rainwater demand is provided by rainwater inflow into the storage. In this study effectiveness of RRWHS was determined the for the modern period 2000–2014 using DES index. The effectiveness depends on the roof area.The investigation has shown that roof area of about 50 m^2 is not economically viable for water consumption greater than 0.1 m^3 day^{-1}. In this case the water storage remains empty on average 20–23 days a month in the southern and eastern regions of Ukraine, in the western region – 15–18 days, in the Ukrainian Carpathians – up to 10–12 days. On an average, the roof area of about 100 m^2 with an average water demand of 0.15 m^3 day^{-1} keeps preserving the water storage from drying up to 50–60% of the days of a month in southern and south-eastern regions and up to 70–90% in the west of Ukraine.

2) Climate change impact on the efficiency of usage RRWHS is manifested through the changes of precipitation regime. Because of large precipitation variability, the efficiency also changes. The greater is the area of the roof, the more sensitive is performance of RRWHS to precipitation changes. There are three periods with different precipitation regimes were found (1970–1984, 1985–1999 and 2000–2014). These differences determines the performance of RRWHS. But in general, from April to October the most of the territory is characterized by approximately stable DES values in each of three time periods. For the last 15 years, six highlighted regions demonstrate specific features in comparison with previous 30 years. There are four areas

where anomaly is negative: north-western region, central-eastern; and four regions with positive anomalies: northeastern, central, southern and southwestern region. In the northeastern and central regions water supply conditions for RRWHS is worsening especially in the spring. In the eastern region improving of conditions has occurred in the summer. In the north-western region conditions have improved in the spring and early summer. Comparison of the water supply conditions in the 21st century with 1970–1984 and 1985–1999 periods has shown a deterioration of water supply conditions in the central, south-western and north-eastern regions. Here DES index has increased by 1–3 days a month. On the contrary, in the central and north-eastern regions it has decreased by 1–2 days a month, probably due to the increase in daily precipitation rate but not the frequency of precipitation days. The water supply conditions are improved in the north-western regions by decreasing DES index by 1–2 days a month. The biggest changes are observed during the period from April to June.

REFERENCES

1. SAZAKLI, E., ALEXOPOULOS, A., LEOTSINIDIS, M., Rainwater harvesting, quality assessment and utilization in Kefalonia Island, Greece. *Water Research,* 2007, 41 (9), 2039-2047.
2. PACEY, A., CULLIS, A., *Rainwater Harvesting: The Collection of Rainfall and Runoff in Rural Areas, London, UK.* 1989.
3. POLKOWSKA, Z., GO´ RECKI, T., NAMIESNIK, J., Quality of roof runoff waters from an urban region (Gdansk, Poland). *Chemosphere,* 2002, 49, 1275-1283.
4. FARRENY, R., GABARRELL, X., RIERADEVALL, J., Cost-efficiency of rainwater harvesting strategies in dense mediterranean neighbourhoods. *Resources, Conservation and Recycling,* 2011, doi: 10.1016/j.resconrec.2011.01.008.
5. GHISI, E., TAVARES, D.D.F., ROCHA, V.L., Rainwater harvesting in petrol stations in Brası´lia: potential for potable water savings and investment feasibility analysis. *Resources, Conservation and Recycling,* 2009, 54, 79-85.
6. KIM, R.-H., LEE, S., KIM, Y.M., LEE, J.H., KIM, S.K., KIM, J.G., Pollutants in rainwater runoff in Korea: their impacts on rainwater utilization. *Environmental Technology,* 2005, 26, 411-420.
7. SIMMONS, G., HOPE, V., LEWIS, G., WHITMORE, J., GAO, W.Z., Contamination of potable roof-collected rainwater in Auckland, New Zealand. *Water Research* 2001, 35 (6), 1518-1524.
8. VILLARREAL, E.L., DIXON, A.,. Analysis of a rainwater collection system for domestic water supply in Ringdansen, Norrkoping, Sweden. *Building and Environment* 2005, 40, 1174-1184.
9. *IPCC, 2013: Climate Change 2013*: The Physical Science Basis. Contribution of Working Group I to the Fifth Assessment Report of the Intergovernmental Panel on Climate Change [Stocker, T.F., D. Qin, G.-K. Plattner, M. Tignor, S.K. Allen, J. Boschung, A. Nauels, Y. Xia, V. Bex and P.M. Midgley (eds.)]. Cambridge University Press, Cambridge, United Kingdom and New York, NY, USA, 1535 pp, doi:10.1017/CBO9781107415324.
10. *Клімат України* / За ред. В.М. Ліпінського, В.А. Дячука, В.М. Бабіченко. – Київ: вид-во Раєвського, 2003. 343 с.
11. МАРТАЗИНОВА В.Ф., ИВАНОВА Е.К., ЩЕГЛОВ А.А. Тенденция современного температурно-влажностного режима Украины к аномально сухим и знойным атмосферным процессам в летний сезон. *Наук. пр. УкрГМІ*, 2016, Вип. 268, С. 15-24.

12. ТИМОФЕЄВ В.Є., ЩЕГЛОВ О.А., ТАТАРЧУК О. П. Деталізація багаторічної зміни атмосферних опадів у літній сезон. *Вісник Київського ун-ту. Серія геогр*, 2012, Вип. 60, С. 30-33.
13. MEEHL G. A. et al. *Global climate projections*. 2007.
14. *Розроблення сценаріїв зміни кліматичних умов в україні на середньо- та довгострокову перспективу з використанням даних глобальних та регіональних моделей*, 2013, [Електронний ресурс]: <http://uhmi.org.ua/project/rvndr/climate.pdf>
15. *Перший Всеукраїнський перепис населення: історичні, методологічні, соціальні, економічні, етнічні аспекти*. – К.: ІВЦ Держкомстату України, 2004, С. 395.
16. LIAW, C.H., TSAI, Y.L., Optimum storage volume of rooftop rain water harvesting systems for domestic use. *Journal of the American Water Resources Association*, 2004, 40, 901-912.
17. СТАСЮК С. Р., ХОРУЖИЙ П. Д. Нормування господарсько-питного водоспоживання в системах сільськогосподарського водопостачання. *Меліорація і водне господарство*, 2014, Вип. 101, С. 97-105.
18. КОНСТАНТИНОВ А.Р. *Испарение в природе*. – Л.: Гидрометеоиздат, 1968, 531 с.
19. WILLEMS P. Multidecadal oscillatory behaviour of rainfall extremes in Europe. *Climatic Change*, 2013, Т. 120, №. 4, p. 931-944.
20. SINGH, V. P., AND C. Y. XU. Evaluation and generalization of 13 mass-transfer equations for determining free water evaporation. *Hydrological Processes*, 1997, 11.3, 311-323.
21. NNAJI, C.C., EMENIKE, P.C. & TENEBE, I.T. An Optimization Approach for Assessing the Reliability of Rainwater Harvesting. *Water Resour Manage*, 2017, 31, 2011. doi:10.1007/s11269-017-1630-9.
22. CAMNASIO E., BECCIU G. Evaluation of the feasibility of irrigation storage in a flood detention pond in an agricultural catchment in Northern Italy. *Water Resour.] Manag*, 2011 25(5), 1489-1508.
23. CAMPISANO A., MODICA C. Selecting time scale resolution to evaluate water saving and retention potential of rainwater harvesting tanks. *Procedia Eng*, 2014, 70, 218-227.
24. RAHMAN A., KEANE J., IMTEAZ MA. Rainwater harvesting in greater Sydney: water savings, reliability and economic benefits. *Resour Conserv Recycl*, 2012, 61, 16-21.
25. ŞEN Z, ALSHEIKH AA, AL-TURBAK AS, AL-BASSAM AM, AL-DAKHEEL AM. Climate change impact and runoff harvesting in arid regions. *Arab J Geosci*, 2013, 6(1), 287-295.

CYSENI 2017, May 25-26, Kaunas, Lithuania
ISSN 1822-7554, www.cyseni.com

ENERGY TRANSITION IMPACT ON LIQUEFIED NATURAL GAS (LNG) SECTOR

Jurgita Lunytė
University of Oslo
Blindern, 0313 – Norway
E-mail: j.lunyte@gmail.com

ABSTRACT

The liquefied natural gas (LNG) industry counts over 50 years. Yet, over the last decade, this sector has rapidly changed. Energy transition has affected each of the energy sectors, and LNG is not an exception. The LNG industry has faced a major transformation and recently has become more dynamic, depending on the core pillars – adaptability and flexibility. The purpose of this paper is to investigate the effect of changing market conditions on LNG contracts and to analyze how these contracts operate in the current LNG market. The impact of energy transition on the LNG sector is presented accordingly to the cross-cutting LNG markets (Europe, the US and the Asia-Pacific regions). The mechanisms, such as the price provision and destination flexibility that should be adjusted and introduced in the contracts in order to adapt to the current energy market environment, are examined. First, the price keeps being a threshold issue of LNG, but with a significant change in pricing methodologies. The altered pricing mechanisms, such as gas supply and demand pricing methodologies rather than oil-indexed pricing, are indispensable for dynamic LNG markets. Second, the diversion right has been newly introduced to the LNG industry contrary to the previously favored destination restrictions. A reference to a case study of the new generation Klaipėda LNG terminal – as a successful example how these measures have been implemented – is indicated. The results of the paper demonstrates that the LNG sector is a complex issue inherent from the energy transition impact. Nevertheless, the parties are able to address the market volatility within the means of contractual terms. New expectations on LNG industry – particularly the concept of flexibility in adjusting to the market – have led to adopt novel regulatory approaches to solve the world's next energy challenge.

Keywords: LNG, pricing mechanisms, destination, dynamic market, Klaipėda LNG terminal

1. INTRODUCTION

In the event of falling world oil prices in mid-2014 and signed the historic Climate change agreement in Paris an energy transition is underway, reports the International Energy Agency (IEA) [1]. According to the 2015 World Energy Outlook (WEO), the world energy demand is to grow by one-third between 2013 and 2040 [2]. Liquefied natural gas (LNG) accounts for up to 24% of the global energy mix, predicting to grow at 2% per year until 2020 [3]. The energy diversification in terms of energy sources and suppliers remains one of the main pillars in the European Union (EU) policy [4]. "Europe needs to get back on the map when it comes to LNG", says Arias Cañete EU Climate and Energy commissioner [5].

The LNG market is dynamic and constantly developing. Geo-political, social, environmental and economic factors are the impediments of re-shaping LNG industry [6]. Parallel to the growth of the LNG market, the LNG contracts have over time developed their own distinct features and have become more flexible against uncertainties and market fluctuations. The dynamic nature of LNG industry is challenging the terms of LNG contracts. New expectations of law – particularly the concept of flexibility in adjusting to the market – have led to adopt novel regulatory approaches and legal forms to solve the world's next energy challenge [7]. Two the most significant contractual provisions – price provisions and diversion rights – are the ones by which buyers and sellers can provide more flexibility in LNG market disturbance [6].

The article is based on the key concepts: flexibility and dynamic market. Taking into the account that there are neither strict nor legally binding definition of the concepts mentioned above, the article questions how these concepts may be applied within the scope of LNG. Admitting that the dynamic market and flexibility *per se* depend on respective gas markets (e.g. Asian LNG market, the US LNG market, European LNG market percieve these concepts differently), the article chose the general definition to follow the research. The key concepts in the article are defined as following. *Dynamic market* encompasses new LNG players, increased LNG supply and changed market conditions. *Flexibility* is perceived as a principle on which the composition of modern LNG contract is structured; as contractual mechanisms developed in time, such as price and destination flexibility clauses, which are enshrined in contracts for the purpose to deal with the value risks associated with the dynamic markets. In the context of diversion clause, flexibility is perceived as the ability to change the contract parties – buyers and sellers – without terminating the primary agreement [8].

The purpose of this work is to investigate the effect of the changing market conditions on the long-term contracts. It has also been examined what legal mechanisms should be adjusted and introduced in the contracts in order to adapt to the current energy market environment.

The article is structured into five sections. First, the article investigates the dynamic LNG market with specific focus on the pricing clause and destination clause. The key term *flexibility* explains how these clauses adapted to the changing market. Second, the article analysis the pricing mechanisms. Pricing provisions keep to be a threshold issue of the LNG contracts but with a significant change in pricing methodologies. For, instance, oil-linked pricing became uncompetitive in comparison to the hub-based pricing adaptation in gas markets. Third, the article examines the diversion clause which is a new term introduced. The findings of the article indicate that certainty in LNG market is far from the rule, fixed terms are not efficient as it used to be. As a result, the LNG players – the sellers and the buyers – require more flexibility. In other words, the parties are looking for the ability how to adjust LNG contracts in the event of changed environment. The reflection of this trend is clear on the recently signed contracts. In the final chapter the case study of a present-day contract demonstrates the LNG law trends. This is an example of *Statoil-Litgas* contract. Lithuania has built the LNG terminal *Independence*, which brings competition to the Lithuanian gas market and increases the energy security of the whole Baltic region as a consequence of a signed gas contract with Norway.

1.1. Methodology

The research is fulfilled using such research methods as descriptive method, comparative method, legal method and scientific method.

The descriptive method. This research method is used to present the research instruments and to define the main concepts of the article.

Comparative method. Comparative method is used to compare the data and to assess the LNG market. The article analyzes the different market regions and identifies applicable jurisdictions respectfully.

Legal method. The price and destination provisions differ accordingly to the regions and the governing law (civil or common law systems). The research is based on the LNG contracts, which are regulated by the international commercial law and contract law.

Scientific method. The research has been undertaken using the scientific method. This method allows forming the conclusions based on the reliable data. The specific questions addressed stem from the general research investigation: how the energy transition has effected the LNG industry from the market perspective.

This work is premised on the view that the LNG contracts should possess flexibility to respond to the changing market conditions in order to remain efficient. The research questions are as following: whether the LNG contracts are capable to operate throughout market fluctuations; whether flexibility can ensure the longevity of LNG contracts and what contracts forms satisfy the parties today. The specific questions addressed in the paper stems from the general research investigation: how the energy transition has effected the LNG industry.

2. LNG ON THE GLOBAL SCENE

2.1. The Concept of Dynamic Market Today

The *dynamic market* is considered to be a sum of global energy events that have an impact on the LNG industry. The stability of the natural gas industry was triggered in 1990 when an important development occurred as new players joined the LNG market: exporters in Qatar, and importers in Turkey and Greece [9]. Moreover, the gas supply has increased due to the rise of the US exports to Europe. Therefore, in 2015 global LNG trade was increased by 2.5% and 24 new contracts reported to be signed [3]. Consequently, the long-term contracts were substantially amended, especially the price provisions, which were the most affected by the market [9]. Bud Coote identified the effects of US exports on global LNG market: first, it shapes dynamic energy market and continues to unify regional markets into one global market; second, it introduces more flexible contractual terms that help importers to negotiate prices with other gas suppliers [10]. Coote claims that over longer term the prevelance of oil-indexed pricing is going to dimish [10]. The LNG imports from the US have influenced the Asian market as well as their traditional contracts [11]. In Asia long-term contracts are traditionally Japanese Crude Cocktail (JCC) linked. Under JCC contracts the LNG price is indexed on the crude prices. The Petroleum Association of Japan calculates JCC index from the most traded top twenty crude oils by volume. Though the recent trend is that the Asian buyers are moving away from oil-indexation to hybrid pricing terms in order to distribute the risks. Under the hybrid pricing the LNG price formula has several components: the oil product index, gas-indexed component and hub pricings [12]. Generally, in other LNG markets a price term shifted to gas hub or hibrid indexation. Furthermore, due to the change in LNG supply and demand, the spot and short-term contracts have grown substantially since 2000 [13]. Spot contracts are the agreements for immediate sale/purchase of the commodity. The spot price is the key driver of LNG flow and LNG players decisions on cargo diversions. Spot trading time-cycle are days while short-term contracts are fixed term contracts for a period ranging from one year to fifteen years. Practitioners identify two market-related and regulatory-related causes that lead towards shorter contract terms [14]. Regulatory impact on long-term contracts occurs through the Government as long-term contracts often have a state element (in)directly [15]. This can have an adverse impact on the long-term contracts due to the changes in the law [15]. Only in 1970s during the energy crisis the laws were passed to regulate the natural gas price [14]. Today the gas prices are regulated by supply and demand, known as the *market value principle* [16]. That is why the dynamic LNG market – not legal regulations – influences the changes on contracts and have accordingly changed the LNG contracts.

Looking back to the LNG evolution, the LNG market has transferred from the region to international patterns. This gave rise to the modification of LNG framework. Based on the analysis above, the effects of transition are twofold: substantial and formal. First, the dynamic market has invoked the demand for the different sophisticated clauses in LNG contracts. The new contractual provisions, in comparison to the old ones, feature more flexibility in terms of pricing and destination clauses, provide wider opportunities for renegotiation contractual provisions before taking the dispute to the arbitration. Second, despite the fact that the long-term LNG contracts continue to evolve toward offering the increased flexibility (e.g. through contractual provisions), such long-term LNG contracts are expected to decline in the years ahead. Additionally, the increased short-term supply contracts are predicted to take the place.

To conclude, today's LNG dynamic market are influenced by the price clause, the buyer's downstream gas market and its alternative fuels, flexibility in terms of the delivery point, regulation of gas competitors, commercial and political risks [9].

3. PRICE PROVISION

3.1. Price Formation

The symbolic beginning of LNG industry is marked by a 15-year contract between British Gas and Compagnie Algerienne signed in 1961. The price clause *per se* has been started to use basically after the 1973 Oil Crisis. To sum up, in the early days of LNG trade the obligation to purchase the quantity was enough to conclude the contracts, contrary to the current contracts whereas the price clause is a fundamental brick of the contract. Considering that a price clause is a complex area of politics, economics and law, energy security as a policy objective can be the determinant in pricing negotiations – not a price provision itself. Thus, the cases do exist where the issue is the politics on negotiating the price clause rather than a price *per se* as a key pillar in the gas contracts.

At the very beginning of LNG trade, before the pricing mechanisms were based on indices, particularly oil-linked [17], a floor price was included to protect investors from price collapse [18]. Later the floor prices were supported with a crude linked pricing mechanisms that "softened LNG price increases in high-oil-price environments providing a more stable LNG contract pricing mechanism [18].

Before discussing the market effect on the price clause, it may be useful to examine the structure of the price clause. In the long-term contracts the parties used an indexation-based pricing formula – an example of the price formula (1) by linking the price to the other comparable energy sources [24]:

$$P = P1 \times [(f \times An)] \tag{1}$$

P – price; *P1* – the defined base price with the application of the product of (f) (the parties fix a base price which is a product of negotiation according to the commercial circumstances of the particular transaction); *f* – application of the product; *An* – the arithmetic average movements on a particular reference price (A) over defined review period (n); (The base is adjusted over time accordingly to the movement of a nominated index.)

Alternatively, a formula (1) could include more than one index: the more indexes are included, the less sensitive is the price to the periodic movement of any index [24]. Thus, a wide selection of the indices ensures stability but the complexity of the price formula increases accordingly. In addition to the choice of the indices, the parties decide the percentage weightings of each index [9]. The primary purpose of indexation was to make contract parties satisfied throughout the fluctuating market during the lifetime of the LNG contract [9]. It is important to note how the price formula is constructed because the arbitrators review the price clause by adjusting the percentage or/and indices. In addition to this, it is important for the contract to provide a different pricing structure in the event of gas resale in to the other markers. For example, under the contract between Atlantic LNG and Gas Natural, the price clause was very standard and in this case it was a flaw [42]. When Gas Natural faced the difficulties, the contract contained a resale clause, which enabled the party to avoid the unprofitable market and to resell the gas to the US. market [42]. Unfortunately, the price clause did not introduce the pricing structure for resale, regardless the resale clause itself. Thus the same price based on European market applied for the LNG sold in both markets – Europe and the US. To conclude, this example indicates the importance of constructing a price formula and providing different pricing structures in the event of resale or divert in other markets (provided a contract allows reselling).

Apparently, the price formation received the attention of the sellers and buyers after being affected by the changed energy market. Only when the traditional business model began to fail, the price formation became a crucial issue [43].

3.2. The Market Effect on Price Clause

The price term in gas contracts is based on two fundamentals: economic (cost of delivery and operation) and market (competing fuels in the market, degree of competition from other suppliers) [43]. The market fundamental is important due to the simple reason that the market changes are directly responsible for the LNG pricing. According to Japan's trade minister, the global shale gas production from the US has caused a "paradigm shift" in LNG pricing encouraging the LNG players to replace oil-linked indexing to the new pricing mechanisms. The new pricing mechanisms – gas supply and demand pricing methodologies – have been introduced and become the principal metric for gas prices in the period of 2014–2015, and predicting up to 2030 [12].

Furthermore, the world faced the collapse in oil prices in 2014–2015. Thus, is there any impact of the fall in crude oil prices on LNG long-term contracts? In Europe the linkage between oil product prices and long-term gas contract prices discontinued after the oil drop. First starting with Norway: producer Statoil moved away from oil product indexation towards hub indexation [12]. As a consequence, imports from Norway rose 12%, while imports from Gazprom fell 10% as Russia's gas prices remained linked to oil prices [44]. Today, the majority of contracts in Europe in the case of delivery to the UK are linked to the NBP (Great Britain's natural gas exchange) index and the US contracts are mostly linked to the Henry Hub index [45]. In Europe, more than 60% of gas sold is based on hub prices, while the majority of long-term Asian LNG contracts remain based on an indexed pricing to crude oil [12]. Overall, the data suggests the shift from the indexation system to the new price formation contract structures. Alternatively, the LNG contract may apply a hub-price mechanism, which is undependable on the other fuels.

The obvious need to move from oil indexation to new contract price formation structures unveils the other key uncertainty – the price formation of future LNG contracts. To what extent the hub prices will take the dominant position in the market. According to Hartley's study report, there are several changes in the LNG market that led to the decline of long-term contracts[46]. These factors are: changes in average spot prices, changes in the variability of spot prices, effects of increasing spot market liquidity. The market fundamental also adjusted the long-term contracts. These factors are the triggers to the LNG pricing determination.

To conclude, the changed energy geopolitics[1] shows that the gas market and oil market have distinguished and these changes are reflected in the legal practice. This difference is reflected in the current LNG contracts since the tendency is the gas prices *decoupling* from the price of oil. Moreover, the price formation can help to adjust the contract price to the changing market conditions. The parties when negiotiating the LNG contracts have to consider which pricing mechanism match the market fundamental the most: index pricing, a spot gas index or a hub price.

4. DESTINATION CLAUSE VS DIVERSION CLAUSE

The diversion clause, which is defined as a contractual right for the buyer to divert LNG cargoes to re-gasification facilities at other destinations under certain circumstances, is a new trend in today's LNG contracts. In fact, this clause did not exist until 1990s only when the LNG supply chain introduced the buyers operating on Free on board (FOB) basis, which requires the seller to deliver goods on board designated by the buyer [19]. This arrangement provided more flexibility for the long-term buyers in managing LNG supplies [18]. Otherwise, the destinations restrictions were a standard clause in early contracts. Such restrictions existed mostly due to the practical reasons: transportation limitations and location. Although very few contracts provided exceptions to alter the scheduled destination, called *emergency need request*: "the seller in its discretion agrees to change the place of delivery to another port in the same country as the buyer" [9]. Much greater destination

---

[1] Common rationale for oil linkage: gas was developed along to oil industry; many gas exporters were also oil exporters; gas was replacing oil products. Source: http://eneken.ieej.or.jp/data/4817.pdf

flexibility appeared in 2001–2002. Under the pressure of the European Commission (EC) and due to the increased LNG supply to Europe, the diversion clause is now included in almost every contract [9]. Thus, the removal of destination restrictions has introduced more flexibility in the LNG contracts.

Jérôme Ferrier, the President of International Gas Union (IGU), stated that the standard destination clauses in long-term LNG contracts, which restrict where cargoes can be unloaded and prevent buyers from reselling excess LNG, could soon be absent in LNG contracts due to the shale revolution in the US market [20]. The most obvious disadvantage of the destination clauses is that these provisions prevent buyers from reselling cargoes or taking delivery outside their home country, restrict arbitrage and limit trading opportunities in spot markets [21]. The buyers claim that the destination clause impose un unjust trade restriction [20]. At the fourth annual LNG Producer-Consumer Conference in Tokyo the focus was on the restrictive terms on LNG delivery schedules and destinations; the LNG market participants called for increased flexibility in contracts [22]. According to the experts, the removal of destination clauses is necessary to manage the emerging LNG supply surplus [22]. In 2015, two of the largest utilities[2] in Japan declared thay they no longer sign contracts that restrict reselling cargoes by limiting the destination of shipments they buy [23]. Petronet LNG's Chief Executive admits that the increasing supply offers better contractual terms that range from an attractive price to destination flexibility clauses and short-term contracts [21].

For the LNG buyers operating the purchasing the LNG on FOB basis this arrangement provides more flexibility regarding the delivery point in managing LNG supplies under the long-term contracts. Delivery point or delivery as specified in the LNG contracts is the point at which seller's obligation to deliver LNG to the buyer is affected; it is the pivotal point connecting the upstream and downstream interests [24]. The delivery point is defined as a precise geographical location and the buyer's gas reception facilities. [24] Generally, it is a standard clause whose the most common two formulations have derived from the International Chamber of Commerce's Incoterms. Under the first formulation FOB (free on board) the seller delivers goods to the buyer when the goods pass the ship's rail at the named port of shipment [25]. In the LNG contract context the FOB term means that the LNG is placed in the custody of a seller until the point of interconnection between the buyer's LNG ship and seller's loading facilities. Another formulation DES (delivered ex ship) means that the seller delivers goods to the buyer at the named port of destination. Therefore, in the new edition of Incoterms DAT (delivered at terminal) introduced *terminal* as a place of destination. LNG remains the property of the seller until the delivery to the named port of destination [26]. Thus, DES formulation is preferable among the sellers due to the provided control and freedom over the LNG shipping. It gives the opportunity to implement a diversion clause in LNG contracts. Equally, a buyer prefers the FOB term. In practice, the parties do not incorporate plain DES or FOB formulations, instead, the parties negotiate the destination diversion clause, which is defined as "a contractual right for the buyer to divert LNG cargoes to re-gasification facilities at other destinations under certain circumstances" [27]. For instance, in the context of DES, a diversion clause may include a mechanism that provides a compensation to the seller for any additional costs of the diversion and which provides a potential allocation of profits associated with the diversion [27]. The Master Sales and Purchase Agreement (MSPA) is a new regulatory form which embodies flexibility so much needed for the buyers (FOB) and by sellers (DES) to operate in spot markets. Only the parties have to sign a memorandum of understanding (MoU), which is attached to the MSPA and which sets the commercial terms applicable to a specific cargo, in order the purchase and sales of cargoes go into effect [28]. The MSPA looks for a balance between the buyer's and seller's interests, and intends to be sufficiently flexible to be used for trades in any geographical region [27]. MSPA capability to provide such flexibility is analyzed in the case study below.

---

[2] Jera Co., a joint venture created by Tokyo Electric Power Co. and Chubu Electric Power Co.

5. CASE STUDY: NORWAY – LITHUANIA

5.1. Comparisons – the first LNG terminal in the Baltic States

The purpose of this chapter is to reflect the changes in the provisions of contracts on the specific case – an agreement between Statoil and Litgas. Lithuanian gas supplier Litgas signed a five-year contract with Statoil ASA to deliver 540 million cubic meters of LNG annually from 2015 [29]. The LNG terminal Independence is leased from Höegh LNG with an option of buyout and is based on the Floating Storage and Regasification Unit (FSRU) technology[30]. “This vessel is the first one in the world to have the FSRU technology deployed from start to finish“, said Støhle, Höegh LNG CEO [31]. Due to its novelty, significance and distinctiveness this case is a good example of presenting the current LNG trends incorparted in one contract. LNG project is a complex issue. For instance, it covers the political aspects of energy security, the economic aspects of energy diversity, the legal aspects of the price clause and destination provisions, the flexibility issue of applying MSPA as a legal instrument for LNG deal, developing the LNG trends in terms of creating hub trade, spot market and promoting new FSRU technology. These elements, introduced below, are inherent to Independence.

5.1.1. The Price Provision

The contract price is linked to the NBP index [32]. Under this type of pricing the contract price depends on the changes in the supply and demand for natural gas, including LNG on the international markets [33]. Litgas CEO said that: “Linking to natural gas indices is a common practice in North Western Europe which makes it possible to abandon the indexation of natural gas prices to oil prices which dominates in Eastern Europe and often results in natural gas prices that have no relation to the ones prevailing in the rest of Europe” [33]. Thus, this contract reflects the tendency of unlinking gas prices from oil in current international long-term supply contracts. The contract ensures continuity and establishes “a new natural gas pricing policy linked to the natural gas price movements on the international markets“ [33].

In addition to this, in January 2016 the negotiations between Statoil ASA and Lithuania was held that lead to the amendment of the contract and the price was adjusted [34]. Under the new contract terms the price was reduced by 15–20%, the pricing formula was amended by linking the LNG prices closer to the natural gas prices supplied by pipeline and the duration of the agreement had been extended from five to ten years and it coincides with the duration of the leasing agreement of FSRU [34].

5.1.2. Destination Flexibility

Due to the provided flexibility in the contract, the contract enshrines a possibility of LNG reloading which would be a new commercial activity in the Baltic Sea region starting from 2017 [35]. The contract between Litgas and Statoil enables the parties to cooperate on joint development of small scale LNG supply [36]. Following the agreement the two companies signed MoU in 2015 regarding the establishment of a joint venture company to supply small scale LNG [37]. A small scale market in the Baltic Sea is potentially attractive business opportunity therefore this contract marks the first step with LNG business in the Baltic Sea region, says Heitmann, vice president of Statoil LNG Trading and Operations [37].

5.1.3. LNG Master Sale and Purchase Agreement

MSPA is a novel model agreement which provides a defined framework for the parties reliant on short-term transactions. This legal tool is beneficial for the both parties acting in dynamic LNG market. The flexible nature of this agreement stems from the structural charasteristic that the contractual provisions, such as the pricing clause and delivery point, are not the part of MSPA but these terms are confirmed in an individual confirmation notices or MoU between parties when the short term opportunity – transaction – appears [8]. Only afterwards MSPA becomes legally binding. Therefore MSPAs enable the LNG players to trade on the spot market. New spot transactions can be made under the exsisting MSPA without a need to negotiate a new agreement [11]. Consequently, Litgas has signed twelve non-binding MSPAs with global suppliers [33]. Under these MSPAs Litgas purchased the commissioning cargo from Statoil which will be delivered on DES basis [33]. Even though DES delivery or FOB are more common in short-term agreements, there is another option for LNG producers – a cost and freight (CFR). Under CFR based agreement the title and risk pass to the buyer in the loading country and the seller is responsible for the delivery of the cargo.

To conclude MSPAs are valuable for its flexibility and its demand continue to increase in the global energy market.

5.1.4. Regional LNG Hub Development

Lithuania aims to develop Klaipeda as a regional LNG hub. Minister of Energy said the country intends to follow the Dutch LNG experience in developing the LNG business in Lithuania and the Baltic region [38]. The Netherlands, one of the country where LNG industry has been developed most in Europe, has agreed to cooperate and share the best practices [39].

5.1.5. FSRU Technology

The LNG terminal Independence is the fifth in the world3 to use FSRU technology [40]. At the 8th European Gas Conference 2015 in Vienna LNG FSRU won the Project of the Year award. Stricter legislation on shipping emissions stimulates the development of FSRUs worldwide. These LNG projects are distinguished by the high environment, health and safety standards [8]. Furthemore, the technology allows the carbon capture and storage (CCS) facilities that is recently of the utmost importance in Norway [8].

5.1.6. Energy Security

Energy security is a key aspect of the new LNG terminal. It brings the competition in the gas market and increases energy security both in Lithuania and the entire Baltic region. “The LNG terminal is a strategic project to improve energy diversity and security of supply,” says Mantas Bartuska, CEO of the Klaipeda Oil, an operator [41].

6. DISCUSSION

Dynamic LNG Market conditions favour the buyers. As reflected in the current LNG contracts a tendency is to decouple the gas prices from the price of oil. So it is unlikely that LNG buyers will sign up to long term oil-indexed contracts. The price formation can help to adjust the contract price to the changing market conditions. Considering the price clause the parties when negiotiating have to consider which pricing mechanism match the market fundamental the most: index pricing, a spot gas index or a hub price.

The diversion rights provision provides more flexibility for buyers and sellers in today’s dynamic LNG market. LNG buyers benefit from diversion of cargoes in two ways. First, diversion rights protect against swings in demand and second, the buyers can make profit from fluctuations in

---

[3] Four terminals are located in Asia: China, Japan, South Korea, Indonesia and one in Europe: Lithuania. “The LNG Industry in 2014“ , GIIGNL. See: http://www.giignl.org/sites/default/files/PUBLIC_AREA/Publications/giignl_2015_annual_report.pdf

spot prices. From the sellers' perspective, the diversion right is not financially beneficial because of the shipping costs unless the profit-sharing mechanisms are applied. It is necessary to consider that the destination clause has an influence on the other provisions such as pricing clause. The diverted cargo impacts the pricing provisions of the contract.

The buyers benefit from diversion rights because provided flexibility helps to manage: inventory, storage constrains, fluctuations in demand within destination markets. In addition to this, due to destination flexibility the buyers can take an advantage of higher prices in the spot market in comparison to ling term contract prices. Therefore, the buyers can take several opportunities for arbitrage. First, in the case of re-export of oversupply, the buyers seek to resell the exceeded demand in the destination market, thereby taking an advantage of the spot market; or in the case of re-export displacements, buyers can re-export LNG received at the original destination to another terminal allowing diversion of LNG to a third destination.

From a seller's perspective, destination restriction clause or diversion rights should be carefully drafted taking into consideration the key aspects:

- Avoiding the risk of enforcement against the seller by a government for inadvertent breaches of trade sanctions arising from a diversion or re-load;
- Restricting or imitating the quantities of LNG that can be diverted;
- Ensuring that profit sharing mechanisms provide adequate certainty on calculation of profits and distribution of proceeds (...);
- Whether any flexibilities should be incorporated for the seller (for example, flexibility to allow the seller to divert deliveries in certain circumstances).

7. CONCLUSIONS

1. The long-term LNG contracts have been evolving since the first one was signed. The terms of the contract are constantly influenced by the market. It has been concluded that today‘s dynamic market calls for the new generation of LNG contracts.

2. The dynamic market has a significant impact on the price clause. It has been concluded that the contract price is not regulated by law. The price clause is determined by the market value principle. Nethertheless, the parties are able to adapt to the market by the means of flexibility, specifically, by drafting the price formula. The most beneficial formulas incorporate a set of indices, a spot element and decouple from the price of oil.

3. The destination flexibility is a new feature of the new generation contracts. The removal of destination restrictions has introduced more flexibility. The diversion clause enables the parties to schedule the cargo to the different LNG markets. The legal changes invoked LNG business activity. Furthermore, an evolving trend towards the single international gas market is recognized. The destination clauses are inconsistent with EU competition law. Thus, the practice of eliminating the destination clauses creates opportunities for delivery flexibility to the parties. Moreover, the diversion clause promotes the development of spot market and hub trading.

4. Finally, having examined the characteristics incorporated in the contract and the LNG tendencies, it has been suggested that the gas contract between Norway and Lithuania could be an example of the new generation LNG contracts. The parties apply the new model MSPA. To conclude, the article demonstrates that the LNG sector is a complex issue inherent from the dynamic market. Nevertheless, the parties are able to address the market volatility within the means of contractual terms. The flexibility embodied in the legal mechanisms, – such as the price formula (which is beyond the price clause), the diversion clause keep them efficient throughout the changing market conditions and shift them to the new contract generation. The LNG environment has rapidly changed giving the rise to adaptation of different LNG models and development of today‘s LNG trends.

REFERENCES

1. The European Commission Energy News. Global Energy Transition is Underway Way – IEA. <https://ec.europa.eu/energy/en/news/global-energy-transition-underway-iea>
2. International Energy Agency. World Energy Outlook 2015. <http://www.worldenergyoutlook.org/weo2015/#d.en.148701>
3. International Energy Agency. Natural Gas.< http://www.iea.org/topics/naturalgas/>
4. The European Commission. Energy Strategy. Secure, competitive, and sustainable energy <https://ec.europa.eu/energy/en/topics/energy-strategy>
5. LNG World News. EU to focus on important LNG infrastructure. <http://www.lngworldnews.com/eu-to-focus-on-important-lng-infrastructure/>
6. DAJANI, E. MONA and DONOGHUE, M. NEIL – BAKER & McKenzie. Protection in a Dynamic LNG Market. *Infrastructure Journal Oil & Gas* (2012).
7. PENWICK, Mark, Stefan WRBKA, ed. *Flexibility in Modern Business Law: A Comparative Assessment*. Japan: Springer, 2016.
8. GRIFFIN Paul, ed. *Liquefied Natural Gas: The Law and Business of LNG*. London: Globe Law And Business, 2012.
9. WEEMS, Philip. Evolution of Long -term LNG Sales Contracts Trends and Issues. *OGEL* 1 (2006).
10. Atlantic Council conference. US LNG Exports and European Energy Security. <http://www.atlanticcouncil.org/events/webcasts/us-lng-exports-and-european-energy-security-conference>
11. BAILY, James and LIDGATE, Rachel. LNG price reviews: a sign of the times. *Journal of World Energy Law and Business* 7 (2014): 140-152.
12. STERN, Jonathan. The Impact of Lower Gas and Oil Prices on Global Gas and LNG Markets. Oxford Institute for Energy Studies (2015). <https://www.oxfordenergy.org/wpcms/wp-content/uploads/2015/07/NG-99.pdf >
13. HARTLEY. The Future of long-term LNG contracts. < http://www.business.uwa.edu.au/__data/assets/pdf_file/0009/2356524/13-22-The-Future-of-Long-term-LNG-Contracts.pdf>
14. JEFFREY M. Petrash. Long-term Natural Gas Contracts: Dead, Dying, or Merely Resting? *Energy Law Journal* 27 (2006): 575-582.
15. CHIAM, Louis and AHUJA, Vishal. Long-term supply contracts – time for review. *AREL Journal* 25 (2006): 149-174.
16. STERN, P. Jonathan (Oxford Institute for Energy Studies and University of Dundee). Is there a rationale for the continuing link to oil product prices in continental European long-term gas contracts? *International Journal of Energy Sector Management* 3 (2007): 221-239.
17. COGAN, John. Contracting Practices Evolve for New Global LNG Trade. *OGEL* 4 (2006).
18. WOOD, David. Where We Are: Relationships, Contacts Evolve Along Supply Chain. *OGEL* 4 (2006).
19. Incoterms, 2012.
20. SHELDRICK, Aaron. Destination clauses on LNG will soon fade away: gas union president. Reuters. <http://www.reuters.com/article/us-asia-lng-contracts-idUSKBN0LT0YY20150225>
21. STAPCZYNSKI, Stephen. Buyers Market for LNG Turns Tables on Producers Amid Supply Glut. Bloomberg <http://www.bloomberg.com/news/articles/2015-10-05/buyers-market-for-lng-turns-tables-on-producers-amid-supply-glut>

22. S&P Global Platts (Singapore). LNG buyers call for more delivery flexibility to manage supply glut. (2015). <http://www.platts.com/latest-news/natural-gas/singapore/lng-buyers-call-for-more-delivery-flexibility-27817357>
23. World Energy Resources. Unconventional Gas, A Global Phenomenon. *World Energy Council Report* 2016. <https://www.worldenergy.org/wp-content/uploads/2016/02/Unconventional-gas-a-global-phenomenon-World-Energy-Resources_-Full-report-.pdf>
24. ROBERTS, Paul. *Gas and LNG Sales and Transport Agreements*. London: Thomson Reuters, 2014.
25. INCOTERMS, 2000.
26. WAKTARE, Eleonora. Territorial Restrictions and profit sharing mechanisms in the gas sector: Algerian case. *EC Competition Policy Newsletter*, Number 3 (2007):19-21. <http://ec.europa.eu/competition/publications/cpn/2007_3_19.pdf>
27. Secondary Markets for LNG Exports: Legal Implications of „re-loads“ for LNG Sales Agreements, HWL EBSWORTH Lawyers (2014). <http://www.hwlebsworth.com.au/latest-news-a-publications/publications/energy-and-resources/item/1235-secondary-markets-for-lng-exports-legal-implications-of-reloads-for-lng-sales-agreements.html>
28. LNG Master MSPA (2012). See: https://www.aipn.org/mcvisitors.aspx
29. HOVLAND, Kjetil MALKENES. Statoil to Supply Gas to Lithuania in Five-Year Deal. The Wall Street Journal. <http://www.wsj.com/articles/statoil-to-supply-gas-to-lithuania-in-five-year-deal-1408637833>
30. ZVIRBLIS. Future Today in Klaipeda / HighTech LNG Terminal, LinkedIn.
31. Christening of Independence. LNG Terminal News. February 2014. <http://www.oil.lt/fileadmin/user_upload/SGD/Terminalas/Special_edition_Terminalas_EN.pdf
32. Lithuania breaks Gazprom’s monopoly by signing first LNG deal. EurActiv. <http://www.euractiv.com/section/energy/news/lithuania-breaks-gazprom-s-monopoly-by-signing-first-lng-deal/>
33. LITGAS contract with Statoil will help to ensure operations of the LNG terminal and to develop new activities, UAB LITGAS. <http://www.litgas.lt/en/litgas-contract-with-statoil-will-help-to-ensure-operations-of-the-lng-terminal-and-to-develop-new-activities/>
34. LNG World News. Lithuania negotiates LNG price cut with Statoil. <http://www.lngworldnews.com/lithuania-negotiates-lng-price-cut-with-statoil/>
35. LNG World News. Lithuania negotiates LNG price cut with Statoil. <http://www.lngworldnews.com/lithuania-negotiates-lng-price-cut-with-statoil/>
36. Klaipeda's LNG reloading station – inked, BTJ. <http://heklalng.com/news/2016/03/10/klaipedas-lng-reloading-station-inked/>
37. LITGAS and Statoil prepare joint venture to enter the Baltic Sea small scale LNG market. LITGAS. <http://www.litgas.lt/en/litgas-and-statoil-prepare-joint-venture-to-enter-the-baltic-sea-small-scale-lng-market/>
38. LNG World News. Lithuania to use Dutch LNG experience. <http://www.lngworldnews.com/lithuania-to-use-dutch-lng-experience/>
39. 1st Lithuanian Netherlands Gas Forum. Netherlands Embassy in Lithuania. <http://lithuania.nlembassy.org/news/2015%5B2%5D/12/1st-lithuanian-netherlands-gas-forum.html>
40. World‘s LNG Liquefaction Plants and Regasification Terminals. Global LNG Limited. April 2016. See: http://www.globallnginfo.com/World%20LNG%20Plants%20&%20Terminals.pdf
41. Klaipeda LNG terminal: Competition adds energy security. Nordic Investment Bank. <http://www.nib.int/news_publications/cases_and_feature_stories/1544/klaipeda_lng_terminal_competition_adds_energy_security>

42. HEUER, Patrick. Crafting Better Price and Price-Renegotiation Clauses to Navigate the Changes in the Atlantic Basin LNG Market. Case study, Externado University of Colombia, 2013.
43. STERN, Jonathan and Rodgers, Howard. The Pricing of Internationally Trading Gas: the search of new fundamentals. Oxford Institute for Energy Studies (2013). <http://eneken.ieej.or.jp/data/4817.pdf>
44. GOTEV, Georgi. Norway overtakes Russia as EU‘s biggest gas supplier. EurActiv. <http://www.euractiv.com/section/energy/news/norway-overtakes-russia-as-eu-s-biggest-gas-supplier/>
45. HAMMER, Ulf and ROGGENKAMP, M. Martha, ed., *European Energy Law Report III.* Anterpen – Oxford: Intersentia, 2006.
46. HARTLEY. The Future of long-term LNG contracts <http://www.business.uwa.edu.au/__data/assets/pdf_file/0009/2356524/13-22-The-Future-of-Long-term-LNG-Contracts.pdf>

CYSENI 2017, May 25-26, Kaunas, Lithuania
ISSN 1822-7554, www.cyseni.com

PROJECTION OF RURAL ELECTRICITY DEMANDS FOR NIGERIA

Paul Bertheau, Philipp Blechinger, Catherina Cader
Reiner Lemoine Institut gGmbH
Ostendstraße 25, 12459 Berlin - Germany
E-mail: paul.bertheau@rl-institut.de

ABSTRACT

Providing reliable access to electricity is a challenge in Nigeria – especially in rural areas - with a national electrification rate of 46 %. For Nigeria to achieve the SDG #7 (Sustainable Development Goals) it is necessary to design economically and environmentally optimized electrification pathways. A main obstacle for a sound planning of electrification interventions including renewable energy solutions is the uncertainty of the expected electricity demands in rural areas. As it is not feasible to conduct demand assessments for a large number of non-electrified and remote villages we have developed a model which projects rural electricity demands based on key socio-economic input parameters.

The approach is comprised of a GIS analysis for deriving input parameters and of a modelling routine for creating rural electricity demand profiles. Initially, socio-economic parameters that determine electricity demands are identified through literature analysis and include the population, economic activity and infrastructure among others. By transforming the quantified socio-economic parameters into electricity demand projections a daily demand profile is synthesized for each village. Subsequently, harvesting periods reflecting increased demands for agricultural appliances and a randomization reflecting the individuality of electricity consumption patterns are incorporated. Lastly, an annual electricity demand profile in hourly increments is derived for each village which serves for assessing the costs of different electrification interventions.

Keywords: rural electrification, electricity demand projection, load profiles, Nigeria, Sub-Saharan Africa

1. INTRODUCTION

Reliable access to electricity still remains a challenge in many regions of Sub-Saharan Africa as well as for many regions of Nigeria [1]. Advancing renewable energy technologies and storage systems open up novel perspectives for decentralized supply structures of electricity. As a consequence, new planning methods are required to account for innovative solutions comparing existing electrification options.

For achieving rapid electricity access conventional options based on central power generation and the extension of large transmission grids need to be reconsidered, taking into account alternative electrification pathways for regions where access to electricity is still lacking or is insufficient [2]. Such alternatives are represented by hybrid mini-grids, which can combine different power generation and storage technologies to efficiently supply local loads [3]. The increased options and complexity of rural electrification underline the need of sophisticated planning tools to determine the techno-economically optimized electrification pathway. This paper presents parts of an approach which enables a comprehensive electrification planning by the use of GIS (geo-information systems) and energy system simulation tools. This approach is applied for five states in Nigeria namely Cross-Rivers, Niger, Ogun, Plateau and Sokoto. To conduct a least-cost comparison of electrification options for each rural village, in the following referred to as consumer cluster, in these five states, it is necessary to assess the energy demand and load profile per consumption point. Given that far more than 7,000 villages/consumer cluster are considered it is not possible to conduct single measurements, therefore it became necessary to develop an automated approach for deriving energy demand values and load profiles from decisive input parameters. This paper presents an approach for a synthetic load projection model for rural areas of Nigeria.

2. METHOLOGY

In order to develop an automated synthetic load projection model, the following approach was applied. Initially, an expert meeting was conducted for defining a basic framework for developing a load projection methodology. Secondly, an extensive literature assessment was conducted and important data reviewed. Subsequently, a load projection methodology was then developed and programmed based on the outcome of the focus working group meeting and findings of the literature and data review. Finally, the developed load projection model was presented and put into discussion during a workshop with stakeholder committed to rural electrification in Abuja (capital of Nigeria). The feedback received was incorporated into the final version of the load projection model.

2.1. Literature review

2.1.1. Load profile

In terms of load profiles for rural communities, few sources are available for Nigeria. In 2015 Olatomiwa estimated load profiles for villages in six geo-politic zones of Nigeria [4]. These load profiles were synthesized by specifying typical daily data. The researchers distinguished between household (HH) and social loads and wet and dry season. For the household profile a typical evening peak is observable which is characteristic for rural load profiles. Social loads have a higher demand during the day as appliances are used for businesses and services. A similar load profile for households in Northern Nigeria was identified by Ogbanna in 2011 [5]. This particular energy demand survey was conducted mainly in Jos, Plateau which included customers of different income level. The identified load profile shows three distinct peaks during morning (8 am), midday (2 to 3 pm) and evening (8 pm). The load peaks are explained by water heating demands, cooking energy demand and the need for lighting (morning), demand for cooking of lunch (midday) and lighting, cooking, brown goods demand (evening). These findings provide valuable information for further approach. As the assessment was conducted in urban and peri-urban regions some likely differences to rural communities can be worked out: The midday peak is declared to stem from cooking appliance. As most rural households are likely to rely largely on biomass for cooking, we can assume that such a midday peak plays a minor role for the load profiles of the considered consumer clusters. Further information on household electricity demand in Nigeria was collected through a UNDP study for six geopolitical zones (GZ) were the consumption of appliances was measured [6]. The collected data confirms the finding that household consumption profiles are usually characterized by peak demands in the evening hours. It is quite essential to keep in mind that these data was collected for urban areas whereas the majority of the consumer clusters in this study are rural settlements. Therefore, it is only partly possible to draw conclusions from the findings. Especially, high base loads during the night hours (12 pm to 6 am) which reflect demand from ACs and cold storages and will most likely not appear in rural villages due to the absence of these appliances.

2.1.2. Energy demand

Despite the load profiles, it is important to assess whether average energy demand values are provided per capita or per household. Generally, it can be stated that energy demand values for rural communities of Nigeria are hardly published. Nevertheless all values provided in the scientific literature are listed in Table 1. None of the values presented are based on measurements and are derived from assessments of appliances used. The results show a widespread estimation of energy demand values ranging from 4.5 kWh/d to 76 kWh/d per household. These values are taken into account as an orientation, but due to the large range final values were determined after consultation with local experts and stakeholders in Abuja (presented in Table 5).

Table 1. Finding for electricity demand values

Source	**Year**	**State**	**Demand per capita (kWh/d)**	**Demand per household (kWh/d)**
[7]	2001	GZ South-West	2.3 (grid electrified) 1.58 (not electrified)	–
[5]	2011	Plateau	–	12.9
[8]	2011	Ilorin	1.45	–
[6]	2013	6 GZ	–	10.1 (average)
[9]	2015	Taraba & Yobe	–	5.38 (4.5 household use, 0.78 productive use)
[4]	2015	6 GZ	–	76 (household) 15 (social facility)

2.2. Development of load projection model

The developed load projection methodology is programmed as a mathematical function in Python [10] and based on five steps: First, specific information per consumer cluster is derived and gathered in an input datasheet. Second, a daily load curve is synthesized based on demographic and infrastructure data for each cluster. Third, a seasonal load profile is incorporated reflecting increased electricity demands mainly for agricultural appliances. Fourth, each of the hourly values in the projected load curve is modified according to random values within a predefined range. Fifth, the load profile is rescaled according to the initial overall demand value prior to the randomization of values. Finally, a load curve is derived for each consumer cluster.

2.2.1. Cluster information

Prior to applying the load projection model, it is necessary to collect site-specific information per consumer cluster in order to reflect the different energy demands. In an earlier study consumer clusters were identified and its status of electrification was determined [11]. The resulting data from this base dataset for the load projection provides information on the location (state, LGA (Local Government Areas), coordinates) as well as population. This information is extended by number of households, economic activity (GDP per capita), educational facilities (schools), health facilities (clinics, health stations, dispensaries etc.) and water supply facilities in place. Thus, key parameters for conducting a synthetic load projection are derived.

Firstly, the number of households per consumer cluster is calculated based on the overall population number. This is necessary because households are most likely to share electric appliances (light bulbs, fans, refrigerators etc.) and therefore a typical electricity demand will be applied on household level. Average household size statistics from the Nigerian National Bureau of Statistics (NBS) are applied [12]. By dividing the population by the average household size of the corresponding state the number of households per cluster is derived.

Secondly, the economic activity (in terms of USD generated) is calculated per consumer cluster. Studies have revealed that energy consumption is significantly linked to economic activity (GDP). These findings have been confirmed for Nigeria [13]. Therefore a dataset providing the economic activity in USD values per square kilometre is applied [14] and the overall sum of USD generated within the extent of consumer cluster is summed up. Subsequently, this value is divided by the population number per consumer cluster to build the GDP per capita. This value allows for scaling the overall electricity consumption according to the existing economic activity.

Thirdly, the quantity of educational, health and water supply facilities is determined per consumer cluster. Thereby the electricity demand apart from households and economic activity is reflected. The quantities are determined by applying the NMIS dataset on educational, health and water supply facilities and the consumer cluster dataset via a GIS analysis in which the number of facilities per consumer clusters are counted [15]. Finally, the exact number of facilities is determined per consumer clusters (Table 2). Heath facilities are distinguished in large consumers (hospitals & clinics) and small consumers (dispensaries, health posts, health stations) reflecting the spread in electricity demands of large health facilities and small ones.

Table 2. Results from data gathering for consumer cluster.

Avg. HH size (#)	**Md. HH size (#)**	**Avg. GDP per capita (USD)**	**Md. GDP per capita (USD)**	**Schools (#)**	**Water pumps (#)**	**Health large (#)**	**Health small (#)**
253	109	6,234	333	9,102	576	732	2,417

2.2.2. *Daily load curve*

The load projection model includes individual load curves for the following categories: Households (low, middle, high consumption), commercial use, productive use, schools, water pumps, agricultural appliances (mills) and health facilities (large consumers and small consumers). Load profiles were elaborated based on information from literature and recommendations of experts. In Fig. 1 the applied load profiles are presented in percentwise consumption per hour. In top left household profiles distinguished in low, medium and high consumption are presented. As electricity is mainly consumed for lightning purposes in rural Nigeria peak demands are after sunset and before sunrise. The household consumption groups depend on the wealth of a single household and differ in their load factors. Whereas low consumption households only apply light bulbs during

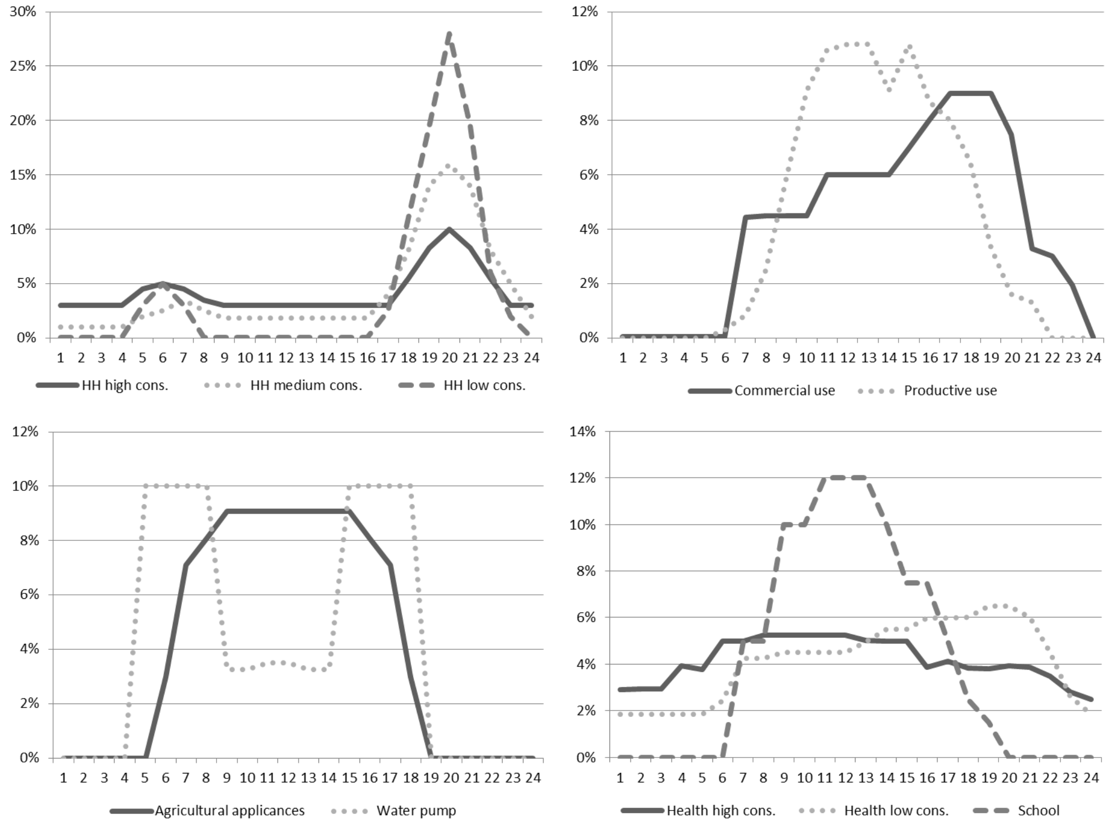

Fig. 1. Daily load profiles in percentwise consumption per hour applied for the different categories

certain periods of the day; medium and high consumption households possess more appliances (television, radio, etc.) which increase the baseload during daytime. Top right illustrates the elaborated load profiles for commercial and productive users. Generally both require electricity for powering appliances during working hours. Productive loads (welder, carpenter, ice factory) peak during noon and afternoon as appliances are operated mainly during daytime. Commercial loads instead (grocery, barber shop, appliance store) peak in the evening hours reflecting higher loads for lighting as these places additionally serve as local meeting points. Bottom left highlights the load curve of water pumps which are applied in the morning and evening hours and agricultural appliances (e.g. mills) which are operated during the day. Bottom right presents load curves of health facilities (high and low consumption) and schools. Health facilities with high consumption reflect rural hospitals with a basic medical infrastructure (e.g. fridges, sterilizers, x-ray machines) characterized by a high baseload and low load factor. Contrasted by that rural health stations (health facilities low consumption) are comprised of few equipment basically fridges and light appliances. Therefore demand peaks in the evening hours. Schools can comprise few electric appliances including ventilators, audio devices and computers for which power is needed during school lessons.

All elaborated load profiles were presented, discussed and approved by experts during the workshop in Abuja. As a result of the previous steps for each of these categories, a specific quantity is known per consumer cluster. Finally, the quantity per category is multiplied with the respective electricity consumption value and distributed over the predefined load profile.

2.2.3. Seasonal load curve

Incorporating a seasonal load curve reflects the increased electricity demand during harvesting periods. The specific seasonal demand is projected according to the expected number of agricultural appliances per consumer cluster. Therefore, a ratio of households to agricultural appliances is defined in order to derive the quantity of appliances. The specific demand per cluster is derived by multiplying the quantity of appliances over a default electricity consumption value and distributing this value over a typical load profile.

Due to the diverse climate zones, landscapes, agricultural productivities and seasons the electricity demands for agricultural appliances (e.g. mill, grinder) differ throughout Nigeria. Generally, two seasonal calendars can be differentiated: A northern seasonal crop calendar (Niger, Plateau, Sokoto) and a southern seasonal crop calendar (Cross Rivers, Ogun). For both seasonal regions a constant electricity demand for agricultural appliances exists as crops are rather stored and processed piecewise as processed at once. The agricultural productivity is higher in the southern regions. This is reflected by an overall higher electricity demand compared to northern regions (see Fig. 2). As agricultural appliances are not operated during the entire day, but rather switched on- and off frequently the overall electricity demand from agricultural appliances is scaled down according to percentage values per month. Finally, the seasonal load curve is added to the annual load curve per consumer cluster derived from the daily load curves.

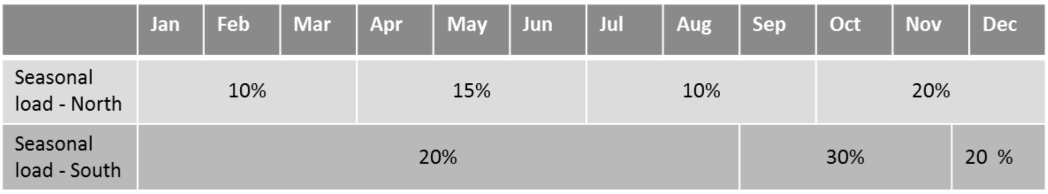

	Jan	Feb	Mar	Apr	May	Jun	Jul	Aug	Sep	Oct	Nov	Dec
Seasonal load - North	10%			15%			10%			20%		
Seasonal load - South	20%								30%			20 %

Fig. 2. Seasonal increased demand from agricultural appliances

2.2.4. *Random variability amd rescaling of loads*

Electricity demand differs from hour-to-hour and day-to-day although typical electricity consumption patterns can be observed throughout consumer groups and seasons. To reflect for this uncertainty a variability factor was included in this load projection model. This variability factor is applied for each hour (e.g. variation from hour-to-hour) and for each day (e.g. variation from day-to-day). Within our load projection model an hourly (8760 values) and daily (365 values) variability value is randomly assigned from a normal gauss distribution with a mean of zero and a standard deviation equal to the "daily variability" or “hourly variability” input value. Subsequently, the variability values are multiplied with the demand value per hour. Finally, the entire year load is rescaled to the overall value before randomization. The overall approach is illustrated in Fig. 3.

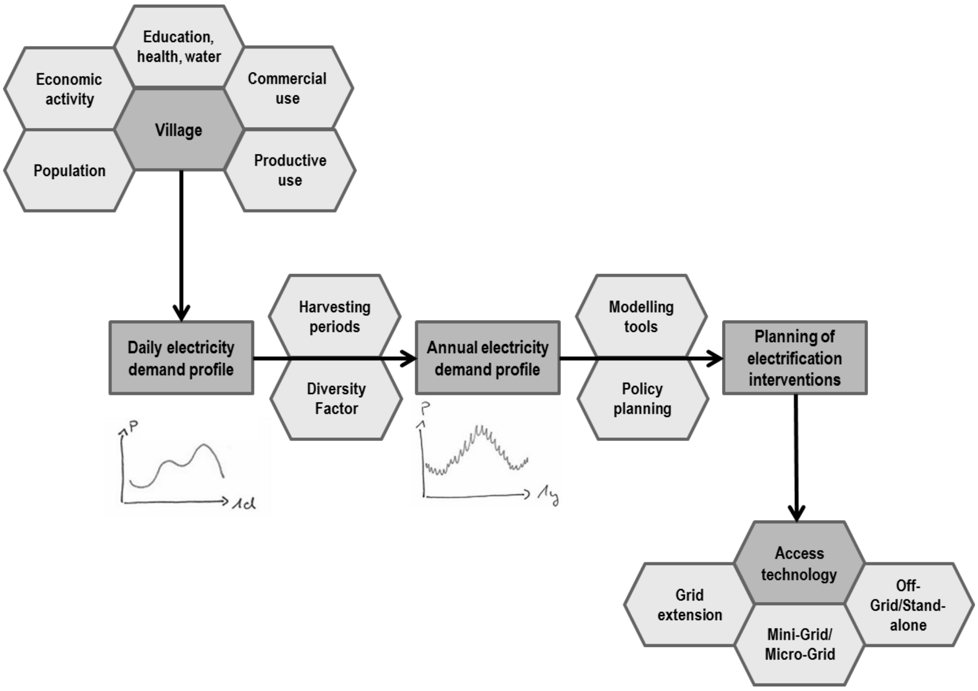

Fig. 3. Scheme of overall load projection and electrification method approach.

3. MODEL ASSUMPTIONS

The load projection model is based on different input datasets: Input parameters, quantities per categories, energy demand values per categories and load profiles per categories. The values applied are based on literature, technical reports from the development aid community and recommendations of experts. Finally the applied values were discussed and adapted according to feedback provided by local stakeholders during a workshop in Nigeria. The different datasets are described in the following sections.

3.1. Input parameters

A number of input parameters allows for scaling the quantity of customer categories. This includes a household connection share which reflects that total electrification of rural villages is rare. Due to the absence of quantitative information on commercial, productive units and agricultural appliances these quantities are derived from a ratio to the overall number of households. To include a random variability as described in methodology section, it is necessary to provide a value in what range random values are derived. All applied values are listed in Table 3.

Table 3. Results from data gathering for consumer cluster

Input value	Value	Description
Share of households connected	80%	Connection rate per consumer cluster. Value is applied for households with low consumption only
Commercial unit per households	1 unit per 10 households	Value derives the number of commercial units from number of households
Productive unit per households	1 unit per 50 households	Value derives the number of productive units from number of households
Agricultural appliance per households	1 unit per 20 households	Value derives the number of agricultural units from number of households
Day-to-day variability	10%	Provided the range for selection of random values per day
Hour-to-hour variability	10%	Provided the range for selection of random values per hour

To reflect the heterogeneity in economic wealth of the consumer clusters, GDP generation was considered in the load projection model. This was conducted by assigning three different thresholds for GDP per capita and year (GDP/capita). The first threshold with an average GDP/capita below 693.5 USD (reflecting the poverty line of 1.9 USD per day), the second threshold with an average GDP/capita below 3,005.5 USD (reflecting the average Nigerian GDP per capita) and the third threshold with an average GDP/capita above 3,005.5 USD. As energy demand rises with economic activity this classification is used for scaling the share of the different household categories and commercial/productive units in order to reflect higher energy demands in wealthier consumer clusters. All discussed values are listed in Table 4.

Table 4. Results from data gathering for consumer cluster.

Input parameter	GDP/capita below 693.5 USD	GDP/capita below 3005.5 USD	GDP/capita above 3005.5 USD
Economic classification	1	2	3
Share of HH low consumption	75%	60%	45%
Share of HH mid. consumption	20%	30%	35%
Share of HH high consumption	5%	10%	20%
Scale value for commer. units	Base value	Base value x 1.2	Base value x 1.5
Scale value for prod. units	Base value	Base value x 1.2	Base value x 1.5

The quantities for household, commercial and productive consumer per cluster are derived according to the parameters presented above. Household quantities are derived from the population number and scaled according to the GDP generation. Afterwards the commercial and productive (including agricultural appliances) quantities are derived from the number of households and scaled according to GDP generation. Contrasted to that the quantities for schools, water pumps, health facilities are site specific and directly derived from datasets. Finally, for each category electricity demand values per day are determined in order to compute the overall electricity demand per category. The values applief per category are listed in Table 5.

Table 5. Electricity demand values applied per category

Category	Electricity demand (kWh/d)	Category	Electricity demand (kWh/d)
Households low consumption	0.74	Schools	3
Households middle consumption	2.35	Water pumps	1
Households high consumption	5.38	Health low consumption	15
Commercial use	3	Health high consumption	150
Productive use	12	Agricultural appliances	5

4. PRELIMINARY RESULTS

4.1. Application of load projection model and results

By applying the elaborated preliminary load projection model for each consumer cluster a randomized load profile (8760 values) reflecting one year comprised of the site specific demand is created. This profile can serve as one of the input datasets for the cost assessment of electrification options. For a total of 7,636 non-electrified villages with a population of 9.8 million we have identified an overall peak demand of 536 MW and energy consumption of 1,202 GWh for these consumers under the current socio-economic conditions (compare Table 6). The results have to be considered as preliminary due to the high uncertainty of input parameters. At the moment it is not possible to evaluate the results due to the lack of comparable data. With further research and efforts in the field of rural electrification such data might be available and will be used for comparison.

Table 6. Results of load projection of rural electricity demand

State	**Villages**	**Rural population (in million)**	**Peak demand (sum in MW)**	**Energy consumption (sum in GWh)**
Cross River	650	1.06	81.5	177
Niger	2,620	2.44	113.6	261
Ogun	1,080	1.06	52.1	119
Plateau	1,808	2.40	120.8	273
Sokoto	1,478	2.90	168.1	371
Total	**7,636**	**9.86**	**536.3**	**1,202**

5. DISCUSSION & CONCLUSION

With this study we present a novel approach for projecting rural electricity demands based on commonly available demographic and socio-economic input parameters. Reliable projections of rural electricity demands are of high importance for the planning of sustainable electrification strategies in developing countries.

For the Nigerian case the results highlight the importance for neatly assessing potential rural electricity demands: For five states with a rural population of approx. 5% of the overall Nigerian population we have projected an electricity peak demand of more than 530 MW and an annual energy consumption of more than 1,200 GWh. To supply these demands will be a huge challenge for the country especially when keeping in mind that the national operational power capacity is currently approx. 4 GW and that Nigeria is comprised of 36 federal states.

The developed load projection model is capable of assessing site specific rural electricity demands but it has several major limitations at the moment. Generally, a projection model can only partly reflect reality. This becomes especially true when taking into account individual behavioural and consumption patterns, which is necessary when projecting electricity demands. In this early stage of development our developed model mainly builds on the relation between economic activity and energy consumption. The overall research field of energy consumption, society and individual consumption in the context of developing countries offers a huge space for further investigation. As a first step it would be beneficial to evaluate the results of this study for individual consumer clusters with real world measured data. As the elaborated model is very sensitive to the input parameters it is essential to increase efforts for collecting reliable and high quality input parameter. Additionally further aspects affecting the electricity demand of rural communities such as cultural or social drivers could be incorporated in the load projection model.

ACKNOWLEDGEMENT

This work partly results from the authors' collaboration with the Nigerian Energy Support Programme (NESP) implemented by the Deutsche Gesellschaft für Internationale Zusammenarbeit (GIZ) GmbH in collaboration with Federal Ministry of Power, Nigeria and funded by the German Government and the European Union. The authors gratefully acknowledge the support from GIZ-NESP and Nigerian FMP. Any conclusions or recommendations expressed in this article do not necessarily reflect the views of GIZ-NESP or FMP.

REFERENCES

1. OHIARE, S. Expanding electricity access to all in Nigeria: a spatial planning and cost analysis. *Energy, Sustainability and Society*, 2015, Vol. 5, No. 1.
2. ZEYRINGER, M., PACHAURI, S., SCHMID, E., SCHMIDT, J., WORRELL, E., MORAWETZ, U.B. Analyzing grid extension and stand-alone photovoltaic systems for the cost-effective electrification of Kenya. *Energy for Sustainable Development*, 2015, Vol. 25, pp. 75–86.
3. IRENA [INTERNATIONAL RENEWABLE ENERGY AGENCY]. Battery storage for renewables: Market status and technology outlook. *Retrieved from http://www.irena.org/documentdownloads/publications/irena_battery_storage_report_2015.pdf*
4. OLATOMIWA, L., MEKHILEF, S., HUDA, A., OHUNAKIN, O. S. Economic evaluation of hybrid energy systems for rural electrification in six geo-political zones of Nigeria. *Renewable Energy*, 2015, Vol. 83, pp. 435–446.
5. OGBONNA, A.C., ONAZI, O., DANTONG, J.S. Domestic energy consumption patterns in a Sub Saharan African City: the study of Jos-Nigeria. *Journal of Environment Science and Resource Management*, 2011; Vol. 3, pp. 48–62.
6. ENERTECH 2013. End-use Metering Campaign for Residential Houses in Nigeria. Metering Campaign Report. DRAFT VERSION, Energy Commission of Nigeria, Federal Ministry of Environment, commissioned by United Nations Development Programme supported by Global Environment Facility. Retrieved the 9th September 2015 from http://www.undp.org/content/dam/nigeria/docs/Sustainable%20Development/UNDP_NG_sustaindev_Metering_Campaign.pdf
7. ADEOTI, O., OYEWOLE, B.A., ADEGBOYEGA, T.A. Solar photovoltaic-based home electrification system for rural development in Nigeria: domestic load assessment. *Renewable Energy*, 2001, Vol. 24, pp. 155–161.
8. AJAO, K.R., OLADOSU O.A., POPOOLA O.T. Using homer power optimization software for cost benefit analysis of hybrid-solar power generation relative to utility cost in Nigeria. *International Journal of Research and Reviews in Applied Sciences*, 2011, Vol. 7, pp. 96–102.
9. AKPAN, U. Technology options for increasing electricity access in areas with low electricity access rate in Nigeria. *Socio-Economic Planning Sciences*, 2015, Vol.51, pp.1–-12.
10. PYTHON CORE TEAM. Python: A dynamic, open source programming language. Python Software Foundation. 2015, URL https://www.python.org/.
11. BERTHEAU, P., CADER, C., BLECHINGER, P. Electrification Modelling for Nigeria, *Energy Procedia*, Volume 93, August 2016, Pages 108-112.
12. NBS 2012 – National Bureau of Statistics – Nigeria General Household Survey Basic Information Document. *Received personally*.
13. TRACTEBEL ENGINEERING SUEZ. 2009 - National Load Demand Study National Energy Development project Draft Final Report - Volume 1 - National Load Demand Forecast.
14. GHOSH, T., POWELL, R., ELVIDGE, C. D., BAUGH, K. E., SUTTON, P. C., ANDERSON, S. Shedding light on the global distribution of economic activity. *The Open Geography Journal*, 2010, Vol. 3, pp. 148–161.
15. NMIS – Nigeria MDG Information System. 2015. Datasets retrieved from http://nmis.mdgs.gov.ng/.